Metal-Organic Frameworks: Concepts from Glass Science and High-Pressure Behavior

Dissertation

Pascal Kolodzeiski

August 2025

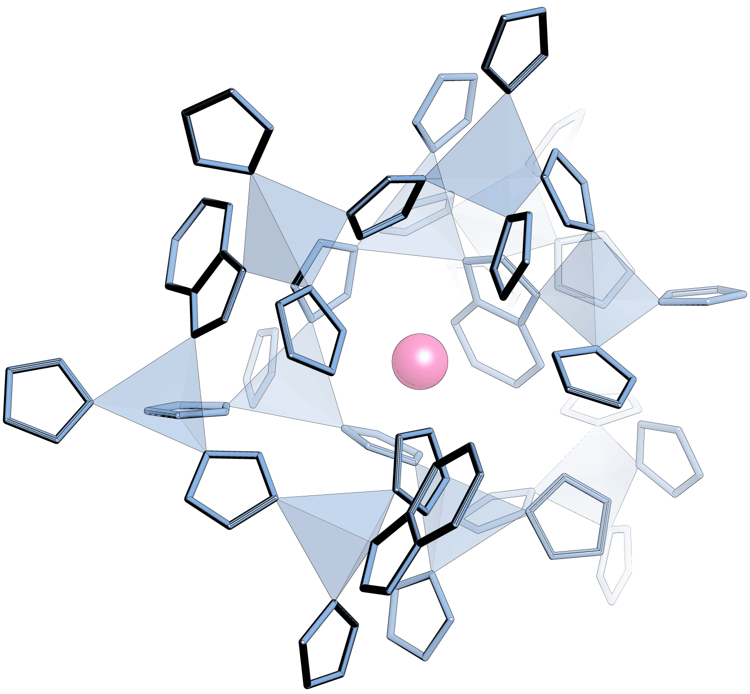

Technische Universität Dortmund

Metal-Organic Frameworks: Concepts from Glass Science and High-Pressure Behavior

Faculty of Chemistry and Chemical Biology
Technische Universität Dortmund

The present work was conducted from September 2020 to August 2025 in the Department of Inorganic Chemistry, Faculty of Chemistry and Chemical Biology, at TU Dortmund University.

Note on the Use of AI Tools

AI-based tools (e.g., ChatGPT, DeepL, Grammarly) were used to support the linguistic revision of certain sections of this thesis. Their use was limited to improving style and grammar, without altering or generating any substantive content. Full responsibility for the content, structure, and academic integrity of this work lies solely with the author.

1. Examiner : Prof. Dr. Sebastian Henke
2. Examiner : apl. Prof. Dr. Claus Czeslik

Date of submission: 28 August 2025

Keep swimming!

And when life gets tough – What will we do?

We'll swim!

– *inspired by a blue surgeonfish*

I would like to express my profound gratitude to *Prof. Dr. Sebastian Henke* for allowing me to work on this exciting research topic, for his excellent mentorship, continuous support, and unwavering motivation throughout this project, including the valuable experiences I gained from visiting and presenting at many international conferences.

I would like to sincerely thank Prof. Dr. Claus Czeslik for kindly agreeing to serve as the second reviewer of this dissertation.

Furthermore, I would like to warmly thank all current and former members of the *Henke Group* for creating a constructive and friendly work environment, for the enjoyable group events, regular synchrotron visits, conference trips, and the joyful lunch and coffee breaks: Jannik Engel, Leandro Straeter, Dr. Zeyu Fan, Nuttaporn Krittametaporn, Tim Krokowski, Guoquiang Li, Christian Nelle, Giulia Rosano, Dagmar Schürmann, Kai Terlinden, Jan-Benedikt Weiß, Fabian Niefer, Katrin Vollmari, as well as Dr. Roman Pallach, Dr. Wen-Long Xue, Dr. Athanasios Koutsianos, Dr. Chinmoy Das, Dr. Jianbo Song, Dr. Louis Frentzel-Beyme, Lennard Richter, and Michael Strobl.

In particular, I would like to thank Jan and Kai for many fruitful and heartwarming discussions about science and other closely related topics, as well as Lennard Richter for enriching the constructive atmosphere in our office.

I would also like to thank all those who have contributed to this project as students, interns, or colleagues: Michael Strobl, Lennard Richter, Dagmar Schürmann, and Jan Philip Schulte.

I would also like to express my gratitude to Jannik Engel, Jana Nolte, Astrid Riedel, Peggy Sieg, Birgit Thormann, Dr. Benjamin Hupp, Dr. Gabriele Trötscher-Kaus, and Dr. Christina Krabbe for their support with everyday problems, organizing internships, and assistance with administrative matters.

Furthermore, I would like to thank all the beamline scientists for their invaluable support during the beamtime: Dr. Christian Sternemann and Dr. Michael Paulus (DELTA, Dortmund), Dr. Volodymyr Baran, Dr. Alexander Schökel, and Dr. Alba San José Méndez (DESY, Hamburg), as well as Dr. Phil Chater and colleagues (DLS, Oxfordshire).

I also thank the group of Prof. Clever for access to their glovebox, and especially Simon Kotnig for maintenance and technical support.

I am deeply grateful to all the friends I met along the way. My heartfelt thanks go to my best friend Annika for her unwavering support during difficult times and for the many meaningful moments we have shared over the years. I would also like to thank my school friends Lina, Kristina, and Milena, as well as those I met during my studies – Kevin, Jelena, Dörte, and Christian – and those I met along the way: Frauke, Tim, and Maria.

Finally – and above all – I would like to thank my beloved family for their tremendous and tireless support throughout my studies and my entire life. I am deeply grateful to my sister and collaborator, Dr. Elena Kolodzeiski, and, of course, to my parents for their unwavering encouragement. Without your trust and unconditional support, this work would not have been possible.

Meiner Familie.

Abstract

Metal-organic frameworks (MOFs) are an emerging class of hybrid functional materials with proposed applications in industrial processes, such as catalysis and gas separation, as well as in environmental technologies, including carbon capture. For practical use, MOFs must be immobilized—typically as pellets via high-pressure pelletization or as glass membranes manufactured through high-temperature melt-casting. Controlling their structural properties and response to these processing conditions is crucial for successful large-scale implementation. In this context, this work addresses two key aspects of MOF immobilization: The modification of MOF glasses to tailor material properties (Part I), and the investigation of high-pressure structural responses in another family of MOFs (Part II).

The number of meltable and glass-forming MOFs is currently largely limited to the subfamily of zeolitic imidazolate frameworks (ZIFs), restricting the accessible structural and chemical space. In contrast, silicate glasses—though based on a single glass former (SiO_2)—are ubiquitous in today's world due to their tunable properties, enabled by the systematic incorporation of glass modifiers (e.g., metal oxides). In this work, the concept of traditional silicate glass modification is transferred to a prototypical MOF glass former by introducing alkali modifiers across a broad compositional range to mimic silicate glass chemistry and investigate resulting trends in thermal and structural properties. The modified MOF glasses parallel the trends of corresponding silicate glass systems, such as a modifier-induced decrease in the glass transition temperature, amongst others. Advanced structural analysis provides insights into local structural changes upon alkali incorporation, pushing the boundaries of current understanding and extending even into the field of silicate glass chemistry. Selective removal of the modifiers via water leaching demonstrates that this approach not only expands the chemical versatility of MOF glasses but also generates additional porosity, providing a powerful toolbox for systematic material design. This work thereby broadens the chemical landscape of MOF glasses and supports their future application as membrane materials.

Due to their structural and chemical diversity, MOFs exhibit a wide range of structural responses, not only at high temperatures but also under high pressures. Such high-pressure conditions are encountered frequently during pelletization and can arise under catalytic reaction conditions. In this work, the high-pressure response (up to 4000 bar) of a series of closely related MOFs is investigated, with particular focus on the role of the metal ion and organic linker. The findings provide insight into the structural origins of mechanical behavior under pressure and highlight how the structure and composition influence the material's compressibility and mechanical stability. These results lay the groundwork for future implementation of MOFs in high-pressure industrial applications.

Kurzfassung

Metallorganische Gerüstverbindungen (engl.: Metal-organic frameworks, MOFs) stellen eine Klasse hybrider Funktionsmaterialien dar, deren potenzielle Anwendungen von industriellen Prozessen wie Katalyse und Gastrennung bis hin zu umwelttechnologischen Anwendungen wie der CO_2-Speicherung reichen. Für den praktischen Einsatz müssen MOFs immobilisiert werden – typischerweise entweder in Form von Pellets durch Hochdruckverpressung oder als Glasmembranen mittels Hochtemperatur-Schmelzgießen. Die Kontrolle der strukturellen Eigenschaften und des Verhaltens unter diesen Verarbeitungsbedingungen ist entscheidend für die erfolgreiche Anwendung im großtechnischen Maßstab. Vor diesem Hintergrund befasst sich die vorliegende Arbeit mit zwei zentralen Aspekten der MOF-Immobilisierung: Die Modifikation von MOF-Gläsern zur gezielten Einstellung ihrer Materialeigenschaften (Teil I) sowie mit der Untersuchung des strukturellen Verhaltens einer weiteren MOF-Familie unter Hochdruck (Teil II).

Die Zahl schmelzbarer und glasbildender MOFs ist derzeit größtenteils auf die Subfamilie der zeolitischen Imidazolat-Gerüstverbindungen (engl.: Zeolitic Imidazolate Frameworks, ZIFs) beschränkt, was den strukturell-chemischen Gestaltungsspielraum limitiert. Silikatgläser hingegen – obwohl sie auf einem einzigen Glasbildner (SiO_2) basieren – sind allgegenwärtig und zeichnen sich durch eine breite Palette einstellbarer Eigenschaften aus, die durch die systematische Zugabe von Glasmodifikatoren (z.B. Metalloxide) ermöglicht wird. In dieser Arbeit wird das Konzept der klassischen Silikatglasmodifikation auf einen prototypischen MOF-Glas-Bildner übertragen. Dazu werden Alkali-Modifikatoren über einen weiten Konzentrationsbereich zugesetzt, um Prinzipien der Silikatglaschemie zu imitieren und die Auswirkungen auf thermische und strukturelle Eigenschaften zu untersuchen. Die modifizierten MOF-Gläser zeigen ähnliche Trends wie entsprechende Silikatglassysteme, etwa eine durch Modifikatoren verursachte Absenkung der Glasübergangstemperatur. Strukturuntersuchungen liefern Einblicke in lokale Strukturveränderungen infolge der Alkali-Inkorporation die das derzeitige Verständnis erweitern und auch im Kontext der Silikatglaschemie von Bedeutung sind. Die gezielte Entfernung der Modifikatoren durch Auslaugen mit Wasser zeigt zudem, dass dieser Ansatz nicht nur die chemische Vielfalt von MOF-Gläsern erweitert, sondern auch zusätzliche Porosität erzeugt und damit ein vielseitiges Werkzeug für das gezielte Design von porösen Materialien darstellt. Diese Arbeit erweitert somit die chemische Landschaft der MOF-Gläser und ebnet den Weg für deren zukünftige Anwendung als Membranmaterialien.

Aufgrund ihrer strukturellen und chemischen Vielfalt zeigen MOFs ein breites Spektrum an struktureller Responsivität – nicht nur bei hohen Temperaturen, sondern auch unter erhöhtem Druck. Bedingungen hoher Drücke treten häufig während der Verpressung von Pellets auf und können auch unter katalytischen Reaktionsbedingungen entstehen. In dieser Arbeit wird das Hochdruckverhalten (bis zu 4000 bar) einer Reihe strukturell verwandter MOFs untersucht, mit besonderem Fokus auf die Rolle der organischen und anorganische

Baueinheit. Die Ergebnisse liefern Einblicke in die strukturellen Ursprünge des mechanischen Verhaltens unter Druck und zeigen, wie Struktur und Zusammensetzung die Kompressibilität und mechanische Stabilität beeinflussen. Damit schaffen die Ergebnisse eine Grundlage für die zukünftige Integration von MOFs in Hochdruckprozesse in der chemischen Industrie.

Contents

List of Abbreviations

ADP atomic displacement parameter

AIRSS *ab initio* random structure searching

APT atom probe tomography

bdc^{2-} 1,4-benzenedicarboxylate

bim^{-} benzimidazolate

BO bridging oxygen

BMEOS Birch-Murnaghan equation of state

CCDC Cambridge Crystallographic Data Centre

COD Crystallography Open Database

DFT density-functional theory

DMF *N,N*–dimethylformamide

dobdc^{4-} 2,5-dioxido-1,4-benzenedicarboxylate

dobpdc^{4-} 4,4'-dioxido-[1,1'-biphenyl]-3,3'-dicarboxylate

DSC differential scanning calorimetry

EDX energy dispersive X-ray spectroscopy

EFG electric-field gradient

EXAFS extended X-ray absorption fine structure

FSDP first sharp diffraction peak

FWHM full width half maximum

GFA glass-forming ability

GS glass stability

gZIF-4 glass of ZIF-4

gZIF-62 glass of ZIF-62

HPPXRD high-pressure powder X-ray diffraction

im^{-} imidazolate

IR infrared

LFSE ligand field stabilization energy

MAS magic angle spinning

mbim 5-methylbenzimidazolate

mim$^-$ 2-methylimidazolate

mmen *N*,*N*'-dimethylethylenediamine

MOF metal-organic framework

MRO medium-range order

NBO non-bridging oxygen

NMR nuclear magnetic resonance

NTE negative thermal expansion

PEL potential energy landscape

PDF pair distribution function

PTM pressure transmitting medium

PXRD powder X-ray diffraction

RDF radial distribution function

RMSD root mean square deviation

SBU secondary building unit

SCL supercooled liquid

SEM scanning electron microscopy

ss solid-state

STA simultaneous thermogravimetric and differential thermal analysis

STEM scanning transmission electron microscopy

T_d decomposition temperature

TEM transmission electron microscopy

T_f fictive temperature

T_g glass transition temperature

THF tetrahydrofuran

T_m melting temperature

$tpdc^{2-}$ [*p*-terphenyl]-4,4”-dicarboxylate

VT-PXRD variable-temperature powder X-ray diffraction

ZIF zeolitic imidazolate framework

1 Motivation and Project Outline

From established industrial applications such as heterogeneous catalysis in the synthesis of pharmaceuticals and polymers, or gas separation for the purification of base chemicals, to emerging environmental technologies like carbon capture, water harvesting, and gas storage — Metal-organic frameworks (MOFs) are a diverse class of porous coordination polymers that hold great promise due to their tunable chemical composition, structural versatility, and exceptionally high surface areas. MOFs follow a modular building scheme and are built from inorganic building units (metal ions, metal-oxo clusters) which are interconnected by organic linkers (i.e., multidentate ligands). To enable their practical application, MOFs must be immobilized and shaped into solid forms, such as pellets produced under elevated pressure or membranes fabricated by melt-casting. However, these processing steps introduce external stimuli like pressure and temperature, which can induce complex structural responses that affect their functional performance. Understanding the behavior of MOFs under such conditions remains a significant challenge, and further elucidating the underlying structure–property relationships may help to optimize the materials' mechanical and thermal properties alongside their (e.g., catalytic or separative) performance. In pursuit of this overarching goal, two distinct aspects will be addressed in Part I and Part II of this thesis:

Part I: Traditional Modification of Metal-Organic Framework Glasses

So far, a very limited number of MOFs have been found to melt and form glasses. These glass-forming MOFs mostly originate from the subgroup of zeolitic imidazolate frameworks (ZIFs) and gave rise to a new class of glassy materials. The outstanding combination of a partially maintained porosity during melt-quenching, even accessible for larger hydrocarbons, together with the improved processability of the glass state (i.e., by melt-casting), renders them promising for the manufacturing of seamless monolithic membranes, possibly improving gas-separation efficiency.

Silicate glasses, in contrast, have been thoroughly investigated over the centuries of their application. Throughout this time, a conceptual understanding of the (silicate) glass state and the influence of modifiers (e.g., various (alkali) metal oxides) on the structure and resulting material properties has been established. The addition of an alkali oxide, such as Na_2O, for example, was found to interrupt the glass network structure, thereby lowering the average network connectivity, thus affecting the materials' properties (e.g., lowering of the glass transition temperature). The ability to tailor essential material properties — including thermal characteristics, chemical and mechanical robustness, and optical quality — is central to the technological relevance and economic importance of specialized silicate glasses.

Currently, MOF glasses lack this kind of profound conceptual understanding, hampering the systematic development of further MOF glass materials with tunable material properties. Within the scope of Part I, the transferability of these well-established concepts to a prototypical ZIF-glass former is investigated by choosing compatible glass modifiers to mimic concepts of traditional silicate glass modification:

1. **Synthesis and Characterization of Glass Modifiers**
   The prototypical glass former ZIF-62 (chemical composition: $Zn(im)_{1.8}(bim)_{0.2}$, im^-= imidazolate, bim^- = benzimidazolate) is a mixed-linker glass-forming ZIF. To mimic the concept of silicate glass modification, the corresponding lithium and sodium salts of the bim^- linker need to be synthesized and characterized. Here, the following questions arise:
   (a) Synthesis and structural characterization
   How can Na(bim) and Li(bim) be synthesized, and what is the structure of both materials?
   (b) Thermal behavior
   Are the modifiers thermally stable beyond the melting temperature of ZIF-62? How does the structure of both materials behave upon heating? Do Na(bim) and Li(bim) exhibit melting or glass formation themselves?
   (c) Influence of the alkali-cation
   In which way does the alkali-ion influence the structure and thermal behavior of both materials?

2. **Traditional Glass Modification of ZIF-62**
   Here, the modification of the glass-former ZIF-62 with the modifiers Na(bim) and Li(bim) is investigated by preparing a series of physical mixtures of the glass former and the modifier. Subsequently, melt-quenching of the mixtures of the crystalline starting materials is used to prepare modified glasses with various ratios of glass former and modifier. This systematic study is performed to answer the following questions:
   (a) A protocol for the preparation of modified glasses
   How can homogeneous modified glasses be prepared over a wide compositional range?
   (b) Thermal behavior of physical mixtures and glasses
   How does the modifier incorporation influence the materials' (thermal) properties?
   (c) Local structure
   How is the modifier incorporated into the glass network on a structural level?

(d) Modifier leaching
Can the modifier be removed from the modified glass via water leaching, and how does this leaching influence the porosity of the material?

Part II: Understanding the High-Pressure Behavior of MOF-74-Type Materials

MOF-74 (chemical composition: M_2(dobdc), $M^{2+} = Mg^{2+}$, Co^{2+}, Ni^{2+}, Cu^{2+}, Zn^{2+}, dobdc^{4-} = 2,5-dioxido-1,4-benzenedicarboxylate) is a family of metal-organic frameworks featuring hexagonal channels and unsaturated binding sites at the metal ion (i.e., open metal sites). The presence of these hexagonal channels allows for high diffusion rates of guest molecules through the material, while the high density and accessibility of open metal sites are a promising prerequisite for their application in catalysis and guest-adsorption technologies. The structurally closely related, geometrically extended Mg_2(dobpdc) (dobpdc^{4-} = 4,4'-dioxido-[1,1'-biphenyl]-3,3'-dicarboxylate) features an even larger pore volume and has been found to exhibit a step-shaped CO_2 sorption isotherm if loaded with various amines, rendering it promising for application in direct air capture.[1] Understanding the structural response of these materials under elevated pressure is essential for their implementation in gas-capture and catalytic applications, where such conditions typically occur either during pelletization and immobilization or as reaction conditions. Here, the following questions arise:

(a) Structural behavior of MOF-74(M) materials under high pressure
What is the structural response of MOF-74 materials under high pressure? How is the structural response influenced by the incorporated metal ion, its electronic structure, and its coordination geometry?

(c) Influence of the linker and guest loading
How does the application of a geometrical extended linker influence the high-pressure structural response of the resulting MOF-74-type material? How does guest loading alter the structural behavior under these conditions?

The following work provides valuable insights into the topical areas outlined above.

2 Introducing Metal-Organic Frameworks

2.1 A Family of Functional Hybrid Materials

In our modern world, porous materials can be found in numerous industrial applications and domestic products. From porous carbon acting as an absorbent in various medical products[2] or in the purification of H_2 from natural gas,[3] to zeolites, which are widely used as catalysts in the petrochemical industry,[4] or as detergents,[5] to porous polymeric membranes employed in wast water treatment.[6]. In 1995, the first report on another class of porous hybrid materials called metal-organic frameworks (MOFs) was published by O. M. Yaghi, which since then have moved into the center of scientific research.[7,8] MOFs are composed of inorganic building units (e.g. metal-ions, metal-oxo clusters), which are interconnected by organic building units (i.e., multidentate neutral or charged organic ligands, so-called *linkers*) to form a supramolecular network structure.[9] The organic linkers can contain two or more (anionic or neutral charged) functional groups, such as amines or carboxylates, acting as electron pair donors for the coordinative bonding to two or more metal ions (see Figure 2.1). In contrast to other coordination networks, the MOF structure features potential porosity, which is reflected in their definition according to IUPAC:[10]

> "A metal–organic framework, abbreviated to MOF, is a coordination network with organic ligands containing potential voids."

Numerous methods for the synthesis of MOFs are reported. They range from simple precipitation from solution, electro- and mechanochemical approaches, microwave and ultrasonic-assisted synthetic protocols, to the self-assembly of the MOF under solvothermal conditions, which remains one of the most common synthetic approaches.[11] After synthesis, solvent molecules, which template the pores during the self-assembly of the MOF, can be removed in a process called *activation*, providing the activated MOF with vacant pores.[12]

A key characteristic of MOFs is their exceptionally high surface area (up to $9140\,m^2\,g^{-1}$)[13,14] and thermal stability (up to $\sim$600 °C)[15], which has led to growing academic and industrial interest in their use for typical host–guest chemistry applications such as gas storage, separation, catalysis, sensing and many others.[16] In response to the growing demand for MOFs, the first industrial-scale productions have been developed, making MOFs commercially available, such as under the brand name Basolite® by BASF SE.[17] In addition, companies like *framergy*, *NUMAT*, and *novoMOF* have emerged, specialising in the application of MOFs in various commercial products such as for (gas) purification, chemical packaging and protection, as well as CO_2 capture.[18–20]

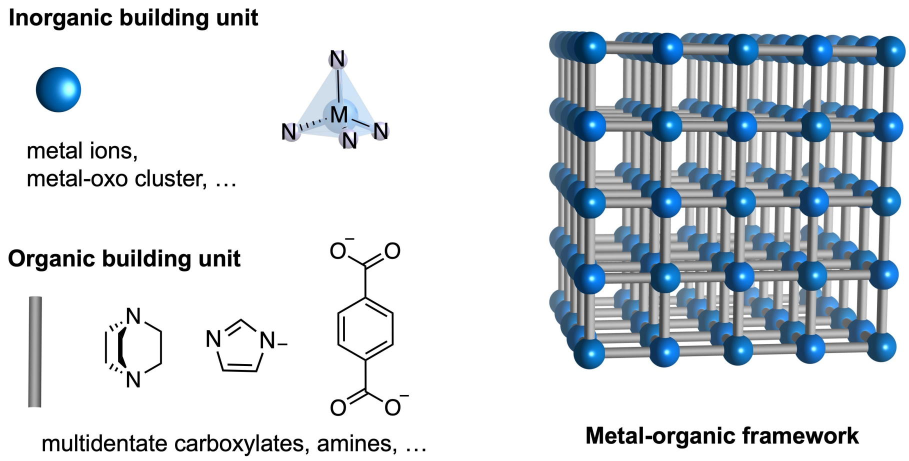

Figure 2.1. Schematic representation of the building scheme of MOFs. Left: Organic and inorganic building units with structural examples for possible nodes and linkers. Right: Structure of the assembled framework.

2.2 The Concept of Reticular Synthesis

The nearly unlimited chemical variation in organic and inorganic building units, combined with the modular building scheme of MOFs, leads to a constantly growing number of new MOF materials. Currently, over 12,505 different porous MOF structures out of more than 100,000 MOF-like frameworks are reported,* covering an immense structural and chemical diversity. The systematic tunability of key material properties such as specific surface area, catalytic activity as well as the thermal, chemical, and mechanical stability is a major advantage that is unprecedented compared to other classes of (conventional) porous materials such as zeolites.[21]

The underlying connectivity of the building units composing the framework is described by the network's *topology*.† The topology depends on the coordination geometry of the metal ions or metal-oxo-cluster, the number and orientation of donor groups in the organic building unit as well as the interconnection of the same. The prediction of network topologies is facilitated by the concept of *reticular synthesis*.[22] This concept is based on the reduction of the inorganic and organic building unit to geometrical descriptors, so-called secondary building units (SBUs), which represent the linkers and metal-nodes underlying geometry. An overview of selected organic and inorganic building units and the corresponding SBUs is depicted in Figure 2.2.

Accordingly, the formal substitution of the metal ion by another metal ion featuring similar coordination geometry and size (i.e both metal ions are represented by the same

*According to the number of crystal structures categorized as MOFs in the Cambridge Crystallographic Data Center (CCDC), `https://www.ccdc.cam.ac.uk/`.

†Network topologies are denoted with three-letter codes (such as **dia** for diamond topology). An overview of framework nets and topologies can be found in the Reticular Chemistry Structure Resource (`https://rcsr.anu.edu.au/`).

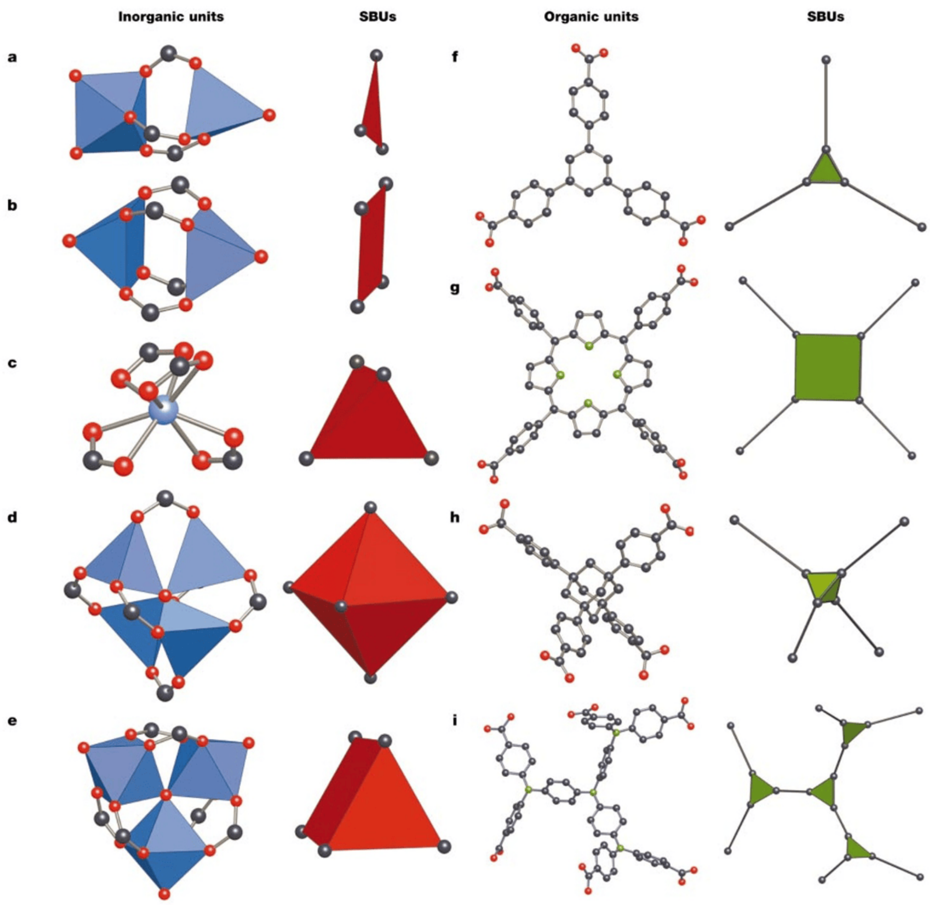

Figure 2.2. Structural examples for organic and inorganic building units with the corresponding SBUs assigned based on their geometry. Color code: Metal ions (blue), O (red), C (black). The metal ions' coordination environments are shown as blue polyhedra. Red and green polyhedra illustrate the SBU's geometry. From reference[22] and reproduced with permission from Springer Nature.

SBU) in a given MOF structure can result in a new MOF with identical topology. These MOFs are then called *isoreticular*.[22] Similarly, the exchange of the linker by a structurally modified (e.g. geometrically extended) analogue is anticipated to result in an isoreticular extended MOF, given that both linkers share the same SBU (see Figure 2.3).[23]

In the case of MOF-5 (chemical composition: $Zn_4O(bdc)_3$), the formal substitution of the bdc^{2-} linker by $tpdc^{2-}$ in IRMOF-16 results in an increase of the relative free volume from 79% (MOF-5) to 91% (IRMOF-16).[21] The possibility of tailoring of pore size in a micropore (pore diameter < 2 nm) or mesopore (pore diameter: 2 nm – 50 nm) regime as well as controlling the resulting pore volume, surface area and pore aperture size is another major advantage compared to traditional porous materials.[24] Today, many literature-known examples of isoreticular extended MOFs exist. Many of these studies focus on the manipulation of host-guest interactions to improve the materials' performance in guest transport (e.g., gas sorption, separation) or conversion (e.g., catalysis) processes.[25,26]

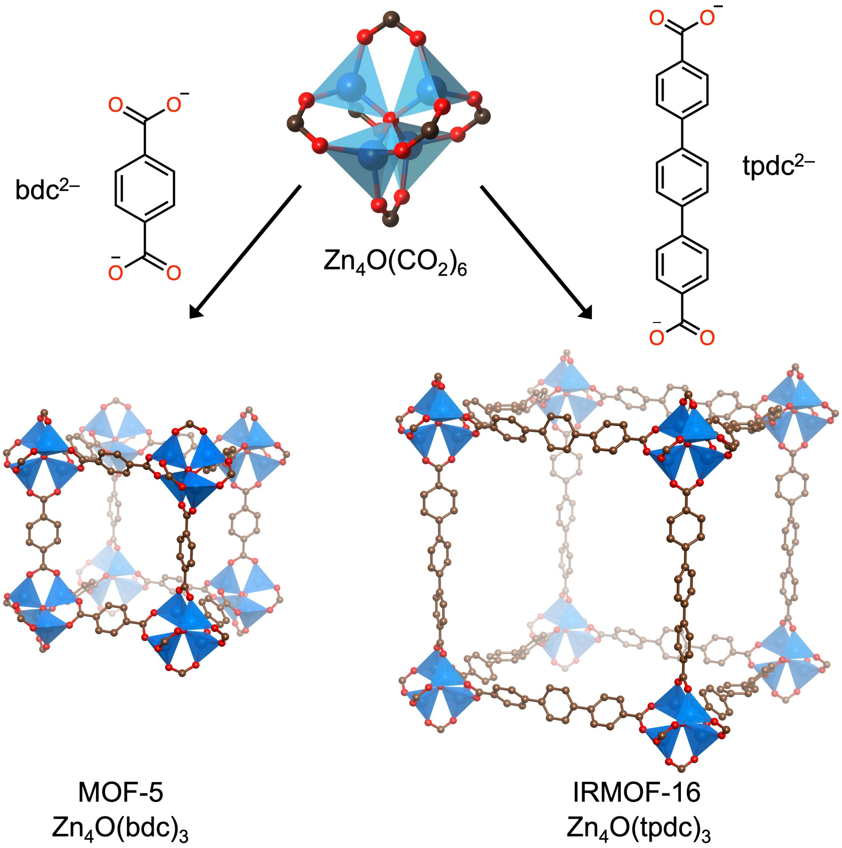

Figure 2.3. Schematic representation of the modular building scheme of isoreticular MOF-5 and IRMOF-16 exhibiting **pcu** (i.e. primitive cubic) topology. Both materials share the same inorganic $Zn_4O(CO_2)_6$ building unit. Formal substitution of the 1,4-benzenedicarboxylate (bdc^{2-}) linker in MOF-5 by [*p*-terphenyl]-4,4"-dicarboxylate ($tpdc^{2-}$) results in the structure of isoreticular IRMOF-16. Color code: Zn (blue), O (red), C (black), hydrogens are omitted for clarity. Coordination environments are shown as blue polyhedra. (CCDC: EDUSOL, EDUWAB).

2.3 Structural Responsiveness

In addition to the structural diversity of this family of functional materials, which results from their modular building scheme, their structural response upon external stimuli such as changes in temperature or pressure is plentiful (see Figure 2.4).[27] Some MOFs exhibit structural flexibility, which enables the framework to adjust its structure reversibly upon external stimuli such as guest loading, changes in temperature, pressure, or light irradiation.[27] Such structural behavior forms the basis for numerous applications of MOFs in sorption and separation processes, chemical sensing, biomedical applications, optoelectronic devices, and many others.[28–30]

Similar to conventional (i.e., non-porous, inorganic) crystalline materials, MOFs are known to exhibit (an)isotropic elastic structural responses, such as thermal expansion and contraction in response to changes in temperature or pressure.[31,32] The porous nature of these metal-organic coordination compounds, however, renders them mechanically soft materials with exceptionally low bulk moduli of mostly 4 - 30 GPa compared to purely inorganic materials such as zeolites, which feature bulk moduli in the range of 30 - 80 GPa.[33,34]

In some cases, MOFs have been observed to undergo (ir)reversible amorphization under high pressures or temperatures.[35,36] Beyond this transformation of a MOF into an amorphous solid material, melting at elevated temperatures represents a rare but remarkable phenomenon, which provides access to a liquid MOF phase. Subsequent rapid cooling of this liquid can lead to vitrification, resulting in the formation of an amorphous MOF glass.[37]

In regard to the various areas of application, understanding the structural response of MOFs —particularly under elevated temperatures and pressures— is of critical importance, as these conditions are frequently encountered in industrial chemical processes. Moreover, the structural behavior of MOFs under such conditions is often complex, and their prediction is challenging, which further highlights the need for further systematic investigations.[38] The distinctive mechanical properties of MOFs, including their inherent softness and possible responsiveness, also demand the development of novel processing strategies, particularly for immobilization purposes (e.g., shaping by pelletization).[39] In this context, the accessibility of a liquid MOF phase offers significant potential, enabling liquid-processing techniques such as melt-casting and exfoliation, and thus the fabrication of grain-boundary-free glassy MOF membranes exhibiting a potentially enhanced separation performance.[40]

These aspects will be investigated in the upcoming Parts I and II of this thesis.

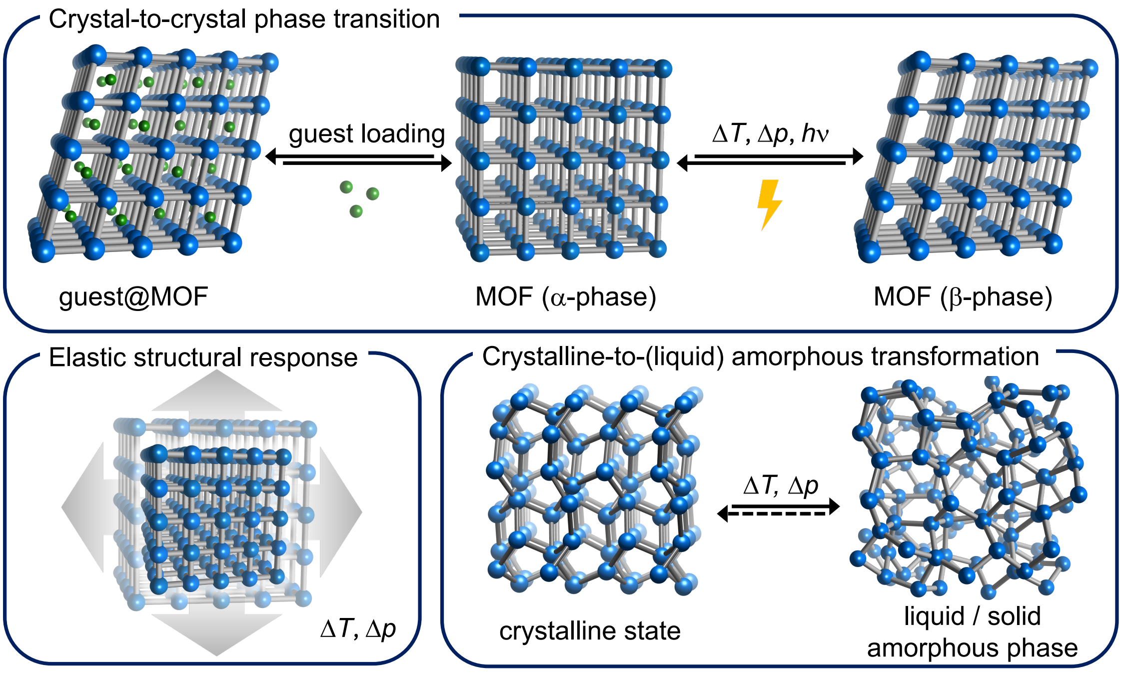

Figure 2.4. Schematic overview of the various kinds of structural behavior of MOFs towards external stimuli such as changes in temperature (ΔT), pressure (Δp), upon light irradiation ($h\nu$) or guest loading. The structural response includes crystal-to-crystal phase transitions (top) from an initial α-phase to a β-phase in response to various external stimuli, including light irradiation (i.e., in the case of photoresponsive MOFs) or even upon guest loading as a result of an inherent structural flexibility. Other MOFs feature solid or liquid amorphous phases (bottom, right), usually accessible at elevated temperature or pressure. Apart from these structural transformations, MOFs feature elastic structural behavior (bottom, left) in the sense of an (an)isotropic thermally or pressure-induced expansion or contraction of the structure. Crystal structures were taken from the Cambridge Crystallographic Data Centre (CCDC) (CCDC: GIZJOP).

Part I – Traditional Modification of Metal-Organic Framework Glasses

3 Introduction

3.1 A Short History of (Silicate) Glass

Over a million years ago, humankind started to employ natural glasses such as obsidian for tool manufacturing, as archeological findings from the Paleolithic age demonstrate.[41] The unique properties of these natural glasses - their brittleness and the formation of sharp edges upon breaking - proved to be an advantageous prerequisite for shaping and the fabrication of sharp cutting tools. The process of melt-quenching, i.e., the melting of a glass former followed by sufficiently fast cooling of the melt to reach vitrification, was only developed much later in history. Glass fragments from ancient Egypt and Mesopotamia dated to the early 1500 BC are the first evidence of the use of the melt-quenching technique and the processing of glass in its liquid state.[42,43] Early glass findings from the late Bronze Age comprise numerous objects such as fragments of vessels, beads, and ingots of various colors.[44] These artifacts not only underline the cultural importance of glass to these early civilizations but also prove these vitreous materials to be important trading goods at the time.[45] Since then, new processing techniques such as glass blowing and casting, as well as further technical advances, have given access to an immense variety of glass products.[46]

In 2005, glass production reached 124 million metric tons worldwide, ranging from domestic items and windows to screens and optical fibers.[47] This non-exhaustive list highlights the ubiquity of this unique material in our modern world. Despite the high demand for vitreous products and although the development of new glassy materials is ongoing, the understanding of the glass state itself is still the subject of current research.

3.2 Glass: A Non-Equilibrium State of Matter

The fundamental nature of the glass state is best understood by examining the behavior of the glass formers' enthalpy and molar volume during the melt-quenching process (see Figure 3.1).[48] When the initially crystalline glass former is heated, its enthalpy and molar volume increase steadily, accompanied on a structural level by thermal excitation of vibrational modes and expansion of the crystal lattice. At the melting temperature (T_m), the glass former undergoes a first-order phase transition into the liquid state, characterized by a discontinuous jump in enthalpy, entropy, and molar volume.[49]

Beyond T_m, the liquid phase exhibits a more pronounced increase in these quantities with rising temperature, reflecting the growing contributions from vibrational and configurational degrees of freedom enabled by bond dissociation during melting. Upon subsequent cooling, the liquid surpasses T_m and reaches the metastable supercooled liquid (SCL) state.[49]

Throughout the SCL state, a transition to the crystalline thermodynamic equilibrium state can occur. According to the classical nucleation theory, the process of crystallization is governed by the diffusion rates of the network-forming species through the melt and the associated activation barriers for nucleation and crystal growth.[50,51] In the case of successful glass formation, crystallization is circumvented by sufficiently high cooling rates, leading to a fast increase in viscosity, thus limiting diffusion rates in the supercooled liquid state until solidification is achieved at glass transition temperature (T_g).[52] Enthalpy and molar volume decrease continuously during this first cooling step, while the increase in liquid viscosity upon cooling limits the accessibility of vibrational and configurational states. Finally, the increase in liquid viscosity leads to the solidification of the SCL at the T_g.[49] Compared to the crystalline starting compound, the glass state remains of higher enthalpy, entropy, and molar volume and is therefore characterized as a metastable state, which can be understood as a frozen liquid state on a structural level.[46]

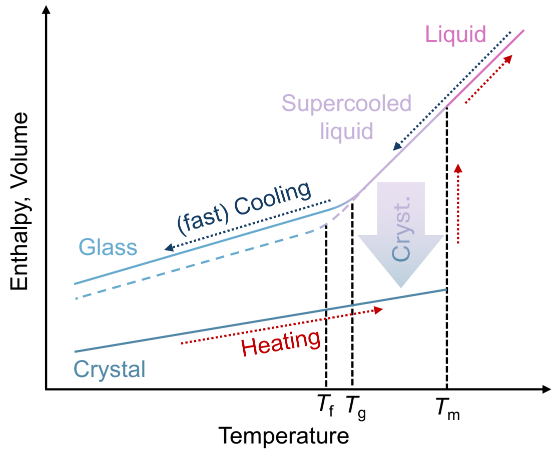

Figure 3.1. Schematic representation of the behavior of the enthalpy and volume of a typical glass former (e.g. SiO_2) during a heating-cooling (i.e., melt-quenching) cycle.[53] The melting temperature (T_m) indicates the melting of the initially crystalline glass former. Upon sufficiently fast cooling, the liquid surpasses the supercooled liquid state and solidifies at the glass transition temperature (T_g) to form the glass. The dashed blue graph corresponds to an alternative glass state reached by applying smaller cooling rates, resulting in a decreased glass transition temperature (T_f). The vertical arrow indicates the possibility of crystallization from the SCL state.[48]

The glass formers' tendency for crystallization upon cooling is described as glass-forming ability (GFA), whereas its resistance towards crystallization upon heating is denoted as glass stability (GS).[54] A frequently used parameter for the GFA, which was introduced by W. Kauzmann in 1948 is the ratio of T_g/T_m, which empirically was found to result in $\sim 2/3$ for a wide range of investigated melt-quenched glass formers.[55,56] Systems with high GFA values (i.e., $T_g/T_m > 2/3$) exhibit a strong increase in viscosity throughout the SCL state, effectively inhibiting crystallization processes.[57] As the glass state is a kinetically trapped state of matter, its properties (e.g., molar volume, density, thermal expansivity) depend on the applied cooling rate during vitrification from the (supercooled) liquid.[58] Slower cooling rates provide more time for structural relaxation processes, leading to a lower glass transition temperature and a glass with increased density and reduced molar volume.[46]

The ambiguity of the glass state as a solid state of matter featuring structural characteristics of the liquid state and the impact of the glass's thermal history on the glass structure leads to many different definitions reported in the literature. In 2017, a comprehensive definition of the glass state was given by E.D. Zanotto and J. C. Mauro:[59]

> "Glass is a non-equilibrium, non-crystalline condensed state of matter that exhibits a glass transition. The structure of glasses is similar to that of their parent supercooled liquids (SCL), and they spontaneously relax toward the SCL state. Their ultimate fate, in the limit of infinite time, is to crystallize."

3.3 Unveiling the Structures of Crystals and Glasses

The process of vitrification involves the transformation of a crystalline glass former to the amorphous glass state. Figure 3.2 shows a two-dimensional depiction of the structure of an exemplary glass-forming material (such as SiO_2) in the crystalline and glass state. While the Crystalline state exhibits translational periodicity along both directions, the glass state shows a complete lack of the same. Instead, both structures can be compared in terms of the presence of short- and long-range order. While the short-range order (i.e., nearest-neighbor connections) is mostly preserved during vitrification, a complete lack of long-range order renders the glass state crystallographically amorphous.[46]

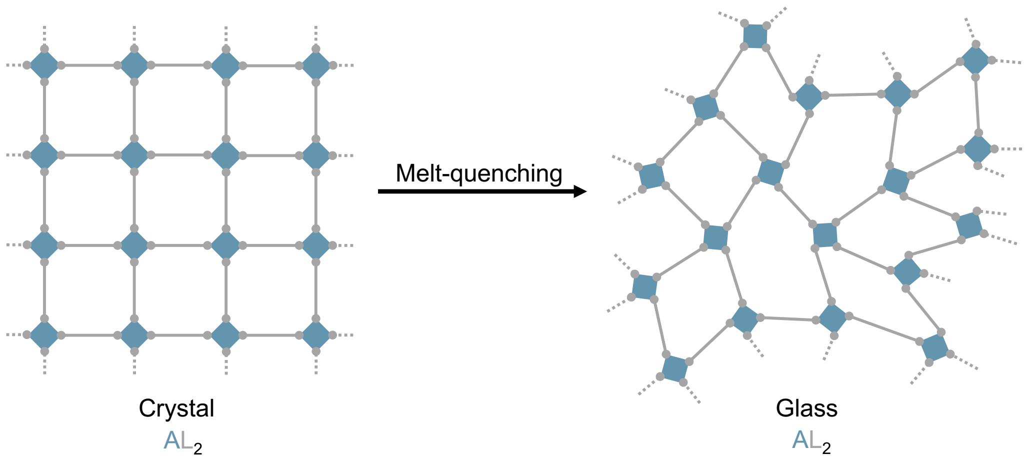

Figure 3.2. Two-dimensional representation of an excerpt of the structure of a crystalline material with the general chemical composition AL_2 and the corresponding amorphous glass structure after melt-quenching.

3.3.1 Powder X-Ray Diffraction

For crystalline materials, structural information can be obtained from the diffraction of X-rays by the crystal (Figure 3.3, left). This process is understood as the elastic scattering of the initial coherent incident X-ray beams by the regular arrangement of a structural basis —i.e., the electron density of the atoms forming the crystal—which are periodically arranged on the underlying crystal lattice. According to BRAGGs law (3.1) constructive interference of the X-rays diffracted by a set of parallel crystallographic planes, separated by the lattice distance d can only occur under the diffraction angle Θ if the additional pathway δ equals an integer multiple n of the wavelength λ.[60]

$$n\lambda = 2d\sin(\Theta) \tag{3.1}$$

In case the Bragg condition (3.1) is fulfilled, the intensity of the diffracted X-rays I_{hkl}, which correspond to the interplanar spacing d_{hkl},* depends on the distribution of electron density within the unit cell, i.e., on the type and position of the atoms that constitute the crystal structure. This relationship is expressed by the square of the absolute value of the structure factor F_{hkl} (3.2).[60]

$$I_{hkl} \propto |F_{hkl}|^2 \tag{3.2}$$

The structure factor is a complex quantity composed of the atomic form factors f_j, which are characteristic for each atomic species j and their respective positions (x_j, y_j, z_j) in the unit cell. F_{hkl} therefore quantifies the contribution of each atom in the unit cell to the intensity of X-rays diffracted from the set of lattice planes indexed by (hkl).[60]

$$F_{hkl} = \sum_j f_j \mathrm{e}^{-i2\pi(hx_j+ky_j+lz_j)} \tag{3.3}$$

In powder X-ray diffraction (PXRD), the random orientation of crystallites in the powdered specimen averages the three-dimensional diffraction information into a one-dimensional pattern. As a result, the diffracted intensity is recorded as a function of the diffraction angle 2Θ and provides information about the bulk composition of the sample (e.g., phase purity) (see Figure 3.3, right).

*hkl correspond to the MILLER indices and specify a set of lattice planes denoted by (hkl).

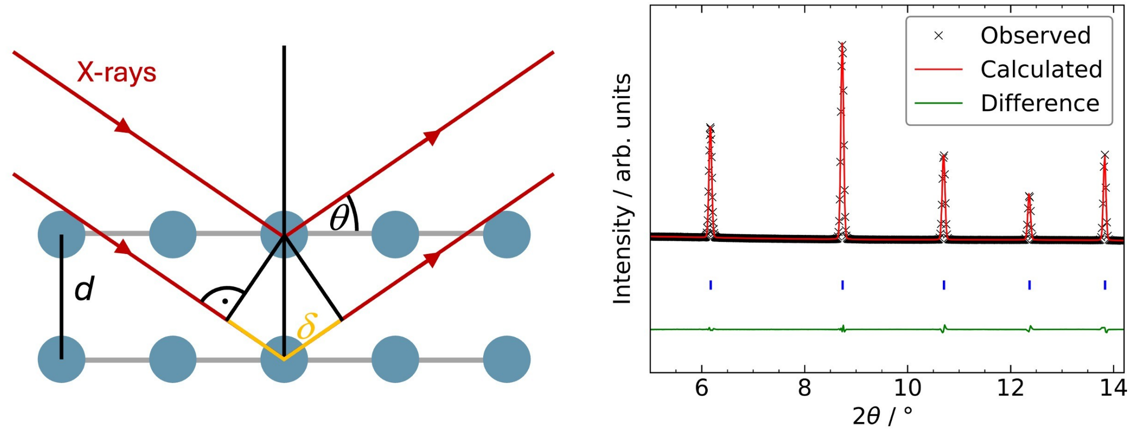

Figure 3.3. Left: Illustration for the classical geometrical derivation of Bragg's law depicting the reflection of X-rays from a set of crystal planes with the lattice distance d, additional beam path δ and diffraction angle Θ; Right: Structureless profile fit performed on an exemplary diffraction pattern. Blue tick marks indicate allowed Bragg peak positions.

Various methods have been reported to analyze PXRDs via profile fitting.[61] Structureless profile fitting approaches (e.g., Pawley method[62], LeBail method[63]) refine the unit cell parameters according to the Bragg peak positions observed in the diffraction pattern, whereas reflection intensities are refined freely (Figure 3.3, right). Rietveld-refinement, in contrast, is based on the refinement of an atomistic structural model, which constrains the calculated reflection intensity based on the calculated atomic position of the model.[64]

3.3.2 X-ray Total Scattering

The absence of translational periodicity in the atomic structure of the specimen results in diffuse scattering rather than sharp Bragg peaks in a powder diffraction experiment. In X-ray total scattering, this diffuse scattering is analysed, as it contains valuable structural information. The total scattering intensity consists of coherent and incoherent contributions (e.g., Compton scattering), as well as multiple scattering and background contributions (e.g., scattering from the capillary or air).[65] To obtain reliable structural information from the scattered intensity, a sufficiently large range in reciprocal space must be covered. This quantity is expressed by the magnitude of the scattering vector Q, as defined in Equation (3.4).

$$Q = \frac{4\pi \sin(\Theta)}{\lambda} \tag{3.4}$$

For structural analysis, the coherent scattering component—obtained by correcting the measured total scattering intensity (e.g., by background subtraction)—is normalized using the specimen's atomic density and average scattering factors to yield the structure function $S(Q)$.[65] The reduced pair distribution function $G(r)$ is then calculated as the Fourier transform of the reduced structure function $F(Q) = Q(S(Q)-1)$. $F(Q)$ contains information about the correlation density of scatterers in reciprocal space, expressed as the deviation from an average correlation density corresponding to a random pair distribution.[65]

$$G(r) = \frac{2}{\pi} \int_{Q_{\min}}^{Q_{\max}} Q(S(Q) - 1) \sin(Qr)\, \mathrm{d}Q \tag{3.5}$$

The Fourier transform $G(r)$ thus describes the deviation of the atomic pair correlation density at the real-space pair distance r from the specimen's average correlation density. Consequently, as $r \to \infty$, $G(r)$ converges to zero because the pair correlation density approaches the average value at large real-space distances.[66]

While $G(r)$ is commonly used as the basis for structural analysis of amorphous materials due to its direct relation to experimental data, an alternative representation is often used for intuitive interpretation: the radial pair distribution function $R(r)$. It can be derived from $G(r)$ and represents a pair correlation function with signal intensities that are weighted by the relative abundance of atomic pairs and their corresponding scattering powers.[†] Quantitative information about specific atomic pair densities can be extracted by integrating the corresponding peaks in $R(r)$ (see Figure 3.4).[67] However, as the total number of pair correlations increases with increasing distances, $R(r)$ diverges to infinity as $r \to \infty$. Due to this global behavior of $R(r)$, quantitative evaluation by integration is only sensible in the low-r region where correlation signals appear well separated.[67]

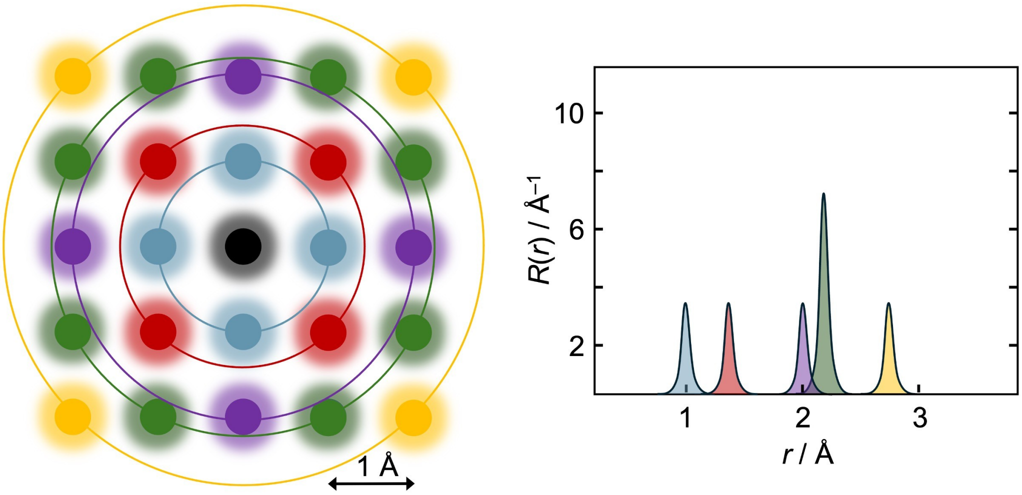

Figure 3.4. Left: Schematic representation of a structure with atoms arranged on a square grid (mesh distance: 1 Å).[68] The atoms exhibit the same individual scattering power and exhibit some kind of local disorder, which may reduce the material's crystallinity, as indicated by the smearing of atomic positions. Right: Radial pair distribution function $R(r)^\dagger$, displaying peaks that correspond to atomic pair correlations within the structure. Integration of a peak yields the number of atomic pairs contributing to that correlation.

[†] The radial distribution function can be obtained from $G(r)$ using $R(r) = r(G(r) + 4\pi r \rho_0)$ with ρ_0 as the atomic number density.

3.4 Thermal Analysis of Glasses: From Fragility Indices to Potential Energy Landscapes

An important characteristic of glasses is their viscous flow behavior after surpassing the glass transition temperature upon heating. In 1991, C. A. Angell investigated the structural origin of the viscous flow behavior of various glass-forming compounds.[69]

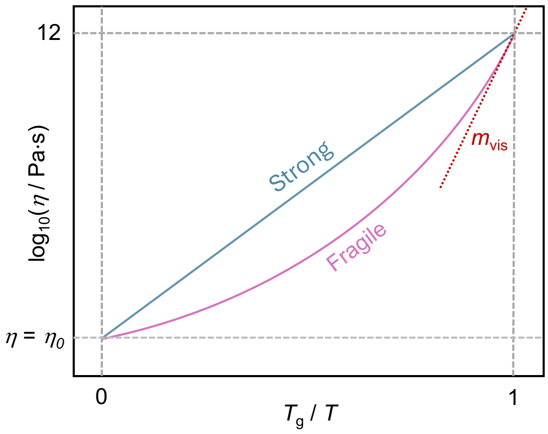

Figure 3.5. Angell plot with a schematic depiction of the viscosity-temperature curves of strong and fragile liquids. The fragility index m_{vis} corresponds to the tangent gradient at $T = T_{\text{g}}$ (red dashed line) where the viscosity η reaches a limit of 10^{12} Pa s upon cooling. Adapted from reference[69].

It was found that the temperature dependency of the liquid viscosity $\eta(T)$ for some network-forming compounds (such as SiO_2) follows an Arrhenius-like behavior. Liquids that behave according to equation 3.6, with η_0 as the respective limit of $\eta(T)$ at infinite temperature, E_{vis} as the activation energy for shear viscous flow and the ideal gas constant R, were characterized as "strong".[69]

$$\eta(T) = \eta_0 e^{\frac{E_{\text{vis}}}{RT}} \tag{3.6}$$

Other (molecular) glass-formers that do not exhibit a network structure were found to follow a super-Arrhenius trend and are characterized as more "fragile" liquids (see Figure 3.5). In the Arrhenius plot (often referred to as the Angell plot), these fragile liquids exhibit a bigger gradient in their temperature-viscosity curves as the temperature approaches T_g upon cooling. In an approach to quantify this behavior, Angell introduced the fragility index m_{vis} which is defined as:[69]

$$m_{\text{vis}} = \frac{\mathrm{d}\log_{10}(\eta(T))}{\mathrm{d}(T_{\text{g}}/T)}\Big|_{T=T_{\text{g}}} \tag{3.7}$$

According to equation 3.7, m_{vis} describes the rate of viscosity change with temperature at T_{g}, which is defined as the point at which the shear viscosity of the liquid reaches an upper limit of $\eta(T_{\text{g}}) = 10^{12}$ Pa s.[51] Strong glass formers (such as SiO_2, $m_{\text{vis}} = 20$)[70] have low fragility indices and exhibit a network structure interconnected by directional bonds. This is opposed to more fragile glass formers (such as Glycerol, $m_{\text{vis}} = 50$), which have high fragility indices and are structurally characterized as molecular compounds, interconnected by non-directional interactions such as Coulomb, van der Waals or $\pi - \pi$ interactions.[70,71]

Combining (3.6) and (3.7) provides Equation 3.8, which illustrates that m_{vis} contains information about the activation energy for shear viscous flow E_{vis}. The latter was found to be in good agreement with the activation energies for structural relaxation of the liquid (i.e., the rearrangement of the liquid's structure to changes in temperature).[72]

$$m_{\mathrm{vis}} = \log_{10}(e) \cdot \left(\frac{E_{\mathrm{vis}}}{RT} \right) \tag{3.8}$$

The time associated with these internal structural relaxation processes in the liquid state is therefore tightly correlated to its viscosity.[72–74] Consequently, the liquid structure of fragile liquids is more sensitive to slight changes in temperature and fluctuates over a larger range of different local configurations compared to strong liquids. This relation and its meaning with regard to the kinetic origin of the glass transition was put in words by Angell in 1995:[70]

> "[...] the glass transition, as actually observed in the laboratory during cooling, is strictly kinetic in origin. [It] is observed [...] when an internal relaxation time, one intrinsic to the liquid, crosses an experimental time scale."

Thus, it is unsurprising that the experimental time scale (i.e. the applied heating/cooling rate) influences the temperature at which the glass transition is observed.[75]

3.4.1 The Calorimetric Fragility Index

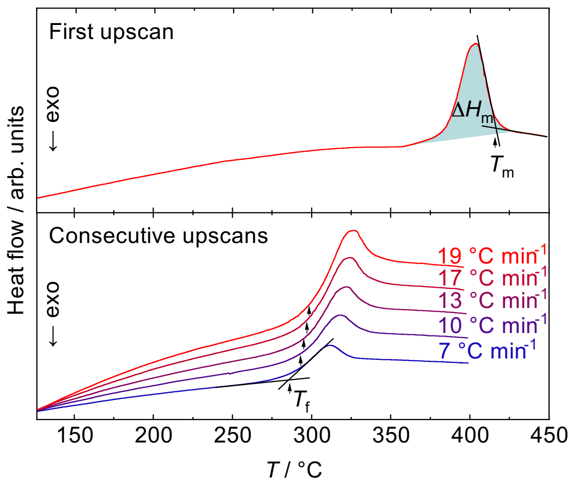

Figure 3.6. Differential scanning calorimetry (DSC) measurements monitoring the heat flow curves of an exemplary glass-former. Top: First thermal upscan depicting the endothermic melting signal. The melting temperature T_m is defined as the offset temperature. ΔH_m refers to the enthalpy of melting calculated from the integral of the melting signal. Bottom: Consecutive heating scans after glass formation illustrating the shift in the glass transition. Various heating/cooling rates were applied during the previous cooling of the melt (not shown) and the depicted subsequent thermal upscans. The glass transition temperatures with heating/cooling rates $\neq \pm 10\,°\mathrm{C\,min^{-1}}$ are denoted as fictive temperature T_f and determined as the onset temperature.

The key parameter that thermally characterizes a vitrified material is the temperature at which the glass transition occurs. Differential scanning calorimetry (DSC) is a widely used method to quantify thermal events such as the glass transition, which occurs upon heating/cooling of a compound.[48] A DSC measurement is typically performed against an (empty) reference pan. The resulting DSC thermogram records the heat flow ($\mathrm{d}Q/\mathrm{d}t$) to or from the sample relative to the reference during a controlled temperature increase or decrease, usually at a constant heating or cooling rate of $(\mathrm{d}T/\mathrm{d}t) = \pm 10\,°\mathrm{C\,min^{-1}}$. Figure 3.6 shows the heat flow curve recorded during the first and consecutive thermal upscans of an exemplary crystalline glass former in a DSC apparatus. The first upscan depicts the melting of the glass former at the melting temperature T_m, which is associated with an endothermic signal (see 3.6, top). Under the assumption of constant pressure and at a constant heating rate, integration of a given signal provides the enthalpy of the associated underlying process ΔH according to:[76,77]

$$\Delta H = \int_{T_1}^{T_2} \frac{1}{q} \left(\frac{\mathrm{d}H}{\mathrm{d}t}\right)_p \mathrm{d}T = \int_{T_1}^{T_2} \frac{1}{q} \left(\frac{\mathrm{d}Q}{\mathrm{d}t}\right)_p \mathrm{d}T \tag{3.9}$$

with T_1 and T_2 as the respective limits of the heat flow signal $(\mathrm{d}Q/\mathrm{d}t)_p$ and with the heating rate $q = (\mathrm{d}T/\mathrm{d}t) = \mathrm{const.}$ After cooling the melt until vitrification at a constant cooling rate and subsequent heating of the formed glass at the same heating rate, a glass transition is observed in the corresponding heat flow curve (see Figure 3.6, bottom). The glass transition appears as a step in the heat flow curve which is due to the increased specific heat capacity C_p (referenced on the sample mass m) of the supercooled liquid state compared to the glass state:[76]

$$\left(\frac{\mathrm{d}Q}{\mathrm{d}t}\right)_p = \left(\frac{\mathrm{d}H}{\mathrm{d}t}\right)_p = m \cdot C_\mathrm{p} \left(\frac{\mathrm{d}T}{\mathrm{d}t}\right) \tag{3.10}$$

T_g is determined as the onset of the glass transition step and is dependent on the rate at which cooling of the melt and the subsequent thermal upscan are performed, with slower heating/cooling rates resulting in lower T_g values.[75] The heating/cooling-rate dependence of the glass transition temperature is given by Equation 3.11 connecting the heating/cooling-rate q with the activation enthalpy for structural relaxation of the liquid ΔH^* which was empirically found to be in good agreement with the activation energy of shear viscous flow ΔE_vis.[72,75,78]

$$\frac{\mathrm{d}\ln(q)}{\mathrm{d}(1/T_\mathrm{g})} = -\frac{\Delta H^*}{R} \approx -\frac{\Delta E_\mathrm{vis}}{R} \tag{3.11}$$

Based on this relation and in accordance with the definition of the fragility index m_vis derived from temperature-dependent viscosity measurements (Equation 3.8), the calorimetric fragility index m_cal was defined as:[48,79]

$$m_\mathrm{cal} = \frac{\mathrm{d}\log_{10}\left(\frac{1}{q}\right)}{\mathrm{d}\left(\frac{T_g}{T_f}\right)} = \log_{10}(e) \cdot \left(\frac{E_\mathrm{vis}}{RT_g}\right) \tag{3.12}$$

Equation 3.12 enables the determination of m_cal from the heating/cooling-rate dependent shift of the fictive temperature T_f (i.e., the glass transition temperature with $q \neq 10\,°\mathrm{C\,min^{-1}}$) and the glass transition temperature T_g (i.e., $q = 10\,°\mathrm{C\,min^{-1}}$) via linear regression of $\log_{10}(1/q)$ against $(T_\mathrm{g}/T_\mathrm{f})$. For a series of various silicate-based glasses, the obtained values for m_cal and m_vis were found to correlate linearly, making the calorimetric approach a convenient method for determining fragility indices.[80]

3.4.2 Heat Capacity and Potential Energy Landscapes

The glass transition is associated with a sudden increase in heat capacity C_p as the material transitions from the solid to the SCL state upon heating. C_p is composed of vibrational and configurational contributions according to:

$$C_\mathrm{p} = C_\mathrm{p,vib} + C_\mathrm{p,conf} \tag{3.13}$$

In the glass state, the transitions between different configurations are slow as the activation barrier for such processes in the solid state is high.[81] Upon surpassing T_g, the gradual drop in viscosity enables the transition between different configurational states. The difference in heat capacity ΔC_p between the glass $C_\mathrm{p,g}$ and the liquid $C_\mathrm{p,l}$ at the glass transition temperature can therefore be identified as the isolated configurational heat capacity contribution ($\Delta C_\mathrm{p} = C_\mathrm{p,l} - C_\mathrm{p,g} \approx C_\mathrm{p,conf}$) (see Figure 3.7).[81]

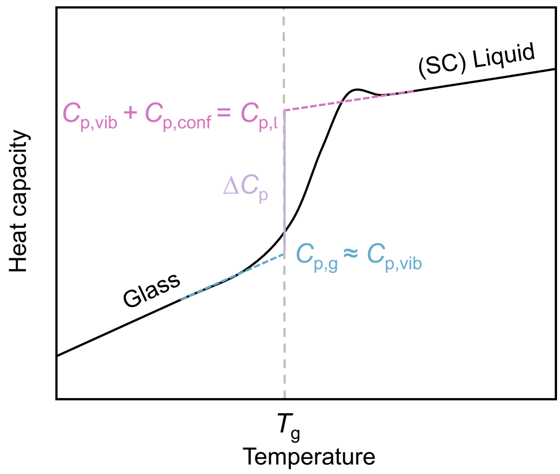

Figure 3.7. Schematic representation of a DSC thermogram showing the heat capacity of a glass upon surpassing the glass transition during a thermal upscan. The jump in heat capacity ΔC_p at the glass transition temperature T_g is interpreted as configurational heat capacity and corresponds to the difference between the heat capacity of the supercooled liquid ($C_\mathrm{p,l}$) and the glass ($C_\mathrm{p,g}$). The illustration was adapted from reference[81].

It was found that glass former characterized as more fragile exhibit larger jumps in heat capacity at T_g compared to strong glass formers.[69,70] This relation can be explained by the higher density of local minima representing different configurational states in their respective potential energy landscape (PEL) (see Figure 3.8). For a strong glass former, the PEL can be understood as a single global basin containing structurally closely related configurational states.[70] As indicated by the low fragility index (see Equation 3.8), the associated activation energy for structural relaxation of the glass structure to an ideal glass state (see blue arrows in Figure 3.8) is comparably low. In contrast, in the fragile case, the PEL exhibits multiple global basins representing structurally more different glass states with high activation barriers associated with inter-basin transitions.[82] Due to the higher number of configurational glass states, the ΔC_p accompanying the glass transition of fragile liquids is generally higher.[70,81]

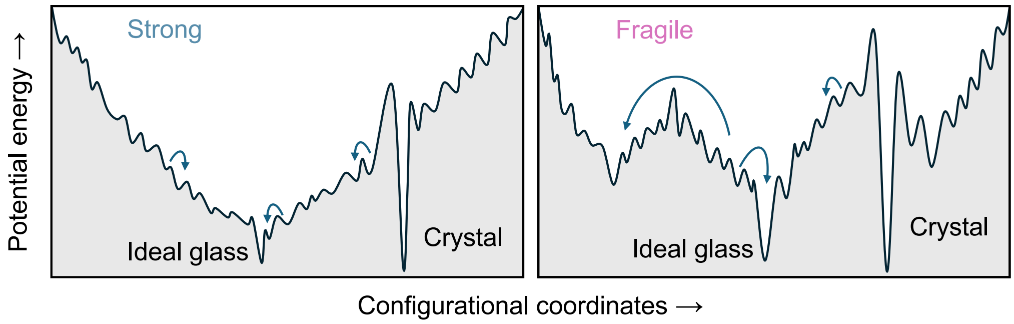

Figure 3.8. Schematic representation of a two-dimensional potential energy landscape of a strong (left) and fragile (right) glass. The arrows indicate the possible transitions between different configurational states and illustrate the presence of larger activation barriers associated with the inter-basin transitions in the fragile case. The scheme was adapted from reference[83].

3.5 A new Class of Glass Former: Zeolitic Imidazolate Framework Glasses

While silicate glasses remain the best-investigated and most abundant glass systems, other glass-forming compounds have been found and transformed into the glass state. Today, several different groups of glass-forming systems have evolved including:[47]

1. Inorganic oxide glasses (e.g., silicates, phosphates, borates, ...)
2. Metallic glasses
3. Organic glasses (e.g,. molecular organic, polymeric glasses)
4. Metal-organic framework glasses

Metal-organic framework glasses represent a new class of glass formers mostly based on the subgroup of ZIFs.[37,84] The characterization as "zeolitic" imidazolate framework is based on the fact that many members of this group adopt topologies known from the well-investigated materials class of zeolites.[85] The zeolite structure is built from tetrahedral TO_4 (T = Si, Al) units with the oxygen bridging between adjacent tetrahedral sites. The counter-cations are located in the zeolite's pores for charge neutrality.[86] ZIFs share a number of topological features such as the tetrahedral geometry of their inorganic building unit, which can be composed of a variety of divalent (transition-) metal ions. These include mostly Zn^{2+}[87] and Co^{2+},[85] but also Fe^{2+},[88] Cd^{2+},[89,90] Mn^{2+}[91] and Mg^{2+}[92] as well as mixed-metal ZIFs incorporating different metal ions.[93] In ZIFs, the metal ions are tetrahedrally coordinated by the nitrogen atoms of the imidazolate-type linkers, which act as organic building units and bridge between neighboring metal centers to form the ZIF.[85] Figure 3.9 illustrates the close structural relation between zeolites and ZIFs, which is based on the imidazolates structure-directing effect, resulting in similar binding angles.[94]

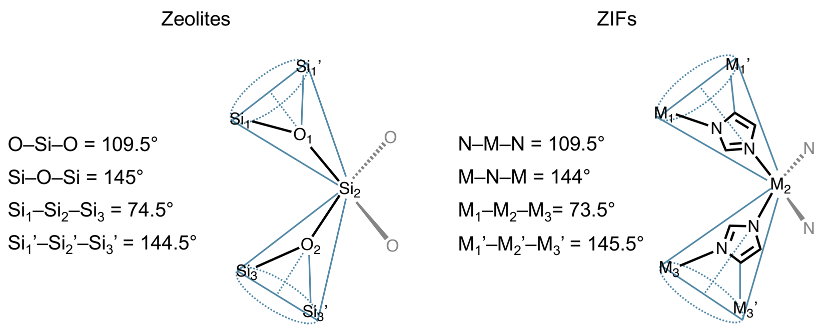

Figure 3.9. Comparison between the angles found in the structures of zeolites and ZIFs. Adapted from reference[94].

The chemical and structural diversity of known ZIF structures is immense due to the large selection of possible metal ions and imidazolate-type linkers which can be incorporated (see Figure 3.10).[95] Their building scheme further enables the specific tuning of material properties. Some ZIFs exhibit large specific surface areas as well as exceptionally high chemical and thermal stability. The zeolitic imidazolate framework ZIF-8 (chemical composition: $Zn(mim)_2$, $mim^- = $ 2-methylimidazolate, **sod** topology, specific surface area: $1.95\,m^2\,g^{-1}$), for instance, exhibits a remarkably high resistance towards boiling alkaline water.[87] While the majority of ZIFs and MOFs, including ZIF-8 decompose at elevated temperatures without prior melting, a very limited number of ZIFs are reported to melt before decomposition and vitrify upon cooling of the melt.

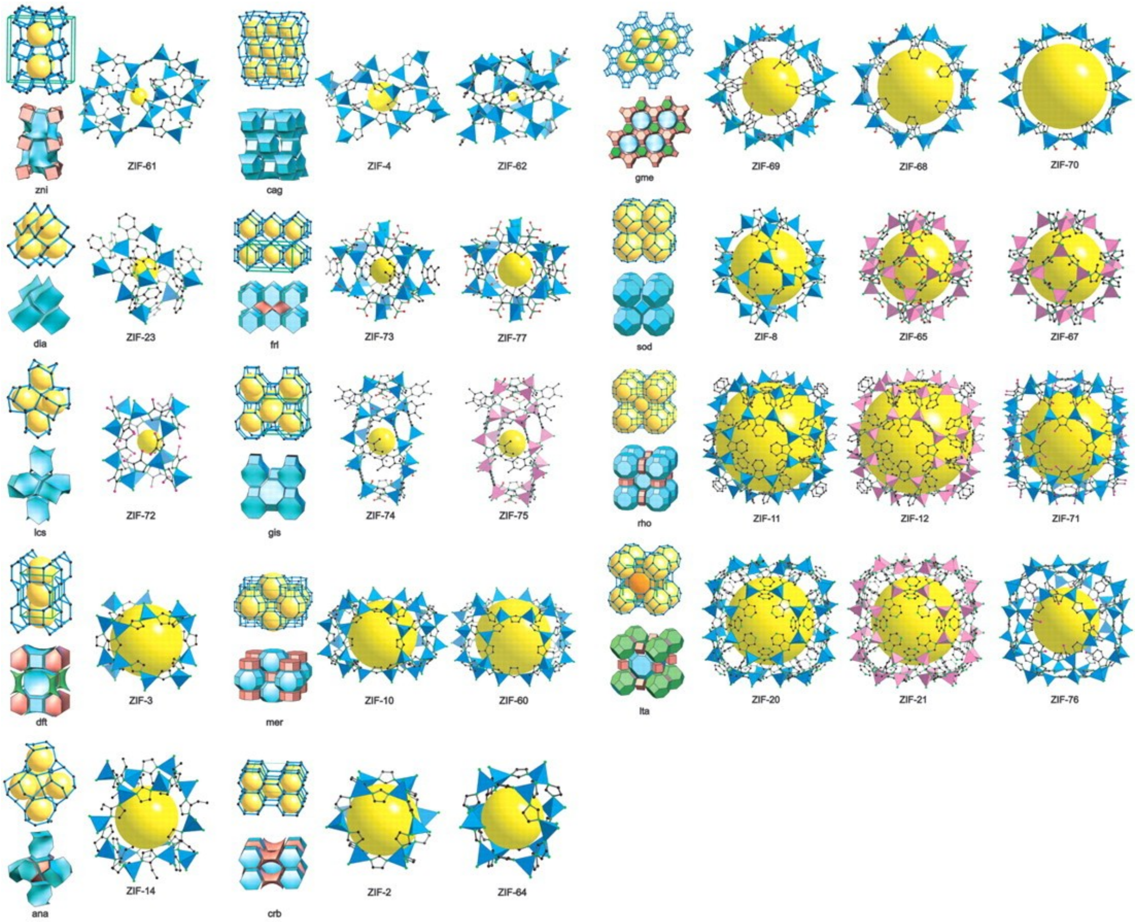

Figure 3.10. Representation of a variety of different ZIFs. Each line depicts underling topology of the material depicted as net (top) and tiling (bottom) which is followed by the crystal structure of the respective ZIF. The topologies are denoted as a three-letter code. The coordination polyhedra in the crystal structure are shown in blue (ZnN_4) or pink (CoN_4). Yellow spheres indicate the free pore volume. From reference[85]. Reprinted with permission from AAAS.

3.5.1 ZIF-4: The first Glass-forming MOF

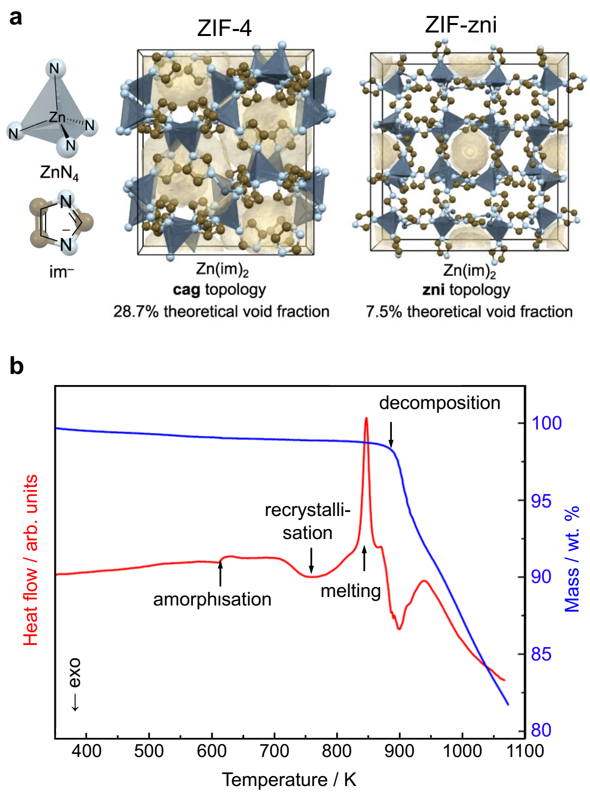

Figure 3.11. **a** Crystal structure of ZIF-4 and ZIF-zni with a view along the crystallographic *b*- and *c*-axis respectively. Hydrogen atoms are omitted for clarity. Pale yellow spheres represent the free volume of the pores. The theoretical void fraction was calulated with a probe radius of 1.6 Å. Adapted from reference[96]. **b** Simultaneous thermogravimetric and differential thermal analysis (STA) curve of the heating of ZIF-4 showing the heat flow signal and mass change during a thermal upscan performed under an inert gas atmosphere. The figure was adapted from reference[97] with permission from WILEY.

ZIF-4 (chemical composition: $Zn(im)_2$, im^- = imidazolate, **cag**‡ topology) is the first MOF reported to show melting upon heating beyond its melting temperature.[84,98] Figure 3.11b illustrates the thermal behavior of ZIF-4 upon heating. The crystalline material first undergoes an exothermic thermal amorphization at ∼ 620 K (∼ 347 °C) followed by recrystallization to a dense, polymorphous ZIF-zni phase at ∼ 770 K (∼ 497 °C). The recrystallization is indicated by an exothermic heat flow signal which is succeeded by an endothermic signal of high enthalpy associated with the melting of the previously formed ZIF-zni phase (exhibiting **zni**‡ topology) at ∼ 866 K (∼ 593 °C). The melting signal is followed by thermal decomposition of the liquid phase, indicated by an exothermic heat flow signal and simultaneous mass loss.

The mechanism of melting and the dynamics of the liquid were investigated using first-principle molecular dynamic simulations, which show that the initially four-fold coordinated Zn^{2+} first undergoes fluctuation of the coordination unit (see Figure 3.12). This is followed by one im^- leaving the former four-fold coordination unit. Finally, another im^- approaches the Zn^{2+} and restores the four-fold tetrahedral coordination environment.[99]

Quenching of the melt just before the onset of thermal decomposition yields a melt-quenched glass (denoted as *g*ZIF-4). XPDF measurements performed on *g*ZIF-4 and a number of other ZIF glasses further indicate that the short-range order (i.e., next-neighbor Zn−im−Zn connections) is maintained during vitrification, while the loss of long-range order

‡The topological codes (e.g. **cag**, **zni**) are used to describe framework topologies. An overview of framework nets and topologies can be found in the Reticular Chemistry Structure Resource (`https://rcsr.anu.edu.au/`)

is in line with the amorphous nature of the glass state.[98] In 2020, Madsen *et. al* performed an ultrahigh-field ^{67}Zn MAS NMR study which indicated an increase in the average Zn−N bond length and increased structural disorder in the tetrahedral ZnN_4 coordination unit in the glass state.[100] Consequently, the overall connectivity (i.e., the average number of neighboring Zn centers directly connected to a given Zn center) remains unchanged during vitrification (i.e., a connectivity of four).

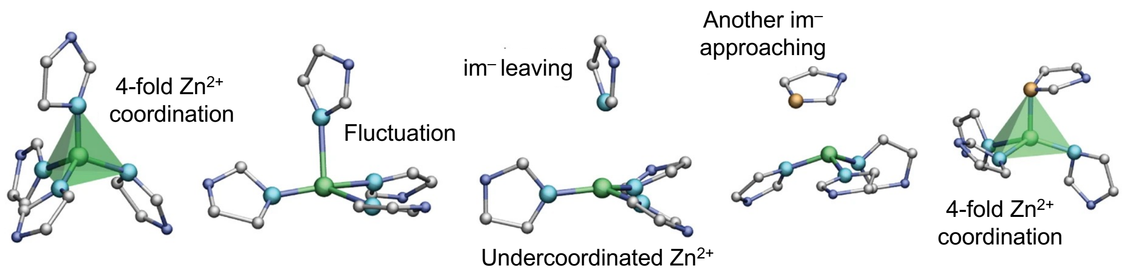

Figure 3.12. Visualization of an imidazolate-exchange representing the structural dynamic of molten ZIF-4. Color code: Zn (green), N (blue, orange), C (grey), coordination environments are shown as green polyhedra, hydrogens were omitted for clarity. From reference[99]. Reproduced with permission from Springer Nature.

During the structural evolution of the porous ZIF-4 parent framework (37.2% theoretical void fraction, $\rho^{\dagger} = 1.22\,\mathrm{g\,cm^{-3}}$) the material densifies upon heating throughout the amorphization and recrystallization to ZIF-zni (8.1% theoretical void fraction, $\rho^{\dagger} = 1.54\,\mathrm{g\,cm^{-3}}$).[96] However, glass formation results in a less dense material compared to ZIF-zni with pores accessible even for larger hydrocarbons ($\rho^{\S} = 1.38\,\mathrm{g\,cm^{-3}}$).[96] The presence of microporosity after melt-quenching of a highly porous crystalline parent framework represents one of the most important aspects in MOF glass research. The facilitated processability of the glass state due to liquid processing methods such as melt casting, molding, or exfoliation, the absence of grain boundaries, in addition to the presence of microporosity has led to a wide range of proposed applications. These range from membrane manufacturing for gas separation to the use as solid-state electrolytes in energy storage applications.[101,102]

However, in the case of ZIF-4, the narrow temperature window between melting and decomposition hinders the preparation of clear, decomposition-free glasses and poses a major challenge for potential applications.

3.5.2 ZIF-62: A prototypical ZIF Glass Former

Partial formal substitution of the im$^-$ linker in ZIF-4 by benzimidazolate (bim$^-$) yields a mixed-linker ZIF denoted as ZIF-62 (chemical composition:† $Zn(im)_{2-x}(bim)_x$, $0.05 <$

†Calculated based on the crystal structure.

§Apparent density calculated based on CO_2 sorption data.

†The chemical composition of ZIF-62 varies depending on the amount of bim$^-$ incorporation within the given limits of x. The isoreticular cobalt analogue ZIF-62(Co) (chemical composition: $Co(im)_{2-x}(bim)_x$, **cag** topology) is not further discussed for the sake of consistency.

$x < 0.35$, **cag** topology) (see Figure 3.13a).[57] Throughout a large range of possible compositions (i.e., variations in x), the thermal behavior of ZIF-62 consists of melting at elevated temperature, followed by thermal decomposition upon further temperature increase. Figure 3.13b depicts the increasing trend in T_m and T_g with growing amounts of bim^- incorporated in ZIF-62. The thermal stability window of the liquid state of ZIF-62 is much larger compared to ZIF-4 which is due to the reduced melting temperature of 370 °C ($x \approx 0.05$)(T_m(ZIF−zni) = 593 °C) while the decomposition temperature remains largely unaltered at ∼ 550 − 600 °C.[103] The higher thermal stability window enables the formation of decomposition-free clear ZIF-62 glasses (denoted as gZIF-62) via melt-quenching of the liquid ZIF-62 phase.[104]

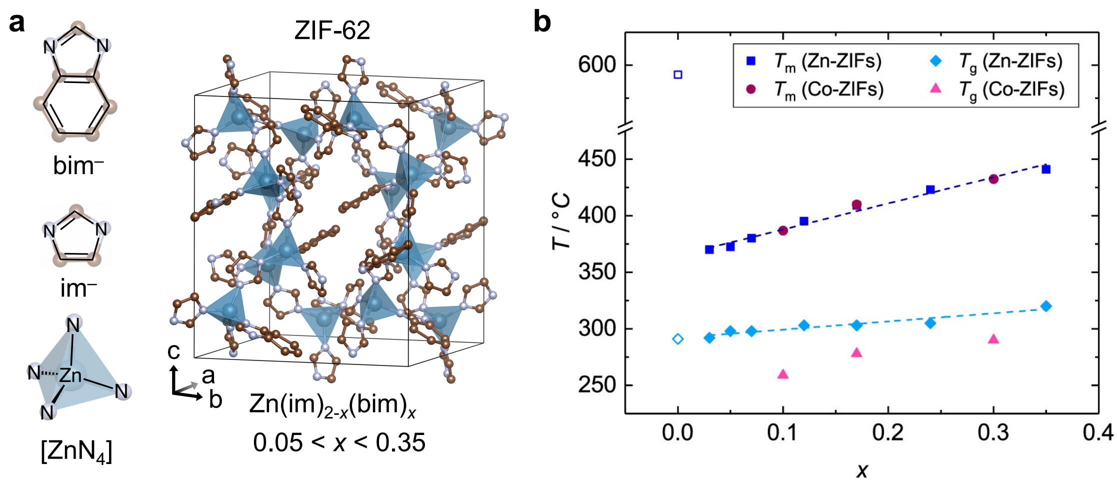

Figure 3.13. **a** Perspective view on the unit cell of ZIF-62 (CCDC: GIZJOP). **b** Melting temperature T_m and glass transition temperature T_g for ZIF-4 ($x = 0$) shown as open blues symbols and ZIF-62 ($Zn(im)_{2-x}(bim)_x$, $0.02 < x < 0.35$) represented as solid blue symbols plotted against the amount x of incorporated bim^-. Purple symbols correspond to the isoreticular cobalt analogues† ($Co(im)_{2-x}(bim)_x$). Reprinted and adapted with permission from reference[103]. Copyright 2019 American Chemical Society.

The significantly different thermal behavior of ZIF-62 and ZIF-4 has been widely discussed in the literature.[57,98,103] ZIF-62 exhibits an ultra-high GFA throughout the large majority of its compositional range.[57] Recrystallization into a denser crystalline phase upon heating, analogous to ZIF-zni formation upon heating of ZIF-4, is effectively prevented by the steric demand of the bulkier bim^- linker. In fact, lower bim^- contents ($x \lesssim 0.05$) fail to suppress the recrystallization to ZIF-zni at around 500 °C.[103]

Bennett *et. al.* further suggested that the drop in T_m between ZIF-4/ZIF-zni and ZIF-62 is caused by the bulky bim^- linker causing a steric constraint on the local coordination environment.[98] Other studies suggest that the larger bim^- linker exhibits a weaker Zn−N bond strength compared to im^- and enables a stronger distribution of the negative charge. Both factors have been found to be correlated with lower melting and glass transition temperatures in various glass-forming ZIFs exhibiting **cag** topology.[105] Furthermore, the enthalpy and entropy of melting was found to be significantly lower for ZIF-62, compared to ZIF-zni, indicating lower enthalpic and entropic differences between the crystalline and liquid state for ZIF-62.[103]

Surprisingly, while the pore volume* of crystalline ZIF-62 ($V_{pore} = 0.16\,cm^3\,g^{-1}$) is lower compared to ZIF-4 ($V_{pore} = 0.25\,cm^3\,g^{-1}$), the respective glasses show the opposite relation with gZIF-62 ($V_{pore} = 0.12\,cm^3\,g^{-1}$) having a slightly larger pore volume than gZIF-4 ($V_{pore} = 0.10\,cm^3\,g^{-1}$).[96] Consequently, V_{pore} decreases by $\sim 60\%$ for ZIF-4 upon vitrification, whereas for ZIF-62 only a reduction of $\sim 25\%$ was observed, suggesting that the crystalline and glass state of ZIF-62 exhibit a similar pore structure.[96]

ZIF-62 remains the best-investigated ZIF glass former in the field of MOF glasses. Its large thermal stability window allows for advanced processing techniques such as vacuum hot-pressing, remelting, and annealing providing bubble-free, transparent glasses with promising mechanical properties.[104] Other studies have been investigating the application of ZIF-62 glass membranes, which were shown to achieve remarkable separation performances for various gas mixtures, such as H_2/CH_4, CO_2/N_2 and CO_2/CH_4.[40,106] Further examples for applications-related studies employing ZIF-62 glass underline the immense potential that lies in the application of this prototypical ZIF glass former.[101,107]

3.5.3 Other glass-forming ZIFs

Despite the intense research that has been done to investigate the origin and the structural prerequisites for the melting of MOFs, this phenomenon is still not fully understood and subject of ongoing research.[103,105,108,109] Consequently, the structural variety of identified ZIF glass formers is still strongly limited. Examples range form im^--based ZIF-4 ($Zn(im)_2$) polymorphs which transition to a high-temperature ZIF-zni phase ($T_m \approx 580\,°C$) and do not exhibit a stable liquid phase,[110] to a variety of mixed-linker ZIFs which generally employ imidazolate (im^-) in combination with another bulkier imidazolate-type linker (e.g. bim^-, 5-methylbenzimidazolate (mbim)) in various ratios.[111–113] A frequently mentioned approach to tuning the (thermal) properties of ZIF glasses focuses on manipulating the nitrogen-metal bond strength and stability to influence corresponding dissociation events in the liquid state. This strategy gave rise to ZIFs employing linkers decorated with electron-withdrawing groups (e.g., halogen-, nitro- or cyano-decorated imidazolate-type linkers) which aim to weaken the M−N (M = metal) bond strength thus promoting glass formation[105,114] as well as the used of different metal ions, such as Co^{2+}[115] or Fe^{2+}[116]. Recently, post-synthetic linker exchange was demonstrated to even induce glass-forming behavior in non-melting ZIF-8.[109]

A recent study by W.-L. Xue *et al.* explored the direct transformation of both meltable and non-meltable ZIFs into the glass state via ball milling (i.e., automated grinding of the crystalline ZIF). The resulting mechanically amorphized materials exhibit high network

*Micropore volumes are derived from CO_2 gas sorption isotherms collected at 195 K. The values correspond to ZIF-62 with $x = 0.35$.

disorder, an increased density, as well as a glass transition upon heating. This approach demonstrates a novel route to access ZIF glasses that are not thermally accessible.[117]

3.6 Modification of Glasses

3.6.1 Traditional Modification of (Silicate-) Glasses

Up to this point, only single-component, initially crystalline glass-formers such as ZIF-62 or SiO_2 were discussed (see Section 3.5.2). Both materials have in common that they exhibit a network structure in the crystalline and in the glass state. However, a glass with the chemical composition SiO_2, so-called quartz glass, can only be found in specialized applications, such as optical fibres, or halogen lamps.[46] In many other real-life applications, the glass former is modified by the addition of modifiers, so-called *fluxes*. Commonly, these fluxes are metal(-loid) oxides, such as Na_2O, CaO, Al_2O_3 or B_2O_3, which are added to the crystalline glass former before melt-quenching. The name *flux* refers to the resulting lower melting temperature and enhanced degree of sintering upon the addition of the modifiers during melt-quenching.[118] In the liquid state, the compounds intermix and react, yielding a modified silicate glass upon cooling of the melt with distinctly different material properties compared to quartz glass.

This concept of traditional silicate glass modification has been developed throughout human history and forms the basis of an immense variety of silicate glasses with various properties depending on the respective chemical composition. Today, numerous commercially available silicate glass systems have evolved, each with their unique set of properties and applications (see Table 3.1).[119]

Table 3.1. Selection of common types of silicate glasses together with their respective chemical composition and commercial name. Adapted from reference[119].

Glass type	Composition (wt.%)				
	SiO_2	B_2O_3	Al_2O_3	Na_2O	CaO/MgO
Borosilicate (Pyrex®)	> 65	> 8	$0 - 5$	–	–
Alumino-silicate (Xensation®)	< 60	–	$10 - 25$	–	–
Alumino-borosilicate (EagleXG®)	$55 - 65$	$5 - 10$	$15 - 20$	–	–
Soda-lime	≈ 71	–	$0 - 2$	15	$13 - 16$

Borosilicate glasses, for instance, are characterized by their exceptionally high chemical durability and thermal shock resistance, justifying their use for labware and consumer products like ovenware.[120]. Gorilla® glass, which is a trademark of the Corning company, is an ion-exchanged alkali-aluminosilicate glass, which is widely used in touchscreen applications due to its improved scratch resistance and toughness.[121] The most abundant type of glasses is soda-lime glasses, which exhibit a low liquid-state viscosity, resulting in facilitated processing conditions for the production of bottles and flat glass.[46]

The development of an understanding of the relation between the structural motives of the incorporated modifier and the modifier-induced changes in the material's properties is a focal point of glass science. In this regard, sodium-silicate glasses (i.e., Na_2O modified SiO_2 glass) represent a well-investigated binary silicate glass system where the influence of Na^+ incorporation has been thoroughly investigated. The incorporation of only 20 mol % Na_2O is known to lower the glass transition temperature from 1200 °C (T_g of quartz glass) to only around 500 °C with a monotonously reduction of T_g upon further Na_2O addition up to ca. 66 mol % Na_2O.[56] A similar trend in the compositional dependency was found for the liquid viscosity of sodium silicate glasses at 1200 °C with a decrease in about 10 orders of magnitude from ca. 10^{12} Pa s (for quartz glass) to $< 10^2$ Pa s for glass compositions containing > 25 mol % Na_2O at 1200 °C.[122,123]

On a structural level, the effect of alkali oxide and alkaline earth oxide incorporation is often discussed in terms of a depolymerization mechanism that lowers the average network connectivity* by the creation of non-bridging oxygens (NBOs) (see Figure 3.14).[54] While unmodified SiO_2 glass mostly maintains an average network connectivity close to four (i.e., most $[SiO_4]$ tetrahedra are connected to four neighboring $[SiO_4]$ tetrahedra), the average network connectivity is continuously reduced upon growing amounts of Na_2O incorporation.[124]

*The term connectivity is understood as the average number of Si centers that are directly linked to a neighboring Si center via a bridging oxygen (BO).

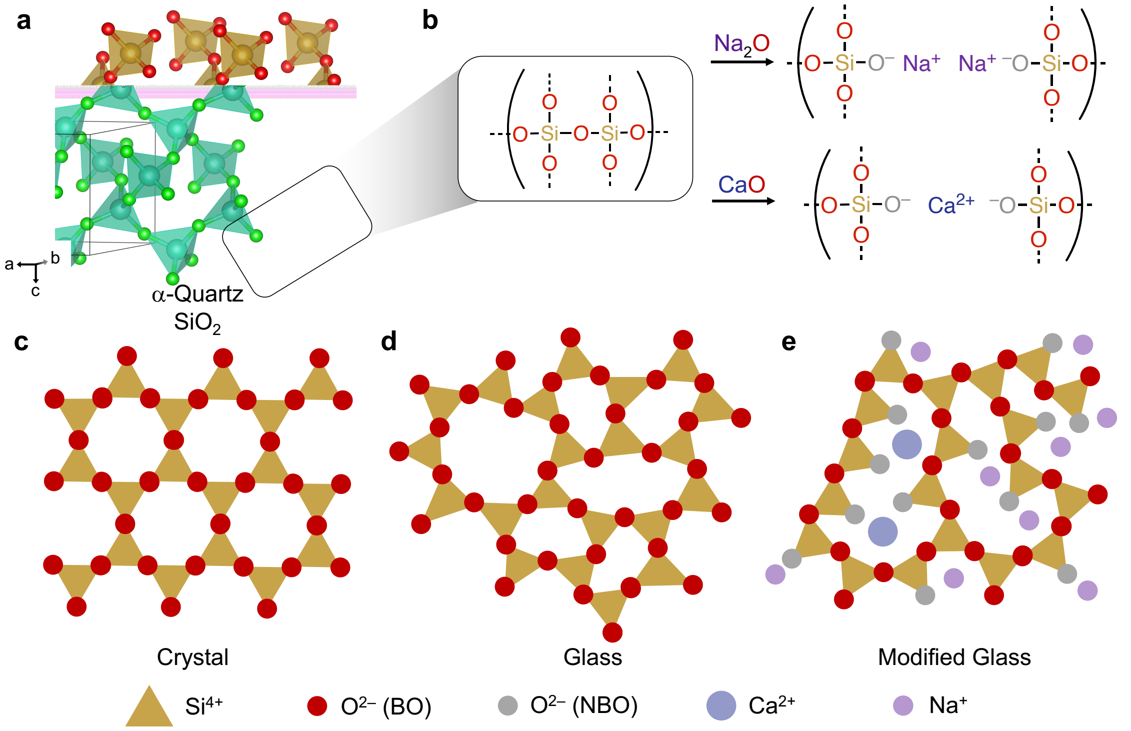

Figure 3.14. **a** Crystal structure of SiO_2 in the form of α-Quartz (Crystallography Open Database (COD): 9012602). **b** Schematic representation of the reaction of the glass-forming SiO_2 network with modifiers (Na_2O and CaO) during melt-quenching showing the formation of NBOs (grey) upon modifier incorporation. **c**,**d**,**e** Schematic representation of the structure of crystalline SiO_2 (**c**), the corresponding unmodified glass (**d**), and the modified glass (**e**) as a two-dimensional projection (four-fold connected [SiO_4] tetrahedra are represented as three-fold connected yellow triangles). Panel **e** demonstrates the reduction of the average network connectivity through modifier incorporation (i.e., network depolymerization) by the transformation of binding oxygens (BO, red) into non-binding oxygens (NBO, grey). Adapted and modified from reference[41] and[118].

The incorporation of an alkali modifier can be understood as a dilution of the SiO_2 network consisting of (partly) directional covalent Si–O bonds by the undirectional electrostatic interaction formed by the alkali or alkaline earth ions with the oxide anions of the glass network upon incorporation (see Figure 3.14e).[124] The drop in viscosity is therefore rationalized by the decrease in network connectivity allowing for diffusion of structural units near T_g.[54] Consequently, the GS of alkali silicate glasses is significantly reduced compared to unmodified silicate glass as the reduced network connectivity facilitates the structural rearrangements necessary for crystallization.[54] Extended X-ray absorption fine structure (EXAFS) spectroscopic studies found that Na^+ in sodium silicate glass exhibits a variety of local structures with Na–O coordination numbers ranging from five to six.[125] Further studies performed by Greaves *et al.* suggest the presence of sodium channels in sodium silicate glasses.[125] These percolation channels are seen as dynamic in origin rather than the result of microsegregation processes in the modified glass and are present on a larger structural scale.[124,126]

However, these structural features evoke further changes in material properties, including a decreased chemical stability and increased hydrophilicity, hampering their use in real-life applications. To overcome this limitation, the low chemical stability of sodium silicate glass can be enhanced by incorporation of a second modifier, CaO. The resulting soda-lime glass exhibits an enhanced chemical durability caused by the less mobile Ca^{2+} ions, which form a chemical barrier preventing water-induced leaching of Na^{+} ions from the soda-lime glass (see Table 3.1).[47,127]

Hence, the application of the concept of glass modification is vital to the field of silicate glasses and paved the way for countless areas of applications in our modern world.

3.6.2 Modification of ZIF glasses – General Strategies

For the modification of ZIF glasses, several general strategies have been developed so far. The earliest approach deals with the manipulation of the chemistry of the initially crystalline glass former. Strategies, such as employing linkers, which weaken the metal-linker bond strength, thus promoting bond dissociation in the liquid state, have already been discussed in Section 3.5.3. This Section, however, focuses on a variety of strategies of ZIF glass modification reported in the literature, which include a second modifying compound that is added before melt-quenching. An overview of the reported approaches on ZIF glass modification is given below:[128]

1. **Guest-impregantion of a crystalline glass-former**
   One well-established strategy to influence glass-forming behavior in ZIFs is guest-impregnation of a porous (non-) meltable ZIF. The additional stabilizing host-guest interactions in the denser infiltrated material reduce the barrier for bond dissociation via charge balancing in the liquid state, while the infiltration-associated structural disorder acts as an entropic contribution to the T_m reduction.[129,130] This strategy not only influences the materials properties of glass-forming ZIFs but was also shown to initiate glass-forming behavior in non-melting ZIFs. The ionic liquid impregnation of initially non-meltable ZIF-8 represents a prominent example amongst others.[129,130] In a recent study, high-pressure water infiltration was shown to reduce T_m and T_g in ZIF-62 significantly by $> 100\,°C$.[131]

2. **Melt-quenching of a glass-forming ZIF with another MOF**
   a) **Glass composites**
      Another strategy to modify ZIF glasses consists of a combination of a glass-forming ZIF with another non-melting MOF. The resulting crystal-glass composite represents a further widely reported possibility for introducing new properties such as higher porosity and enhanced gas uptake to the glass former.[132,133] Prominent examples are the embedding of non-melting high porous and crystalline UiO-66* in an amorphous *g*ZIF-62 glass matrix.[132]

*UiO-66 (chemical composition: $Zr_6O_4(OH)_4(bdc)$, bdc^{2-} = 1,4-benzenedicarboxylate)

b) Flux-melted and liquid-blended ZIF glasses

A homogenous incorporation of the modifying second compound can be achieved via the liquid blending of two meltable ZIFs which intermix in the liquid phase or by the dissolution of a non-melting ZIF in the glass-forming ZIF in the liquid state (i.e., flux-melting). Examples range from the liquid phase blending of ZIF-4(Co)[†] with ZIF-62,[134] to the flux-melting of non-meltable ZIF-8 with ZIF-62.[135] Both approaches provide homogenous and amorphous vitrified materials, which exhibit a single glass transition upon heating of the modified glass.[128]

These literature-known approaches to modifying ZIF glasses differ from the established strategies of traditional (silicate-) glass modification. In only a limited number of examples, a homogeneous incorporation of the modifier into the glass former can be achieved. These examples mostly include the mentioned flux-melting approaches as well as the results achieved via liquid-phase blending of ZIFs (category 2b). These approaches, however, although yielding homogenously modified ZIF glass materials either involve a third organic linker like the 2-methylimidazolate (mim^-) of ZIF-8 or they introduce a further type of transition-metal node which does not substantially differ from the metal node of the pure glass former regarding the directionality and strength of the metal-linker bond and their respective coordination geometry. Consequently, modifier-induced changes in the network connectivity are not expected.

During the preparation of this thesis, a publication by F. Cao *et al.* appeared, investigating the modification of glass-forming ZIF-4 and ZIF-62, as well as the non-glass-forming ZIF-8, using hydrohalide salts of benzimidazole ($bim \cdot HCl$, $bim \cdot HBr$, $bim \cdot HI$) and other heterocycles.[136] The authors produced clear and homogeneously modified ZIF glasses in most cases, except for ZIF-8-based systems, and reported a modifier-induced decrease in T_g.

Structural and thermal analyses indicate a depolymerization of the ZIF glass network upon modification. The modified glasses feature halide–Zn bonds as well as “dangling” (i.e., singly bound) and formally unbound (benz-)imidazoles. Upon sintering, the modified glasses showed an increase in T_g, attributed to repolymerization of the framework after evaporation of unbound or singly bound (benz-)imidazoles accompanied by the substitution of bridging imidazolates by bridging halides.[136]

Although the observed trend in T_g is rationalized by a framework depolymerization mechanism, resembling established structure–property relations from silicate glass chemistry, the use of hydrohalide salts of (benz-)imidazoles leads to a formal substitution of former bridging imidazolate linkers by halides. This approach therefore differs fundamentally from classical silicate glass modification (see Figure 3.14), where network depolymerization is induced by the incorporation of (alkali) metal(loid) oxides rather than substitution of the oxide anion itself.

[†] ZIF-4(Co) refers to the Co analog of ZIF-4 (**cag** topology) with the chemical composition $Co(im)_2$, im^- = imidazolate.

Consequently, the reported ZIF glass modification approaches lack the conceptual framework of structure–property relationships that is well established for silicate glass systems, where material properties can be systematically tuned through compositional changes. In the following, this research gap will be addressed, starting with the synthesis and characterization of appropriate ZIF glass modifiers Na(bim) and Li(bim) to closely mimic the concept of silicate glass modification.

4 Lithium and Sodium Benzimidazolate Coordination Networks: Syntheses, Structures, and Thermal Properties

The work presented in this chapter was published in a peer-reviewed research article.[137] The text and figures are reproduced or adapted from the preprint version of the manuscript,[138] which is available under a Creative Commons Attribution 4.0 International License (CC BY 4.0, https://creativecommons.org/licenses/by/4.0/legalcode). Adaptations include modifications in nomenclature and rearrangements of figures. Full citation details and author contributions are provided below.

Authors

Pascal Kolodzeiski[1], Erik Svensson Grape[2,#], Roman Pallach[1], Lennard Richter[1], A. Ken Inge[2], Sebastian Henke[1,*]

[1] Department of Chemistry and Chemical Biology, Technische Universität Dortmund, 44227 Dortmund, Germany.

[2] Department of Materials and Environmental Chemistry, Stockholm University, SE-10691 Stockholm, Sweden.

[#] Present address: Department of Chemistry and Biochemistry, Materials Science Institute, University of Oregon, Eugene, Oregon 97403, United States.

Publisher: Crystal Growth and Design (ACS Publications)
Date of Publication: August 23, 2024

Author Contributions

P.K. and L.R. synthesized the materials and conducted and analyzed the thermal analysis data and spectroscopic measurements. 3DED data collection and analysis was performed by E.S.G. and A.K.I.. P.K. collected and analyzed the XRPD data. R.P. performed the Rietveld refinement of β-Na(bim). The manuscript was written by P.K. and S.H. with contributions from the other authors.

Acknowledgements

This project received funding from Deutsche Forschungsgemeinschaft within the project 447344931 (HE 7628/7-1). P.K. acknowledges the Fonds der Chemischen Industrie for a

Kekulé-Fellowship. The authors thank DELTA Dortmund for allocation of beamtime at beamline BL9 and Christian Sternemann and Michael Paulus for their help with XRPD experiments at DELTA. We thank Diamond Light Source (DLS) for access to beamline I15-1 (CY31642) which contributed to the results presented here. Beamline scientist Philip Chater is acknowledged for supporting the XRPD experiments at DLS. We thank Jan-Benedikt Weiß, Wen-Long Xue and Chinmoy Das for their help with collecting the data at DLS.

4.1 Abstract

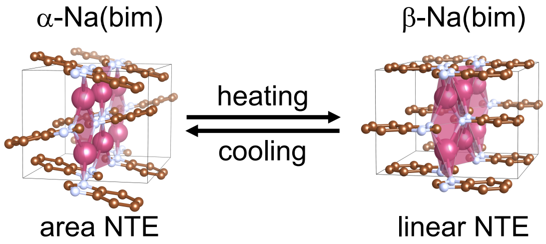

Alkali metal imidazolates are important compounds, serving as intermediates in organic synthesis and additives in alkali ion electrolytes. However, their solid-state structures and thermal behaviors remain largely unexplored. In this study, we present the synthesis, structural analysis and thermal characterization of lithium and sodium benzimidazolate (bim^-). The crystal structures of these microcrystalline materials, determined by 3D-electron diffraction, reveal closely related layered coordination networks. In these structures, fourfold N-coordinated alkali ions are bridged in two dimensions by bim^- linkers, with the networks' surfaces decorated by the phenyl rings of the bim^- linkers, stacking atop one another in the solid state. Differential scanning calorimetry combined with variable temperature X-ray powder diffraction indicate that both materials melt above 450 °C. Additionally, Na(bim) undergoes a displacive phase transition from an ordered α-phase to a highly disordered β-phase before melting. Structural variations, primarily attributable to the differing ionic radii of Li^+ and Na^+, result in distinct coordination environments of the alkali metal ions and varying orientations of the bim^- linkers. These differences lead to markedly distinct thermal behaviors: Li(bim) exhibits positive thermal expansion along all crystal axes, whereas Na(bim) switches from area negative thermal expansion (NTE) to linear NTE during the $\alpha \rightarrow \beta$ phase transition.

4.2 Introduction

Metal imidazolates form the basis for several different functional materials. The most prominent example is the family of zeolitic imidazolate frameworks (ZIFs), a subgroup of metal-organic frameworks (MOFs), exhibiting zeolitic topologies with open pores.[85,95] ZIFs consist of divalent transition metal ions, such as Zn^{2+} and Co^{2+}, which are tetrahedrally coordinated by the nitrogen atoms from imidazolate-type linkers that bridge adjacent metal centers. The imidazolates' structure-directing effect arises from the close resemblance of the metal–imidazolate–metal bond angle (around 145°) to the Si–O–Si bond angle observed in silicates and zeolites.[94] ZIFs are often subject to studies focusing on gas physisorption and separation applications due to their porous nature combined with a rather high chemical and thermal stability inherent to some members of this class of materials.[87,139] In the last decade many ZIF structures have been reported including mixed linker and mixed metal ZIFs[93,103,105] that feature different metal ions, such as Fe^{2+},[88] Cd^{2+},[89,90] Mn^{2+},[91] and Mg^{2+}.[92] By formal substitution of half of the divalent metal ions by trivalent B^{3+} and the other half by monovalent metal ions, such as Cu^+ or Li^+, a related class of materials denoted as boron imidazolate frameworks (BIFs) can be obtained.[140,141] While some BIFs exhibit zeolitic topologies, others such as BIF-40 (chemical composition: $CuBH(bim)_3$, bim^- = benzimidazolate) feature coordination units with trigonal connectivity and exhibit reductive properties originating from the hydridic hydrogen atom of $[BH(bim)_3]$.[141,142] In addition to the highly porous crystalline structures of ZIFs, their thermal properties have recently attracted significant interest.[143] Studies have shown that certain ZIFs, specifically those based on Zn^{2+}, Co^{2+}, and Fe^{2+}, can melt when heated to temperatures between around 400 °C to 600 °C under an inert atmosphere.[84,98,115,116] Upon cooling, these melts form amorphous glasses that retain some of their microporosity,[96,109] making them valuable for applications such as gas separation membranes[40,101] and (quasi-)solid electrolytes.[102,144] This melting and glass-forming ability is particularly noteworthy as it allows the materials to be shaped and molded in their liquid state, a capability not available in conventional non-meltable MOFs or coordination networks.[104,106] This unique property expands the practical applications and processing possibilities of ZIF-based materials, offering new opportunities for innovation in various fields.

Compared to the extensive structural information available for divalent metal imidazolates (e.g., ZIFs) and BIFs, very little is known about the solid-state structures of the simplest alkali imidazolate salts. This is surprising given the chemical simplicity of such compounds and their role in chemical synthesis and as additives for liquid lithium ion electrolytes. Examples from chemical synthesis include the preparation of N-functionalized imidazoles or the synthesis of imidazolium-based ionic liquids,[145–147] while several derivatives of lithium 4,5-dicyanoimidazolate salts are highly potent additives for liquid lithium ion electrolytes.[148–150] Given the demand for such alkali imidazolate salts is high, advanced knowledge about their synthesis, solid-state structures and thermal properties is crucial for their application. Due to their high hydrophilicity and the challenges associated with growing larger single crystals, only a very small number of alkali imidazolates have been structurally characterized to date. These include some alkali imidazolate salts A(im) (im^- = imidazolate; A^+ = Li^+, Na^+, K^+) as well as some mixed alkali and alkaline earth metal imidazolates.[151–153] A notable example is a microporous high-temperature polymorph of Na(im), which is obtained by heating the dense room temperature polymorph of Na(im) to 212 °C under an inert atmosphere.[153] In this work, we report the synthesis, structural analysis and thermal characterization of lithium and sodium benzimidazolate, Li(bim) and Na(bim). The crystal structures of the microcrystalline materials were derived from 3D electron diffraction (3DED) and variable temperature (VT) X-ray powder diffraction (PXRD). Both materials form 2D coordination networks with closely related structures. Differential scanning calorimetry (DSC) reveals that both materials melt at temperatures beyond 450 °C and fully recrystallize upon cooling the liquid phases. DSC and VTPXRD uncover that Na(bim) undergoes a thermally induced phase transition from a room temperature α-phase to a high-temperature β-phase before melting. The displacive phase transition can be explained by a highly anisotropic thermal expansion behavior of the α-phase which displays the very rare phenomenon of area NTE.

Analysis of the VTPXRD data reveals that the unusual thermal expansion behavior of Na(bim) originates from lattice vibrations and dynamical disorder in the crystal structure.

4.3 Results and Discussion

4.3.1 Synthesis and Structural Characterization

Li(bim) and Na(bim) were synthesized via an acid-base reaction of benzimidazole (Hbim) dissolved in dry THF with *n*-butyllithium (*n*-BuLi) or sodium hexamethyldisilazide (NaHMDS) as the metalation agents (see Experimental Section). While Li(bim) precipitates directly from the reaction solution, precipitation of Na(bim) was initiated by the addition of *n*-hexane to the reaction mixture. After washing the obtained powders with *n*-hexane, solvent residues and unreacted Hbim were removed by heating the products at 280 °C under a dynamic vacuum. Li(bim) was obtained as a colorless and Na(bim) as a slightly yellow but strongly hygroscopic microcrystalline powder. ^{1}H NMR spectra of the alkali salts dissolved in DMSO-d_6 and DCl/D_2O display only signals assigned to the hydrolysis product benzimidazole (Figures A1.1 and A1.2). The absence of HMDS byproducts in Na(bim) was proven by ^{29}Si NMR measurements (Figure A1.3). The absence of N–H stretching vibrations in the range from 2500 cm^{-1} to 3200 cm^{-1} in Fourier transform infrared (FTIR) spectra of the reaction products additionally proves the full deprotonation of Hbim (Figure A1.12). To further verify the chemical identity of the reaction product, thermal decomposition of the alkali salts under air was studied with simultaneous thermogravimetric and differential thermal analysis (STA), resulting in a total mass loss of 90.0% for Li(bim) (calc.: 90.6% for complete combustion to Li_2O) and 78.8% for Na(bim) (calc.: 78.0% for complete combustion to Na_2O) in the temperature range from 50 °C up to 1200 °C (see Figures A1.6 and A1.7). The crystal structures of Li(bim) and α-Na(bim) (i.e., the room temperature phase of Na(bim); the high temperature β-phase is discussed below) were solved by 3DED from submicron-sized crystals (Figure 4.1 and A1.8).* Both materials crystallize in the orthorhombic crystal system in the space groups *Cmme* (Li(bim)) and *Pbcm* (α-Na(bim)). In both cases, the alkali ions are fourfold coordinated by the N atoms of four bim$^-$ linkers. The [LiN_4] polyhedra in Li(bim) exhibit a flattened tetrahedral coordination geometry with a geometry index $\tau_4 = 0.68$ (with $\tau_4 = 1$ for the perfect tetrahedral environment and $\tau_4 = 0$ for the perfect square planar environment)[154], whereas the [NaN_4] polyhedra in α-Na(bim) feature an unusual coordination environment that is close to a square planar configuration ($\tau_4 = 0.23$). In both structures, each N atom of the bim$^-$ linkers bridges between two adjacent Li^+ or Na^+ ions so that each linker has contact to four alkali ions. The [LiN_4] and [NaN_4] polyhedra are connected with neighboring polyhedra by edge-sharing forming 1D inorganic rods that are bridged in the second dimension by bim$^-$ linkers to generate layered coordination networks. The phenyl rings of the bim$^-$ linkers are oriented alternatingly on opposite sides of the layer plane. The alkali ions as well as the bim$^-$ units

*CCDC 2364871-2364872 and 2365470 contain the supplementary crystallographic data for this paper. These data can be obtained free of charge via www.ccdc.cam.ac.uk/data_request/cif.

can both be regarded as four connecting vertices, so that the network topology can be classified as a binary square lattice (**sql**). In Li(bim), the bim$^-$ linkers are arranged perfectly perpendicular to the layer plane, whereas in Na(bim) they alternatingly tilt away from the plane normal, leading to a herringbone-like pattern when viewed along the crystallographic c-axis. The 2D coordination networks are tightly stacked on top of each other in the third dimension, forming a layered van-der-Waals crystal. The layer-layer distance (c-axis of Li(bim) and a-axis of α-Na(bim)) is much shorter for α-Na(bim) ($a_{3\mathrm{DED}} = 8.7500(17)$ Å) than for Li(bim) ($c_{3\mathrm{DED}} = 11.921(2)$ Å). This is because neighboring layers feature a stronger interdigitation of the bim$^-$ linkers in α-Na(bim) because of their alternate tilting.

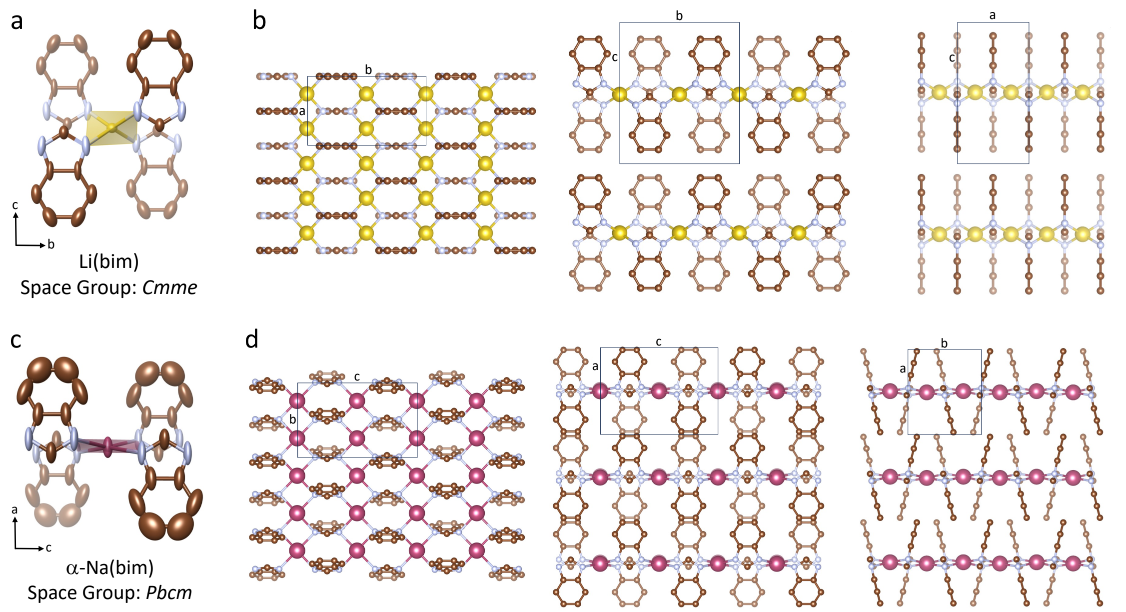

Figure 4.1. Crystal structures of Li(bim) and α-Na(bim) with Li (yellow), Na (purple), C (brown), N (blue). Hydrogen atoms are omitted for clarity. **a**, **c** Perspective view on the coordination environments of the metal sites in Li(bim) and α-Na(bim) with displacement ellipsoids drawn at the 50% probability level. **b**, **d** Orthographic representations of supercells of the crystal structures of Li(bim) and α-Na(bim) viewed along the crystallographic main axes.

The phase purity of the bulk materials was proven by structureless profile fits (Pawley method[62]) to PXRD patterns recorded at room temperature (see Figure A1.13 and A1.13). The lattice parameters obtained from the profile fit (Table A1.4) are 3% to 6% smaller than those derived from 3DED (Table A1.1), resulting in significantly smaller unit cell volumes from PXRD data. Specifically, the unit cell volume of Li(bim) from PXRD is 11.6% smaller, and that of Na(bim) is 13.7% smaller, compared to 3DED. This discrepancy can be attributed to the lower accuracy of the unit cell parameters provided by 3DED, due to various experimental challenges associated with the method and instrument.[155] We note that a synthesis protocol for Li(bim) and some basic structural characterization, including unit cell parameters and space group symmetry, were recently reported in a doctoral thesis.[152] However, atomic coordinates were not provided. The thesis proposed the space group symmetry *Pmca*, which is a non-isomorphic subgroup (albeit in a different axis setting) of the space group *Cmme* derived via 3DED.[152] We confirmed the validity of the structure with space group *Cmme* by profile fitting of the PXRD data of Li(bim), which showed that none of the additional Bragg reflections of the subgroup *Pmca* have non-zero intensity in the PXRD pattern (Figure A1.15).

4.3.2 Thermal Phase Behavior

STA of Li(bim) and Na(bim) in open alumina crucibles under an inert N2 flow revealed that the materials thermally decompose at 406 °C and 384 °C, respectively (Figure A1.4 and A1.5). In contrast, DSC analyses up to a temperature of 500 °C in hermetically sealed aluminum crucibles (Figure 4.2a) display endothermic melting signals at 487 °C with a melting enthalpy (ΔH_m) of 26.9 kJ mol^{-1} for Li(bim) and at 453°C with a ΔH_m of 24.7 kJ mol^{-1} for Na(bim). The assignment of the endothermic signals to melting events is based on the loss of Bragg reflections in variable temperature (VT)PXRD patterns collected at 500 °C (Figure 4.2b; samples sealed in quartz capillaries) and the transformation of a loose microcrystalline powder to monolithic shapes of sintered particles after heating the materials across their melting point in the DSC apparatus (see Figure A1.11). The slightly higher T_m and ΔH_m of Li(bim) compared to Na(bim) can be explained by the higher charge density of the smaller Li^+ ion compared to Na^+, leading to stronger ionic bonds for Li(bim). The observation that the materials only melt when heated in sealed vessels suggests they have a high vapor pressure below their melting temperatures. Consequently, if the samples are in an open environment, they decompose rather than melt, while they have a higher thermal stability and form a liquid if they are in a closed vessel. Na(bim) shows an additional weaker endothermic signal in the DSC upscan at 166 °C. This signal corresponds to a first-order solid-solid phase transformation from the room-temperature α-phase to a high-temperature β-phase. Determination and refinement of the crystal structure of the β-phase of Na(bim) from the VTPXRD data was successful and is discussed below. Li(bim) shows no additional phase change besides the melting event in the temperature range studied.

Cyclic DSC experiments, consisting of two consecutive heating-cooling cycles, prove that all phase transitions are reversible (Figure A1.9 and A1.10). While cooling the liquid Na(bim) from 470 °C to 100 °C, the exothermic recrystallization of the material occurs at 412 °C followed by the exothermic $\alpha \rightarrow \beta$ transition at 157 °C. The absolute value of the corresponding phase change enthalpies of Na(bim) is very close to those of the heating branch, thus indicating that thermal decomposition of the liquid Na(bim) at high temperatures is negligible. In contrast, the absolute value of the melting and recrystallization enthalpies of Li(bim) decreases during thermal cycling between 100 °C and 500 °C, suggesting partial thermal decomposition of the material at high temperature.

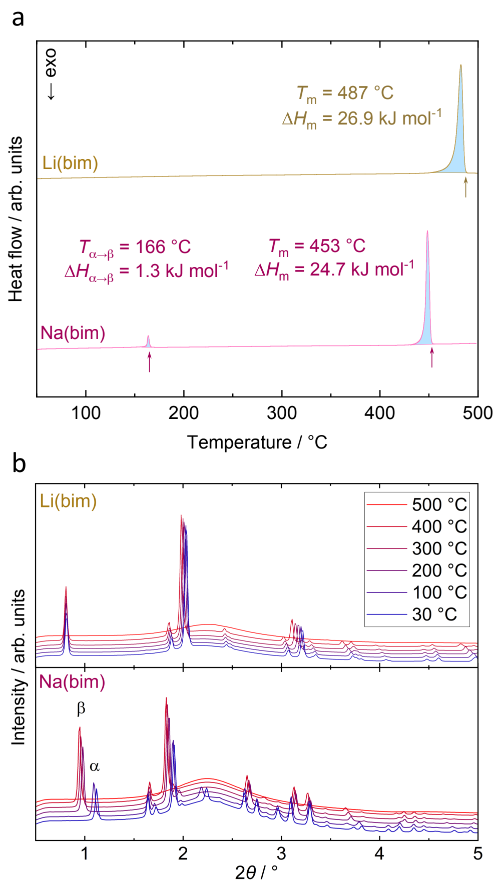

Figure 4.2. **a** Heat flow curves of Li(bim) and Na(bim) in a DSC experiment with a constant heating rate of 10 °C min^{-1} from room temperature up to 500 °C. **b** *In-situ* VTPXRD patterns of Li(bim) and Na(bim) ($\lambda = 0.1616$ Å) monitoring the thermal expansion and the phase transition from α- to β-Na(bim). The PXRD pattern recorded at 500 °C features only diffuse scattering in agreement with the melting signal in the DSC data.

The sharp peak observed in the heat flow curve of the DSC data during the $\alpha \to \beta$ phase transition of Na(bim) suggests that the transition is of a displacive nature, while the rather low $\Delta H_{\alpha\to\beta}$ (1.3 kJ mol^{-1}) and $\Delta S_{\alpha\to\beta}$ (2.9 J K^{-1} mol^{-1} indicate that the transition does not involve a major rearrangement of the structure.[156] The PXRD pattern of the β-phase has fewer reflections than the pattern of the α-phase, implying that β-Na(bim) has a higher symmetry (see Figure 4.2b). Indeed, the diffraction pattern of β-Na(bim) can be indexed with a slightly expanded unit cell in the space group *Aemm*, a minimal non-isomorphic supergroup of space group *Pbcm* (the symmetry of α-Na(bim)).[157] For structureless profile fitting (Pawley method[62]), the non-standard space group setting *Aemm* was transformed to the conventional setting *Cmme* by axis transformation (see Supplementary Information for details), yielding an excellent fit to the experimental PXRD pattern recorded at 200 °C. All other minimal non-isomorphic subgroups of *Pbcm* failed to provide a good fit to the data.

An initial structural model for β-Na(bim) was generated from the structure of α-Na(bim) through axis transformation and enforcement of *Cmme* symmetry (Figure 4.3). Subsequent Rietveld refinement[64] against the VTPXRD data of Na(bim) recorded at 200 °C resulted in a highly disordered structural model providing a good fit to the experimental data with satisfactory reliability factors ($R_{\mathrm{wp}} = 1.49\%$, $R_{\mathrm{exp}} = 1.80\%$, $R_{\mathrm{Bragg}} = 0.95\%$; details in the Supplementary Information). The derived structure of β-Na(bim) closely resembles that of Li(bim), which is also crystallizing in *Cmme*. The model for β-Na(bim) depicts a structure where the bim$^-$ linkers are oriented perfectly perpendicular to the coordination network layers. The refined isotropic atomic displacement parameters (ADPs) of the C and N atoms of the bim$^-$ linker indicate that these units strongly oscillate about the direction of the crystallographic *a*-axis (Figure 4.3a). Additionally, a dynamic displacement of all network atoms orthogonal

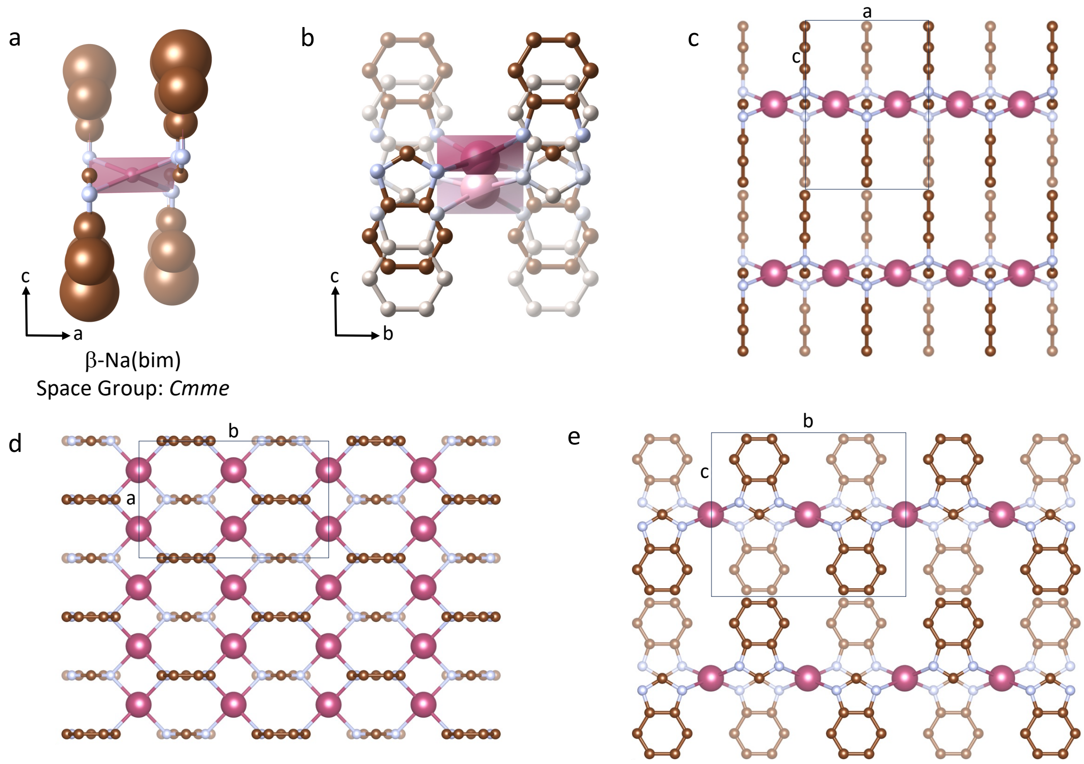

Figure 4.3. Crystal structure of β-Na(bim) with Na (purple), C (brown) and N (blue). Hydrogen atoms are omitted for clarity. **a** Coordination environment of Na atoms without positional disorder (i.e., only the atoms of one half-occupied molecular fragment are shown). The atomic radii correspond to the atoms' isotropic displacement parameters (drawn at a 50% probability level). **b** View on the coordination environment of Na atoms featuring positional disorder. The two Na(bim) molecular fragments (full-colored and color-desaturated) are translated along the c-axis and have an atomic occupancy of 1/2 each. **c**, **d**, **e** Orthographic views of supercells of a simplified ordered structure of β-Na(bim) obtained by averaging the atomic positions of the two molecular fragments shown in panel **b**. Views along the crystallographic main axes are shown.

to the plane of the 2D coordination network was evident in the Fourier difference map. Modeling this transverse displacement using anisotropic ADPs was not feasible due to the limited number of observed reflections in the PXRD data, resulting from the relatively poor scattering power of β-Na(bim) at 200 °C. Consequently, the displacement was accounted for by a split model representing two sets of atoms, each with 50% occupancy, displaced along the c-axis (Figure 4.3b). The large dynamic displacement of the atoms perpendicular to the plane of the 2D network is already apparent in the anisotropic ADPs of the Na, N and C atoms in the structural model of α-Na(bim) derived by 3DED (Figure 4.1c). Therefore, it is proposed that large amplitude transverse lattice vibrations drive the phase transition from the α- to the β-phase in Na(bim). Remarkably, the coordination environment of the Na^+ ions markedly changes from close to square-planar in α-Na(bim) ($\tau_4 = 0.23$) to a more tetrahedral environment in β-Na(bim) ($\tau_4 = 0.45$)[154].

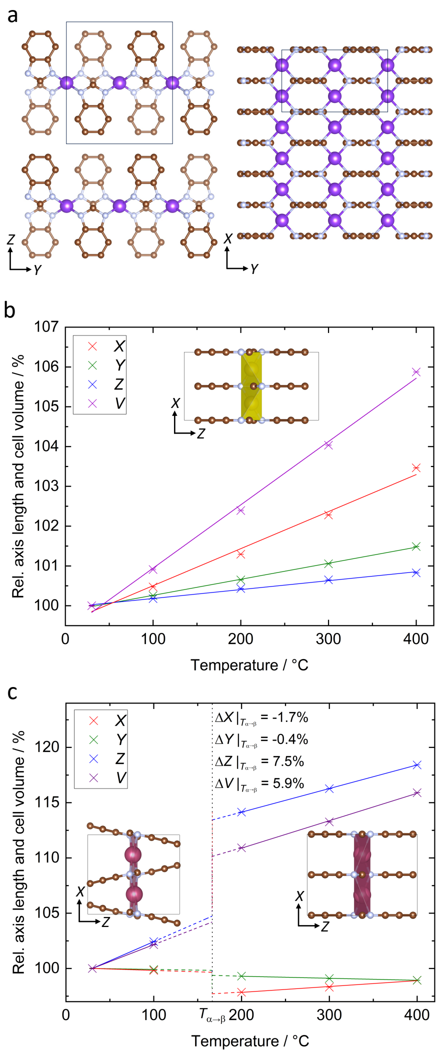

Figure 4.4. **a** Definition of the principal axes of expansion X, Y and Z illustrated with a generic A(bim) crystal structure with the metal ion A^+ = Li^+, Na^+ (violet), N (blue), and C (brown). **b**,**c** Progression of the principal axes X, Y and Z and the unit cell volume V of Li(bim) (**b**) and Na(bim) (**c**) in the temperature range from 30 °C to 400 °C. Na(bim) exhibits the $\alpha \to \beta$ phase transition at $T_{\alpha\to\beta} = 166$ °C. The lines are linear fits to the data. The uncertainties of the data are smaller than the size of the symbols. The graphical insets show excerpts of the crystal structures of the corresponding phases present in the respective temperature ranges with Li (yellow), Na (pink), C (brown), N (blue). Hydrogen atoms are omitted for clarity.

Structureless profile fitting of the VT PXRD patterns of Li(bim) and Na(bim) (Figure 4.2b) in the temperature range from 30 °C to 400 °C provided comprehensive information on the thermal expansion of the coordination networks and gave more insights into the $\alpha \to \beta$ phase transition of Na(bim) (Figure A1.17 and A1.19). To aid the comparison of the different phases involved, we define a set of orthogonal principal axes X, Y and Z (Figure 4.4a), which correspond to the lattice vectors lying parallel to the layer of the coordination networks (i.e. X along the rods of edge-connected $[LiN_4]/[NaN_4]$ polyhedra and Y along the bridging direction of the bim^- linkers) and the lattice vector perpendicular to it (Z). The relationship between the crystallographic lattice vectors a, b, c and the principal axes is given in Table A1.6. The corresponding linear thermal expansion coefficients α_l ($l = X, Y, Z$) describe the temperature-dependent change of the length of the principal axes l at constant pressure ($\alpha_l = \frac{1}{l}\frac{\mathrm{d}l}{\mathrm{d}T}$, whereas the volumetric thermal expansion coefficient α_V provides the magnitude of the volume change with increasing temperature ($\alpha_V = \frac{1}{V}\frac{\mathrm{d}V}{\mathrm{d}T}$) (see Section A1.9 for details). The thermal expansion coefficients are in the order of $10^{-6}\,\mathrm{K}^{-1}$ and are given in the unit MK^{-1} ($1\,\mathrm{MK}^{-1} = 10^{-6}\,\mathrm{K}^{-1}$).

Li(bim) continuously expands along all principal axes with the largest coefficient of thermal expansion (α) along the principal axis X ($\alpha_X = 92(5)\,\mathrm{MK}^{-1}$), which is the direction along the $[LiN_4]$ polyhedral rods (Figure 4.4b, Table 4.1). Along the principal axis Y (direction of bim^- linkers bridging between the polyhedral rods) and the principal axis Z (stacking direction of the 2D network), the thermal expansion is substantially smaller ($\alpha_Y = 40.0(6)\,\mathrm{MK^{-1}}$, $\alpha_Z = 22.3(10)\,\mathrm{MK^{-1}}$), resulting in a volumetric thermal expansion coefficient α_V of $154(5)\,\mathrm{MK^{-1}}$ and a total expansion by about 6% during heating from 30 °C to 400 °C (see Section A1.9 for details).

The thermal expansion behavior of Na(bim) differs substantially from the one of Li(bim) (Figure 4.4c, Table 4.1). Up to the $\alpha \rightarrow \beta$ phase transition at approximately 166 °C, α-Na(bim) shows a very large volumetric thermal expansion coefficient α_V of about $304\,\mathrm{MK^{-1}}$. The strong volumetric expansivity originates from the drastic expansion of the material along the Z axis ($\alpha_Z \approx 343\,\mathrm{MK^{-1}}$), whereas X and Y both contract upon heating ($\alpha_X \approx -26\,\mathrm{MK^{-1}}$, $\alpha_Y \approx -13\,\mathrm{MK^{-1}}$).

Thus, α-Na(bim) displays the very rare phenomenon of area NTE[158] with an area expansivity $\alpha_A = \alpha_X + \alpha_Y \approx -39\,\mathrm{MK^{-1}}$. The magnitude of α_A of α-Na(bim) is substantially larger than those of other materials featuring this property, for example $LiBeBO_3$ ($\alpha_A = -5.07(21)\,\mathrm{MK^{-1}}$)[159] and Zn(isonicotinate)$_2$ ($\alpha_A = -21.8(10)\,\mathrm{MK^{-1}}$[158]. The area NTE of α-Na(bim) acts in the layer of the 2D networks and can be explained by the large amplitude vibrations transverse to the layer plane (i.e., parallel to Z). These vibrations are also responsible for the $\alpha \rightarrow \beta$ phase transition (Figure 4.1c and 4.3b). In accordance with this rationale, the principal axes X and Y further contract by 1.7% and 0.5%, respectively, during the $\alpha \rightarrow \beta$ phase transition, while Z expands by 7.5%, resulting in a volume increase of 5.9%. The large expansion of Z is driven by the vibrational motion of the network's building units in β-Na(bim) and the change in the geometry of the [NaN_4] polyhedra from close to square planar (α-phase) to more tetrahedral (β-phase) as discussed above. Upon further heating, β-Na(bim) keeps expanding primarily along the Z axis, even though α_Z ($183.7(4)\,\mathrm{MK^{-1}}$) is only about half as large as for α-Na(bim). Moreover, α_X is positive ($54(5)\,\mathrm{MK^{-1}}$) and α_Y remains negative ($-18.5(17)\,\mathrm{MK^{-1}}$) in α-Na(bim), so that the material switches from area NTE to linear NTE at the $\alpha \rightarrow \beta$ phase transition. The volumetric expansivity is smaller in β-Na(bim) compared to β-Na(bim) but α_V is still larger than the one of Li(bim) and amounts to $219(6)\,\mathrm{MK^{-1}}$. This again is a signature of the large amplitude lattice vibrations of β-Na(bim) and the weaker metal-nitrogen bonds in Na(bim) compared to Li(bim), consistent with the lower melting temperature of the sodium derivative.

4.4 Conclusion

We have successfully synthesized and characterized the crystal structures and thermal properties of Li(bim) and Na(bim). 3DED revealed that both materials crystallize in the orthorhombic crystal system, forming closely related layered coordination networks. DSC and VTPXRD revealed that both Li(bim) and Na(bim) melt above 450 °C. Notably, Na(bim) undergoes an additional displacive phase transition from an ordered α-phase to a dynamically disordered β-phase at approximately 166 °C. Li(bim) exhibits positive thermal expansion along all principal axes within the studied temperature range. In contrast,

Table 4.1. Linear and volumetric thermal expansion coefficients of Li(bim), α- and β-Na(bim). The principal axes X, Y, and Z correspond to the crystallographic axes a, b, and c for Li(bim) and β-Na(bim), and to b, c, and a for α-Na(bim). Standard deviations for the thermal expansion coefficients of α-Na(bim) are not provided, as only two datasets have been recorded for this phase. Overall, the reliability of the reported uncertainties is constrained by the limited number of diffraction patterns recorded at varying temperatures (see Table A1.7 and A1.8).

	$\alpha_X/\mathrm{MK}^{-1}$	$\alpha_Y/\mathrm{MK}^{-1}$	$\alpha_Z/\mathrm{MK}^{-1}$	$\alpha_V/\mathrm{MK}^{-1}$
Li(bim)	92(5)	40.0(6)	22.3(10)	154(5)
α-Na(bim)	–26	–13	343	304
β-Na(bim)	54(5)	–18.5(17)	183.7(4)	219(6)

α-Na(bim) displays the very rare phenomenon of area NTE, due to large amplitude lattice vibrations orthogonal to the layer plane of the coordination network. These vibrations also drive the $\alpha \rightarrow \beta$ phase transition in Na(bim), resulting in a significant change in the coordination environment of the Na^+ ions from close to square planar in the α-phase to more tetrahedral in the dynamically stabilized β-phase. As a result, Na(bim) switches from strong area NTE in the α-phase to linear NTE in the β-phase. This study underscores the influence of the differing ionic radii of Li^+ and Na^+ on the structural and thermal properties of their respective benzimidazolate compounds. Na(bim) exhibits weaker metal-nitrogen bonds compared to Li(bim), consistent with its lower melting temperature. These structural variations lead to distinct thermal behaviors, with Na(bim) displaying complex thermal expansion characteristics, unlike the consistently positive thermal expansion observed in Li(bim). Due to the markedly different thermal expansion behaviors of the β-Na(bim) and Li(bim) phases, the presence of a low-temperature α-Na(bim)-like phase of Li(bim) is considered unlikely. Overall, this research provides valuable insights into the structural dynamics and thermal properties of alkali metal benzimidazolates, contributing to a deeper understanding of these materials and their potential applications. The discovery of strong area NTE in α-Na(bim), associated with large magnitude transverse vibrations, provides a guide for the design of this unusual property in other layered coordination networks. Moreover, the accessible liquid phase of Li(bim) and Na(bim) opens up new possibilities for their use as fluxes in the preparation of various vitreous composite materials. Specifically, these compounds could serve as effective network modifiers in the preparation of MOF and coordination polymer glasses.[160]

5 From Glass Modifiers to Modified Glasses

As illustrated in the published peer-reviewed research article that constitutes the foregoing Chapter 4, the glass modifiers Na(bim) and Li(bim) have been synthesized and characterized successfully regarding their thermal and structural properties.[137] With this achievement, the first work package presented in the project outline in Chapter 1 is completed.

The crystal structures of Li(bim) and Na(bim) reveal layered two-dimensional coordination networks, in which fourfold N-coordinated alkali ions are bridged by benzimidazolate linkers. The compounds melt at 453 °C (Na(bim)) and 487 °C (Li(bim)) respectively, and recrystallize upon cooling. Due to the larger ionic radius of Na^{+}, the metal–linker bonds in Na(bim) are weaker, resulting in a lower melting temperature (T_{m}) compared to Li(bim). Both melting temperatures further fall below the decomposition temperature of the designated glass former ZIF-62 ($T_{\mathrm{d}} = 555-600\,°\mathrm{C}$).[103] In addition to this important prerequisite as an adequate glass modifier for ZIF-62, Na(bim) exhibits an endothermic, displacive phase transition at 166 °C, which appears as a helpful indicator for monitoring the chemical incorporation of the modifier into the glass former, observable in calorimetric measurements.

Given these intermediate results, the following Chapter 6 explores the application of Na(bim) and Li(bim) as modifiers in the glass modification of the glass former ZIF-62 upon melt-quenching and analyzes the modifiers' influence on the thermal and structural properties of the modified glasses. This approach parallels the chemistry of traditional silicate glass modification and investigates the transferability of long-established concepts of (silicate) glass modification to the class of modified ZIF-62 glasses.

6 Alkali-Ion-Modified Zeolitic Imidazolate Framework Glasses

The work presented in this chapter is currently under review for publication in a peer-reviewed journal. The text and figures are reproduced or adapted from the preprint version of the manuscript,[161] which is available under a Creative Commons Attribution 4.0 International License (CC BY 4.0, https://creativecommons.org/licenses/by/4.0/legalcode). Adaptations include modifications in nomenclature and rearrangements of figures, while supplementary analytical data were added to improve clarity and completeness. Full citation details and author contributions are provided below.

Authors

Pascal Kolodzeiski[1], Benjamin M. Gallant[2], Lennard Richter[1], Mario Antonio T. Ongkiko[3], Carlo Franke[4],Aleksander Kostka[5],Wen-Long Xue[1], Chinmoy Das[1,6], Jan-Benedikt Weiß[1], Elena Kolodzeiski[7], Thomas Kress[8], Gregor Kieslich[7], Tong Li[4], Andrew J. Morris[3], Dominik Kubicki[2], Sebastian Henke[1,*]

[1] Fakultät für Chemie und Chemische Biologie, Technische Universität Dortmund, Otto-Hahn-Straße 6, 44227 Dortmund, Germany.

[2] School of Chemistry, University of Birmingham, Edgbaston, B15 2TT, United Kingdom.

[3] School of Metallurgy and Materials, University of Birmingham, Elms Road, Edgbaston, Birmingham, B15 2TT, United Kingdom.

[4] Faculty of Mechanical Engineering, Atomic-scale Characterisation, Ruhr-Universität Bochum, Universitätsstraße 150, 44801 Bochum, Germany.

[5] Center for Interface-Dominated High Performance Materials (ZGH), Ruhr-Universität Bochum, Universitätsstraße 150, 44801 Bochum, Germany.

[6] Department of Chemistry, SRM University-AP, Amaravati, Andhra Pradesh-522240, India.

[7] Department of Chemistry, TUM School of Natural Sciences, Technical University of Munich, Lichtenbergstraße 4, 85748 Garching, Germany.

[8] Yusuf Hamied Department of Chemistry, University of Cambridge, Cambridge, CB2 1EW, United Kingdom.

Date of Submission: January 24, 2025

Author Contributions

The project was conceptualised by S.H and P.K. Synthesis and thermal analysis were performed by P.K., L.R. and J.-B.W.. W.-L. X. and C.D. helped with the collection of (*in-situ*) X-ray diffraction and total scattering data. W.-L.X. analyzed the XAFS measurements. XPDF analysis, IR spectroscopy and gas sorption measurements were performed by P.K.. B.M.G. and D.K. conducted and analysed the (*in-situ*) MAS NMR measurements. Corresponding DFT calculations were performed by M.A.T.O. and A.J.M.. T.K. analysed the MAS NMR spin-lattice relaxation measurements. C.F. and T.L. collected and analysed the APT data and performed SEM imaging. STEM-EDX measurements were performed by A.K.. E.K. provided the DFT calculations on the vibrational states of Na(bim). G.K. provided advisory support throughout the work on this project. The manuscript was drafted by P.K. and S.H. with contributions from the other authors.

Acknowledgements

This project received funding from Deutsche Forschungsgemeinschaft within the project 447344931 (HE 7628/7-1) and by an Exploration Grant of Boehringer Ingelheim Foundation (S.H.). P.K. acknowledges the Fonds der Chemischen Industrie for a Kekulé-Fellowship. The authors thank DELTA Dortmund for the allocation of beamtime at BL9 as well as Christian Sternemann and Michael Paulus for their support with PXRD experiments at DELTA. We thank Diamond Light Source (DLS) for access to beamline I15-1 (CY31642-1) and beamline scientist Philip Chater for the support in the total scattering experiments. We further acknowledge Deutsches Elektronen-Synchrotron (DESY) for access to beamline P02.1 (I-20220350) and the associated beamline scientists for their help with the total scattering experiments. Computations have been carried out using computational and data resources provided by the Leibniz Supercomputing Centre (www.lrz.de). T.L. and C.F. thank the DFG Major Research Instrumentation Programme (GZ: INST 213/1049-1FUGG) for financial support in purchasing the Ferrovac VCTM VSN40S and customized Sylatech GB1500-E glovebox. T.L. and C.F. acknowledge the Zentrum für Grenzflachendominierte Hochstleistungswerkstoffe (ZGH) at Ruhr University Bochum for the access to infrastructures (Cameca LEAP 5000 XR, FEI Helios G4 CX SEM/FIB, and JEOL JEMARM 200F). Computing resources were provided by the University of Birmingham's BlueBEAR HPC service and the Sulis Tier 2 HPC platform (EP/T022108/1), with 25 networking support from CCP-NC (EP/T026642/1), CCP9 (EP/T026375/1), and UKCP (EP/X035891/1). This work was facilitated by software tools (specifically Soprano) developed by the Collaborative Computing Project for NMR

Crystallography, funded by EPSRC grant EP/T026642/1. B.M.G. and D.J.K. acknowledge the UKRI Horizon Europe guarantee funding (PhotoPeroNMR, Grant Agreement EP/Y01376X/1) and the UK High-Field Solid-State NMR Facility at the University of Warwick (funded by EPSRC; EP/T015063/1,EP/R029946/1), which have been used in this research to support the solid-state NMR measurements in this work.

6.1 Abstract

Modifying glass compositions is key to creating silicate-based glasses for technologies like optical fibres, catalytic supports, protective coatings, and separation membranes. Here, we extend this concept to metal-organic framework (MOF) glasses by modifying the MOF glass former ZIF-62 ($Zn(im)_{1.8}(bim)_{0.2}$, im^- = imidazolate, bim^- = benzimidazolate) with Na(bim) and Li(bim) as a compatible glass modifier. Melt-quenching of physical mixtures with varying Na(bim) content ($x\,Na(bim) \cdot Zn(im)_{1.8}(bim)_{0.2}$, $0 < x < 1.5$) produces modified MOF glasses with a systematic decrease in the glass transition temperature (T_g), and increased liquid fragility, configurational heat capacity (ΔC_V) at T_g, and density as x increases – paralleling the chemistry in silicate glasses due to partial network depolymerization. Structural and spectroscopic analysis, coupled with density-functional theory calculations, confirm that Na(bim) is incorporated homogeneously into the MOF glass network rather than in the MOF pores and reveal the presence of undercoordinated sodium ion environments. Finally, extraction of the modifier by water treatment increases glass porosity, akin to established borosilicate glass processes. Thereby, we introduce a transferable approach for tailoring the structure and properties of MOF glasses, expanding possibilities for these functional glass materials.

6.2 Introduction

Glass manufacturing dates back to ancient civilizations, with early glass fragments from Egypt and Mesopotamia demonstrating an early understanding of how additives influence silicate glass properties.[42] The addition of fluxes, such as metal oxides and carbonates, to SiO_2 lowers processing temperatures and facilitates glass formation by disrupting the network of corner-sharing $[SiO_4]$ tetrahedra (Figure 6.1a).[118] Modifiers like Na_2O reduce the number of bridging oxygens, creating non-bridging oxygens and depolymerizing the framework, which alters the glass's thermal, optical, and mechanical properties.[46,118] This ability to tailor glass properties through compositional changes has made glass modification a cornerstone of modern glass science and technology, enabling applications from everyday products such as windows to advanced aerospace seals and pharmaceutical packaging.[162,163] The remarkable versatility of silicate glasses stems directly from their tunability through compositional changes, which continues to drive innovation across diverse industries.[46]

Recently, metal-organic framework (MOF) glasses emerged as a new class of glass formers offering unique structural and functional properties.[37,84] Among them, zeolitic imidazolate frameworks (ZIFs) have garnered significant attention due to their structural similarities to aluminosilicate zeolites, including tetrahedral coordination of the metal ions and similar metal-ligand-metal bond angles.[85,87] ZIF-62 ($Zn(im)_{1.8}(bim)_{0.2}$, im^- = imidazolate, bim^- = benzimidazolate) is one of the first ZIFs shown to exhibit melting upon heating and glass formation upon subsequent cooling of the melt (i.e. melt-quenching).[98] The ultrahigh glass-forming ability and the partially maintained microporosity make ZIF-62 glass an interesting candidate for gas separation applications.[57,96,103] The absence of grain boundaries and the potential for melt-processing (e.g. moulding) further enhance its appeal for membrane applications.[107,164] However, the number of MOFs capable of forming glasses is strongly limited, and the factors governing their glass formation remain a topic of vast research interest.[105,109,112,113,117]

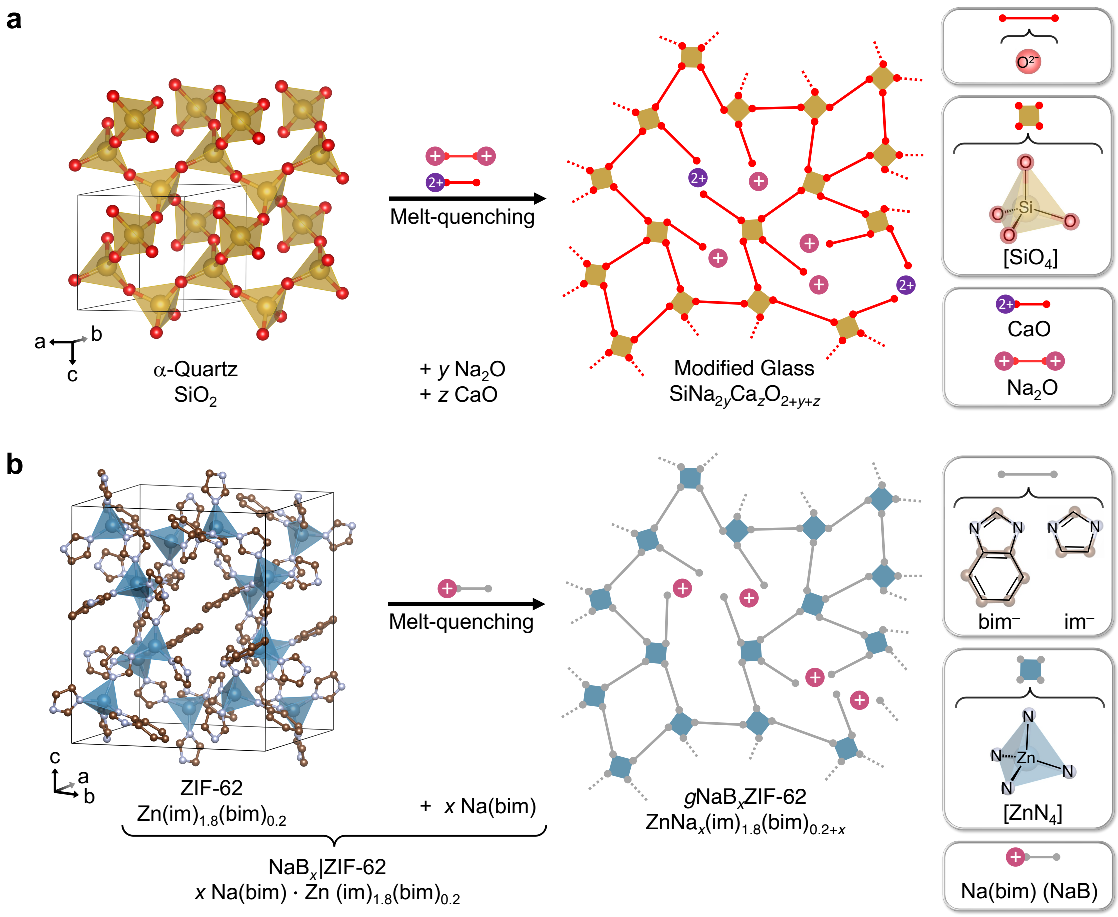

Figure 6.1. Conceptual scheme of glass modification in silicate and MOF glasses. **a** Traditional modification of SiO_2 glass with Na_2O and CaO as network modifiers. **b** Extension of this concept to the MOF glass former ZIF-62 using Na(bim) as a modifier. The schematics illustrate the crystal structures of SiO_2 and ZIF-62, alongside a 2D depiction of the modified glass networks, highlighting the effect of modifiers on SiO_2 or $Zn(im/bim)_2$ glass network connectivity. In the MOF case, physical mixtures are labelled NaB$_x$|ZIF-62, with the corresponding glasses denoted gNaB$_x$ZIF-62, where x represents the molar amount of Na(bim) added. color code: Si (yellow), O (red), Na (purple), Ca (violet), Zn (turquoise), N (light blue), C (brown); hydrogens were omitted for clarity.

To broaden the structural and compositional space of ZIF glasses, prior studies have (i) modified the crystalline glass former via linker/node substitution or guest impregnation to shift melting and glass formation, and (ii) mixed the glass former with additional phases,[103,109,115,129,131,165] yielding heterogeneous composites[132,133] or, in some cases, flux-melted/blended glasses.[134–136] While valuable, these routes are either synthesis-intensive and system-specific, or they lack a unifying framework for how an added phase modifies the network. Critically, the deliberate use of a "modifier" in the sense established for silicate glasses – enabling composition-property trends and mechanistic insight into network depolymerization – has remained largely unexplored for MOF glasses.

Inspired by the traditional principles of silicate glass modification, we show the modification of ZIF-62 glass using sodium benzimidazolate Na(bim)[137] as the glass modifier (Figure 6.1b). We comprehensively examine the structural, thermal, and chemical properties of the modified glass as a function of modifier concentration, demonstrating drastically decreased glass transition temperatures (T_g) and increased liquid fragilities, aiding materials processing and shaping. Moreover, we demonstrate that the extraction of the incorporated modifier via a water-leaching process increases the porosity of the glass. This approach, analogous to the Vycor process in silicate glass manufacturing,[166,167] highlights the potential for applying concepts from traditional glass chemistry to MOF-based glasses, unlocking a new toolbox for designing and tuning vitreous MOF materials.

6.3 Result and Discussions

6.3.1 ZIF glass modification

Physical mixtures of the glass former ZIF-62 and the modifier Na(bim) in varying ratios were prepared by manual grinding of the crystalline starting materials. All sample handling and analysis were done under an inert atmosphere due to the hygroscopic nature of Na(bim). The derived physical mixtures are denoted as NaB_x|ZIF-62 and feature variable composition $x\,Na(bim) \cdot Zn(im)_{1.8}(bim)_{0.2}$, with $x = 0.1, 0.3, 0.5, 1.0, 1.5$. Heating these mixtures to 450 °C in a DSC setup (small scale, ca. 10 mg) or in a custom-made hermetic steel crucible with a tube furnace (larger scale, ca. 250 mg, Figure A2.9), followed by cooling to room temperature yielded amorphous materials proven by powder X-ray diffraction data (see Figure 6.2a,b). The obtained materials exhibit clear signs of macroscopic material flow and glass shard formation (Figure 6.2c, A2.6). At low Na(bim) concentrations ($x = 0.1$), the melt-quenched glasses (denoted as gNaB$_x$ZIF-62) contained crystalline residues of ZIF-zni ($Zn(im)_2$)[97] when held at 450 °C for only 30 min (Figure A2.18). Extending the isothermal hold to 1 h at 450 °C resulted in fully amorphous materials, even for $x = 0.1$ (Figure A2.19). This tempering step was found to be essential for the homogenization of the melt (see Section 11).

Solution-phase ^{1}H nuclear magnetic resonance (NMR) spectroscopy of digested glass samples verified the absence of organic decomposition products following glass preparation (Figure A2.22-A2.31)). STA, combining thermogravimetry with differential thermal analysis, revealed a reduced decomposition temperature (T_d) of $\sim 480 - 540$ °C for the modified glasses, compared to gZIF-62 ($T_d = 603$ °C; Figure A2.11 – A2.14). Scanning transmission electron microscopy (STEM) with energy dispersive X-ray spectroscopy (EDX) confirmed a homogenous distribution of Zn^{2+} and Na^+ ions in the gNaB$_x$ZIF-62 materials with both low ($x = 0.3$) and high ($x = 1.0$) modifier contents (Figure A2.85-A2.88). Further insights into the three-dimensional distribution of the Zn- and Na-containing (complex-) ions in the modified glasses were obtained by atom probe tomography (APT) on gNaB$_{0.3}$ZIF-62 (Figure 6.2d). APT is a mass-spectrometry technique that maps the spatial distribution of individual ionic species with sub-nanometer resolution in three dimensions.[168,169] The 3D-APT reconstruction reveals a homogeneous distribution of Zn- and Na-containing (complex-) ions at the nanometer scale, which was confirmed by a statistical analysis comparing the experimental with computed randomised data (see Figure A2.84).

6.3.2 Thermal behavior

Cyclic DSC and *in situ* variable-temperature powder X-ray diffraction (VT-PXRD) provide comprehensive insights into the thermal behavior of the NaB$_x$|ZIF-62 physical mixtures and the resulting glasses. In the first DSC heating scans, weak endothermic signals at 166 °C correspond to the solid-state $\alpha \rightarrow \beta$ phase transition of Na(bim), consistent with previous findings (Figure 6.2e).[137] This is followed by overlapping endothermic events that scale with Na(bim) concentration, indicating simultaneous melting, material intermixing and reaction processes during melt homogenization up to 450 °C (Figure A2.41-A2.43). The flux-melting process of the NaB$_x$|ZIF-62 mixtures is supported by VT-PXRD data, which show the complete disappearance of Bragg reflections for Na(bim) and ZIF-62 around 350 °C, followed by internal crystallization of either the dense ZIF-zni (Zn(im)$_2$)[97] at low modifier concentrations ($x = 0.1, 0.3$) or ZIF-7-III (Zn(bim)$_2$)[170] at higher concentrations ($x = 1.0, 1.5$) (Figure A2.33-A2.39). The absence of the Na(bim) $\alpha \rightarrow \beta$ phase transition and the stable T_g observed in subsequent heating scans confirm the complete incorporation of the modifier in the glass matrix (Figure 6.2f). Increasing Na(bim) content leads to a substantial reduction in T_g, from 294 °C for gZIF-62 down to 161 °C for gNaB$_{1.0}$ZIF-62, indicating progressive depolymerization of the glass network as x increases (Figure 6.2g). This trend aligns with observations in traditional sodium silicate glasses, where alkali ion incorporation reduces network connectivity, leading to a decreased T_g and liquid viscosity.[46] Similar to sodium silicate systems, the Tg reduction is steep at low modifier concentrations but asymptotically approaches a limiting minimum at higher concentrations (Figure A2.125). At the highest Na(bim) contents (gNaB$_{1.5}$ZIF-62), the glass transition signal is followed by an exothermic peak at 293 °C succeeded by an endothermic event of similar magnitude around 407 °C, suggesting intermediate crystallization and dissolution of a transient phase of ZIF-7-III, as supported by VT-PXRD data (Figure A2.37, A2.39).

Further DSC experiments evaluated the calorimetric fragility indices (m) of the modified glasses to evaluate changes in the activation energy of viscous flow at T_g (Figure A2.46 – A2.50).[171,172] The fragility index differentiates strong glass-formers, such as SiO_2 ($m = 20$), which features a network structure of strongly associated SiO_4 units, from fragile ones ($m >> 20$), such as molecular (e.g. organic) glass-forming compounds.[70] For gZIF-62, we determined a fragility index of 19 ± 2, classifying it as a strong liquid and aligning with previous reports ($m \approx 23$).[57,105] However, as the Na(bim) concentration increases, m reaches approximately 51 for gNaB$_{1.0}$ZIF-62, approaching values typical of molecular glass formers like glycerol ($m = 53$).[71] This increase indicates a more complex energy landscape in Na(bim)-modified ZIF glasses with a greater diversity of configurational states and higher activation energies required for viscous flow (Table A2.6).[70] The indicated steeper decline in melt viscosity with rising temperature is advantageous regarding the liquid processability of gNaB$_x$ZIF-62 materials. Additionally, the heat capacity change (ΔC_V) at T_g increases with higher Na(bim) content, again reflecting a successively larger number of accessible configurational states beyond T_g (see Figure 6.2g, S48).[70,81]

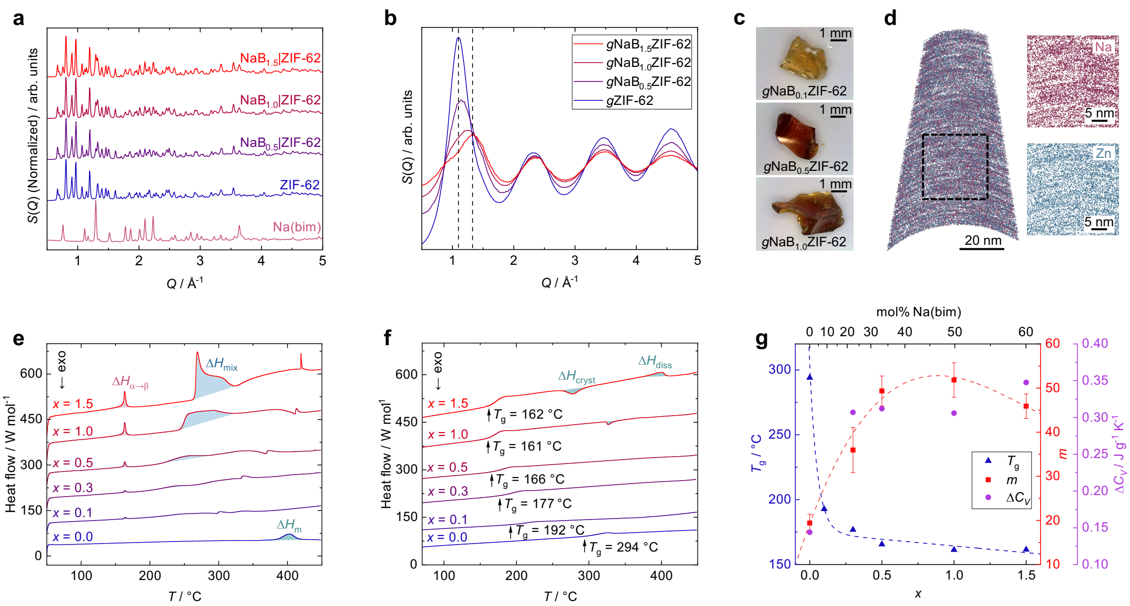

Figure 6.2. X-ray total scattering, thermal analysis, microstructural and microscopic characterization of modified ZIF glasses. **a,b** X-ray total scattering functions $S(Q)$ of the crystalline compounds and selected physical mixtures (**a**), and the corresponding glasses (**b**) Dashed lines mark the first sharp diffraction peak (FSDP) positions for non-modified and heavily modified glasses. **c** Optical microscopy images of glass shards from large scale gNaB$_x$ZIF-62 preparations. **d** Slice of the reconstructed APT model for gNaB$_{0.3}$ZIF-62, displaying the Na and Zn ion distributions. The right insets detail the Na (top) and Zn (bottom) ion distributions in the highlighted region. **e** DSC thermograms of NaB$_x$|ZIF-62 mixtures across different x values recorded at 10 °C min^{-1}. Endothermic events correspond to ZIF-62 melting (ΔH_m), the $\alpha \rightarrow \beta$ phase transition of Na(bim) ($\Delta H_{\alpha \rightarrow \beta}$) and reaction and intermixing process ΔH_{mix}. **f** DSC thermograms of gNaB$_x$ZIF-62 materials with varying modifier contents (x) recorded at 10 °C min^{-1}, highlighting the glass transition onset (T_g, arrow). Endothermic and exothermic events are attributed to crystallization (ΔH_{cryst}) and dissolution (ΔH_{diss}) of the dense ZIF-7-III phase. Scans are offset by 80 W mol^{-1} (molar unit: ZnNa$_x$(im)$_{1.8}$(bim)$_{0.2+x}$). **g** Trends in T_g, the liquid fragility index (m) and heat capacity change (ΔC_V) at T_g for gNaB$_x$ZIF-62. The dashed lines are visual guides.

The reduced glass stability, as indicated by crystallization events observed during the heating of gNaB$_x$ZIF-62 glasses with $x \leq 0.3$ and $x \geq 1.0$ is attributed to partial network depolymerization (reduced network connectivity), lower melt viscosity and local excesses of im$^-$ and bim$^-$ linkers, which encourage partial crystallization from the SCL state.[173] Consequently, phase separation, structural rearrangement, and nucleation at these modifier concentrations promote the intermediate crystallization of dense, thermodynamically favourable phases – ZIF-zni for $x \leq 0.3$ and ZIF-7-III for $x \geq 1.0$ – at elevated temperature.

6.3.3 Local structure analysis

The local structural changes induced by Na(bim)-modification of ZIF-62 glasses were investigated through infrared (IR) spectroscopy, X-ray total scattering combined with pair distribution function (PDF) analysis and solid-state ^{23}Na and ^{13}C NMR spectroscopy, revealing detailed insights into bond modifications and medium-range order (MRO).

In the mid-infrared (IR) spectra (Figure 6.3a,b), the distinct vibrational bands of Na(bim) at 1468 cm^{-1} and 1445 cm^{-1}, identified via DFT-based vibrational analysis, correspond to bim$^-$ ring stretching modes (Figure A2.5). For ZIF-62, analogous im$^-$/bim$^-$ ring stretching modes appear at 1499 cm^{-1}, 1475 cm^{-1} and 1456 cm^{-1}, which broaden and shift to 1494 cm^{-1}, 1474 cm^{-1} and 1455 cm^{-1} in gZIF-62.[174] In the physical mixtures, IR bands from Na(bim) and ZIF-62 are well separated. Upon vitrification, they merge into three broader bands located at 1494 cm^{-1}, 1468 cm^{-1} and 1455 cm^{-1}. The intensity ratio of these three peaks varies as Na(bim) content increases, with a substantial increase in the band at 1455 cm^{-1} with concurrent loss of the strong band at 1494 cm^{-1}. These changes are consistent with an increased density of Na$^+$-coordinated im$^-$/bim$^-$, resulting in increased disorder and reduced bond stiffness, leading to band broadening and vibrational modes with lower wavenumbers, respectively.

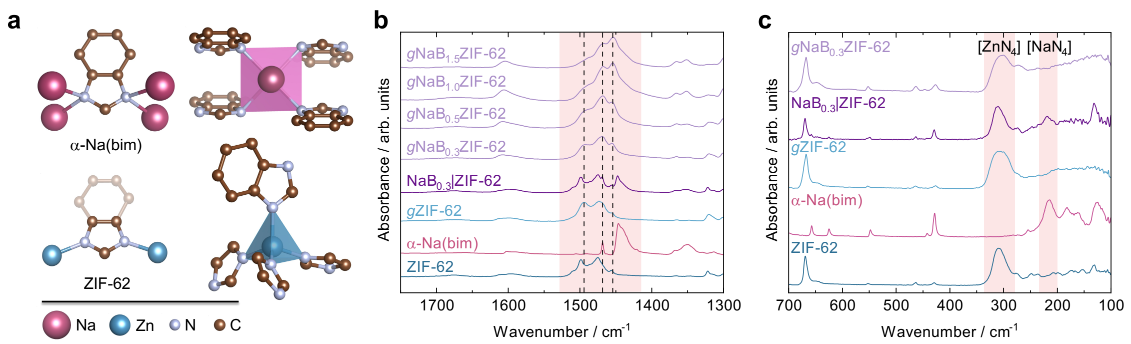

Figure 6.3. Vibrational spectroscopic analysis of Na(bim) incorporation in ZIF-62 glasses. **a** Ball-and-stick representation of the local environment surrounding bim$^-$/im$^-$ linkers and the Na$^+$/Zn^{2+} ions in α-Na(bim) (top) and ZIF-62 (bottom). Hydrogens are omitted for clarity. **b** Excerpt of the mid-IR spectra of ZIF-62, Na(bim), the physical mixture NaB$_{0.3}$|ZIF-62, and gNaB$_x$ZIF-62 glasses with varying Na(bim) contents. The red-highlighted region corresponds to the bim$^-$/im$^-$ ring stretching bands, with dashed lines indicating the peak positions in the modified glasses. **c** Far-IR spectra focussing on the asymmetric [ZnN$_4$] stretching band (309 cm^{-1}) and the [NaN$_4$] stretching band (214 cm^{-1}).

The far-IR spectra provide further information on the structural changes in metal coordination (Figure 6.3a,c). The asymmetric [ZnN_4] stretching band[175] at 309 cm^{-1} in crystalline ZIF-62 broadens and shifts to lower wavenumbers in *g*ZIF-62, reflecting the disturbance of Zn^{2+} coordination resulting in non-ideal coordination geometries. The asymmetric [NaN_4] stretching band of Na(bim) at 214 cm^{-1} is detectable in the spectrum of the physical mixtures but blends into the background after glass formation, confirming the loss of the distinct coordination environment of Na^+ ions in crystalline Na(bim). As an effect of Na(bim) incorporation in the ZIF glass, the [ZnN_4] stretching band shifts towards even lower wavenumbers, indicating that the modifier weakens the Zn−N bond strength and further disturbs the Zn^{2+} coordination environment.

Complementary insights into the local structure and MRO of the Na(bim)-modified ZIF glasses are obtained from X-ray total scattering experiments. In the scattering function $S(Q)$, the FSDP shifts from 1.10 Å^{-1} to 1.33 Å^{-1} as Na(bim) concentration increases, suggesting progressive densification of the glass (Figure 6.2b).[176,177] This shift is accompanied by a substantial decrease in scattering intensity, reflecting a loss of contrast in electron density as former interstitial voids within the ZIF glass network are successively occupied by the modifier. Concurrent broadening of the FSDP suggests a reduction in real-space correlation length, indicative of a diminished MRO as Na(bim) disrupts network connectivity.[176]

To further investigate these structural changes, PDFs, represented as $G(r)$, were extracted from the X-ray total scattering data for both the NaB_x|ZIF-62 physical mixtures and the corresponding *g*NaB_xZIF-62 glasses with comparisons made to ZIF-62 and *g*ZIF-62 (Figure 6.4a-e). Due to the high scattering cross-section of Zn^{2+}, Zn-based interatomic distances dominate the PDFs at $r \leq 2$ Å. The data reveal that, while short-range order, reflecting the immediate environment of Zn^{2+} and the organic linkers, is maintained during melting and glass formation, long-range order ($r > 10$ Å) is lost, consistent with the amorphization process (Figure A2.62-A2.66).

To quantify the structural deviations of the Na(bim)-modified glasses from pristine *g*ZIF-62, the $G(r)$ functions were rescaled to a common molar unit, $ZnNa_x(im)_{1.8}(bim)_{0.2+x}$ (Figure 6.4b-c, see Section A2.12 for details). The rescaled PDFs, $G^*(r)$, of the ZIF glasses show significant broadening and reduced intensity of the Zn$\cdots$Zn next-neighbor peak at 5.9 Å as x increases. This observation supports the formation of non-Zn^{2+}-bridging im^-/bim^- linkers in Na(bim)-modified glasses, where linkers are attached to only one Zn^{2+} and one Na^+ rather than bridging two Zn^{2+} ions, thereby reducing connectivity in the network.

Differential PDF analysis[178,179] was performed to isolate changes in interatomic distances upon glass modification (Figure 6.4d). By subtracting the $G^*(r)$ of physical mixtures from that of their glasses, difference functions $\Delta G^*(r) = G^*_{\mathrm{i}}(r) - G^*_{\mathrm{ii}}(r)$, were obtained, with i = *g*NaB_xZIF-62 and ii = NaB_x|ZIF-62. These difference functions reveal a progressing reduction in the population of ideal Zn⋯Zn distances ($r = 5.9$ Å) as Na(bim) content increases, along with a gradual shift towards slightly longer Zn⋯Zn distances. This shift indicates modifier-induced perturbations of Zn^{2+} coordination sites, resulting in a broader distribution of Zn···Zn distances, consistent with the redshift and broadening of the $[ZnN_4]$ vibrational band (see Figure 6.3c). Additionally, the loss of pair correlations around 7 Å is largely attributed to the loss of Na···Na distances specific to crystalline Na(bim), while new Na···Zn distances may be evident in the range from 4.5 to 5.5 Å, as this region is increasingly populated in the $G(r)$ of the glasses with higher x.

Additional Zn K-edge EXAFS measurements on crystalline ZIF-62, gZIF-62 and gNaB$_x$ZIF-62 materials provide a coordination number of CN = 4 across all samples, confirming that tetrahedral Zn^{2+} network nodes are largely preserved during glass formation and modification (Table A2.11).

To further investigate the local structure of gNaB$_x$ZIF-62 materials, we employed a combined theoretical and experimental approach using solid-state ^{23}Na magic angle spinning (MAS) NMR spectroscopy, a powerful technique for probing atomic-level structures in materials, even in the absence of long-range order. Figures 4f-h show ^{23}Na MAS NMR spectra of gNaB$_x$ZIF-62 with x = 0.1, 0.5, and 1.0 at 20.0 T (MAS = 20 kHz).

At $x = 0.1$, three signals are observed: two narrow peaks at 6.8 and –6.3 ppm, and a broad peak centred around 0 ppm. The large full-width half-maximum (FWHM = 13.9 ppm) of this signal indicates significant static disorder in the Na+ local environment within the glass network. As the Na(bim) content increases, the intensity of the broad component grows, dominating other spectral features. To further interrogate these overlapping components, we employed a longer echo delay during acquisition of ^{23}Na spectra, effectively suppressing signals with short spin-spin relaxation times (T_2).[180] This filtering reveals the same two narrow components in gNaB$_{0.5}$ZIF-62 and gNaB$_{1.0}$ZIF-62 as in gNaB$_{0.1}$ZIF-62 that are obscured by the broad signal in the unfiltered spectra (Figure 6.4f-h and A2.95). This suggests that, at low Na(bim) content, Na^+ predominantly occupies two well-defined coordination sites, corresponding to the narrow peaks. However, the presence of the broad signal even at $x = 0.1$, and the disappearance of narrow peaks at higher Na(bim) content, indicate that these preferred coordination sites support limited Na^+ occupancy ($x < 0.1$), while excess Na^+ populates a diverse distribution of local coordination environments.

To structurally identify the Na^+ coordination modes observed experimentally, we generated possible Na^+ environments using *ab initio* random structure searching (AIRSS).[181] Experimental NMR spectra suggest a wide Na(bim)-concentration-dependent range of Na^+ coordination environments. To simulate this range, we geometry-optimised supercells of $(Na_{2y}Zn_{16-y})[(im)_{1.75}(bim)_{0.25}]_{16}$ for integer y = 1-4, where $y = 2$ corresponds to a Na^+:Zn^{2+} ratio consistent with $x = 0.29$. Structures were relaxed to minima in the potential energy surface by minimising DFT forces. For each y, AIRSS yielded ten distinct, local energy-minimised structures for a total of 200 unique Na^+ coordination environments (Figure A2.89). We simulated solid-state ^{23}Na NMR spectra (20.0 T, 20 kHz) for all 200 Na^+ environments using calculated chemical shielding and electric-field gradient (EFG) tensors (Figure A2.96).

As expected, DFT-relaxed structures reveal diverse Na^+ environments, ranging from Na^+ incorporation at node sites (i.e., sites that are occupied by Zn^{2+} in unmodified ZIF-62) to

Na^+ attachment on the framework's pore walls. The degree of Na^+ coordination by the nitrogen lone pairs of im^- and bim^- linkers varies substantially, with observed coordination numbers of 0, 1, 2, 3, and 4 (Figure A2.89). To investigate the correlation between ^{23}Na NMR shift and both Na^+ positioning and $N-Na^+$ coordination, we classified all 200 calculated Na^+ sites by these criteria and generated corresponding cumulative predicted ^{23}Na spectra (Figure 6.4i-n). Spectra with both 50 and 4000 Hz Gaussian broadening applied are shown to simulate broadening due to static disorder in the material.

As a result, we identified three distinct Na^+ site categories: (i) Na^+ attached to the pore walls of the framework (Figure 6.4o), (ii) Na^+ replacing a tetrahedral Zn^{2+} node (Figure 6.4p), and (iii) two Na^+ jointly replacing a tetrahedral Zn^{2+} node (Figure 6.4q). Grouping predicted ^{23}Na spectra corresponding to Na^+ sites in these three categories (Figure 6.4i) reveals minimal overlap between experimental data and shifts predicted for Na^+ on pore wall sites, indicating that Na^+ preferentially adopts coordination sites similar to those of Zn^{2+} nodes, either with single or double Na^+ occupancy. This preference is likely caused by π-coordination of im^- and bim^- to Na^+ in pore wall sites, which results in short, energetically disfavoured $Na^+ \cdots Zn^{2+}$ distances upon π-coordination of im^- and bim^- to Na^+ in pore wall sites (mean 3.49 Å across calculated pore wall sites).

Figures 6.4j-n show cumulative predicted ^{23}Na NMR spectra grouped by the $N–Na^+$ coordination number of each DFT-simulated Na^+ environment, with a coordinate bond defined by $N \cdots Na^+$ distances < 2.7 Å (based on distances of 2.55 - 2.62 Å in the crystal structure of α-Na(bim)[137]). Table A2.14 provides a complete classification of all DFT-simulated Na^+ sites. A strong correlation between $N–Na^+$ coordination number and ^{23}Na shift is evident, with minimal overlap between predicted ^{23}Na shifts for 2-, 1- and 0-coordinated Na^+ and the experimental spectral region. The strongest correlation is seen with 3-coordinated Na^+, confirming that Na^+ substitution for Zn^{2+} in gNaB$_x$ZIF-62 distorts the network, reduces connectivity and causes partial pore collapse. Supporting this, we find a close correlation between the Na^+ coordination number and Na^+ site assignment (Figure A2.90), with mean coordination numbers of 1.35 for pore wall sites, 3.17 for doubly occupied node sites, and 3.60 for singly occupied node sites.

While overlapping predicted ^{23}Na line shapes prevent definitive assignment of the narrow, low-intensity experimental signals at 6.8 and –6.3 ppm, simulated spectra suggest these signals arise from singly or doubly occupied node sites (Figure A2.92). Additionally, the cumulative predicted spectrum of doubly occupied node sites centres around the broad experimental peak at ~0 ppm. (Figure 6.4i). Collectively, the simulated spectra suggest that at low Na(bim) concentrations, Na^+ resides in coordination environments similar to those of distorted Zn^{2+} sites; as Na(bim) content increases, doubly occupied Na^+ node sites become more populated, which gradually increases the intensity of the broad spectral component centred at ~0 ppm.

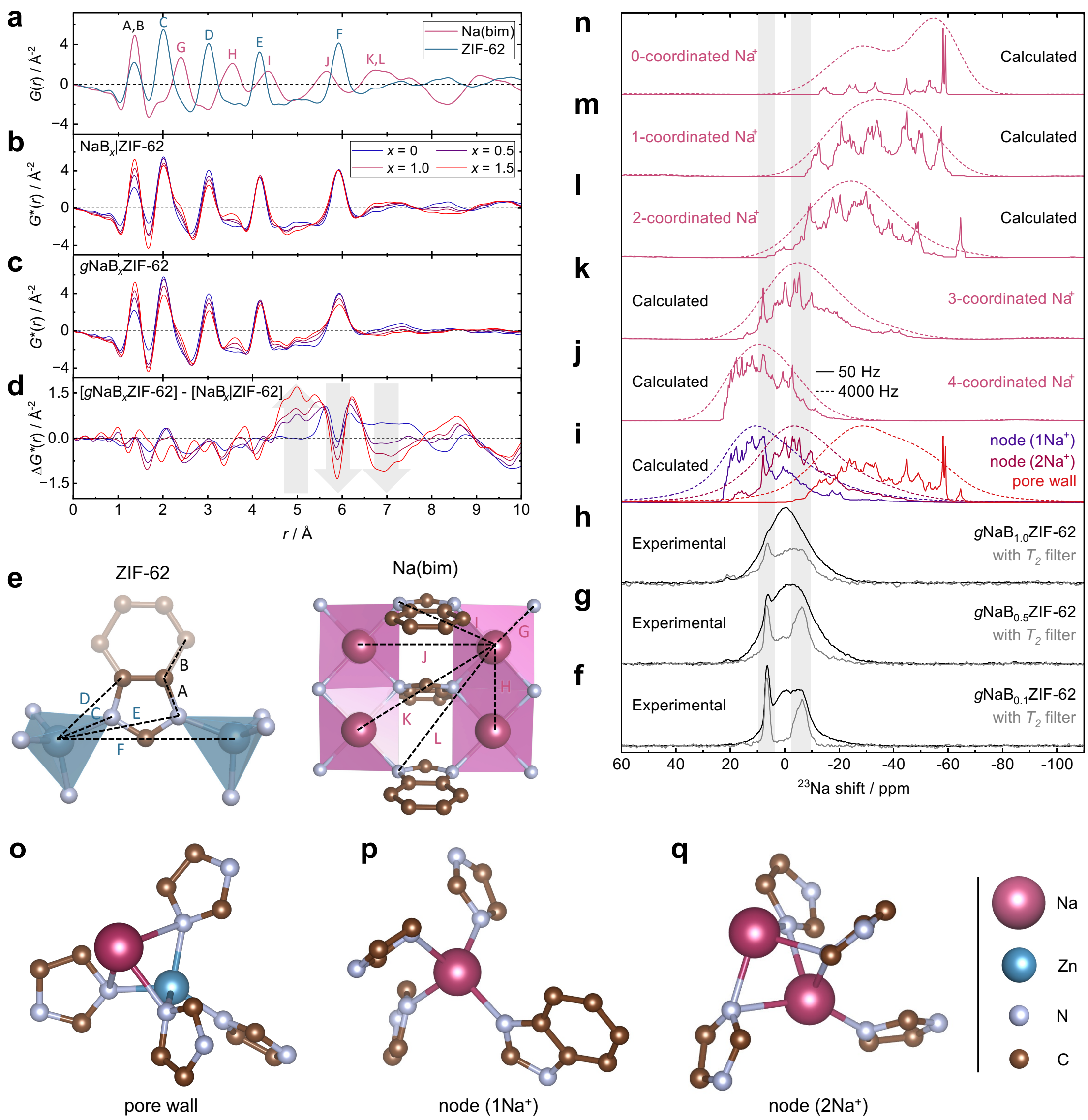

Figure 6.4. PDF, NMR and DFT analysis of structural changes during vitrification. **a-d** PDFs in the form of $G(r)$ (scaled by number density) or $G^*(r)$ (rescaled to the molar unit $ZnNa_x(im)_{1.8}(bim)_{0.2+x}$) of crystalline Na(bim) and ZIF-62 (**a**), the crystalline physical mixtures NaB$_x$|ZIF-62 (**b**), and the corresponding glasses gNaB$_x$ZIF-62 (**c**). **d** Differential PDFs ($\Delta G^*(r)$) illustrating the structural changes between the rescaled PDFs of the physical mixtures and their glasses, highlighting modifications induced by vitrification. **e** Representation of short-range connectivity of ZIF-62 (left) and α-Na(bim) (right), with key interatomic distances highlighted. **f-h** Experimental ^{23}Na NMR (20.0 T, 20 kHz MAS) spectra of gNaB$_x$ZIF-62 with $x = 0.1, 0.5, 1.0$. Spectra acquired with both a short (0.1 ms, black) and long (25.6 ms, grey) echo delay are shown, with the latter effectively filtering components in the spectra with short spin-spin relaxation times (T_2). **i-n** Predicted ^{23}Na NMR spectra of Na$^+$ sites in DFT-simulated gNaB$_x$ZIF-62 structures, categorised by Na$^+$ occupation in the gNaB$_x$ZIF-62 structure (1Na$^+$ and 2Na$^+$ correspond to singly and doubly occupied node sites, respectively) (**i**) and N$-$Na$^+$ coordination number (**j-n**). **o-p** Examples of local structures surrounding Na$^+$ in DFT-simulated gNaB$_x$ZIF-62: (**o**) a MOF pore wall site, (**p**) a singly occupied node site, and (**q**) a doubly occupied node site. Gaussian line broadening of 50 Hz (solid) and 4000 Hz (dashed) is applied to calculated spectra to simulate the effect of static disorder.

These structural insights reveal a surprising contrast between the Na^+ environments in Na-modified ZIF glasses and those in Na-modified silicate glasses. In sodium silicate glasses, Na^+ typically exhibits a coordination number of 5 to 6, coordinated by oxide anions, and is envisioned as forming percolation channels that intersect the glass network.[125] In Na-modified ZIF glasses, however, the coordination number is significantly lower, ranging between 3 and 4, with Na^+ coordinated by the nitrogen lone pairs of imidazolate ligands. This fundamental difference arises from the nature of the bonding and the distinct geometric constraints imposed by the imidazolate linkers. Unlike the compact, spherical oxide anions in silicate glasses, the extended organic imidazolate linkers introduce steric hindrance, limiting the number of nitrogen atoms that can coordinate to a single Na^+ ion. Furthermore, the directional character of the nitrogen lone pairs enhances the specificity of the $Na^+ \cdots N$ interaction, favouring fewer contacts compared to the non-directional ionic interactions between Na^+ and oxide anions. Together, these factors result in lower coordination numbers for Na^+ in ZIF glasses and highlight the unique structural role of Na^+ in these materials. This distinction underscores the potential of adapting glass modification principles to MOF-based systems to achieve fundamentally different structural and functional outcomes.

6.3.4 Modifier extraction and gas sorption

The porosity of ZIF glasses is typically much lower than that of their crystalline parent frameworks, prompting recent efforts to enhance and control the glasses' porosity for applications in hydrocarbon separation and carbon capture.[96,106,109] Here, Na(bim)-modified ZIF glasses (gNaB$_x$ZIF-62) were subjected to a water-extraction process to investigate potential porosity changes through selective modifier leaching. Upon submersion in water, the gNaB$_x$ZIF-62 materials undergo hydrolysis of Na–N bonds, releasing NaOH and imH/bimH, resulting in a strongly basic aqueous medium (Figure A2.101), while preserving the integrity of the Zn-im/bim network. Optical microscopy reveals progressive changes in the glass shards over several days (Figure 6.5a, A2.100). The initially transparent glass pieces become opaque and swell once in contact with water. After 7 days in water, glass pieces with low Na(bim) content ($x = 0.1$) largely retain their structure, while those with higher Na(bim) levels develop lamellar cracks ($x = 0.5$) or disintegrate into smaller particles ($x = 1.0$). This increasing water sensitivity is attributed to the higher proportion of hydrophilic modifier relative to the hydrophobic, water-stable ZIF glass former[164] as Na(bim) content increases.

Quantitative ^{1}H solution NMR spectroscopy of acid-digested samples of water-leached gNaB$_{0.3}$ZIF-62 (denoted lgNaB$_x$ZIF-62, lg = leached glass) demonstrates preferential removal of Na(im) over Na(bim), ascribed to the increased bulkiness of bim^- compared to im^-. Nonetheless, these findings support the presence of Na–im bonds in the modified ZIF glasses. (Figure 6.5b, S87). The aqueous washing solution contains about 95% imidazole and 5% benzimidazole (Figure A2.104,A2.105). Notably, despite these modifications, all the leached glasses remain amorphous, as confirmed by PXRD (Figure A2.102, A2.103). Further analysis of solid leached glass samples by far-IR spectroscopy shows a slight blueshift of the [ZnN_4] stretching band, indicating stronger Zn–N bonds post-leaching (Figure A2.107). DSC measurement of lgNaB$_{0.3}$ZIF-62 shows several broad endothermic events in a first heating scan (Figure A2.111). After heating at 450 °C for 30 minutes, a second heating scan displays a glass transition with an increase in T_g from 117 °C to 275 °C, suggesting a structural rearrangement and restoration of network rigidity in the temperature-treated leached glass.

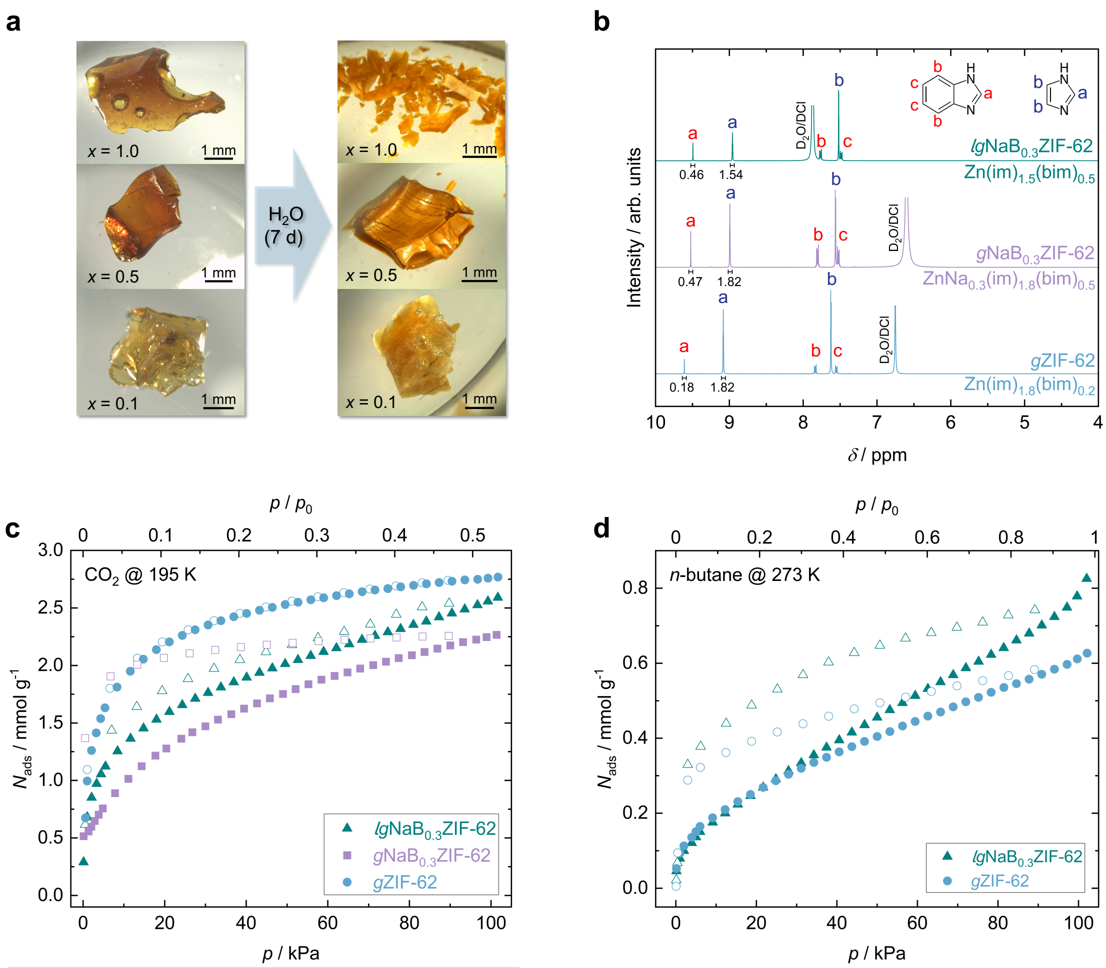

Figure 6.5. The influence of water-leaching on the material's porosity. **a** Optical microscopy images of gNaB$_x$ZIF-62 glasses before and after suspension in water for seven days for different modifier contents x. **b** ^{1}H solution NMR spectra of the modified glass before and after water leaching, digested in D_2O/DCl and DMSO-d_6. The chemical shift of the protons of the solvent D_2O/DCl is strongly pH-dependent, leading to variations in their positions across the spectra. **c** Sorption isotherms for CO_2 collected at 195 K. **d** n-Butane gas sorption isotherm collected at 273 K. Points in the ad- and desorption branches are shown as solid and open symbols, respectively.

The modifier extraction process draws parallels to the well-established Vycor process, developed in the 1930s to produce porous silicate glasses for applications in catalysis, adsorption, and membrane technologies.[166,167] In the Vycor process, phase-separated alkali borosilicate glasses undergo heat treatment, resulting in silicate-rich and alkali-borate-rich domains. An acid treatment then removes the soluble borate-rich phase, leaving behind a porous silicate network with tailored pore structures.[182] Similarly, the leaching of Na(im) and Na(bim) from gNaB$_x$ZIF-62 provides an accessible pathway for creating additional porosity in MOF-derived glasses.

To assess porosity changes induced by modifier incorporation and subsequent extraction, gas sorption isotherms were recorded for gZIF-62, gNaB$_x$ZIF-62, and lgNaB$_x$ZIF-62 (Figure 6.5c). The materials' porosity is assessed by CO_2 (kinetic diameter 3.30 Å[183]) gas sorption at 195 K, as CO_2 is a well-established probe for quantifying the microporosity of ZIF glasses, which typically possess narrow pores largely inaccessible to N_2 (kinetic diameter 3.64 Å[183]) at 77 K. At 195 K, the CO_2 sorption isotherm reaches complete micropore filling at the maximum pressure of 100 kPa.[184] The parent glass gZIF-62 shows a Langmuir-type (Type I) isotherm with a maximum CO_2 uptake of 2.77 mmol g^{-1}, in agreement with previously reported values.[105] By contrast, the modified glass gNaB$_{0.3}$ZIF-62 shows a lower maximum uptake (2.27 mmol g^{-1}) and pronounced hysteresis between the adsorption and desorption branches. This reduced CO_2 uptake of gNaB$_{0.3}$ZIF-62 compared to gZIF-62 aligns with the higher density of the modified glass observed in the FSDP analysis (Figure 6.2b) and further suggests that the incorporated Na(bim) modifier further limits interstitial void volume, thus reducing accessible microporosity.

After modifier extraction, the resulting glass lgNaB$_x$ZIF-62 exhibits an increased CO_2 uptake of 2.59 mmol g^{-1}, approaching that of gZIF-62. The recovered microporosity of lgNaB$_x$ZIF-62 also facilitates faster diffusion, substantially reducing the hysteresis associated with the CO_2 sorption process. The slightly lower micropore volume and increased hysteresis of lgNaB$_{0.3}$ZIF-62, compared to gZIF-62, are likely due to the increased proportion of the bulkier bim$^-$ linker in the leached glass. Given the maximum relative pressure (p/p_0) for CO_2 sorption at 195 K is about 0.55,[185–187] these measurements are limited to evaluating microporosity without access to meso- or macropore volume. However, fitting the CO_2 sorption data to a dual-site Langmuir model, followed by extrapolation to a hypothetical CO_2 saturation pressure, suggests that lgNaB$_{0.3}$ZIF-62 possesses a total pore volume about 26% greater than that of gZIF-62 (Figure A2.112, Table A2.16). This finding is corroborated by n-butane sorption recorded at a higher temperature (273 K), which shows a 26% higher n-butane capacity of lgNaB$_{0.3}$ZIF-62 compared to gZIF-62 at saturation, further confirming the generation of additional meso- and macropores post-leaching (Figure 6.5d).

These results demonstrate that selective extraction of Na(im) from ZIF glasses offers a versatile approach to tuning porosity. This strategy enables the recovery of micropores and the creation of meso- and macropores. It represents a significant advancement in tailoring ZIF glass porosity for applications in gas storage, separation, and catalysis, bridging a critical gap in functionalizing MOF-derived glasses.

6.3.5 Lithium benzimidazolate modification

In an effort to further expand the chemical range of alkali-modified ZIF-62 glasses, Li(bim) was investigated as a modifier. Melt-quenching of physical mixtures LiB_x|ZIF-62 (with $x = 0.3$, 0.6, 1.1) in sealed DSC pans at 425 °C produced clear, decomposition-free glasses with evidence of macroscopic flow, as confirmed by solution ^{1}H NMR measurements of acid-digested samples (Figures A2.120–A2.122) and microscopy images (Figure A2.117). PXRD patterns of the resulting gLiB$_x$ZIF-62 glasses verified their amorphous nature (Figure A2.119). Additional PXRD measurements of the physical mixtures after the application of heating programs with maximum temperatures below 425 °C, together with VTPXRD data of $LiB_{1.1}$|ZIF-62, indicated a tendency towards crystallization of ZIF-zni and ZIF-7-III at low and high Li(bim) contents, respectively (Figures A2.118 and A2.126). As in the case of gNaB$_x$ZIF-62 glasses, a modifier-induced decrease in T_g was observed. The relative drop in T_g compared to the unmodified glass former remained similar for Li(bim)- and Na(bim)-modified ZIF-62, whereas sodium silicate glasses show a much steeper decrease upon Na_2O addition (Figure A2.125). The slightly higher T_g of gLiB$_x$ZIF-62 compared to gNaB$_x$ZIF-62 at similar x is rationalized by the smaller ionic radius of Li^+ and resulting stronger Li−N bonds inhibiting bond dissociation upon reaching the glass transition during heating. Analogous to Na(bim)-modified glasses, the incorporation of Li(bim) is accompanied by a fusion and broadening of vibrational bands in the infrared spectrum, reflecting modifier-induced structural disorder (Figures A2.116–A2.117), and by broadening of the PDF signal at ~ 6 Å associated with a potential loss of Zn$\cdots$Zn pair correlation density (Figure A2.127). The observed similarities in the thermal and structural analysis of Li(bim)- and Na(bim)-modified ZIF-62 glasses underline the robustness and general applicability of the glass-modification concept to the field of MOF glasses and highlight how material properties can be controlled systematically by the choice of the modifiers alkali cation.

6.4 Conclusion

The vitrification of the MOF glass former ZIF-62 with Na(bim) via a flux-melting approach has successfully yielded modified ZIF glasses, analogous to traditional (silicate) glass modification systems. Key properties, including a modifier-induced decrease in glass transition temperature (T_g), increased hydrophilicity, and enhanced liquid fragility, were shown to be tunable in a controlled, continuous manner. Structurally, these trends correspond to an increased glass network disorder and depolymerization, mirroring mechanisms observed in inorganic glasses. The identification of the Na^+ structural motifs through ^{23}Na MAS NMR and DFT calculations represents an important advance in understanding the network structure and chemistry of MOF glasses, addressing fundamental questions that remain even in the well-established field of inorganic glass science. Unlike in silicate glasses, Na^+ primarily integrates into the ZIF glass network by replacing Zn^{2+} nodes, creating denser materials with highly disordered and undercoordinated Na^+ environments. This substitution reduces network connectivity and partially collapses the pore structure compared to gZIF-62, underscoring the profound impact of modifiers on the structural and functional properties of MOF glasses. The use of Li(bim) as a modifier further demonstrates the broad applicability and robustness of the glass-modification concept, with trends in thermal and structural properties closely paralleling those observed for the sodium analogues.

Beyond these valuable insights, the post-synthetic removal of the Na-based modifier via water extraction highlights the adaptability of leaching processes, such as Vycor, to MOF glasses. This process offers a versatile tool for tailoring porosity enabling control of pore structures and expanding the functional capabilities of MOF glasses for applications in gas separation, storage, and catalysis.

This work also opens new avenues in MOF glass science by expanding the chemical and functional diversity of these materials through non-stoichiometric modifications, akin to strategies established for inorganic glasses. Although the adjustable T_g and improved flowability resulting from reduced viscosity may facilitate processing at lower temperatures, practical manufacturing can be constrained by the requirement of autogenous pressure during melt-quenching and the material's strong adhesion of the Na(bim)-modified MOF glasses to crucible surfaces, which impede the production of large glass monoliths with the current set-up. Additionally, this flux modification strategy may enable the transformation of previously non-meltable ZIFs into processable glasses, expanding the landscape of accessible MOF glass materials. The potential to access unique phase behaviors, such as spinodal decomposition, lays the foundation for exploring new glass phase dynamics. Together, these advances underscore the versatility and transformative potential of MOF glasses, paving the way for next-generation porous and functional glasses.

7 Conclusion and Outlook - From High Temperature to High Pressure

Part I of this thesis focuses on the transferability of well-established concepts of (silicate) glass modification to the young materials class of MOF glasses. The presented work further expands the variety of available MOF glass materials by validating the applicability of long-known tools to introduce structural changes to the glass on a molecular level. The presented study found that a large portion of these concepts established for silicate glass systems, such as the modifiers' influence on structure-property relationships, are still valid for the investigated case of Na(bim) and Li(bim)-modified ZIF-62 glass. The systematic tunability of the glass transition temperature, the material density, and porosity, along with liquid viscosity and hydrophilicity, pinpoint key processing parameters that are at the center of interest for future MOF-based industrial applications such as membranes for gas-separation, as a medium for gas-storage, or as solid-state electrolytes.

In this context, the successful extraction of the modifier in analogy to the Vycor process established for (boro-)silicate glasses is a further tool to modulate the material's porosity and potentially impose additional porosity to the material in a hierarchical manner. This process provides potential control over the performance of future MOF-glass-based hydrocarbon separation or carbon capture technologies and underlines the potential value of these findings to tackle major environmental and economic challenges of our time.

However, the obtained structural insights reveal subtle differences in the modified glass network and modifier incorporation between the traditional (silicate) glass systems and the investigated Na(bim) and Li(bim)-modified ZIF-62 glasses. Differences such as the lower coordination number of sodium ions in the modified ZIF-62 glass compared to sodium silicate glasses and resulting effects on the glass network's structure open up further areas of research. Finally, questions remain about how the cation identity of the modifier and potential synergistic effects in multi-modified ZIF-62 glasses influence the resulting material properties. This research question, however, lies beyond the scope of the present work and remains to be explored in future work.

The results presented in Part I of this thesis enhance current knowledge on the possibilities of modifying ZIF-62 glasses in a traditional manner. This contributes to the development of future MOF glass membranes by offering additional tools to tune material properties and optimize processing parameters. Part II continues to explore a related area of research by focusing on the structural stability and response of MOFs under high pressure, as these conditions are common in the manufacturing of MOF pellets used to immobilize MOFs in catalysis, gas storage, and gas separation technologies without impeding the functionality of the materials (e.g., catalytic activity or separation performance). MOF-74-type materials represent a promising class of MOF materials with high potential regarding their application in the aforementioned industrial processes. Investigating their structural response upon high hydrostatic pressure is the subject of the following Part II.

Part II - Understanding the High-Pressure Behavior of MOF-74-Type Materials

8 Understanding the High-Pressure Behavior of MOF-74-Type Materials: The Influence of Metal Identity and Linker Extension

The work presented in this chapter is currently under review for publication in a peer-reviewed journal. The text and figures are reproduced or adapted from the preprint version of the manuscript,[188] which is available under a Creative Commons Attribution 4.0 International License (CC BY 4.0, https://creativecommons.org/licenses/by/4.0/legalcode). Adaptations include modifications in nomenclature and rearrangements of figures. Full citation details and author contributions are provided below.

Authors

Pascal Kolodzeiski[1], Michael Strobl[1], Louis Frentzel-Beyme[1], Michael Paulus[2], Christian Sternemann[2], Christian Nelle[1], Kai Terlinden[1], Jianbo Song[1], Sebastian Henke[1,*]

[1] Fakultät für Chemie und Chemische Biologie, Technische Universität Dortmund, Otto-Hahn-Straße 6, 44227 Dortmund, Germany.

[2] Fakultät Physik/DELTA, Technische Universität Dortmund, 44221 Dortmund, Germany.

Date of Submission: August 13, 2025

Author Contributions

P.K. and M.S. synthesized and characterized the materials. L.F.B, M.P. and C.S. optimized the high-pressure cell for in-situ HPPXRD measurements. C.N. contributed to the automated evaluation of the data. L.F.B., K.T. and J.S. helped with the collection of synchrotron data. The manuscript was written by P.K. and S.H. with contributions from the other authors.

Acknowledgement

P.K. acknowledges the Fonds der Chemischen Industrie for a Kekulé fellowship. The authors thank DELTA Dortmund for the allocation of beamtime. We acknowledge the mechanical workshops of the Department of Chemistry and Chemical Biology, TU Dortmund, for the manufacturing and modification of the high-pressure powder diffraction cell. We acknowledge DESY (Hamburg, Germany), a member of the Helmholtz Association HGF, for the provision of experimental facilities. High-pressure PXRD experiments of this research were carried out at PETRA III on beamline P02.1 (proposal I-20200047). We thank the associated beamline scientists Alexander Schökel, Alba San José Méndez, Volodymyr Baran, and Martin Etter for their support during data collection.

8.1 Abstract

MOF-74 (M_2(dobdc); dobdc^{4-} = 2,5-dioxido-1,4-benzenedicarboxylate) and its isoreticular derivatives represent a chemically versatile class of metal-organic frameworks (MOFs) with high densities of open metal sites and one-dimensional channels. These features underpin their utility in gas storage, separation, and catalysis. However, their mechanical behavior under hydrostatic pressure, critical for shaping, membrane integration, and high-pressure separations, remains insufficiently understood. Here, we report a comparative high-pressure powder X-ray diffraction study of six M_2(dobdc) materials (M^{2+} = Mg^{2+}, Mn^{2+}, Co^{2+}, Ni^{2+}, Cu^{2+}, Zn^{2+}) and the expanded analogue Mg_2(dobpdc) (dobpdc^{4-} = 4,4'-dioxido-[1,1'-biphenyl]-3,3'-dicarboxylate), both in its activated and diamine-loaded forms, under hydrostatic pressure up to 4000 bar. Two distinct compression mechanisms are identified: M_2(dobdc) frameworks compress primarily along the crystallographic *c*-axis through distortion of the square-pyramidal [MO_5] coordination units. The bulk modulus varies from 10 to 24 GPa and correlates strongly with metal ion hardness as well as bond length and angular distortion parameters. In contrast, Mg_2(dobpdc) undergoes compression via bending of the extended dobpdc^{4-} linker in the *a,b*-plane, resulting in an exceptionally low bulk modulus of ~3 GPa. Notably, while guest-free Mg_2(dobpdc) amorphizes irreversibly, the diamine-loaded variant transitions reversibly to a severely distorted, non-periodic high-pressure phase and fully recovers its crystallinity upon decompression. Together, these findings establish how metal identity, linker architecture and guest loading govern pressure response in MOF-74-type materials, offering guiding principles for their integration in pressure-intensive industrial applications.

8.2 Introduction

Metal-organic frameworks (MOFs) represent a class of porous materials composed of metal nodes interconnected by organic linkers. Their exceptional structural diversity, permanent porosity, large internal surface areas and pore volumes have made them the focus of intense research in the past decades, particularly in the fields of adsorption[189] and catalysis[190], gas separation[9] and sensing[191]. Several MOF families have emerged as strong candidates for integration into industrial processes that address urgent environmental and technological challenges.[16] Their performance in applications such as carbon capture,[192] gas storage,[193] gas separation[194] and catalysis[195] relies on specific structural features, including tunable pore sizes and shapes, rapid guest diffusion pathways, and tailored chemical environments at active sites.[196,197]

Among these materials, the MOF-74/CPO-27 family (general formula: M_2(dobdc), dobdc^{4-} = 2,5-dioxido-1,4-benzenedicarboxylate) is of particular significance. M_2(dobdc) frameworks are built from various divalent metal ions (M^{2+} = Mg^{2+}, Mn^{2+}, Fe^{2+}, Co^{2+}, Ni^{2+}, Cu^{2+}, Zn^{2+}, Cd^{2+}) interconnected by the dobdc^{4-} linker (Figure 8.1).[198–204] The M_2(dobdc) structure exhibits one-dimensional hexagonal channels (~15 Å diameter) lined with coordinatively unsaturated metal sites, arising from the square-pyramidal $[MO_5]$ coordinated geometry. These open metal sites act as Lewis-acidic adsorption sites and endow the materials with a high density of guest-accessible binding centres.[205] Consequently, M_2(dobdc) derivatives have been widely studied for their guest adsorption behavior,[199,206] magnetic properties,[207] catalytic activity[208–210] and chemical stability in the presence of small molecules such as water and ammonia.[211,212] Although the topology of M_2(dobdc) is retained across different metal centres due to the derivatives' isoreticular nature, the choice of metal exerts a profound influence on functional properties via differences in ionic radius, coordination strength, and electronic structure.

Several M_2(dobdc) derivatives have demonstrated catalytic activity in industrially relevant reactions, such as ammonia synthesis,[210] Friedel-Crafts acylation[209] and NO_x reduction.[213] Comparative studies have highlighted the importance of metal identity, with Mg_2(dobdc) offering superior CO_2 uptake,[206] while Ni_2(dobdc) shows enhanced hydrogen sorption.[199] Synergetic effects have also been exploited in mixed-metal systems; for example, thermally treated $(Ni/Mg)_2$(dobdc) acts as a bifunctional catalyst for the CO_2 methanation, exploiting the high CO_2 capacity of Mg_2(dobdc) along with Ni-centered hydrogenation activity under confinement.[214]

Geometric expansion of the organic linker yields the isoreticular M_2(dobpdc) framework, incorporating the extended 4,4'-dioxido-[1,1'-biphenyl]-3,3'-dicarboxylate ($dobpdc^{4-}$) linker (4,4'-dioxido-[1,1'-biphenyl]-3,3'-dicarboxylate).[1] This structural modification increases the pore diameter to ∼22 Å, enhancing guest diffusion and enabling dative post-synthetic functionalization at the open metal sites with various diamines (Figure 8.1).[1,215–219] Loading of the material with *N*,*N*'-dimethylethylenediamine (mmen) results in occupation of each of the open metal sites by one mmen ligand, inducing a cooperative CO_2 sorption mechanism with high selectivity and fast kinetics. These features render mmen@Mg_2(dopbdc) a benchmark material for direct air capture technologies.[1,216]

Despite the extensive literature on the adsorption and catalytic properties of MOF-74-type materials, comparatively little is known about their behavior under mechanical stress and elevated pressure.[220,221] This is a critical gap, as high pressures are encountered not only in process environments (e.g., fixed-bed reactors, high-pressure separations) but also during manufacturing steps such as pelletization and membrane fabrication. For instance, Ni_2(dobdc) microcrystalline powder irreversibly amorphizes under a pelletization pressure of 10 kbar, resulting in complete loss of porosity, whereas pelletization at only 1 kbar retains crystallinity and methane uptake capacity.[222] A deeper understanding of the structural response of MOF-74-type materials under pressure is thus essential for guiding their integration into industrial processes and technological devices.

In general, MOFs are considered as mechanically soft materials, with bulk moduli ranging from 3 – 30 GPa,[33] even though few examples with extraordinarily high bulk moduli up to about 80 GPa have been reported.[223–225] Their pressure responses span a wide spectrum, from rigid compression and amorphization (MOF-5,[36] ZIF-8,[226] UiO-66[227]) to more complex transitions, such as the open-to-closed pore transformation in MIL-47 at only

1400 bar, driven by a wine-rack-type flexibility.[228] While M_2(dobdc) materials are generally viewed as rigid, structural modifications, particularly through linker elongation, may impart additional degrees of flexibility.[220]

In this work, we investigate the high-pressure behavior of a series of M_2(dobdc) materials ($M^{2+} = Mg^{2+}$, Mn^{2+}, Co^{2+}, Ni^{2+}, Cu^{2+}, Zn^{2+}) as well as the expanded Mg_2(dobpdc) with and without mmen loading. Using in situ PXRD under hydrostatic pressures up to 4000 bar, we systematically analyze compression mechanisms, assess the influence of metal identity, and evaluate the role of linker extension. The resulting structure-property relationships offer key insights into the mechanical response of MOF-74-type frameworks and provide a valuable basis for the rational design of MOFs for pressure-intensive industrial applications.

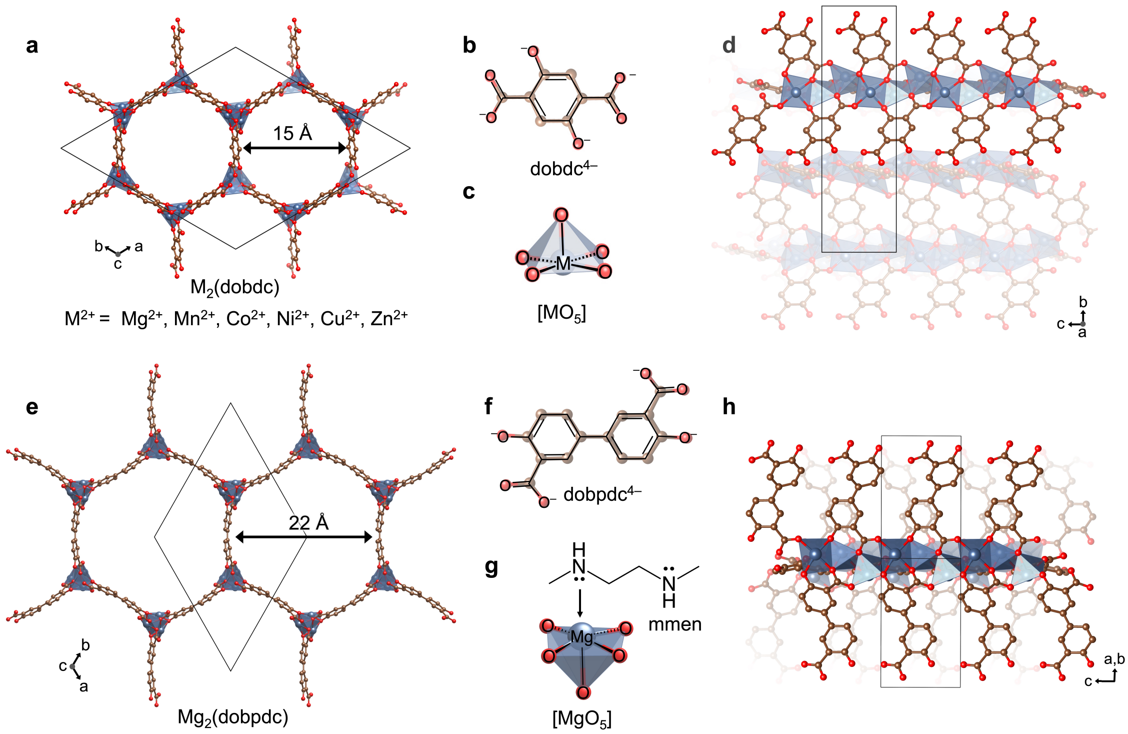

Figure 8.1. **a** Crystal structure of M_2(dobdc) materials featuring a series of metal ions M^{2+} interconnected by the 2,5-dioxido-1,4-benzenedicarboxylate ($dobdc^{4-}$) linker (**b**). The square-pyramidal coordination units (**c**) feature an open metal site and constitute rods of edge-shared coordination units along the hexagonal channels (**d**). **e** Crystal structure of Mg_2(dobpdc) featuring the geometrically extended $dobpdc^{4-}$ linker (**f**) as well as an open metal site at the square pyramidally coordinated Mg^{2+}. The pore diameters shown in panels **a** and **e** correspond to the Zn-analogues, respectively. Guest loading with mmen leads to occupation of the former open metal site through the coordinative bond of the diamine nitrogen atom. **h** Rods of edge-sharing coordination units running along the *c*-axis.

8.3 Results and Discussion

8.3.1 Synthesis of MOF-74-Type Materials

M_2(dobdc) materials (M^{2+} = Mg^{2+}, Mn^{2+}, Co^{2+}, Ni^{2+}, Cu^{2+}, Zn^{2+}) and Mg_2(dobpdc) were synthesized according to published protocols.[201,204,206,209,229,230] After a solvent exchange with methanol or ethanol over several days, the materials were activated under dynamic vacuum at 110−250 °C. Phase purity of all materials was confirmed by structureless profile fits (Pawley method[62]) of PXRD patterns (Figure A3.15–A3.22). Solid-state IR spectroscopy (Figure A3.11–A3.12) as well as solution ^{1}H NMR spectroscopy (materials digested in DMSO-d_6 and DCl, Figure A3.1–A3.10) prove successful activation. The degree of activation, defined as the fraction of open metal sites, exceeded 95% for most samples. Only Mg_2(dobdc) exhibited a lower degree of activation of 91% due to the presence of residual *N*,*N*-dimethylformamide (Table A3.1).

In addition to guest-free Mg_2(dobpdc), a second batch of diamine-loaded mmen@Mg_2(dobpdc) was prepared by immersion of the MOF in a solution of mmen in *n*-hexan, followed by thermal activation. An mmen-loading of 84% (i.e., 84% of the Mg sites are occupied by mmen) was determined from the ^{1}H NMR spectrum of a digested sample (see Figure A3.8, Table A3.1).

8.3.2 High-Pressure PXRD Analysis of M_2(dobdc) Derivatives

To probe the mechanical response of the M_2(dobdc) derivatives, high-pressure (HP)PXRD experiments were conducted under hydrostatic conditions up to 4000 bar. A custom-built high-pressure cell equipped with X-ray transparent diamond windows enabled controlled hydraulic compression, with silicone oil employed as the pressure transmitting medium (PTM).[231,232] Activated microcrystalline MOF powders were loaded into Kapton capillaries (1 mm outer diameter) under an inert atmosphere in a glovebox. The PTM was subsequently added, and the capillaries were centrifuged to ensure complete removal of gas bubbles prior to hermetic sealing (Figure A3.13). The sealed capillaries were then mounted in the high-pressure cell, where hydrostatic pressure was applied using water and a hydraulic pump. Each experiment commenced with the collection of a PXRD pattern at ambient pressure, followed by incremental increases in pressure up to 4000 bar. After pressure release, a final PXRD pattern was recorded at ambient conditions (denoted as 1* bar) to evaluate structural reversibility.

Unit cell parameters at each pressure step were extracted via sequential Pawley profile fits. Pressure-dependent unit cell volumes were fitted using the second-order Birch-Murnaghan equation of state (BMEOS) to extract the bulk modulus (K_0). To quantify the anisotropy of structural contraction, linear compressibilities along the a,b directions ($\alpha_{a,b}$) and along the c-axis (α_c) were also calculated. Since both M_2(dobdc) and M_2(dobpdc) frameworks crystallize in the trigonal system (space groups $R\bar{3}$ and $P3_121$, respectively) with $a = b$, $\alpha = \beta = 90°$ and $\gamma = 120°$, these parameters provide insight into directional deformation behavior. The pressure fitting range for each sample was adjusted to exclude data points affected by the onset of amorphization or excessive peak broadening.

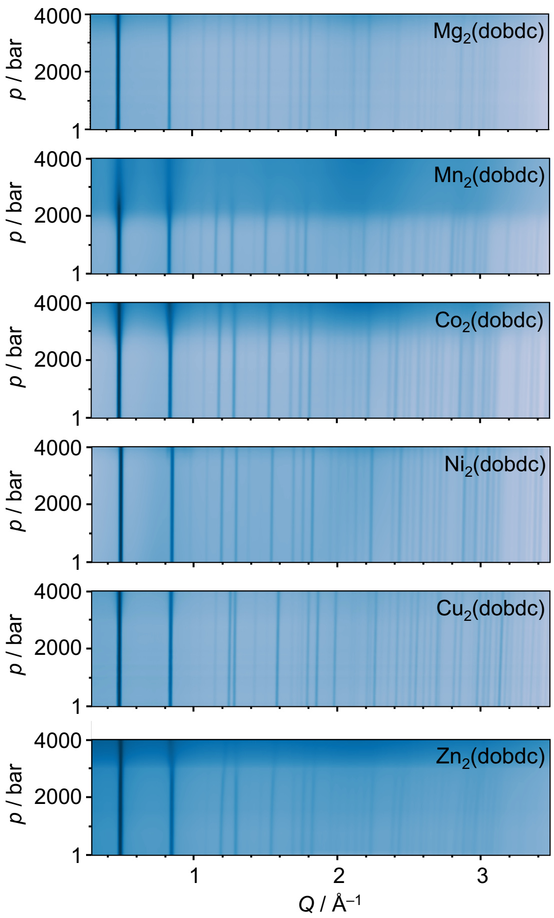

Figure 8.2. Contour maps of the HPPXRD patterns of the M_2(dobdc) materials in the pressure range from atmospheric pressure (1 bar) to 4000 bar. Each map is generated by interpolation from 15 – 34 diffraction patterns recorded at varying pressure points between 1 and 4000 bar. The normalized diffraction intensities are shown on a color scale from dark blue (high intensity) to light purple (low intensity).

The experimental procedure and data evaluation workflow were validated using KBr as a pressure standard. The extracted bulk modulus of KBr ($K_0 = 15.1 \pm 0.2$ GPa; Figure A3.23, A3.35–A3.37 and Table A3.4) is in excellent agreement with literature values (14.2–14.6 GPa),[233,234] confirming the accuracy of the setup.

All M_2(dobdc) derivatives show a continuous contraction of the unit cell upon compression, as evidenced by a sample-dependent, progressive shift of Bragg reflections to higher Q (Figure 8.2). With increasing pressure, a rise in background intensity is observed, attributed to water accumulation in the beam path. While Mg_2(dobdc), Ni_2(dobdc), and Cu_2(dobdc) retain sharp Bragg peaks and high crystallinity up to 4000 bar, Mn_2(dobdc), Zn_2(dobdc) and Co_2(dobdc) exhibit progressively stronger peak broadening and partial amorphization. Amorphization sets in around 1500 bar for Mn_2(dobdc), 2000 bar for Zn_2(dobdc), and 2500 bar for Co_2(dobdc). These trends persist after full pressure release (1* bar): Mn_2(dobdc) and Zn_2(dobdc) remain largely amorphous with only broad and weak reflections, while Co_2(dobdc) shows partial recovery of crystallinity (Figure 8.3a). In contrast, Mg_2(dobdc), Ni_2(dobdc), and Cu_2(dobdc) maintain well-defined PXRD patterns with only minor peak broadening relative to their initial states.

To further elucidate the origin of peak broadening, Pawley profile fits were carried out on selected HPPXRD patterns of Ni_2(dobdc) across the entire pressure range using TOPAS V6.1. Instrument-specific peak shape function and macros that account for sample-specific broadening contributions from crystallite domain size and microstrain were applied (see Chapter A3 for details).[235] This analysis reveals a modest increase in microstrain ($\epsilon_0 =$ 0.07 – 0.2%) and a continuous decrease in domain size from 160 nm at ambient pressure to

70 nm at 4000 bar (see Figure 8.3b, A3.34). These results indicate that pressure-induced peak broadening is primarily due to a reduction in domain size induced by mechanical stress.

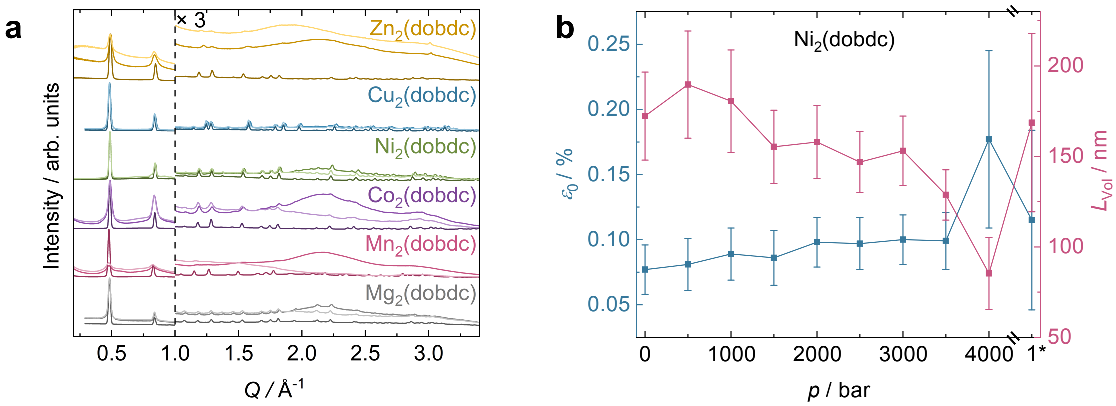

Figure 8.3. **a** HPPXRD patterns of M_2(dobdc) materials, with line colors fading from full (1 bar) to intermediate (4000 bar) to pale (after decompression from 4000 to 1 bar) intensity. **b** Trend in microstrain ϵ_0 and crystalline domain size L_{Vol} provided by the analysis of pressure-induced Bragg peak broadening for Ni_2(dobdc). Lines serve as a guide to the eye.

The extracted bulk moduli span a wide range, from ~10 GPa for Zn_2(dobdc) to ~24 GPa for Ni_2(dobdc) and Mg_2(dobdc) (Table 8.1). Linear compressibilities along the a,b axes ($\alpha_{a,b}$) are similar across all derivatives, ranging from ~9.1 $\mathrm{TPa^{-1}}$ for Mg_2(dobdc) to ~14.2 $\mathrm{TPa^{-1}}$ for Zn_2(dobdc), indicating comparable lateral rigidity. In contrast, compressibility along the c-axis (α_c) is up to four times larger than $\alpha_{a,b}$ and varies markedly with the metal identity, spanning 19.6 to 62.1 $\mathrm{TPa^{-1}}$ (Figure 8.4a,b). Notably, Zn_2(dobdc) exhibits by far the highest α_c, consistent with its low bulk modulus and early onset of amorphization. The experimentally determined bulk moduli and linear compressibilities of Mg_2(dobdc) and Zn_2(dobdc) are in excellent agreement with those predicted in previous theoretical studies.[220,221] Given that the ionic radii of Mg^{2+} (0.66 Å[236]) and Zn^{2+} (0.68 Å[236]) are almost identical and that both ions do not feature any ligand field stabilization energy (LFSE), the higher compressibility of Zn_2(dobdc) compared to Mg_2(dobdc) may be explained by the higher polarizability and lower chemical hardness of Zn^{2+} (Pearson chemical hardness:[237] 10.3 eV) compared to Mg^{2+} (32.5 eV), reducing the stiffness of the [ZnO_5] polyhedra.

The generally pronounced anisotropy between $\alpha_{a,b}$ and α_c present in all M_2(dobdc) derivatives reflects the structural architecture of these frameworks: the c-axis runs parallel to the rod-shaped inorganic building unit of edge-sharing square-pyramidal [MO_5] polyhedra. Consequently, the variation in K_0 across the series is primarily governed by differences in α_c and hence the elastic response of the chain of [MO_5] polyhedra.

These differences in mechanical behavior, can be rationalized by considering the electronic structure of the metal ions. According to ligand field theory,[238] high-spin square-pyramidally coordinated Mn^{2+} ($3d^5$) has an LFSE of zero,[239] while Co^{2+} ($3d^7$), Ni^{2+} ($3d^8$)

Table 8.1. Linear compressibilities ($\alpha_{a,b}$, α_c) bulk moduli (K_0), reference volume (V_0), reference volume per formula unit ($V_{0,\mathrm{f.u.}}$) and utilized fitting range for all MOF-74-type materials under study here.

Material	$\alpha_{a,b}$ / TPa^{-1}	α_c / TPa^{-1}	$\alpha_c/\alpha_{a,b}$	K_0 / GPa	V_0 / Å^3	$V_{0,\mathrm{f.u.}}$ / Å^3	fitting range / bar
Mg_2(dobdc)	9.1 ± 0.5	22.3 ± 0.6	2.45	24.0 ± 0.3	3934.5 ± 0.3	437.2	50 – 4000
Mn_2(dobdc)	10.8 ± 0.2	35.6 ± 0.6	3.30	17.1 ± 0.3	4229.4 ± 0.4	469.9	1 - 1500
Co_2(dobdc)	13.6 ± 0.3	23.9 ± 0.3	1.76	19.1 ± 0.2	3978.3 ± 0.3	442.0	1 – 2500
Ni_2(dobdc)	10.3 ± 0.1	19.6 ± 0.1	1.90	24.1 ± 0.1	3905.1 ± 0.1	433.9	1 – 3500
Cu_2(dobdc)	13.6 ± 0.4	26.8 ± 0.5	1.97	17.4 ± 0.2	3616.2 ± 0.5	401.8	1 – 4000
Zn_2(dobdc)	14.2 ± 0.5	62.1 ± 3.3	4.37	10.3 ± 0.4	3912 ± 2	434.7	1 – 2000
Mg_2(dobpdc)	136.9 ± 1.3	32.3 ± 7.4	0.24	3.1 ± 0.1	2668 ± 1	889.3	1 – 1200
mmen@ Mg_2(dobpdc)	85.4 ± 3.4	58.1 ± 2.3	0.68	4.0 ± 0.2	2791 ± 2	930.3	1 – 1200

and Cu^{2+} (3d^9) possess modest LFSEs that enhance coordination rigidity. Mg^{2+} (3s^0) and Zn^{2+} (3d^{10}) engage minimal geometric stabilization via orbital interactions, relying instead on non-directional electrostatic bonding. As a result, frameworks incorporating metals with no LFSE (Mg^{2+}, Mn^{2+}, and Zn^{2+}) exhibit more pronounced strain-softening at elevated pressure; i.e., the increase in compressibility with pressure due to facile distortion of the coordination sphere (Figure 8.4c).

In an attempt to evaluate the influence of structural and electronic factors, we performed linear correlation analyses between K_0 and various descriptors: ionic radius, electronegativity, LFSE, and coordination distortion parameters derived from literature-reported high-resolution M_2(dobdc) crystal structures.[240] Cu_2(dobdc) was excluded from the analysis due to the strong Jahn-Teller distortion of its [CuO_5] polyhedra, which results in a unit cell volume 8–14% smaller than the other analogues (Table 8.1). The already more compact ambient-pressure structure of Cu_2(dobdc) naturally features a comparatively high $K0$ of ~17.4 GPa. Mg_2(dobdc) was also excluded due to its main group character.

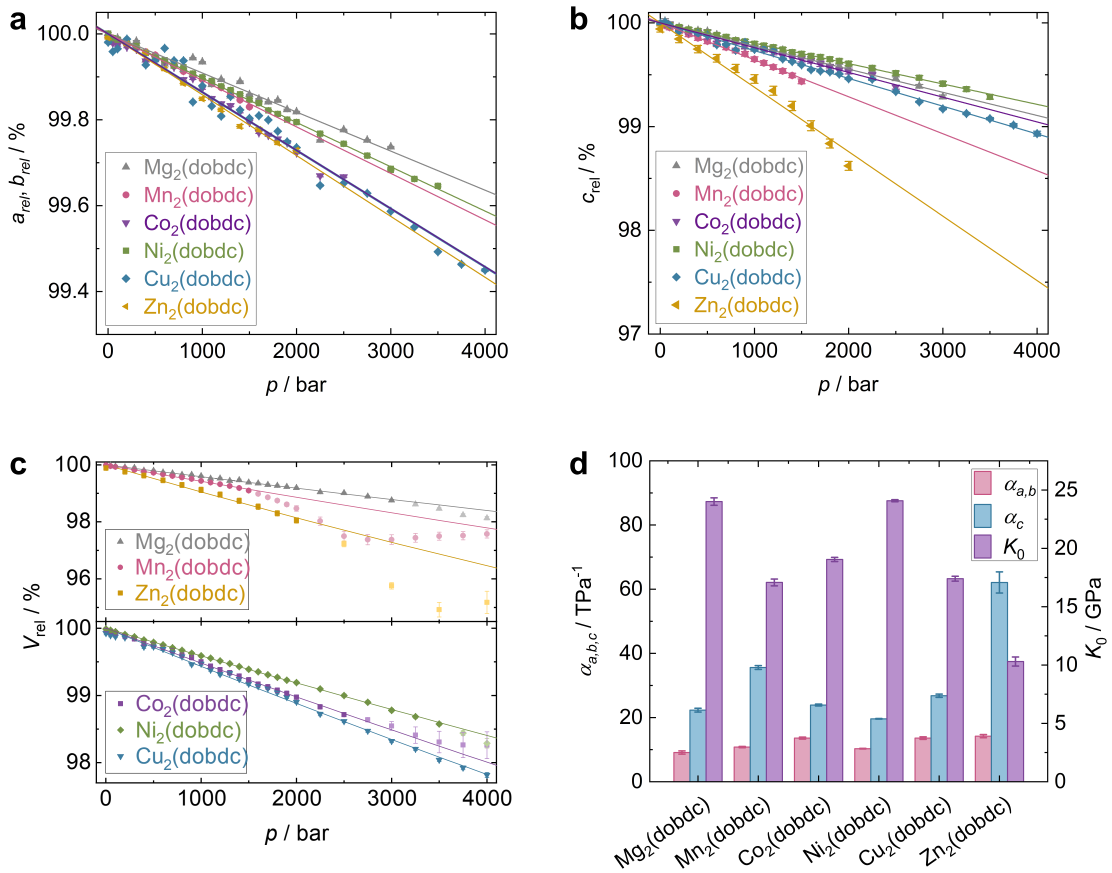

Figure 8.4. **a**,**b** Trends in the unit cell parameters upon pressure increase (data points) with linear fits (lines) providing the linear compressibility values shown in panel **d** and Table 8.1. **c** Pressure-induced reduction of the relative unit cell volume V_{rel} for M_2(dobdc) materials (data points) with fits to the second-order BMEOS (lines) performed on the full-colored data points. Data points shown in pale colors were excluded from the evaluation because of pronounced strain-softening behavior (upper part) or other deviations from the initial trend. **d** Comparison of the linear compressibilities $\alpha_{a,b}$ and α_c and the bulk modulus K_0 for all investigated M_2(dobdc) materials.

Among all tested parameters, only the bond length distortion index (root mean square deviation (RMSD), of M−O distances) and the angular distortion index (RMSD of bond angles within the $[MO_5]$ unit from their ideal values in a square-pyramidal geometry) exhibited strong correlations (i.e., Pearson coefficient $|r| > 0.9$) with K_0, with Pearson coefficients of −0.98 and −0.91, respectively. Other parameters yielded weaker correlations ($|r| \leq 0.8$, see Chapter A3 for details). These results demonstrate that mechanical compliance is linked to deviations from ideal square-pyramidal coordination geometry. Frameworks with more distorted $[MO_5]$ polyhedra are more susceptible to pressure-induced deformation and display lower stiffness, and, in some cases, irreversible amorphization.

8.3.3 High-Pressure PXRD Analysis of Mg_2(dobpdc) Derivatives

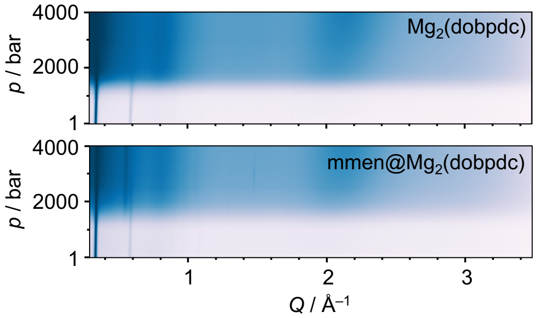

Figure 8.5. high-pressure powder X-ray diffractions (HPPXRDs) of Mg_2(dobpdc) materials in the pressure range from atmospheric pressure (1 bar) to the maximum pressure of 4000 bar. The normalized diffraction intensities are shown on a color scale from dark blue (high intensity) to light purple (low intensity).

To investigate the role of linker elongation on the governing mechanical response under pressure, we examined the high-pressure behavior of Mg_2(dobpdc) and its diamine-loaded derivative mmen@Mg_2(dobpdc), using the same pressure cell setup and data analysis routines applied to the M_2(dobdc) series. In contrast to the parent framework Mg_2(dobdc), both expanded Mg_2(dobpdc) derivatives exhibit a pronounced tendency toward pressure-induced amorphization, with amorphization initiating at pressure as low as ∼1500 bar (Figure 8.5).

Sequential profile fitting of the HPPXRD data up to 1200 bar (i.e., before the onset of amorphization) reveals that the Mg_2(dobpdc) compresses predominantly along the a,b axes, with $\alpha_{a,b} = 137 \pm 1\,\mathrm{TPa}^{-1}$, four times higher than along the c-axis ($\alpha_c = 32 \pm 7\,\mathrm{TPa}^{-1}$) (Figure 8.6, Table 8.1). Upon mmen loading, this anisotropy is reduced since steric hindrance from the coordinated guest molecules restricts contraction in the a,b plane ($\alpha_{a,b} = 86 \pm 3\,\mathrm{GPa}$), resulting in compensatory contraction along the c-axis ($\alpha_c = 62 \pm 2\,\mathrm{GPa}$). Despite these changes in directional compressibility, the bulk moduli of both materials remain exceptionally low ($K_0 = 3.1 \pm 0.1\,\mathrm{GPa}$ for Mg_2(dobpdc) and $K_0 = 4.0 \pm 0.2\,\mathrm{GPa}$ for mmen@Mg_2(dobpdc)). The steric demand of the mmen guests is further reflected in the ∼5% increase in the reference unit cell volume V_0 relative to the guest-free framework (Table 8.1).

The high compressibility of the Mg_2(dobpdc) derivatives is attributed to the conformational flexibility of the geometrically elongated $dobpdc^{4-}$ linker. The linker already adopts a bend configuration under ambient conditions, and further bending under pressure is presumed to facilitate efficient volume reduction through a linker distortion mechanism. This mode of compression, dominated by deformation in the a,b plane, is in stark contrast to the c-axis-dominated compression observed for the M_2(dobdc) series, where structural contraction is accommodated by distortion of the square-pyramidal $[MO_5]$ polyhedra.

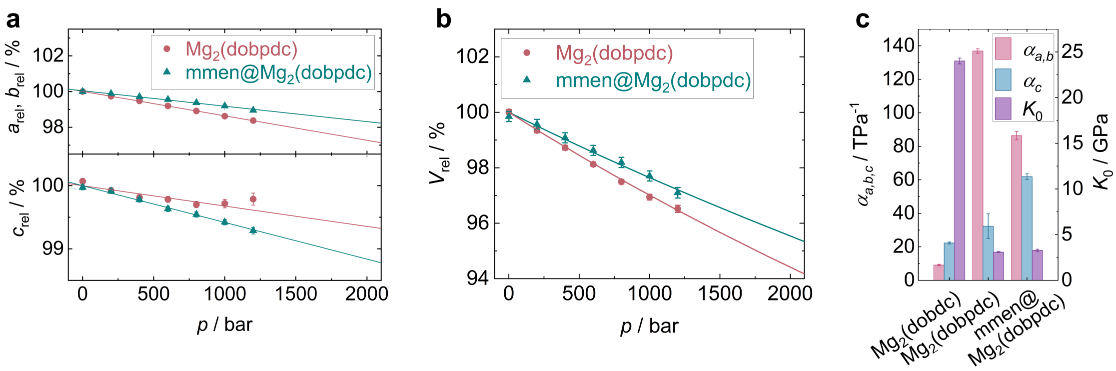

Figure 8.6. **a** Trends in the unit cell parameters upon pressure increase (data points) with linear fits (lines) providing the linear compressibility values shown in panel **c** and Table 8.1. **b** Pressure-induced change in the relative unit cell volume V_{rel} (data points) with fits of the second-order BMEOS (lines) providing the bulk moduli depicted in panel **c** and Table 8.1. **c** Comparison between the linear compressibilities $\alpha_{a,b}$ and α_c and bulk moduli (K_0) of Mg_2(dobdc) and the Mg_2(dobpdc) materials before and after guest loading with mmen.

At pressures above ~1500 bar, guest-free Mg_2(dobpdc) exhibits a drastic loss of crystallinity, with the emergence of broad diffuse scattering features indicative of far-reaching structural collapse. This amorphization is irreversible, as demonstrated by the nearly featureless PXRD pattern observed after decompression to ambient pressure (Figure 8.7a).

By contrast, mmen@Mg_2(dobpdc) displays a more complex response. Beginning at ~1400 bar, a weak but distinct scattering peak emerges at $Q = 0.55\,\text{Å}^{-1}$ and gradually intensifies with increasing pressure, while the Bragg reflections of the original trigonal phase fade and largely disappear above 2500 bar (Figure 8.7b). This behavior is indicative of a pressure-induced phase transition to a highly disordered, distorted phase, characterized by a single broad scattering peak. The scattering vector of $0.55\,\text{Å}^{-1}$ corresponds to a real space distance of ~11.4 Å, which is slightly shorter than the lateral spacing between adjacent [MO_5] polyhedra chains in the ambient-pressure single crystal structure of the Zn-derivative mmen@Zn_2(dobpdc) (~12.4 Å).[241] Thus, we propose that the peak at $0.55\,\text{Å}^{-1}$ serves as a signature for the average distance between neighboring [MgO_5] chains in the high-pressure phase of mmen@Mg_2(dobpdc).[242] The emergence of a single broad peak at this Q value strongly suggests that mmen@Mg_2(dobpdc) undergoes a transition to a topologically conserved yet highly distorted phase, characterized by anisotropic and non-periodic deformations of the honeycomb-like channels.

We propose that this high-pressure phase involves an ensemble of elliptically distorted channel geometries, with the major and minor axes of the ellipses having locally varying lengths and crystallographic directions (Figure 8.7c). The combination of lost long-range periodicity and preserved intra-framework connectivity is consistent with a locally ordered, non-periodic structure.[242] Critically, the initial trigonal phase is fully restored upon pressure release, as evidenced by the recovery of sharp Bragg reflections without residual broadening (Figure 8.7b). This demonstrates the reversibility of the transformation and the absence of irreversible structural collapse in the high-pressure phase.

Elliptical distortions of honeycomb-like channels have been previously reported for another expanded MOF-74 derivative (i.e., IRMOF-74-V) under Ar adsorption.[220,243] In the present case, the presence of mmen guest molecules significantly enhances the mechanical resilience of Mg_2(dobpdc), stabilising the framework well beyond the pressure threshold at which the guest-free material undergoes irreversible amorphization. The mmen guests not only prevent collapse but also enable the framework to recover crystallinity after a full pressure cycle. These findings highlight the critical role of guest molecules in modulating mechanical response and point to a broader strategy for improving the pressure tolerance of large-pore, channel-based MOFs through targeted guest incorporation.

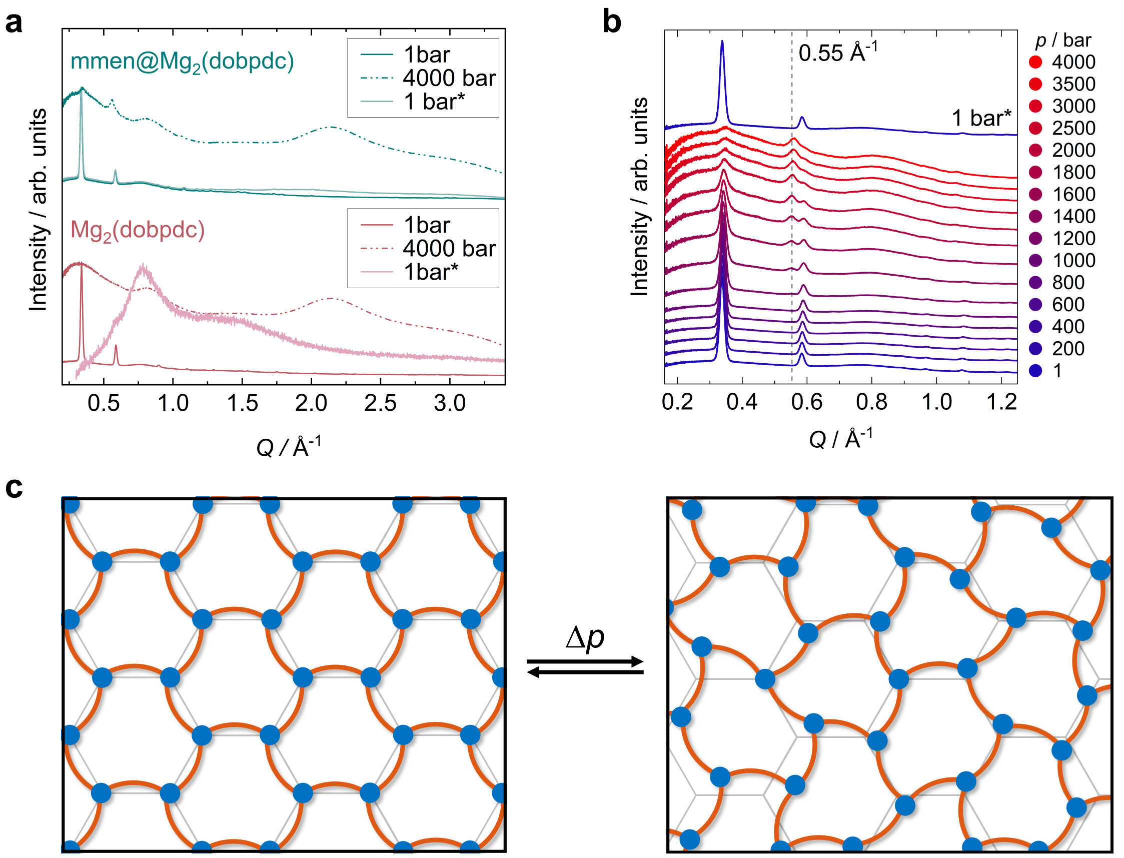

Figure 8.7. **a** HPPXRD pattern of the mmen-loaded and guest-free Mg_2(dobpdc) materials before (1 bar) and after (1 bar*) a complete pressure cycle, together with the pattern collected at the maximum pressure of 4000 bar. The pattern of Mg_2(dobpdc) (1 bar*) was collected using CuK_α radiation. **b** HPPXRD patterns of mmen@Mg_2(dobpdc) during a full pressure cycle monitoring the reversible transition to a disordered high-pressure phase indicated by the scattering peak at 0.55 $Å^{-1}$. **c** Schematic illustration of the envisaged pressure-induced phase transition of mmen@Mg_2(dobpc) viewed along the hexagonal channels of the framework (i.e., along the *c*-axis) with dobpdc^{4-} linkers shown as orange lines between the rod-shaped inorganic building units (blue nodes). mmen guests are omitted in the illustration.

8.4 Conclusion

High-pressure PXRD measurements reveal two fundamentally different compression mechanisms in MOF-74-type materials. For M_2(dobdc) (M^{2+} = Mg^{2+}, Mn^{2+}, Co^{2+}, Ni^{2+}, Cu^{2+}, Zn^{2+}) pressure-induced volume contraction occurs primarily along the crystallographic *c*-axis, driven by distortions of the square-pyramidal [MO_5] coordination environment. The bulk moduli span 10–24 GPa, reflecting the critical influence of the metal center. Correlation analyses highlight that a complex interplay of ionic radii, chemical hardness, ligand field effects and local distortions of the [MO_5] polyhedra is responsible for the large variation in bulk modulus and the differing propensities for (irreversible) pressure-induced amorphization.

In contrast, the expanded analogue Mg_2(dobpdc), compresses mainly through deformation of the flexible dobpdc^{4-} linkers in the *a*,*b*-plane, resulting in exceptionally low bulk moduli of only ~3 GPa. Guest-loading with the diamine mmen modifies this response by restricting lateral compression and inducing a compensatory contraction along the *c*-axis. While guest-free Mg_2(dobpdc) amorphizes irreversibly already at ~1500 bar, mmen@Mg_2(dobpdc) undergoes a reversible transition to a non-periodic, topologically preserved high-pressure phase, likely featuring anisotropic channel distortions, and fully recovers its crystallinity upon decompression from 4000 bar.

These results highlight the critical roles of metal ion electronic structure, coordination geometry, and linker flexibility in determining the mechanical response of MOFs. Beyond advancing the fundamental understanding of framework compression, the results provide key design principles for improving the pressure resistance of MOFs through ligand selection and guest incorporation. This is particularly relevant for large-pore, adsorption-active frameworks such as mmen@Mg_2(dobpdc), a benchmark material in carbon capture.[1] Enhancing their mechanical resilience is essential for their long-term deployment in devices, process engineering, and industrial gas separation technologies operating under elevated pressures.

9 General Summary and Outlook

Recently, metal–organic frameworks (MOFs) have emerged as promising candidates for various industrial and environmental applications due to their great potential for catalysis, gas separation, carbon capture, and sensing.[9,189–191] The implementation of MOFs in such processes requires reliable strategies to immobilize the material without compromising its catalytic or separation performance.

In this context, the present work addresses two key aspects of MOF immobilization: MOF glasses—which offer the advantage of liquid-phase processing and enable the fabrication of seamless (i.e., grain-boundary free) membranes via melt-casting or exfoliation (Part I)—and the high-pressure structural response of a particularly promising subfamily of MOFs, along with the structural origins of their mechanical behavior (Part II).

While Part I aimed to expand the currently limited chemical diversity of MOF glasses by transferring established concepts from silicate glass chemistry, Part II focused on elucidating the structural factors that govern the compressibility and mechanical stability of MOF-74-type materials under high pressure. A fundamental understanding of the structural origins of the high-pressure response is essential for both the fabrication of MOF pellets, typically pelletized under high pressure, and their deployment under reaction conditions involving elevated pressures.

Part I - Traditional Modification of Metal-Organic Framework Glasses

In Part I of this work, the concept of traditional silicate glass modification was transferred successfully to the MOF glass former ZIF-62. In a first step, the conceptual approach required the synthesis of appropriate alkali modifiers.

(i) Lithium and Sodium Benzimidazolate Coordination Networks

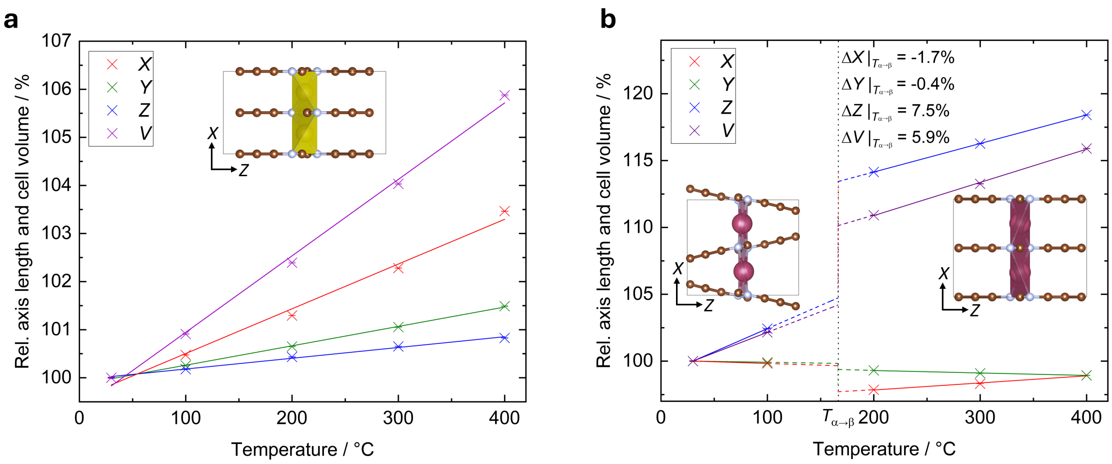

Figure 9.1. Thermal expansivity of Li(bim) (**a**) and Na(bim) (**b**). The Na(bim) $\alpha \to \beta$ phase transition is indicated by the jump in the unit cell parameters at 166 °C. Adapted and modified from reference[137]. For further details, see Figure 4.4 in Chapter 4.

Lithium and sodium benzimidazolate were synthesized and characterized regarding their solid-state structures and thermal behavior. Both compounds were found to crystallize in two-dimensional layered structures, consisting of 4-fold N-coordinated alkali ions bridged by benzimidazolate linkers. Thermal analysis revealed that both compounds undergo melting upon heating, followed by recrystallization upon cooling. Notably, their respective upper thermal stability limit under autogenous pressure lies beyond the melting point of ZIF-62, rendering them suitable candidates as modifiers for ZIF-62 glasses.

Furthermore, Na(bim) exhibits a displacive phase transition at 166 °C to a high-temperature β-phase characterized by pronounced structural disorder. Interestingly, while the low-temperature α-phase displays area NTE, the β-phase shows linear NTE.

(ii) Alkali-Ion-Modified ZIF-62 Glasses

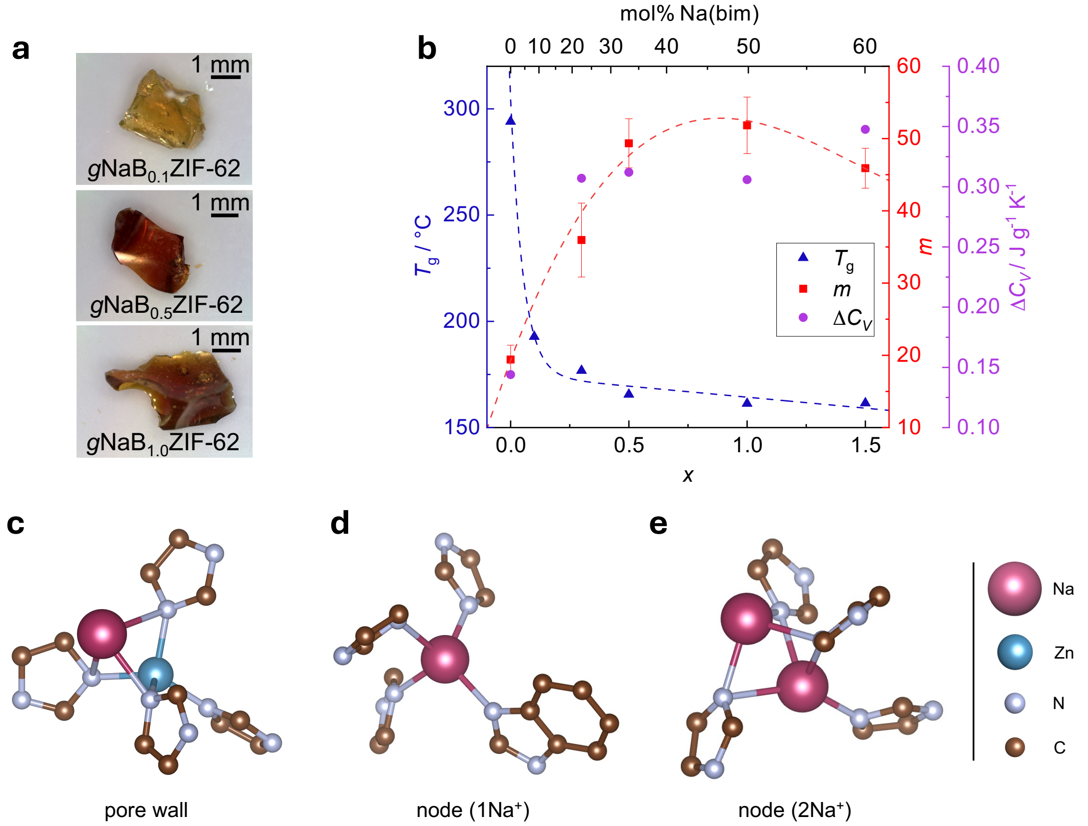

Figure 9.2. **a** Microscope images of shards of Na(bim)-modified ZIF-62 glasses, **b** Trend in thermal parameters such as the glass transition temperature (T_g), calorimetric fragility index (m) and jump in heat capacity at T_g (ΔC_V) as a function of modifier content. **c**,**d**,**e** Structural motives of Na^+ incorporation in the Na(bim)-modified ZIF-62 glass. Adapted and modified from reference[161]. For further details, see Figures 6.2 and 6.4 in Chapter 6.

Melt-quenching of physical mixtures of the ZIF-62 glass former and an alkali-based modifier enables the formation of alkali-ion-modified ZIF-62 glasses across a broad compositional range for both Na(bim) and Li(bim) (see Figure 9.2a). Due to the metal–organic nature of the system and the associated lower decomposition temperatures (ca. 600 °C), significantly lower processing temperatures of 425 °C (for Li(bim)) and 450 °C (for Na(bim)) are required, in contrast to silicate glass systems.[244]

Thermal analysis of the mixtures and glasses revealed the tendency for crystallization of dense $Zn(im)_2$ or $Zn(bim)_2$ phases (i.e., ZIF-zni and ZIF-7-III) at the respective compositional lower and upper limits of the investigated modifier content. Notably, the reduced glass stability observed at low modifier contents is rationalized by the alkali ions' effect of lowering the liquid viscosity.

Systematic investigations showed that an increasing Na(bim) content leads to a decrease in the glass transition temperature, accompanied by an increase in the fragility index, heat capacity jump at T_g, and density (see Figure 9.2b). These trends closely resemble those observed in sodium silicate glass systems and are attributed to network depolymerization and structural disorder resulting from sodium-ion incorporation.

Solid-state ^{23}Na NMR spectroscopy, supported by DFT calculations, revealed a broad range of undercoordinated Na^+, which were grouped into three distinct structural motifs based on their coordination environment (see Figure 9.2c-e). This structural insight into local Na^+ incorporation supports the conceptual depolymerization model and extends the current understanding of alkali ion modification in glass networks.

The incorporation of the modifier also induces partial pore collapse, which aligns well with the increased structural complexity, evidenced by a higher liquid fragility, enhanced configurational degrees of freedom, and a decrease in Zn$\cdots$Zn correlation density with increasing modifier content.

These results demonstrate that the concept of alkali modification, well-established in silicate glass chemistry, as well as the associated structure–property relationships, are transferable to the emerging class of MOF glasses. Hence, this study not only serves as a proof-of-concept but also introduces a powerful tool for tailoring key material properties, including glass transition temperature, porosity, liquid viscosity, density, glass stability, and hydrophilicity.

Despite these conceptual similarities, notable structural differences arise from the steric demand and geometric characteristics of the (benz)imidazolate anion and its coordination behavior in the modified ZIF-62 glasses compared to the oxide anion in silicate glasses. These differences manifest in significantly lower coordination numbers of 3-4 for Na^+ in the modified ZIF-62 glasses, compared to coordination numbers of 5–6 in sodium silicate glasses.[125] The modified ZIF-62 glasses further exhibit unique topological features, including the partial retention of their intrinsic porosity, which is an exceptional property and advantage of MOF glasses.

While the requirement for autogenous pressure during thermal processing at elevated temperatures presents a potential burden for industrial scalability, this challenge was shown to be manageable through appropriate adjustments of the processing parameters.

(iii) Modifier Leaching

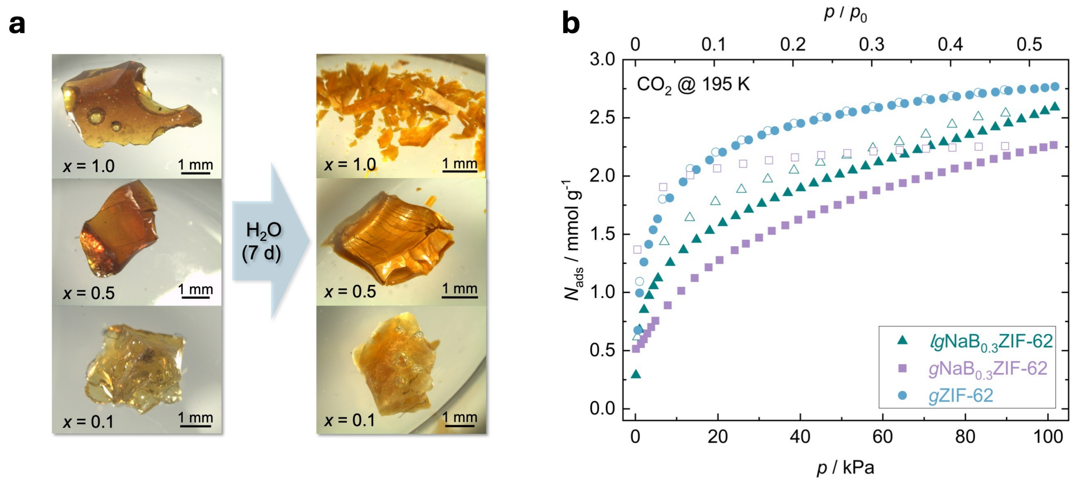

Figure 9.3. **a** Microscope images of Na(bim)-modified ZIF-62 glasses gNaB$_x$ZIF-62 before and after water-leaching. **b** CO_2 gas (physi-) sorption isotherms of gZIF-62, gNaB$_{0.3}$ZIF-62 and water-leached lgNaB$_{0.3}$ZIF-62. Adapted and modified from reference[161]. For further details, see Figure 6.5 in Chapter 6.

While the incorporation of Na(bim) reduces the porosity and increases the density of the resulting modified glasses, it was shown that subsequent water leaching partially removes sodium imidazolate from the modified glass. The conventional Vycor process for producing porous silicate glasses, in contrast, typically relies on acid leaching to create porosity.[166,167] The water-leaching of modified ZIF-62 glasses was demonstrated to generate mesopores within an already microporous network, enabling hierarchical pore architectures. This hierarchical tuning of porosity in a glassy material offers a powerful strategy for optimizing the separation performance in potential membrane applications.

In total, these findings represent a substantial step forward for the field of MOF glasses by demonstrating how well-established concepts and methods can be employed to systematically enhance the chemical and structural diversity of MOF glasses, thus facilitating their way into various areas of application.

Nonetheless, the extent to which these established concepts from traditional glass chemistry can be transferred to MOF glasses remains an open question. State-of-the-art silicate glasses incorporate a wide variety of modifiers to tailor properties such as mechanical stability, chemical durability, thermal expansivity, shock resistance, and color.[46] Properties, which remain of high importance for the manufacturing of MOF glass products, such as membranes for industrial separation purposes. Translating this chemical complexity into the MOF glass domain via the use of boro-, alumino-, or alkali metal (benz)imidazolates presents an intriguing direction for future research. These studies may also include the exploration of alternative MOF glass formers as base materials for modifier incorporation, as well as the transfer of other established concepts, such as post-synthetic ion exchange, which is widely applied in the manufacturing of advanced silicate glasses like Gorilla® glass.[119]

Part II - Understanding the High-Pressure Behavior of MOF-74-Type Materials

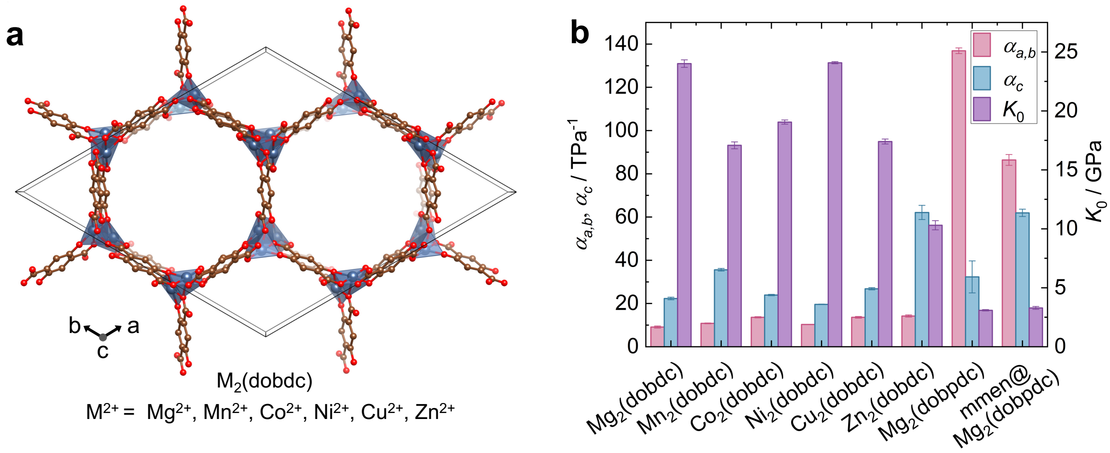

Figure 9.4. **a** Excerpt of the crystal structure of MOF-74(M) featuring various metal ions M^{2+}. **b** Linear compressibilities α and bulk moduli K_0 for all investigated MOF-74-type materials. Adapted and modified from reference[188]. For further details, see Figures 8.1, 8.4 and 8.6 in Chapter 8.

Several MOF-74-type materials have been identified as promising candidates for a wide range of applications, including catalysis and carbon capture.[1,214] In this work, their structural response to high pressures of up to 4000 bar was investigated, revealing two distinct contraction mechanisms that manifest as elastic responses in these materials.

All investigated isoreticular MOF-74 materials exhibit a predominant contraction along the crystallographic c axis, which results in a progressive distortion of the coordination environments of the square-pyramidally coordinated metal ions with increasing pressure (see Figure 9.4a). Materials containing metal ions with minor to no directional preference in their coordination geometry (e.g., Mg^{2+}, Zn^{2+}) or with zero LFSE (e.g., Mn^{2+}) were found to display pronounced strain-softening behavior upon pressure increase. The bulk modulus of MOF-74 materials (excluding MOF-74(Mg) and (Cu)) was found to correlate with the degree of geometric distortion of the coordination polyhedra at ambient pressure, with stronger distortion resulting in lower bulk moduli. Surprisingly, but following preceding theoretical studies,[220,221] MOF-74(Mg) was found to feature a rather high bulk modulus, which is attributed to the low polarizability of Mg^{2+} (see Figure 9.4b).

The structurally closely related Mg_2(dobpdc), which incorporates the geometrically extended dobpdc^{4-} linker, exhibits a larger pore diameter and higher surface area compared to MOF-74. Interestingly, this extension causes a switch in the compression mechanism: Instead of a contraction along the c axis, Mg_2(dobpdc) predominantly contracts along the

a,b axis under pressure, indicating progressive distortion of the linker itself rather than the coordination units. The material shows an exceptionally low bulk modulus of only ~3 GPa and undergoes irreversible amorphization above ~1200 bar.

Upon guest loading with mmen, the high-pressure response changes significantly. While the bulk modulus remains unchanged at ~ 4 GPa, amorphization at elevated pressures becomes reversible. This suggests that guest incorporation increases the mechanical stability of the framework, likely through stabilization of the metal coordination environment by occupation of the former open metal sites. The appearance of a diffuse scattering peak in the HPPXRD pattern of the guest-loaded material during amorphization indicates a reversible transition to a highly disordered high-pressure phase.

This study offers new insights into the structural response of a subclass of MOFs under pressure, experimentally confirming previously reported theoretical predictions regarding their mechanical properties. These findings were made possible by the development of a custom-built high-pressure PXRD setup, which enables precise pressure control in a range suitable for relatively soft MOFs. Thus, this work not only advances MOF-74-type materials toward industrial applications in catalysis and CO_2 capture but also demonstrates the broader applicability of the newly developed high-pressure PXRD setup for future investigations of other promising materials. In this context, the anisotropic elastic response of MOF-74-type materials under pressure was successfully traced back to structural features such as the degree of distortion of coordination environments, the linker geometry, and the electronic structure of the metal ion (e.g., bond character and ligand field stabilization). These underlying structure–property relationships were shown to govern trends in the materials' mechanical behavior and enable a deeper understanding of the structural origin of the high-pressure response.

Future studies may focus on the transferability of this understanding to other MOFs of high relevance, aiming to expand current knowledge of their mechanical behavior across a broader structural and topological range. In this context, the described structure–property relationships could contribute to the development of general design principles, enabling the rational design of future MOFs with tailored mechanical properties optimized for industrial-scale applications such as catalysis or gas separation.

All in all, this work addresses two key aspects of MOF immobilization, thereby deepening our understanding of structure–property relationships and paving the way for a future industrial implementation of MOFs.

10 Experimental Section to Chapter 4

All chemicals and solvents used in the synthesis were purchased from commercial sources. The benzimidazole was dried by resublimation at 100 °C under dynamic vacuum (10^{-3} mbar) overnight prior to the syntheses.

10.1 Synthesis of Li(bim)

1.5 g (12.7 mmol) of dry benzimidazole (Hbim) was dissolved in 55 mL of dry tetrahydrofuran (THF) in a purged Schlenk flask (250 mL) under constant argon flow. The solution was then cooled to approx. –70 °C and 4.5 mL (11.5 mmol) *n*-butyllithium (2.5 M in *n*-hexane) was slowly added using a syringe. The cooling bath was removed, and the solution was allowed to warm up to room temperature (25 °C) while stirring overnight. The next day the mother liquor was decanted from the precipitate, the solid was washed with dry *n*-hexane (1 x 40 mL) and dried at 100 °C under a dynamic vacuum for 2 h. Subsequently, the solid was heated to 250 °C for 3 h under a dynamic vacuum to remove any excess Hbim. Li(bim) was obtained as a white powder and stored in a glovebox under Ar atmosphere (yield 1.15 g, 81%).

10.2 Synthesis of α-Na(bim)

1.5 g (12.7 mmol) of dry Hbim was dissolved in 30 mL of dry THF in a purged Schlenk flask (250 mL) under constant argon flow. The solution was cooled with an ice bath and 6 mL (12.0 mmol) of sodium hexamethyldisilazane (NaHMDS, 2 M in THF) was added under Ar flow. The ice bath was removed, and the reaction mixture was allowed to warm up to room temperature under stirring for 1 h. The yellow solution was filtered through a syringe filter (PTFE, 0.2 µL) and transferred into another Schlenk flask (250 mL). 40 mL of dry *n*-hexane was added to form a white precipitate. The suspension was stored in a fridge at 8 °C overnight. Subsequently, the supernatant fluid was removed, and the white powder was washed with dry *n*-hexane (2 x 20 mL). After solvent removal under dynamic vacuum at 100 °C for 2 h, the solid material was transferred to a Schlenk-tube which was introduced to a tube furnace and heated at 280 °C for 3 h under dynamic vacuum to remove any excess Hbim. α-Na(bim) was obtained as a light-yellow powder and stored in a glovebox under Ar atmosphere (yield 1.43 g, 85%).

10.3 X-ray powder diffraction (XRPD)

XRPD measurements were performed at Beamline BL9 at DELTA (Dortmunder Elektronenspeicherring-Anlage, Dortmund, Germany) with a monochromatic X-ray beam

($\lambda = 0.4603$ Å) using a Dectris Pilatus 100K detector in an angular range from 2° – 35° (2Θ) and a capillary rotor. The thoroughly ground sample material was filled in a borosilicate capillary (1.0 mm diameter) in a glovebox under an inert atmosphere (N_2) and sealed using epoxy glue (UHU Schnellfest). Variable temperature (VT)XRPD experiments were conducted at beamline I15-1 at DLS (Diamond Light Source, UK) using a monochromatic X-ray beam ($\lambda = 0.161669$ Å), a Perkin Elmer XRD 4343 CT 2D plate detector, a capillary rotor and a hot air blower for adjusting the sample temperature. The finely ground sample material was filled in a borosilicate glass capillary (1.0 mm outer diameter) and sealed using epoxy glue (UHU Schnellfest) in a N_2-filled glovebox. Data integration and processing were performed in DAWN 2.30.0.[245,246] Structureless profile fits (Pawley method[62]) as well as the Rietveld Refinement44 were performed using the routines provided by the TOPAS-academic v6 software package.[235]

10.4 3D Electron Diffraction (3DED)

The samples were handled in an argon-filled glovebox and prepared by sprinkling the powders onto holey carbon grids. The prepared grids were then loaded into a JEOL vacuum transfer holder and inserted into the TEM column. 3DED data were collected using a JEOL JEM2100 TEM, equipped with a Timepix detector from Amsterdam Scientific Instruments, while continuously rotating the crystal at $0.45\,°\,s^{-1}$. The experiments were carried out using Instamatic,[247] with initial data assessment, as well as data reduction and merging (a single dataset for the lithium phase and 6 datasets for the sodium phase) being performed in edtools and XDS, respectively.[248,249] The acquired intensities were then used to solve the structure of each phase using SHELXT,[250] and refined using SHELXL,[251] with electron scattering factors as previously published by Peng.[252] From the 3DED data, all non-hydrogen atoms could be located in the initial structure solution from SHELXT.

10.5 Simultaneous Thermogravimetric and Differential Thermal Analysis (STA)

STA was performed on a Discovery SDT 650 instrument from TA Instruments under a constant nitrogen flow or airflow of $100\,mL\,min^{-1}$. For the measurement, a small amount (~ 10 mg) of the powdered sample was placed in a 90 µL alumina crucible in a glovebox with N_2 atmosphere. The thus prepared sample was removed from the inert atmosphere and quickly transferred into the STA instrument where it was heated with a constant heating rate of $10\,°C\,min^{-1}$ in a range from 50 °C to 800 °C (N_2 flow) or 1200 °C (airflow). In the latter case, the sample was held at the maximum temperature isothermally for 5 min to ensure complete thermal decomposition. Data evaluation was carried out in TA instruments TRIOS version 5.1.1.46572.

10.6 Differential Scanning Calorimetry (DSC)

DSC measurements were measured on a DSC25 from TA instruments. The samples were ground thoroughly and placed in a hermetically sealed aluminium crucible under N_2 atmosphere. All experiments were carried out under constant N_2 flow (50 mL min^{-1}) in a temperature range from 50 °C to approx. 500 °C with a constant heating and cooling rate of ±10 °C min^{-1}. Data evaluation was carried out in TA instruments TRIOS version 5.1.1.46572. Temperature and enthalpy calibration was performed with an indium standard. The integrals of the heat flow curves are given as enthalpies ΔH even though the measurements were performed under hermetic conditions (V = constant) since it is generally assumed that enthalpies ΔH and internal energies ΔU are similar for processes involving only condensed phases.[253]

10.7 Nuclear Magnetic Resonance (NMR) Spectroscopy

Solution ^{1}H NMR and ^{29}Si INEPT (insensitive nuclei enhanced by polarization transfer) NMR spectroscopy was performed on a Bruker DPX-300, DPX 500 or Agilent DD2 500 spectrometer. The crystalline material was dissolved in DMSO-d_6 (0.5 mL) and DCl/D2O (35 wt%, one drop, $<$ 0.1 mL). Data processing was performed in MestReNova (v14.2.0). The data was referenced to the residual proton signals of DMSO-d_6 and all chemical shifts are given relative to tetramethylsilane.

10.8 Fourier Transform (FT)IR Spectroscopy

Infrared spectra were collected on a Spectrum 3 FTIR spectrometer in a range from 4000 – 400 cm^{-1}. A Gladi ATR-300 unit from Pike Technologies with a diamond crystal was used as an attenuated total reflectance (ATR) unit. During the measurement all samples were compressed with a stamp securing the sample on the diamond and an inert-gas (N_2) flow was put in place to minimize the samples' reaction with atmospheric water.

11 Experimental Section to Chapter 6

All chemicals and solvents used in the synthesis were purchased from commercial suppliers and used without further purification if not stated otherwise.

11.1 Synthesis of ZIF-62 ($Zn(im)_{1.8}(bim)_{0.2}$)

2.4 g of $Zn(NO_3)_2 \cdot 6\,H_2O$ (8.1 mmol, 8.1 eq.), 122 mg benzimidazole (1.0 mmol, 1.0 eq.) and 1.727 g imidazole (25.4 mmol, 25.4 eq.) were dissolved in 14 mL of *N*,*N*-dimethylformamide in a Teflon lined autoclave (25 mL). The autoclave was sealed tightly, transferred to a preheated oven at 130 °C, and heated for 45 h. After cooling to room temperature, the colorless crystals were washed with iso-propanol (3 × 10 mL) and ground thoroughly. The powder was thermally activated under a dynamic vacuum (10^{-3} mbar) at 280 °C for 4 h in a tube furnace. $Zn(im)_{1.8}(bim)_{0.2}$ was obtained as a colorless powder (yield 511 mg, 1.8 mmol, 36%).

11.2 Synthesis of α-Na(bim)

Na(bim) was synthesized according to a synthetic protocol reported in the literature.[137] Prior to the synthesis, benzimidazole (bimH) was dried by resublimation at 100 °C under a dynamic vacuum (10^{-3} mbar) overnight. In a purged Schlenk flask (250 mbar), 1.5 g (12.7 mmol, 1.1 eq.) of dry bimH was dissolved in 30 mL of dry tetrahydrofuran (THF) under constant argon flow. 6 mL (12.0 mmol, 1.0 eq.) of sodium hexamethyldisilazane (NaHMDS, 2 M in THF) was added while the solution was cooled with an ice bath. Within 1 h, the reaction mixture was allowed to warm up to room temperature under constant stirring. Next, the yellow reaction mixture was filtered through a syringe filter (PTFE, 0.2 µL) and transferred into another purged Schlenk flask (250 mL). 40 mL of dry *n*-hexane was added to initiate the formation of a white precipitate. The reaction mixture was stored in a refrigerator (8 °C) overnight. The next day, the mixture was decanted, and the obtained white powder was washed with dry *n*-hexane (2 × 20 mL). The residual solvent was removed under dynamic vacuum (10^{-3} mbar) at 100 °C for 2 h and the solid material was then heated at 280 °Cin a tube furnace for 3 h under dynamic vacuum (10^{-3} mbar) to remove any excess bimH. α-Na(bim) was obtained as a light-yellow powder and stored in a glovebox under an inert N_2 atmosphere (yield 1.43 g, 10.2 mmol, 85%).

11.3 Preparation of *g*NaB$_x$ZIF-62 glasses (x = 0.0, 0.1, 0.3, 0.5, 1.0, 1.5)

Table 11.1. Composition of NaB$_x$|ZIF-62 materials. The physical mixtures comprise various amounts of glass former ZIF-62 and glass modifier Na(bim).

x	$m_{\mathrm{ZIF-62}}$/mg	$n_{\mathrm{ZIF-62}}$/mmol	$m_{\mathrm{Na(bim)}}$/mg	$n_{\mathrm{Na(bim)}}$/mmol
0	250	1.19	0	0
0.1	234.3	1.12	15.7	0.11
0.3	208.2	0.99	41.8	0.3
0.5	187.4	0.89	62.6	0.45
1	149.8	0.71	100.2	0.71
1.5	124.8	0.6	125.2	0.89

Na(bim) modified glasses were prepared by mixing the corresponding amount of the glass former ZIF-62 with the modifier Na(bim) in an N_2-filled glovebox. The physical mixture was ground thoroughly for 5 min to ensure sufficient homogenization after being transferred to either a hermetically sealed DSC crucible (10 mg scale) or a custom-made hermetically sealed quartz glass lined stainless steel crucible (250 mg scale). The small-scale glass preparation (x = 0.1, 0.3, 0.5, 1.0, 1.5) temperature program was applied in a DSC apparatus. It consists of an initial heating step from room temperature to a maximum temperature (450 °C) followed by an isothermal segment of 30 min and a final cooling step back to room temperature. All heating and cooling rates were executed at a constant rate of ±10 °C min^{-1}. For large-scale glass preparation (x = 0.1, 0.5, 1.0), the stainless-steel crucible equipped with a quartz glass inlet was filled with 250 mg of the corresponding physical mixture, sealed tightly under an N_2 atmosphere (glovebox) and transferred into a purged Schlenk tube which was introduced to a tube furnace. For the large-scale approach, the isothermal segment in the aforementioned temperature program was extended to 1 h to allow for complete mixing in the liquid state. Finally, the Schlenk tube was removed from the furnace and cooled to room temperature within 40 min using pressurized airflow on the outside of the Schlenk tube as a cooling agent. Further handling of the obtained glasses was performed in a glovebox under an N_2 atmosphere. In the case of x = 0 (preparation of *g*ZIF-62) the large-scale approach was chosen. In the modified temperature program, the maximum temperature was increased to 470 °C, followed by an isothermal segment (1 h) and final cooling back to room temperature according to the procedure mentioned above.

11.4 Preparation of *lg*NaB$_{0.3}$ZIF-62

The modified glass gNaB$_{0.3}$ZIF-62 (250 mg) was prepared in a large-scale approach as described above. After vitrification, the material was ground thoroughly for 5 min and subsequently dispersed in distilled water (25 mL). The water was exchanged five times over the course of 24 h, and the suspension was stirred for the next two days. After that time, the mixture was decanted, and the material was washed with MeOH (3 × 25 mL). The remaining solid material was transferred to a Schlenk tube and heated at 100 °C under a dynamic vacuum overnight to remove any remaining solvent residues. The washing solutions were collected, and the bulk solvent was removed via rotary evaporation at 60 °C.

11.5 Powder X-ray diffraction (PXRD)

Room temperature PXRD measurements were conducted on a Siemens D5005 diffractometer in Bragg-Brentano geometry using CuK$_\alpha$ radiation in the range from 5° to 50° 2Θ with a step size of 0.01°. The sample material was ground using n-hexane and the resulting suspension was deposited on a single crystal zero background sample holder made from silicon (cut along the (610) plane). Variable temperature powder X-ray diffraction (VT-PXRD) measurements were performed at Beamline BL9 at DELTA (Dortmunder Elektronenspeicherring Anlage, Dortmund, Germany) with a monochromatic X-ray beam ($\lambda = 0.4568$ Å) using a MAR345 plate detector in an angular range from ca. 2 – 12° 2Θ. The thoroughly ground sample material was filled in a borosilicate capillary (1.0 mm diameter) under an inert N_2 atmosphere (glovebox) and sealed using epoxy glue (UHU Schnellfest). An Anton Parr DHS1100 sample stage was used for the temperature adjustment. The temperature program consisted of a stepwise temperature increase from room temperature to the respective maximum temperature using a constant heating rate of ca. 30 °C min^{-1}. The heating ramp was interrupted by isothermal segments at the respective temperature steps of 120 s for data collection. Data integration and processing were performed in DAWN Science Version 2.30.0.[245,246] Structureless profile fits (Pawley method[62]) were performed using the routines provided by the TOPAS-academic v6 software package.[235]

11.6 Variable temperature X-ray total scattering (VT-PXRD)

In-situ VT-PXRD experiments were conducted at beamline I15-1 at Diamond Light Source (DLS, UK) or at Beamline P02.1 at Deutsches Elektronen Synchrotron (DESY). At DLS a monochromatic X-ray beam ($\lambda = 0.1617$ Å) was used for data collection in combination with a Perkin Elmer XRD 4343 CT 2D plate detector. Under an inert N_2 atmosphere (glovebox), the finely ground sample material was filled in a borosilicate glass capillary (1.0 mm outer diameter) and sealed using epoxy glue (UHU Schnellfest). A hot air blower was used to adjust the sample temperature stepwise up to 450 °C with a constant heating rate of 20 °C min^{-1} followed by an isothermal segment of 5 min for data collection and subsequent cooling back to room temperature. PDFgetX3 version 2.2.0[254] was used for further processing (calculation of $I(Q)$, $S(Q)$ data) and the calculation of PDF data in the form of $G(r)$. For the differential PDF approach, the total scattering data was evaluated using Gudrun (Version 2017). The subsequent data manipulation (LC-fitting approach) was performed with algorithms provided by the NumPy (version 1.21.5) and SciPy (version 1.9.1) libraries in Python 3.9.13. For $NaB_{0.3}$|ZIF-62 *in-situ* variable temperature X-ray total scattering measurements were performed at DESY with a wavelength of 0.2071 Å in combination with a Varex XRD 4343CT plate detector and an Oxford Instruments hot air blower for temperature adjustment applying the same temperature program as at DLS. The measurements were collected using borosilicate capillaries (1 mm outer diameter), which were filled with the finely ground sample material and sealed under an inert N_2 atmosphere (glovebox). Additionally, a room temperature measurement of *ex-situ* prepared finely ground gNaB$_{0.3}$ZIF-62 material was conducted. Sample preparation, filling of the capillaries and sealing with UHU Schnellfest was performed under an inert N_2 atmosphere (glovebox). Data integration and processing were performed in DAWN Science Version 2.30.0 and PDFgetX3.[245,246]

11.7 Simultaneous thermogravimetric and differential thermal analysis (STA)

STA measurements were performed on a Discovery SDT 650 instrument from TA Instruments under a constant nitrogen flow of 100 mL min^{-1}. For the measurement, a small amount (∼10 mg) of the powdered sample was placed in an open alumina crucible under an inert (N_2) atmosphere. The sample crucible was removed from the inert atmosphere and quickly transferred into the STA instrument, where it was heated with a constant heating rate of 10 °C min^{-1} in a range from 50 °Cto ∼600 °C under constant N_2 flow. Data evaluation was carried out in TA instruments TRIOS version 5.1.1.46572. Decomposition temperatures T_d were determined as the onset of mass loss in the thermogravimetric curve.

11.8 Differential scanning calorimetry (DSC)

DSC measurements were performed on a DSC25 from TA instruments. The samples were ground thoroughly and placed in a hermetically sealed aluminium crucible under an inert N_2 atmosphere. All experiments were conducted under constant N_2 flow (50 mL min^{-1}) in a temperature range from 50 °C to approx. 500 °C. If not stated differently, a constant heating and cooling rate of ±10 °C min^{-1} was applied. Temperature and enthalpy calibration was performed with different metal standards (indium, zinc, lead) using the same temperature program. Data evaluation was carried out in TA instruments TRIOS version 5.1.1.46572. The integrals of the heat flow curves are given as enthalpies ΔH even though the measurements were performed under hermetic conditions (V = constant) since it is generally assumed that enthalpies ΔH and internal energies ΔU are similar for processes involving only condensed phases.[253] Modulated DSC (MDSC) measurements for ΔC_V calculation were carried out with a heating rate of 2 °C min^{-1}, a modulation period of 120 s and an amplitude of ±1 °C min^{-1}.

11.9 Solution ^{1}H nuclear magnetic resonance (NMR) spectroscopy

Solution ^{1}H NMR were performed on a Bruker DPX-300, DPX 500 or Agilent DD2 500 spectrometer. The crystalline material was dissolved in DMSO-d_6 (0.5 mL) and DCl/D_2O (35 wt%, one drop, < 0.1 mL). Data processing was performed in MestReNove (v14.2.0). The data was referenced to the residual proton signals of DMSO, and chemical shifts are given relative to tetramethylsilane.

11.10 Fourier transform infrared (FTIR) spectroscopy

Far- and mid-infrared spectra were collected on a Spectrum 3 FTIR spectrometer in a range from 4000 – 400 cm^{-1} (mid IR) or 30 – 700 cm^{-1} (far IR) respectively. A Gladi ATR-300 unit from Pike Technologies was used as an attenuated total reflectance unit. During the measurement, all samples were compressed with a stamp securing the sample on the ATR diamond and an inert-gas (N_2) flow was put in place to minimize the sample's reaction with atmospheric water.

11.11 Isothermal gas physisorption

Gas sorption isotherms were collected in a Quantachrome iQ MP porosimeter. The ground sample material (50 – 90 mg) was degassed at 100 °Cfor ca. 2 h under dynamic vacuum ($p \approx 10^{\breve{}5}$ kPa) prior to the measurement. Isothermal physisorption measurements were conducted by using N_2 (77 K, purity > 99.999%), CO_2 (195 purity > 99.995%) and n-butane (273 K, purity > 99.9%) as gas probes. The temperature was adjusted using a 3P Instrument CryoTune filled with liquid nitrogen. Between two measurements the samples were degassed under dynamic vacuum ($p \approx 10^{\breve{}5}$ kPa) at ambient temperature for ca. 2 h. After the sorption measurements with n-butane, the sample was degassed under a dynamic vacuum at 100 °Cfor 30 min additionally.

11.12 Electron microscopy

The STEM-EDX investigations were performed on an aberration-corrected JEOL JEM-ARM200F NEOARM. scanning electron microscopy (SEM) images were taken with the FEI G4 CX FIB/SEM. For the preparation of SEM and transmission electron microscopy (TEM) samples, a small amount of the particles was dispersed in hexane by ultrasonication and then dropped onto Cu TEM grids. To prevent the particles from reacting with humidity, this process was carried out in a Sylatech GB1500-E glovebox. The individual TEM grids were then sealed airtight in plastic bags in the glovebox to protect them from exposure to humidity during transportation to the TEM.

11.13 Atom probe tomography (APT)

To prepare the APT samples, the particles were placed on aluminium sample holders in a Sylatech GB1500-E glovebox at a humidity of <1 ppm. Individual particles were then picked up with a micromanipulator in a FEI G4 CX focused ion beam/scanning electron microscope (FIB/SEM), welded to a microtip coupon, and subsequently shaped into a cone-shaped specimen (size: $50 \times 50 \times 100$ nm) using a standard annular milling procedure. To prevent the hygroscopic particles from reacting with the air humidity between the preparation steps, a Ferrovac Ultra High Vacuum Cryo Transfer Suitcase (UHVCTS) was used to transfer the samples between the glovebox, FIB/SEM and APT in ultra-high vacuum. The APT measurements were performed in a Cameca LEAP 5000 XR operating in laser mode at a temperature of 60 K, a pulse frequency of 125 kHz, a laser pulse energy of 20 pJ and a detection rate of 0.4%. The APT data was reconstructed and analyzed with the commercial software AP Suite 6.3.0.90.

11.14 Solid-state nuclear magnetic resonance (ssNMR) spectroscopy

The powdered gNaB$_x$ZIF-62 samples were packed into 3.2 mm zirconia rotors (room temperature ^{23}Na measurements) or zirconia crucible inserts then placed inside 7 mm zirconia rotors (variable temperature ^{23}Na measurements). Solid-state MAS NMR spectra of ^{23}Na (224.8 MHz) were recorded on a Bruker Avance Neo 20.0 T spectrometer equipped with a 3.2 mm MAS probe using 62.5 kHz RF field. A MAS rate of 20 kHz was used for all such samples. Variable temperature ^{23}Na MAS spectra were recorded on the same spectrometer but equipped with a 7 mm laser-heated MAS probe and using 250 kHz RF field. The temperature of samples in this probe was calibrated using the ^{79}Br shift variation of KBr.[255] A MAS rate of 4 kHz was used for all such samples. ^{23}Na chemical shifts were referenced to NaCl (7.71 ppm). Quantitative ^{23}Na spectra were recorded using a recycle delay of 5 × measured T_1 component for each sample. All rotors were spun using dry nitrogen.

11.15 Density-functional theory (DFT) calculations

The magnetic shielding and EFG tensors were calculated using CASTEP (version 23.1)[256] sing density-functional perturbation theory and the gauge-including projector augmented wave (GIPAW) method.[257–260] The PBE functional and on-the-fly ultrasoft pseudopotentials were used.[261] A cut-off energy of 900 eV was used for the plane-wave basis set. The convergence criteria for electronic self-consistency was 10^{-10} eV. A Monkhorst-Pack grid with k-point spacing of 0.03 $Å^{-1}$ was used for Brillouin-zone integration.[262] Structures were relaxed to a force threshold of 0.01 eV $Å^{-1}$ before the calculation of NMR tensors. Van der Waals forces in the system were described using the Grimme D3 dispersion correction.[263,264] Configurations of $(Na_{2y}Zn_{16-y})[(im)_{1.75}(bim)_{0.25}]_{16}$ were constructed using the Atomic Simulation Environment (ASE) Python package. The DFT-relaxed structure of ZIF-62 $(Zn_{16})[(im)_{1.75}(bim)_{0.25}]_{16}$ was used as a base structure. Na^+ ions were introduced by randomly inserting Na atoms into the base cell and removing a corresponding number of Zn^{2+} ions for charge balancing. The number of Na^+ ions $N = 2,4,6$, and 8 correspond to $x = 0.13, 0.29, 0.46$, and 0.67, respectively, in gNaB$_x$ZIF-62. Ten configurations for each of the specified Na-loading were created and geometry optimised. We used the Python packages Soprano and mrsimulator[265] to transform CASTEP NMR outputs into finite speed MAS solid-state (ss)NMR spectra. Soprano was used to scrape CASTEP .magres files for their chemical shielding and EFG tensors. Mrsimulator combined the tensor information with experimental parameters to simulate finite speed MAS ssNMR. The experimental parameters included a rotor frequency of 20,000 Hz and an external magnetic field of 20 T. Isotropic chemical shielding of ^{23}Na was referenced against calculated and experimental NaCl at 551.59 and 7.21 ppm, respectively.

12 Experimental Section to Chapter 8

12.1 MOF Synthesis

All chemicals were purchased from commercial suppliers and used without further purification steps.

12.1.1 Synthesis of Mg_2(dobdc)

Mg_2(dobdc) was prepared using a synthetic protocol from the literature.[201] Solutions of 2,5-dihydroxyterephthalic acid (H_4dobdc) (150 mg, 0.75 mmol) in THF (10 mL), NaOH (120 mg, 3 mmol) in H_2O (3 mL) and $Mg(NO_3)_2 \cdot 6\,H_2O$ (384 mg, 1.5 mmol) in H_2O (3 mL) were prepared. The solutions were united in a 15 mL Teflon-lined autoclave, which was sealed tightly and heated to 100 °C for 24 h. Next, the reaction mixture was decanted and the remaining solid was suspended in 25 mL ethanol. The supernatant liquid was exchanged three times over the course of 5 days. After thermal activation under a dynamic vacuum (10^{-3} mbar) at 250 °C for 5 h, Mg_2(dobdc) was obtained as a colorless powder. The product was stored in a glovebox under an inert (Ar) atmosphere.

12.1.2 Synthesis of Mn_2(dobdc)

Mn_2(dobdc) was synthesized according to a published synthetic protocol.[230] Manganese(II) acetate tetrahydrate (0.368 g, 1.50 mmol) and H_2O (1 mL) were placed in a Teflon-lined autoclave (15 mL). A solution of H_4dobdc (0.152 g, 0.75 mmol) in *N*-methyl-2-pyrrolidone (8 mL) was added. The autoclave was sealed and heated to 110 °C for 23 h. The reaction mixture was decanted, and the remaining solid was washed with MeOH and H_2O (3 × 10 mL each) and subsequently suspended in MeOH (10 mL). The supernatant liquid was exchanged three times over 6 days. After thermal activation at 200 °C for 18 h under a dynamic vacuum (10^{-3} mbar), Mn_2(dobdc) was obtained as an orange powder and stored in a glovebox (inert Ar atmosphere).

12.1.3 Synthesis of Co_2(dobdc)

Co_2(dobdc) was prepared according to a literature-known protocol.[206] H_4dobdc (0.48 g, 2.43 mmol) and $Co(NO_3)_2 \cdot 6\,H_2O$ (2.37 g, 8.6 mmol) were dissolved in 200 mL of a volumetric mixture from DMF:EtOH:H_2O = 1:1:1. The reaction mixture was transferred to a 250 mL Schott flask, which was tightly sealed and heated at 100 °C for 24 h. Subsequently, the reaction mixture was washed with DMF (3 × 20 mL) and the remaining solid was suspended in 25 mL methanol. The supernatant liquids was exchanged three times over the course of 5 days. Thermal activation of the material under dynamic vacuum (10^{-3} mbar) at

250 °C overnight provided Co_2(dobdc) as a dark purple crystalline powder. The material was transferred to a glovebox and stored under an inert Ar atmosphere.

12.1.4 Synthesis of Ni_2(dobdc)

Ni_2(dobdc) was prepared following a synthetic protocol from the literature.[204] Solutions of nickel (II) acetate tetrahydrate (150 mg, 0.60 mmol) in H_2O (5 mL) and H_4dobdc (187 mg, 0.94 mmol) in 5 mL THF were prepared. Both solutions were combined in a Teflon-lined autoclave (15 mL), which was sealed tightly and heated at 110 °C for 3 days. Next, the reaction mixture was decanted and washed with ethanol (3 × 20 mL). The remaining solid was suspended in 25 mL of methanol and the supernatant solvent was exchanged ten times throughout the course of ten days. During that time the mixture was heated at 65 °C in an oven. Thermal activation of the material under a dynamic vacuum (10^{-3} mbar) at 250 °C for 5 h provided Ni_2(dobdc) as a brown powder. The material was transferred to a glovebox and stored under an inert Ar atmosphere.

12.1.5 Synthesis of Cu_2(dobdc)

Cu_2(dobdc) was prepared according to a literature-known protocol.[209] H_4dobdc (0.50 g, 2.52 mmol) and $Cu(NO_3)_2 \cdot 3\,H_2O$ (1.34 g, 5.55 mmol) were dissolved in DMF (57 mL) and isopropanol (3 mL) in a 90 mL screw cap vial. The reaction solution was purged saturating the gas phase with Ar. The flask was sealed tightly and heated at 80 °C for 2 days. Next, the reaction mixture was decanted and the obtained solid was washed with DMF (3 × 20 mL). The remaining solid was suspended in 25 mL methanol and the supernatant solvent was exchanged three times throughout the course of 5 days. Thermal activation of the material under a dynamic vacuum (10^{-3} mbar) at 110 °C overnight provided Cu_2(dobdc) as a red powder. The product was transferred into a glovebox and stored under an inert Ar atmosphere.

12.1.6 Synthesis of Zn_2(dobdc)

Zn_2(dobdc) was prepared following a literature-known synthetic protocol.[266] H_4dobdc (0.50 g, 2.52 mmol) and $Zn(NO_3)_2 \cdot 4\,H_2O$ (2.25 g, 7.56 mmol) were dissolved in DMF (100 mL) and H_2O (5 mL) in a 250 mL Schott flask. The tightly sealed reaction flask was heated at 100 °C for 3 days. The obtained solid was washed with DMF (3 × 20 mL) and subsequently suspended in methanol (25 mL). The supernatant solvent was exchanged three times over the course of 5 days. Thermal activation under a dynamic vacuum (10^{-3} mbar) at 250 °C for 10 h provided Zn_2(dobdc) as a yellow micro-crystalline powder. The material was transferred to a glovebox and stored under an inert Ar atmosphere.

12.1.7 Synthesis of Mg_2(dobpdc) and mmen@Mg_2(dobpdc)

Mg_2(dobpdc) was synthesized according to a synthetic protocol from the literature.[229]

H_4dobpdc (27.4 g, 0.10 mmol) and $Mg(NO_3)_2 \cdot 6\,H_2O$ (64.0 mg, 0.25 mmol) were dissolved in methanol and DMF (V/V = 55:45, 10 mL) in a Teflon-lined autoclave (15 mL). The solution was heated at 120 °C overnight. Next, the reaction mixture was decanted, the obtained solid was washed with DMF and methanol (3 × 20 mL) and the residual solid material was suspended in methanol (10 mL). The supernatant solvent was exchanged three times over the course of 5 days. After that, the first batch was subject to thermal activation under a dynamic vacuum (10^{-3} mbar) at 250 °C for 5 h. This process provided Mg_2(dobpdc) as a colorless powder, which was stored in a glovebox under an inert (Ar) atmosphere.

For the preparation of mmen@Mg_2(dobpdc), 57 mg of Mg_2(dobpdc) (0.18 mmol) were suspended in 10 mL of dry n-hexane under an inert atmosphere (glovebox). N,N-dimethylethylenediamine (mmen, 0.4 mL, 0.819 g mL^{-1}, 3.61 mmol) was added, and the reaction mixture was stirred at room temperature overnight. Next, the solid material was washed with n-hexane (3 × 2 mL) and dried under a dynamic vacuum (10^{-3} mbar) at 100 °C for 5 h. mmen@Mg_2(dobpdc) was obtained as a colorless material and was stored in a glovebox under an inert Ar atmosphere.

12.2 ^{1}H Nuclear Magnetic Resonance (NMR) Spectroscopy

^{1}H NMR spectroscopic measurements were performed on a Bruker DPX-300, DPX 500 or Agilent DD2 500 spectrometer. The crystalline materials were dissolved in DMSO-d_6 and D2O/DCl (35 wt%, one drop < 0.1 mL). The spectra are referenced to the residual proton signals of DMSO-d_6 and the chemical shifts are given relative to tetramethylsilane. Data processing was performed in MestReNova v14.2.0.

12.3 Infrared (IR) Spectroscopy

Infrared spectra were collected on a Perkin Elmer Spectrum 3 equipped with a Gladi ATR-300 unit, a Perkin Elmer Spectrum 2 with a diamond ATR unit or a Bruker Alpha II FTIR spectrometer equipped with a platinum diamond ATR in a wavenumber range from 4000 − 400 cm^{-1} in attenuated total reflectance (ATR) mode. Using a stamp, the powdered sample material was secured and compressed on the ATR unit. To minimize the reaction of the sample with atmospheric water, the measurement was either performed in a glovebox under an inert Ar atmosphere (Bruker Alpha II) or under an inert-gas (N_2) flow if data collection was conducted outside the glovebox.

12.4 High-Pressure Powder X-ray Diffraction (HPPXRD)

High-pressure PXRD (HPPXRD) measurements were conducted at beamline BL9[267] at Dortmund Electron Accelerator (DELTA, Dortmund) or at beamline P02.1[268] (PETRA III) at Deutsches Elektronen Synchrotron (DESY, Hamburg). The measurements were performed using a modified custom-made high-pressure powder diffraction cell available at DELTA, originally used for conducting high-pressure SAXS measurements.[232] Modifications include changes in the sample holder enabling the insertion of capillaries, as well as an increased diameter of the beam exit window for creating a maximum diffraction angle range of 15° 2Θ.[231] Further details on the modified setup are shown in Figure A3.13 in the Supporting Information.

Sample preparation was performed in a glovebox under an inert Ar atmosphere. For the preparation of the capillaries, Kapton tubes (2 cm long, 1 mm outer diameter) were cut and closed on one end using epoxy glue (UHU Schnellfest). In the glovebox, the materials were ground thoroughly and filled into the Kapton capillaries. Silicone oil was injected on top of the sample material into the capillary as a pressure-transmitting medium. For the M_2(dobdc) samples poly(methylphenylsiloxane) (CAS: 63148-58-3, viscosity $125\,\mathrm{mm^2\,s^{-1}}$ (25 °C)) and for the Mg_2(dobpdc) samples poly(methylphenylsiloxane) (CAS: 63148-58-3, viscosity $450 - 550\,\mathrm{mm^2\,s^{-1}}$ (25 °C)) was used. After the addition of silicone oil, the capillary was centrifuged to ensure complete immersion of the crystalline sample material. To prevent the inclusion of gas bubbles, more silicon oil was added to the capillary, and the tip of the open end was bent to close. A metal ring was put over the bent end and squeezed tightly using a pair of pliers (see Figure A3.13 for further details).

Diffraction patterns were collected at atmospheric pressure up to 4000 bar ($p = 1 - 4000$ bar, with an error of $\Delta p = \pm 5$ bar) with a stepwise increase in the applied hydrostatic pressure. Sample-detector distance calibrations were performed with LaB_6.

Data collection was performed using a monochromatic X-ray beam with a wavelength of 0.4460 Å or 0.4537 Å at beamline BL09 of DELTA or a wavelength of 0.2074 Å at beamline P02.1 of PETRAIII, DESY. Dawn Science Version 22.30.0 was used for data integration.[245] The structureless profile fits (Pawley method[62]) were performed with the routines provided by TOPAS-academic v6.[235]

Appendix

A1 Appendix to Chapter 4

A1.1 Solution NMR Spectroscopy

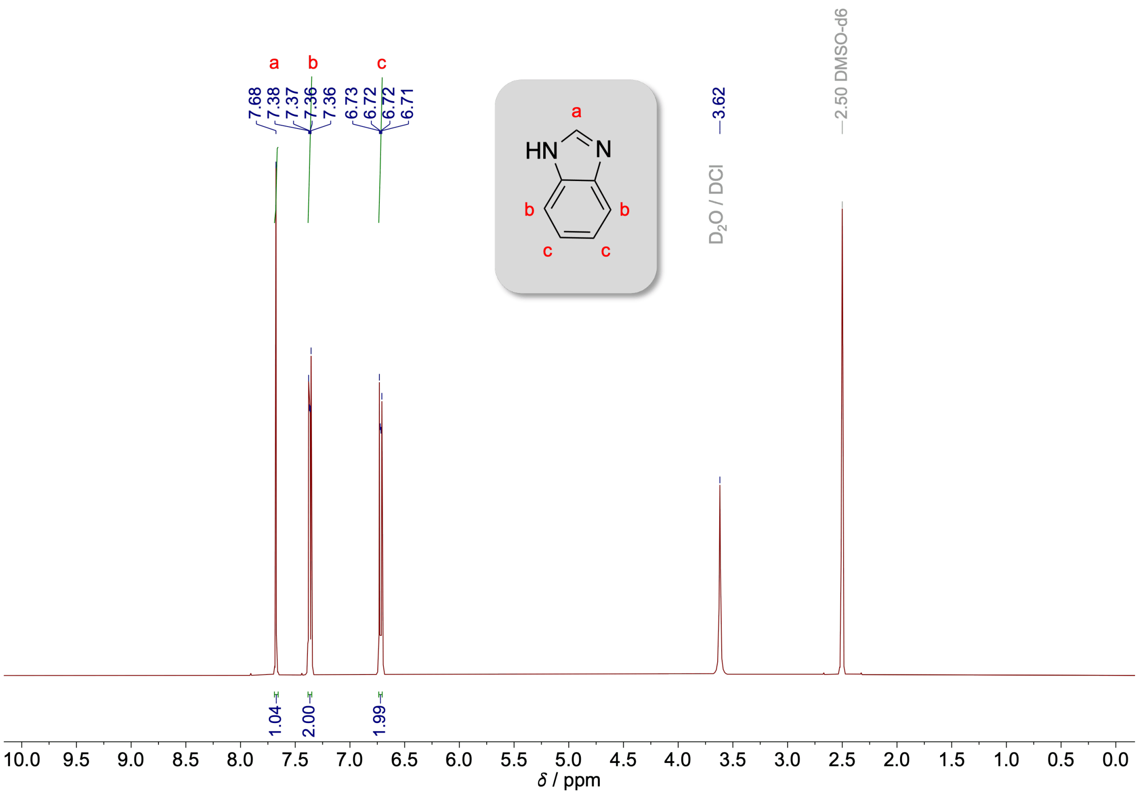

Figure A1.1. ^{1}H NMR spectrum of Li(bim) dissolved in DMSO-d_6 and DCl/D_2O.

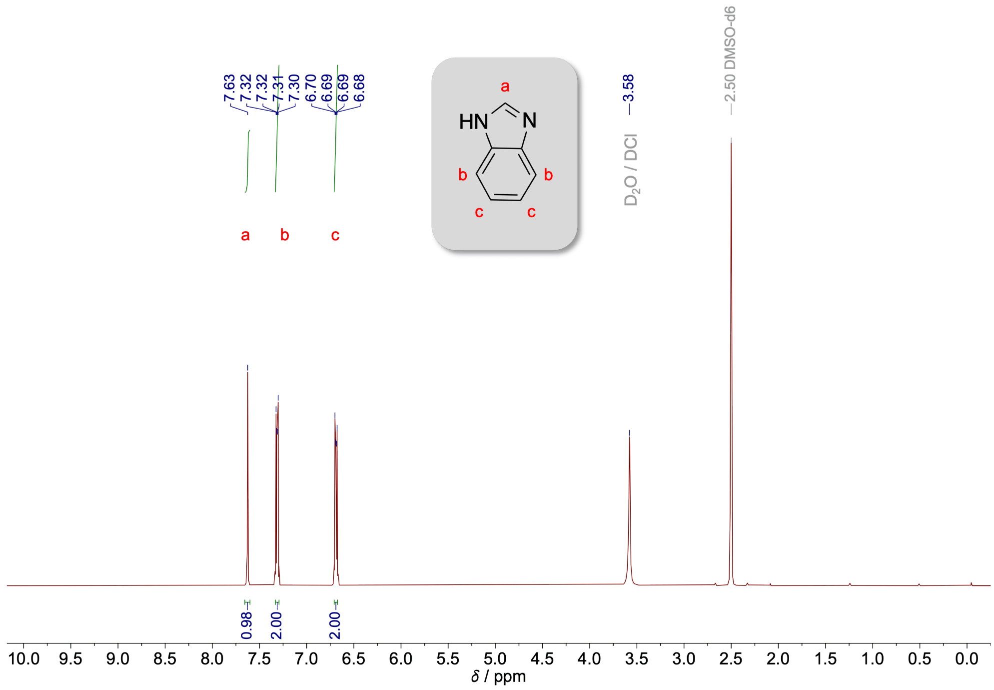

Figure A1.2. ^{1}H NMR spectrum of Na(bim) dissolved in DMSO-d_6 and DCl/D_2O.

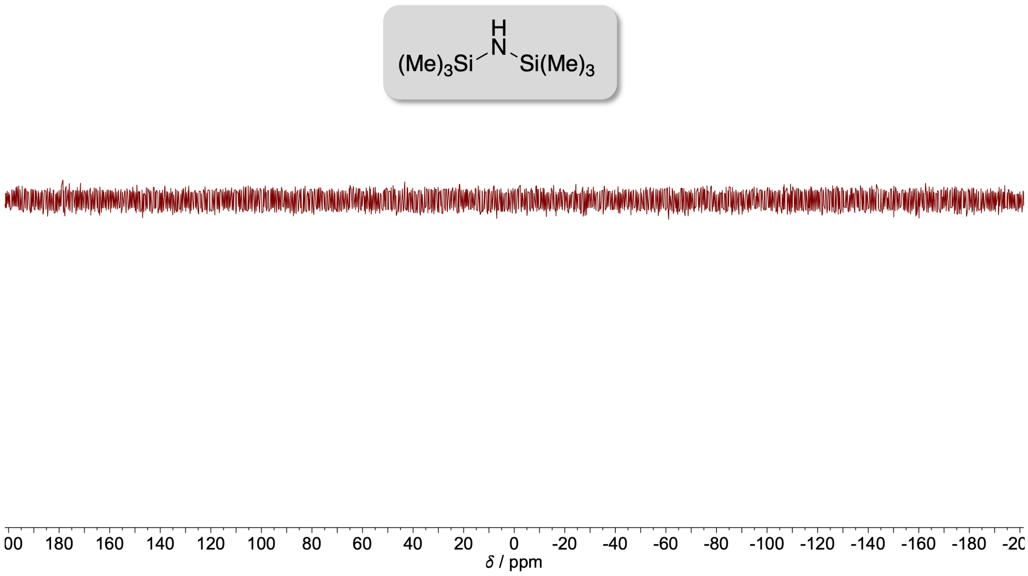

Figure A1.3. ^{29}Si INEPT (insensitive nuclei enhancement by polarization transfer) long-range NMR spectrum of Na(bim) dissolved in DMSO-d_6 and DCl/D_2O proving the absence of HMDS by-product in the investigated sample. The resonance of HMDS is expected at −2.2 ppm.[269]

A1.2 Simultaneous Thermal Analysis

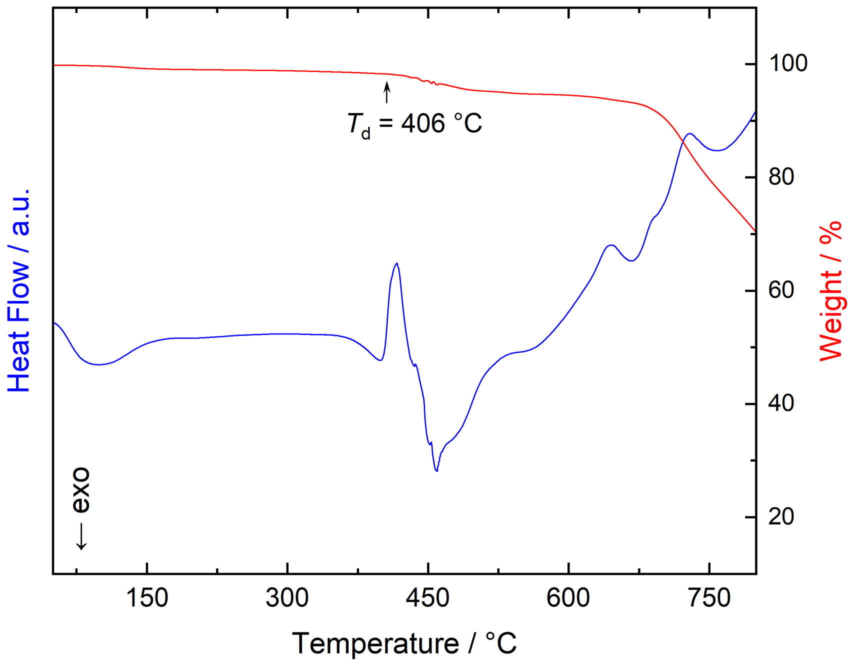

Figure A1.4. STA analysis of Li(bim) under an inert atmosphere (N_2 flow) from 50 °C to 800 °C with a constant heating rate of 10 °C min^{-1}. The thermal decomposition temperature was determined by the intersection of two tangents and is indicated by an arrow.

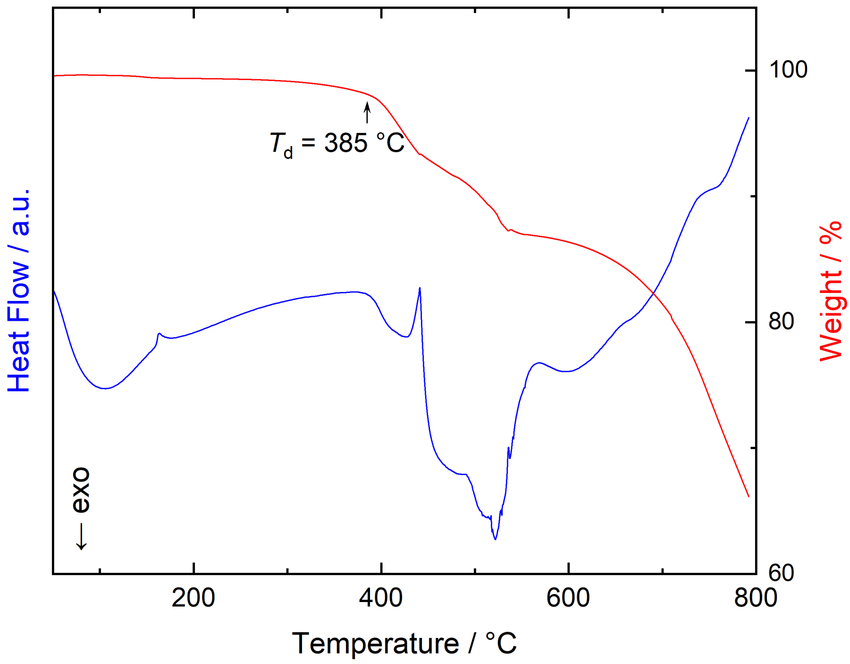

Figure A1.5. STA analysis of Na(bim) under an inert atmosphere (N_2 flow) from 50 °C to 800 °C with a constant heating rate of 10 °C min^{-1}. The thermal decomposition temperature was determined by the intersection of two tangents and is indicated by an arrow.

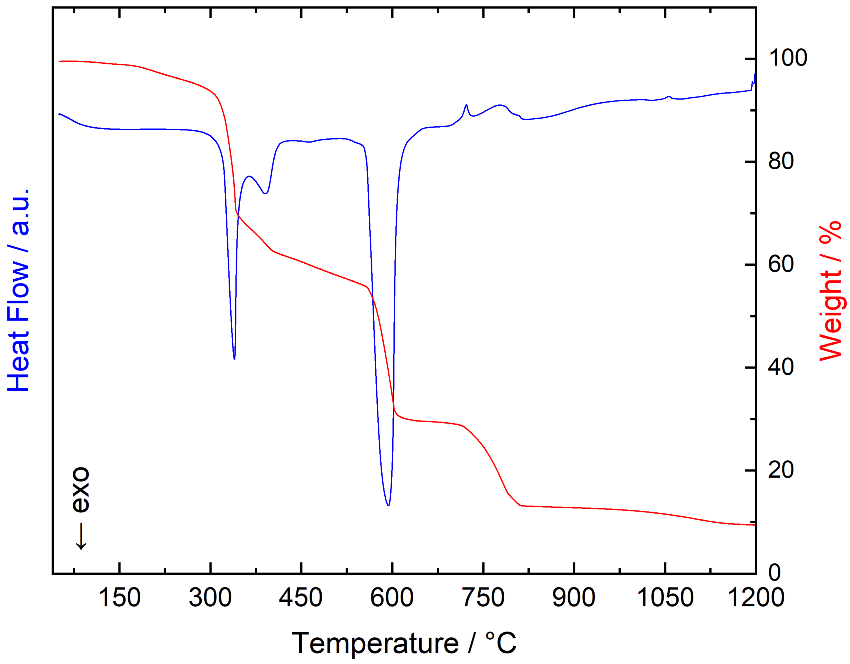

Figure A1.6. STA analysis of the thermal decomposition of Li(bim) under air flow from room temperature to 1200 °C with a constant heating rate of 10 °C min^{-1} followed by an isothermal segment at 1200 °C of 5 min. The recorded mass loss of 90.0% is in accordance with the calculated mass loss of 90.6%

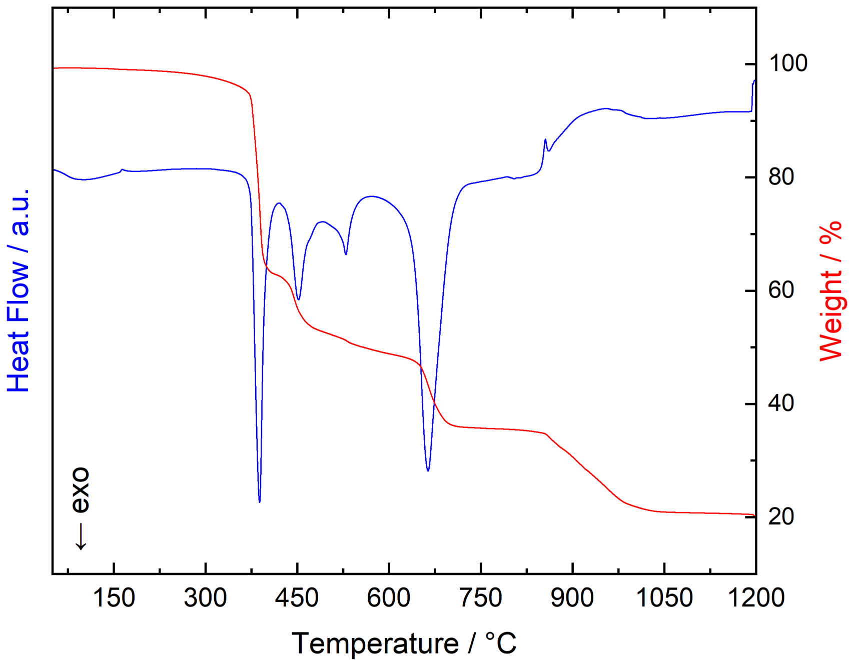

Figure A1.7. STA analysis of the thermal decomposition of Na(bim) under air flow from room temperature to 1200 °C with a constant heating rate of 10 °C min^{-1} followed by an isothermal segment at 1200 °C of 5 min. The recorded mass loss of 78.8% is in accordance with the calculated mass loss of 78.0%

A1.3 3D Electron Diffraction (3DED)

Table A1.1. Crystallographic data of the 3D electron diffraction data of Li(bim) and α-Na(bim).

	Li(bim)	α-Na(bim)
Empirical formula	$C_7H_5LiN_2$	$C_7H_5N_2Na$
Wavelength	0.0251 Å	0.0251 Å
Crystal system	Orthorhombic	Orthorhombic
Space group	*Cmma* (No. 67)	*Pbcm* (No. 57)
Unit cell dimensions	a = 5.9670 (12) Å	a = 8.7500(17) Å
	b = 10.291(2) Å	b = 7.4000(15) Å
	c = 11.921(2) Å	c = 11.830(2) Å
Volume	732.0(3) $Å^3$	766.0(3) $Å^3$
Z	4	4
Index ranges	$-5 \leq h \leq 5$	$-9 \leq h \leq 8$
	$-11 \leq k \leq 9$	$-9 \leq k \leq 9$
	$-13 \leq l \leq 11$	$-14 \leq l \leq 14$
Reflections collected	616	11183
Independent reflections	272	641
	[R(int) = 0.1051]	[R(int) = 0.1720]
Completeness (to 0.83 Å resolution)	69.2%	77.0%
R_1 (ED model) [I > 2σ(I)]	0.1472	0.1330

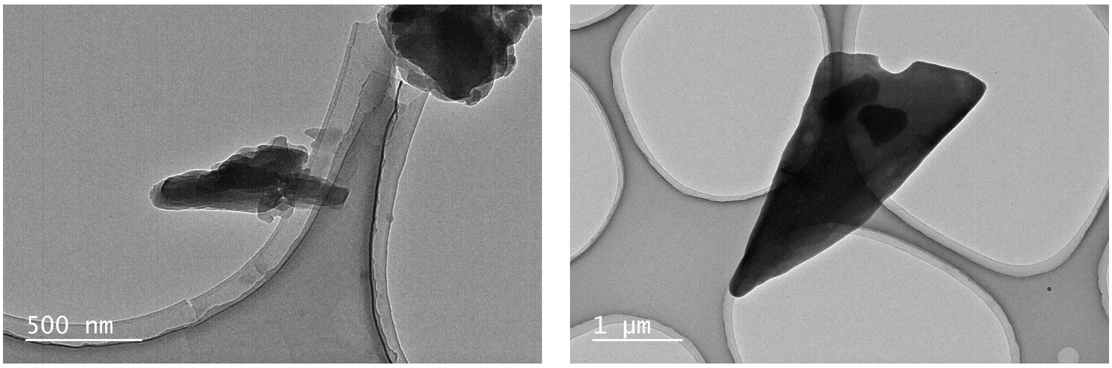

Figure A1.8. Transmission electron microscopy images of crystallites of Li(bim) (left) and Na(bim) (right)prior to 3DED data collection.

A1.4 Differential Scanning Calorimetry

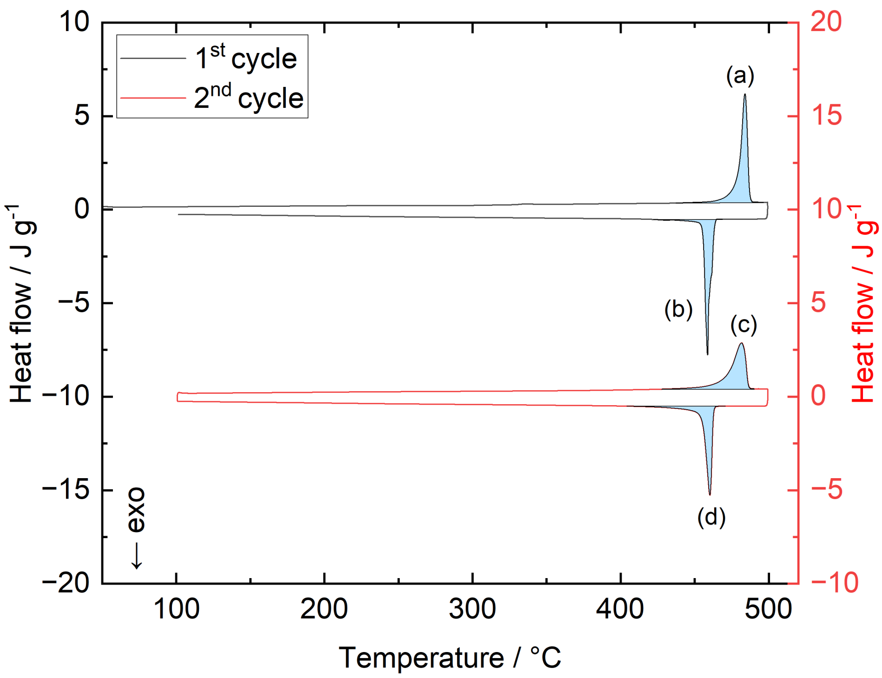

Figure A1.9. Heat flow curves of two consecutive heating-cooling cycles of Li(bim) in a DSC experiment with a constant heating/cooling rate of $10\,°\mathrm{C\,min^{-1}}$. The signals corresponding to melting and crystallization events are labelled alphabetically. The corresponding melting temperatures, enthalpies and entropies are given in Table A1.2.

Table A1.2. Temperatures (T), change in enthalpy (ΔH) and change in entropy (ΔS) associated with the events in the heat flow curves in the DSC experiment of Li(bim) shown in Table A1.9. The temperature is given as the offset temperature of the corresponding thermal event with respect to the direction of the temperature change (e.g. thermal up- or downscan).

Cycle	Signal	Event	T/°C	ΔH/kJ mol^{-1}	ΔS/J mol^{-1} K^{-1}
1st	(a)	melting	487	26.9	35.4
	(b)	crystallization	460	23.0	31.4
2nd	(c)	melting	486	23.1	30.4
	(d)	crystallization	463	20.6	28.0

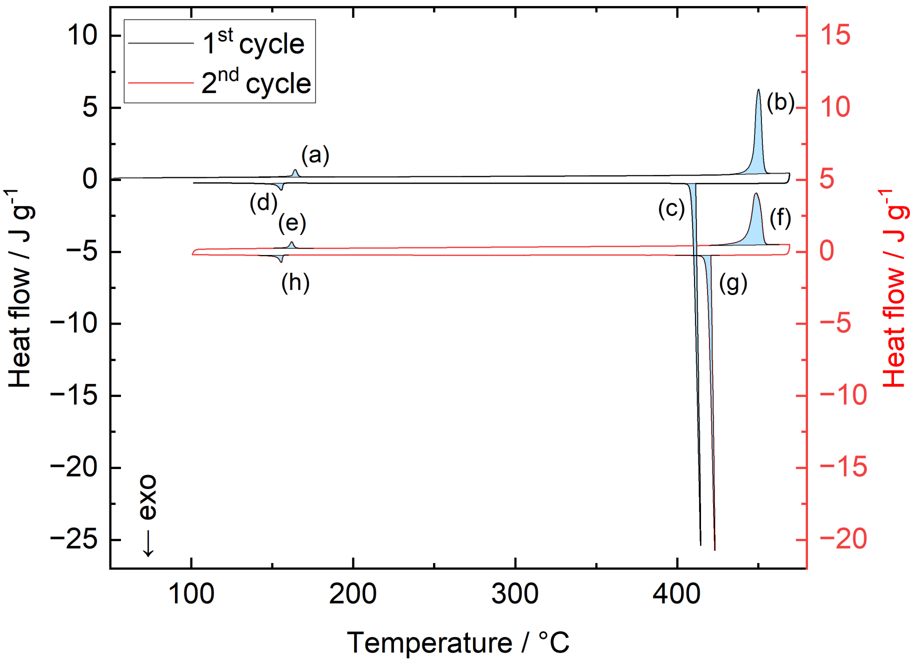

Figure A1.10. Heat flow curves of two consecutive heating-cooling cycles of Na(bim) in a DSC experiment with a constant heating/cooling rate of $10\,°C\,min^{-1}$. The signals corresponding to solid-solid phase transition and melting/crystallization events are labeled alphabetically. The corresponding transition temperatures, enthalpy, and entropy changes are given in Table A1.3.

Table A1.3. Temperatures (T), change in enthalpy (ΔH) and change in entropy (ΔS) associated with the events in the heat flow curves in the DSC experiment of Na(bim) shown in Figure A1.10. The temperature is given as the offset temperature of the corresponding thermal event with respect to the direction of the temperature change (e.g. thermal up- or downscan).

Cycle	Signal	Event	T/°C	ΔH/kJ mol^{-1}	ΔS/J mol^{-1} K^{-1}
1st	(a)	$\alpha \rightarrow \beta$ transition	166	1.3	2.9
	(b)	melting	453	24.7	34.0
	(c)	crystallization	412	22.8	33.3
	(d)	$\beta \rightarrow \alpha$ transition	157	1.2	2.8
2nd	(e)	$\alpha \rightarrow \beta$ transition	164	1.5	3.4
	(f)	melting	454	23.6	32.5
	(g)	crystallization	421	22.3	32.1
	(h)	$\beta \rightarrow \alpha$ transition	157	1.4	3.3

A1.5 Optical Microscopy

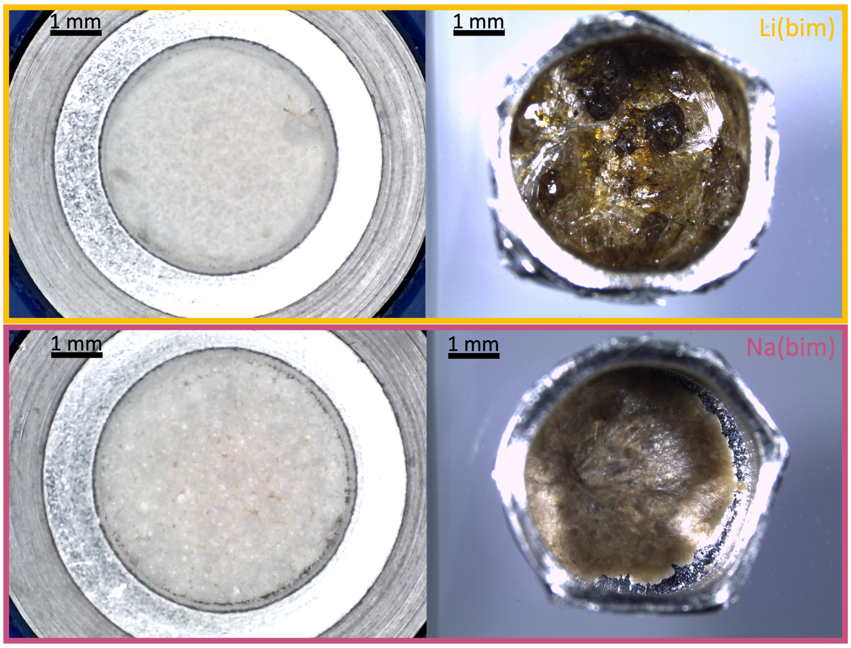

Figure A1.11. Optical microscopy images of Li(bim) and Na(bim) before (left) and after (right) a thermal heating-cooling cycle up to 500 °C (Li(bim)) and 470 °C (Na(bim)). The experiment was performed under hermetic conditions in a DSC apparatus with a constant heating and cooling rate of 10 °C min^{-1} under N_2 atmosphere. The original colorless microcrystalline powder particles fuse into larger pieces due to melting of the material at high temperature.

A1.6 Infrared Spectroscopy

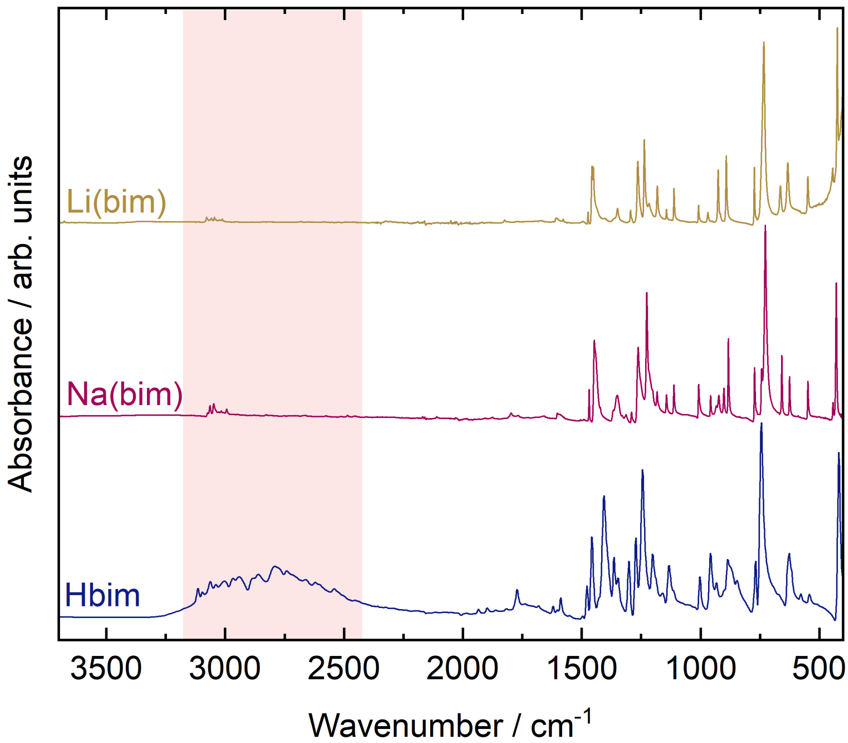

Figure A1.12. Infrared spectra of benzimidazole (Hbim), Na(bim) and Li(bim). The highlighted region displays vibrational bands corresponding to N–H stretching modes which are no longer present in the spectra of the alkali benzimidazolates. The weak bands above 3000 cm^{-1}in the spectra of Li(bim) and Na(bim) correspond to C–H stretching vibrations of bim^{-}.

A1.7 X-ray Powder Diffraction

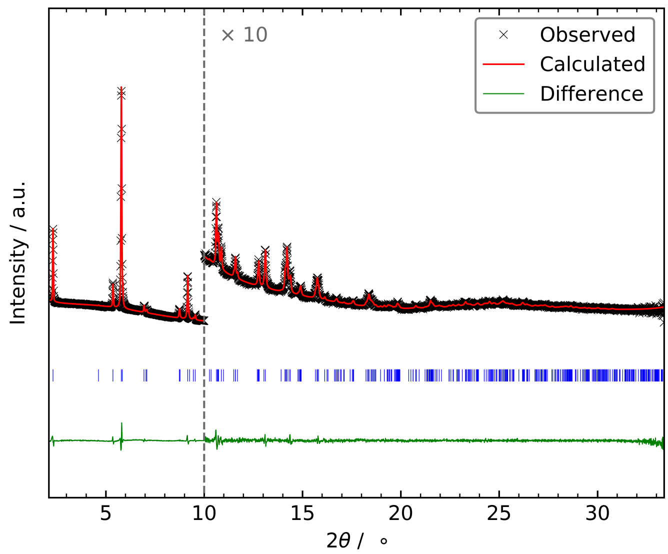

Figure A1.13. Profile fit (Pawley method) to the XRPD pattern of Li(bim) recorded with $\lambda = 0.4603$ Å at 25 °C at BL09 the synchrotron radiation facility DELTA. The blue tick marks indicate allowed Bragg peak positions. The refined unit cell parameters are compiled in Table A1.4.

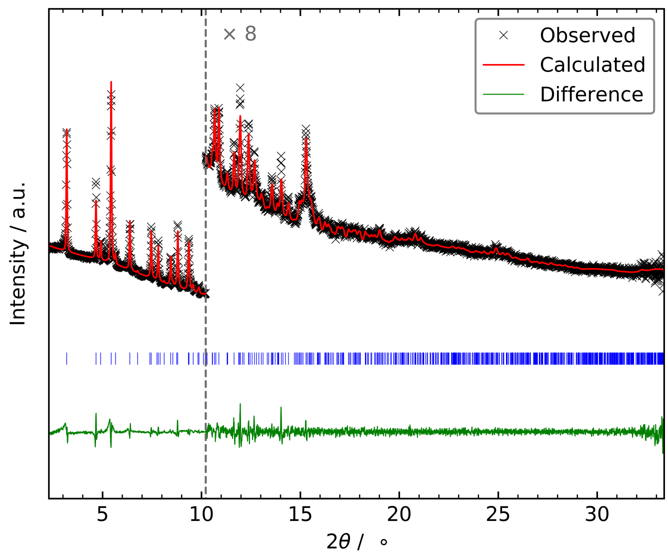

Figure A1.14. Profile fit (Pawley method) to the XRPD pattern of α-Na(bim) recorded with $\lambda = 0.4603$ Å at 25 °C at BL09 of the synchrotron radiation facility DELTA. The blue tick marks indicate allowed Bragg peak positions. The refined unit cell parameters are compiled in Table A1.4.

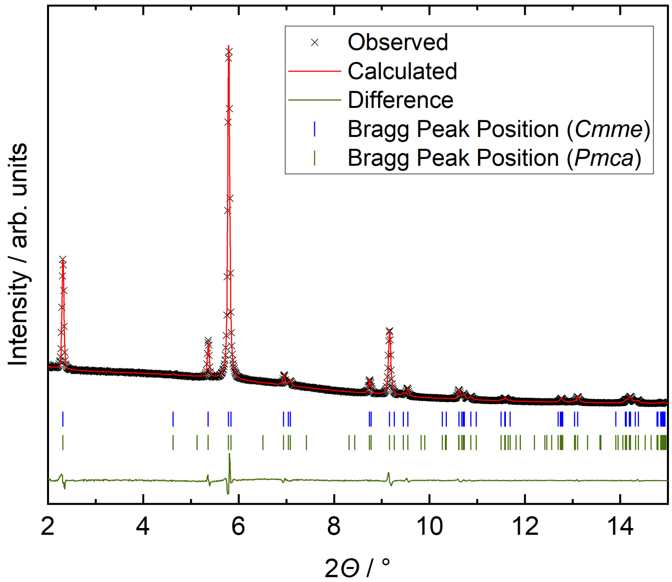

Figure A1.15. Profile fit (Pawley method) to the XRPD pattern of Li(bim) recorded at 25 °C with $\lambda = 0.4603$ Å at BL09 of the synchrotron radiation facility DELTA according to the space group *Cmme*. The blue tick marks indicate allowed Bragg peak positions for the space group *Cmme* while the green tick marks were calculated based on a fit in the non-isomorphic subgroup *Pmca* previously reported[152].* The additional reflections allowed in the subgroup *Pmca* have zero intensity in the experimental diffraction pattern, thus confirming *Cmme* symmetry as observed in the 3DED experiment. The refined unit cell parameters are compiled in Table A1.4.

*The previously proposed space group *Pmca* corresponds to a non-standard setting of space group *Pbcm*. The relationships between the unit cell axes of the (correct) higher symmetry space group *Cmme*, the non-standard subgroup *Pmca* and the standard subgroup *Pbcm* are as follows: $a_{Cmme} = c_{Pmca} = b_{Pbcm}$;$b_{Cmme} = a_{Pmca} = c_{Pbcm}$; $c_{Cmme} = b_{Pmca} = a_{Pbcm}$.

Table A1.4. Crystallographic parameters obtained by profile fitting (Pawley method) performed on the XRPD data of α-Na(bim) and Li(bim) recorded at 25 °C (see Figures A1.13 - A1.15). Starting parameters were derived from the 3DED data. In the case of Li(bim) the profile fit was also performed based on the unit cell parameters from the literature (in the assigned space group *Pmca*, see footnote above).[152]

Compound	Li(bim)	Li(bim)	α-Na(bim)
crystal system	orthorhombic	orthorhombic	orthorhombic
space group	*Cmme*	*Pmca*	*Pbcm*
a/ Å	5.76306(14)	9.8418(8)	8.242(16)
b/ Å	9.8424(7)	11.4032(8)	7.065(6)
c/ Å	11.4028(8)	5.76298(15)	11.272(16)
α/°	90	90	90
β/°	90	90	90
γ/°	90	90	90
V/ Å^3	646.79(6)	646.76(7)	660.78(18)
R_{wp}/%	3.97	3.88	4.32
R_{exp}/%	18.01	16.93	18.73
χ	0.22	0.23	0.23

A1.8 Rietveld Refinement

Rietveld refinement was performed using the routines implemented in the TOPAS-Academic v6 software package,[235] peak shapes were fitted using the Thompson-Cox-Hastings profile[270] and a Chebychev polynomial as a background function. The starting structural model for β-Na(bim) was constructed from the single crystal structure of α-Na(bim) derived from 3DED by, firstly, changing the space group from *Pbcm* to *Pbma* via axis transformation according to $a_{Pbcm} \rightarrow c_{Pbma}$, $b_{Pbcm} \rightarrow a_{Pbma}$, $c_{Pbcm} \rightarrow b_{Pbma}$ and, secondly, changing the space group symmetry to the supergroup *Cmme*. This yields a starting model, which is structurally very similar to the structure of Li(bim) but features a two-fold disorder of the bim^- units enforced by the mirror plane perpendicular to the a-axis. A structureless profile fit (Pawley method) to XRPD data recorded at beamline I15-1 of Diamond Light Source ($\lambda = 0.161669$ Å, $T = 200\,°C$) gave the initial unit cell parameters, peak shapes and background function, which were then applied to the Rietveld refinement One-half of the bim^- unit (the asymmetric unit) was described as a rigid body, which was allowed to rotate only along the b-axis due to symmetry restrictions of the space group in the initial refinement cycles. The location of the bim^- unit on the b-c-plane without the two-fold disorder proved to give the best fit to the data. Furthermore, inspection of the Fourier difference map indicated disorder of the Na^+ and the bim^- unit along the c-direction (i.e. perpendicular to the plane of the 2D layers), likely as a consequence of thermal motion. Due to the anisotropic displacement, this feature could not be modeled sufficiently by isotropic displacement parameters. Refinement of anisotropic displacement parameters was not feasible due to the limited number of observed reflections in the XRPD pattern. Hence, the anisotropic displacement was modeled by introducing a second bim^- unit (occupancy 0.5 for both bim^- units) and by moving the Na^+ ion away from its special position (Wyckoff position *4b*; ¼, 0, ½) by changing its z-coordinate to about 0.55 and giving the Na^+ ion an occupancy of 0.5. The later step generated a two-fold disorder along the c-axis of the Na^+ ions located around the Wyckoff position *4b*. Symmetry restrictions allowed refinement of the atomic coordinates (z) along the c-axis only since Na^+ is located on the 2-fold rotation axis parallel to the c-axis (Wyckoff position *8l*; ¼, 0, z) and the bim^- units are centered on Wyckoff position *4g* (coordinates 0, ¼, z) with site symmetry *mm2*. In later refinement cycles the isotropic thermal displacement parameters (one set shared between both bim^- units) were refined as well (with the values of C1/C12 and N1/N12 being restricted to minimum values of $B = 3.0\,\text{Å}^2$) to account for thermal motions along the a- and b-axes as well. In the final refinement cycle, the background function, peak shape parameters and unit cell parameters were refined together with the structure model.

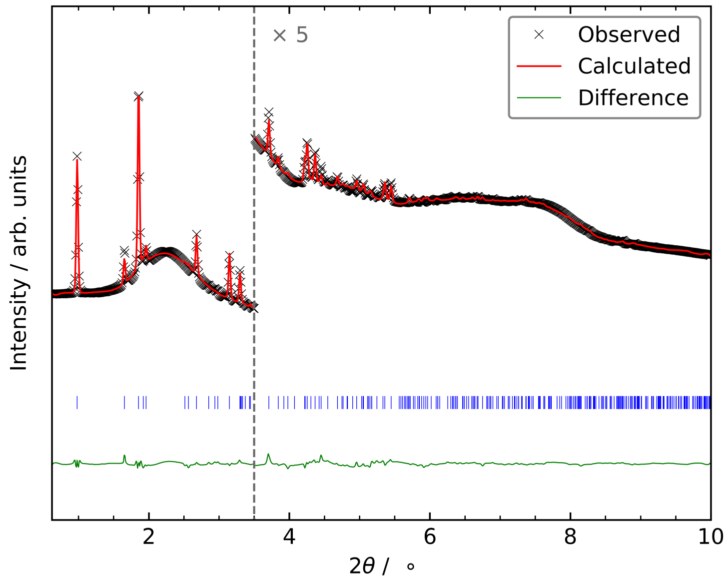

Figure A1.16. Profile fit (Rietveld refinement) to the XRPD pattern of β-Na(bim) recorded at 200 °C with a wavelength of $\lambda = 0.1616$ Å at beamline I15-1 at Diamond Light Source. The blue tick marks indicate allowed Bragg peak positions. The refined unit cell parameters are shown in Table S5.

Table A1.5. Refined parameters obtained by profile fitting (Rietveld refinement) performed on the XRPD data of β-Na(bim) collected at 200 °C (see Figure A1.16).

Compound	β-Na(bim) (200 °C)
crystal system	orthorhombic
space group	*Cmme*
a/ Å	6.9158(6)
b/ Å	11.2126(19)
c/ Å	9.4510(18)
$\alpha/°$	90
$\beta/°$	90
$\gamma/°$	90
V/ Å^3	732.9(2)
R_{wp}/%	1.49
R_{exp}/%	1.8
R_{Bragg}/%	0.96
χ	0.83

A1.9 Analysis of Thermal Expansion

In the following the volumetric thermal expansion coefficient α_V is calculated based on the integrated form of its definition:[271]

$$\ln\left(\frac{V(T)}{V_0}\right) = \alpha_V \cdot T + C_V \tag{A1.1}$$

where $V(T)$ is the unit cell volume at temperature T and C_V is a dimensionless constant. The reference volume V_0 was arbitrarily set to $1\,\text{Å}^3$. The linear thermal expansion coefficients α_l (with $l = a$, b or c) are calculated based on the following related definition:[271]

$$\ln\left(\frac{l(T)}{l_0}\right) = \alpha_l \cdot T + C_l \tag{A1.2}$$

where $l(T)$ is the lattice parameter (a, b or c) at temperature T and C_l is a dimensionless constant. The reference lattice parameter l_0 was arbitrarily set to $1\,\text{Å}$.

In order to avoid confusion due to the different axis settings of the involved space groups *Cmme* and *Pbcm* of the different phases, we define a set of principal axes X, Y and Z, which describe the lattice vectors parallel to the layer of the coordination networks (X and Y) and the lattice vector perpendicular to it (Z). The following table assigns the lattice vectors a, b, c to the corresponding principal axis.

Table A1.6. Assignment of the lattice vectors a, b and c of the orthorhombic crystal structures of Li(bim), α-Na(bim) and β-Na(bim) to the principal axes of thermal expansion X, Y and Z. X and Y lie parallel to the plane of the layered coordination networks and Z represents the direction orthogonal to the layers.

Phase	Space group	X	Y	Z
Li(bim)	*Cmme*	a	b	c
α-Na(bim)	*Pbcm*	b	c	a
β-Na(bim)	*Cmme*	a	b	c

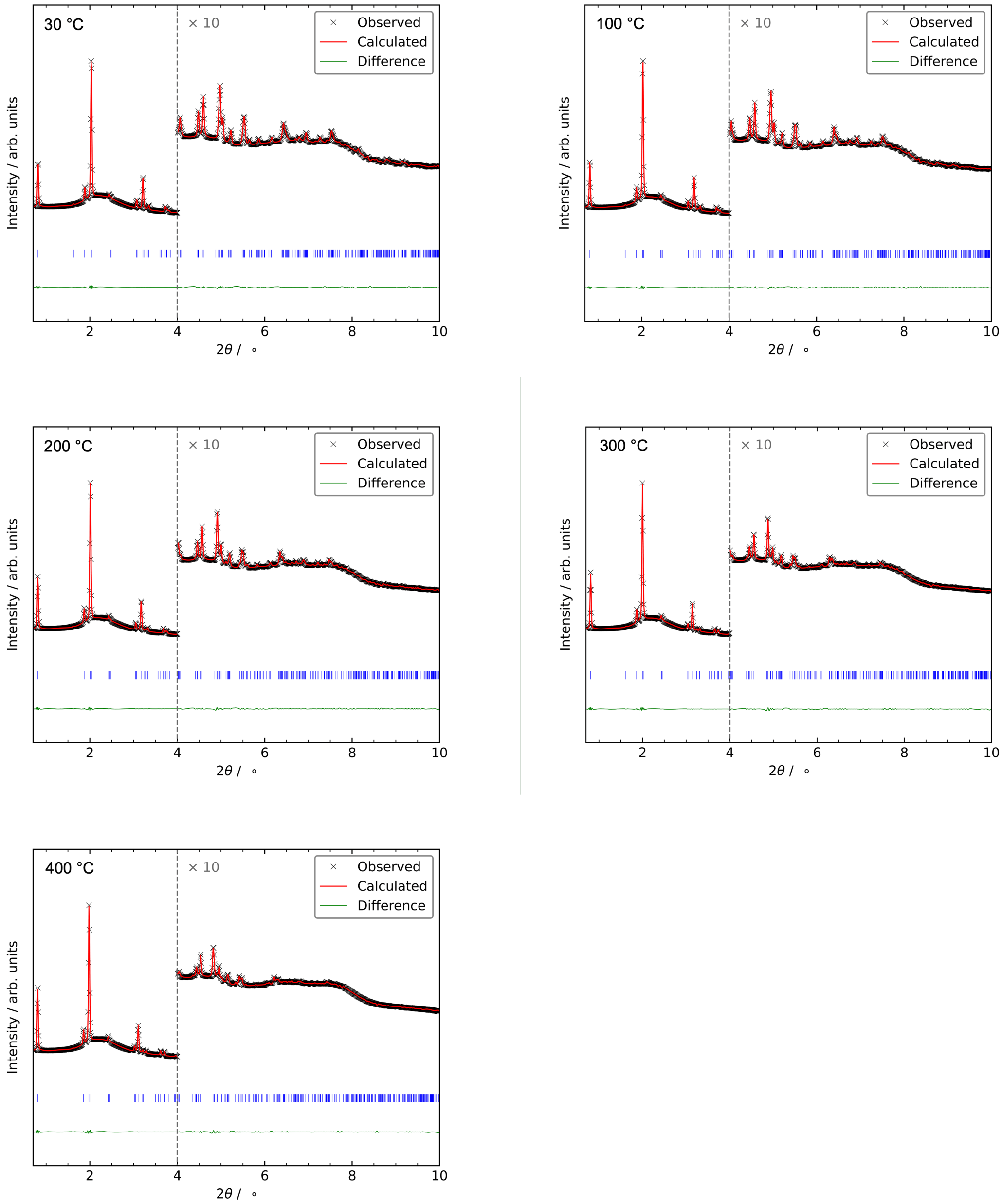

Figure A1.17. Structureless profile fits (Pawley method) to the VTXRPD patterns of Li(bim) recorded at different temperatures with a wavelength of 0.1617 Å. Blue tick marks indicate the position of allowed Bragg peaks. The refined unit cell parameters are shown in Table A1.7

Table A1.7. Refined crystallographic parameters obtained by profile fitting (Pawley method) of the VTPXRD data of Li(bim) (see Figure A1.17).

$T/°C$	30	100	200	300	400
crystal system	orthorhombic	orthorhombic	orthorhombic	orthorhombic	orthorhombic
space group	*Cmme*	*Cmme*	*Cmme*	*Cmme*	*Cmme*
a/ Å	5.76577(17)	5.79305(16)	5.84040(15)	5.89728(16)	5.96552(18)
b/ Å	9.8448(9)	9.8700(8)	9.9088(8)	9.9487(8)	9.9915(9)
c/ Å	11.3910(0)	11.4114(9)	11.4402(8)	11.4651(8)	11.4852(8)
$\alpha/°$	90	90	90	90	90
$\beta/°$	90	90	90	90	90
$\gamma/°$	90	90	90	90	90
V/ Å^3	646.59(8)	652.47(8)	662.06(7)	672.66(8)	684.57(8)
$R_{wp}/\%$	1.05	1.04	1.03	1.07	1.07
$R_{exp}/\%$	1.39	1.96	1.97	2	2.02
χ	0.75	0.53	0.52	0.54	0.53

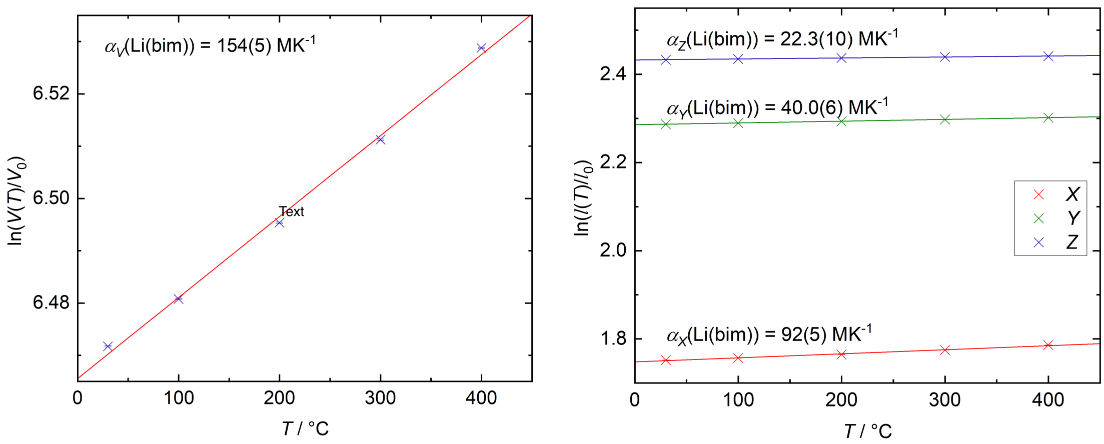

Figure A1.18. Left: Determination of the volumetric thermal expansion coefficient α_V of Li(bim) by an error-weighted linear fit according to equation (A1.1). Right: Determination of the linear thermal expansion coefficients α_l (with $l = X, Y, Z$) of Li(bim) by error-weighted linear fits according to equation (A1.2). See Table A1.6 for the assignment of principle axes X, Y, Z to the lattice vectors a, b and c. The estimated standard deviations of V, X, Y and Z are smaller than the size of the symbols.

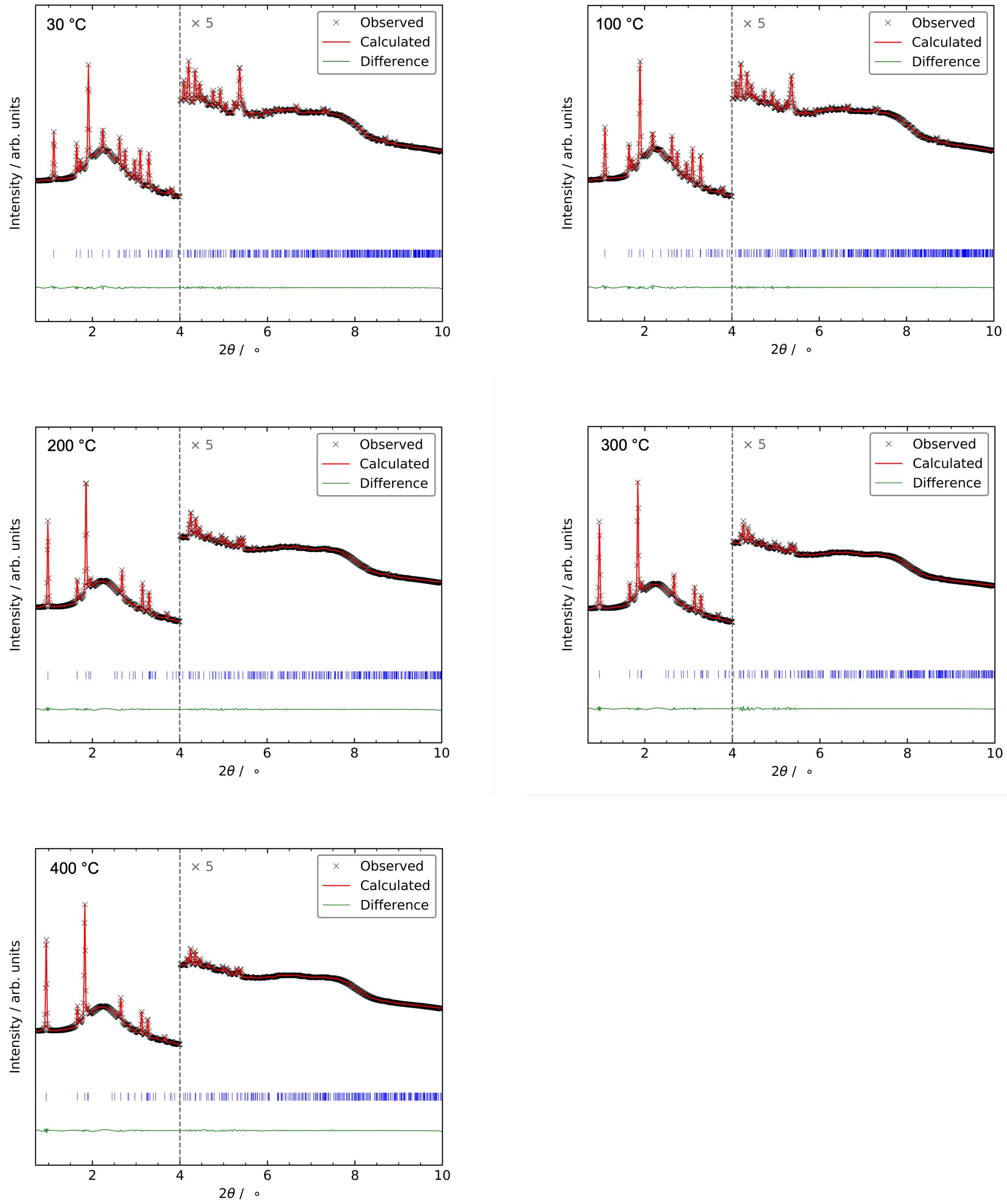

Figure A1.19. Structureless profile fits (Pawley method) to the VTXRPD patterns of Na(bim) recorded at different temperatures with a wavelength of 0.1617 Å. Blue tick marks indicate the position of allowed Bragg peaks. The refined unit cell parameters are shown in Table A1.8.

Table A1.8. Refined crystallographic parameters obtained by profile fitting (Pawley method) of the VTPXRD data of Na(bim) (see Figure A1.19).

$T/°C$	30	100	200	300	400
crystal system	orthorhombic	orthorhombic	orthorhombic	orthorhombic	orthorhombic
space group	*Pbcm*	*Pbcm*	*Cmme*	*Cmme*	*Cmme*
a/ Å	8.282(2)	8.4833(8)	6.9164(3)	6.9481(4)	6.9921(4)
b/ Å	7.0677(9)	7.0551(4)	11.2128(11)	11.1887(13)	11.1717(13)
c/ Å	11.292(2)	11.2817(14)	9.4537(6)	9.6297(6)	9.8075(6)
$\alpha/°$	90	90	90	90	90
$\beta/°$	90	90	90	90	90
$\gamma/°$	90	90	90	90	90
V/ Å^3	661.0(2)	675.22(11)	733.15(9)	748.62(11)	766.10(11)
$R_{wp}/\%$	0.81	0.83	0.74	0.85	0.8
$R_{exp}/\%$	1.16	1.17	1.45	1.44	1.42
χ	0.7	0.71	0.51	0.59	0.56

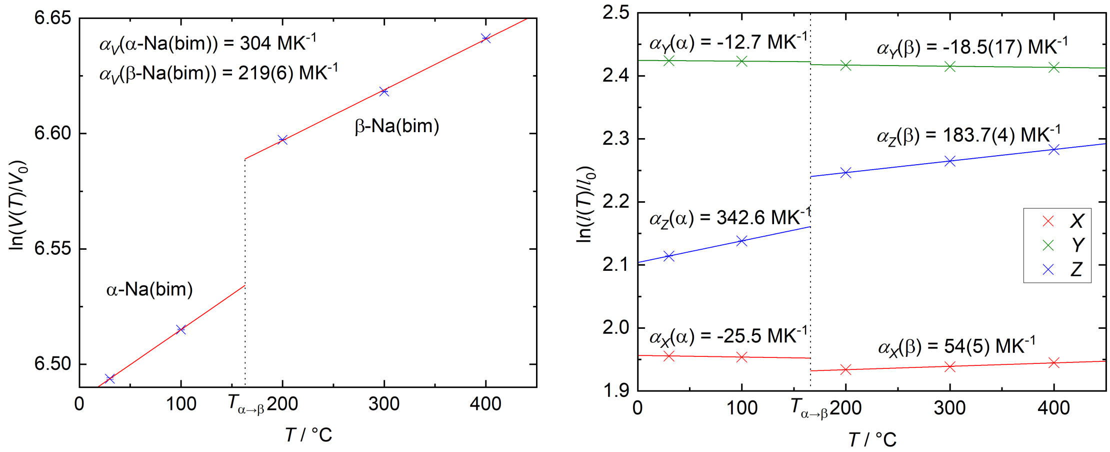

Figure A1.20. Left: Determination of the volumetric thermal expansion coefficients α_V of both Na(bim) phases extracted by error-weighted linear fits according to equation (A1.1). Right: Determination of the linear thermal expansion coefficients α_l (with $l = X, Y, Z$) of both Na(bim) phases by error-weighted linear fits according to equation (A1.2). See Table A1.6 for the assignment of principle axes X, Y, Z to the lattice vectors a, b and c. The estimated standard deviations of V, X, Y and Z are smaller than the size of the symbols.

A2 Appendix to Chapter 6

A2.1 Infrared Spectroscopy

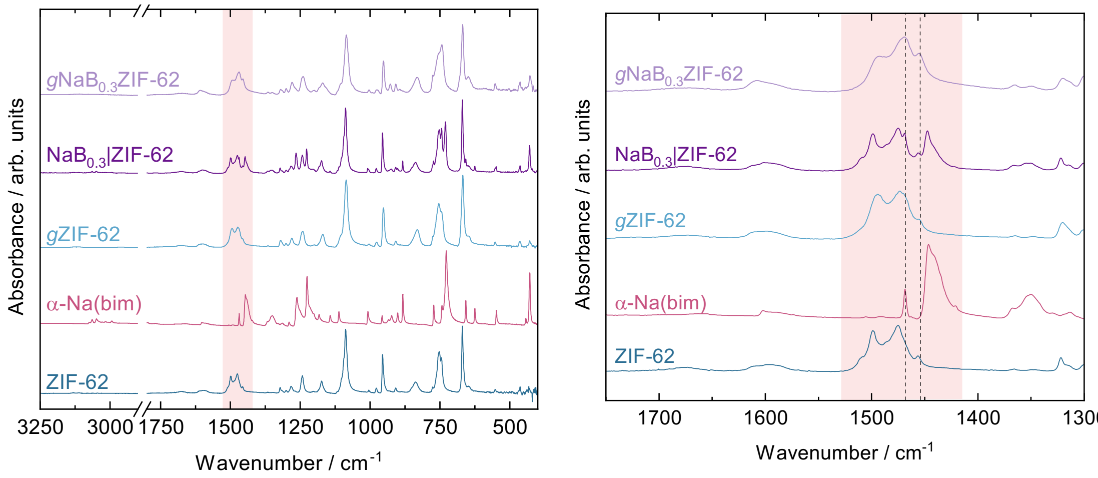

Figure A2.1. Mid-infrared spectra of ZIF-62, the corresponding glass *g*ZIF-62, the modifier α-Na(bim), the physical mixture of modifier and glass former $NaB_{0.3}|ZIF\text{-}62$ and the corresponding glass of the physical mixture $g$$NaB_{0.3}ZIF\text{-}62$ with a zoom into the highlighted wavenumber range (right).

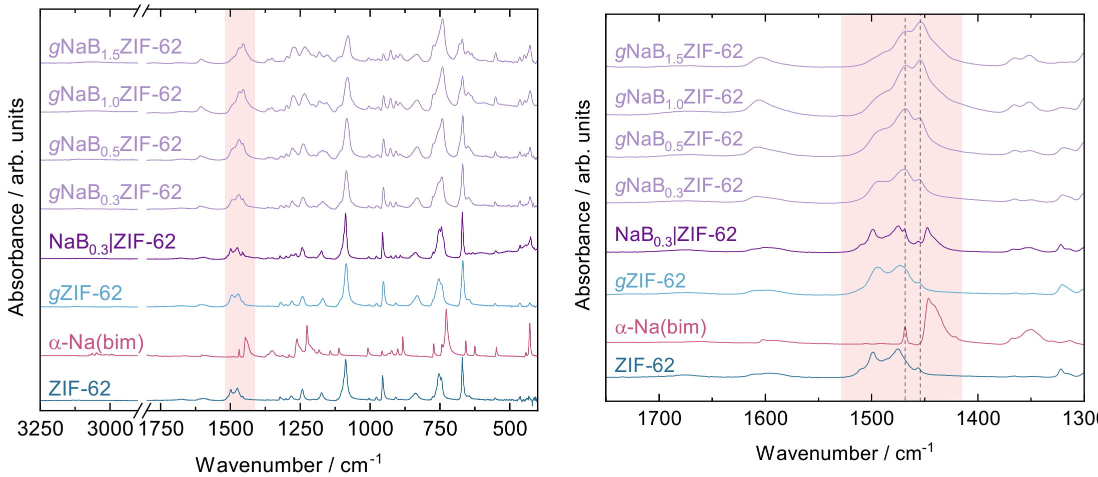

Figure A2.2. Mid-infrared spectra of ZIF-62, the corresponding glass *g*ZIF-62, the modifier α-Na(bim), and Na(bim)-modified ZIF-62 glasses $g$$NaB_xZIF\text{-}62$ with different amounts of modifier incorporated x. The right figure shows a zoom into the region from $1300 - 1750\,cm^{-1}$.

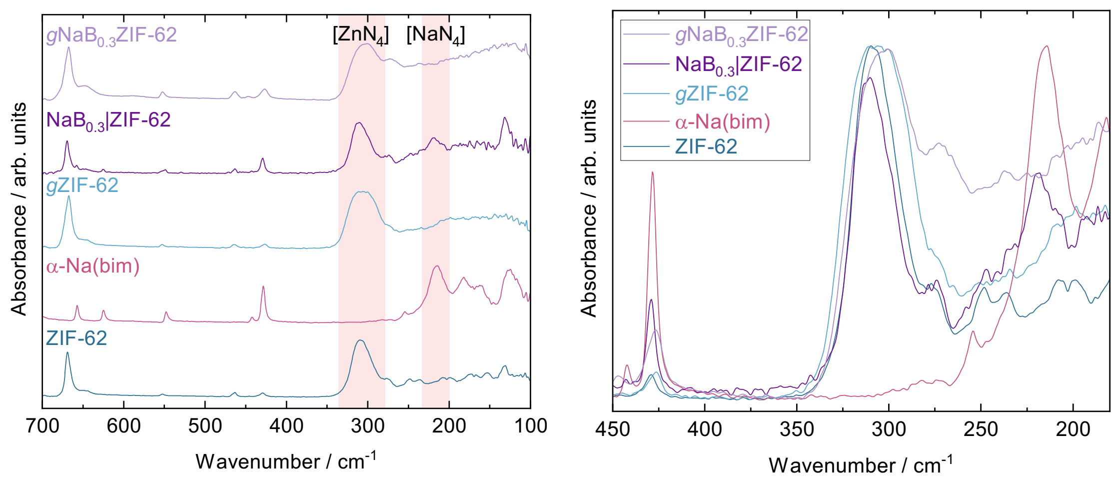

Figure A2.3. Far-infrared spectra of ZIF-62, the corresponding glass *g*ZIF-62, the modifier α-Na(bim), the physical mixture of modifier and glass former $NaB_{0.3}$|ZIF-62 and the corresponding glass of the physical mixture $g$$NaB_{0.3}$ZIF-62 with a zoom into the highlighted wavenumber range (right).

A2.2 Density Functional Theory Calculation and Vibrational Analysis

The IR spectra of α-Na(bim) were calculated using the Vienna Ab Initio Simulation Package (VASP, version 5.4)[272,273], using periodic density functional (DFT) with the optPBE-vdw functional and projected augmented wave (PAW) pseudo-potentials. The IR calculations are based on a geometry-optimized structure, which included both the relaxation of the cell parameters as well as the relaxation of the nuclei position. The cut-off energy of the plane wave basis set is 400 eV. For describing the electronic states, the Methfessel-Paxton smearing method was employed with a smearing width of 0.2 eV. The convergence criteria for the forces on the nuclei was 0.02 eV $\mathrm{\AA}^{-1}$ and the criterion for the electronic relaxation is set to 10^{-7} eV. The Brillouin zone integration is based on a $6 \times 6 \times 1$ k-point grid. The optimised lattice constants of the used unit cell are $a = 8.2672$ Å, $b = 7.0732$ Å, and $c = 11.3000$ Å (see Figure A2.4). The IR calculations were carried out using the density functional perturbation theory (DFPT) vibrational analysis approach.[274–276]

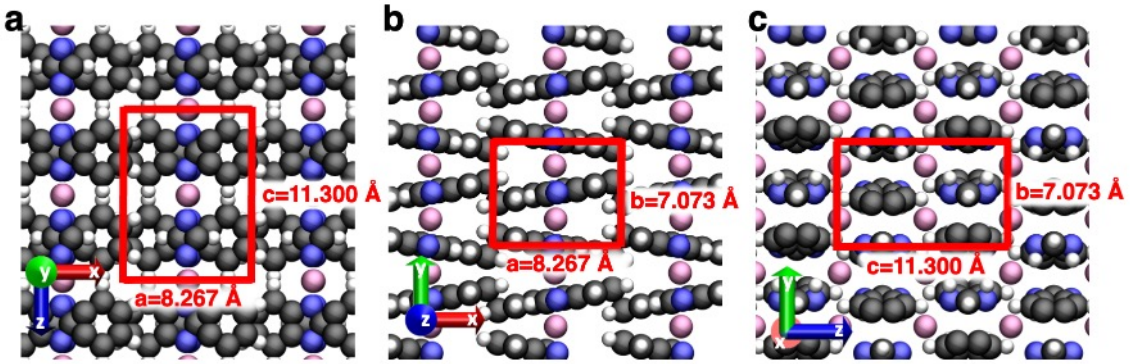

Figure A2.4. Visualization of the geometry-optimized molecular structure of α-Na(bim). The C-atoms are coloured in black, the N atoms in blue, H in white, and Na in light purple. a), b), and c) show the structure, including the unit cell (red rectangle), along three different orientations. The respective orientation is highlighted by the axes at the bottom left corner of each panel.

Table A2.1. Wavenumbers of prominent vibrational bands found in the experimental far-IR spectra ($\tilde{\nu}_{exp}$), the corresponding vibrational band obtained by DFT ($\tilde{\nu}_{calc}$) and a description of the vibrational mode. Animations of the corresponding molecular vibrations are available at `http://doi.org/10.6084/m9.figshare.28264145`.

$\tilde{\nu}_{exp}$/cm^{-1}	$\tilde{\nu}_{calc}$/cm^{-1}	Description of vibrational mode
657	650	Symmetric N_4 in-plane vibration ,Na-N stretching contribution
624	626.8	Aromatic in-plane deformation ,Na-N stretching contribution
547	555.4	Aromatic in-plane deformation vibration
442	435.4	Benzimidazolate in-plane vibration ,Na-N stretching vibration contribution
428	429.8	Phenyl out-of-plane vibration
253	269.2	Benzimidazolate out-of-plane vibration
214	211.4	NaN_4 in-plane vibration
182	194.6	NaN_4 in-plane vibration

Table A2.2. Wavenumbers of prominent vibrational bands found in the experimental mid-IR spectra ($\tilde{\nu}_{\mathrm{exp}}$), the corresponding vibrational band obtained by DFT ($\tilde{\nu}_{\mathrm{calc}}$) and a description of the vibrational mode. Animations of the corresponding molecular vibrations are available at http://doi.org/10.6084/m9.figshare.28264145.

$\tilde{\nu}_{\mathrm{exp}}/\mathrm{cm}^{-1}$	$\tilde{\nu}_{\mathrm{exp}}/\mathrm{cm}^{-1}$	Description of vibrational mode
3048 - 3075	3084	C-H stretching vibration
1601	1575	In-plane-ring stretching vibration
1468	1462	In-plane ring-stretching vibration
1446	1437	In-plane ring-stretching vibration
1446	1424	In-plane C-N stretching vibration (asymmetric)
1261	1249	In-plane C-N stretching vibration (symmetric)
1225	1218	In-plane C-N stretching vibration (asymmetric)
882	874.2	In-plane ring stretching vibration
882	873.4	C-N out-of-plane vibration
882	872.8	C-N out-of-plane vibration
727	724.4	C-N out-of-plane vibration

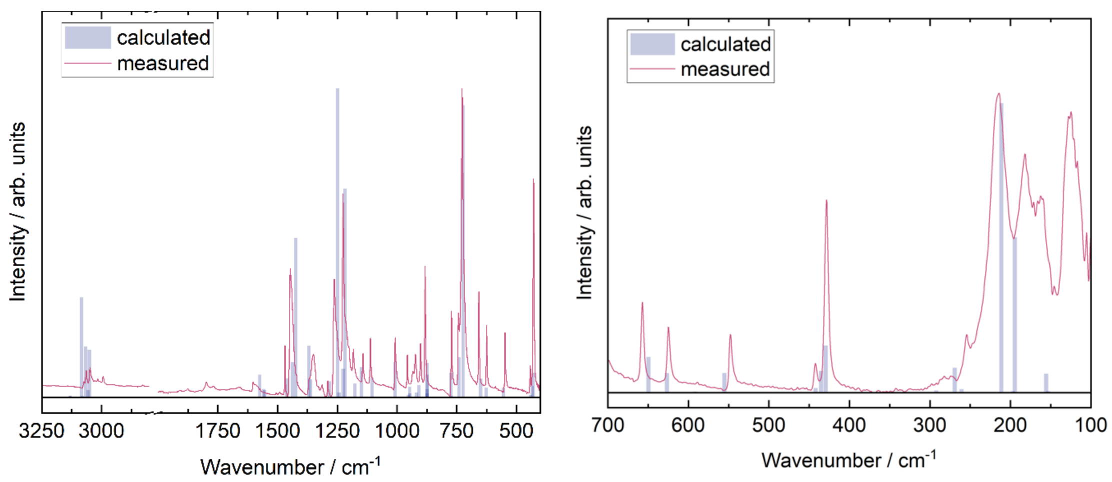

Figure A2.5. MIR (left) and FIR (right) spectra of α-Na(bim) shown together with the intensity distribution of vibrational bands obtained by DFT calculations.

A2.3 Optical Microscopy Images

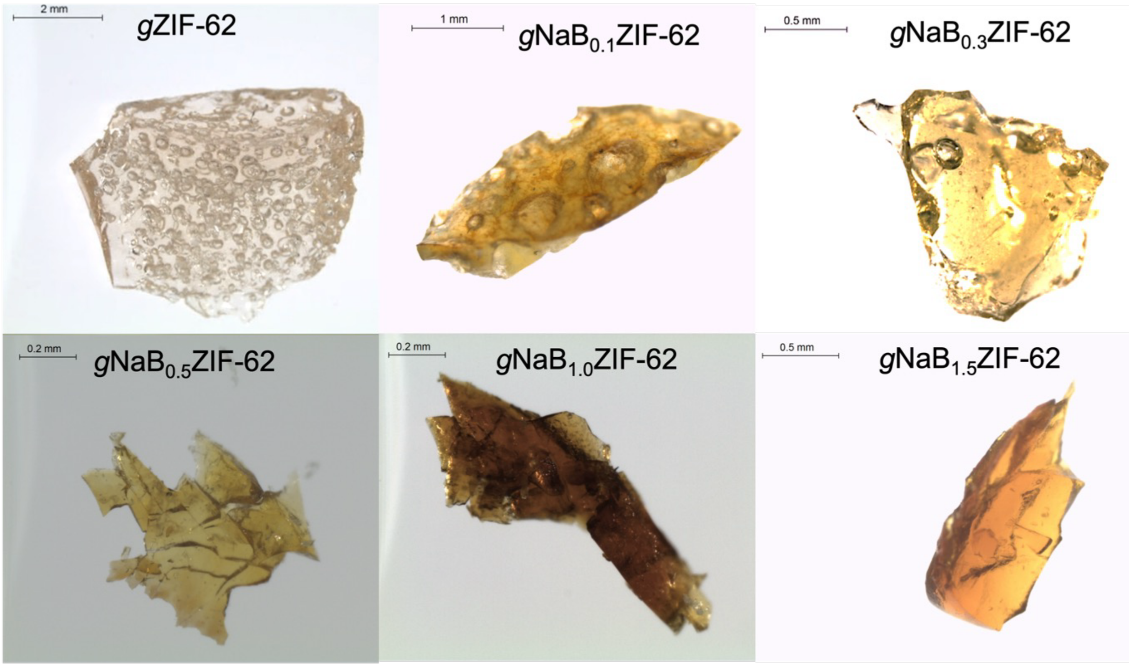

Figure A2.6. Optical microscopy images of shards of gZIF-62 (large-scale) and gNaB$_x$ZIF-62 materials with different Na(bim) contents x prepared on a small scale in a DSC apparatus.

Figure A2.7. Optical microscopy images of shards of gNaB$_x$ZIF-62 materials with different Na(bim) contents x. The glasses were prepared using the large-scale approach.

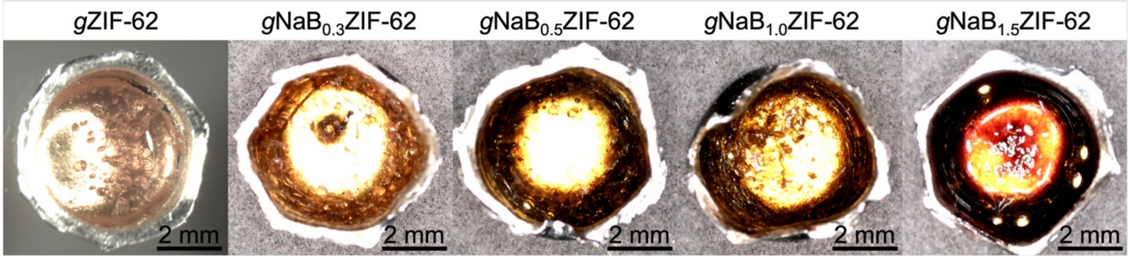

Figure A2.8. Optical microscopy images of gZIF-62 and gNaB$_x$ZIF-62 materials in DSC pans with different Na(bim) contents x. The glasses were prepared in a DSC apparatus (~10 mg scale) in a sealed DSC pan, which was opened after the heating-cooling cycle for melting and glass formation. The images illustrate the pronounced wetting behavior of the modified glasses compared to pure gZIF-62 and the formation of a meniscus on the glass surface. This behavior is in accordance with the lower viscosity of the modified glasses, as the meniscus formation requires sufficient fluidity in the liquid state.

A2.4 Large-Scale Vitrification Set-up

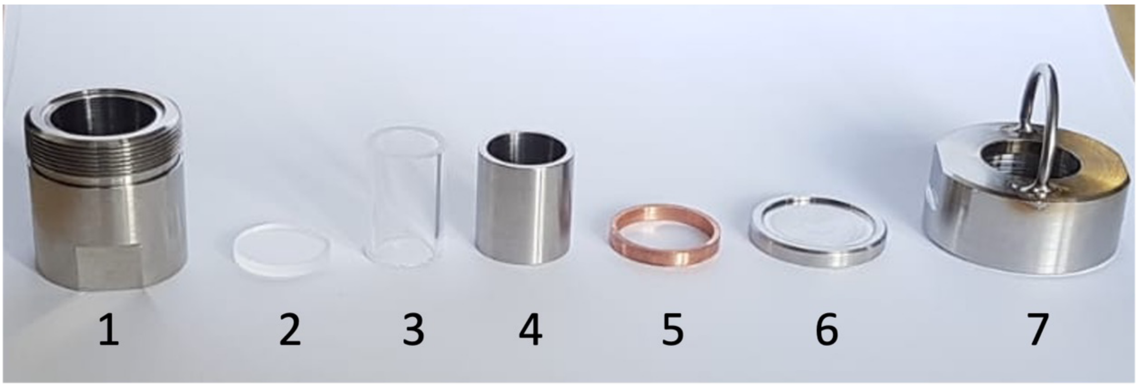

Figure A2.9. Photograph of the disassembled custom-made hermetic crucible for large-scale vitrification approaches consisting of a stainless-steel mantle (1), the top plate (6), the screw cap (7) and a copper sealing ring (5) sitting between the mantle and the top plate. The sample material itself is placed in a quartz-glass inlet consisting of the bottom plate (2) and the quartz-glass mantle (3), which is stabilised against tilting by the inner stainless-steel mantle (4).

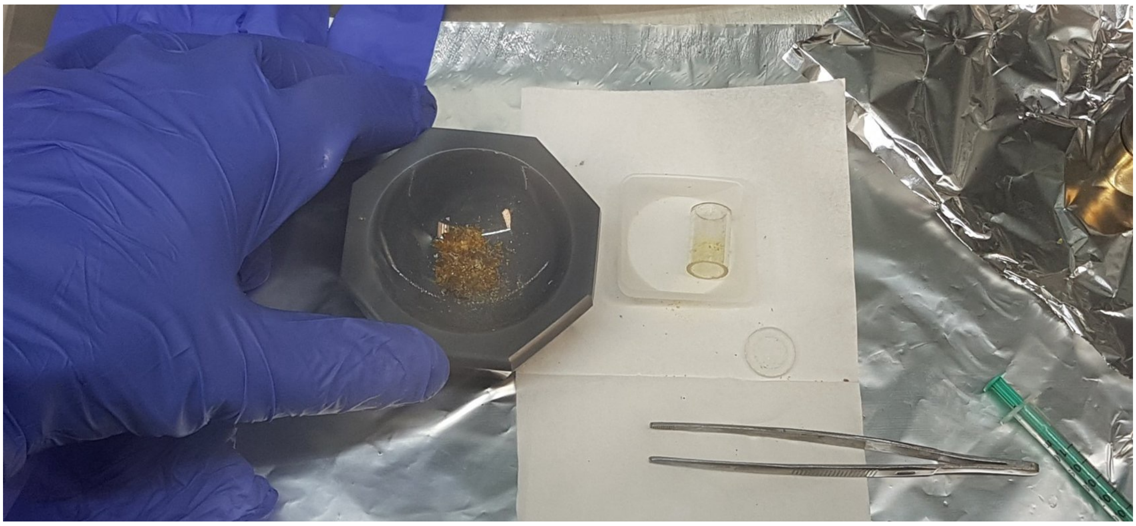

Figure A2.10. Photograph taken during the removal of melt-quenched gNaB$_{0.5}$ZIF-62 from the custom-made hermetic crucible (autoclave approach). The strong adhesion of the modified glass to the quartz glass inlet after melt-quenching required breaking the monolith.

A2.5 Simultaneous Thermal Analysis

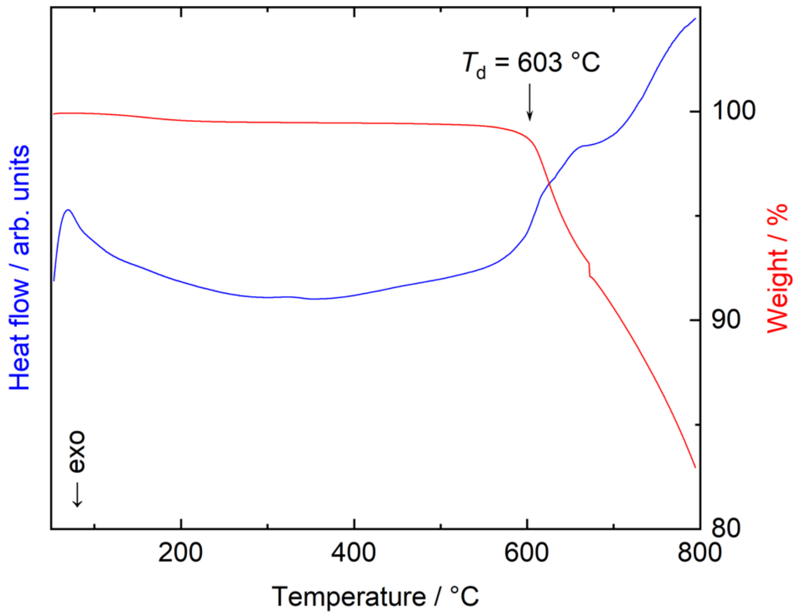

Figure A2.11. STA thermogram of gZIF-62 recorded with a constant heating rate of $10\,°\mathrm{C\,min^{-1}}$ under constant N_2 flow. The arrow indicates the decomposition temperature T_d.

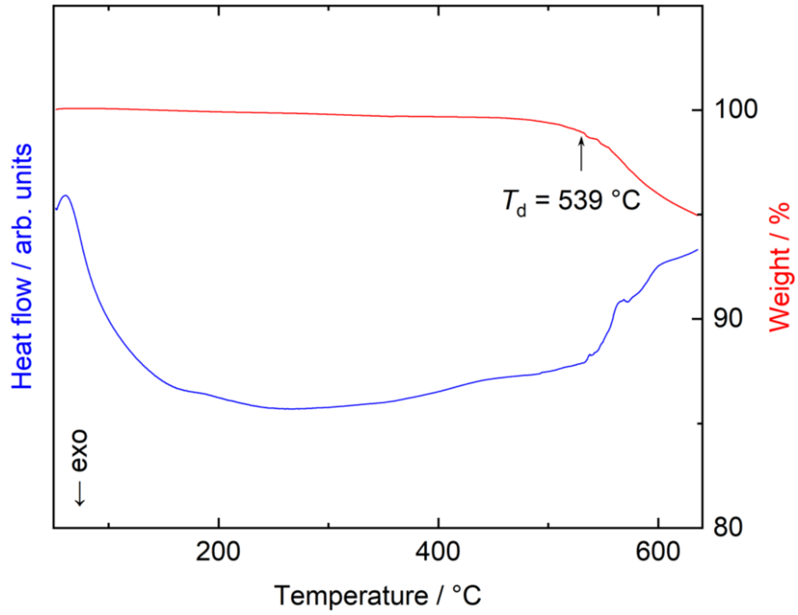

Figure A2.12. STA thermogram of gNaB$_{0.5}$ZIF-62 recorded with a constant heating rate of $10\,°C\,min^{-1}$ under constant N_2 flow. The arrow indicates the decomposition temperature T_d.

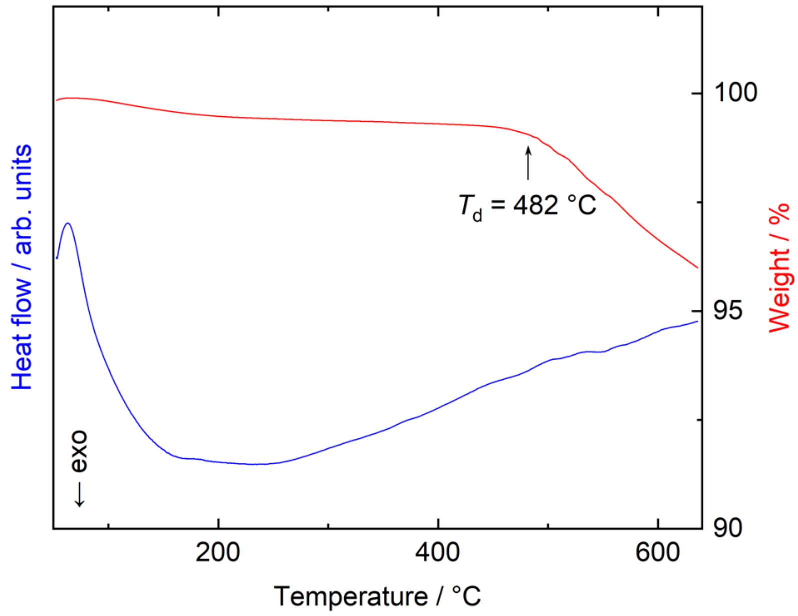

Figure A2.13. STA thermogram of gNaB$_{1.0}$ZIF-62 recorded with a constant heating rate of $10\,°C\,min^{-1}$ under constant N_2 flow. The arrow indicates the decomposition temperature T_d.

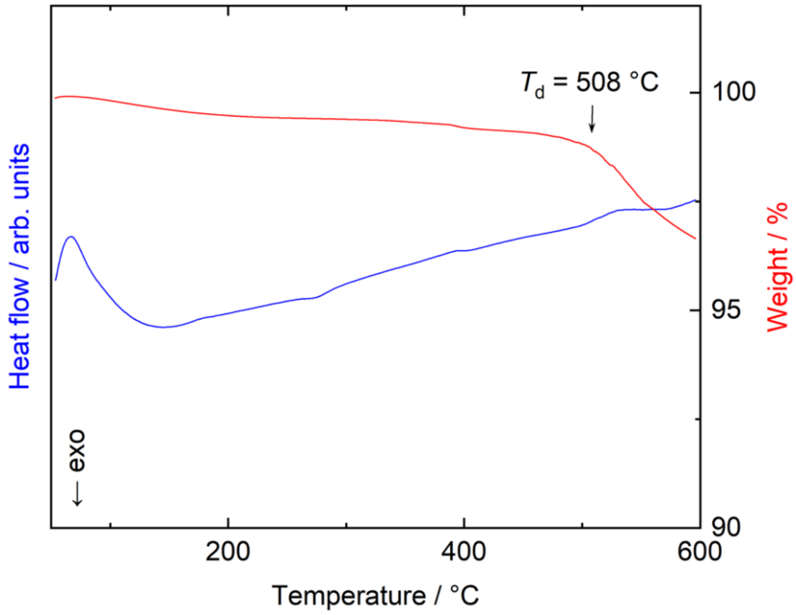

Figure A2.14. STA thermogram of gNaB$_{1.5}$ZIF-62 recorded with a constant heating rate of 10 °C min^{-1} under constant N_2 flow. The arrow indicates the decomposition temperature T_d.

A2.6 Powder X-Ray Diffraction

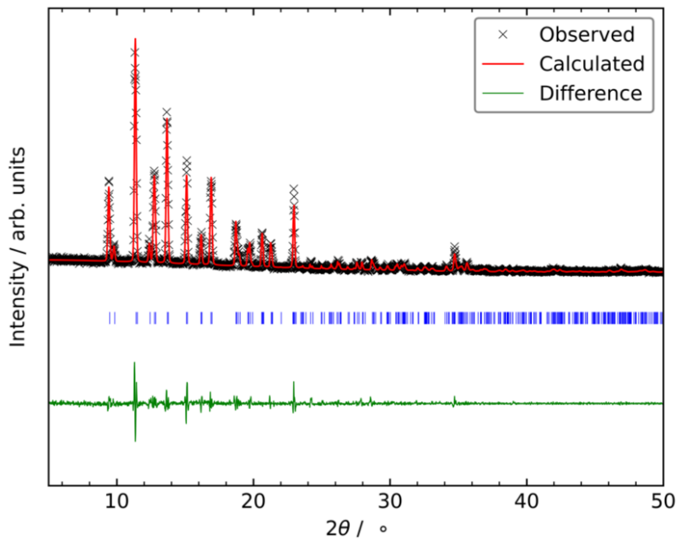

Figure A2.15. Structureless profile fit (Pawley method[62]) performed on the PXRD measurement of ZIF-62 recorded with CuK$_\alpha$ radiation. The blue tick marks indicate allowed Bragg peak positions. Refined unit cell parameters are shown in Table A2.3.

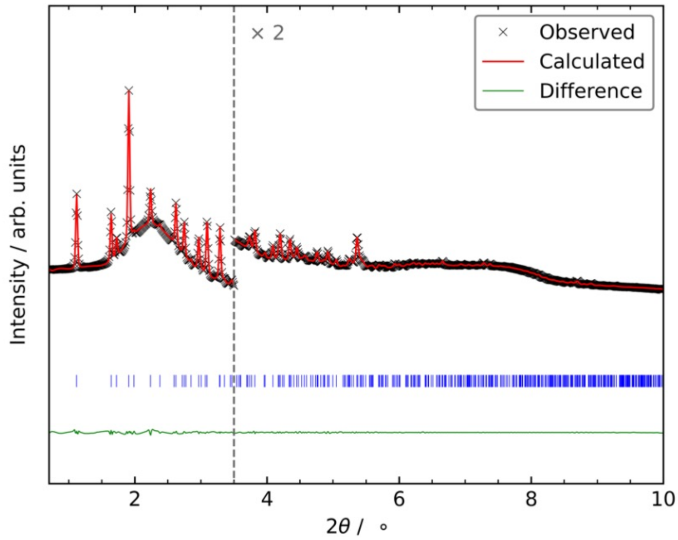

Figure A2.16. Structureless profile fit (Pawley method[62]) performed on the PXRD measurement of α-Na(bim) recorded at room temperature with a wavelength of 0.1617 Å at DLS. Blue tick marks indicate the position of allowed Bragg peaks. Refined unit cell parameters are shown in Table A2.3.

Table A2.3. Refined parameters obtained by profile fitting (Pawley method[62]) performed on the PXRD data of ZIF-62 and α-Na(bim).

Material	ZIF-62	α-Na(bim)
crystal system	orthorhombic	orthorhombic
space group	*Pbca*	*Pbcm*
a/Å	15.371(4)	8.282(2)
b/Å	15.494(3)	7.0677(9)
c/Å	17.940(4)	11.292(2)
α/°	90	90
β/°	90	90
γ/°	90	90
V/Å^3	4272(2)	661.0(2)
R_{wp}/%	13.85	0.81
R_{exp}/%	9.33	1.16
χ	1.49	0.7

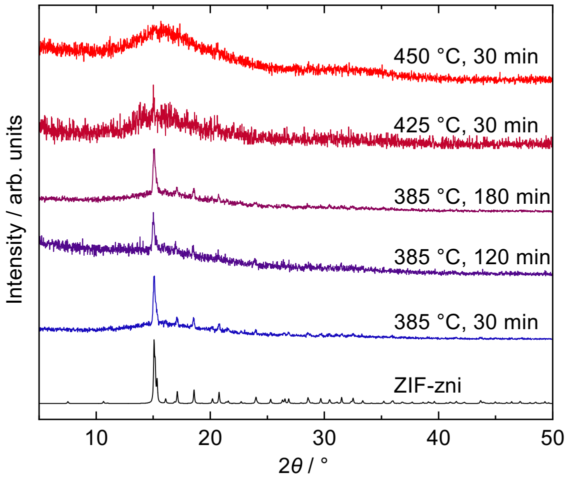

Figure A2.17. PXRD patterns of $NaB_{0.3}$|ZIF-62 after different temperature treatments consisting of a heating segment from room temperature up to a maximum temperature, followed by an isothermal segment of several minutes and subsequent cooling back to room temperature. The heating and cooling were performed at a constant rate of 10 °C. The maximum temperature and time of the isothermal segment are given next to the corresponding PXRD patterns of the materials after the temperature treatment. The PXRD patterns were recorded with CuK_α radiation under air. The black pattern (bottom) corresponds to a simulated diffraction pattern of ZIF-zni (CCDC: IMIDZB).

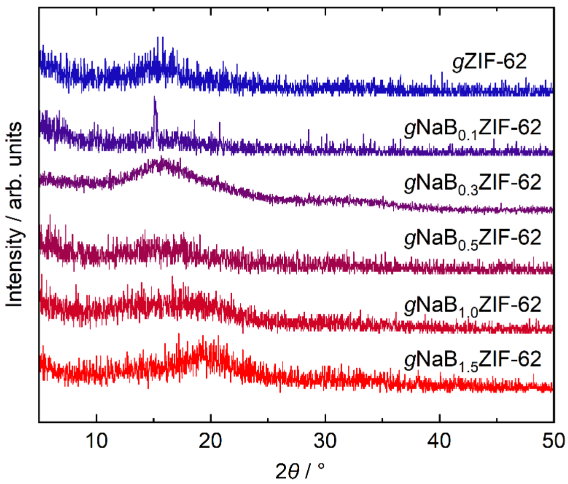

Figure A2.18. PXRD patterns of gNaB$_x$ZIF-62 materials after the melt-quenching procedure performed in a DSC apparatus (∼10 mg scale) consisting of a heating segment from room temperature up to 450 °C, followed by an isothermal segment of 30 mins and subsequent cooling back to room temperature. The heating and cooling were performed at a constant rate of 10 °C min^{-1}. Diffraction patterns were recorded with CuK_α radiation under air.

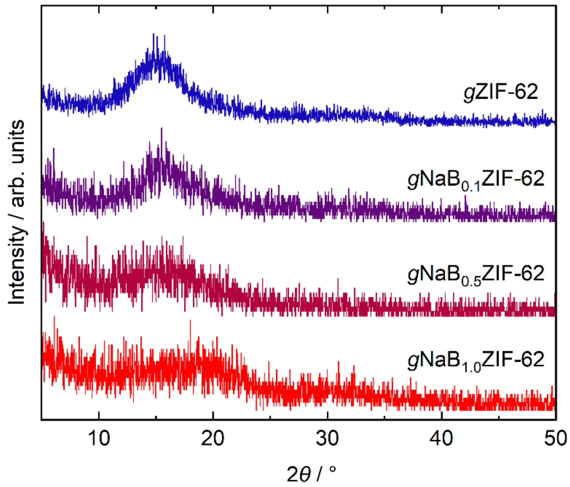

Figure A2.19. PXRD patterns of gNaB$_x$-ZIF-62 materials after the melt-quenching procedure in the large-scale melt-quenching approach (~250 mg scale) consisting of a heating segment from room temperature up to 450 °C, followed by an isothermal segment of 30 mins and subsequent cooling back to room temperature. The heating was performed at a constant rate of 10 °C min^{-1} while cooling was performed under external airflow (cooling rate ca. -10 °C min^{-1}). Diffraction patterns were recorded with CuK$_\alpha$ radiation under air.

A2.7 Solution NMR Spectroscopy

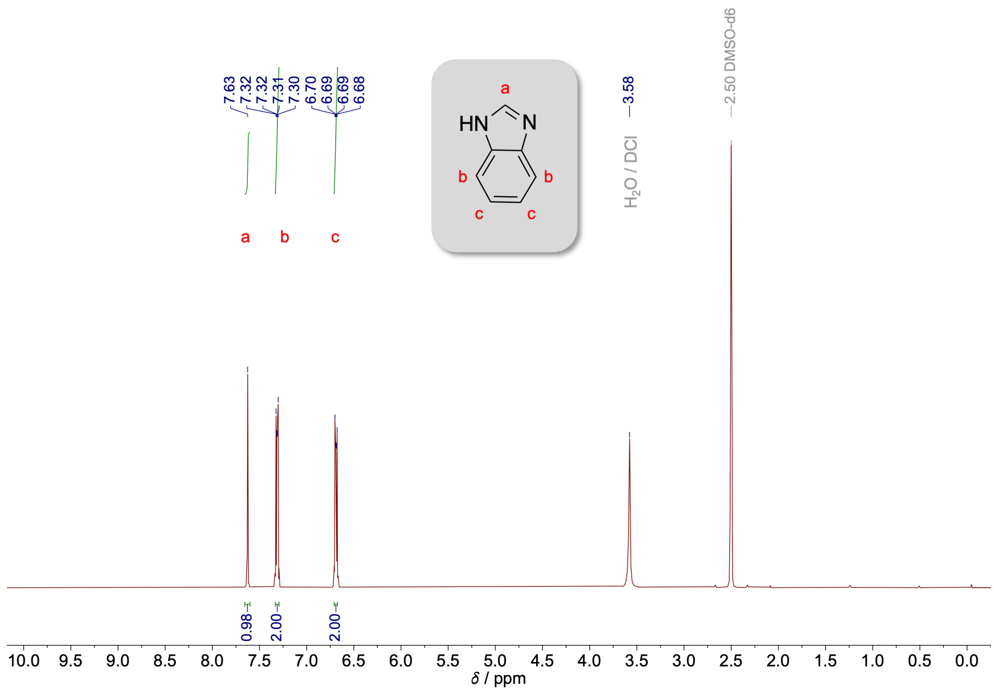

Figure A2.20. ^{1}H NMR spectrum of Na(bim) dissolved in DMSO-d_6 and DCl/D_2O (35 wt%, one drop, < 0.1 mL).

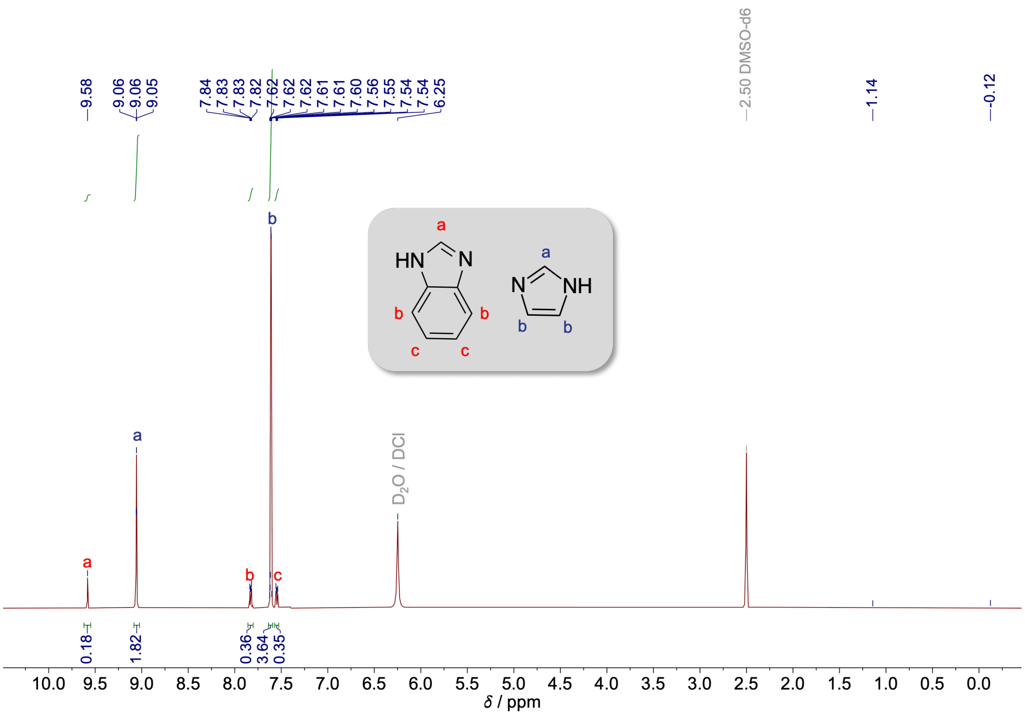

Figure A2.21. ^{1}H NMR spectrum of ZIF-62 dissolved in DMSO-d_6 and DCl/D_2O (35 wt%, one drop, < 0.1 mL).

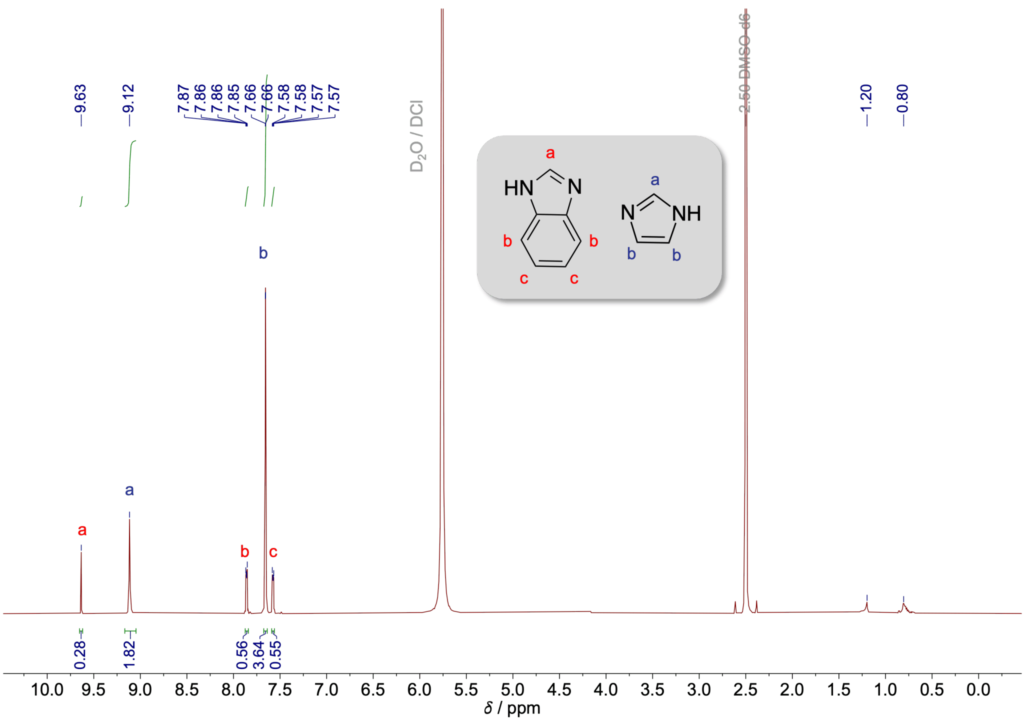

Figure A2.22. ^{1}H NMR spectrum of gNaB$_{0.1}$ZIF-62 (prepared in ∼10 mg scale) dissolved in DMSO-d_6 and DCl/D_2O (35 wt%, one drop, < 0.1 mL). Signals at around 0.8 and 1.2 ppm are assigned to residues of n-hexane, which was added during the grinding of the obtained glass monolith.

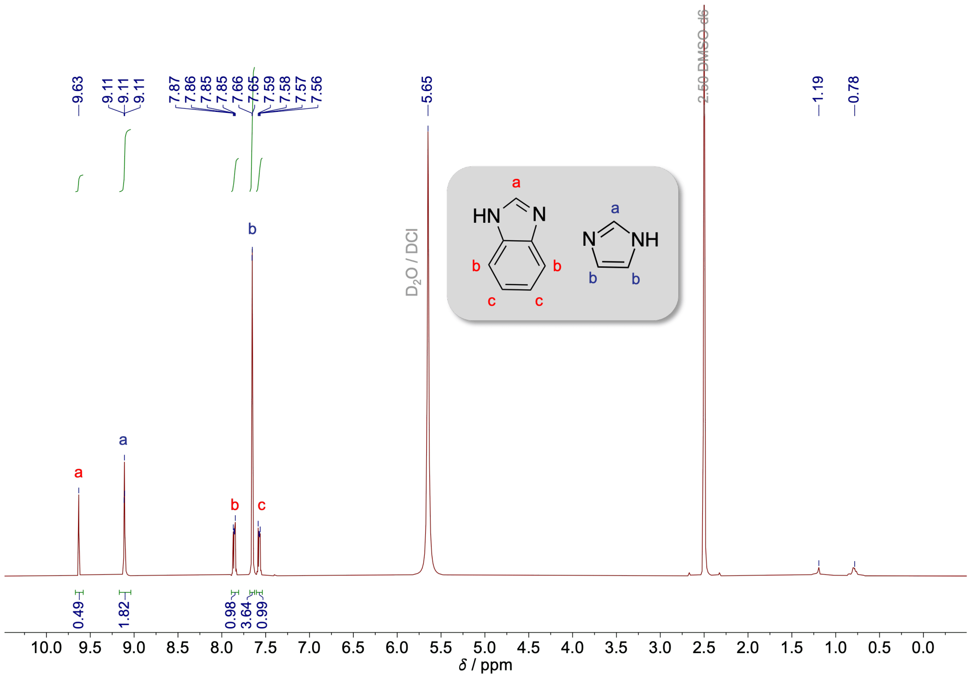

Figure A2.23. [1]H NMR spectrum of gNaB$_{0.3}$ZIF-62 (prepared in ~10 mg scale) dissolved in DMSO-d_6 and DCl/D_2O (35 wt%, one drop, < 0.1 mL). Signals at around 0.8 and 1.2 ppm are assigned to residues of n-hexane, which was added during the grinding of the obtained glass monolith.

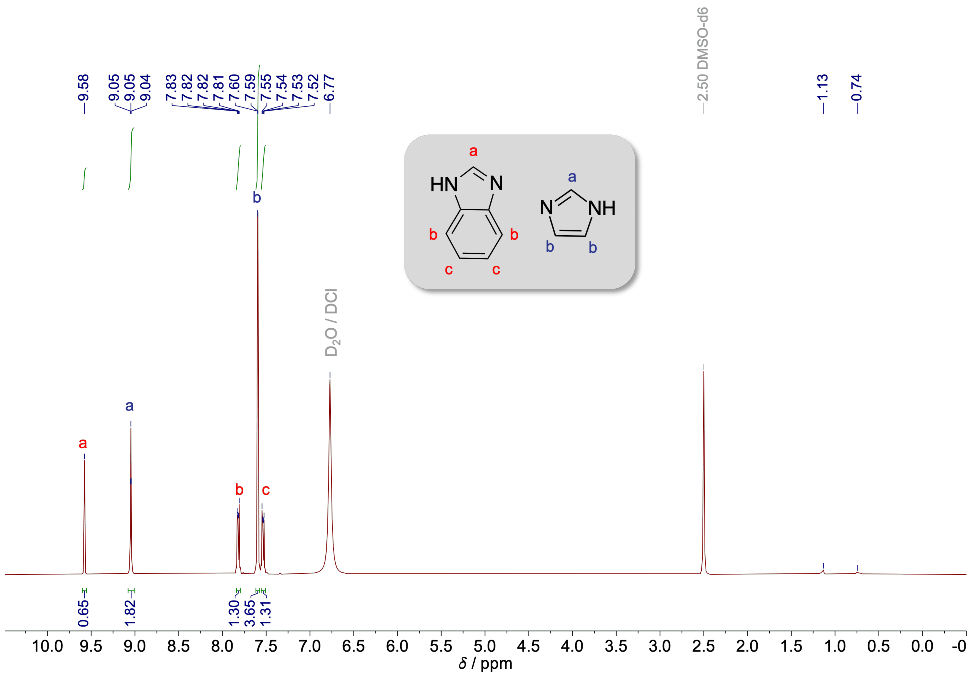

Figure A2.24. [1]H NMR spectrum of gNaB$_{0.5}$ZIF-62 (prepared in ~10 mg scale) dissolved in DMSO-d_6 and DCl/D_2O (35 wt%, one drop, < 0.1 mL). Signals at around 0.8 and 1.2 ppm are assigned to residues of n-hexane, which was added during the grinding of the obtained glass monolith.

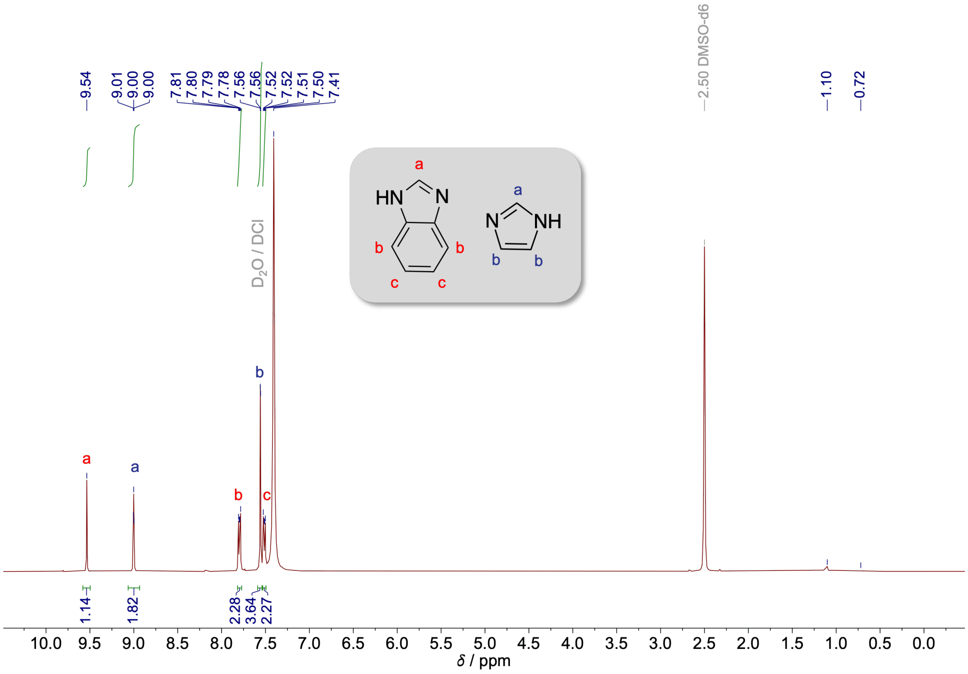

Figure A2.25. ^{1}H NMR spectrum of gNaB$_{1.0}$ZIF-62 (prepared in ~10 mg scale) dissolved in DMSO-d_6 and DCl/D_2O (35 wt%, one drop, < 0.1 mL). Signals at around 0.8 and 1.2 ppm are assigned to residues of n-hexane, which was added during the grinding of the obtained glass monolith.

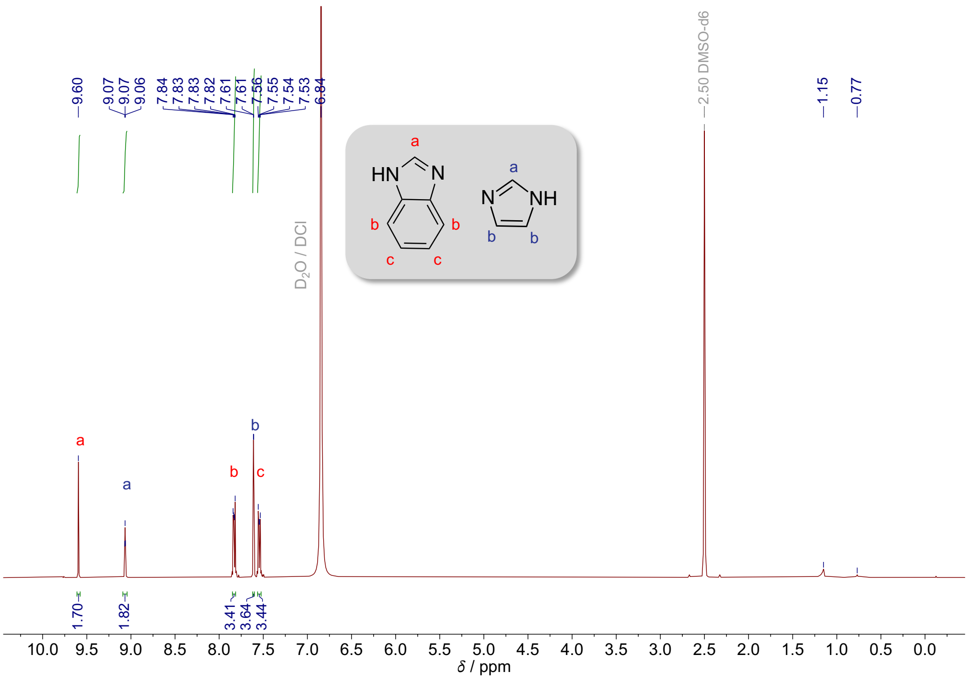

Figure A2.26. ^{1}H NMR spectrum of gNaB$_{1.5}$ZIF-62 (prepared in ~10 mg scale) dissolved in DMSO-d_6 and DCl/D_2O (35 wt%, one drop, < 0.1 mL). Signals at around 0.8 and 1.2 ppm are assigned to residues of n-hexane, which was added during the grinding of the obtained glass monolith.

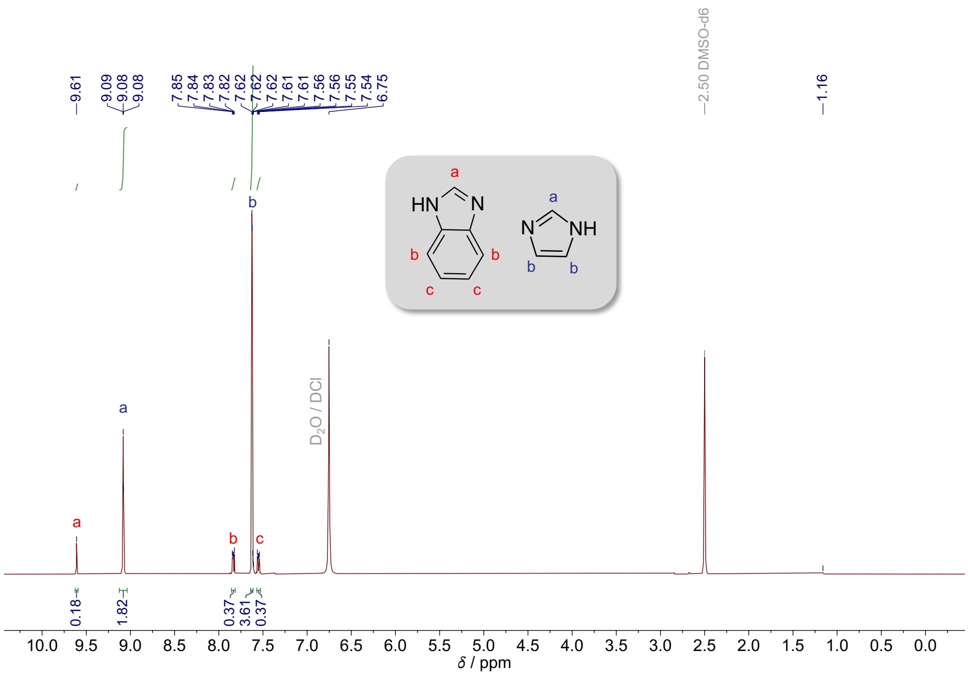

Figure A2.27. [1]H NMR spectrum of *g*ZIF-62 (prepared in ~250 mg scale) dissolved in DMSO-d_6 and DCl/D_2O (35 wt%, one drop, < 0.1 mL). Signals at around 0.8 and 1.2 ppm are assigned to residues of *n*-hexane, which was added during the grinding of the obtained glass monolith.

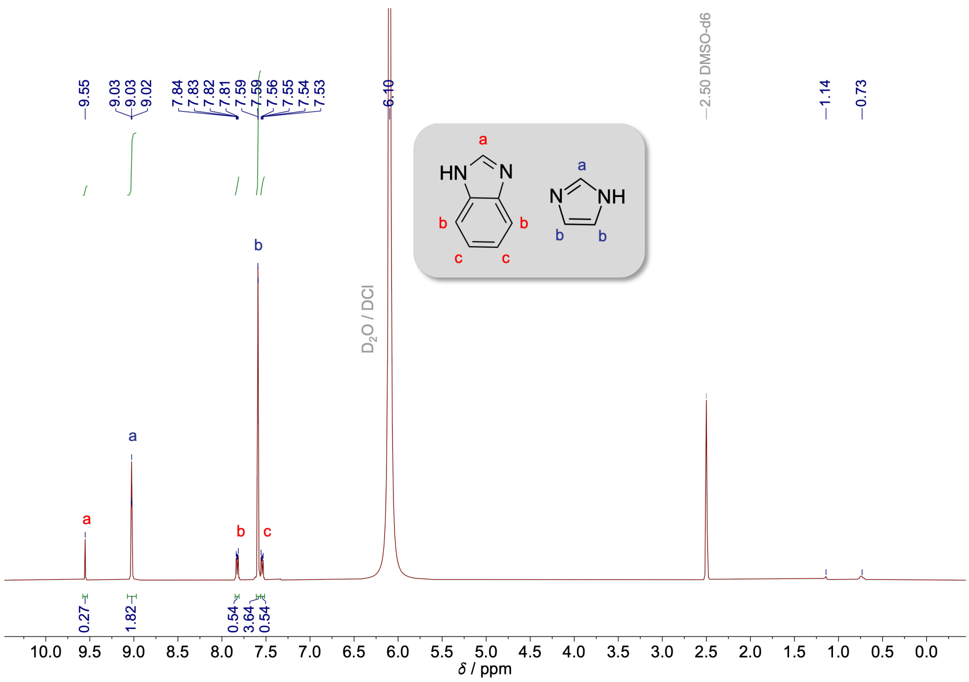

Figure A2.28. [1]H NMR spectrum of *g*NaB$_{0.1}$ZIF-62 (prepared in ~250 mg scale) dissolved in DMSO-d_6 and DCl/D_2O (35 wt%, one drop, < 0.1 mL). Signals at around 0.8 and 1.2 ppm are assigned to residues of *n*-hexane, which was added during the grinding of the obtained glass monolith.

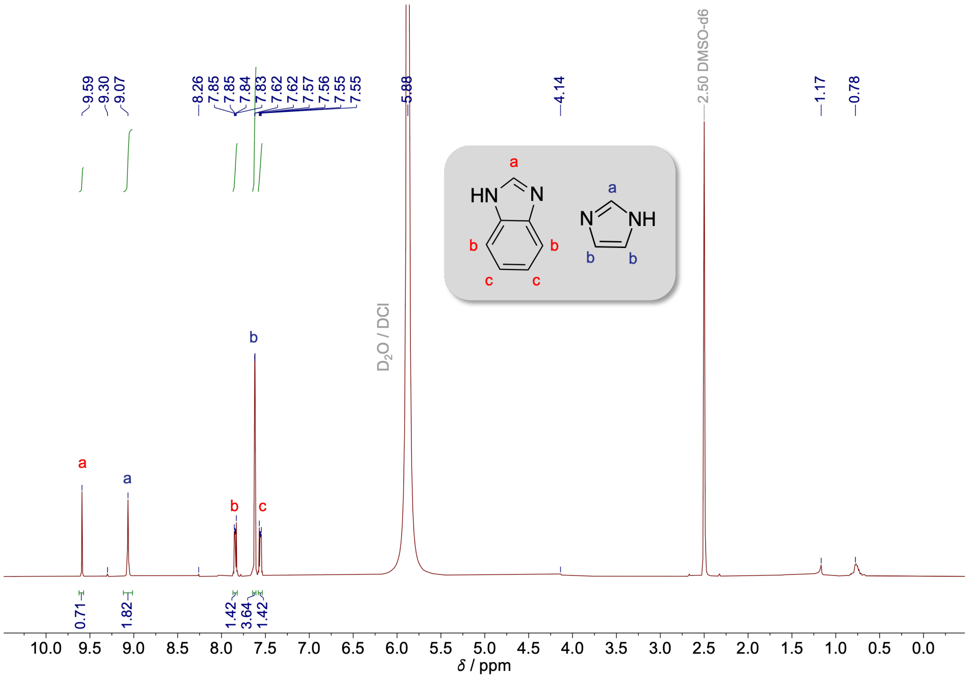

Figure A2.29. ^{1}H NMR spectrum of gNaB$_{0.5}$ZIF-62 (prepared in ~250 mg scale) dissolved in DMSO-d_6 and DCl/D_2O (35 wt%, one drop, < 0.1 mL). Signals at around 0.8 and 1.2 ppm are assigned to residues of n-hexane, which was added during the grinding of the obtained glass monolith.

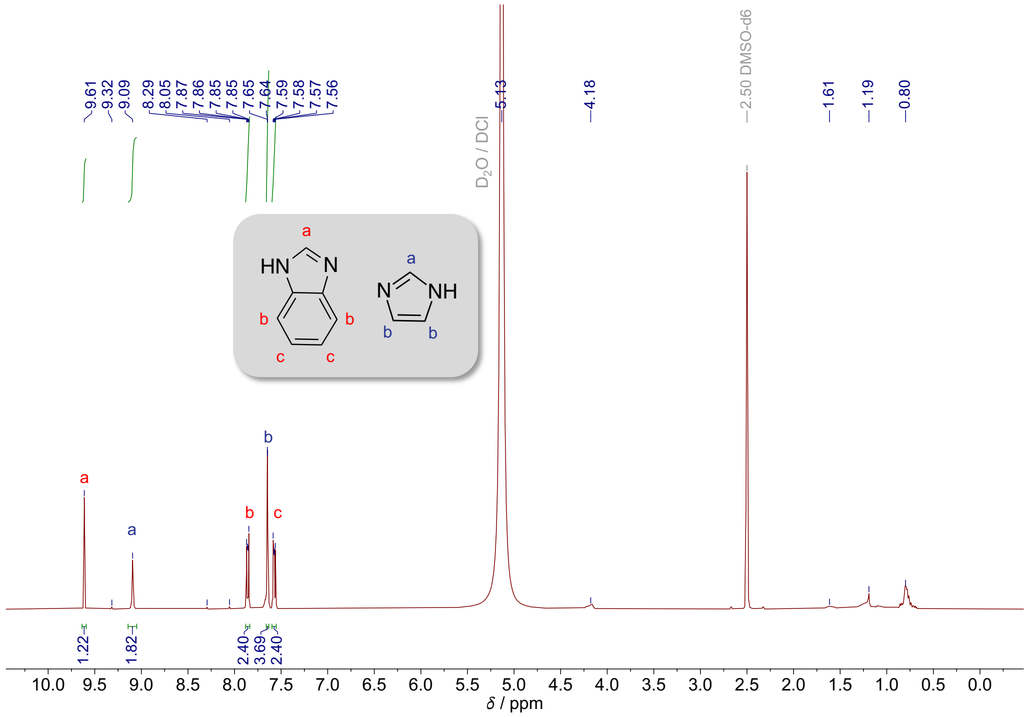

Figure A2.30. [1]H NMR spectrum of gNaB$_{1.0}$ZIF-62 (prepared in ~250 mg scale) dissolved in DMSO-d_6 and DCl/D_2O (35 wt%, one drop, < 0.1 mL). Signals at around 0.8 and 1.2 ppm are assigned to residues of n-hexane, which was added during the grinding of the obtained glass monolith.

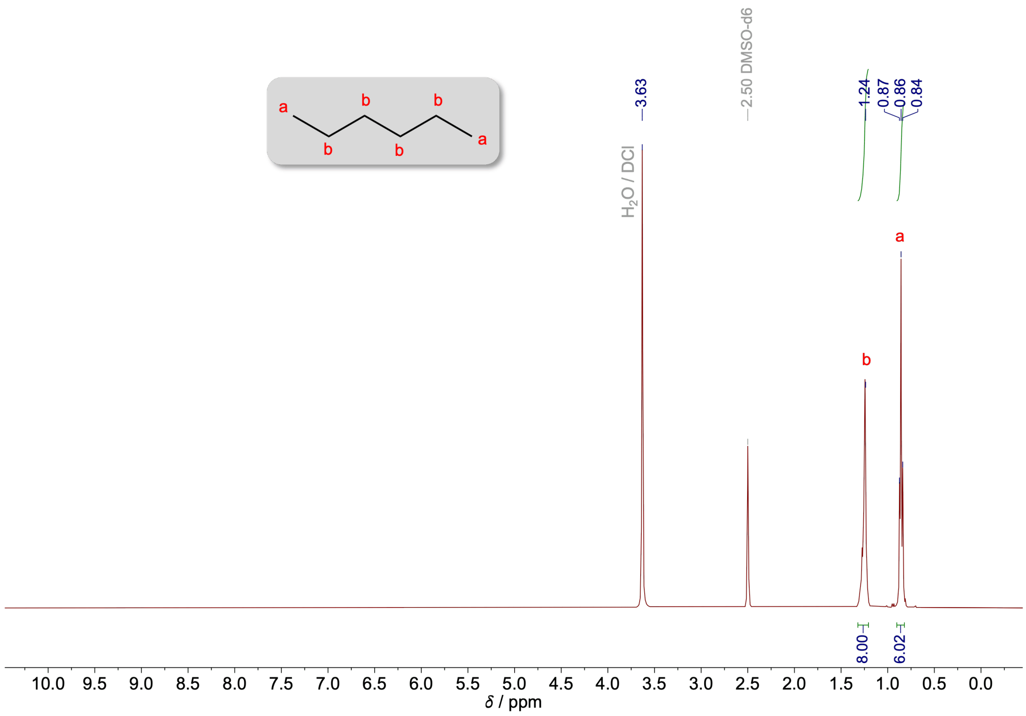

Figure A2.31. [1]H NMR spectrum of n-hexane dissolved in DMSO-d_6 and DCl/D_2O (35 wt%, one drop, < 0.1 mL).

Table A2.4. Name and chemical composition of prepared Na(bim)-modified ZIF-62 glasses gNaB$_x$ZIF-62 for different Na(bim) contents x and ZIF-62. Materials were obtained via two different approaches (i.e. small and large scale) and their chemical composition was calculated according to the bim-to-im ratio obtained from solution ^{1}H NMR spectroscopic measurements of the glass samples digested in DMSO-d_6 and DCl/D_2O (35 wt%, one drop, < 0.1 mL). The thus calculated Na(bim) content x shown here does not necessarily coincide with the x used in the nomenclature (gNaB$_x$ZIF-62) due to rounding. It is assumed that the x values in the nomenclature are in accordance with the solution ^{1}H NMR results with regard to the error margin of the NMR measurement. The chemical composition of the corresponding physical mixtures NaB$_x$|ZIF-62 is expected to be identical to those of the respective glasses. Deviations between the intended chemical composition and the composition found in ^{1}H NMR spectroscopy may be attributed to weighting errors during the preparation of the physical mixtures and measurement inaccuracies of ^{1}H NMR spectroscopy.

Scale	Name	bim$^-$	im$^-$	Chemical composition	x
Small	ZIF-62	0.18		$Zn(im)_{1.82}(bim)_{0.18}$	–
(∼10 mg)	gNaB$_{0.1}$ZIF-62	0.28		$Na_{0.10}Zn(im)_{1.82}(bim)_{0.28}$	0.10
	gNaB$_{0.3}$ZIF-62	0.49	1.82	$Na_{0.31}Zn(im)_{1.82}(bim)_{0.49}$	0.31
	gNaB$_{0.5}$ZIF-62	0.65		$Na_{0.47}Zn(im)_{1.82}(bim)_{0.65}$	0.47
	gNaB$_{1.0}$ZIF-62	1.14		$Na_{0.96}Zn(im)_{1.82}(bim)_{1.14}$	0.96
	gNaB$_{1.5}$ZIF-62	1.7		$Na_{1.52}Zn(im)_{1.82}(bim)_{1.70}$	1.52
Large	gZIF-62	0.18		$Zn(im)_{1.82}(bim)_{0.18}$	–
(∼250 mg)	gNaB$_{0.1}$ZIF-62	0.27	1.82	$Na_{0.09}Zn(im)_{1.82}(bim)_{0.27}$	0.09
	gNaB$_{0.5}$ZIF-62	0.71		$Na_{0.53}Zn(im)_{1.82}(bim)_{0.71}$	0.53
	gNaB$_{1.0}$ZIF-62	1.22		$Na_{1.04}Zn(im)_{1.82}(bim)_{1.22}$	1.04

A2.8 Variable Temperature Powder X-Ray Diffraction

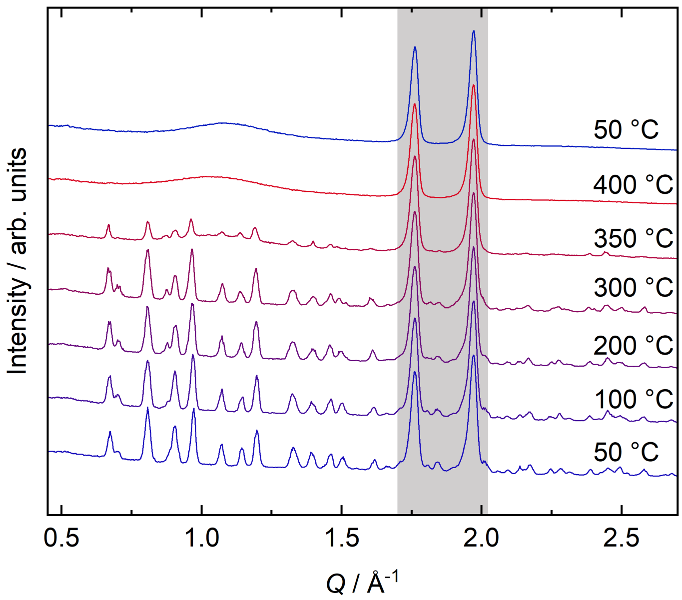

Figure A2.32. VT-PXRD patterns of a heating-cooling-cycle of ZIF-62 recorded with $\lambda = 0.4568$ Å at DELTA starting with the heating from 50 °C (blue, bottom) up to 400 °C (red) and subsequent cooling back to 50 °C (blue, top). The greyed-out reflections are related to the used experimental set up and do not originate from the sample material. The blue tick marks correspond to the allowed Bragg peak positions of ZIF-62 (CCDC: GIZJOP).

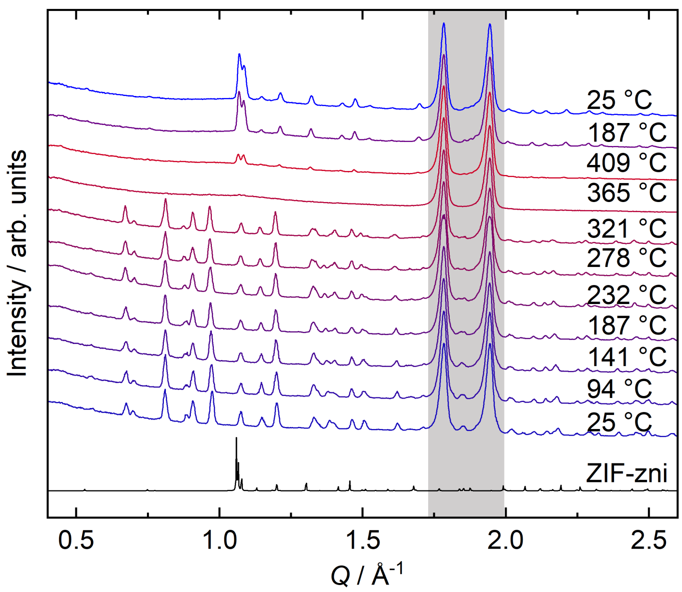

Figure A2.33. VT-PXRD patterns of a heating-cooling-cycle of $NaB_{0.1}$|ZIF-62 recorded with $\lambda = 0.4616$ Å at DELTA starting with the heating from 25 °C (blue, bottom) up to 409 °C (red) and subsequent cooling back to 25 °C (blue, top). The tick marks correspond to the allowed Bragg peak positions of ZIF-62 (blue) and ZIF-zni (red) (CCDC: GIZJOP, IMIDZB). The greyed-out reflections are related to the used experimental set up and do not originate from the sample material.

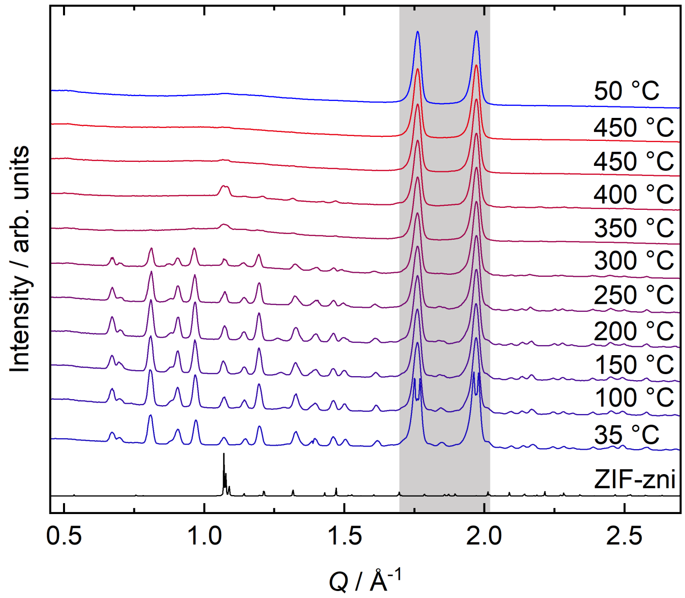

Figure A2.34. VT-PXRD patterns of a heating-cooling-cycle of $NaB_{0.3}$|ZIF-62 recorded with $\lambda = 0.4568$ Å at DELTA starting with the heating from 35 °C (blue, bottom) up to 450 °C (red) followed by an isothermal segment (2nd 450 °C measurement) and subsequent cooling back to 50 °C (blue, top). The tick marks correspond to the allowed Bragg peak positions of ZIF-62 (blue) and ZIF-zni (red). The latter crystallises at 350 °C and dissolves again above 400 °C (CCDC: GIZJOP, IMIDZB). The greyed-out reflections are related to the used experimental set up and do not originate from the sample material.

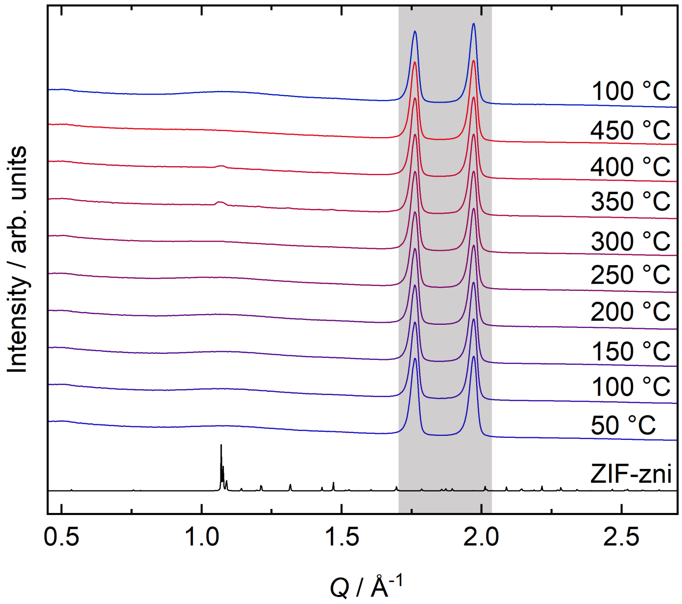

Figure A2.35. VT-PXRD patterns of a heating-cooling-cycle of gNaB$_{0.3}$ZIF-62 recorded with $\lambda = 0.4568$ Å at DELTA starting with the heating from 50 °C (blue, bottom) up to 450 °C (red) and subsequent cooling back to 100 °C (blue, top). The black line corresponds to a simulated diffraction pattern of ZIF-zni (bottom) (CCDC: IMIDZB). The greyed-out reflections are related to the used experimental set up and do not originate from the sample material. The depicted VT-PXRD data show the intermediate crystallization of ZIF-zni during the heating of gNaB$_{0.3}$ZIF-62 starting at 350 °C and the subsequent dissolution of the crystalline phase at even higher temperatures.

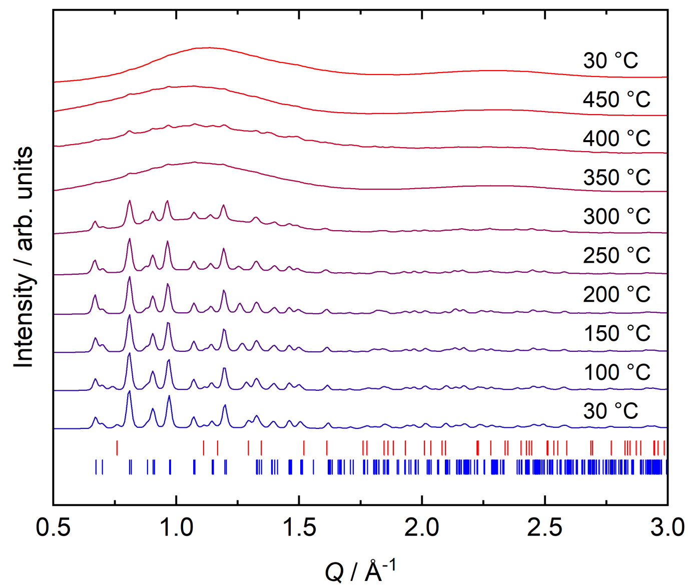

Figure A2.36. VT-PXRD patterns of a heating-cooling-cycle of $NaB_{0.5}$|ZIF-62 recorded with λ = 0.1616 Å at DLS starting with the heating from 30 °C (blue, bottom) up to 450 °C (red) and subsequent cooling back to 30 °C (blue, top). The tick marks correspond to the allowed Bragg peak positions of ZIF-62 (blue) and α-Na(bim) (red) (CCDC: GIZJOP, QOVDAK). The intermediate appearance of reflections in the pattern collected at 400 °C is likely caused by residual microcrystalline ZIF-62 from the unheated part of the capillary, moving into the path via the flow of the (amorphous) liquid.

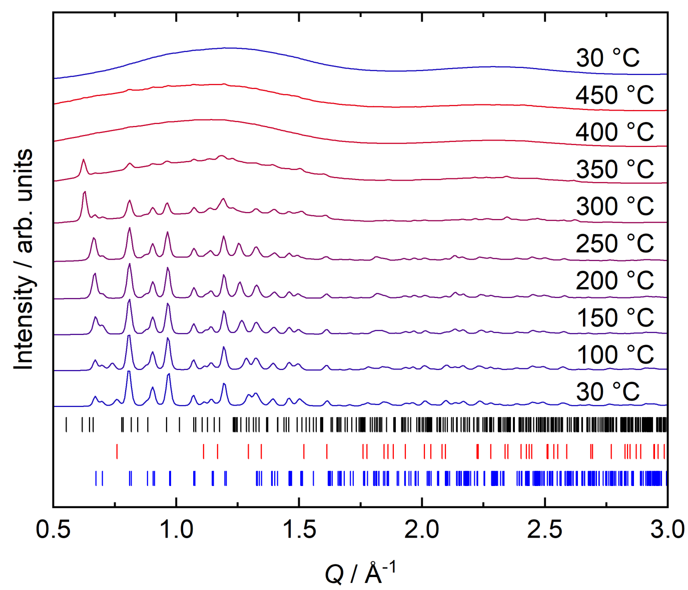

Figure A2.37. VT-PXRD patterns of a heating-cooling-cycle of $NaB_{1.0}$|ZIF-62 recorded with λ = 0.1616 Å at DLS starting with the heating from 30 °C (blue, bottom) up to 450 °C (red) and subsequent cooling back to 30 °C (blue, top). The tick marks indicate the allowed Bragg peak positions of ZIF-62 (blue), α-Na(bim) (red) as well as ZIF-7-III (black) after crystallization at 300 °C (CCDC: GIZJOP, QOVDAK, KOLYAM).

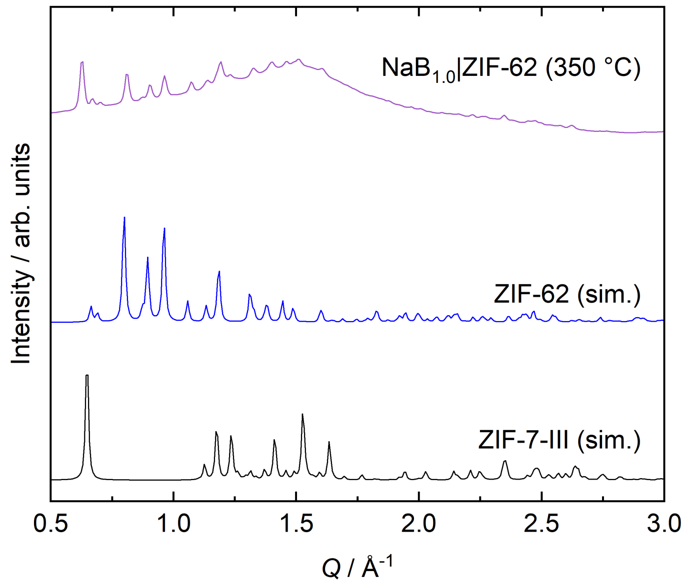

Figure A2.38. PXRD pattern of $NaB_{1.0}$|ZIF-62 recorded at 350 °C with $\lambda = 0.1616$ Å at DLS, together with simulated diffraction patterns of ZIF-62 (blue) and ZIF-7-III (black) demonstrating the presence of residual ZIF-62 and crystallised ZIF-7-III in the physical mixture during the thermal upscan shown in Figure A2.36 (CCDC: GIZJOP, KOLYAM). The first reflection of ZIF-7-III ($hkl = 002$) is slightly shifted compared to the first reflection observed in the pattern of $NaB_{1.0}$|ZIF-62 due to the thermal expansion of the crystalline phase at elevated temperatures.

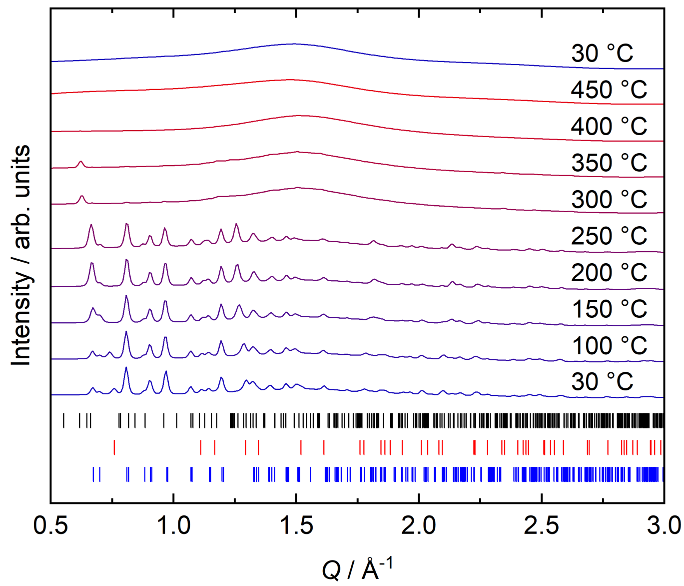

Figure A2.39. VT-PXRD patterns of a heating-cooling-cycle of $NaB_{1.5}$|ZIF-62 recorded with $\lambda = 0.1616$ Å at DLS starting with the heating from 30 °C (blue, bottom) up to 450 °C (red) and subsequent cooling back to 30 °C (blue, top). The tick marks correspond to the allowed Bragg peak positions of ZIF-62 (blue) and α-Na(bim) (red) as well as ZIF-7-III (black) which crystallises at 300 °C followed by dissolution of the formed crystalline phase at 400 °C (CCDC: GIZJOP, QOVDAK, KOLYAM).

A2.9 Differential Scanning Calorimetry

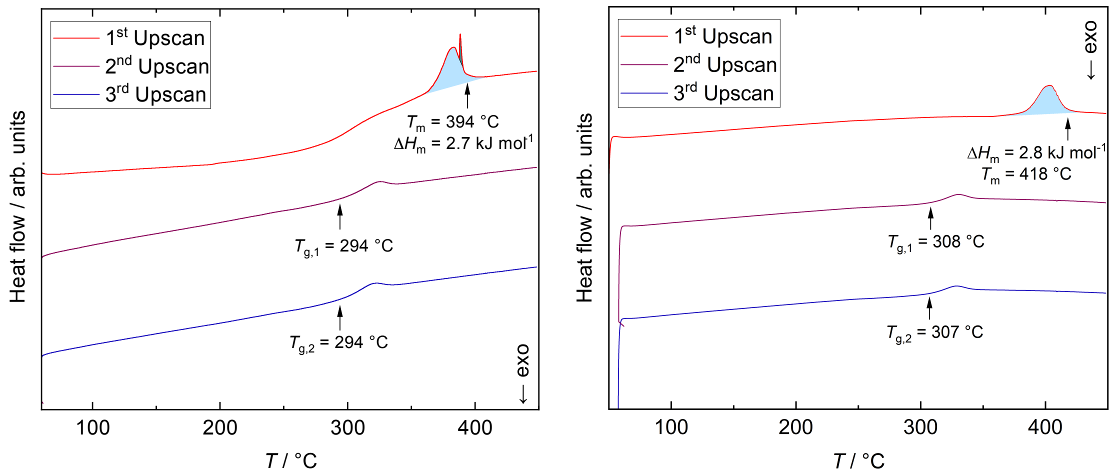

Figure A2.40. Heat flow curves of consecutive thermal upscans of ZIF-62 measured under hermetic conditions in a sealed crucible (left) and in a perforated one (right). The autogenous pressure build-up leads to artefacts in the first thermal upscan, which are assigned to the deformation of the crucible (left). Further, the thermal events of melting (T_m) and the glass transition (T_g) appear at lower temperatures (left) compared to the measurement performed under atmosphere pressure (right). Heating and cooling were performed at a constant rate of $\pm 10\,°\mathrm{C\,min^{-1}}$.

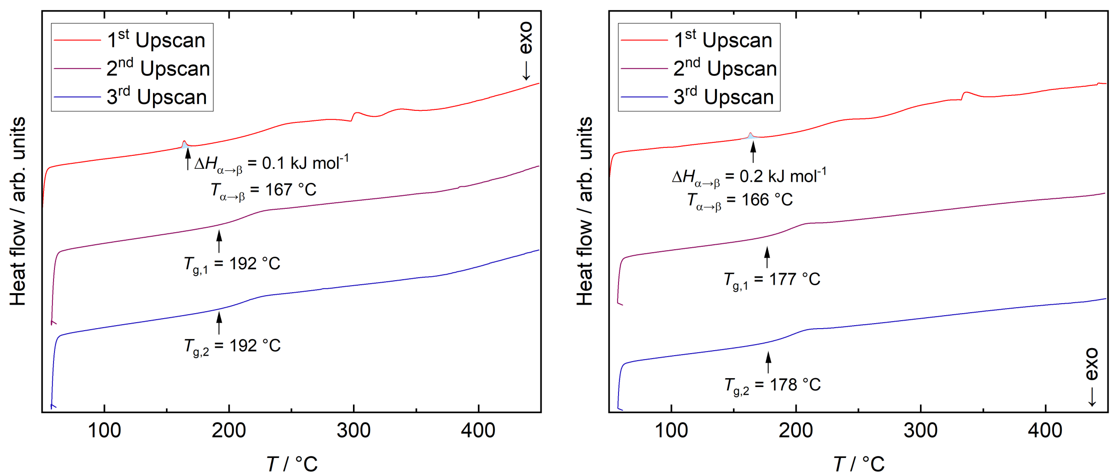

Figure A2.41. Heat flow curves of consecutive thermal upscans of the physical mixture $\mathrm{NaB_{0.1}}$|ZIF-62 (left) and $\mathrm{NaB_{0.3}}$|ZIF-62 (right). An isothermal segment of 30 mins was applied after the first upscan to improve homogenization. Heating and cooling were performed at a constant rate of $\pm 10\,°\mathrm{C\,min^{-1}}$. Enthalpies ΔH were calculated based on the mean molar mass of the corresponding physical mixture. Sharp features in the first upscan beyond 350 °C are considered artefacts resulting from crucible deformation under the autogenous pressure build-up. The arrows indicate the temperature of the glass transition T_g, the temperature of the $\alpha \rightarrow \beta$-phase transition of pure Na(bim) in the physical mixture $T_{\alpha\rightarrow\beta}$ and the temperature of the intermixing process T_mix during the reaction of ZIF-62 with Na(bim).

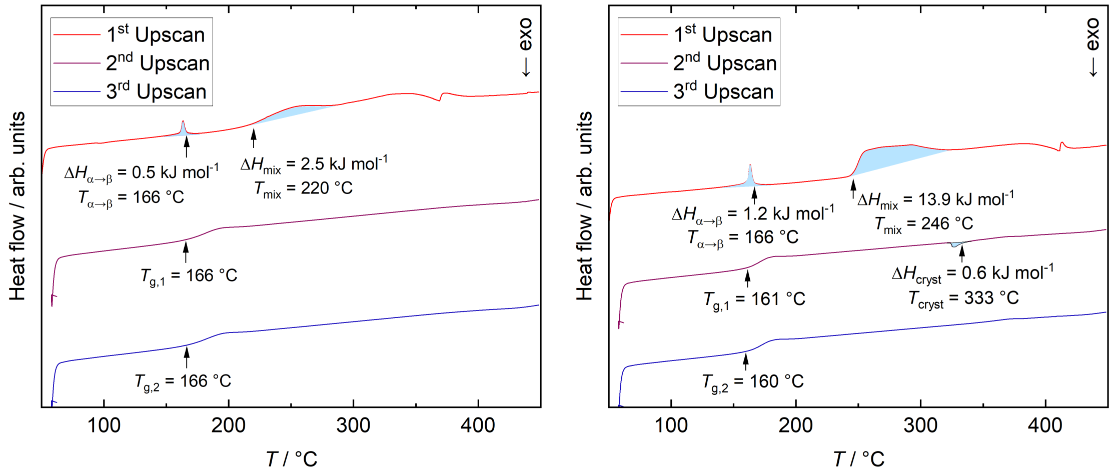

Figure A2.42. Heat flow curves of consecutive thermal upscans of the physical mixture $NaB_{0.5}|ZIF$-62 (left) and $NaB_{1.0}|ZIF$-62 (right). An isothermal segment of 30 mins was applied after the first upscan to improve homogenization. Heating and cooling were performed at a constant rate of $\pm 10\,^{\circ}C\,min^{-1}$. Enthalpies ΔH were calculated based on the mean molar mass of the corresponding physical mixture. Sharp features in the first upscan beyond 350 °C are considered artefacts resulting from crucible deformation under the autogenous pressure build-up. The arrows indicate the temperature of the glass transition T_g, the temperature of the $\alpha \rightarrow \beta$-phase transition of pure Na(bim) in the physical mixture $T_{\alpha\rightarrow\beta}$ and the temperature of the intermixing process T_{mix} during the reaction of ZIF-62 with Na(bim).

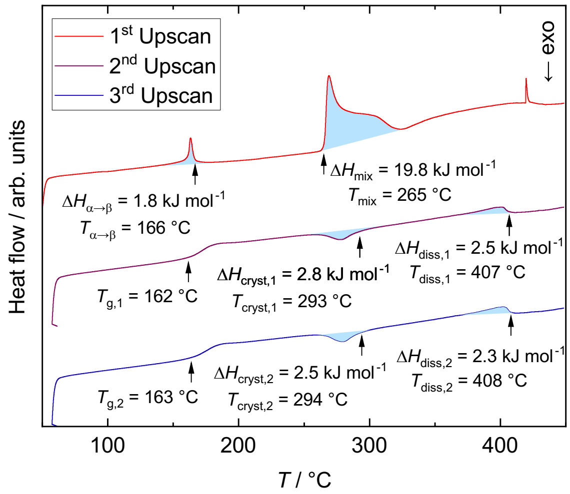

Figure A2.43. Heat flow curves of consecutive thermal upscans of the physical mixture $NaB_{1.5}$|ZIF-62. An isothermal segment of 30 mins was applied after the first upscan to improve homogenization. Heating and cooling were performed at a constant rate of $\pm 10\,°C\,min^{-1}$. Enthalpies ΔH were calculated based on the mean molar mass of the corresponding physical mixture. Endothermic features in the first upscan beyond 350 °C are considered artefacts resulting from crucible deformation under the autogenous pressure build-up. The arrows indicate the temperatures of the glass transition T_g, the temperature of the $\alpha \rightarrow \beta$ phase transition of pure Na(bim) in the physical mixture $T_{\alpha\rightarrow\beta}$ or the temperature of the intermixing process T_{mix} during the reaction of ZIF-62 with Na(bim) in the first thermal upscan. T_{cryst} and T_{diss} correspond to the crystallization and subsequent dissolution process of the intermediately formed crystalline ZIF-7-III phase in the second and third thermal upscan.

Table A2.5. Enthalpies associated with the $\alpha \rightarrow \beta$ phase transition of Na(bim) ($\Delta H_{\alpha\rightarrow\beta}$) in the first thermal upscan of the physical mixtures with different Na(bim) contents x as well as the enthalpy which is assigned to the process of intermixing (ΔH_{mix}) during the reaction of ZIF-62 and Na(bim) in the first thermal upcan in the corresponding DSC thermograms (see Figure A2.40 – A2.43). The extracted molar enthalpies are calculated based on the molar unit $ZnNa_x(im)_{1.8}(bim)_{0.2+x}$. The obtained $\Delta H_{\alpha\rightarrow\beta}$ values ($\Delta H_{\alpha\rightarrow\beta}$(Na(bim)) = 1.3 kJ mol^{-1})[137] are in rough accordance with the amount of Na(bim) in the physical mixtures as reflected by the solution ^{1}H NMR spectroscopy results.

x	$\Delta H_{\alpha\rightarrow\beta}$ / J g^{-1}	$\Delta H_{\alpha\rightarrow\beta}$/ kJ mol^{-1}	ΔH_{mix} / J g^{-1}	ΔH_{mix} / kJ mol^{-1}
0.1	0.5	0.1	–	–
0.3	0.8	0.2	–	–
0.5	1.7	0.5	9	2.5
1	3.6	1.2	40.4	13.9
1.5	4.3	1.8	47	19.7

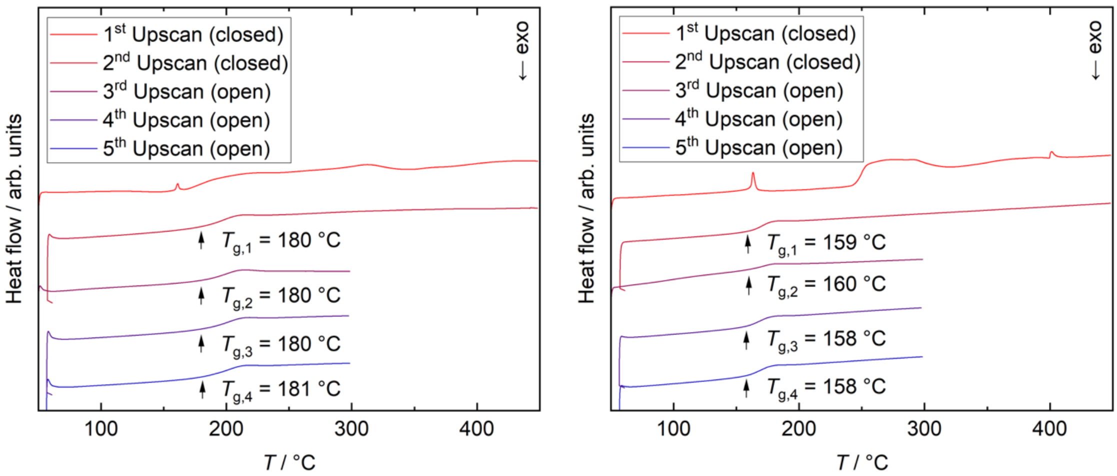

Figure A2.44. Heat flow curves of consecutive thermal upscans of the physical mixture $NaB_{0.3}$|ZIF-62 (left) and $NaB_{1.0}$|ZIF-62 (right). An isothermal segment of 30 min was applied after the first upscan to improve homogenization of the melt. To investigate the influence of the autogenous pressure build-up in the hermetically sealed crucible, only the first two upscans were collected in a sealed crucible (closed) while the 3^{rd} to 5^{th} upscans were collected with a pierced crucible lid (open). Heating and cooling were performed at a constant rate of $\pm 10\,°C\,min^{-1}$. Sharp features in the first upscan beyond 350 °C are considered artefacts resulting from crucible deformation under the autogenous pressure build-up. The arrows indicate the temperature of the glass transition T_g, and monitor only minor changes in the glass transition temperature between the first two and the following upscans at ambient pressure.

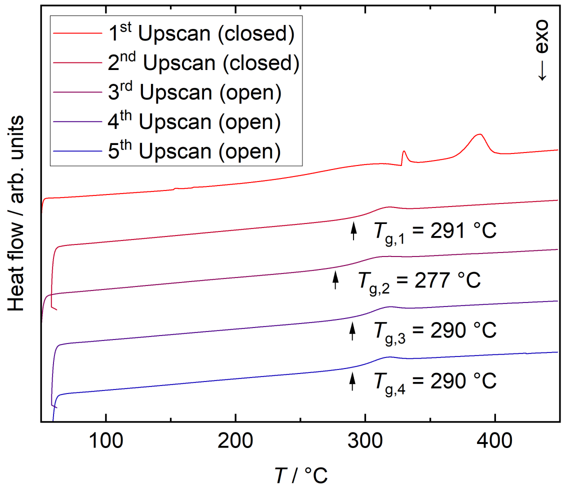

Figure A2.45. Heat flow curves of consecutive thermal upscans of ZIF-62. An isothermal segment of 30 mins was applied after the first upscan to improve homogenization of the melt. To investigate the influence of the autogenous pressure build-up in the hermetically sealed crucible, only the first two upscans were collected in a sealed crucible (closed) while the 3rd to 5th upscans were collected with a pierced crucible lid (open). Heating and cooling were performed at a constant rate of $\pm 10\,°C\,min^{-1}$. Sharp features in the first upscan are considered artefacts resulting from crucible deformation under the autogenous pressure build-up. The arrows indicate the temperature of the glass transition T_g, and monitor a decrease of T_g in the first upscan after opening of the crucible (3rd upscan). After the relaxation of the glass (i.e. after undergoing $T_{g,2}$) the glass transition temperature increases in upscans 4 and 5 back to the initial value of 290 °C.

A2.10 Calorimetric Fragility Measurements

A2.10.1 Experimental Details

All DSC experiments were performed on the DSC25 from TA Instruments under a constant N_2 flow of $50\,\mathrm{mL\,min^{-1}}$. Data processing was carried out in TA Instruments TRIOS version 5.1.1.46572.

Calorimetric fragility measurements were performed according to the experimental protocol first published by Zheng *et al.*[171] For the measurement, a powdered sample was filled in an aluminium crucible, which was hermetically sealed under an inert atmosphere (N_2). The sample was subject to a temperature program consisting of an initial vitrification process (heating to 450 °C, followed by an isothermal segment of 30 min at the maximum temperature), followed by the actual fragility measurement procedure. For this, the sample was subject to several consecutive cooling and heating cycles, each with a different but constant cooling/heating rate (q_c) of ± 7, 10, 13, 16, $19\,\mathrm{K\,min^{-1}}$. The fictive temperature fictive temperature (T_f), as well as the glass transition temperature T_g was defined as the inflexion point of the heat flow curve during the glass transition. After the measurement, the obtained glass was subject to PXRD measurements to make sure that the sample was not altered during the temperature program applied for fragility determination (e.g., by partial crystallization of ZIF-zni or ZIF-7-III). The liquid fragility index m was obtained as the slope of a linear fit to the data plotted according to its definition given in Equation A2.1. The following equation further shows the relation between m and the activation energy of viscous flow E_a at T_g and the ideal gas constant R:

$$m = \frac{\mathrm{d}\log(\frac{1}{q_c})}{\mathrm{d}(\frac{T_\mathrm{g}}{T_\mathrm{f}})} = \frac{1}{2.303} \cdot \frac{\mathrm{d}\ln(\frac{1}{q_c})}{\mathrm{d}(\frac{T_\mathrm{g}}{T_\mathrm{f}})} = \frac{E_\mathrm{a}}{2.303 \cdot R \cdot T_\mathrm{g}} \tag{A2.1}$$

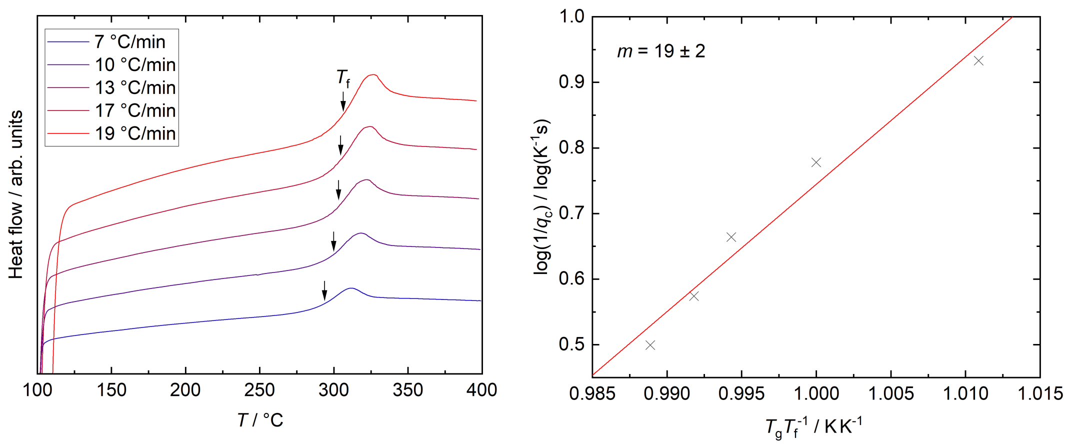

Figure A2.46. Left: Consecutive heating branches with different heating rates in a cyclic DSC experiment of gZIF-62. The black arrows indicate the determined fictive temperatures T_f at the glass transition. Right: Linear regression performed on the data points extracted from the DSC experiments providing the calorimetric fragility index m ($R^2 = 0.97$).

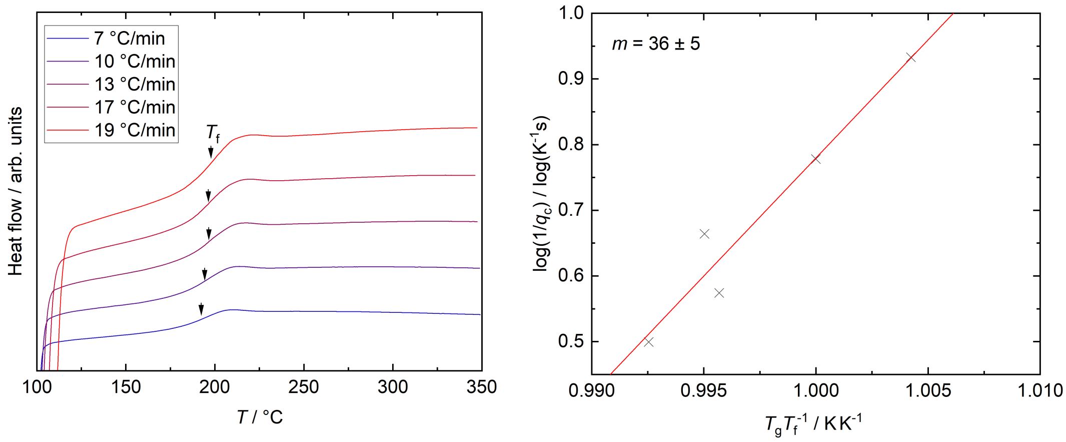

Figure A2.47. Left: Consecutive heating branches with different heating rates in a cyclic DSC experiment of gNaB$_{0.3}$ZIF-62. The black arrows indicate the determined fictive temperatures T_f at the glass transition. Right: Linear regression performed on the data points extracted from the DSC experiments providing the calorimetric fragility index m ($R^2 = 0.94$).

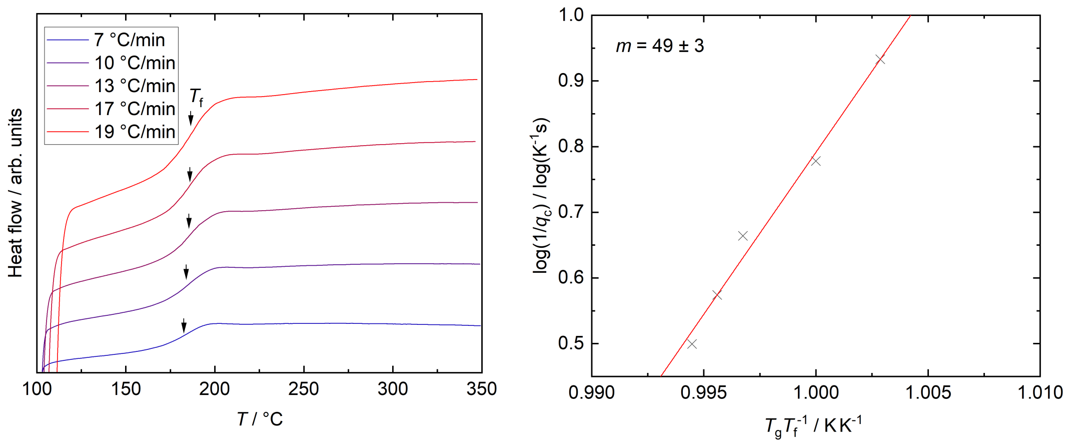

Figure A2.48. Left: Consecutive heating branches with different heating rates in a cyclic DSC experiment of gNaB$_{0.5}$ZIF-62. The black arrows indicate the determined fictive temperatures T_f at the glass transition. Right: Linear regression performed on the data points extracted from the DSC experiments providing the calorimetric fragility index m ($R^2 = 0.96$).

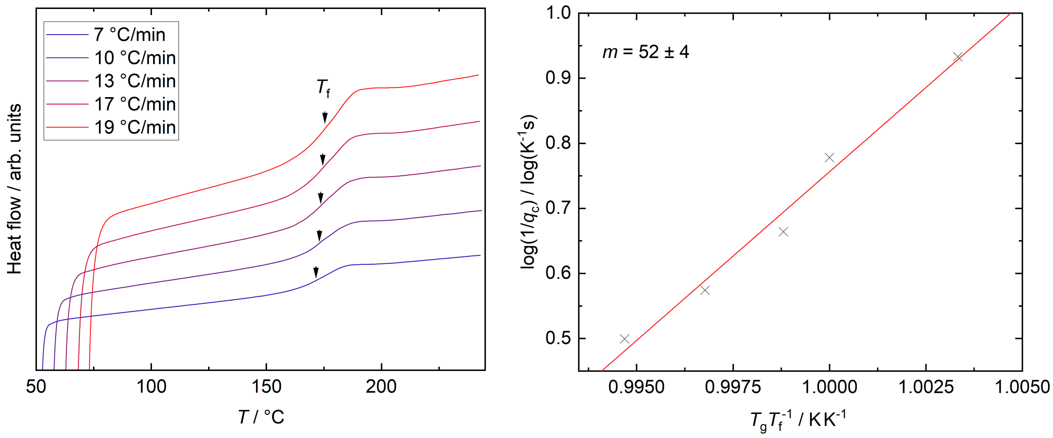

Figure A2.49. Left: Consecutive heating branches with different heating rates in a cyclic DSC experiment of gNaB$_{1.0}$ZIF-62. The black arrows indicate the determined fictive temperatures T_f at the glass transition. Right: Linear regression performed on the data points extracted from the DSC experiments providing the calorimetric fragility index m ($R^2 = 0.98$).

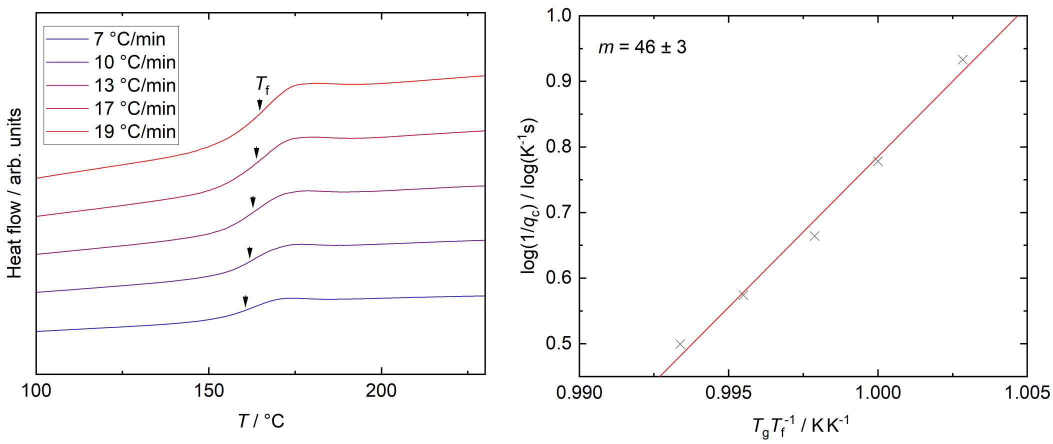

Figure A2.50. Left: Consecutive heating branches with different heating rates in a cyclic DSC experiment of gNaB$_{1.5}$ZIF-62. The black arrows indicate the determined fictive temperatures T_f at the glass transition. Right: Linear regression performed on the data points extracted from the DSC experiments providing the calorimetric fragility index m ($R^2 = 0.99$).

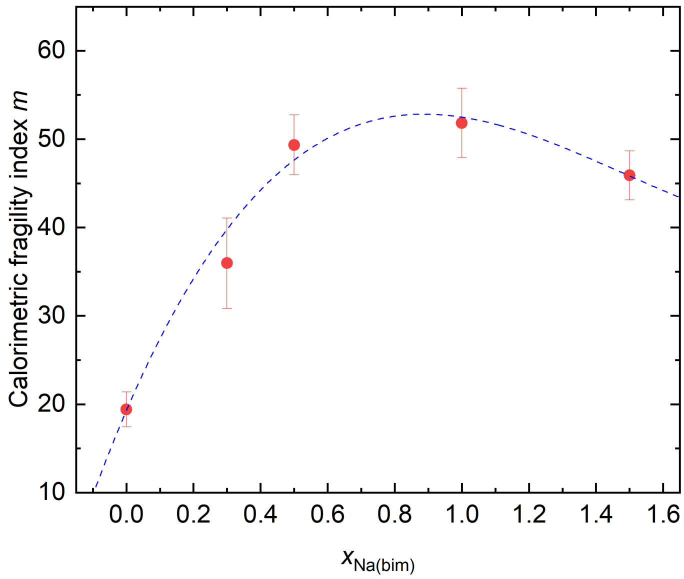

Figure A2.51. Calorimetric fragility index m for different modified ZIF-62 glasses with various amounts of modifier x Na(bim) according to the general chemical formula x Na(bim) $\cdot$ $\mathrm{Zn(im)_{1.8}(bim)_{0.2}}$. The blue dashed line serves as a guide to the eye.

Table A2.6. Calorimetric fragility index m of Na(bim)-modified ZIF-62 glasses with the chemical formula $\mathrm{Zn\,Na_{\mathit{x}}(im)_{1.8}(bim)_{0.2+\mathit{x}}}$, their glass transition temperature T_g and the resulting activation energy of viscous flow E_a at T_g calculated according to Equation A2.1.

x	m	$T_\mathrm{g}/°\mathrm{C}$	$E_\mathrm{a}/\mathrm{kJ\,mol^{-1}}$
0.0	19 ± 2	299.9	213 ± 22
0.3	36 ± 5	194.3	322 ± 46
0.5	49 ± 3	183.9	432 ± 31
1.0	52 ± 4	173.0	443 ± 34
1.5	46 ± 3	161.9	382 ± 24

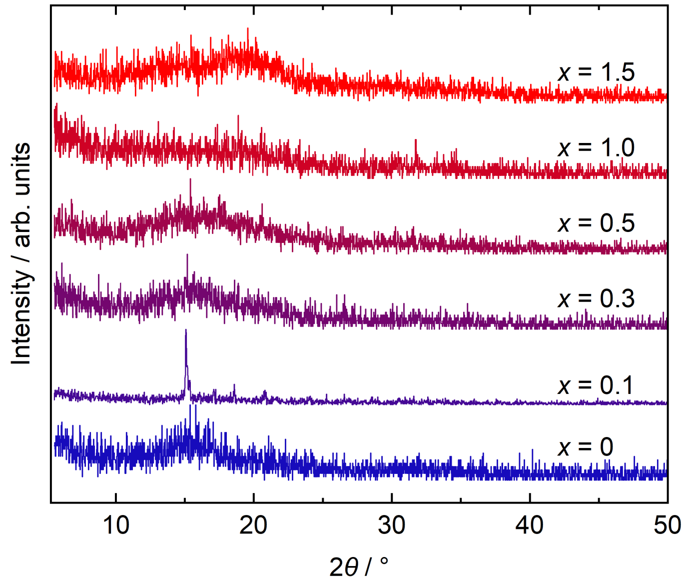

Figure A2.52. PXRD pattern of gNaB$_x$ZIF-62 materials after undergoing the temperature program applied during the calorimetric fragility determination. The measurement was conducted using CuK$_\alpha$ radiation and performed under air. The diffraction patterns show diffuse scattering for all glasses except for gNaB$_{0.1}$ZIF-62. Here, partial recrystallization of ZIF-zni is observed. Thus, the calorimetric fragility index of gNaB$_{0.1}$ZIF-62 could not be determined, as the material experiences partial crystallization to ZIF-zni upon thermal cycling.

A2.11 Heat Capacity Measurements

A2.11.1 Experimental Details

Reversing heat capacity measurements were performed on a DSC25 from TA instruments. The samples were ground thoroughly and placed in a hermetically sealed aluminium crucible under an inert N_2 atmosphere. All experiments were carried out under constant N_2 flow ($50\,\mathrm{mL\,min^{-1}}$) via modulated DSC (MDSC) with a mean heating rate of $2\,^\circ\mathrm{C\,min^{-1}}$, a modulated temperature amplitude of $\pm 1\,^\circ\mathrm{C}$ and a modulation period of 120 s. Baseline and heat capacity calibration were performed with a sapphire standard before the measurement. Data evaluation was carried out in TA instruments TRIOS version 5.1.1.46572.

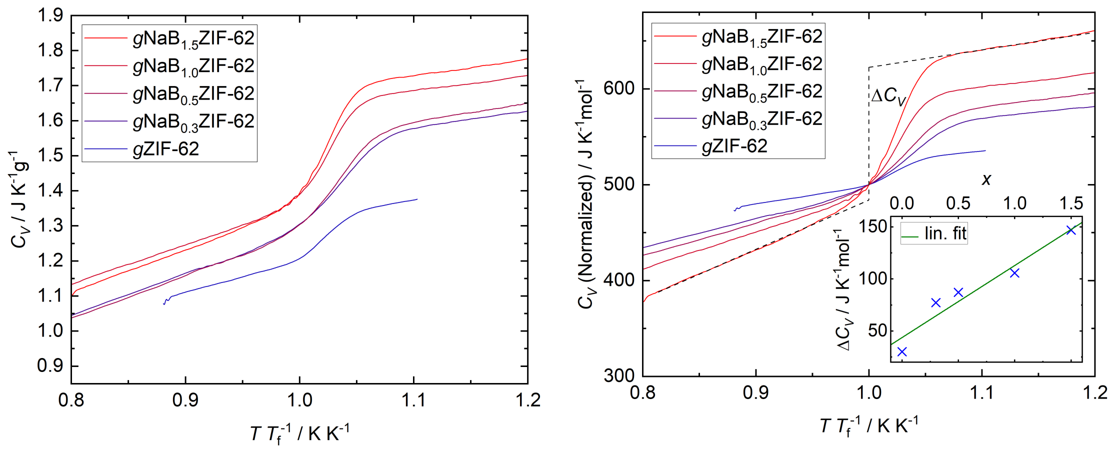

Figure A2.53. Reversing heat capacities C_V of gNaB$_x$ZIF-62 materials with various amounts of modifier x according to the general chemical formula Zn Na$_x$(im)$_{1.8}$(bim)$_{0.2+x}$ defined as molecular unit. Left: Absolut gravimetric reversing heat capacities of gNaB$_x$ZIF-62 materials in the unit J K^{-1} g^{-1}. Right: Molar reversing heat capacities of gNaB$_x$ZIF-62 materials. The offset in molar heat capacity was chosen arbitrarily according to the intersection point ($TT_f^{-1} = 1$) and corrected accordingly. The inset shows the change of the heat capacity ΔC_V at the temperature of the glass transition recorded with a heating rate of 2 °C min^{-1} (T_f) plotted against the modifier content x.

Table A2.7. Reverse heat capacity ΔC_V, at the temperature of the glass transition T_f measured with a heating rate of 2 °C min^{-1} for the modified ZIF-62 glasses with different Na(bim) contents x.

x	ΔC_V/J mol^{-1} K^{-1}	T_f/°C
0.0	30	304.8
0.3	77	174.9
0.5	87	171.1
1.0	106	160.7
1.5	146	154.4

A2.12 X-Ray Pair Distribution Function Analysis

A2.12.1 Experimental Details

Variable temperature *in-situ* X-ray total scattering measurements were performed at Diamond Light Source (DLS), UK, and Deutsches Elektronen Synchrotron (DESY), Germany. At DLS three different physical mixtures with x = 0.5, 1.0, and 1.5 of glass-former ZIF-62 with varying amounts of Na(bim) modifier were investigated under heating to 450 °C and after melt-quenching as well as the pure starting compounds Na(bim) and ZIF-62. For the measurements, the powdered sample material was filled in quartz capillaries (1 mm outer diameter) under an inert Ar atmosphere and sealed with epoxy glue (UHU-Schnellfest). X-rays with a wavelength of 0.1617 Å were used for data collection. Data processing was performed using PDFgetX3. For $NaB_{0.3}$|ZIF-62 *in-situ* variable temperature X-ray total scattering measurements were performed at DESY with a wavelength of 0.2071 Å starting at room temperature with a stepwise increase up to 450 °C as well as after returning to room temperature. The variable temperature measurements were collected using quartz capillaries (1 mm outer diameter). Additionally, a room temperature measurement of finely ground $g$$NaB_{0.3}$ZIF-62 material (prepared in a DSC apparatus via the small-scale approach, see Experimental Section) was conducted using a borosilicate capillary (1 mm outer diameter). Sample preparation, filling of the capillaries, and sealing with UHU Schnellfest was performed under an inert atmosphere (Glovebox). Data processing was performed using DAWN Science Version 2.30.0 and PDFgetX3.

For the differential PDF analysis, only the data collected at DLS (NaB_x|ZIF-62 with x = 0, 0.5, 1.0, 1.5) were included as these data were collected under identical measurement conditions regarding the *in-situ* glass preparation procedure (heating rates, temperature steps, data collection time) as well as the wavelength and the choice of capillaries. The total scattering data were reevaluated using Gudrun (Version 2017), which is expected to provide pair distribution functions with higher accuracy in the low r region than PDFGetX3. In the latter case, the applied polynomial correction leads to artefacts in the extracted $G(r)$ functions at low r.[254] The densities of the physical mixtures and their glasses were calculated based on the respective ratio of the crystallographic densities of the isolated crystalline starting compounds Na(bim) and ZIF-62 (see Table A2.8). The maximum Q-space used in the Fourier transformation was set to $Q_{\max} = 18.5$ Å. Gudrun provides PDF data denoted as the differential correlation function "$D(r)$". These data, which were used for the evaluation presented here, are in accordance with the $G(r)$ functions obtained from PDFgetX3 regarding their physical meaning as defined in Equation 2 with $S(Q)$ as the scattering function with the respective limit of $S(Q \rightarrow \infty) = 1$.[66] For the sake of consistency, the $D(r)$ functions are denoted as $G(r)$ in the following evaluation.

$$G(r) = \frac{2}{\pi} \int_{Q_{\min}}^{Q_{\max}} Q[S(Q) - 1] \sin{(Qr)} \mathrm{d}Q \tag{A2.2}$$

A2.12.2 Variable Temperature *I(Q)* Data

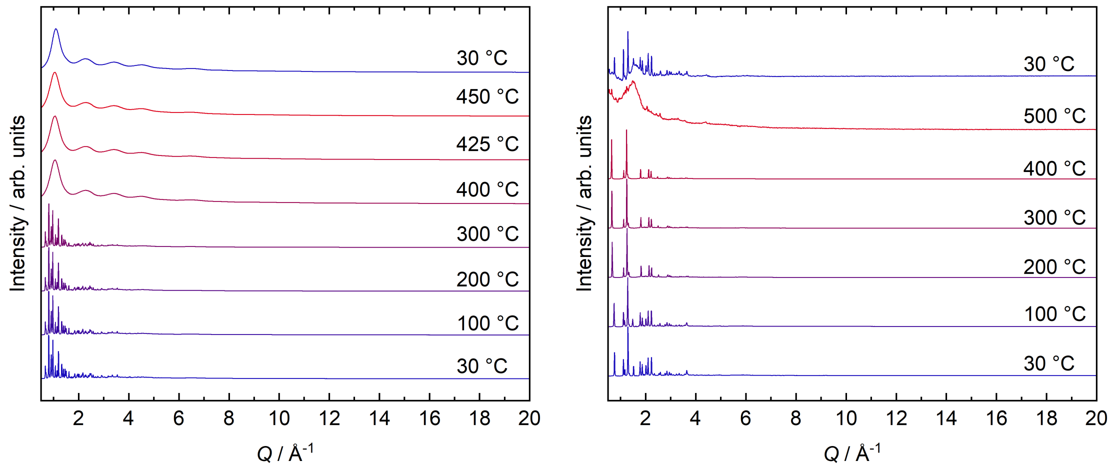

Figure A2.54. Normalized, background-subtracted and scattering-corrected diffraction data collected for PDF analysis of the glass former ZIF-62 (left) and modifier Na(bim) (right) with increasing temperature and after temperature-quenching (top-pattern in blue). Data collection was performed at DLS with a wavelength of 0.1617 Å.

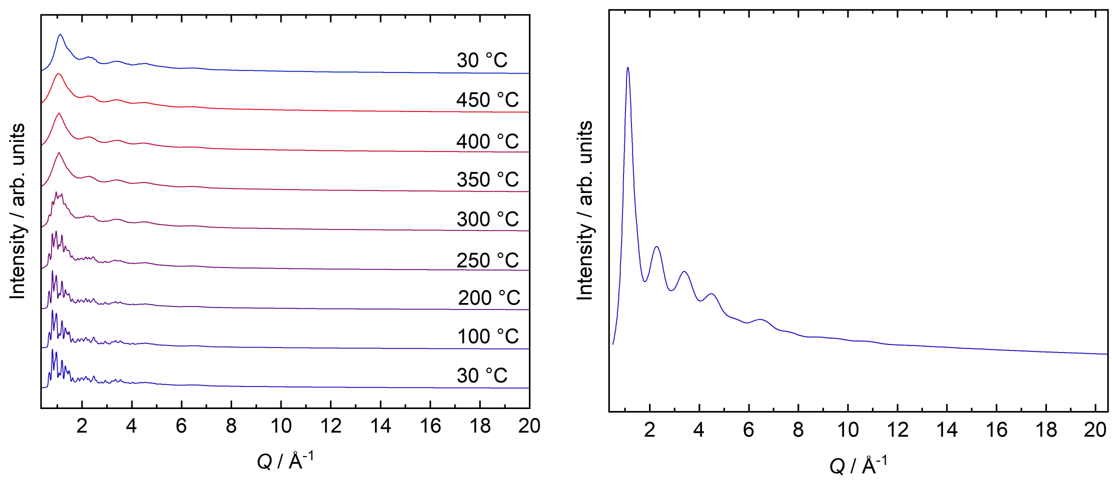

Figure A2.55. Left: Normalized, background-subtracted, and scattering-corrected diffraction data collected for PDF analysis of the physical mixtures NaB$_{0.3}$|ZIF-62 with increasing temperature and after temperature-quenching (top-pattern in blue). Right: Normalized, background-subtracted, and scattering-corrected diffraction data collected for PDF analysis of gNaB$_{0.3}$ZIF-62 prepared *ex-situ*. Data collection was performed at DESY with a wavelength of 0.2077 Å.

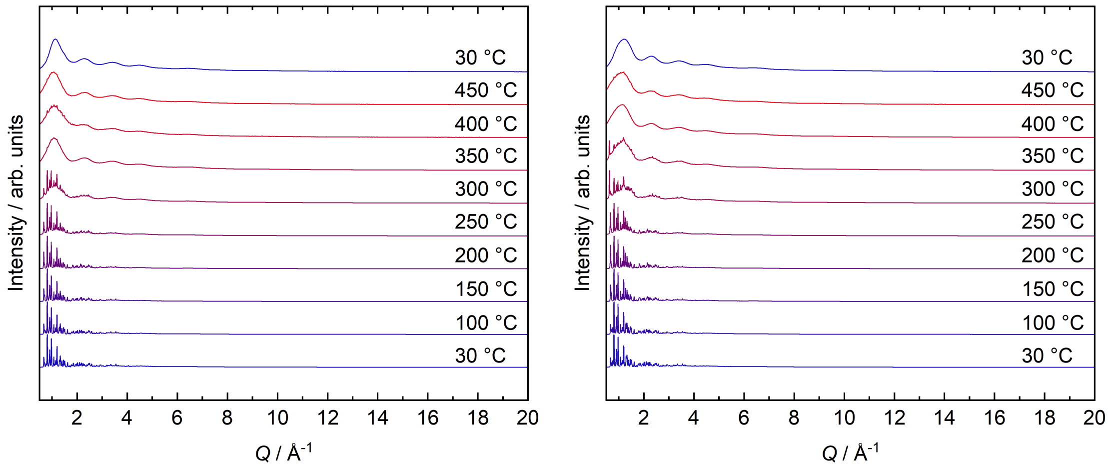

Figure A2.56. Normalized, background-subtracted, and scattering-corrected diffraction data collected for PDF analysis of the physical mixtures NaB_x|ZIF-62 with $x = 0.5$ (left), 1.0 (right) with increasing temperature and after temperature-quenching (top-pattern in blue). Data collection was performed at DLS with a wavelength of 0.1617 Å.

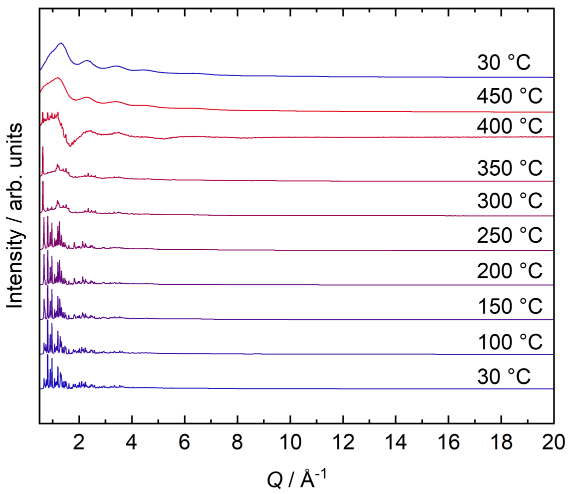

Figure A2.57. Normalized, background-subtracted, and scattering-corrected diffraction data collected for PDF analysis of the physical mixtures NaB_x|ZIF-62 with $x = 1.5$ with increasing temperature and after temperature-quenching (top-pattern in blue). Data collection was performed at DLS with a wavelength of 0.1617 Å. The overall low intensity in the pattern collected at 400 °C is the result of the liquid material moving out of the beam path.

A2.12.3 Variable Temperature *S(Q)* Data

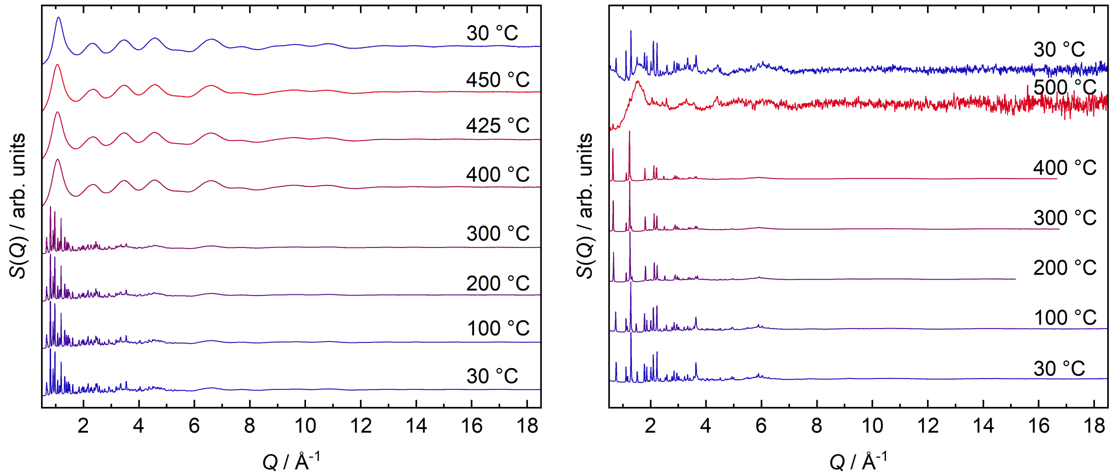

Figure A2.58. Structure function $S(Q)$ extracted from X-ray total scattering data for the glass former ZIF-62 (left) and Na(bim) (right) with increasing temperature and after temperature-quenching (top-pattern in blue). Data collection was performed at DLS with a wavelength of 0.1617 Å. The overall low intensity in the pattern of Na(bim) (right) collected at 500 °C is the result of the liquid material moving out of the beam path.

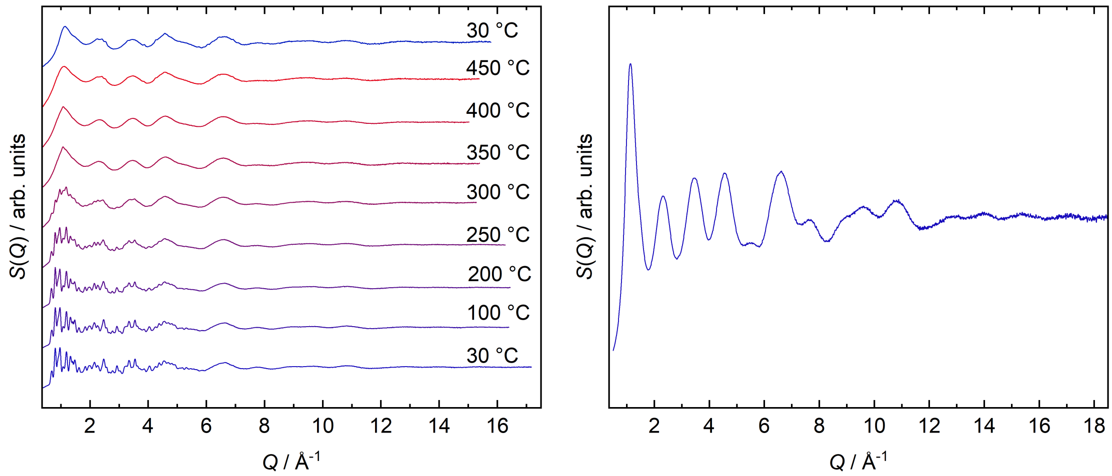

Figure A2.59. Right: Structure function $S(Q)$ extracted from X-ray total scattering data of $NaB_{0.3}$|ZIF-62 with increasing temperature and after temperature-quenching (top-pattern in blue). Left: Structure function $S(Q)$ extracted from X-ray total scattering data of $g$$NaB_{0.3}$ZIF-62 prepared *ex-situ*. Data collection was performed at DESY with a wavelength of 0.2077 Å.

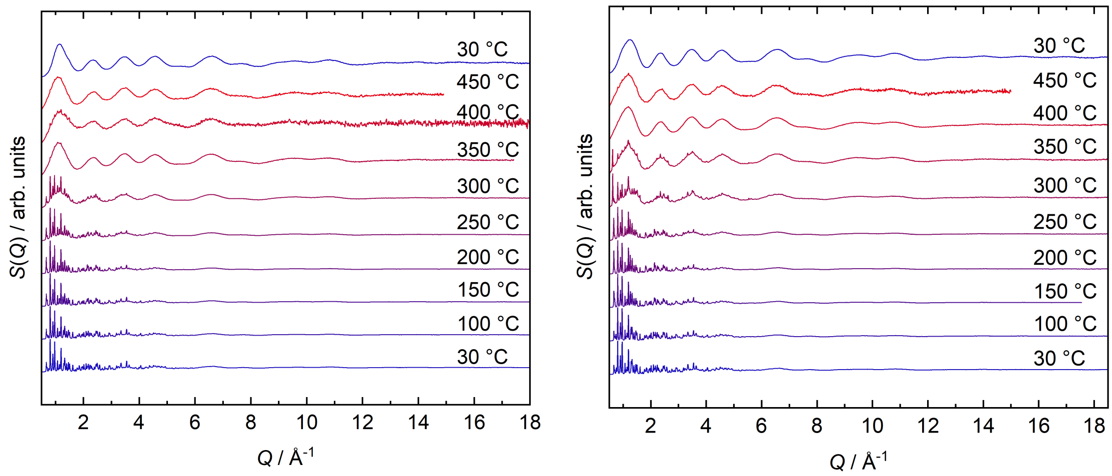

Figure A2.60. Structure function S(Q) extracted from X-ray total scattering data for the physical mixtures NaB_x|ZIF-62 with $x = 0.5$ (left), 1.0 (right) with increasing temperature and after temperature-quenching (top-pattern in blue). Data collection was performed at DLS with a wavelength of 0.1617 Å. The overall low intensity and high noise level in the pattern of $NaB_{0.5}$|ZIF-62 (left) collected at 400 °C is the result of the liquid material moving out of the beam path.

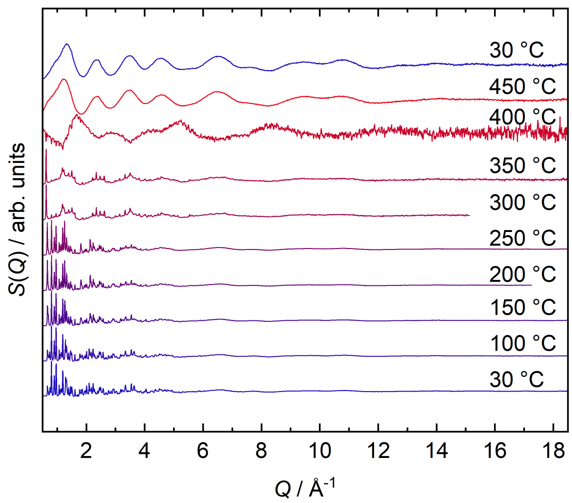

Figure A2.61. Structure function $S(Q)$ extracted from X-ray total scattering data for the physical mixture NaB_x|ZIF-62 with $x = 1.5$ with increasing temperature and after temperature-quenching (top-pattern in blue). Data collection was performed at DLS with a wavelength of 0.1617 Å. The overall low intensity and high noise level in the pattern collected at 400 °C is the result of the liquid material moving out of the beam path.

A2.12.4 Variable Temperature *G(r)* Data

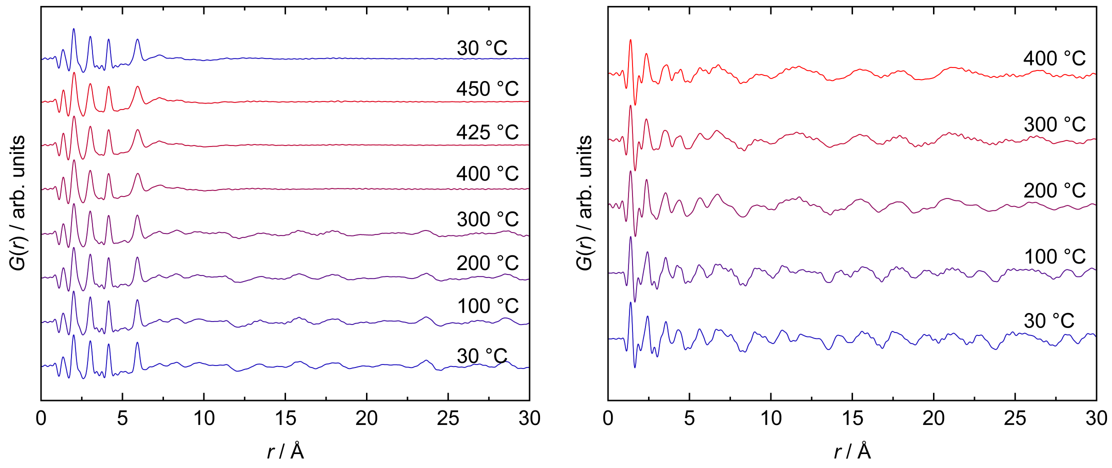

Figure A2.62. *In-situ* PDF data in the form of $G(r)$ of the glass former ZIF-62 (left) and Na(bim) (right) with increasing temperature and after temperature-quenching (top-pattern in blue). Data collection was performed at DLS with a wavelength of 0.1617 Å.

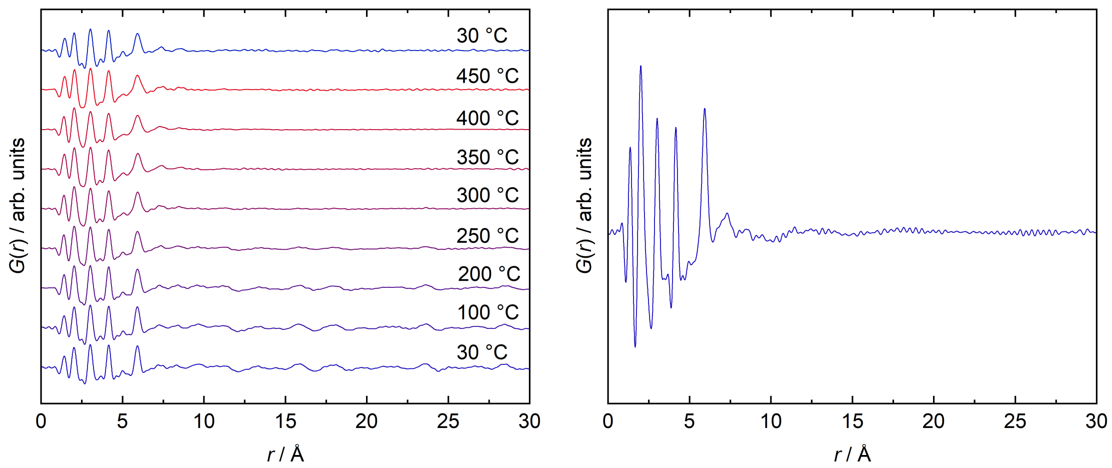

Figure A2.63. Left: *In-situ* PDF data in the form of G(r) of the physical mixture $NaB_{0.3}$|ZIF-62 with increasing temperature and after temperature-quenching (top-pattern in blue). Right: PDF data in the form of $G(r)$ of $g$$NaB_{0.3}$ZIF-62 prepared *ex-situ*. Data collection was performed at DESY with a wavelength of 0.2077 Å.

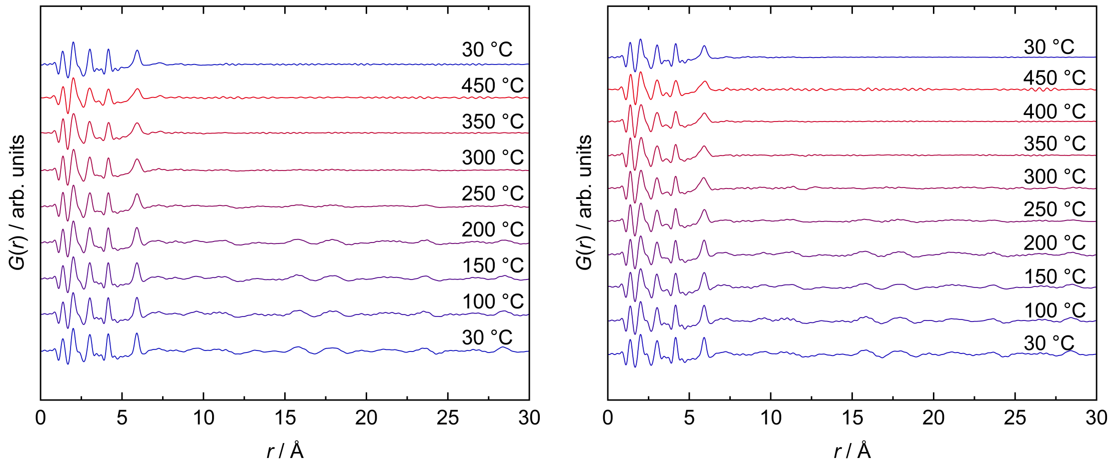

Figure A2.64. *In-situ* PDF data in the form of $G(r)$ of the physical mixtures NaB_x|ZIF-62 with $x = 0.5$ (left), 1.0 (right) with increasing temperature and after temperature-quenching (top-pattern in blue). Data collection was performed at DLS with a wavelength of 0.1617 Å.

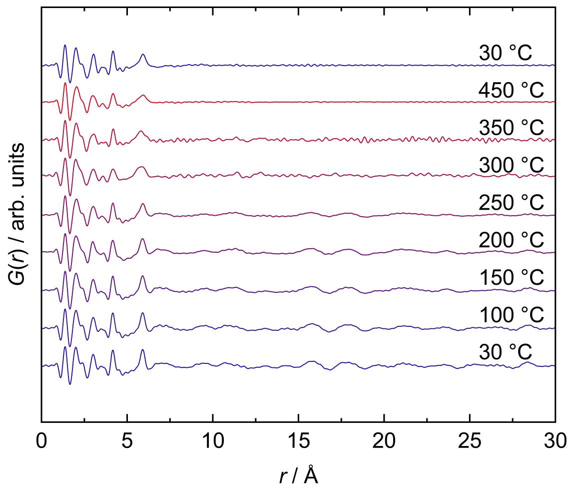

Figure A2.65. *In-situ* PDF data in the form of $G(r)$ of the physical mixtures NaB_x|ZIF-62 with $x = 1.5$ with increasing temperature and after temperature-quenching (top-pattern in blue). Data collection was performed at DLS with a wavelength of 0.1617 Å

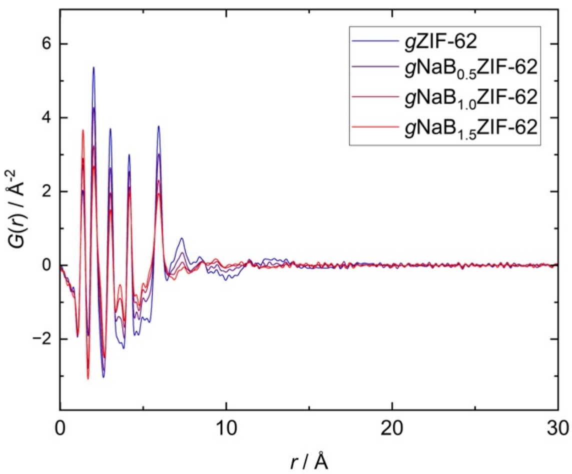

Figure A2.66. PDF data in the form of $G(r)$ of the modified glasses gNaB$_x$ZIF-62 collected at room temperature proving the absence of long-range order for the modified glasses. Data collection was performed at DLS with a wavelength of 0.1617 Å.

A2.12.5 First Sharp Diffraction Peak Analysis

A closer look at the FSDP provides more information about the MRO of the modified glass.[81,96,177,277] An accepted theory by ELLIOTT describes the FSDP's origin as a consequence of the periodicity of boundaries of small voids, which are homogenously distributed throughout the material.[176] As shown in Figure A2.68, the intensity of the total scattering structure functions $S(Q)$ decreases with increasing amount of modifier incorporated. Within the void model, this intensity decrease can be explained by a loss of contrast in electron density as former voids are successively occupied by the modifier. A similar behavior was observed for sodium-ion-modified silicate glasses investigated by neutron scattering.[176,278] The shift of the FSDP's maximum from 1.10 Å^{-1} to 1.33 Å^{-1} with an increase in modifier content is associated with the densification of the material, while the broadening of the FSDP corresponds to a loss of real-space correlation length ($L = 2\pi/\Delta Q$). Hence, the incorporation of the modifier seems to reduce the MRO of the glass while increasing the density and reducing the porosity of the glassy material.

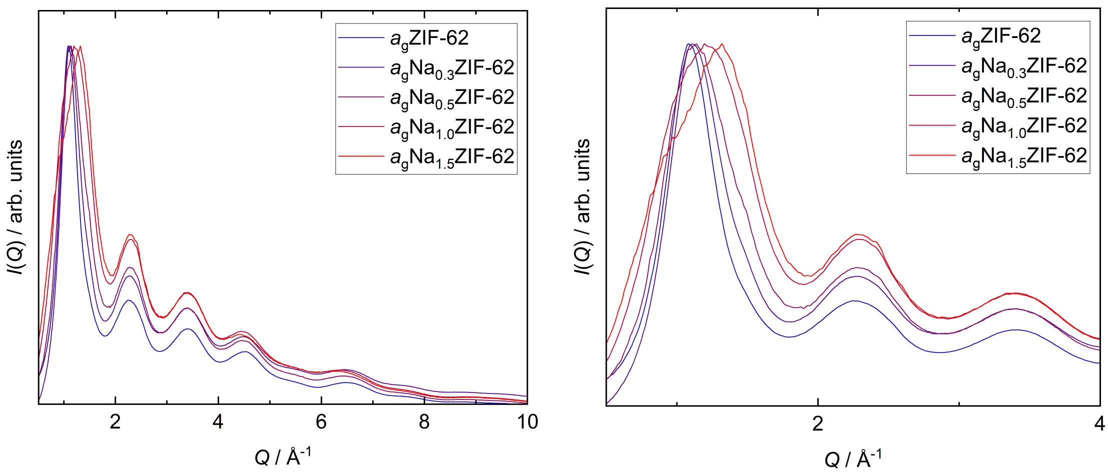

Figure A2.67. Normalized, background-subtracted and scattering-corrected diffraction data collected for PDF analysis of gNaB$_x$ZIF-62 materials for $x = 0$ (gZIF-62), 0.3, 0.5, 1.0 and 1.5 (left) and zoom into the low-Q region displaying the systematic shift in the FSDP with increasing modifier content x (right).

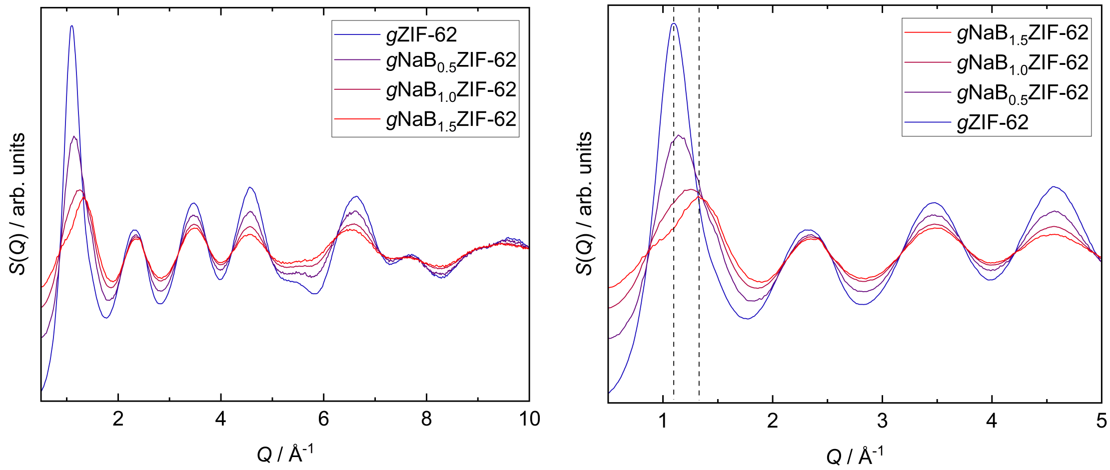

Figure A2.68. Total scattering structure functions $S(Q)$ of gNaB$_x$ZIF-62 materials for $x = 0$ (gZIF-62), 0.5, 1.0, 1.5 with a zoom into the low-Q region displaying the shift in the FSDP and the loss of its intensity with increasing modifier contents x.

A2.12.6 Differential PDF Analysis

Table A2.8. Mean crystallographic densities ρ_{m} and number densities ρ_0 of NaB_x|ZIF-62 materials calculated from the densities of the crystalline compounds ZIF-62 and Na(bim). The calculated densities were used in the processing of the PDF data of NaB_x|ZIF-62 and $g\mathrm{NaB}_x$ZIF-62 materials.

Material	$\rho_{\mathrm{m}}/\mathrm{g\,cm^{-3}}$	$\rho_0/\mathrm{Å}^{-3}$
ZIF-62	1.297	0.068
$\mathrm{NaB}_{0.5}$|ZIF-62	1.322	0.073
$\mathrm{NaB}_{1.0}$|ZIF-62	1.338	0.076
$\mathrm{NaB}_{1.5}$|ZIF-62	1.350	0.079
Na(bim)	1.408	0.091

Firstly, the functions $G(r)$ were transformed to the radial distribution function (RDF) $R(r)$ via:

$$R(r) = r(G(r) + 4\pi r \rho_0) \tag{A2.3}$$

The RDFs of the physical mixtures were fitted with a linear combination of the RDFs of the pure compounds Na(bim) and ZIF-62, assuming that the contribution of the RDF of the particle's interface in the physical mixtures can be neglected. This approach is similar to differential PDF analysis and closely related to principal component analysis (PCA) as described in the literature.[178,279]

$$\frac{1}{r} R_{\mathrm{LC}} = \frac{1}{r}(c_1 \cdot R_{\mathrm{ZIF-62}}(r) + c_2 \cdot R_{\mathrm{Na(bim)}}(r)) \tag{A2.4}$$

With c_1 and c_2 being the coefficients representing the intensity contribution of the RDFs of the pure compounds to the RDF of their physical mixtures.

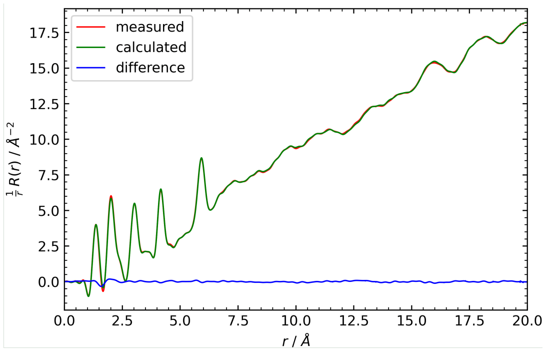

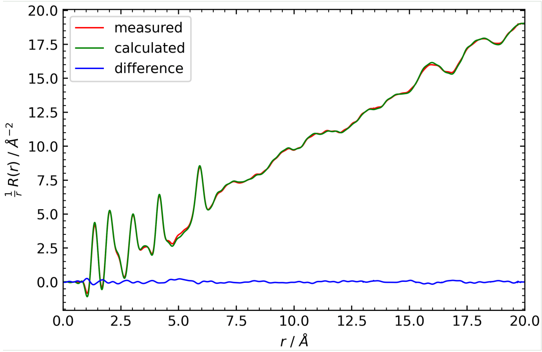

Figure A2.69. RDFs of the physical mixtures NaB_x|ZIF-62 (measured) with $x = 0.5$ (left) and 1.0 (right), fitted with the linear combination function $R_{LC}(r)/r$ (calculated) and the difference between both with $R^2 = 0.999$ (left) and $R^2 = 0.999$ (right). The refined linear combination parameters are shown in Table A2.9.

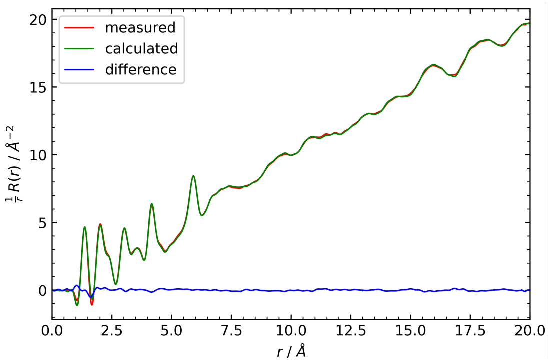

Figure A2.70. RDFs of the physical mixtures NaB_x|ZIF-62 (measured) with $x = 1.5$ fitted with the linear combination function $R_{LC}(r)/r$ (calculated) and the difference between both with $R^2 = 0.999$. The refined linear combination parameters are shown in Table A2.9.

The difference curves for all linear combination fits (Figures A2.69 and A2.70) appear featureless and show excellent agreement between the $R(r)$ of the physical mixtures and $R_{LC}(r)$. Therefore, it can be concluded that the contribution of the particle interfaces to the RDFs and PDF can be neglected. The obtained linear combination coefficients c_1 and c_2 for the construction of the $R_{LC}(r)$ functions obtained as the result of these fits are summarized in Table A2.9.

Table A2.9. Linear combination coefficients c_1 and c_2 of the linear combination function $R_{LC}(r)$ for different physical mixtures with varying ratios of glass former (ZIF-62) and -modifier (Na(bim)) together with the coefficient of determination (R^2) provided by the fits shown in Figures A2.69 and A2.70.

Material	c_1(ZIF-62)	c_2(Na(bim))	R^2
$NaB_{0.5}$|ZIF-62	0.798 ± 0.001	0.208 ± 0.001	0.999
$NaB_{1.0}$|ZIF-62	0.708 ± 0.001	0.312 ± 0.001	0.999
$NaB_{1.5}$|ZIF-62	0.634 ± 0.001	0.395 ± 0.001	0.999

A closer look at the $G(r)$ functions of the isolated starting compounds reveals that the signal associated with next-neighbor Zn$\cdots$Zn correlations in ZIF-62 ($r = 5.9$ Å) are located at the same distance where the PDF of Na(bim) has a value close to zero (see Figure A2.71, left). Consequently, the PDF of Na(bim) does not contribute to the intensity of the physical mixture's $G(r)$ at $r = 5.9$ Å. In the $G(r)$ functions of the physical mixtures, the same signal decreases in intensity upon the addition of Na(bim) (see Figure A2.71, right). This is explained by the decreasing density of next-neighbor Zn$\cdots$Zn correlations as a result of the successive dilution of ZIF-62 upon the addition of Na(bim).

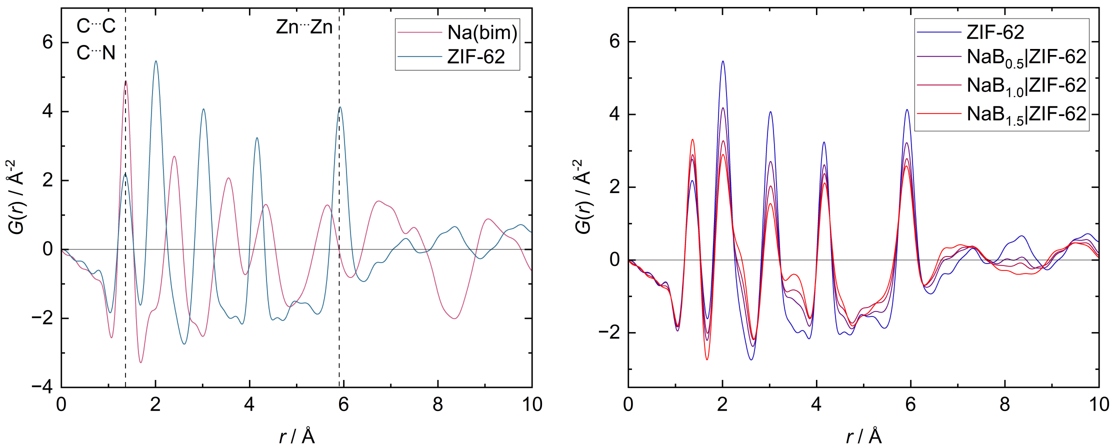

Figure A2.71. PDFs in the form of $G(r)$ for Na(bim) and ZIF-62 (left) as well as for different physical mixtures (right). The dashed lines mark the allocation of next-neighbor C$\cdots$C/C$\cdots$N and Zn$\cdots$Zn correlations.

Next, the signal at 5.9 Å was chosen for rescaling the $G(r)$ functions of the physical mixtures to the intensity found for pure ZIF-62. This step is performed to achieve a renormalization of the physical mixture's $G(r)$ functions to the next-neighbor Zn$\cdots$Zn correlation density of ZIF-62. This normalization is essentially a normalization to a molar unit of $ZnNa_x(im)_{1.8}(bim)_{0.2+x}$. Hence, the scaling factors derived from the respective maxima of the physical mixture's $G(r)$ functions (at 5.9 Å) are in good accordance with the scaling factors calculated from c_1 (c_1^{-1}) in the LC-fitting approach discussed above (see

Table A2.9 and Table A2.10). In the following, all rescaled $G(r)$ functions are denoted as $G^*(r)$. In the $G^*(r)$ functions of the physical mixtures, the intensity of the signal at 5.9 Å remains the same throughout all physical mixtures, whereas the intensity of the signal at 1.37 Å increases with x (see Figure 4 in the main manuscript). This signal, corresponding to next-neighbor C$\cdots$C and C$\cdots$N correlations, increases with x due to the growing number of those correlations per molar unit ($ZnNa_x(im)_{1.8}(bim)_{0.2+x}$).

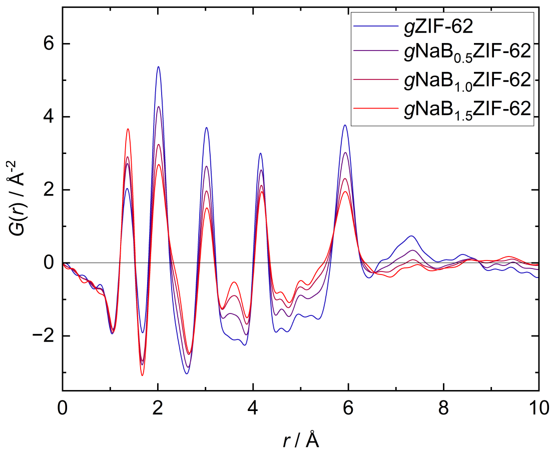

Figure A2.72. $G(r)$ functions of the modified glasses gNaB$_x$|ZIF-62 showing the increase of C$\cdots$C/C$\cdots$N correlation density (signal at 1.4 Å) and decreasing Zn$\cdots$Zn correlation density (signal at 5.9 Å) with growing amount of Na(bim) incorporation.

Upon glass formation, the organic (benz)imidazolate linkers remain intact as proven by solution ^{1}H NMR spectroscopic measurements (see Section S7). Hence, the signal reflecting the number of C$\cdots$C/C$\cdots$N correlations should remain largely unaltered during vitrification. Rescaling the $G(r)$ functions of the glasses according to the maximum intensity of this signal found in the physical mixture's $G^*(r)$ function (first signal at ~1.37 Å) provides $G^*(r)$ functions for the corresponding glasses (see Figure 6.4).

Table A2.10. Scaling factors c for different physical mixtures and their corresponding glasses. The scaling factors were obtained from the linear combination fitting approach ($c_{\mathrm{LC}} = c - 1\check{}^{1}$) and by comparing the maximum intensity of the signal at 5.9 Å (Zn$\cdots$Zn) in the $G(r)$ function of the physical mixtures with the intensity of ZIF-62 ($c_{\mathrm{Zn\cdots Zn}}$). $c_{\mathrm{C\cdots C}}$ refers to the scaling factor of a glass' to the respective physical mixture's $G(r)$ function and is based on the relative maximum intensities of the first signal at 1.4 Å (C$\cdots$C/C$\cdots$N). The far-right column contains the product of the two scaling factors applied to the glasses' $G(r)$ functions to obtain $G^{*}(r)$.

x	c_{LC}	$c_{\mathrm{Zn\cdots Zn}}$	$c_{\mathrm{C\cdots C}}$	$c_{\mathrm{Zn\cdots Zn}} \cdot c_{\mathrm{C\cdots C}}$
0.0	1.000	1.000	1.073	1.073
0.5	1.253	1.268	1.017	1.290
1.0	1.412	1.471	1.004	1.478
1.5	1.577	1.573	0.905	1.424

To further evaluate the change in the abundance of correlations in the $G^{*}(r)$ functions during glass formation, the difference between the $G^{*}(r)$ functions of the physical mixtures and the vitreous counterpart was calculated for the varying chemical compositions. These $\Delta G^{*}(r)$ functions ($\Delta G^{*}(r) = G^{*}_{\mathrm{glass}}(r) - G^{*}_{\mathrm{physical\ mixture}}(r)$) monitor the change in the atomic pair distribution occurring upon the transformation of the crystalline physical mixture to the sodium-modified ZIF glass (see Figure 6.4).

A2.12.7 Discussion of $\Delta G^*(r)$ approach

The $\Delta G^*(r)$ functions show a loss in signal intensity for the correlation at 5.9 Å assigned to an increasing loss of next-neighbor Zn$\cdots$Zn pair correlations with increasing modifier content (see Figure 6.4). The $\Delta G^*(r)$ functions further display an increased population of distances around 4.5 – 5.5 Å and a further decrease in population in the region around 6.5 – 7.5 Å with the growing amount of modifier incorporated in the vitrification process. Nonetheless, interpreting these changes is challenging due to the rather high noise level in the $\Delta G^*(r)$. Further, it must be noted that for the calculation of the $\Delta G^*(r)$ functions and the necessary scaling of the $G(r)$ functions, the approximation of a suitable baseline is crucial. The baseline $f(r)$ of the $G(r)$ function depends on the average number density ρ_0 of the materials (in the chosen normalization) and can be described via the linear Equation A2.5:[65]

$$f(r) = -4\pi r \rho_0 \tag{A2.5}$$

For the PDF evaluation, the number density ρ_0 of the physical mixtures was calculated as the mean number density of ZIF-62 and Na(bim) weighted by their respective ratio (see Table A2.8). The subsequent upscaling of the physical mixture's $G(r)$ functions to $G^*(r)$ (with scaling factors > 0, see Table A2.10) formally increases the number density ρ_0^* (with $f^*(r) = \breve{}4\pi r \rho_0$, for the baseline of $G^*(r)$) to a value where the physical mixture's number density reflects the same Zn$\cdots$Zn pair correlation density as for pure ZIF-62. As a consequence, the signal reflecting Zn...Zn pair correlations (at 5.9 Å) remain of the same maximum intensity in the physical mixture's $G^*(r)$ functions. For the evaluation of the glasses' PDFs, the same number densities ρ_0 were applied as for the physical mixtures. The scaling factors for the calculation of $G^*(r)$ for the modified glasses are very similar to the scaling factors used in the physical mixtures $G^*(r)$ (see Table A2.10). The trend of an increasing density of the gNaB$_x$ZIF-62 materials with x, which is reflected in the calculated ρ_0 (and ρ_0^*) values, is also monitored by the growing shift of the FSDP in $S(Q)$ with x (see Section A2.12.5). However, it is known that the density of gZIF-62 is slightly higher than for the crystalline parent framework.[96] This densification is not taken into account in the evaluation presented here due to the lack of exact density values for the gNaB$_x$ZIF-62 materials. Nonetheless, the densification during glass formation will lead to a slightly steeper falling baseline than anticipated, which will influence the signal intensities used for scaling and, therefore, the resulting $\Delta G^*(r)$ function. However, due to the anticipated higher densities of gNaB$_x$ZIF-62 materials compared to the corresponding physical mixtures, the observed trends in the $\Delta G^*(r)$ functions with varying x are expected to remain unchanged or become even more pronounced even though the real densities of the glasses cannot be applied, as they are unknown.

A2.13 Extended X-Ray Absorption Fine Structure Analysis

A2.13.1 Experimental Details

EXAFS measurements were conducted at BL10 at Dortmund Electron Accelerator (DELTA) from 9.5 keV to 10.5 keV in transmission mode to cover the energy of the Zn K absorption edge. The material was mixed and thoroughly ground with various amounts of hexagonal boron nitride (BN) to reach a dilution of ca. 50 – 80% (w/w). The prepared material was then filled in Kapton capillaries (1 mm inner diameter), and the capillaries were sealed using epoxy glue under an inert (Ar) atmosphere in a glovebox. The calibration of the energy at the Zn K edge was performed using Zn powder diluted to 90% with BN. XAFS data analysis was performed in the ATHENA module of the Demeter software packages.[280] The EXAFS spectra were obtained by subtracting the post-edge background from the overall absorption, followed by normalization of the data with respect to the edge-jump step. Subsequently, the $\chi(k)$ data were Fourier transformed into real (R) space to separate the EXAFS contributions from different coordination shells. To obtain the quantitative structural parameters surrounding Zn atoms, least-squares curve fitting was performed using the ARTEMIS module of the Demeter software package. The following EXAFS equation was used:

$$\chi(k) = \sum_j \frac{N_j S_0^2 F_j(k)}{kR_j^2} \cdot \exp\left[-2k^2\sigma_j^2\right] \cdot \exp\left(\frac{-2R_j}{\lambda(k)}\right) \cdot \sin\left[2kR_j + \phi_j(k)\right] \tag{A2.6}$$

where S_0^2 is the amplitude reduction factor, $F_j(k)$ is the effective curved-wave backscattering amplitude, N_j is the number of neighbors in the j-th atomic shell, R_j is the distance between the X-ray absorbing central atom and the atoms in the j^{th} atomic shell (back scatterer), λ is the mean free path in Å, $\phi_j(k)$ is the phase shift (including the phase shift for each shell and the total central atom phase shift), σ_j is the Debye-Waller parameter of the j^{th} atomic shell (variation of distances around the average R_j). The amplitude reduction factor S_0^2 was determined to be 0.91 by fitting the Zn–N coordination in crystalline ZIF-62, where the coordination number is known to be 4. This fixed value of S_0^2 was subsequently applied to all other samples to extract the Zn−N coordination number and real Zn−N bond length (see Table A2.11).

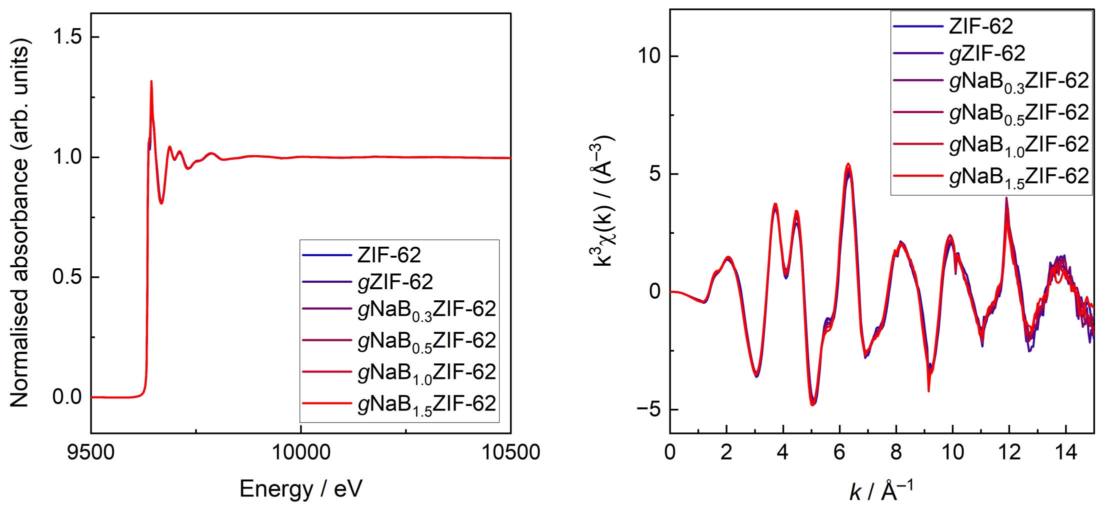

Figure A2.73. Left: Normalized X-ray absorption spectra of ZIF-62, gZIF-62 and the modified glasses gNaB$_x$ZIF-62. Right: EXAFS signal in the form of $k^3\chi(k)$ plotted against the wavenumber k.

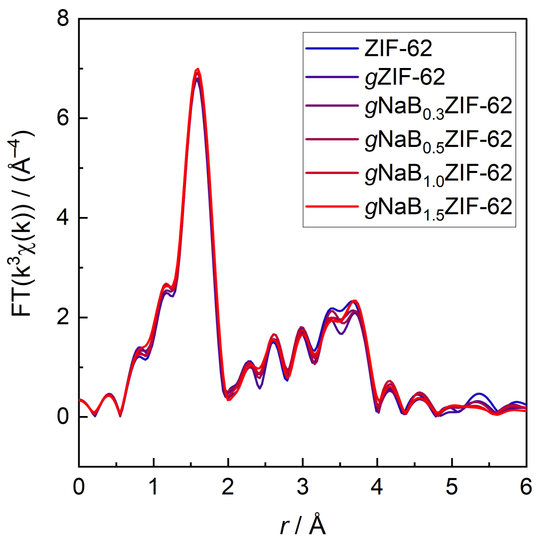

Figure A2.74. Left: Fourier-transform of the EXAFS signal plotted against the real-space distance r for ZIF-62, gZIF-62 and the modified glasses gNaB$_x$ZIF-62.

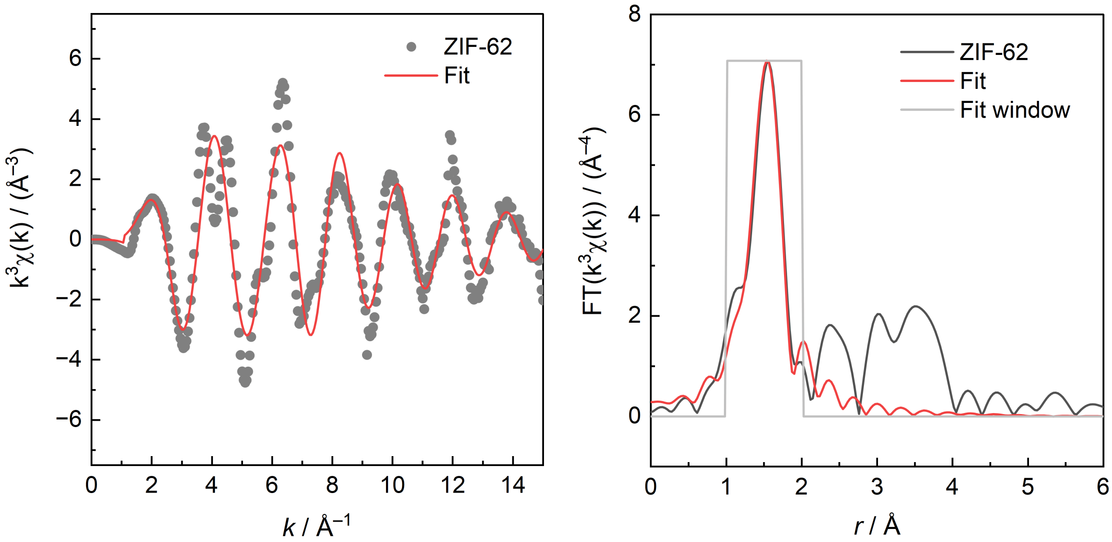

Figure A2.75. Left: Fit to the EXAFS signal in the form of $k^3\chi(k)$ according to Equation A2.6 for ZIF-62. Right: Fourier transform of the EXAFS signal for ZIF-62 plotted against the real-space distance r with the corresponding Fourier transform of the fit shown left. The fitted range covers the interatomic distances of the first coordination shell of Zn^{2+} (i.e., [ZnN_4] units) in the investigated material. The refined parameters of the fitted function are summarized in Table A2.11.

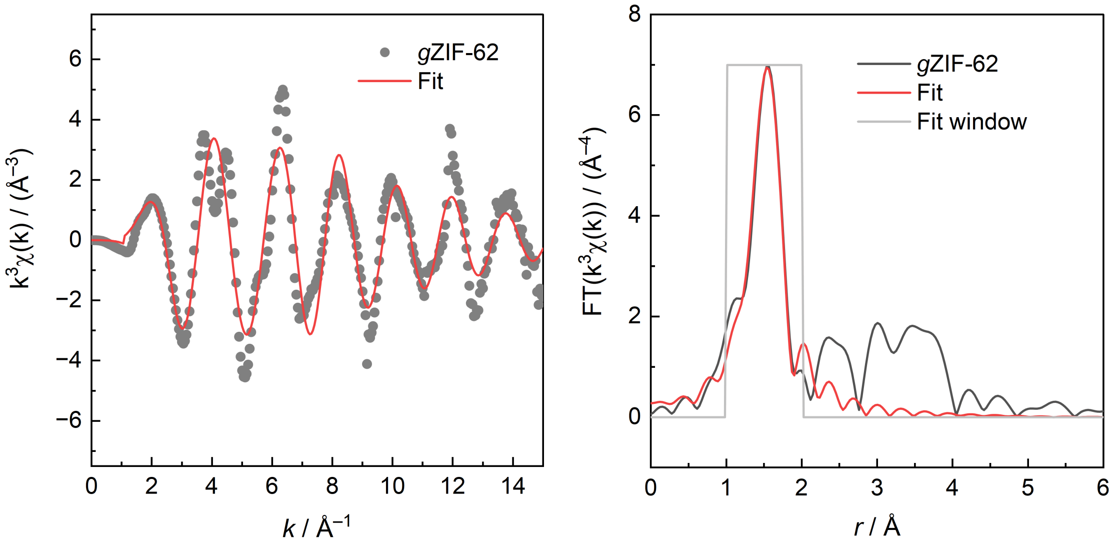

Figure A2.76. Left: Fit to the EXAFS signal in the form of $k^3\chi(k)$ according to Equation A2.6 for *g*ZIF-62. Right: Fourier transform of the EXAFS signal for *g*ZIF-62 plotted against the real-space distance r with the corresponding Fourier transform of the fit shown left. The fitted range covers the interatomic distances of the first coordination shell of Zn^{2+} (i.e., [ZnN_4] units) in the investigated material. The refined parameters of the fitted function are summarized in Table A2.11.

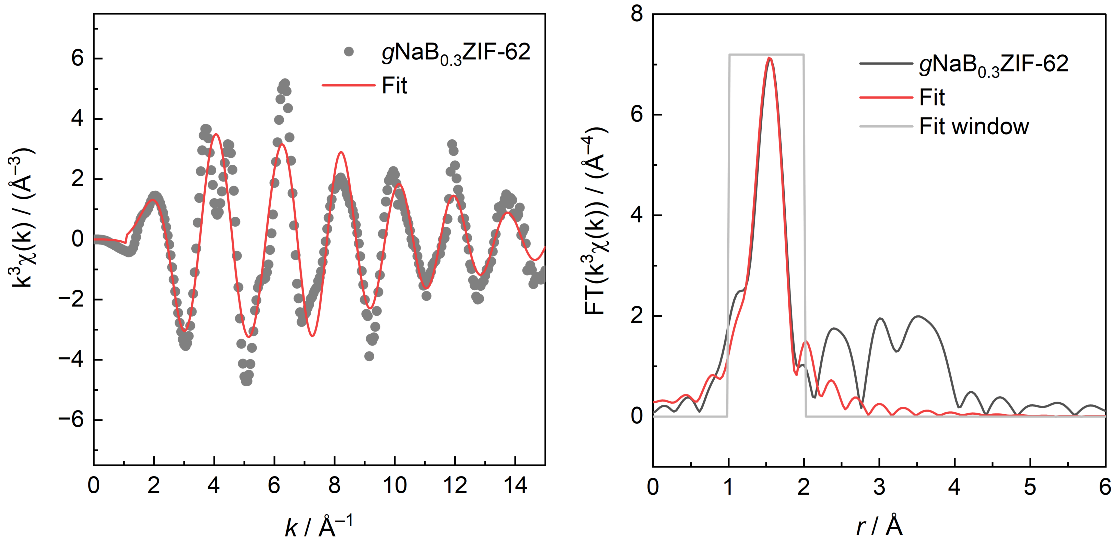

Figure A2.77. Left: Fit to the EXAFS signal in the form of $k^3\chi(k)$ according to Equation A2.6 for gNaB$_{0.3}$ZIF-62. Right: Fourier transform of the EXAFS signal for gNaB$_{0.3}$ZIF-62 plotted against the real-space distance r with the corresponding Fourier transform of the fit shown left. The fitted range covers the interatomic distances of the first coordination shell of Zn^{2+} (i.e., $[ZnN_4]$ units) in the investigated material. The refined parameters of the fitted function are summarized in Table A2.11.

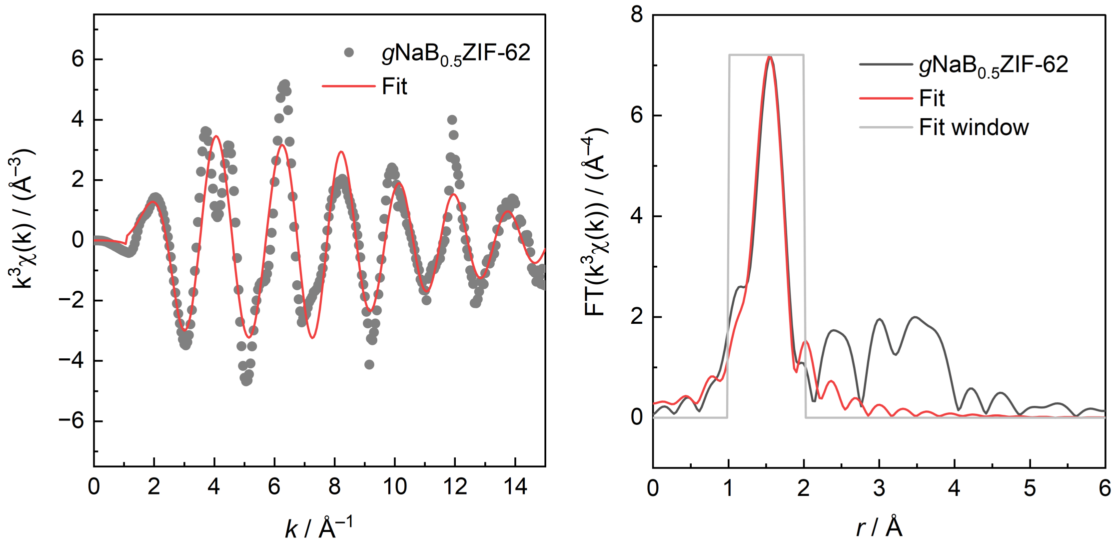

Figure A2.78. Left: Fit to the EXAFS signal in the form of $k^3\chi(k)$ according to Equation A2.6 for gNaB$_{0.5}$ZIF-62. Right: Fourier transform of the EXAFS signal for gNaB$_{0.5}$ZIF-62 plotted against the real-space distance r with the corresponding Fourier transform of the fit shown left. The fitted range covers the interatomic distances of the first coordination shell of Zn^{2+} (i.e., $[ZnN_4]$ units) in the investigated material. The refined parameters of the fitted function are summarized in Table A2.11.

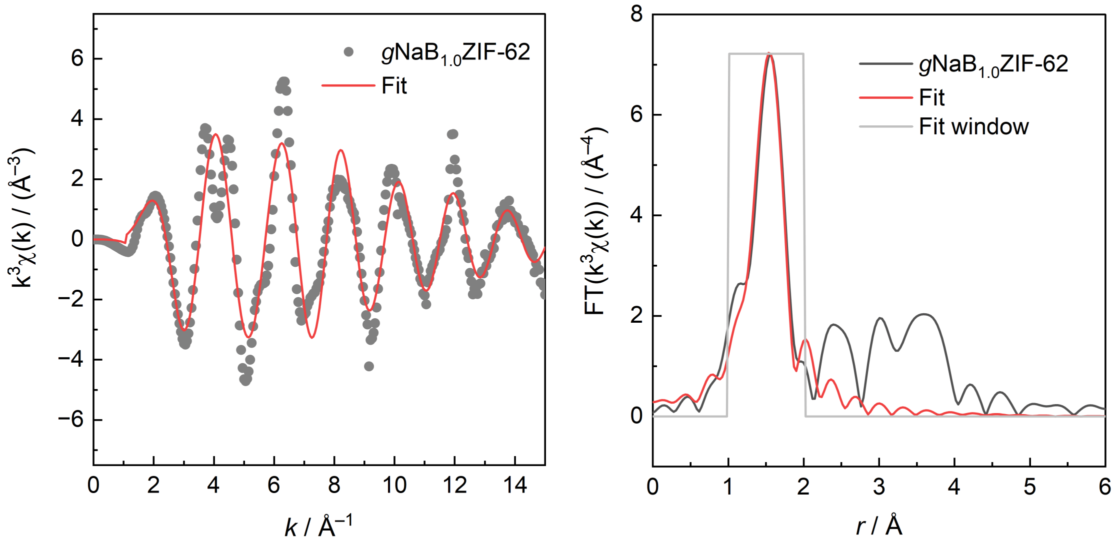

Figure A2.79. Left: Fit to the EXAFS signal in the form of $k^3\chi(k)$ according to Equation A2.6 for gNaB$_{1.0}$ZIF-62. Right: Fourier transform of the EXAFS signal for gNaB$_{1.0}$ZIF-62 plotted against the real-space distance r with the corresponding Fourier transform of the fit shown left. The fitted range covers the interatomic distances of the first coordination shell of Zn^{2+} (i.e., [ZnN_4] units) in the investigated material. The refined parameters of the fitted function are summarized in Table A2.11.

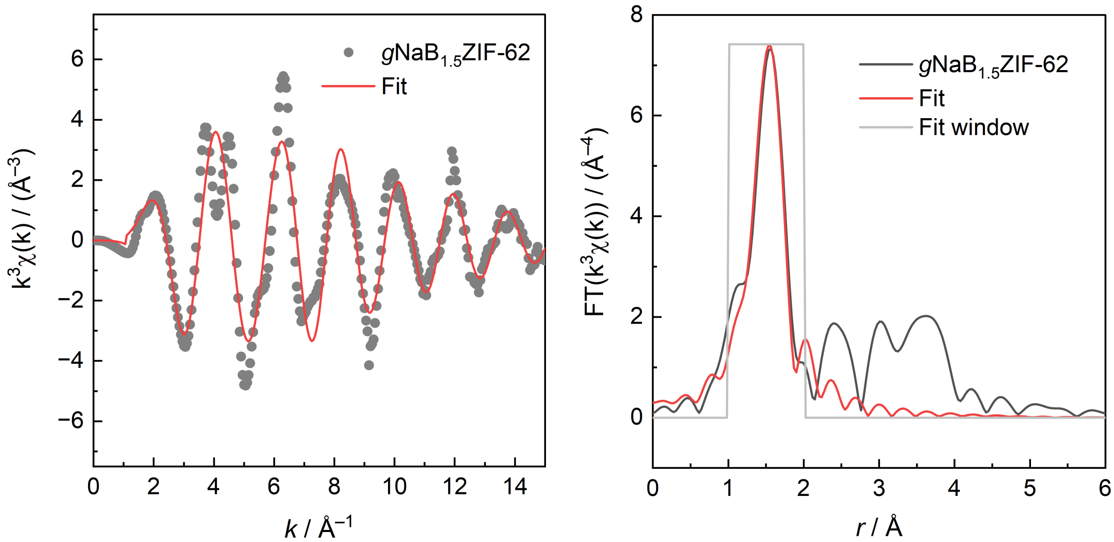

Figure A2.80. Left: Fit to the EXAFS signal in the form of $k^3\chi(k)$ according to Equation A2.6 for gNaB$_{1.5}$ZIF-62. Right: Fourier transform of the EXAFS signal for gNaB$_{1.5}$ZIF-62 plotted against the real-space distance r with the corresponding Fourier transform of the fit shown left. The fitted range covers the interatomic distances of the first coordination shell of Zn^{2+} (i.e., [ZnN_4] units) in the investigated material. The refined parameters of the fitted function are summarized in Table A2.11.

Table A2.11. Refined parameters obtained by fitting Equation A2.6 to the EXAFS signal of ZIF-62, *g*ZIF-62 and the modified glassed *g*NaB$_x$ZIF-62 shown in Figure A2.73 - Figure A2.80. The determined parameters correspond to the first coordination shell (i.e., [ZnN_4] coordination shell) and include the amplitude reduction factor S_0, the Zn coordination number (CN), the average Zn−N distance r, the determined Debye-Waller factor σ^2, the deviation of the Zn K absorption edge from the expected value for Zn^{2+} ΔE_0 and the R factor indicating the goodness if the fit.

Material	Shell	S_o^2	CN	r/Å	σ^2	ΔE_0/eV	R factor
ZIF-62	Zn−N	0.907 ± 0.06	4	1.984 ± 0.001	0.004	4.5 ± 0.6	0.010
*g*ZIF-62	Zn−N	0.91	3.95 ± 0.23	1.987 ± 0.004	0.004	4.4 ± 0.6	0.007
*g*NaB$_{0.3}$ZIF-62	Zn−N	0.91	4.11 ± 0.28	1.989 ± 0.005	0.005	4.4 ± 0.6	0.009
*g*NaB$_{0.5}$ZIF-62	Zn−N	0.91	4.03 ± 0.29	1.988 ± 0.005	0.004	4.3 ± 0.7	0.011
*g*NaB$_{1.0}$ZIF-62	Zn−N	0.91	4.08 ± 0.31	1.989 ± 0.005	0.004	4.3 ± 0.7	0.013
*g*NaB$_{1.5}$ZIF-62	Zn−N	0.91	4.23 ± 0.34	1.989 ± 0.005	0.004	4.2 ± 0.8	0.014

A2.14 Atom Probe Tomography

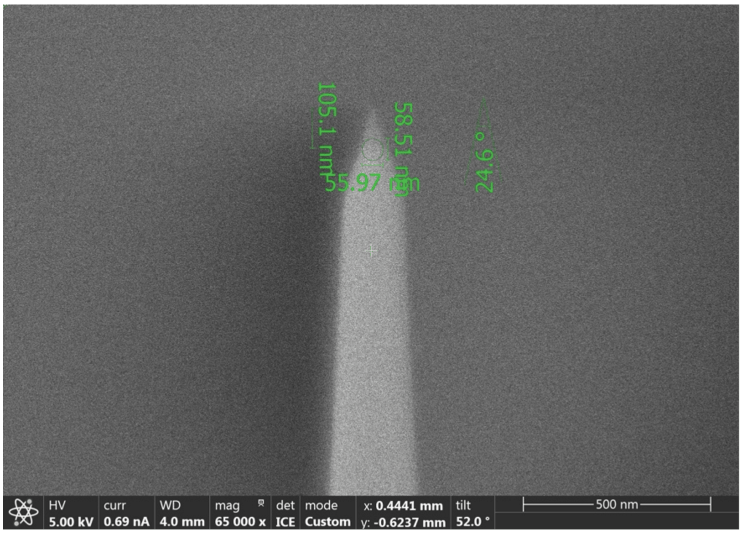

Figure A2.81. Electron microscopy image of the specimen (gNaB$_{0.3}$ZIF-62) prepared for the APT measurement.

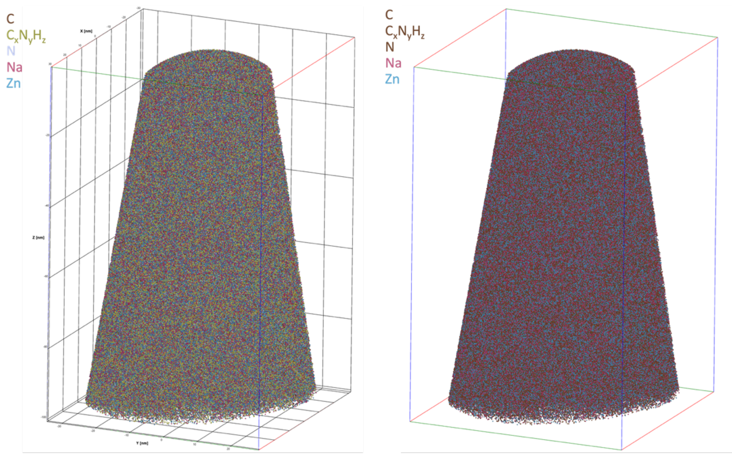

Figure A2.82. Reconstructed atomic model of the specimen based on the ions detected in the APT measurement. Left: Full reconstruction depicting all Na- and Zn-containing (complex) ions represented as Na (red) and Zn (blue). All hydrogens and CNH-complex ions, which do not include Na and Zn, are represented by $C_xH_yN_z$ (green). Carbon and Nitrogen are represented by C (brown) and N (light blue), respectively. Right: Simplified view on the reconstruction showing all organic (complex) ions in brown. All Na and Zn-containing (complex) ions are represented as Na (red) and Zn (blue) respectively.

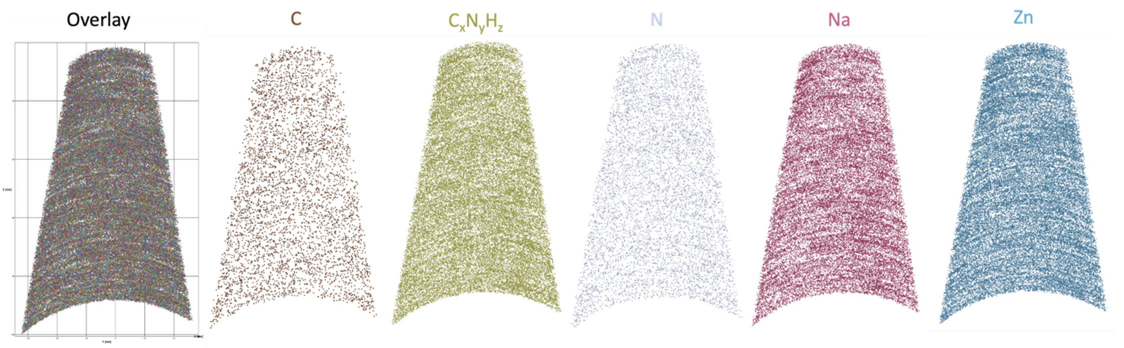

Figure A2.83. Slice of the reconstructed atomic model as shown in Figure S82 applying the same atomic representation scheme as in the full reconstruction (Figure S82, left).

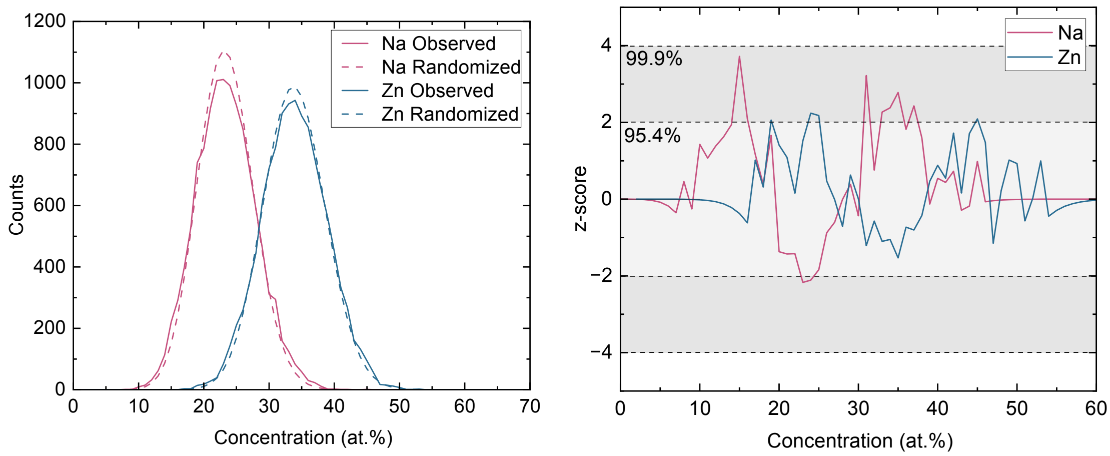

Figure A2.84. Left: Frequency distribution curves of the respective Na and Zn sites in the reconstructed APT model together with computed randomized data as a reference for the distribution of an ideal random distribution. Right: z-Score for the frequency analysis shown left illustrating the deviation of the found ion concentration from the (random) binomial distribution with z-scores exceeding the 99.7% confidence interval hinting towards the presence of Na ion clustering.

A2.15 Electron Microscopy and Energy-Dispersive X-Ray Spectroscopy

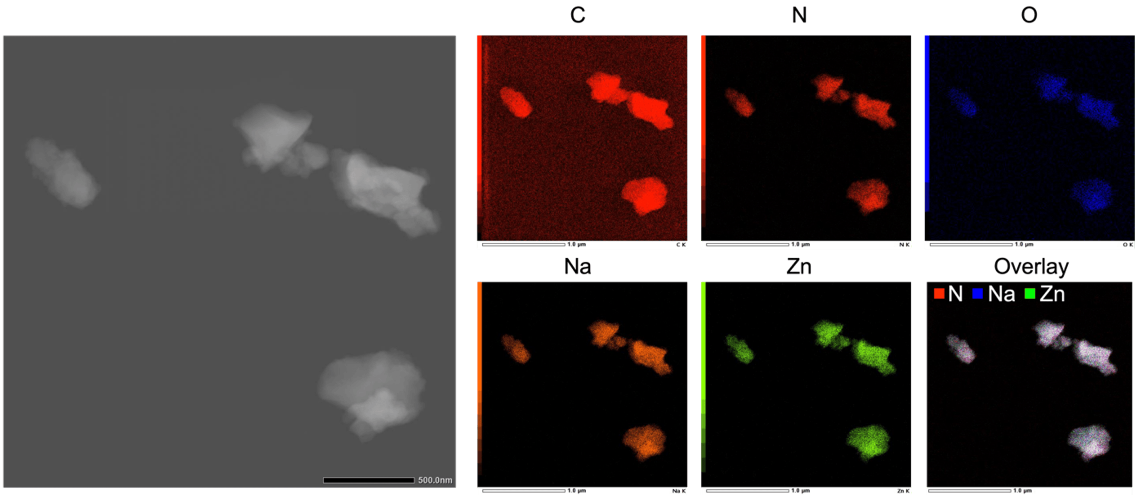

Figure A2.85. STEM image of small shards of gNaB$_{0.3}$ZIF-62 (left) together with colour maps indicating the relative abundance of the respective nuclei obtained by EDX measurements.

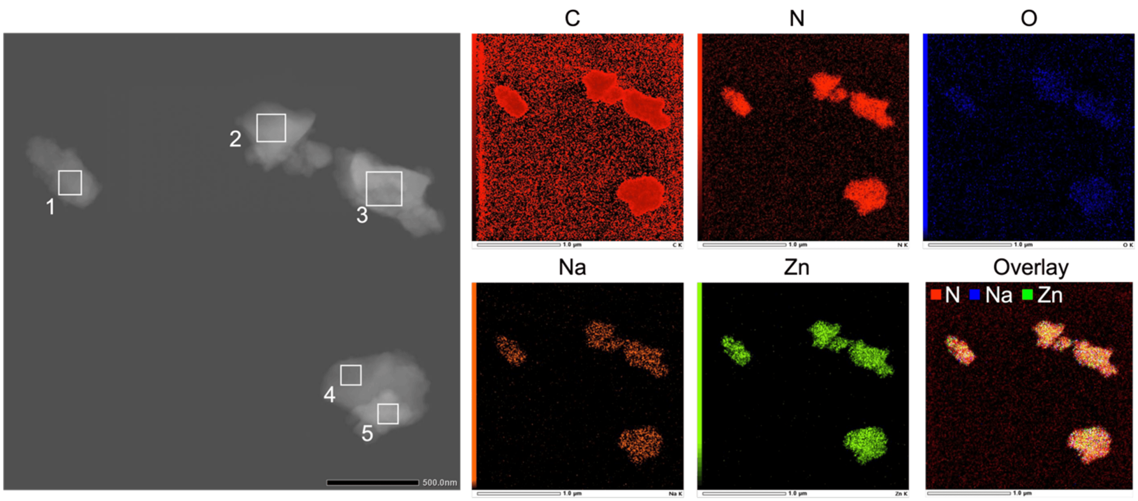

Figure A2.86. STEM image of small shards of gNaB$_{0.3}$ZIF-62 (left) together with colour maps indicating the relative abundance of the respective nuclei obtained by quantitative EDX measurements. The results of the quantification approach are shown in Table A2.12.

Table A2.12. Results of the quantitative analysis of STEM-EDX measurements for gNaB$_{0.3}$ZIF-62. The areas correspond to the areas highlighted in Figure A2.86.

Area	Atomic species / at.%							Zn/Na ratio
	C	N	O	Na	Zn	S	Cl	
1	90.67	6.78	0.70	0.75	1.10	–	–	1.47
2	88.71	8.10	0.81	0.91	1.47	–	–	1.62
3	89.27	7.65	0.76	0.93	1.40	–	–	1.51
4	92.06	5.60	0.73	0.66	0.96	–	–	1.46
5	92.66	4.93	0.56	0.71	1.13	–	–	1.59

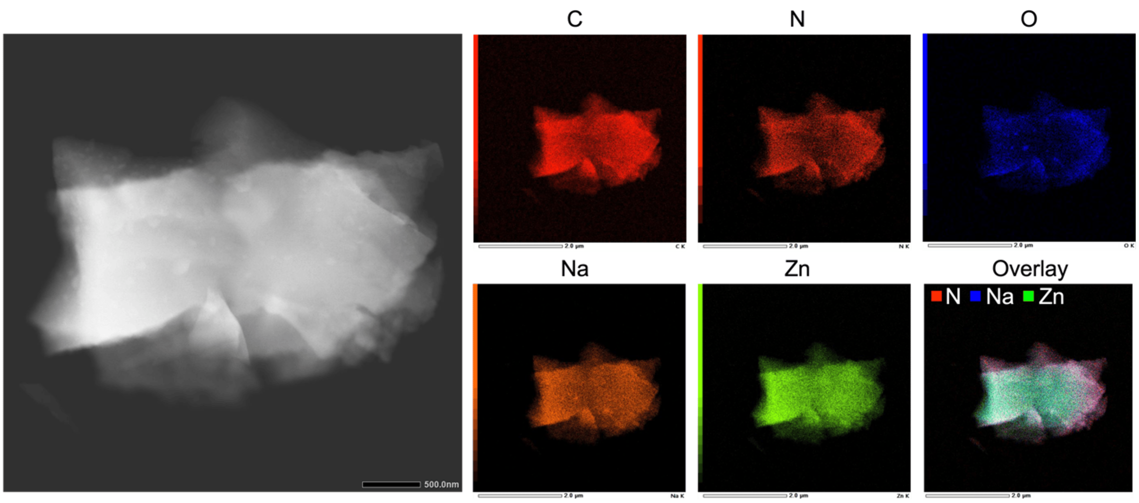

Figure A2.87. STEM image of a shard of gNaB$_{1.0}$ZIF-62 (left) together with colour maps indicating the relative abundance of the respective nuclei obtained by EDX measurements.

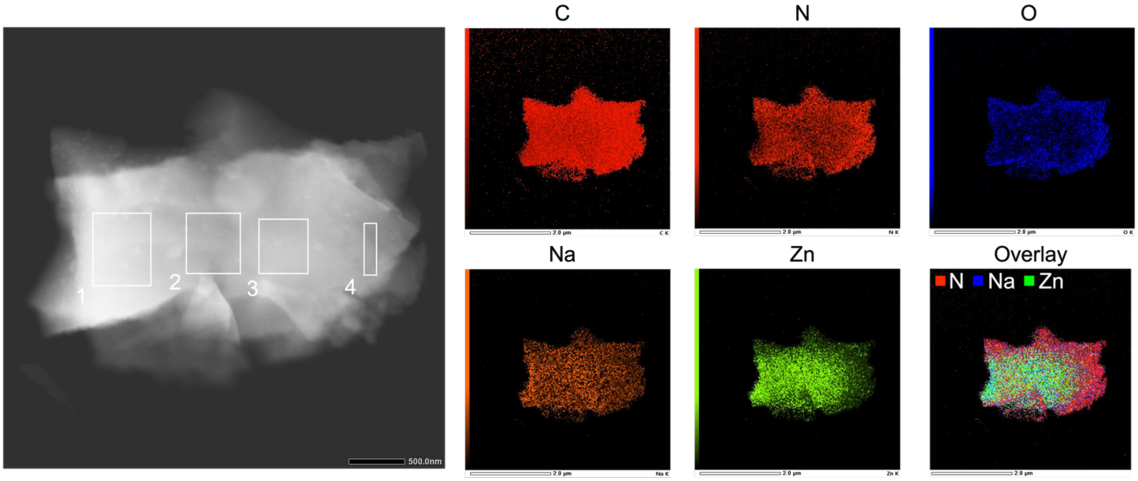

Figure A2.88. STEM image of a shard of gNaB$_{1.0}$ZIF-62 (left) together with colour maps indicating the relative abundance of the respective nuclei obtained by quantitative EDX measurements. The results of the quantification approach is shown in Table A2.13.

Table A2.13. Results of the quantitative analysis of STEM-EDX measurements for gNaB$_{0.3}$ZIF-62. The areas correspond to the areas highlighted in Figure A2.88.

Area	Atomic species / at.%							Zn/Na ratio
	C	N	O	Na	Zn	S	Cl	
1	65.85	8,26	2.25	7.70	15.59	–	–	2.02
2	68.26	7.64	2.11	7.64	14.34	–	–	1.88
3	66.09	6.84	2.12	8.37	16.57	–	–	1.98
4	77.40	11.54	3.14	3.51	4.41	–	–	1.26

A2.16 Density Functional Theory Calculations

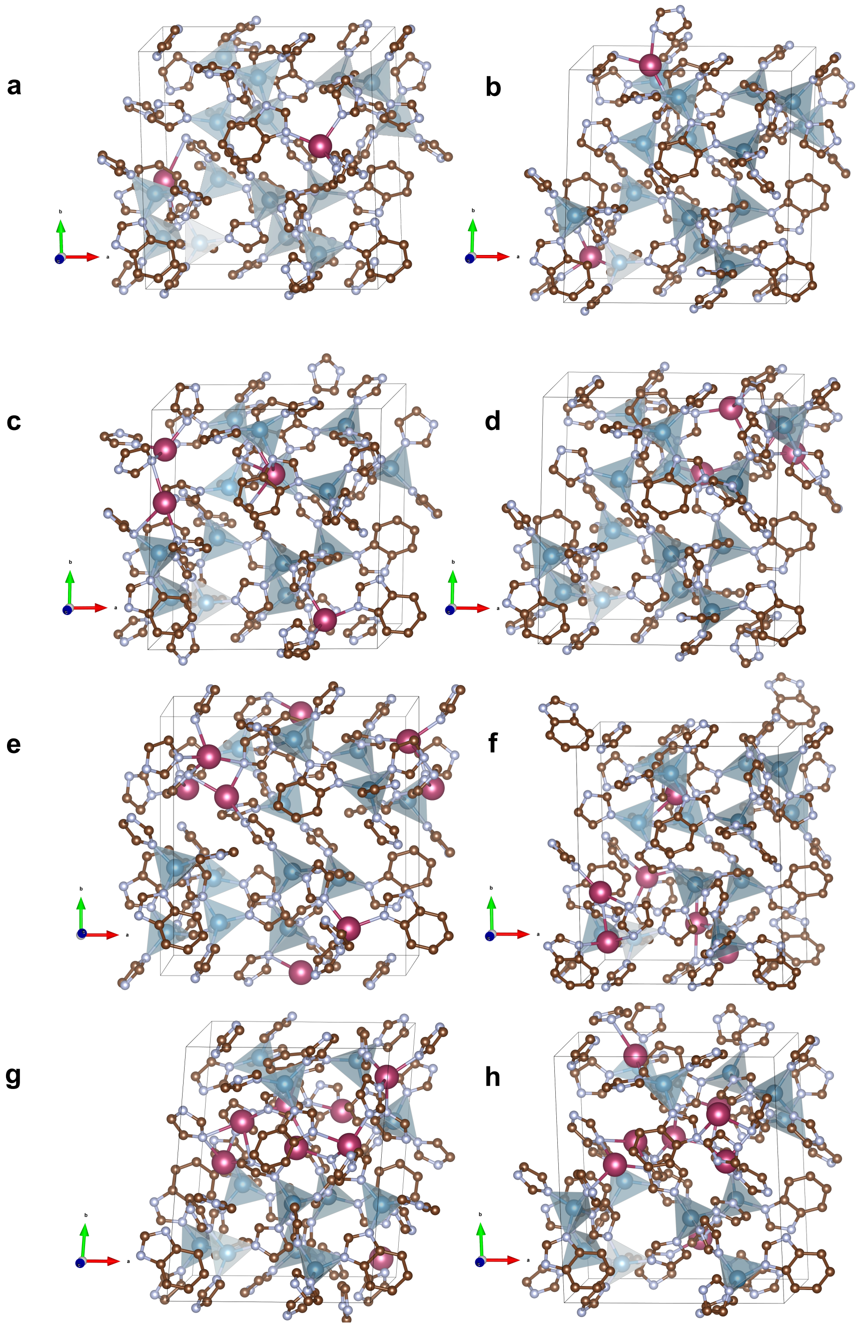

Figure A2.89. Examples of geometry-optimised supercell structures of composition $(Na_{2y}Zn_{16-y})[(im)_{1.75}(bim)_{0.25}]_{16}$. Two examples are shown for each y = 1 (a-b), 2 (c-d), 3 (e-f), and 4 (g-h). All supercells provided as .cell supplementary files. (Na, pink; Zn, dark blue; N, light blue; C, brown)

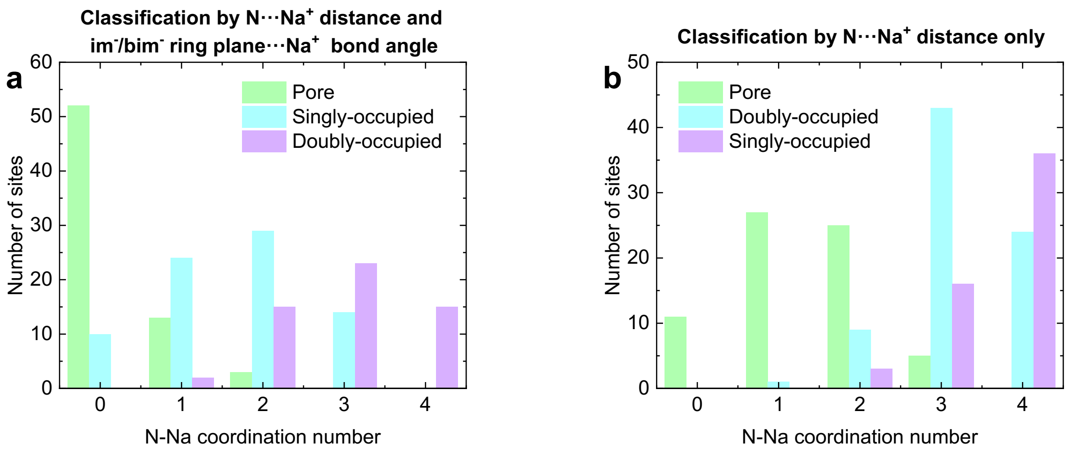

Figure A2.90. Relationship between categorization of geometry-optimised Na^+ as attached to the pore walls of gNaB$_x$ZIF-62, on doubly occupied or singly occupied node site and $N{-}Na^+$ coordination number, defined by $N \cdots Na^+$ distance < 2.7 Å and the im^-/bim^- ring plane$\cdots Na^+$ angle $< 30°$ (a) and $N \cdots Na^+$ distance < 2.7 Å only (b).

Table A2.14. Classification of DFT-simulated Na^+ coordination environments found in .cell files provided as supplementary files. $N-Na^+$ coordination number defined by distance only requires that $N\cdots Na^+$ distance < 2.7 Å only for an $N-Na^+$ coordinate bond to be counted. $N-Na^+$ coordination number defined by distance and angle requires that both $N\cdots Na^+$ distance < 2.7 Å and that a less than 30° angle between the plane of the im^-/bim^- ring and Na^+ for a $N-Na^+$ coordinate bond to be counted. Na^+ site assignment: 1 = singly occupied node site, 2 = doubly occupied node site, 3 = pore wall site.

Supercell	Na # (in .cell file)	N-Na$^+$ coordination (distance only)	N-Na$^+$ coordination (distance + angle)	Na$^+$ site assignment
ZIF-62_Na2_01	1	0	0	3
ZIF-62_Na2_01	2	1	0	3
ZIF-62_Na2_02	1	4	3	1
ZIF-62_Na2_02	2	1	0	3
ZIF-62_Na2_03	1	4	3	1
ZIF-62_Na2_03	2	1	0	3
ZIF-62_Na2_04	1	2	0	3
ZIF-62_Na2_04	2	3	3	1
ZIF-62_Na2_05	1	2	0	3
ZIF-62_Na2_05	2	2	1	3
ZIF-62_Na2_06	1	1	0	3
ZIF-62_Na2_06	2	4	3	1
ZIF-62_Na2_07	1	3	0	3
ZIF-62_Na2_07	2	4	3	1
ZIF-62_Na2_08	1	4	4	1
ZIF-62_Na2_08	2	0	0	3
ZIF-62_Na2_09	1	4	4	1
ZIF-62_Na2_09	2	0	0	3
ZIF-62_Na2_10	1	1	0	3
ZIF-62_Na2_10	2	4	3	1
ZIF-62_Na4_01	1	1	0	3
ZIF-62_Na4_01	2	4	2	2
ZIF-62_Na4_01	3	4	3	2
ZIF-62_Na4_01	4	4	2	2
ZIF-62_Na4_02	1	3	2	1
ZIF-62_Na4_02	2	4	4	1
ZIF-62_Na4_02	3	2	1	3
ZIF-62_Na4_02	4	1	0	3
ZIF-62_Na4_03	1	0	0	3
ZIF-62_Na4_03	2	4	3	1
ZIF-62_Na4_03	3	1	0	3
ZIF-62_Na4_03	4	3	2	1
ZIF-62_Na4_04	1	4	1	2
ZIF-62_Na4_04	2	1	0	3
ZIF-62_Na4_04	3	4	4	1
ZIF-62_Na4_04	4	3	0	2
ZIF-62_Na4_05	1	2	2	1
ZIF-62_Na4_05	2	1	0	3
ZIF-62_Na4_05	3	2	1	1
ZIF-62_Na4_05	4	4	4	1
ZIF-62_Na4_06	1	3	2	2
ZIF-62_Na4_06	2	1	1	3
ZIF-62_Na4_06	3	3	2	2
ZIF-62_Na4_06	4	2	0	3
ZIF-62_Na4_07	1	1	0	3
ZIF-62_Na4_07	2	4	4	1
ZIF-62_Na4_07	3	1	1	3
ZIF-62_Na4_07	4	3	2	1
ZIF-62_Na4_08	1	4	3	1
ZIF-62_Na4_08	2	1	0	3
ZIF-62_Na4_08	3	0	0	3
ZIF-62_Na4_08	4	4	3	1
ZIF-62_Na4_09	1	3	1	3
ZIF-62_Na4_09	2	4	4	1
ZIF-62_Na4_09	3	3	2	1
ZIF-62_Na4_09	4	3	1	1
ZIF-62_Na4_10	1	4	2	2
ZIF-62_Na4_10	2	4	2	2
ZIF-62_Na4_10	3	2	0	3
ZIF-62_Na4_10	4	4	3	2
ZIF-62_Na6_01	1	3	1	2
ZIF-62_Na6_01	2	4	4	1
ZIF-62_Na6_01	3	1	0	3
ZIF-62_Na6_01	4	4	2	2
ZIF-62_Na6_01	5	2	0	3
ZIF-62_Na6_01	6	4	3	1
ZIF-62_Na6_02	1	2	1	3

ZIF-62_Na6_02	2	4	3	2
ZIF-62_Na6_02	3	4	4	1
ZIF-62_Na6_02	4	1	0	3
ZIF-62_Na6_02	5	3	2	1
ZIF-62_Na6_02	6	3	3	2
ZIF-62_Na6_03	1	3	1	2
ZIF-62_Na6_03	2	4	3	2
ZIF-62_Na6_03	3	2	1	3
ZIF-62_Na6_03	4	3	2	2
ZIF-62_Na6_03	5	4	2	2
ZIF-62_Na6_03	6	2	0	3
ZIF-62_Na6_04	1	4	3	2
ZIF-62_Na6_04	2	2	2	3
ZIF-62_Na6_04	3	4	2	2
ZIF-62_Na6_04	4	2	1	3
ZIF-62_Na6_04	5	2	1	2
ZIF-62_Na6_04	6	3	1	2
ZIF-62_Na6_05	1	4	3	1
ZIF-62_Na6_05	2	3	3	1
ZIF-62_Na6_05	3	4	2	1
ZIF-62_Na6_05	4	1	0	3
ZIF-62_Na6_05	5	3	3	2
ZIF-62_Na6_05	6	2	1	2
ZIF-62_Na6_06	1	4	3	2
ZIF-62_Na6_06	2	1	0	3
ZIF-62_Na6_06	3	2	1	2
ZIF-62_Na6_06	4	3	2	2
ZIF-62_Na6_06	5	3	2	2
ZIF-62_Na6_06	6	3	1	2
ZIF-62_Na6_07	1	4	0	2
ZIF-62_Na6_07	2	2	1	2
ZIF-62_Na6_07	3	4	3	1
ZIF-62_Na6_07	4	3	3	1
ZIF-62_Na6_07	5	1	0	3
ZIF-62_Na6_07	6	1	0	3
ZIF-62_Na6_08	1	4	3	1
ZIF-62_Na6_08	2	4	4	1
ZIF-62_Na6_08	3	4	2	1
ZIF-62_Na6_08	4	1	0	3
ZIF-62_Na6_08	5	2	0	3
ZIF-62_Na6_08	6	1	0	3
ZIF-62_Na6_09	1	3	2	2
ZIF-62_Na6_09	2	3	0	2
ZIF-62_Na6_09	3	3	0	3
ZIF-62_Na6_09	4	2	1	2
ZIF-62_Na6_09	5	2	2	1
ZIF-62_Na6_09	6	3	2	2
ZIF-62_Na6_10	1	4	1	2
ZIF-62_Na6_10	2	3	2	2
ZIF-62_Na6_10	3	0	0	3
ZIF-62_Na6_10	4	4	3	1
ZIF-62_Na6_10	5	3	3	1
ZIF-62_Na6_10	6	1	0	3
ZIF-62_Na8_01	1	3	1	2
ZIF-62_Na8_01	2	2	1	3
ZIF-62_Na8_01	3	4	1	2
ZIF-62_Na8_01	4	3	2	2
ZIF-62_Na8_01	5	0	0	3
ZIF-62_Na8_01	6	3	2	2
ZIF-62_Na8_01	7	4	4	1
ZIF-62_Na8_01	8	3	3	1
ZIF-62_Na8_02	1	4	3	1
ZIF-62_Na8_02	2	3	1	2
ZIF-62_Na8_02	3	2	0	3
ZIF-62_Na8_02	4	4	4	1
ZIF-62_Na8_02	5	2	0	3
ZIF-62_Na8_02	6	2	0	3
ZIF-62_Na8_02	7	4	2	2
ZIF-62_Na8_02	8	3	2	2
ZIF-62_Na8_03	1	2	1	2
ZIF-62_Na8_03	2	3	3	2
ZIF-62_Na8_03	3	3	2	2
ZIF-62_Na8_03	4	1	0	3
ZIF-62_Na8_03	5	4	1	2
ZIF-62_Na8_03	6	4	3	2
ZIF-62_Na8_03	7	3	2	2
ZIF-62_Na8_03	8	3	2	2
ZIF-62_Na8_04	1	3	0	2
ZIF-62_Na8_04	2	3	1	3
ZIF-62_Na8_04	3	3	2	2
ZIF-62_Na8_04	4	3	2	2
ZIF-62_Na8_04	5	3	2	1
ZIF-62_Na8_04	6	4	2	1

ZIF-62_Na8_04	7	4	3	1
ZIF-62_Na8_04	8	3	0	3
ZIF-62_Na8_05	1	3	3	2
ZIF-62_Na8_05	2	2	1	3
ZIF-62_Na8_05	3	2	0	3
ZIF-62_Na8_05	4	2	2	3
ZIF-62_Na8_05	5	3	3	1
ZIF-62_Na8_05	6	3	1	2
ZIF-62_Na8_05	7	2	0	3
ZIF-62_Na8_05	8	3	1	2
ZIF-62_Na8_06	1	2	0	2
ZIF-62_Na8_06	2	3	1	2
ZIF-62_Na8_06	3	3	2	2
ZIF-62_Na8_06	4	1	1	3
ZIF-62_Na8_06	5	3	0	2
ZIF-62_Na8_06	6	4	3	2
ZIF-62_Na8_06	7	4	4	1
ZIF-62_Na8_06	8	2	1	2
ZIF-62_Na8_07	1	0	0	3
ZIF-62_Na8_07	2	3	2	1
ZIF-62_Na8_07	3	0	0	3
ZIF-62_Na8_07	4	4	2	1
ZIF-62_Na8_07	5	3	1	2
ZIF-62_Na8_07	6	2	0	3
ZIF-62_Na8_07	7	2	0	2
ZIF-62_Na8_07	8	4	4	1
ZIF-62_Na8_08	1	2	0	3
ZIF-62_Na8_08	2	1	1	2
ZIF-62_Na8_08	3	1	1	3
ZIF-62_Na8_08	4	1	0	3
ZIF-62_Na8_08	5	3	3	2
ZIF-62_Na8_08	6	3	3	1
ZIF-62_Na8_08	7	3	3	1
ZIF-62_Na8_08	8	4	2	1
ZIF-62_Na8_09	1	2	2	3
ZIF-62_Na8_09	2	2	0	3
ZIF-62_Na8_09	3	3	2	2
ZIF-62_Na8_09	4	4	2	1
ZIF-62_Na8_09	5	3	1	2
ZIF-62_Na8_09	6	3	1	2
ZIF-62_Na8_09	7	4	2	2
ZIF-62_Na8_09	8	0	0	3
ZIF-62_Na8_10	1	3	0	2
ZIF-62_Na8_10	2	3	2	2
ZIF-62_Na8_10	3	3	2	2
ZIF-62_Na8_10	4	3	0	2
ZIF-62_Na8_10	5	4	3	1
ZIF-62_Na8_10	6	0	0	3
ZIF-62_Na8_10	7	4	3	2
ZIF-62_Na8_10	8	4	1	2

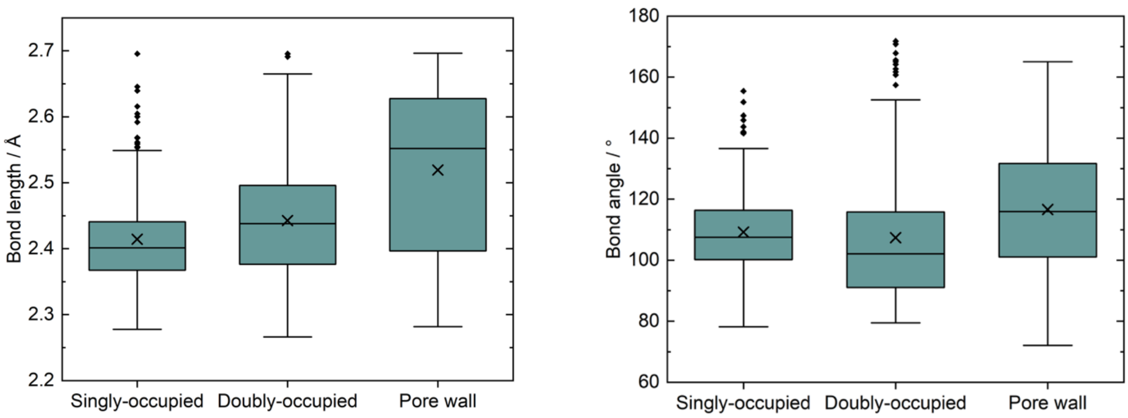

Figure A2.91. Box plots illustrating the distribution of bond lengths and bond angles for the sodium ions categorised according to the identified three distinct Na sites. The box represents the interquartile range (IQR) from the first (Q1) to the third quartile (Q3) and covers 50% of the data points. The line inside indicates the median and the cross the average value of the dataset. The whiskers extend to the smallest and largest values within 1.5 × IQR from the quartiles. Points beyond the whiskers are considered outliers.The broad distribution of bond angles for sodium ions in pore wall sites is a consequence of the large range of coordination numbers found for such sodium sites.

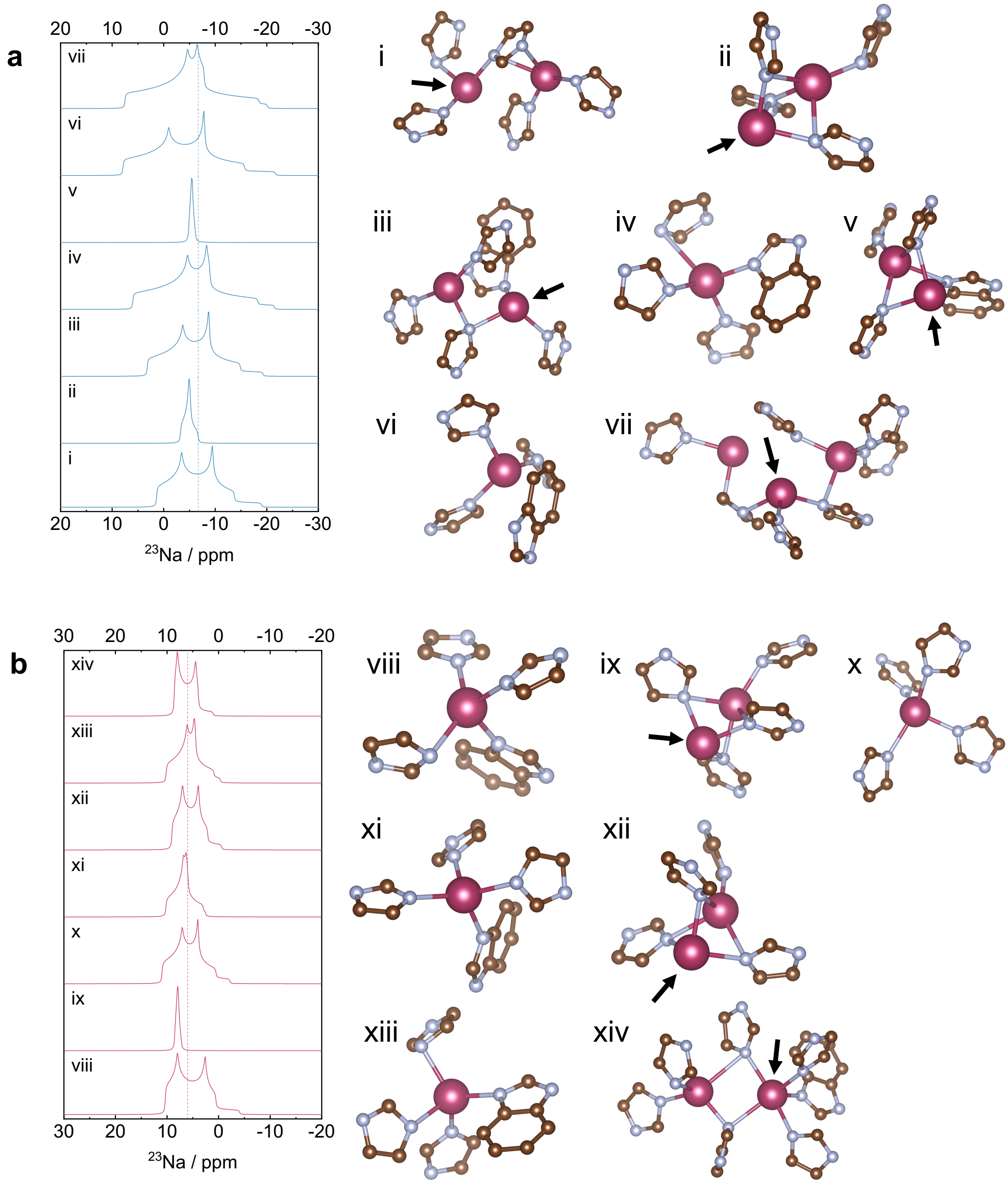

Figure A2.92. DFT-simulated Na^+ coordination environments giving rise to predicted ^{23}Na NMR spectra with maximum intensity in the regions around -6.3 ± 3ppm (a) and 6.8 ± 3ppm (b). Where multiple Na^+ are shown in a single environment, an arrow is used to show the Na^+ corresponding to the predicted ^{23}Na spectrum of interest. (Na, pink; N, light blue; C, brown; hydrogens were omitted for clarity).

A2.17 Solid-State Nuclear Magnetic Resonance Spectroscopy

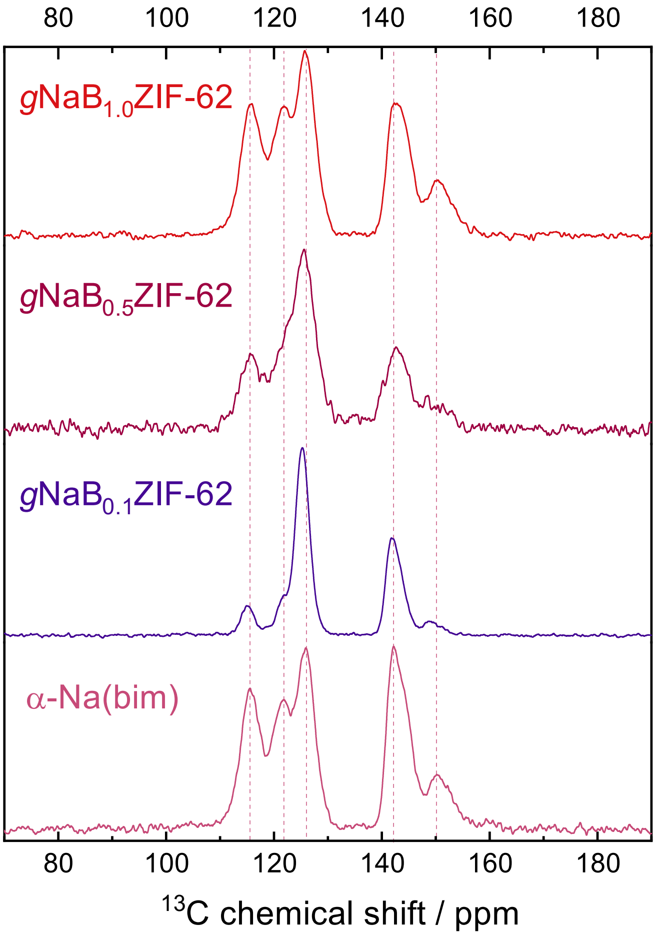

Figure A2.93. ^{1}H-decoupled ^{1}H-^{13}C cross-polarization MAS NMR (11.7 T, 12 kHz) of gNaB$_x$ZIF-62 and its organic salt precursors. Gradual increase in Na(bim) content in gNaB$_x$ZIF-62 is reflected in an increase in the intensity of ^{13}C signals corresponding to bim^{-}. No other signals are observed, which might correspond to organic impurities in the modified MOF glass materials.

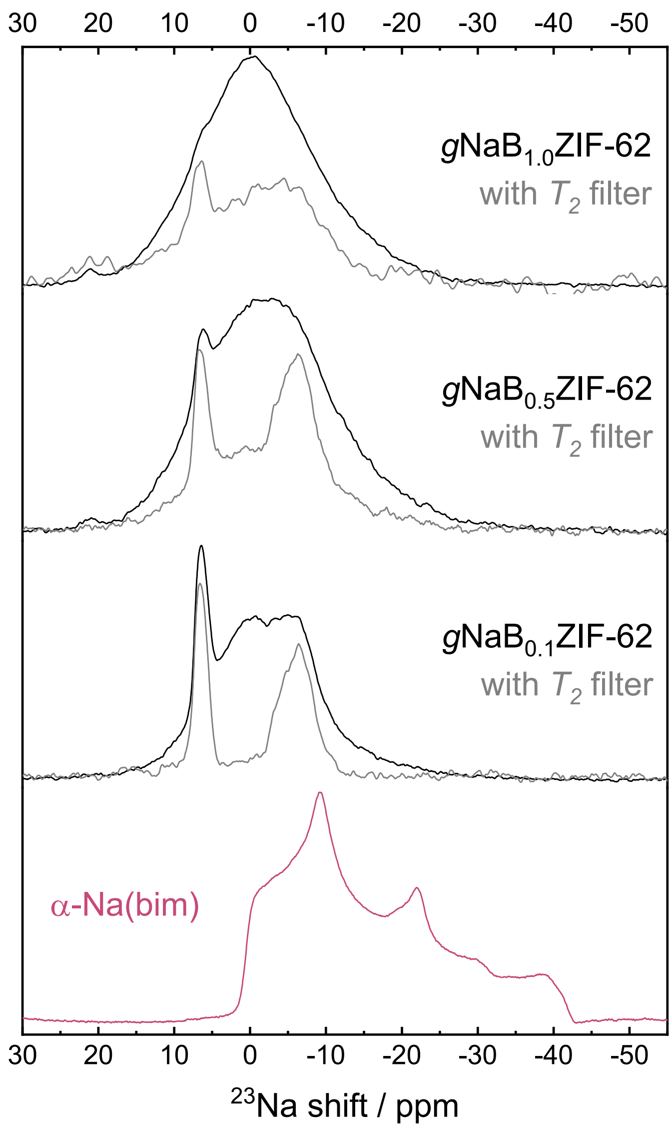

Figure A2.94. ^{23}Na MAS NMR spectra (20.0 T, 20 kHz) of α-Na(bim) and gNaB$_x$ZIF-62 with x = 0.1, 0.5 and 1.0. Spectra of modified MOF glasses are shown with a short (0.05 ms) and long (12.8 ms) echo delay to filter spectral components with short spin-spin relaxation times (T_2) (see Figure A2.95).

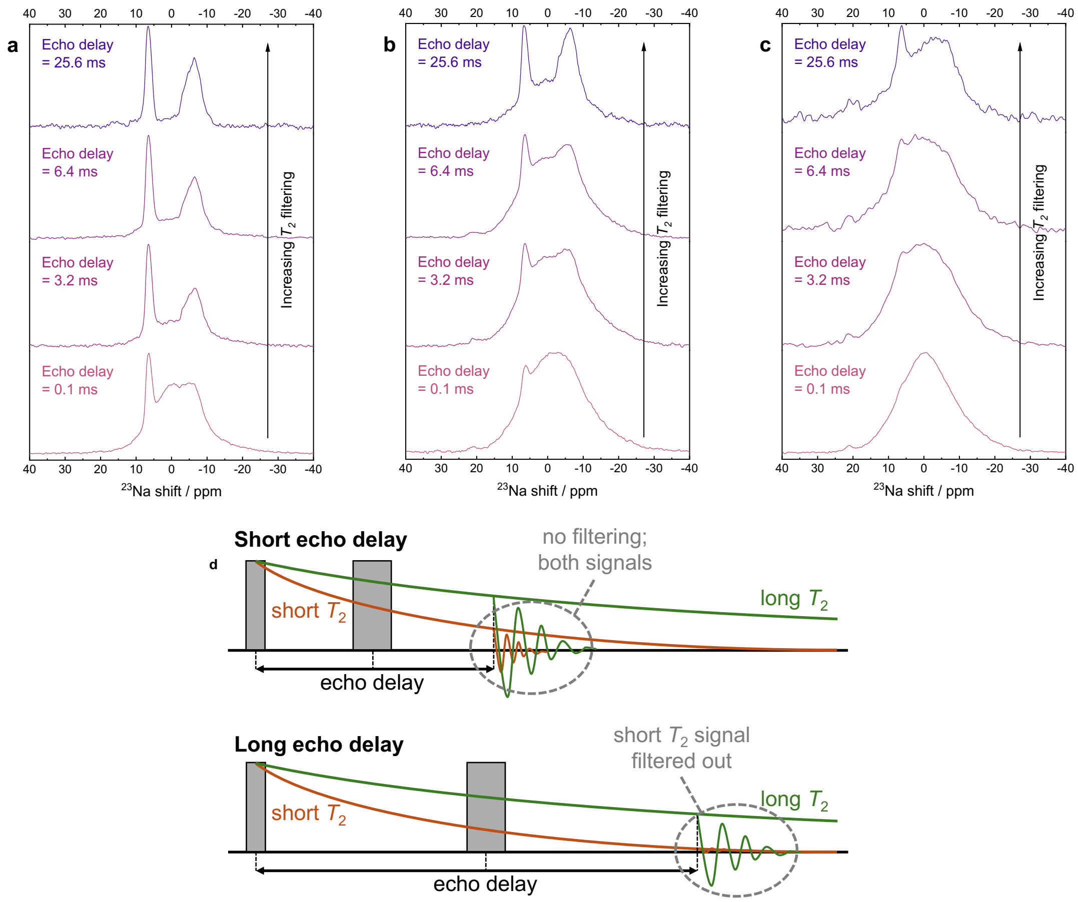

Figure A2.95. Spin-spin relaxation time (T_2) filtering by increasing echo delay time of ^{23}Na MAS NMR (20.0 T, 20 kHz) of gNaB$_x$ZIF-62 with $x = 0.1$ (a), 0.5 (b) and 1.0 (c) acquired via Hahn echo pulse sequence. d, Schematic figure showing the effect of altering echo delay on the signal intensity of Na environments with short and long T_2 values.

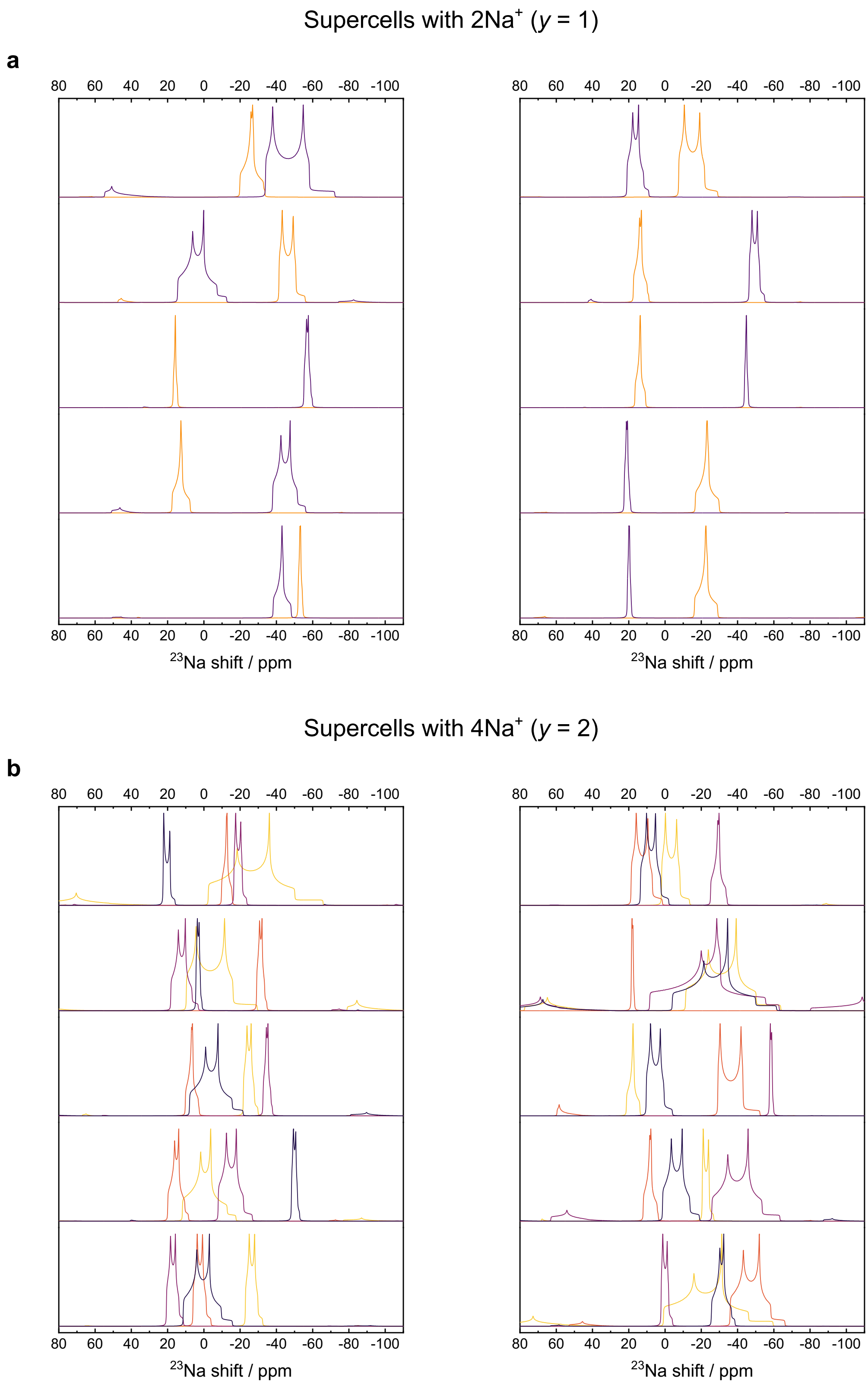

Supercells with 2Na+ (y = 1)
a
Supercells with 4Na+ (y = 2)
b
80 60 40 20 0 -20 -40 -60 -80 -100
23Na shift / ppm

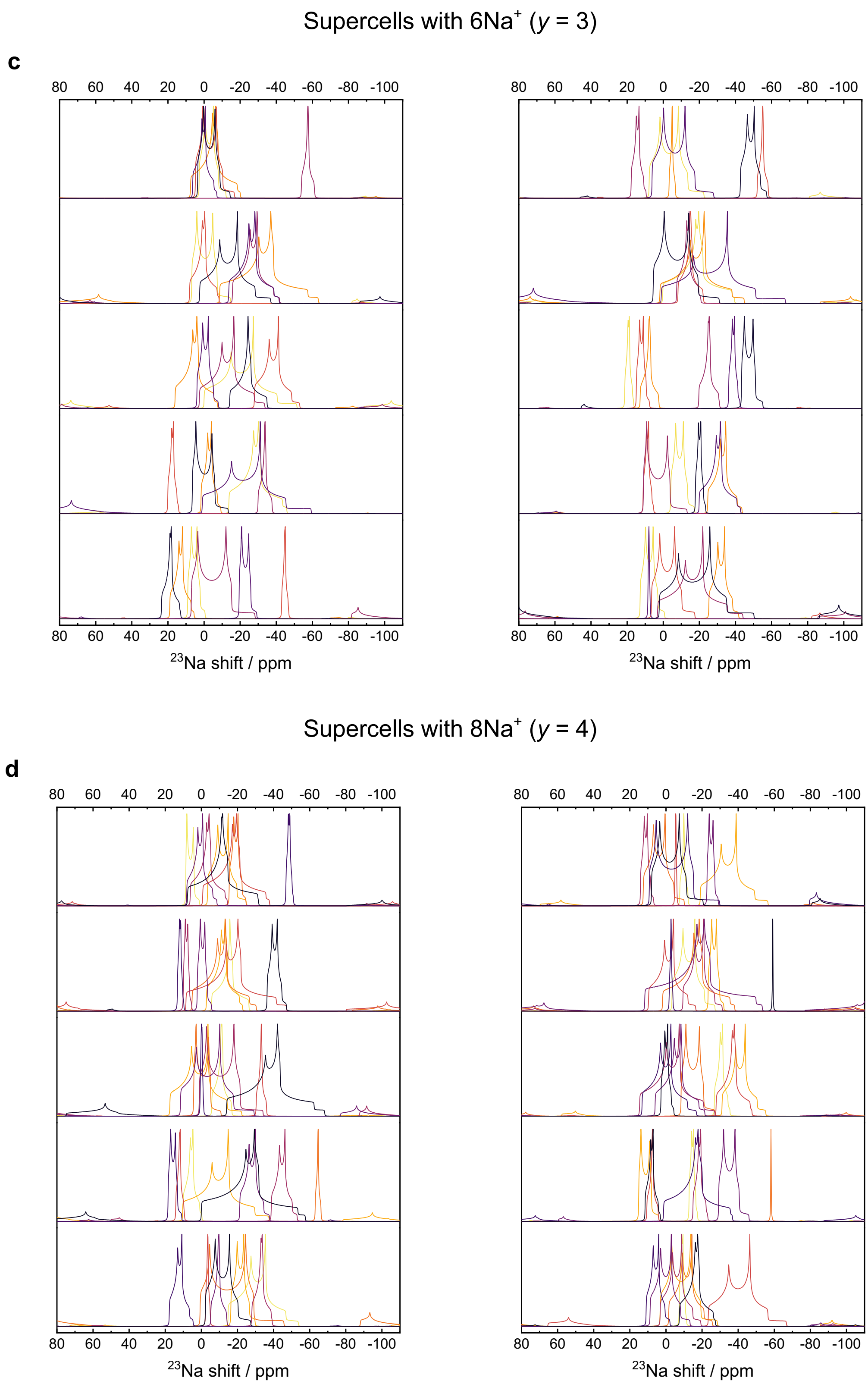

Figure A2.96. Predicted ^{23}Na spectra (20.0 T, MAS = 20 kHz) for all DFT-simulated Na^+ environments, simulated using calculated chemical shielding and EFG tensors. Spectra are grouped by supercell, each with composition $(Na_{2y}Zn_{16-y})[(im)_{1.75}(bim)_{0.25}]_{16}$, with $y = 1$ (a), 2 (b), 3 (c) and 4 (d).

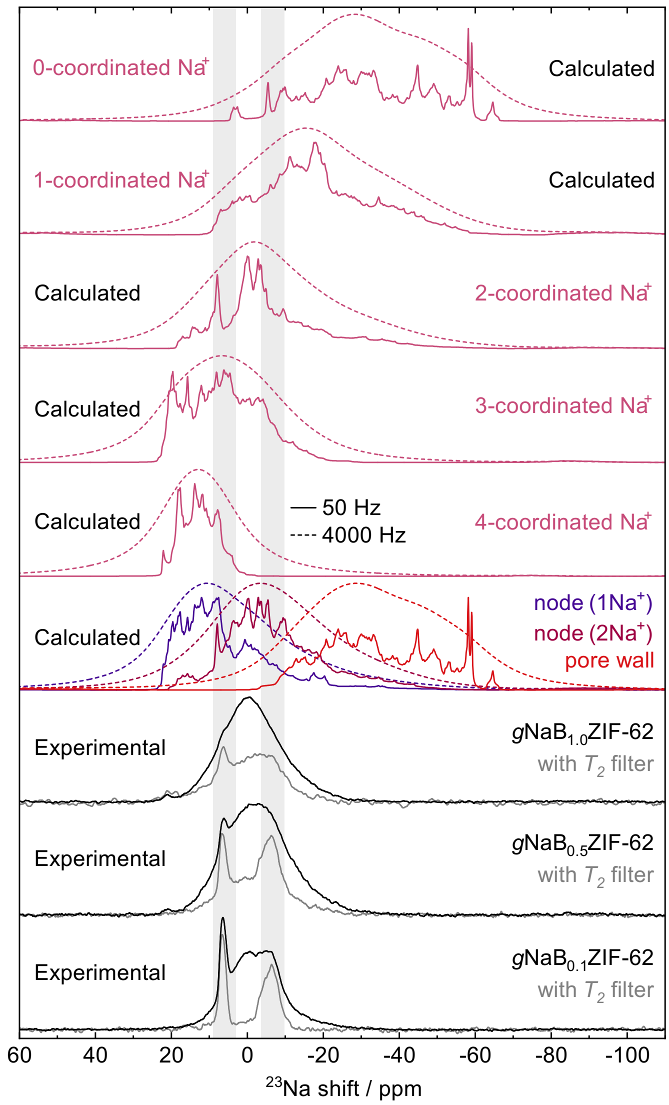

Figure A2.97. This figure is identical to that found in the main text (Figure 6.4f-n), except that N–Na^+ coordination is defined by both N···Na^+ distance and the angle between the line between N and Na^+ and the plane of the im^-/bim^- ring < 30°, as described below. Experimental ^{23}Na NMR (20.0 T, 20 kHz MAS) spectra of gNaB$_x$ZIF-62 with $x = 0.1$, 0.5, 1.0 (f-h). Spectra acquired with both a short (0.1 ms, black) and long (25.6 ms, grey) echo delay are shown, with the latter effectively filtering components in the spectra with short spin-spin relaxation times (T_2). Predicted ^{23}Na NMR spectra of Na^+ sites in DFT-simulated gNaB$_x$ZIF-62 structures, categorised by Na^+ occupation in the gNaB$_x$ZIF-62 structure (1Na^+ and 2Na^+ correspond to singly and doubly occupied node sites, respectively) (i) and N–Na^+ coordination number (j-n).

Doubly occupied Na^+ sites often resemble those observed in the α-Na(bim) structure (Figure 6.4a), with limited direct N–Na^+ coordination. As such, the bonding interactions present in many doubly occupied node sites may not be appropriately represented by the definition of N–Na^+ coordination using the N···Na^+ distance only (Figure 6.4j-n). To investigate this, we introduced a second criterion of N–Na^+ coordination and recategorised all 200 simulated Na^+ sites. This criterion introduces a requirement for a degree of covalency (directionality) in N−Na^+ coordinate bonding by requiring that both (i) N···Na^+ distance < 2.7 Å, and (ii) the angle between the line between N and Na^+ and the plane of the im^-/bim^- ring $<$ 30°. In Figure A2.97 we show cumulative predicted ^{23}Na spectra categorized using this new classification system and find that there is even less spectral overlap between the experimental spectra and the predicted ^{23}Na region corresponding to 4-coordinate Na^+ sites. Instead, lower coordination numbers become experimentally relevant, further supporting our inference that Na^+ incorporation into *g*ZIF-62 distorts the MOF substantially, consistent with reduced network connectivity and partial pore collapse.

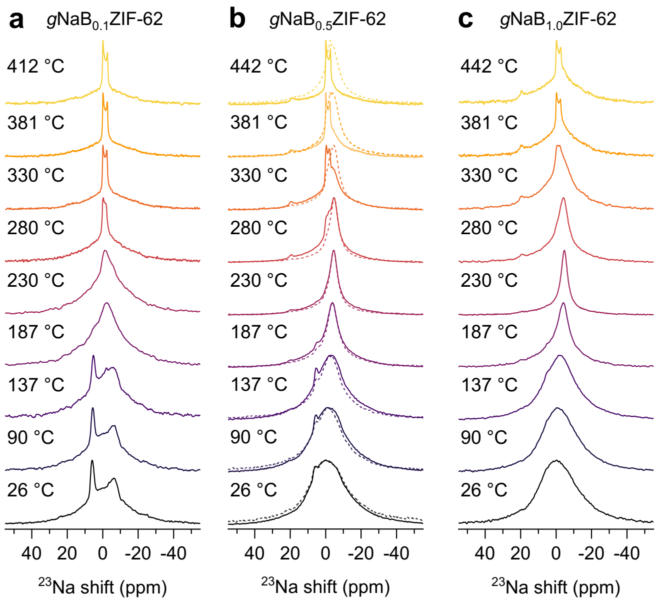

Figure A2.98. Variable temperature solid-state ^{23}Na MAS NMR (20.0 T, 4 kHz magic angle spinning) spectra of *g*NaB$_x$ZIF-62 with $x = 0.1$ (a), 0.5 (b) and 1.0 (c). Solid lines show spectra acquired via a Hahn echo pulse sequence (250 µs echo delay). Dashed lines show spectra acquired via a Bloch decay pulse sequence.

To further understand how the local structure of modified ZIF-62 glasses evolves under heating we conduct variable temperature ^{23}Na MAS NMR (20.0 T, 4 kHz) on *g*NaB$_x$ZIF-62 with $x = 0.1$, 0.5 and 1.0 (Figure A2.98). For all three compositions, we observe three distinct temperature regimes. As temperature increases up to T_g, ^{23}Na spectra narrow, indicating increasing flexibility in the MOF prior to reaching the glass transition. Above T_g, a single peak centred at -4.5 ppm emerges with a still narrower full width half maximum (FWHM). We observe that the intensity of this peak in echo experiments progressively decreases as the temperature increases and, for the highest temperatures, is substantially lower compared to pulse-acquire (Bloch decay) experiments. This result indicates that the spin-spin relaxation time of the broad component decreases with increasing temperature, which we attribute to the onset of Na^+ diffusion in the material. At the highest temperatures (>230 °C), a new ^{23}Na signal is apparent, displaying a pronounced quadrupolar lineshape. Although present for all compositions investigated, the intensity of this high-temperature peak relative to the broad component at –4.5 ppm is greatest for $x = 0.1$. We attribute this peak to a distinct binding mode, or phase, which is present throughout but only becomes visible when the dominant broader component is suppressed due to T_2 shortening.

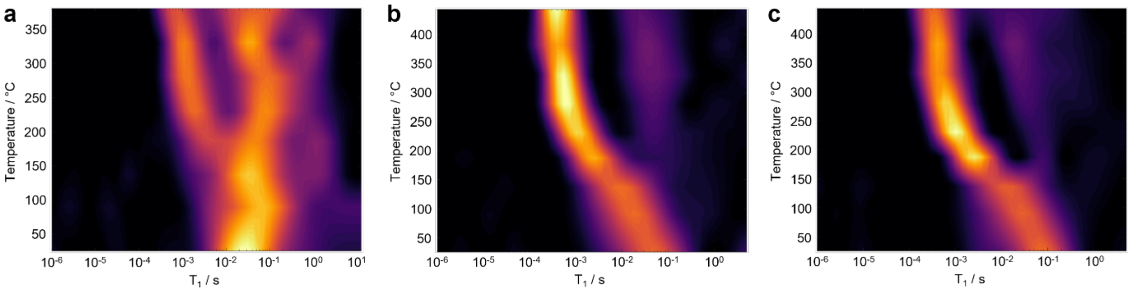

Figure A2.99. Inverse Laplace transform fitting of ^{23}Na spin-lattice time (T_1) as a function of temperature for gNaB$_x$ZIF-62, $x = 0.1$ (a), 0.5 (b), 1.0 (c). Below T_g, a single ^{23}Na T_1 is found for all three materials, while above T_g a second component with notably longer T_1 is observed.

A2.18 Water Leaching Experiments

A2.18.1 Optical Microscopy Images

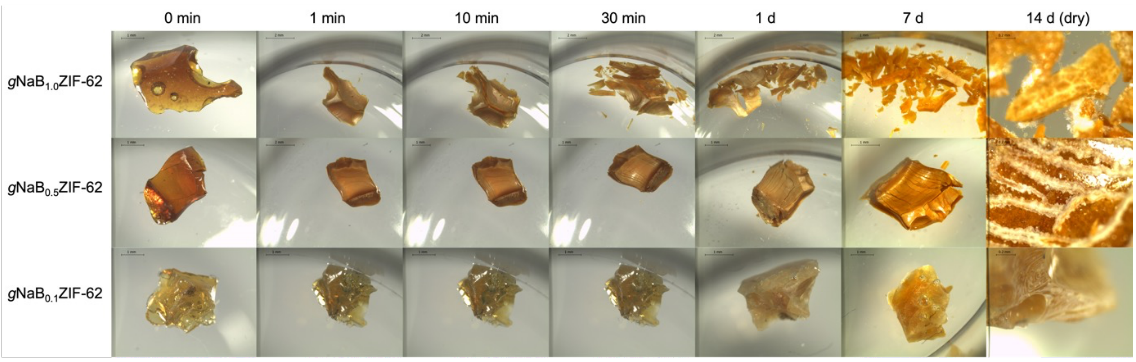

Figure A2.100. Microscope images of gNaB$_x$ZIF-62 ($x = 1.0, 0.5, 0.1$) displaying their reaction with water over a period of two weeks. The images on the right show a zoom into the reaction products after water evaporation (after 14 days). Phase separation into a water-soluble colourless phase (presumably hydrated Na(bim)/Na(im)) and a water-insoluble dark yellowish ZIF glass phase is evident. After 14 days, the remaining liquid was evaporated at room temperature (far-right image). The remaining solid material was washed with water and investigated by PXRD (see Figure A2.102).

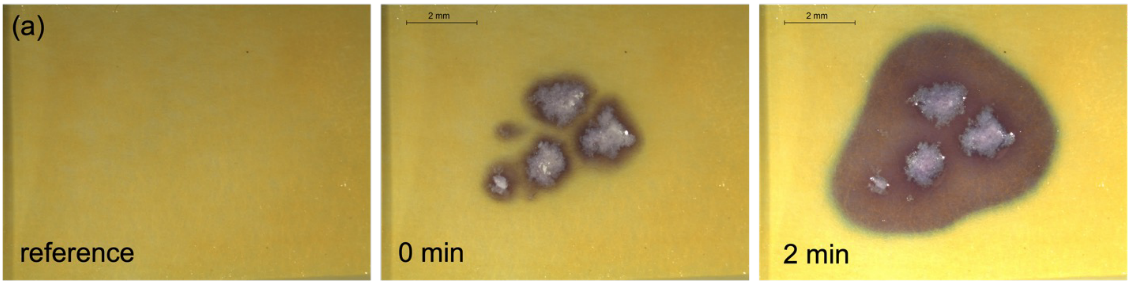

Figure A2.101. Microscope images of the reaction of powdered gNaB$_{0.3}$ZIF-62 on wetted pH indicator paper over the course of 2 minutes. The pH indicator covers a pH range from pH 7 (yellow), pH 10 (green) up to pH 14 (dark brown).

A2.18.2 X-Ray Diffraction Measurements

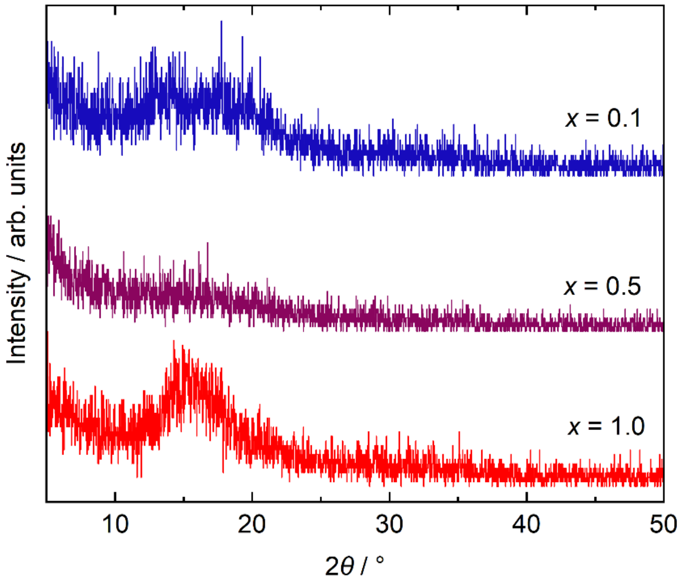

Figure A2.102. PXRD patterns of gNaB$_x$ZIF-62 materials with modifier contents x after two weeks of water treatment and subsequent washing with water (see Figure A2.100). Diffraction patterns were recorded with CuK$_\alpha$ radiation.

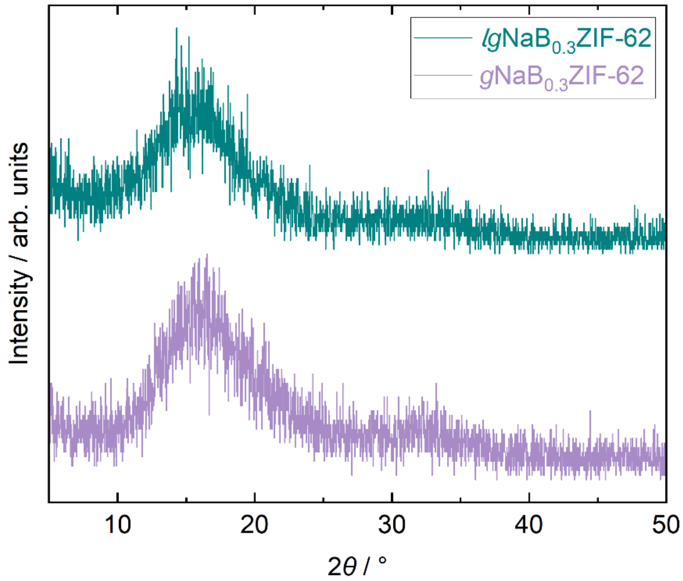

Figure A2.103. PXRD pattern of gNaB$_{0.3}$ZIF-62 before and after (lgNaB$_{0.3}$ZIF-62) the water treatment. Diffraction patterns were recorded with CuK$_\alpha$ radiation.

A2.18.3 Solution ^{1}H NMR Spectroscopy

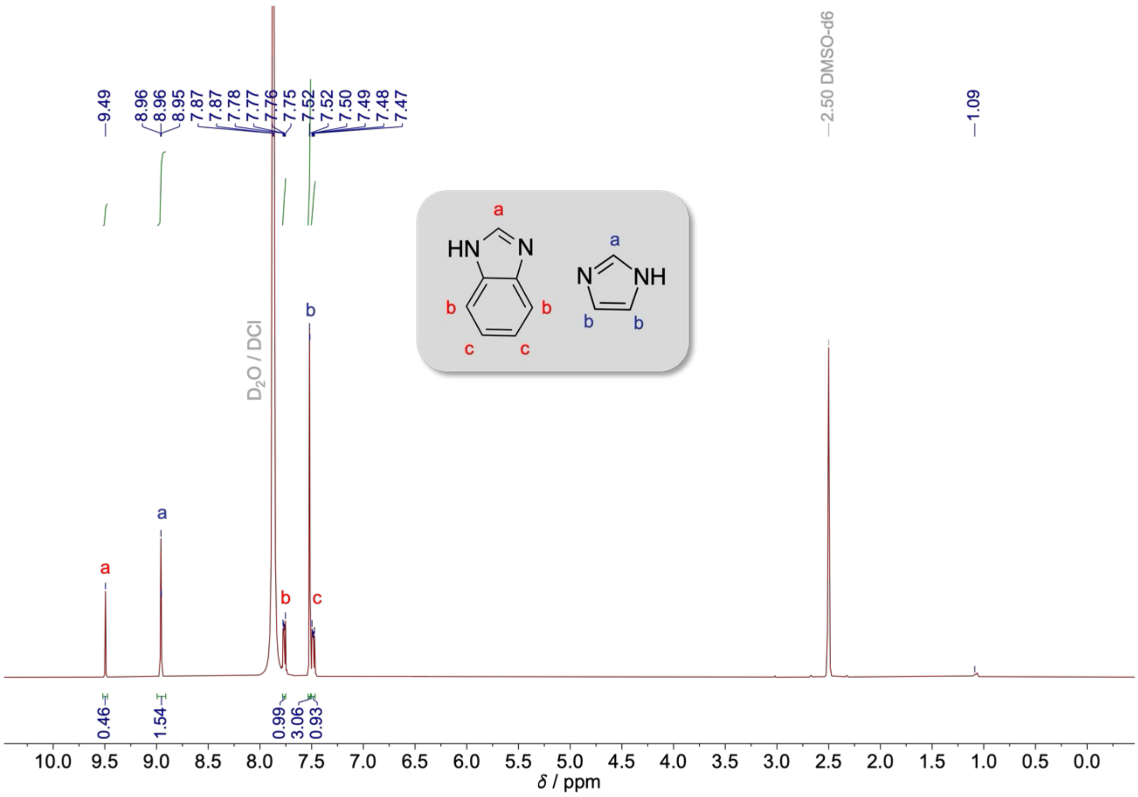

Figure A2.104. ^{1}H NMR spectrum of lgNaB$_{0.3}$ZIF-62 obtained via water-leaching of gNaB$_{0.3}$ZIF-62. The integrated signals suggest a chemical composition of Zn(im)$_{1.5}$(bim)$_{0.5}$ under the assumption of complete sodium ion removal. The material was dissolved in DMSO-d_6 and DCl/D_2O (35 wt%, one drop, <0.1 mL).

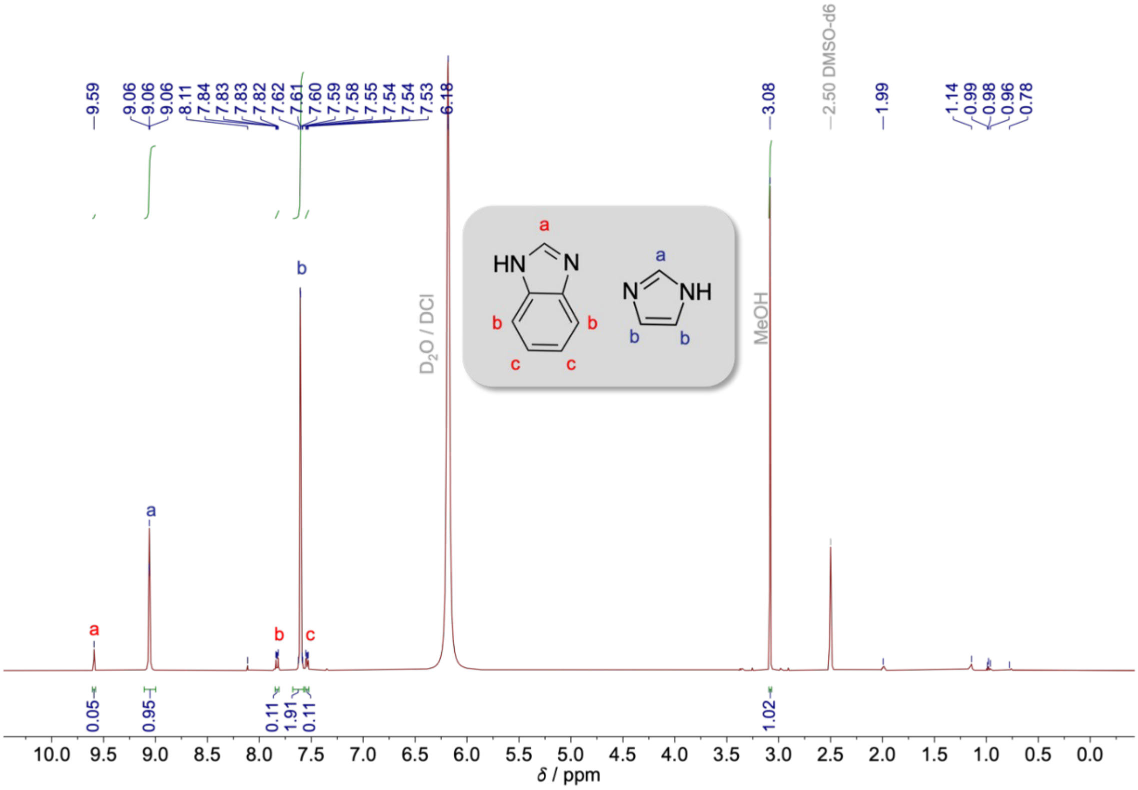

Figure A2.105. ^{1}H NMR spectrum of the leaching products obtained from the washing solution (H_2O, MeOH) as the result of the preparation of *lg*Na$B_{0.3}$ZIF-62 (prepared in ∼250 mg scale. After solvent removal in a rotary evaporator at 60 °C the remaining solid material was dissolved in DMSO-d_6 and DCl/D_2O (35 wt%, one drop, <0.1 mL).

A2.18.4 SEM Imaging

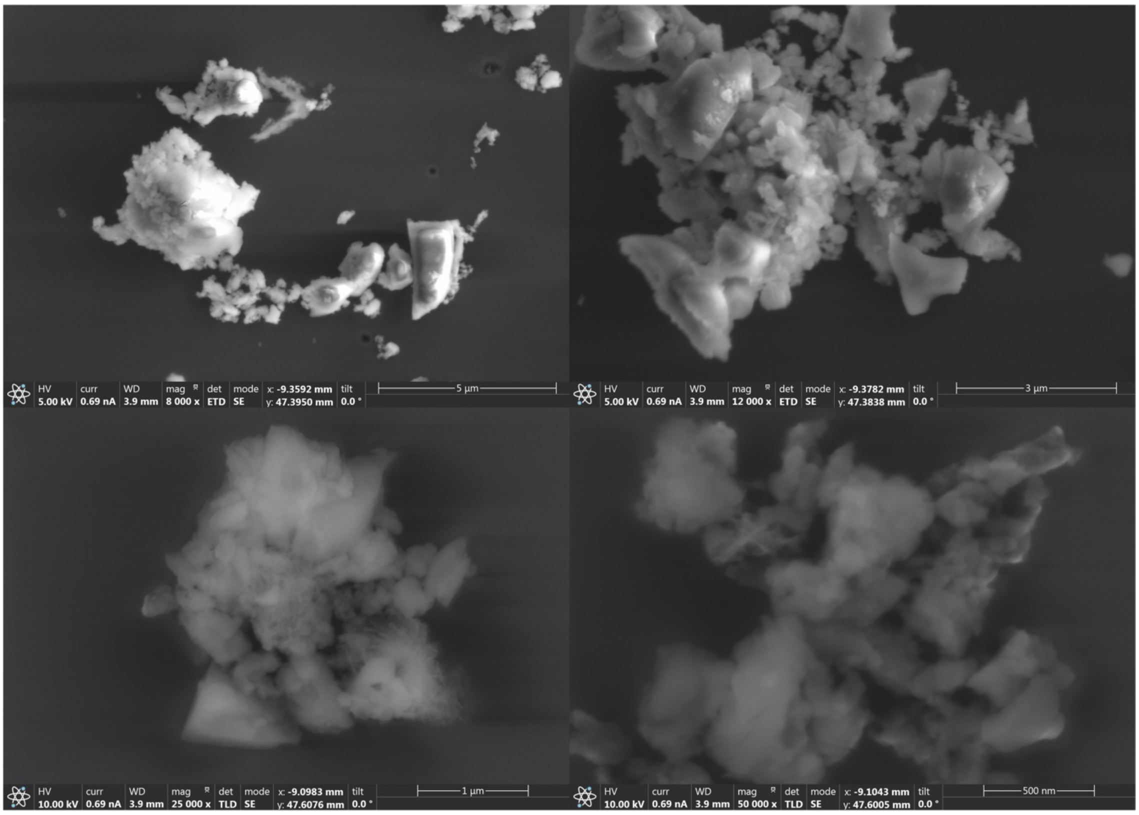

Figure A2.106. SEM images of lgNaB$_{0.3}$ZIF-62 with different magnifications.

A2.18.5 Infrared Spectroscopy

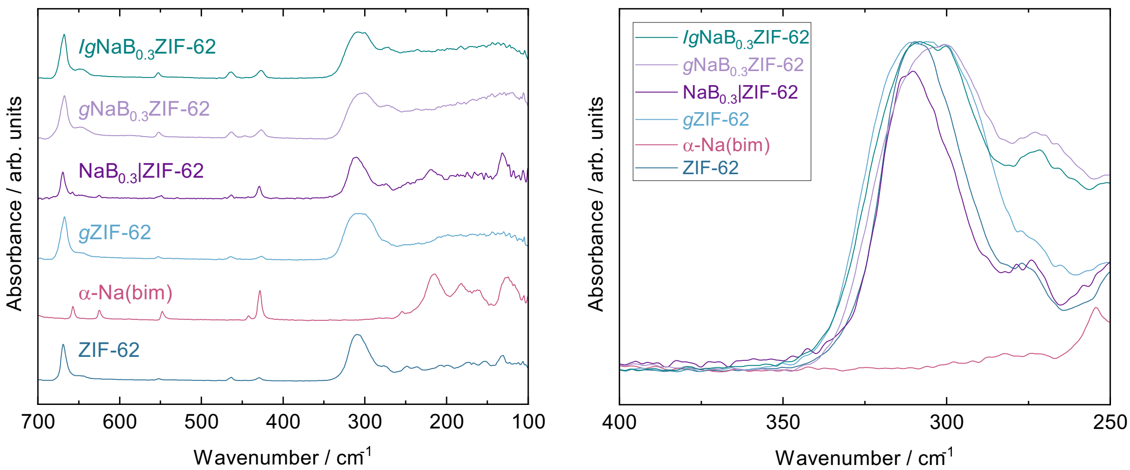

Figure A2.107. Far-infrared spectra of ZIF-62, the corresponding glass gZIF-62, the modifier α-Na(bim), the physical mixture of modifier and glass former NaB$_{0.3}$|ZIF-62, the corresponding glass of the physical mixture gNaB$_{0.3}$ZIF-62 and the glass after the water-leaching treatment lgNaB$_{0.3}$ZIF-62. The figure on the right shows a zoom into the wavenumber range of the [ZnN$_4$] tetrahedra vibration.

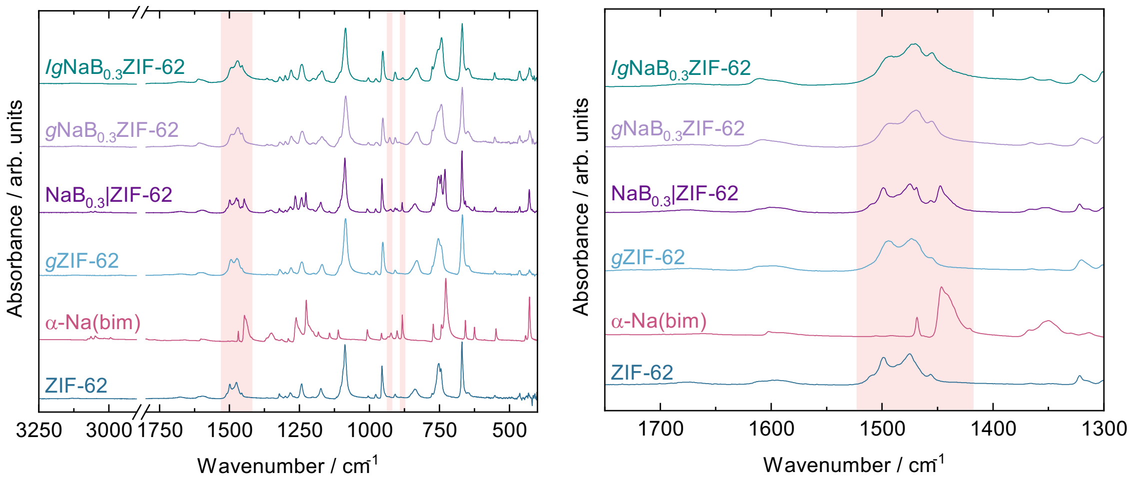

Figure A2.108. Mid-infrared spectra of ZIF-62, the corresponding glass gZIF-62, the modifier α-Na(bim), the physical mixture of modifier and glass former $NaB_{0.3}$|ZIF-62, the corresponding glass of the physical mixture $g NaB_{0.3}$ZIF-62 and the glass after the water-leaching treatment $lg NaB_{0.3}$ZIF-62. The figure on the right shows a zoom into the wavenumber range from 1800 to 1300 cm^{-1}.

A2.18.6 X-Ray Pair Distribution Function Analysis

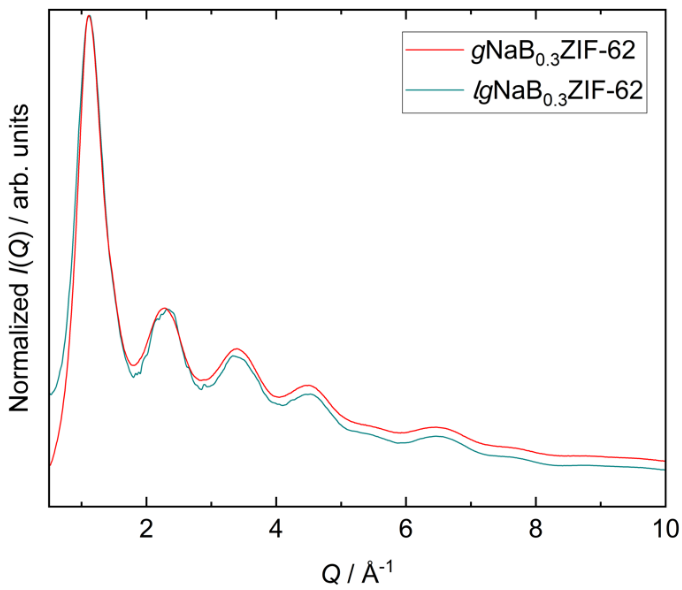

Figure A2.109. Normalized, background-subtracted and scattering-corrected diffraction data collected for the PDF analysis of $g NaB_{0.3}$ZIF-62 and $lg NaB_{0.3}$ZIF-62. The data show no shift in the FSDP after water leaching.

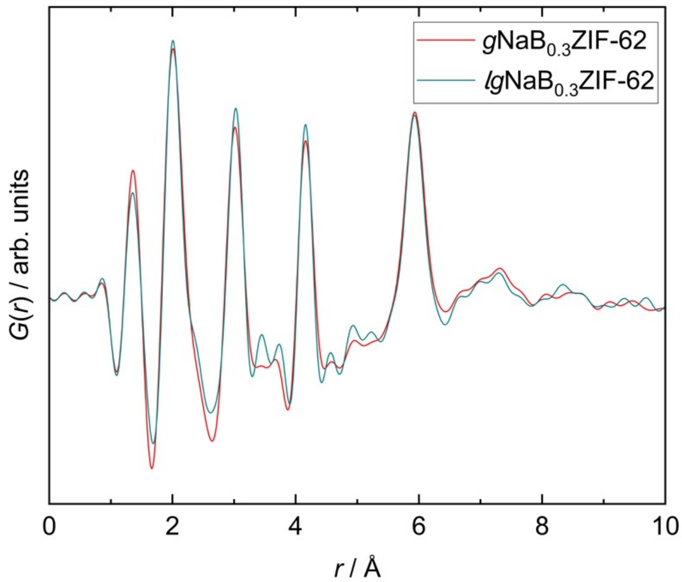

Figure A2.110. X-ray pair distribution function in the form of $G(r)$ for gNaB$_{0.3}$ZIF-62 and lgNaB$_{0.3}$ZIF-62 in an arbitrary scale. The extracted PDFs show a strong similarity between both materials as the water leaching primarily removes Na(im) from the materials, which exhibits a low scattering cross-section.

A2.18.7 Differential Scanning Calorimetry

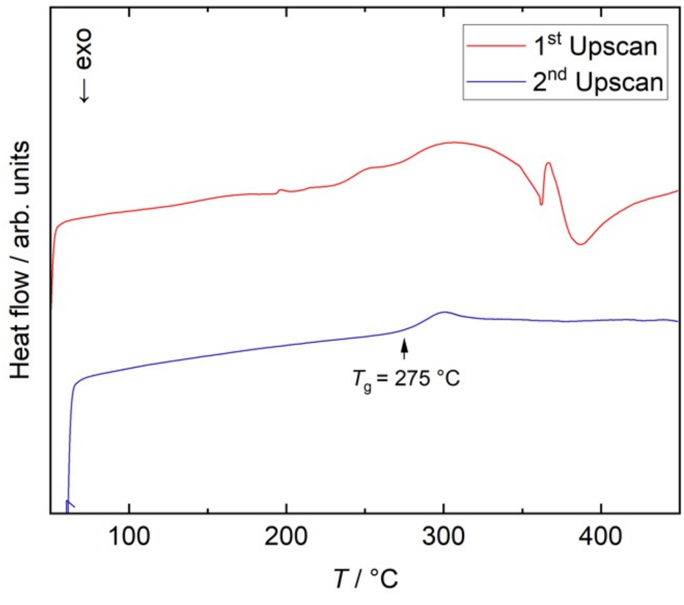

Figure A2.111. Heat flow curves of consecutive thermal upscans of lgNaB$_{0.3}$ZIF-62. An isothermal segment of 30 mins was applied after the first upscan to improve homogenization. Heating and cooling were performed at a constant rate of $\pm 10\,\mathrm{K\,min^{-1}}$.

A2.18.8 (Physi-) Gassorption Experiments

Dual-site Langmuir isotherms were fitted to the desorption branches of the CO_2 sorption isotherms measured at 195 K.[281] This enables the extrapolation of the isotherms to higher relative pressures as accessible experimentally. In the dual-site Langmuir isotherm (Equation A2.7) the relationship between the uptake N_{ads} and the pressure p is expressed via two equilibrium constants K_1 and K_2 and the corresponding maximum adsorption capacities N_1 and N_2:

$$N_{\mathrm{ads}} = \frac{K_1 \cdot p}{1 + \frac{K_1 \cdot p}{N_1}} + \frac{K_2 \cdot p}{1 + \frac{K_2 \cdot p}{N_2}} \tag{A2.7}$$

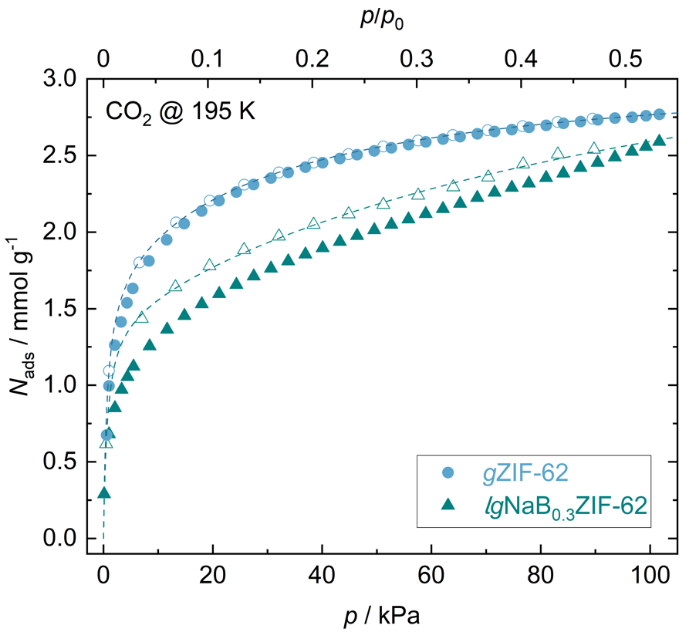

Figure A2.112. CO_2 gas sorption isotherm of *g*ZIF-62, *g*NaB$_{0.3}$ZIF-62 and water-leached *lg*NaB$_{0.3}$ZIF-62 collected at a temperature of 195 K. The dashed lines correspond to a dual-site Langmuir model (6) fitted to the desorption branches of both gas sorption isotherms. The fitting parameters are shown in Table A2.15.

Table A2.15. Parameters obtained from the fitting of the dual-site Langmuir isotherms as shown in Equation A2.7 to the desorption branches of *g*ZIF-62 and *lg*NaB$_{0.3}$ZIF-62 in the gas sorption measurements performed with CO_2 at 195 K.

Material	K_1/ mmol g^{-1} kPa^{-1}	K_2/ mmol g^{-1} kPa^{-1}	N_1/ mmol g^{-1}	N_2/ mmol g^{-1}
*g*ZIF-62	0.045 ± 0.002	2.64 ± 0.05	1.38 ± 0.01	1.72 ± 0.02
*lg*NaB$_{0.3}$ZIF-62	0.021 ± 0.002	2.11 ± 0.13	2.47 ± 0.19	1.45 ± 0.04

At 195 K, CO_2 sorption is limited to a maximum p/p_0 of 0.53.[185–187] This means only micropores can be quantified under these conditions, while larger mesopores are not fully filled with the adsorbate. The virtual CO_2 capacity at saturation ($p/p_0 = 1$), $N_{\text{sat,virt}} = N_1 + N_2$, can be estimated from the saturation capacities N_1 and N_2 derived from the isotherm fits. $N_{\text{sat,virt}}$ is about 26% higher for *lg*NaB$_{0.3}$ZIF-62 ($N_{\text{sat,virt}} = 3.9$ mmol g^{-1}) compared to *g*ZIF-62 ($N_{\text{sat,virt}} = 3.1$ mmol g^{-1}). This reflects the substantially higher overall porosity of *lg*NaB$_{0.3}$ZIF-62 compared to *g*ZIF-62, which is also evident from *n*-butane sorption recorded at 273 K (see Figure 5 in the main manuscript). The experimental n-butane capacity close to saturation ($p/p_0 = 0.95$), $N_{\text{sat,exp}}$, similarly is 26% higher for *lg*NaB$_{0.3}$ZIF-62 ($N_{\text{sat,exp}} = 0.77$ mmol g^{-1}) compared to *g*ZIF-62 ($N_{\text{sat,exp}} = 0.61$ mmol g^{-1}).

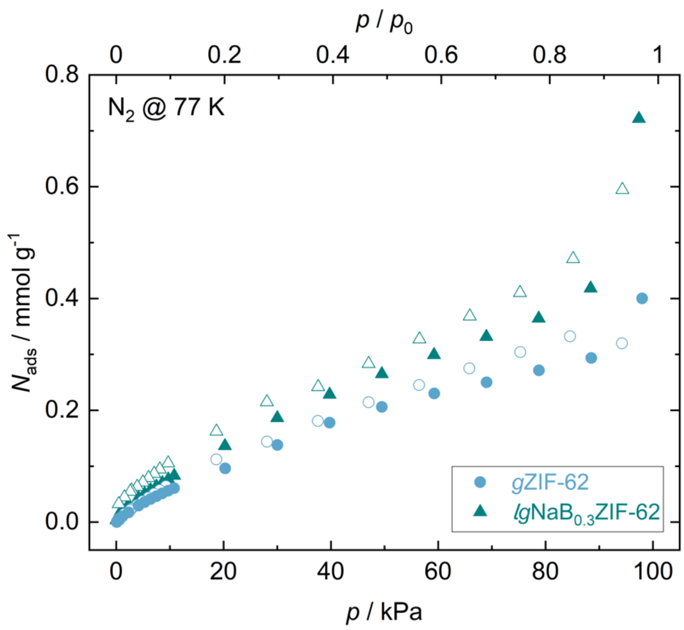

Figure A2.113. N_2 gas sorption isotherm of *g*ZIF-62 and *lg*NaB$_{0.3}$ZIF-62 after the water leaching treatment collected at a temperature of 77 K.

Table A2.16. Maximum gas uptake $N_{ads,max}$ for *g*ZIF-62 and *g*$NaB_{0.3}$ZIF-62 prior to and after the water leaching (*lg*$NaB_{0.3}$ZIF-62) for different gases and at different temperatures. The given values correspond to the maximum uptake of CO_2 (at $p/p_0 \approx 0.53$), N_2 (at $p/p_0 \approx 0.90$), *n*-butane (at $p/p_0 \approx 0.95$) and propene (at $p/p_0 \approx 0.21$) in the corresponding gas sorption isotherm (see Figures A2.112–A2.113 and Figure 6.5.

Material	N_{ads}/mmol g^{-1}		
	CO_2 (195 K)	N_2 (77 K)	C_4H_{10} (273 K)
*g*ZIF-62	2.77	0.29	0.61
lg$NaB_{0.3}$ZIF-62	2.59	0.42	0.77
g$NaB_{0.3}$ZIF-62	2.27	–	–

A2.18.9 Atmospheric Stability

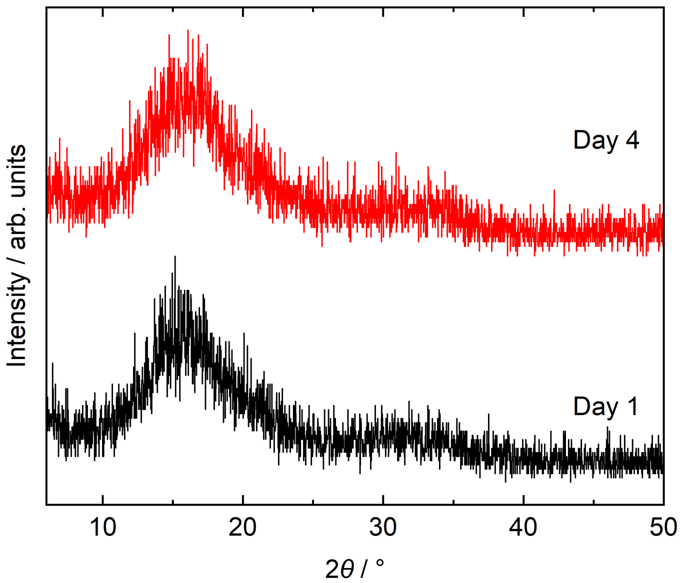

Figure A2.114. PXRD pattern of *g*$NaB_{0.3}$ZIF-62 before and after exposure to the atmosphere for four days. Diffraction patterns were recorded with CuK_α radiation. The scattered intensity indicates no change in the amorphous state of the material due to the exposure to atmospheric water.

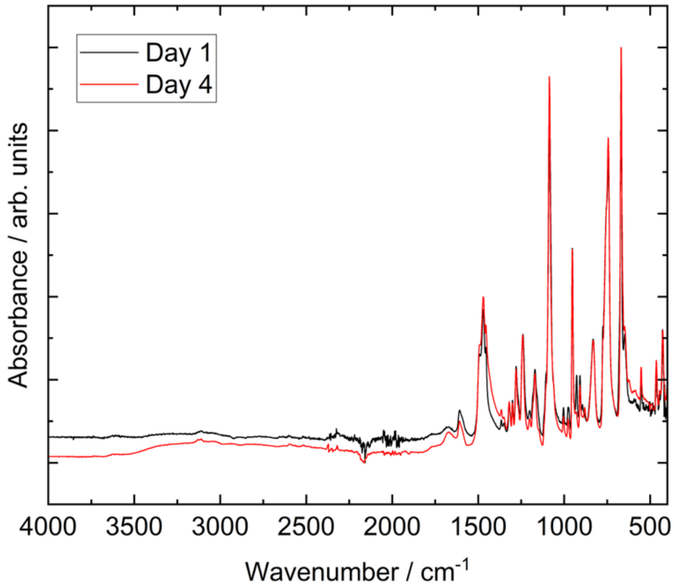

Figure A2.115. Mid-infrared spectra of gNaB$_{0.3}$ZIF-62 before and after exposure to the atmosphere for four days. The increased intensity in the region between 2500 cm^{-1} and 3500 cm^{-1} is assigned to the OH stretch vibration of adsorbed atmospheric water. The sample mass increased by 3% over the course of 4 days due to the adsorption of water.

A2.19 Lithium Benzimidazolate Modification

Lithium benzimidazolate (Li(bim)) was synthesised according to an earlier publication.[137] Further steps in the preparation of the modified glasses via melt-quenching are analogous to the preparation of the Na(bim)-modified ZIF-62 glasses (see Methods Section in the main manuscript). The gLiB$_x$|ZIF-62 materials in this work were prepared in a DSC crucible (10 mg scale) and with a maximum temperature of 425 °C during the isothermal segment in the corresponding temperature program. Manual handling of the materials was performed in a glovebox under an inert atmosphere to prevent the hygroscopic materials from reacting with atmospheric water.

A2.19.1 Infrared Spectroscopy

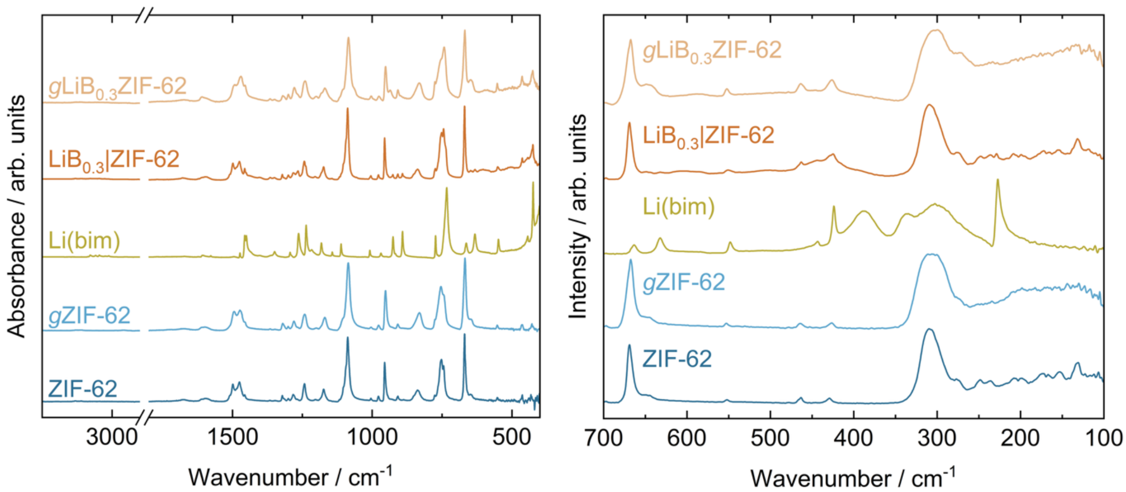

Figure A2.116. Mid-infrared spectra (left) and far-infrared spectra (right) of ZIF-62, the corresponding glass gZIF-62, the modifier Li(bim), the physical mixture of modifier and glass former LiB$_{0.3}$|ZIF-62 and the corresponding glass of the physical mixture gLiB$_{0.3}$ZIF-62.

A2.19.2 Microscope Images

Figure A2.117. Optical microscopy images of shards of gLiB$_x$ZIF-62 materials with different Li(bim) contents x. The glasses were prepared in a 10 mg scale in a DSC apparatus.

A2.19.3 Powder X-ray Diffraction

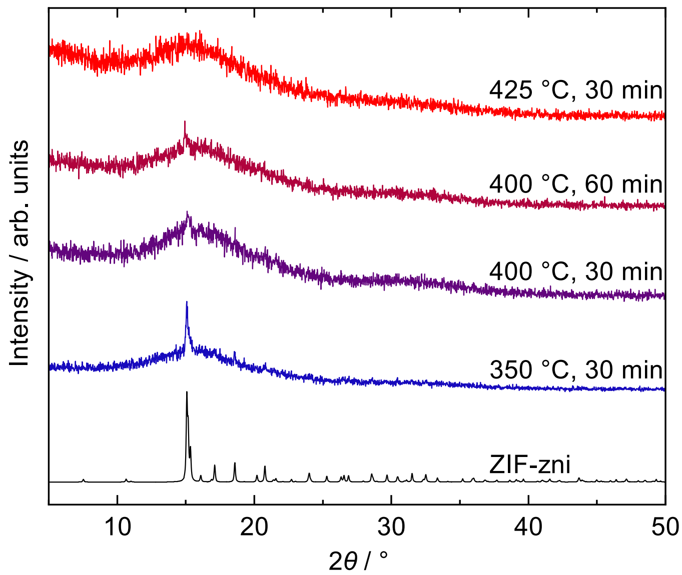

Figure A2.118. PXRD patterns of $LiB_{0.3}$|ZIF-62 after different temperature treatments consisting of a heating segment from room temperature up to a maximum temperature, followed by an isothermal segment of several minutes and subsequent cooling back to room temperature. The heating and cooling were performed at a constant rate of $10\,°C\,min^{-1}$. The maximum temperature and time of the isothermal segment are given next to the corresponding PXRD patterns of the materials after the temperature treatment. The PXRD patterns were recorded with CuK_α radiation under air. The black pattern (bottom) corresponds to a simulated diffraction pattern of ZIF-zni (CCDC: IMIDZB).

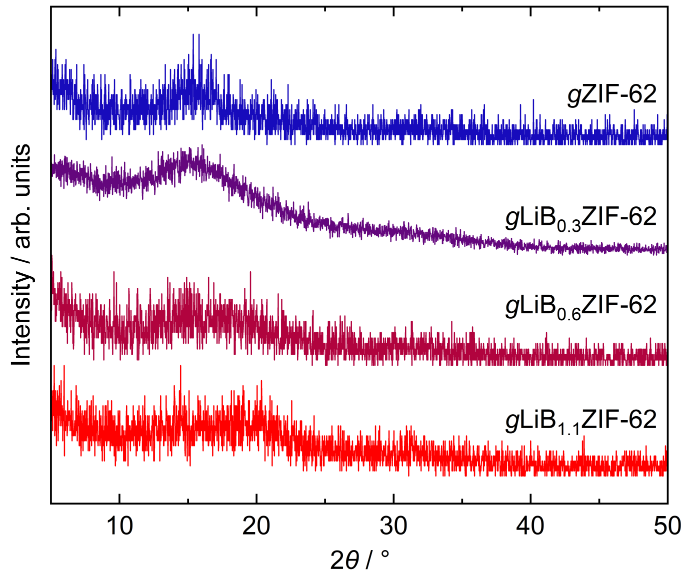

Figure A2.119. PXRD patterns of gLiB$_x$ZIF-62 materials after the melt-quenching procedure performed in a DSC apparatus (~10 mg scale) consisting of a heating segment from room temperature up to 425 °C, followed by an isothermal segment of 30 min and subsequent cooling back to room temperature. The heating and cooling were performed at a constant rate of 10 °C min^{-1}. Diffraction patterns were recorded with CuK$_\alpha$ radiation under air.

A2.19.4 Solution ^{1}H NMR Spectroscopy

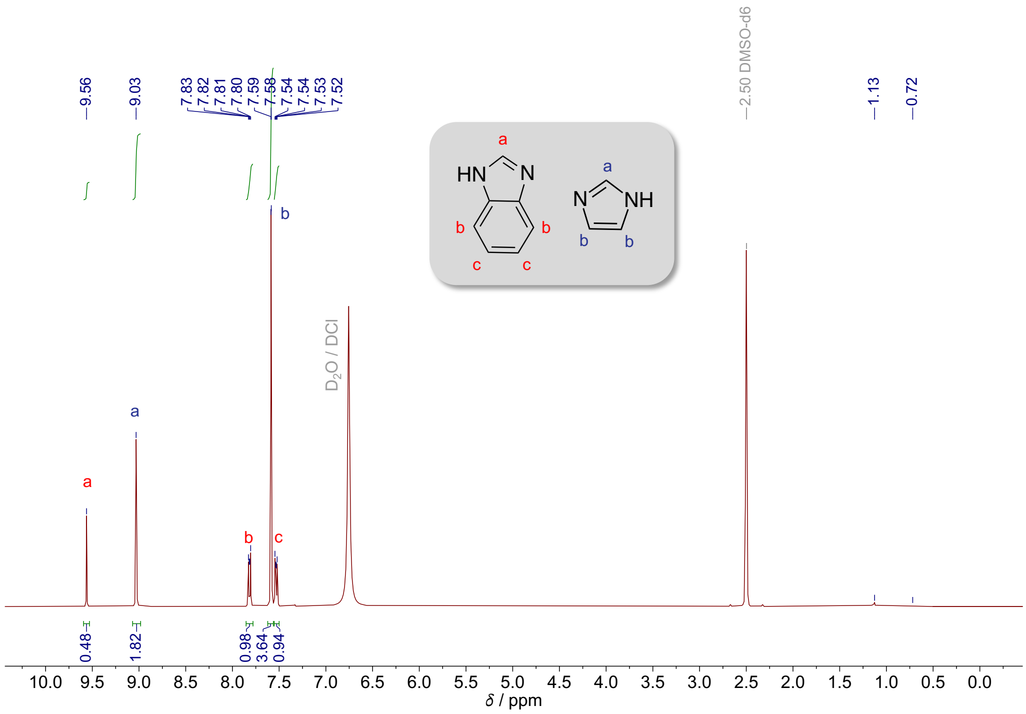

Figure A2.120. ^{1}H NMR spectrum of gLiB$_{0.3}$ZIF-62 (prepared in ~10 mg scale) dissolved in DMSO-d_6 and DCl/D$_2$O (35 wt%, one drop, <0.1 mL). Signals at 1.13 ppm are assigned to residues of n-hexane, which was added during the grinding of the obtained glass monolith.

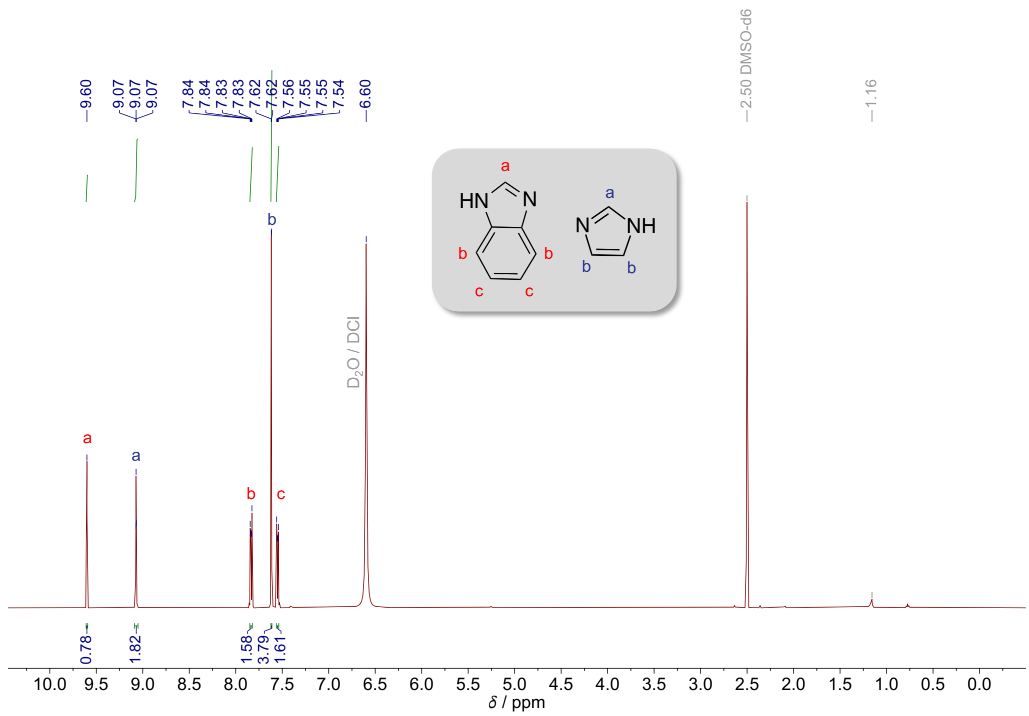

Figure A2.121. [1]H NMR spectrum of gLiB$_{0.6}$ZIF-62 (prepared in ~10 mg scale) dissolved in DMSO-d_6 and DCl/D_2O (35 wt%, one drop, <0.1 mL). Signals at 1.13 ppm are assigned to residues of n-hexane, which was added during the grinding of the obtained glass monolith.

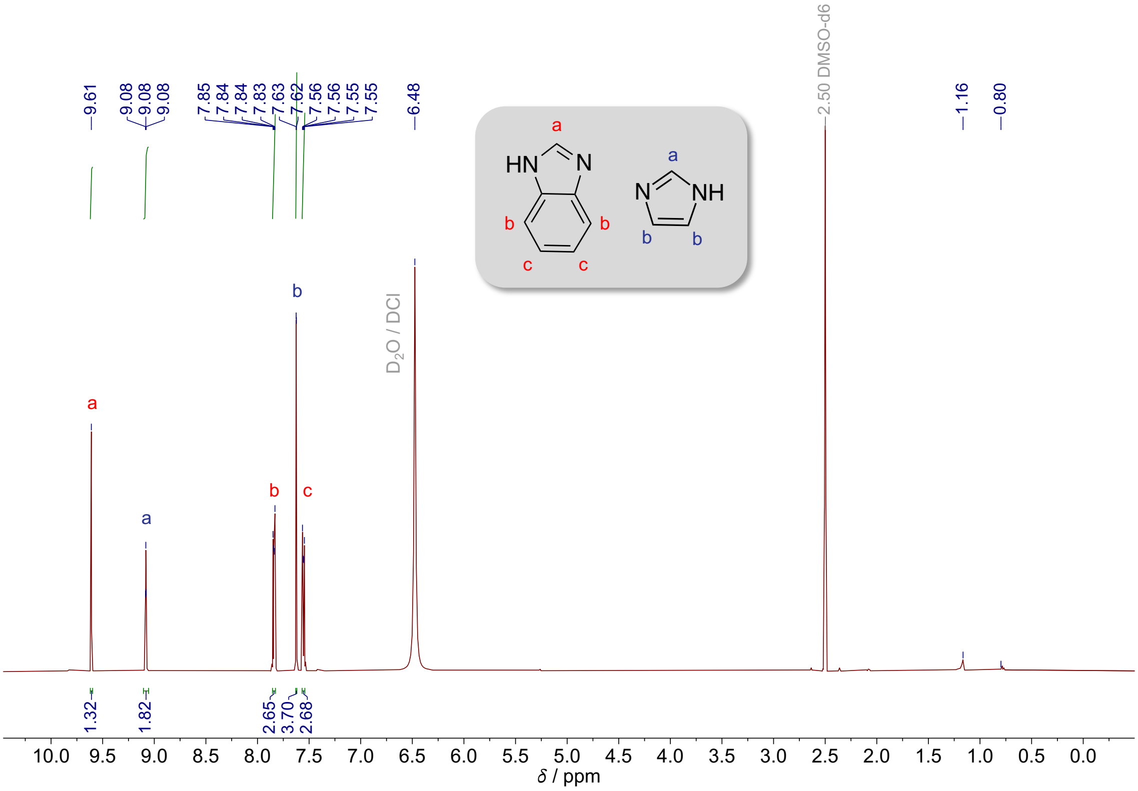

Figure A2.122. ^{1}H NMR spectrum of gLiB$_{1.1}$ZIF-62 (prepared in ~10 mg scale) dissolved in DMSO-d_6 and DCl/D_2O (35 wt%, one drop, <0.1 mL). Signals at 1.13 ppm are assigned to residues of n-hexane, which was added during the grinding of the obtained glass monolith.

Table A2.17. Name and chemical composition of prepared Li(bim)-modified ZIF-62 glasses gLiB$_x$ZIF-62 for different Li(bim) contents x and ZIF-62. The chemical composition was calculated according to the bim/im ratio obtained from solution ^{1}H NMR spectroscopy measurements of the glass samples digested in DMSO-d_6 and DCl/D_2O (35 wt%, one drop, <0.1 mL). The thus calculated Li(bim) content $x(^1H$ NMR) does not necessarily coincide with the x used in the nomenclature (gLiB$_x$ZIF-62) due to rounding. It is assumed that the x values in the nomenclature are in accordance with the solution ^{1}H NMR results with regard to the error margin of the NMR measurement. The chemical composition of the corresponding physical mixtures LiB$_x$|ZIF-62 is expected to be identical to those of the respective glasses. Deviations between the intended chemical composition and the composition found in ^{1}H NMR spectroscopy may be attributed to weighing errors during the preparation of the physical mixtures and measurement inaccuracies of ^{1}H NMR spectroscopy.

Approach	Name	bim^-	im^-	Composition	x
	gLiB$_{0.3}$ZIF-62	0.48		$Li_{0.30}Zn(im)_{1.82}(bim)_{0.48}$	0.30
10 mg scale	gLiB$_{0.6}$ZIF-62	0.78	1.82	$Li_{0.60}Zn(im)_{1.82}(bim)_{0.78}$	0.60
	gLiB$_{1.1}$ZIF-62	1.32		$Li_{1.14}Zn(im)_{1.82}(bim)_{1.32}$	1.14

A2.19.5 Differential Scanning Calorimetry

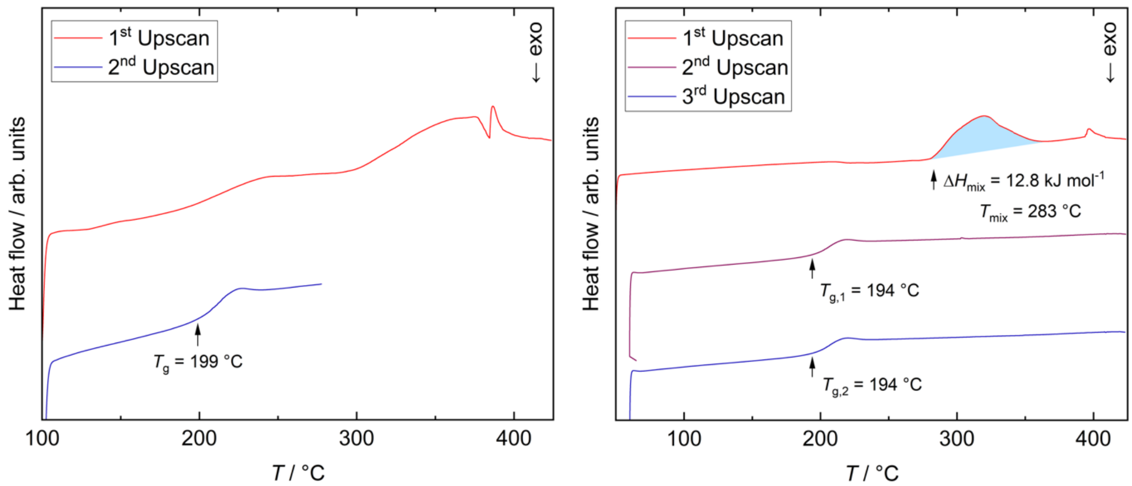

Figure A2.123. Heat flow curves of consecutive thermal upscans of LiB_x|ZIF-62 for $x = 0.3$ (left) and $x = 0.6$ (right) to a maximum temperature of 425 °C in the first upscan. An isothermal segment of 30 min was applied after the first upscan to improve homogenization. Heating and cooling were performed at a constant rate of ±10 °C min^{-1}. Enthalpies ΔH were calculated based on the mean molar mass of the corresponding physical mixture. Sharp features in the first upscan beyond 350 °C are considered artefacts resulting from crucible deformation under the autogenous pressure build-up. The arrows indicate the temperature of the glass transition T_g, and the temperature of the intermixing process T_{mix} during the reaction of ZIF-62 with Li(bim).

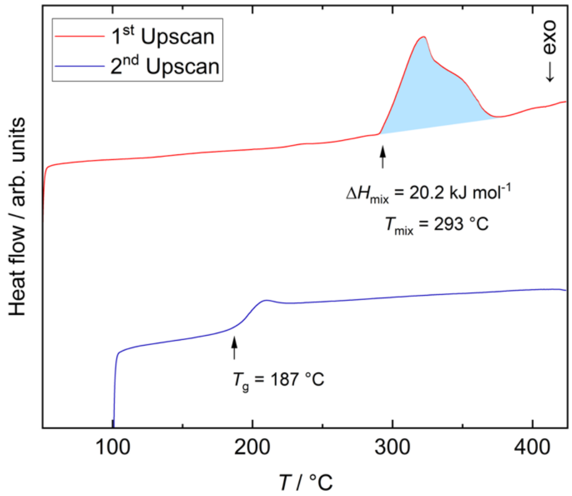

Figure A2.124. Heat flow curves of consecutive thermal upscans of LiB_x|ZIF-62 for $x = 1.1$ to a maximum temperature of 425 °C in the first upscan. An isothermal segment of 30 mins was applied after the first upscan to improve homogenization. Heating and cooling were performed at a constant rate of ±10 °C min^{-1}. Enthalpies ΔH were calculated based on the mean molar mass of the corresponding physical mixture. Sharp features in the first upscan beyond 350 °C are considered artefacts resulting from crucible deformation under the autogenous pressure build-up. The arrows indicate the temperature of the glass transition T_g, and the temperature of the intermixing process T_{mix} during the reaction of ZIF-62 with Li(bim).

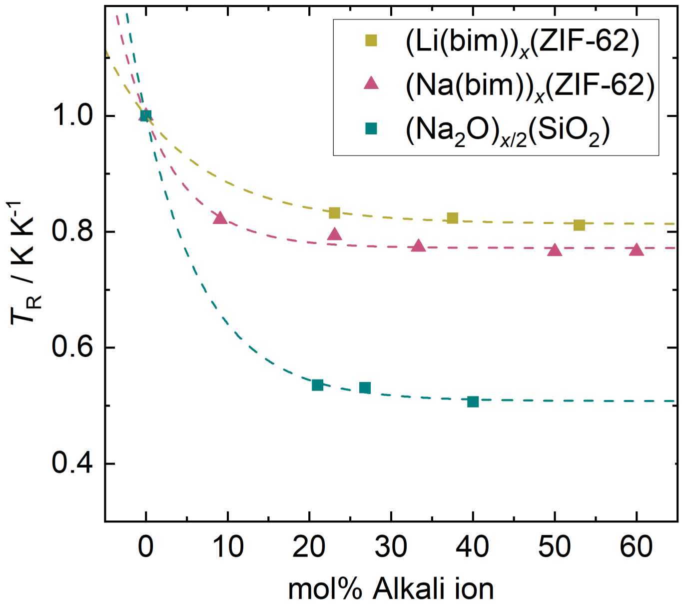

Figure A2.125. Trend in the reduced glass transition temperature T_R with $T_R = T_g/T_g$(glass former) for the investigated ZIF-62 glass systems and a comparison with sodium silicate glasses employing Na_2O as modifier. The temperatures for the sodium silicate glasses were taken from the literature.[244]

A2.19.6 Variable Temperature Powder X-ray Diffraction

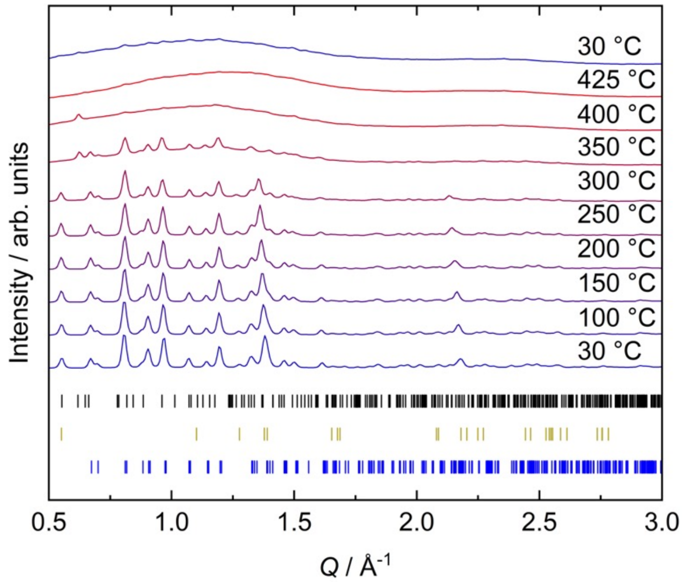

Figure A2.126. VT-PXRD patterns of a heating-cooling-cycle of $LiB_{1.1}$|ZIF-62 recorded with $\lambda = 0.1616$ Å at DLS starting with the heating from 30 °C (blue, bottom) up to 425 °C (red) and subsequent cooling back to 30 °C (blue, top). The tick marks correspond to the allowed Bragg peak positions of ZIF-62 (blue) as well as Li(bim) (light green) and ZIF-7-III (black)(CCDC: GIZJOP, KOLYAM). ZIF-7-III crystallises at 350 °C and dissolves in the ZIF melt above 400 °C.

A2.19.7 X-Ray Pair Distribution Function Analysis

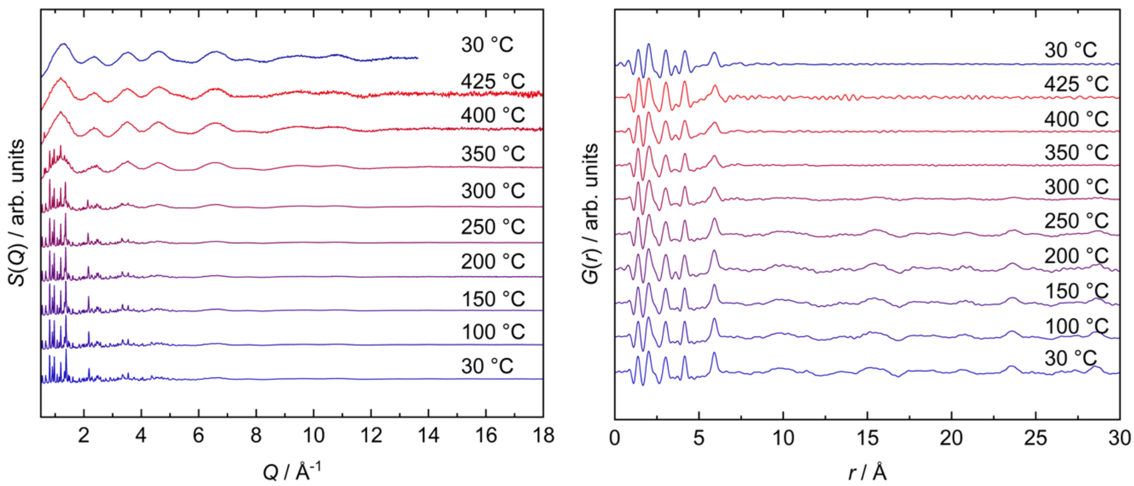

Figure A2.127. Structure function $S(Q)$ extracted from X-ray total scattering data for the physical mixtures $LiB_{1.1}$|ZIF-62 (left) with increasing temperature and after temperature-quenching (top-pattern in blue) together with the corresponding PDFs in the form of $G(r)$. Data collection was performed at DLS with a wavelength of 0.1616 Å. The overall low intensity and high noise level in the pattern of $LiB_{0.5}$|ZIF-62 (left) collected at 425 °C is the result of the liquid material moving out of the beam path.

A3 Appendix to Chapter 8

A3.1 Solution ^{1}H NMR Spectroscopy

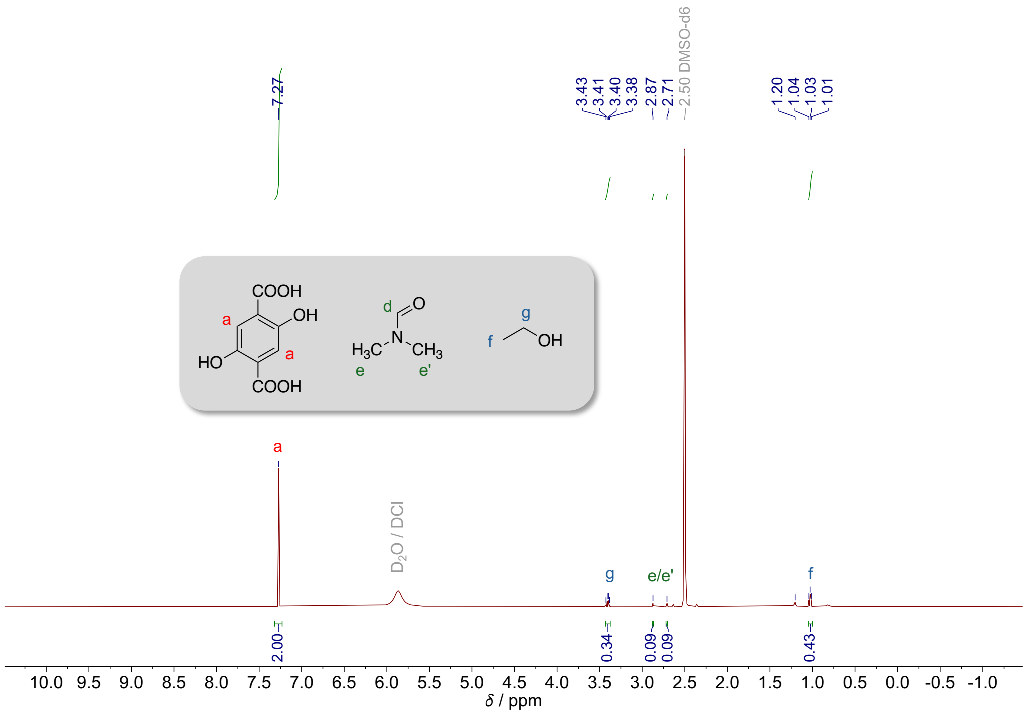

Figure A3.1. Solution ^{1}H NMR spectrum of MOF-74(Mg) digested in DCl/D_2O and DMSO-d_6. Additional signals are assigned to residual solvent molecules. The estimated chemical composition and degree of activation is summarized in Table A3.1.

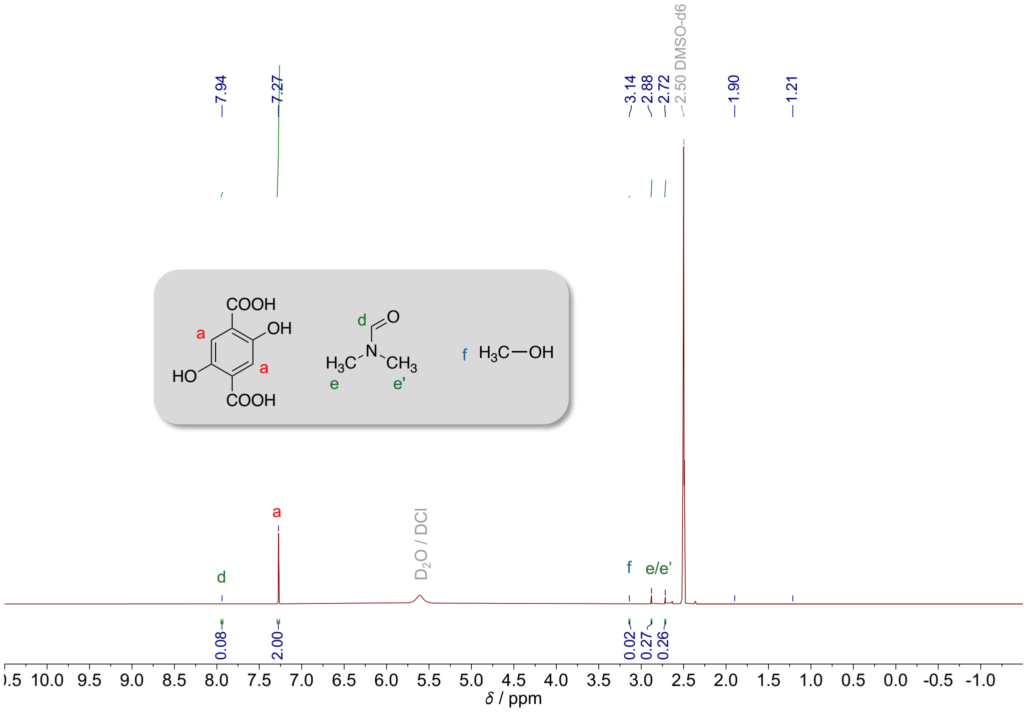

Figure A3.2. Solution ^{1}H NMR spectrum of MOF-74(Mn) digested in DCl/D_2O and DMSO-d_6. Additional signals are assigned to residual solvent molecules. The estimated chemical composition and degree of activation is summarized in Table A3.1.

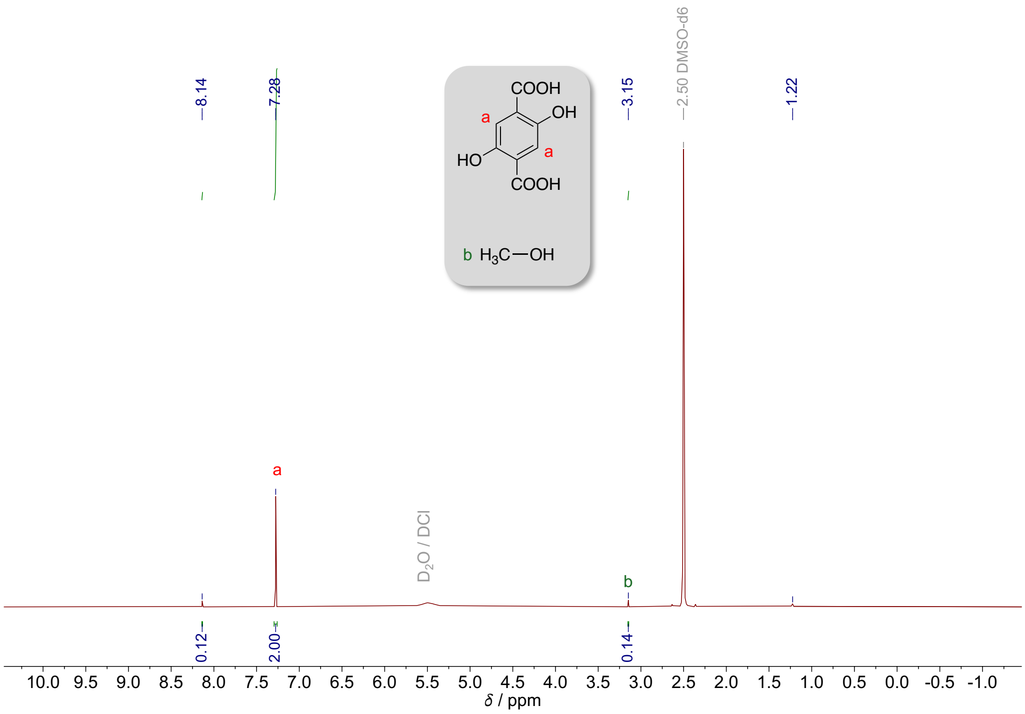

Figure A3.3. Solution ^{1}H NMR spectrum of MOF-74(Co) digested in DCl/D_2O and DMSO-d_6. Additional signals are assigned to residual solvent molecules. The estimated chemical composition and degree of activation is summarized in Table A3.1.

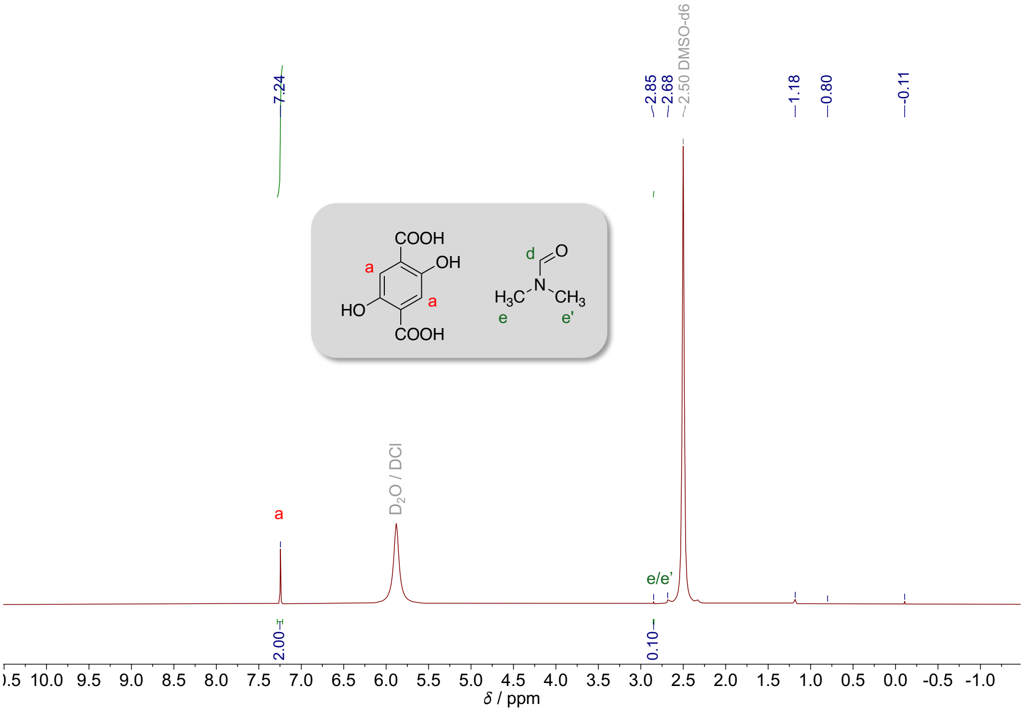

Figure A3.4. Solution ^{1}H NMR spectrum of MOF-74(Ni) digested in DCl/D_2O and DMSO-d_6. Additional signals are assigned to residual solvent molecules. The estimated chemical composition and degree of activation is summarized in Table A3.1.

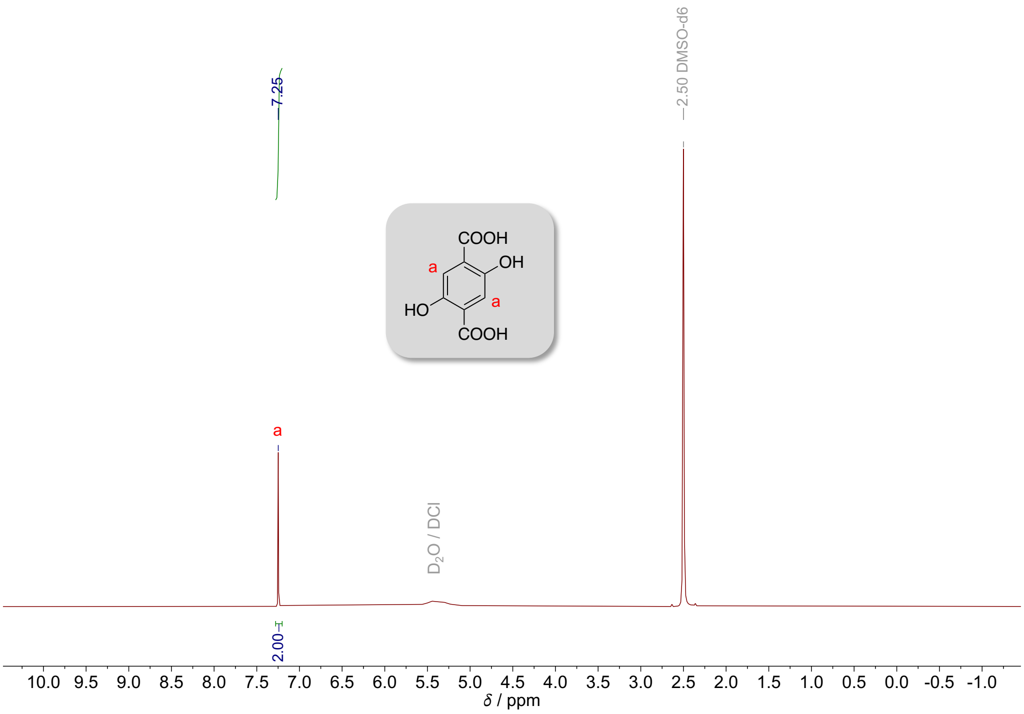

Figure A3.5. Solution ^{1}H NMR spectrum of MOF-74(Cu) digested in DCl/D_2O and DMSO-d_6. Additional signals are assigned to residual solvent molecules. The estimated chemical composition and degree of activation is summarized in Table A3.1.

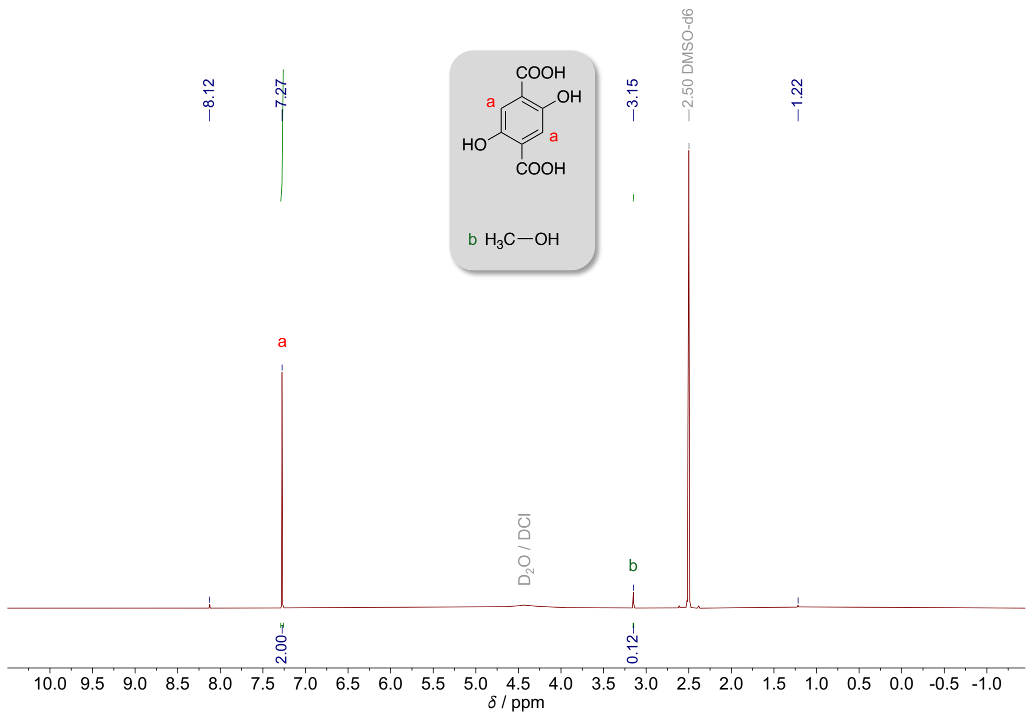

Figure A3.6. Solution ^{1}H NMR spectrum of MOF-74(Zn) digested in DCl/D_2O and DMSO-d_6. Additional signals are assigned to residual solvent molecules. The estimated chemical composition and degree of activation is summarized in Table A3.1.

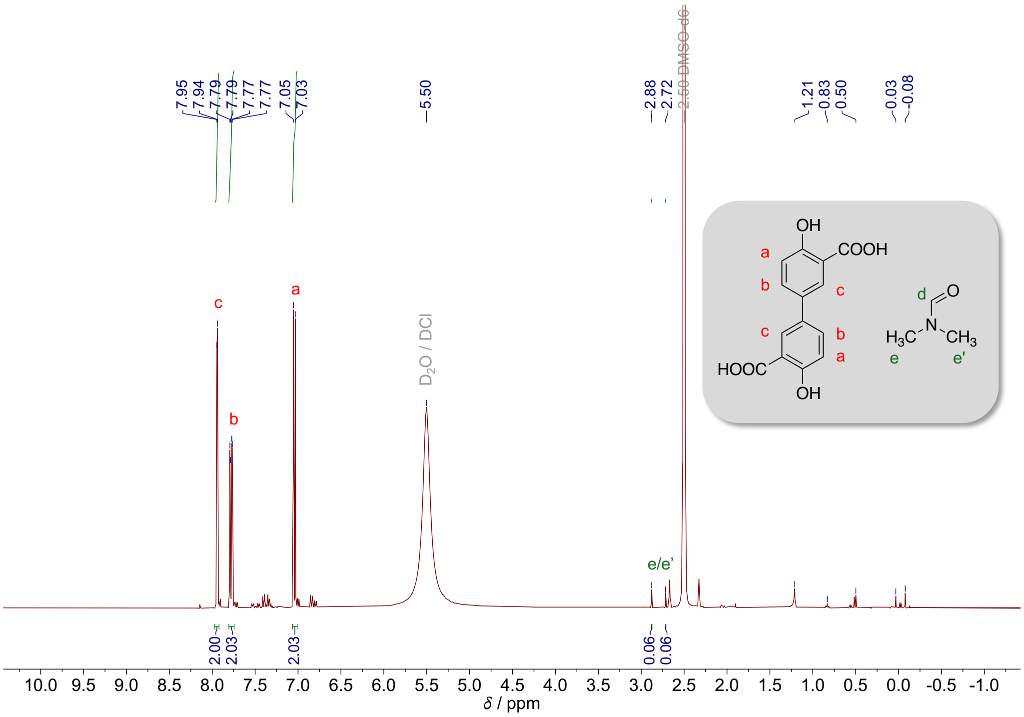

Figure A3.7. Solution ^{1}H NMR spectrum of Mg_2(dobpdc) digested in DCl/D_2O and DMSO-d_6. Additional signals are assigned to residual solvent molecules (DMF). The estimated chemical composition and degree of activation is summarized in Table A3.1. Unassigned signals in the aromatic region are considered solvent impurities (toluene, see Figure A3.10).

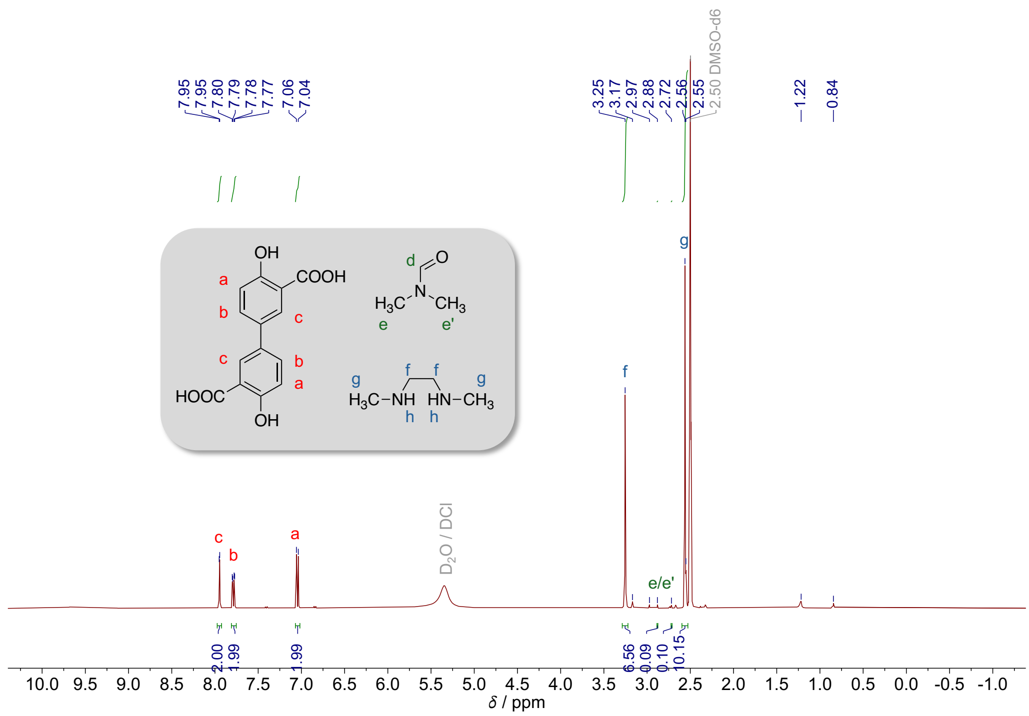

Figure A3.8. Solution ^{1}H NMR spectrum of mmen@Mg_2(dobpdc) digested in DCl/D_2O and DMSO-d_6. Additional signals are assigned to mmen or residual solvent molecules. The estimated chemical composition and degree of activation is summarized in Table A3.1.

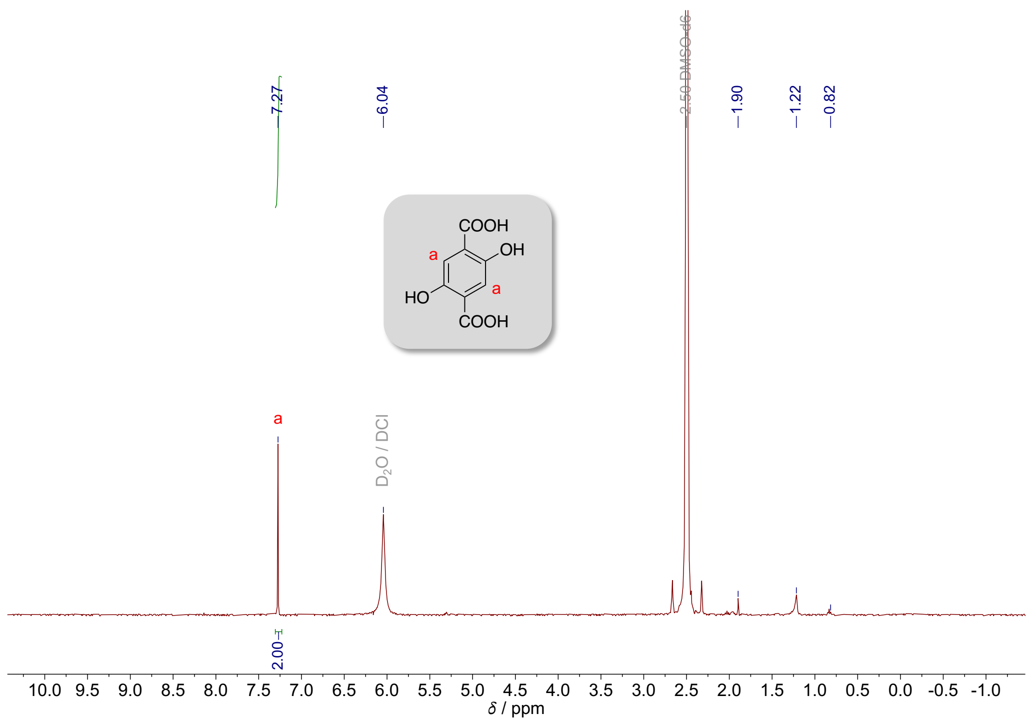

Figure A3.9. Solution ^{1}H NMR spectrum of H_4dobdc digested in DCl/D_2O and DMSO-d_6. Additional signals are assigned to solvent impurities.

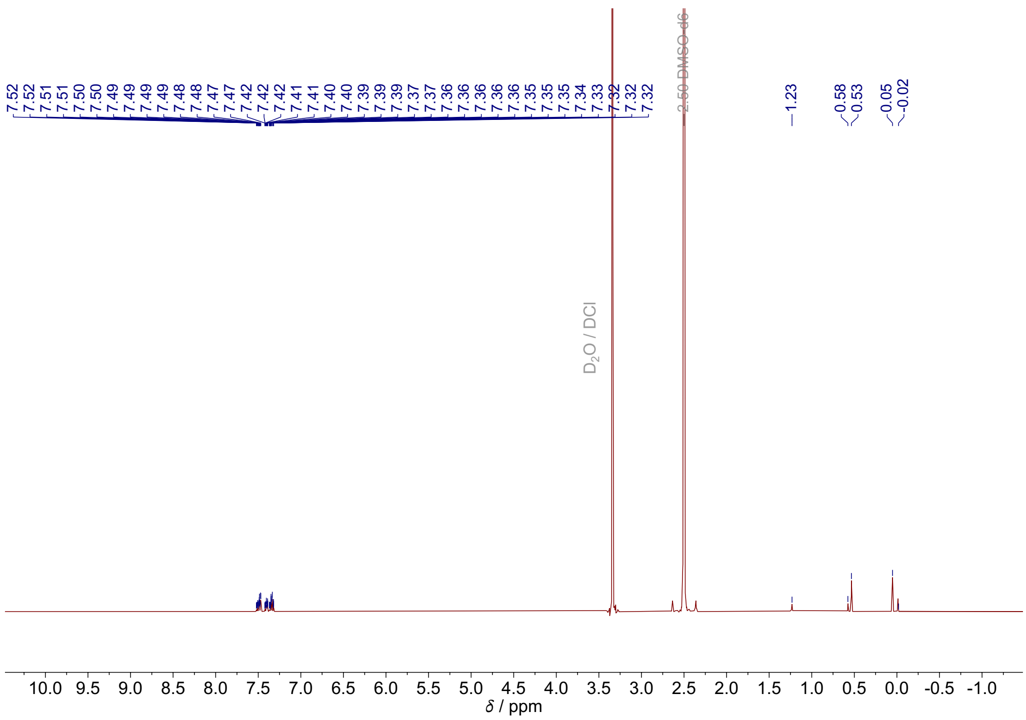

Figure A3.10. Solution ^{1}H NMR spectrum of the solvents used for the preparation of the ^{1}H NMR spectra of Mg_2(dobpdc) and mmen@Mg_2(dobpdc) (DCl/D_2O and DMSO-d_6). Residual signals (i.e., aromatic signals at 7.5 ppm and aliphatic signals in the range from $0 - 1.25$ ppm) are identified as solvent impurities (most prominently toluene).

Table A3.1. Chemical composition of the discussed materials obtained from solution ^{1}H NMR spectroscopy. The degree of activation (i.e., the relative number of unoccupied open metal sites) is estimated based on the amount of identified solvent residues.

Material	Chemical composition	Activation / %
Mg_2(dobdc)	Mg_2(dobdc)$(DMF)_{0.03}(EtOH)_{0.16}$	91
Mn_2(dobdc)	Mn_2(dobdc)$(DMF)_{0.09}(EtOH)_{0.01}$	95
Co_2(dobdc)	Co_2(dobdc)$(MeOH)_{0.05}$	98
Ni_2(dobdc)	Ni_2(dobdc)$(DMF)_{0.03}$	99
Cu_2(dobdc)	Cu_2(dobdc)	100
Zn_2(dobdc)	Zn_2(dobdc)$(MeOH)_{0.04}$	98
Mg_2(dobpdc)	Mg_2(dobpdc)$(DMF)_{0.02}$	99[a]
mmen@Mg_2(dobpdc)	Mg_2(dobpdc)$(DMF)_{0.03}(mmen)_{1.67}$	–

[a]Signals in the aromatic region which do not correspond to H_4(dobpdc) or solvent impurities are assigned to traces of organic decomposition products, diminishing the real degree of activation.

A3.2 Infrared Spectroscopy

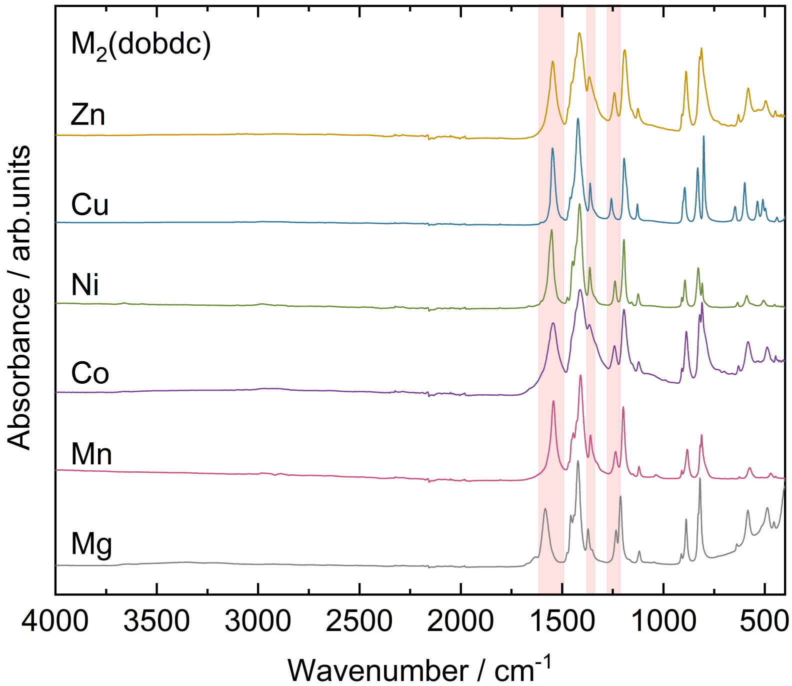

Figure A3.11. Mid-infrared spectra of MOF-74(M) materials with different metals incorporated (M). The highlighted vibrational bands correspond to the asymmetric ($\sim$1550 − 1600 cm^{-1}), and symmetric carboxylate stretching vibration ($\sim$1350 − 1370 cm^{-1}) as well as the phenolic carbon-oxygen stretching vibration ($\sim$1240 cm^{-1}).[174]

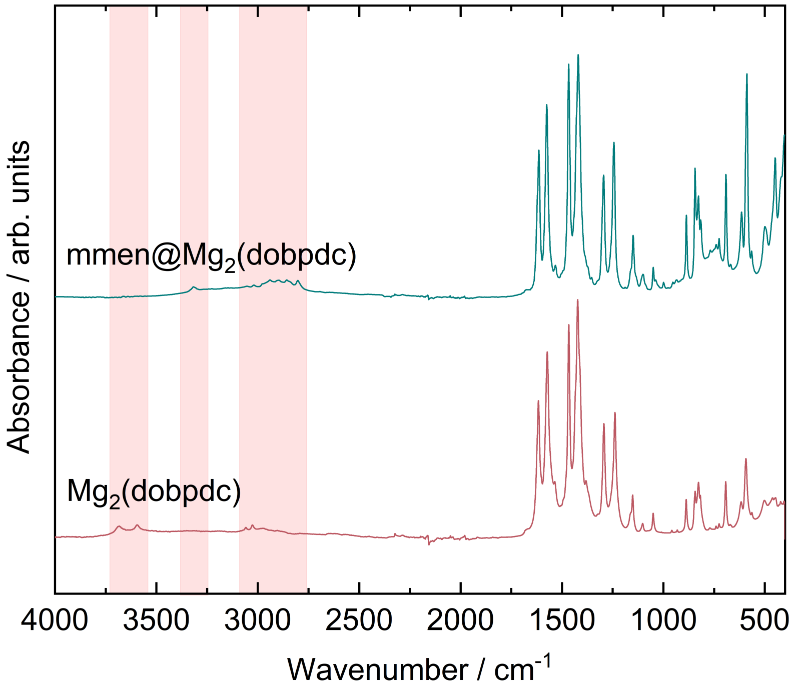

Figure A3.12. Mid-infrared spectra of Mg_2(dobpdc) and the diamin-appended mmen@Mg_2(dobpdc). The highlighted bands correspond to the C−H stretch vibrations of the dobpdc^{4-} linker and mmen ($2750 - 3060\,cm^{-1}$), and the N−H stretching vibration of mmen ($3317\,cm^{-1}$). The additional bands at 3686 and $3592\,cm^{-1}$ present in the spectrum of Mg_2(dobpdc) are assigned to atmospheric water adsorbed by the material during the time of the IR data collection (Table A3.1).

A3.3 High-Pressure X-ray Diffraction Setup

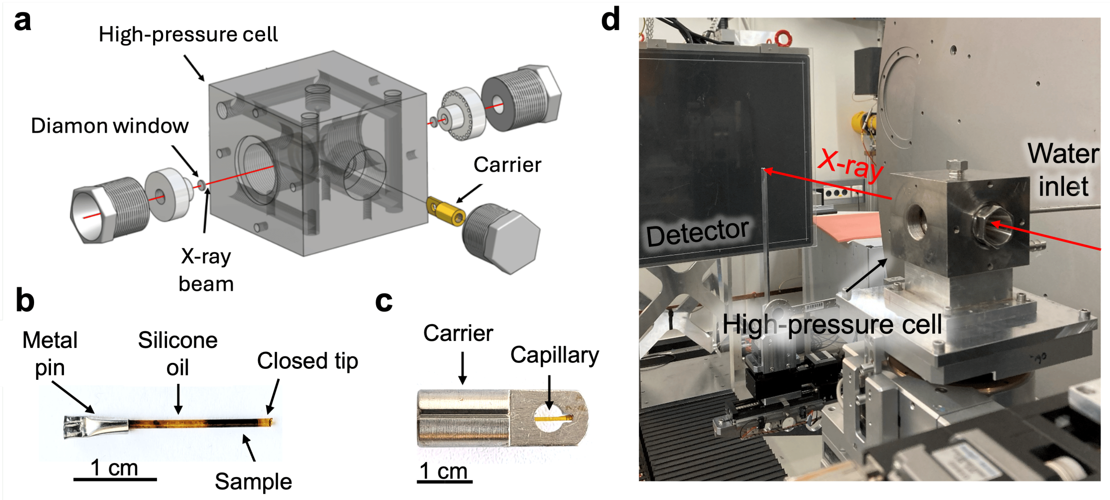

Figure A3.13. **a** Schematic representation of the HPPXRD setup. Figure taken from reference[232] **b** Kapton capillary filled with the crystalline sample material and silicone oil as a pressure-transmitting medium. The squeezed metal pin is used to seal the capillary and prevent water intrusion. **c** Carrier, loaded with an empty Kapton capillary. **d** A photo of the experimental setup taken at beamline P02.1 (DESY) showing the mounted high-pressure cell, the water inlet used for hydraulic pressure control, and the X-ray beam path through the cell to the plate detector.

A3.4 Powder X-ray Diffraction

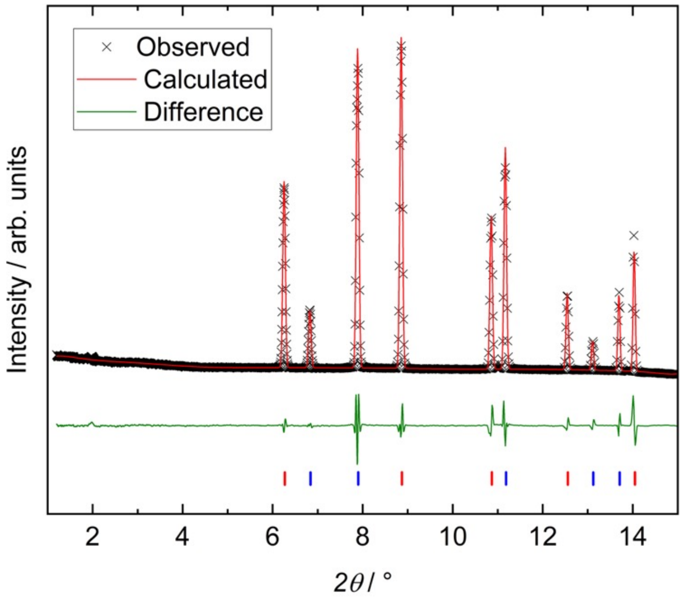

Figure A3.14. Profile fit (Pawley method) performed on the PXRD pattern of KBr and LaB_6 mixture used for pressure and distance calibration. The pattern was recorded at DELTA using a wavelength of 0.4537 Å at atmospheric pressure. Red tick marks indicate the position of allowed Bragg peaks assigned to LaB_6. Blue tick marks indicate reflections originating from KBr. The refined parameters are summarised in Table A3.3 and Table A3.4.

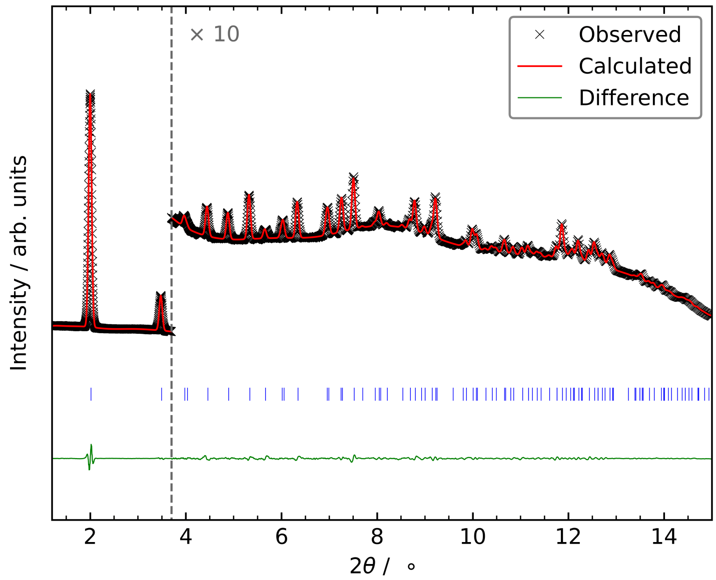

Figure A3.15. Profile fit (Pawley method) performed on the PXRD pattern of MOF-74(Mg). The pattern was recorded at DELTA using a wavelength of 0.4537 Å at a pressure of 50 bar. Blue tick marks indicate the position of allowed Bragg peaks. The refined parameters are summarized in Table A3.5.

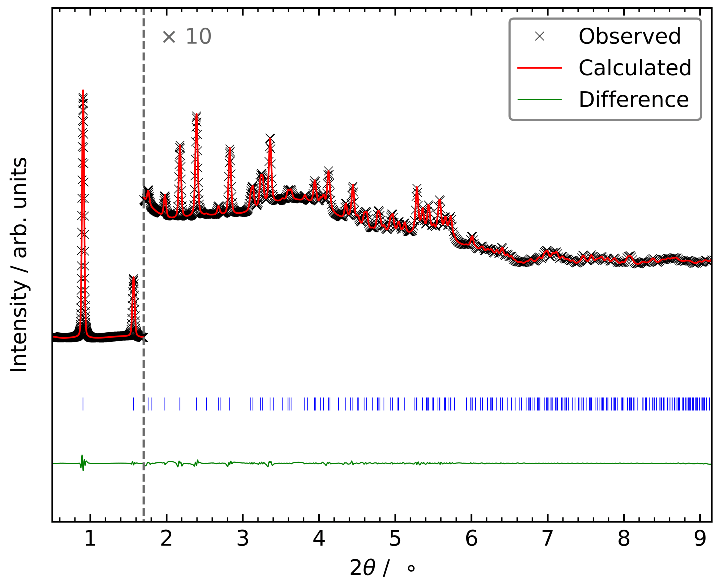

Figure A3.16. Profile fit (Pawley method) performed on the PXRD pattern of MOF-74(Mn). The pattern was recorded at DESY using a wavelength of 0.2074 Å at atmospheric pressure. Blue tick marks indicate the position of allowed Bragg peaks. The refined parameters are summarized Table A3.6.

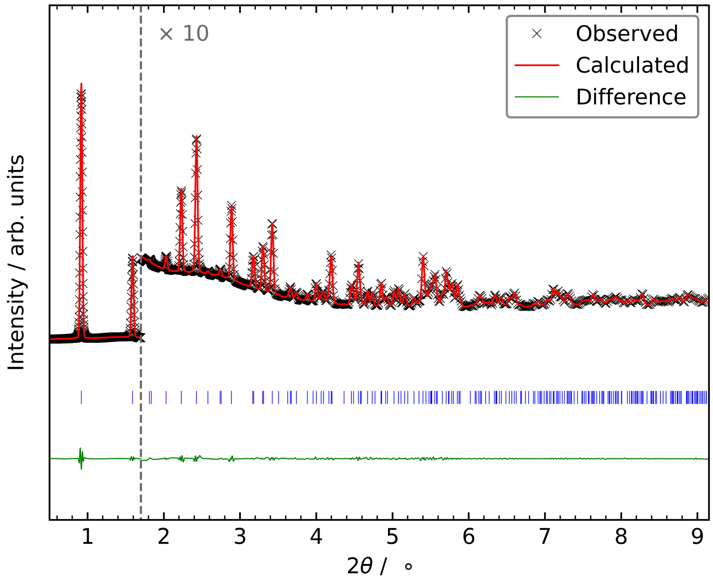

Figure A3.17. Profile fit (Pawley method) performed on the PXRD pattern of MOF-74(Co). The pattern was recorded at DESY using a wavelength of 0.2074 Å at atmospheric pressure. Blue tick marks indicate the position of allowed Bragg peaks. The refined parameters are summarized Table A3.7.

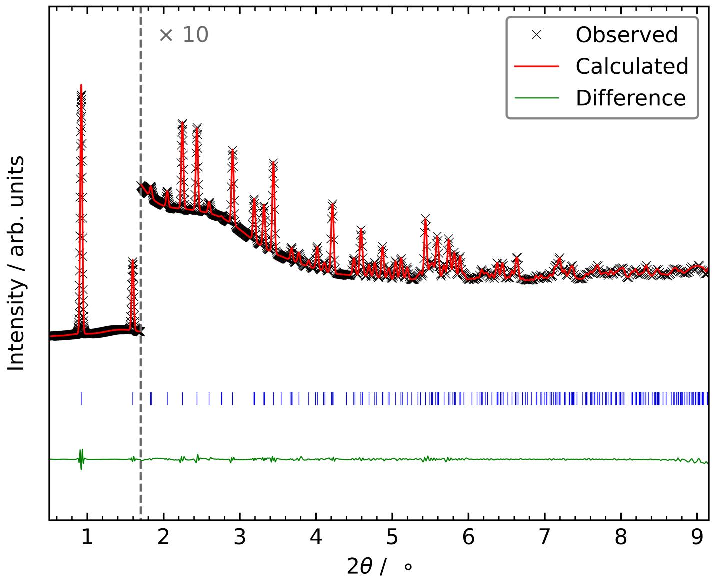

Figure A3.18. Profile fit (Pawley method) performed on the PXRD pattern of MOF-74(Ni). The pattern was recorded at DESY using a wavelength of 0.2074 Å at atmospheric pressure. Blue tick marks indicate the position of allowed Bragg peaks. The refined parameters are summarized Table A3.8.

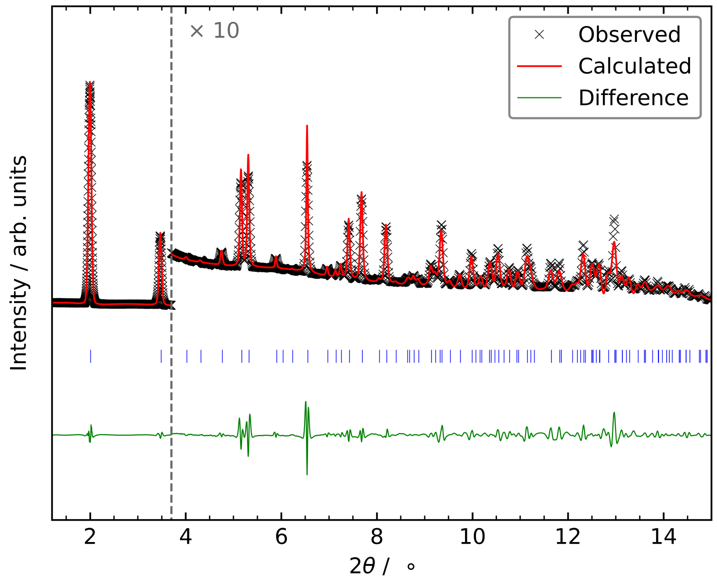

Figure A3.19. Profile fit (Pawley method) performed on the PXRD pattern of MOF-74(Cu). The pattern was recorded at DELTA using a wavelength of 0.4537 Å at atmospheric pressure. Blue tick marks indicate the position of allowed Bragg peaks. The refined parameters are summarized Table A3.9.

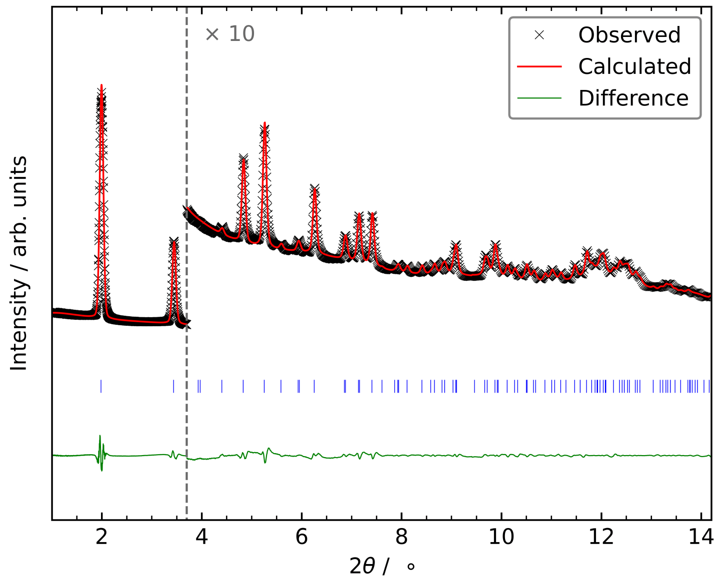

Figure A3.20. Profile fit (Pawley method) performed on the PXRD pattern of MOF-74(Zn). The pattern was recorded at DELTA using a wavelength of 0.4460 Å at atmospheric pressure. Blue tick marks indicate the position of allowed Bragg peaks. The refined parameters are summarized in Table A3.10.

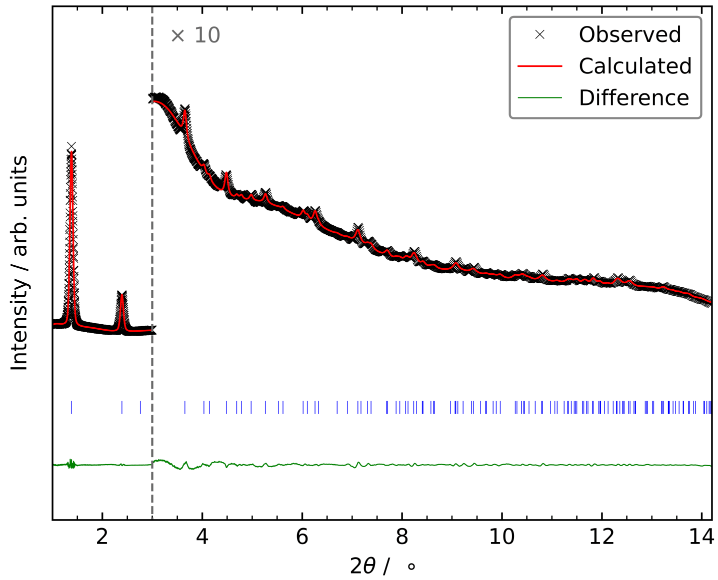

Figure A3.21. Profile fit (Pawley method) performed on the PXRD pattern of Mg_2(dobpdc). The pattern was recorded at DELTA using a wavelength of 0.4460 Å at atmospheric pressure. Blue tick marks indicate the position of allowed Bragg peaks. The refined parameters are summarized in Table A3.11.

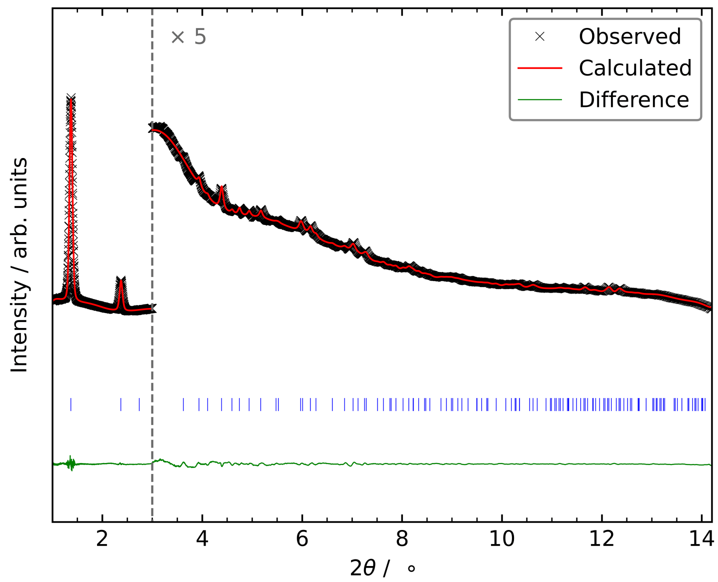

Figure A3.22. Profile fit (Pawley method) performed on the PXRD pattern of mmen@Mg_2(dobpdc). The pattern was recorded at DELTA using a wavelength of 0.4460 Å at atmospheric pressure. Blue tick marks indicate the position of allowed Bragg peaks. The refined parameters are summarized in Table A3.12.

A3.5 High-Pressure Powder X-ray Diffraction

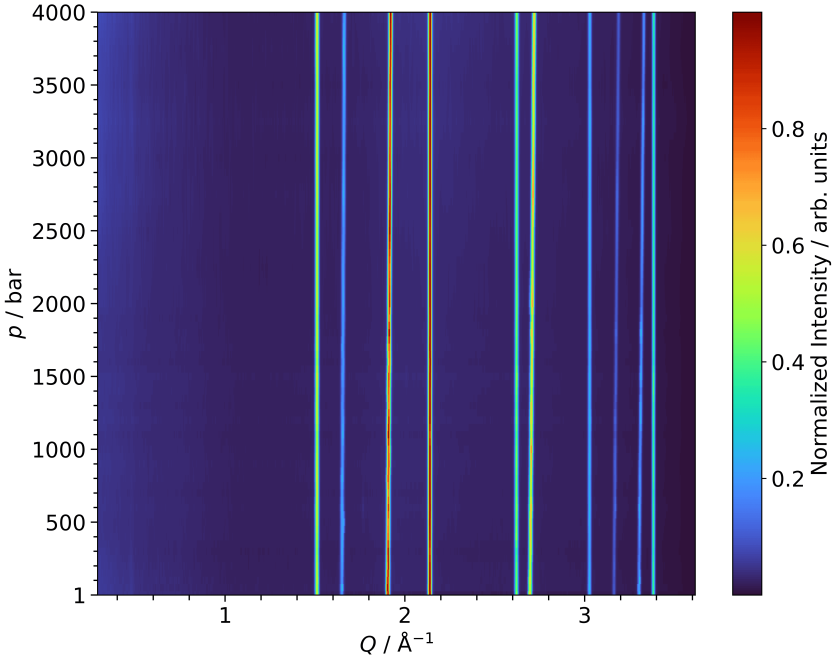

Figure A3.23. Heatmap calculated from the HPPXRD patterns of the calibrant mixture of KBr and LaB_6 (m/m = 1:1) during a stepwise pressure increase from 1 to 4000 bar. The heatmap was calculated based on 34 individual diffraction patterns, which were collected at DELTA using a wavelength of 0.4537 Å.

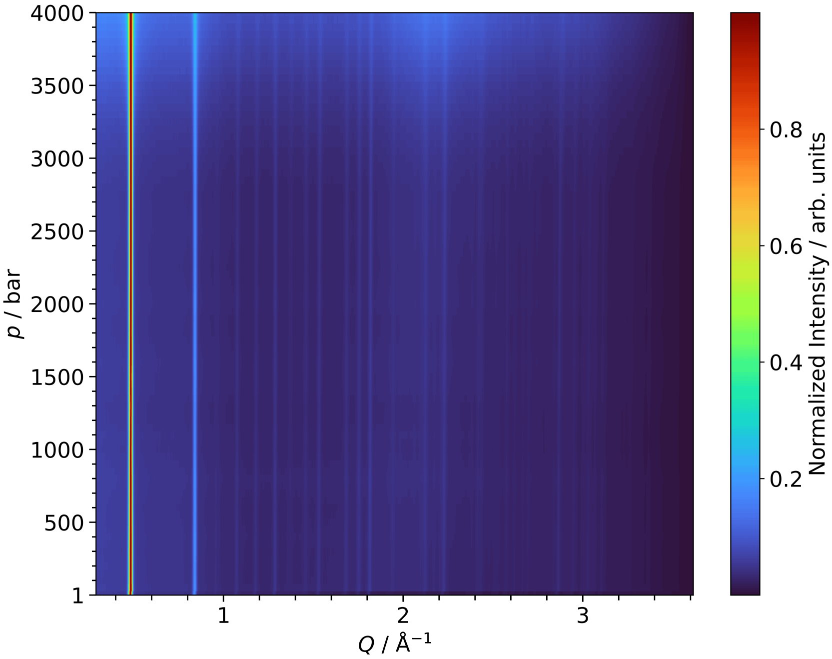

Figure A3.24. Heatmap depicting the HPPXRD patterns of MOF-74(Mg) during a stepwise pressure increase from 1 to 4000 bar. The heatmap was calculated based on 30 individual diffraction patterns, which were collected at DELTA using a wavelength of 0.4537 Å.

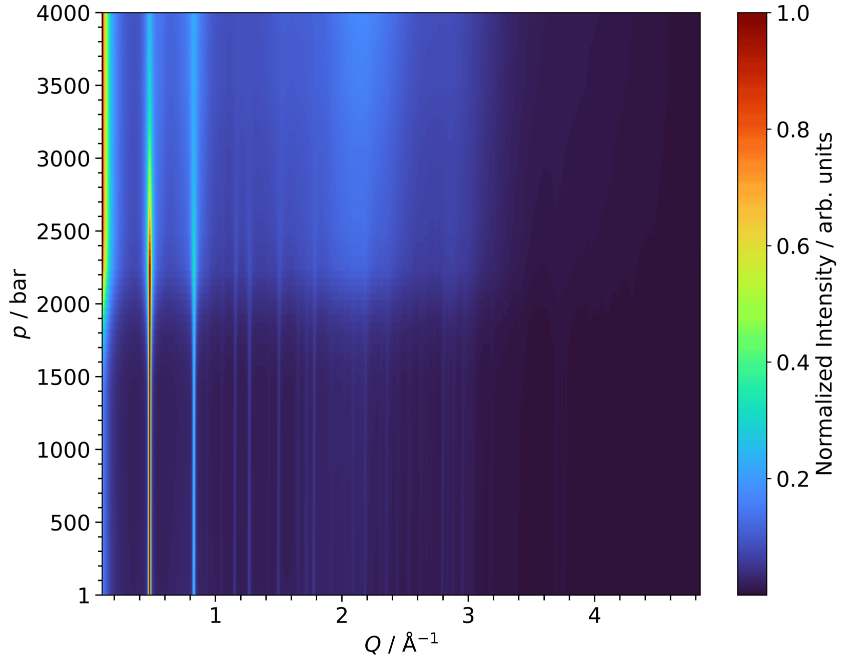

Figure A3.25. Heatmap depicting the HPPXRD patterns of MOF-74(Mn) during a stepwise pressure increase from 1 to 4000 bar. The heatmap was calculated based on 29 individual diffraction patterns, which were collected at DESY using a wavelength of 0.20737 Å.

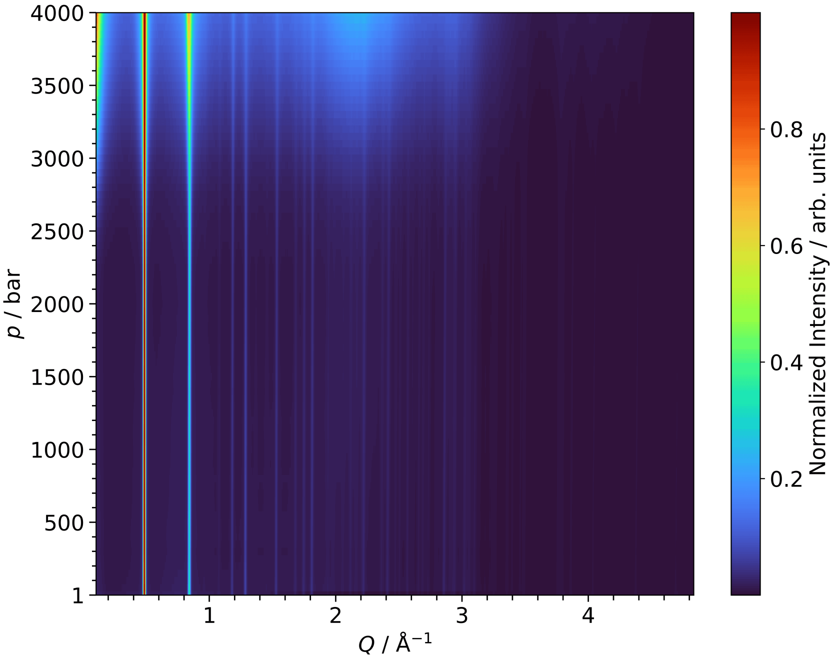

Figure A3.26. Heatmap depicting the HPPXRD patterns of MOF-74(Co) during a stepwise pressure increase from 1 to 4000 bar. The heatmap was calculated based on 29 individual diffraction patterns, which were collected at DESY using a wavelength of 0.20737 Å.

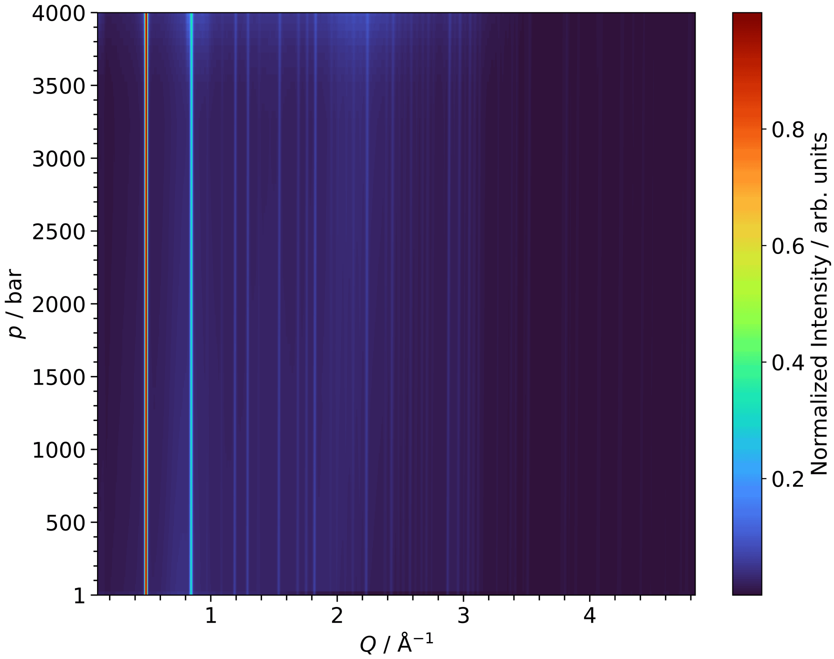

Figure A3.27. Heatmap depicting the HPPXRD patterns of MOF-74(Ni) during a stepwise pressure increase from 1 to 4000 bar. The heatmap was calculated based on 30 individual diffraction patterns, which were collected at DESY using a wavelength of 0.20737 Å.

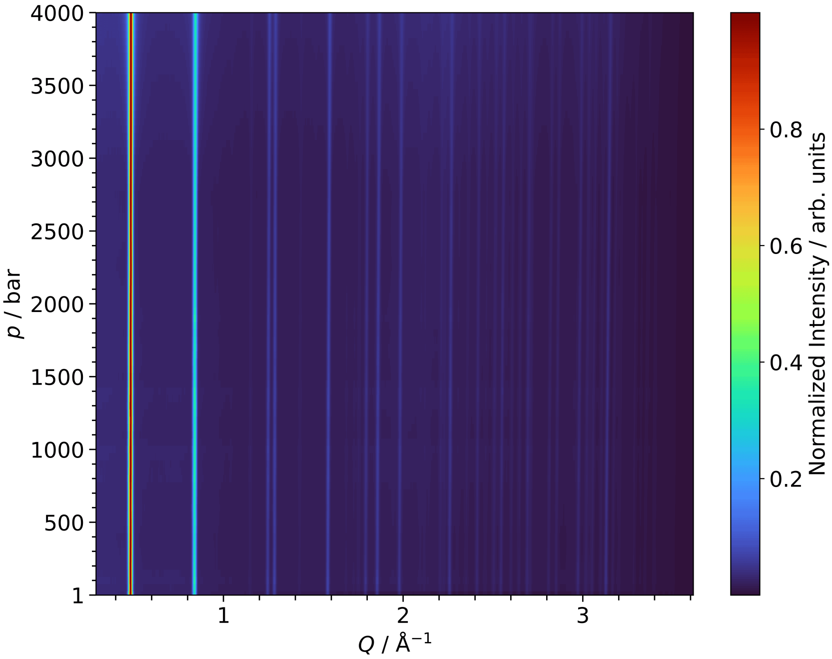

Figure A3.28. Heatmap depicting the HPPXRD patterns of MOF-74(Cu) during a stepwise pressure increase from 1 to 4000 bar. The heatmap was calculated based on 33 individual diffraction patterns, which were collected at DELTA using a wavelength of 0.4537 Å.

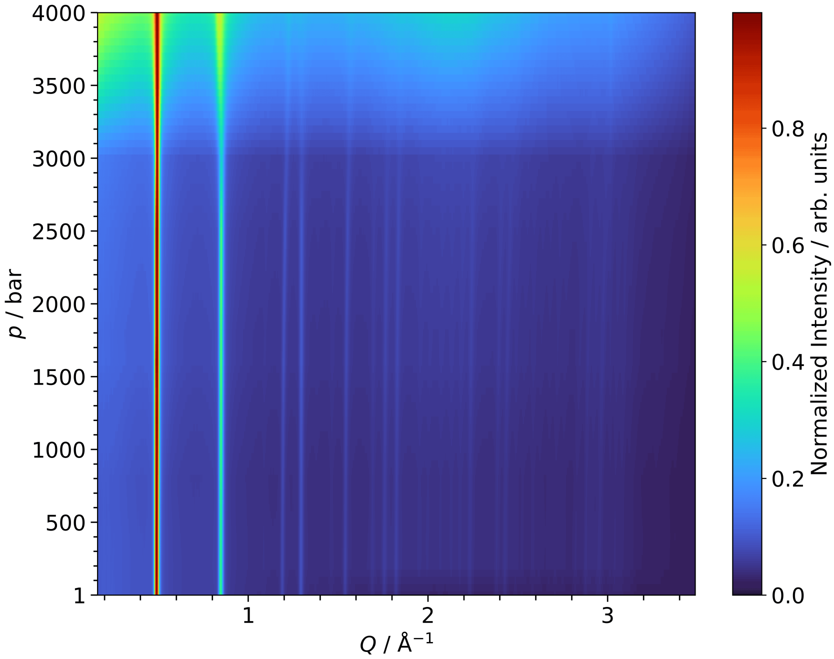

Figure A3.29. Heatmap depicting the HPPXRD patterns of MOF-74(Zn) during a stepwise pressure increase from 1 to 4000 bar. The heatmap was calculated based on 15 individual diffraction patterns, which were collected at DELTA using a wavelength of 0.4460 Å.

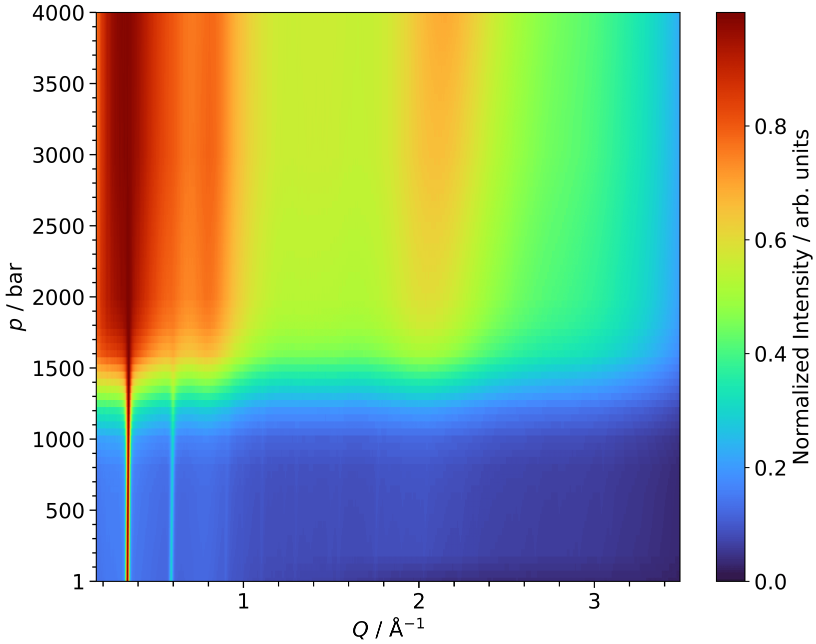

Figure A3.30. Heatmap depicting the HPPXRD patterns of Mg_2(dobpdc) during a stepwise pressure increase from 1 to 4000 bar. The heatmap was calculated based on 13 individual diffraction patterns, which were collected at DELTA using a wavelength of 0.4460 Å.

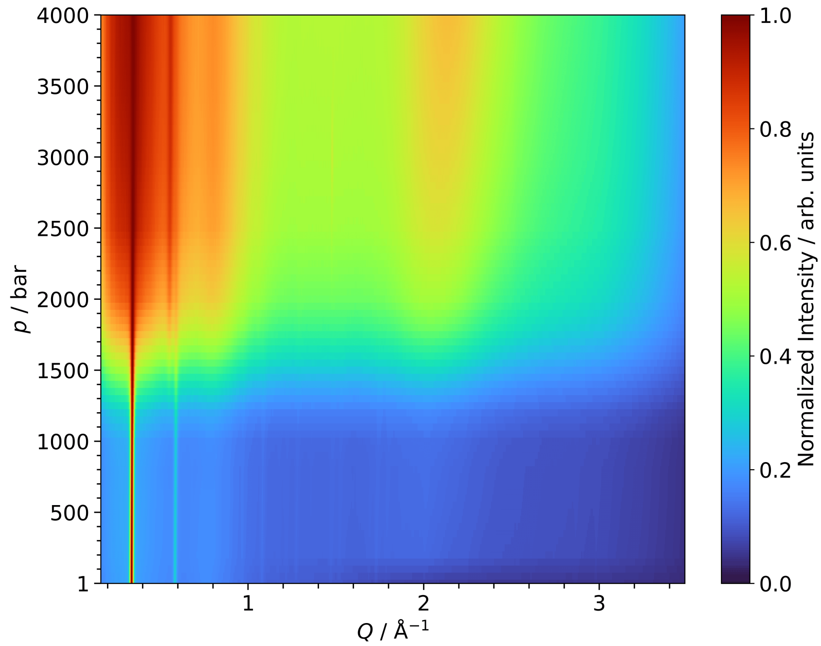

Figure A3.31. Heatmap depicting the HPPXRD patterns of mmen@Mg_2(dobpdc) during a stepwise pressure increase from 1 to 4000 bar. The heatmap was calculated based on 15 individual diffraction patterns, which were collected at DELTA using a wavelength of 0.4460 Å.

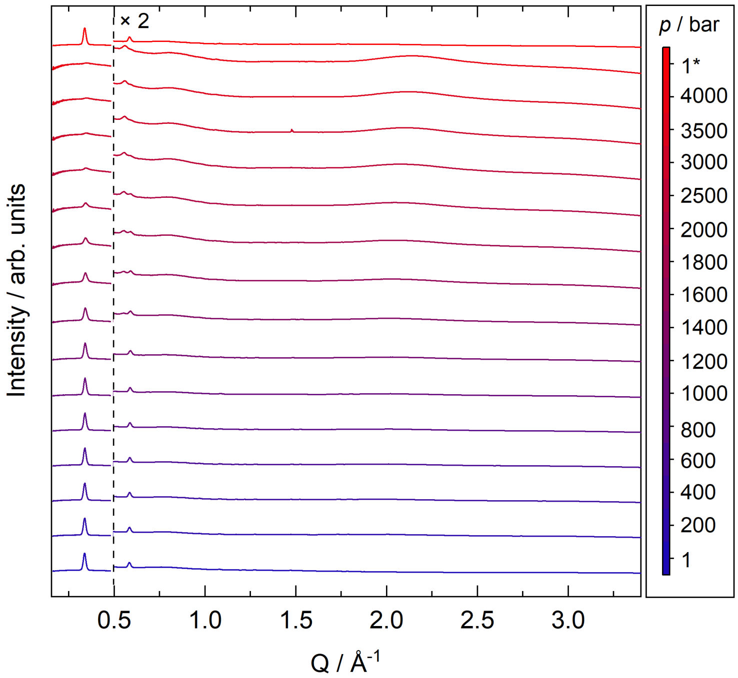

Figure A3.32. Stacked HPPXRD patterns of mmen@Mg_2(dobpdc) during a stepwise pressure increase from 1 to 4000 bar. The pattern denoted as 1* bar corresponds to the diffraction pattern after returning to ambient pressure. The patterns were collected at DELTA using a wavelength of 0.4460 Å.

A3.6 Pressure Cycle Stability

After the pressure was increased from atmospheric pressure to 4000 bar in the HPPXRD experiment, the pressure was reduced back to atmospheric pressure to investigate possible changes. For mmen@ Mg_2(dobpdc), a PXRD pattern after returning to atmospheric conditions was collected *in situ* (in the HP cell) at DELTA and also *ex situ* using CuK_α radiation with a lab diffractometer. In the case of Mg_2(dobpdc), the pattern after returning to atmospheric pressure was only collected *ex situ* using CuK_α radiation.

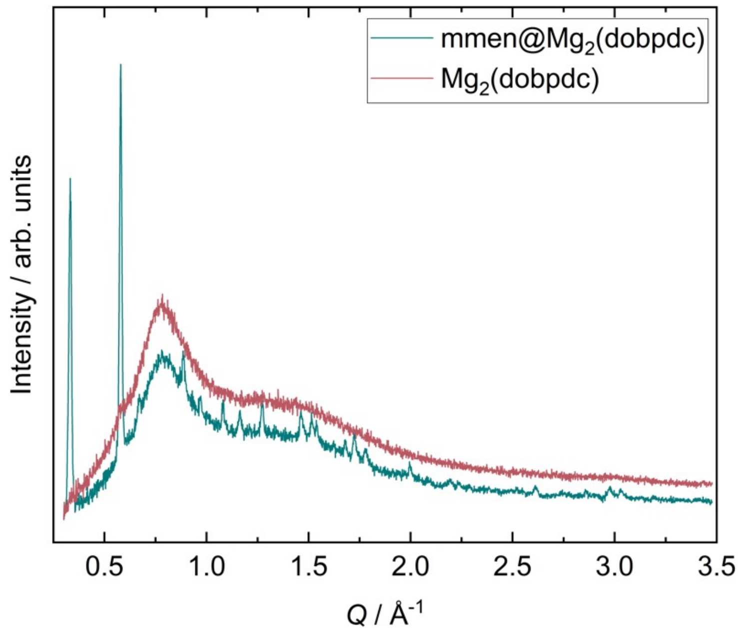

Figure A3.33. PXRD patterns of Mg_2(dobpdc) and mmen@Mg_2(dobpdc) after undergoing a full pressure cycle up to 4000 bar and back to atmospheric pressure (1 bar*). The patterns were measured using the capillaries previously used for the HPPXRD measurements and collected with a wavelength of 1.5418 Å in transmission mode. The diffraction pattern of mmen@Mg_2(dobpdc) is in accordance with the respective synchrotron measurement (see Figure 8.6e), while the diffraction pattern of Mg_2(dobpdc) displays diffuse scattering, indicating complete amorphization of the material due to the pressure cycling.

A3.7 Sequential profile Fitting

A3.7.1 Method

Profile fits (Pawley method[62]) were performed in TOPAS academic V 6.0.[235] For every set of high-pressure PXRD patterns (i.e., for each material), the pattern collected at the lowest pressure (i.e., 1 bar; 50 bar for MOF-74(Mg)) was selected as the starting point for the first profile fit. Apart from the unit cell parameters, the first fit was used to determine the z-parameter (th2_offset macro[61]). This macro adjusts the relative shift of the diffraction pattern on the 2Θ-scale, allowing for corrections of possible displacements of the capillary along the X-ray beam path. To prevent possible correlations between the extracted unit cell volume and the z-parameter, the latter was kept constant throughout the following sequential fits. This is reasonable, as the HPPXRD cell was securely fixed after sample loading, preventing any movement during the pressure cycling experiment. The automated fitting routine started with the fit of the pattern collected at the lowest pressure. The extracted unit cell parameters, background function (Chebyshev background function[61]) and peak shape function (Thompson-Cox-Hastings Peak Shape Function, TCHZ_Peak_Type[270]) are applied to fit the PXRD at the next pressure point. This routine continued up to the pattern collected at the maximum pressure (4000 bar), as well as the pattern collected after returning to 1 bar (denoted as 1* bar). As the background function becomes increasingly complex with increasing pressure (water-induced diffuse X-ray scattering), a recursive strategy was chosen. In the case that the initially chosen degree of the Chebyshev polynomial background function appeared insufficient for fits at higher pressure points, the initial degree of the background function was adjusted, and the sequential fitting was repeated.

A3.7.2 Peak Broadening Analysis

The contribution of isotropic microstrain and crystallite size to the broadening of Bragg peaks in the HPPXRD patterns of MOF-74(Ni) upon pressure increase was analysed by structureless profile fits (Pawley method) performed on several diffraction patterns throughout the range from 1 up to 4000 bar. Firstly, the setup-related peak broadening (i.e., instrument peak function) was determined by a corresponding fit of the LaB_6 calibrant collected at atmospheric pressure. The refined fitting parameters are shown in Table A3.2.

Table A3.2. Refined unit cell parameters and goodness-of-fit values for the profile fits (Pawley method) performed on LaB_6 calibrant for the determination of the instrument-dependent peak profile.

Compound	LaB_6
CS	cubic
SG	$Pm\bar{3}m$
a / Å	4.15727(7)
b / Å	4.15727(7)
c / Å	4.15727(7)
α / °	90
β / °	90
γ / °	90
V / Å^3	71.850(11)
R_{wp} / %	3.06
R_{exp} / %	1.38
χ	2.22

The thus obtained instrument peak function (Thompson-Cox-Hastings Peak Shape Function, TCHZ_Peak_Type[270]) is expected to be unaffected by crystallite size-related or microstrain-related peak broadening contributions and was used as a peak function with constant parameters in the following profile fits. For fitting the MOF-74(Ni) HPPXRD patterns, the broadening of peaks was described using two macros in TOPAS academic v6.0: The e0_from_Strain macro[61] describes microstrain-related peak broadening by introducing both Lorentzian and Gaussian strain broadening components (i.e., a pseudo-Voigt function) in addition to the fixed instrumental peak shape function; the LVol_FWHM_CS_G_L macro[61] is used to introduce crystallite size-related peak broadening (i.e., integral breadthbased volume-weighted column heights, LVol) in addition to the fixed instrument peak shape function in the form of a convoluted Lorentzian and Gaussian (i.e., a pseudo-Voigt function). The physical origin of peak broadening is differentiable by the diffraction angle dependency of the respective size-($1/\cos(\Theta)$ dependency) or strain- ($\tan(\Theta)$ dependency) related broadening.[61] Again, the th2_offset macro (z-parameter) describing the shift of the diffraction pattern on the 2Θ-scale due to changes in sample position was determined for the initial 1 bar pattern and kept constant throughout the subsequent fits. To achieve sensible background functions even for patterns collected at high hydrostatic pressure, the penalties_weighting_K1 keyword[61] was used, limiting the reflection intensity with increasing 2Θ The refined cell parameters are shown in Table A3.13.

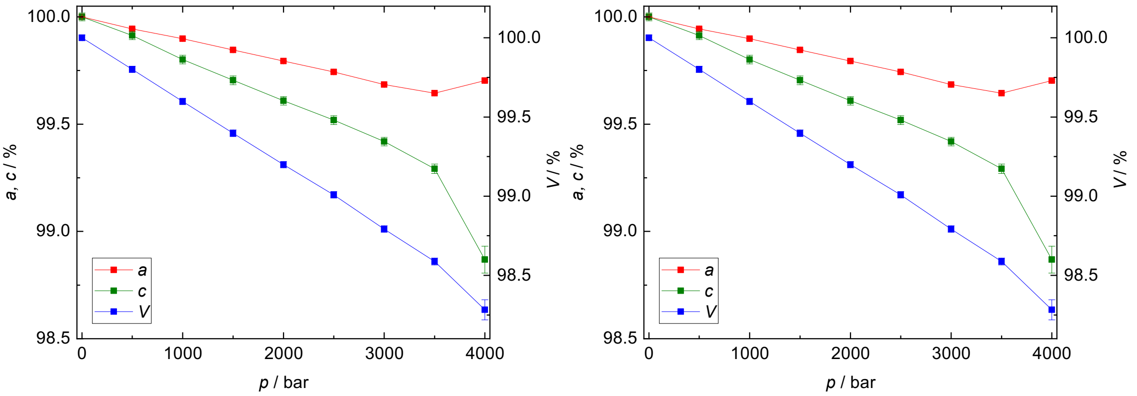

Figure A3.34. Left: Trend in the unit cell parameters upon pressure increase extracted from the profile fits performed on MOF-74(Ni) with applied macros for crystallite size- and microstrain-related Bragg peak broadening. Extracted unit cell parameters are summarized in Table A3.13.

A3.7.3 Crystallographic Tables

Table A3.3. Unit cell parameters and refinement quality indicators provided by sequential profile fits (Pawley method) performed on the HPPXRD patterns of LaB_6.

p / bar	1	50	100	200	300	400	500	600	700	800	900	1000	1100	1200	1300
Crystal system	cubic	cubic	cubic	cubic	cubic	cubic	cubic	cubic	cubic	cubic	cubic	cubic	cubic	cubic	cubic
space group	$Pm\bar{3}m$	$Pm\bar{3}m$	$Pm\bar{3}m$	$Pm\bar{3}m$	$Pm\bar{3}m$	$Pm\bar{3}m$	$Pm\bar{3}m$	$Pm\bar{3}m$	$Pm\bar{3}m$	$Pm\bar{3}m$	$Pm\bar{3}m$	$Pm\bar{3}m$	$Pm\bar{3}m$	$Pm\bar{3}m$	$Pm\bar{3}m$
a / Å	4.14812(4)	4.14868(4)	4.14825(4)	4.14835(4)	4.14850(4)	4.14815(3)	4.14812(4)	4.14798(5)	4.14783(3)	4.14801(4)	4.14787(4)	4.14763(3)	4.14772(4)	4.14766(4)	4.14769(3)
b / Å	4.14812(4)	4.14868(4)	4.14825(4)	4.14835(4)	4.14850(4)	4.14815(3)	4.14812(4)	4.14798(5)	4.14783(3)	4.14801(4)	4.14787(4)	4.14763(3)	4.14772(4)	4.14766(4)	4.14769(3)
c / Å	4.14812(4)	4.14868(4)	4.14825(4)	4.14835(4)	4.14850(4)	4.14815(3)	4.14812(4)	4.14798(5)	4.14783(3)	4.14801(4)	4.14787(4)	4.14763(3)	4.14772(4)	4.14766(4)	4.14769(3)
α / °	90	90	90	90	90	90	90	90	90	90	90	90	90	90	90
β / °	90	90	90	90	90	90	90	90	90	90	90	90	90	90	90
γ / °	90	90	90	90	90	90	90	90	90	90	90	90	90	90	90
V / Å^3	71.3760(20)	71.4050(20)	71.3830(20)	71.3880(20)	71.3960(20)	71.3780(20)	71.3760(20)	71.3690(20)	71.3610(20)	71.3700(20)	71.3640(20)	71.3510(20)	71.3560(20)	71.3520(20)	71.3540(20)
R_{wp} / %	5.31	5	5.01	4.7	4.46	4.07	5.5	6.11	4.17	4.92	4.87	4.24	5.58	4.44	4.35
R_{exp} / %	20.1	20.39	20.3	20.13	19.77	14.37	14.4	14.5	14.65	14.66	14.73	14.7	14.51	14.68	14.79
χ	0.26	0.25	0.25	0.23	0.23	0.28	0.38	0.42	0.28	0.34	0.33	0.29	0.38	0.3	0.29

1400	1500	1600	1700	1800	1900	2000	2250	2500	2750	3000	3250	3500	3750	4000	1*
cubic	cubic	cubic	cubic	cubic	cubic	cubic	cubic	cubic	cubic	cubic	cubic	cubic	cubic	cubic	cubic
$Pm\bar{3}m$	$Pm\bar{3}m$	$Pm\bar{3}m$	$Pm\bar{3}m$	$Pm\bar{3}m$	$Pm\bar{3}m$	$Pm\bar{3}m$	$Pm\bar{3}m$	$Pm\bar{3}m$	$Pm\bar{3}m$	$Pm\bar{3}m$	$Pm\bar{3}m$	$Pm\bar{3}m$	$Pm\bar{3}m$	$Pm\bar{3}m$	$Pm\bar{3}m$
4.14754(4)	4.14700(4)	4.14678(4)	4.14689(5)	4.14674(4)	4.14660(4)	4.14654(4)	4.14665(4)	4.14660(4)	4.14625(4)	4.14610(4)	4.14584(4)	4.14557(4)	4.14575(4)	4.14548(4)	4.14892(4)
4.14754(4)	4.14700(4)	4.14678(4)	4.14689(5)	4.14674(4)	4.14660(4)	4.14654(4)	4.14665(4)	4.14660(4)	4.14625(4)	4.14610(4)	4.14584(4)	4.14557(4)	4.14575(4)	4.14548(4)	4.14892(4)
4.14754(4)	4.14700(4)	4.14678(4)	4.14689(5)	4.14674(4)	4.14660(4)	4.14654(4)	4.14665(4)	4.14660(4)	4.14625(4)	4.14610(4)	4.14584(4)	4.14557(4)	4.14575(4)	4.14548(4)	4.14892(4)
90	90	90	90	90	90	90	90	90	90	90	90	90	90	90	90
90	90	90	90	90	90	90	90	90	90	90	90	90	90	90	90
90	90	90	90	90	90	90	90	90	90	90	90	90	90	90	90
71.3460(20)	71.3180(20)	71.3070(20)	71.3130(20)	71.3050(20)	71.2980(20)	71.2950(20)	71.3000(20)	71.2980(20)	71.2800(20)	71.2720(20)	71.2590(20)	71.2450(20)	71.2540(20)	71.2400(20)	71.4170(20)
5.29	4.5	4.99	5.94	5.16	5.23	5.36	4.44	3.77	3.9	4.25	4.05	3.93	4.12	3.84	3.58
14.8	12.67	11.94	12.66	13.76	15.31	16.74	18.9	20.87	22.77	23.81	24.82	24.68	25.68	25.62	26.83
0.36	0.36	0.42	0.47	0.37	0.34	0.32	0.24	0.18	0.17	0.18	0.16	0.16	0.16	0.15	0.13

Table A3.4. Unit cell parameters and refinement quality indicators provided by sequential profile fits (Pawley method) performed on the HPPXRD patterns of KBr.

p / bar	1	50	100	200	300	400	500	600	700	800	900	1000	1100	1200	1300
crystal system	cubic	cubic	cubic	cubic	cubic	cubic	cubic	cubic	cubic	cubic	cubic	cubic	cubic	cubic	cubic
space group	$Fm\bar{3}m$	$Fm\bar{3}m$	$Fm\bar{3}m$	$Fm\bar{3}m$	$Fm\bar{3}m$	$Fm\bar{3}m$	$Fm\bar{3}m$	$Fm\bar{3}m$	$Fm\bar{3}m$	$Fm\bar{3}m$	$Fm\bar{3}m$	$Fm\bar{3}m$	$Fm\bar{3}m$	$Fm\bar{3}m$	$Fm\bar{3}m$
a / Å	6.58411(8)	6.58453(8)	6.58298(8)	6.57981(8)	6.57851(7)	6.57686(6)	6.57581(8)	6.57409(9)	6.57344(6)	6.57349(7)	6.56892(7)	6.56735(6)	6.56881(8)	6.56639(6)	6.56476(6)
b / Å	6.58411(8)	6.58453(8)	6.58298(8)	6.57981(8)	6.57851(7)	6.57686(6)	6.57581(8)	6.57409(9)	6.57344(6)	6.57349(7)	6.56892(7)	6.56735(6)	6.56881(8)	6.56639(6)	6.56476(6)
c / Å	6.58411(8)	6.58453(8)	6.58298(8)	6.57981(8)	6.57851(7)	6.57686(6)	6.57581(8)	6.57409(9)	6.57344(6)	6.57349(7)	6.56892(7)	6.56735(6)	6.56881(8)	6.56639(6)	6.56476(6)
α / °	90	90	90	90	90	90	90	90	90	90	90	90	90	90	90
β / °	90	90	90	90	90	90	90	90	90	90	90	90	90	90	90
γ / °	90	90	90	90	90	90	90	90	90	90	90	90	90	90	90
V / Å^3	285.425(10)	285.479(10)	285.277(10)	284.865(10)	284.697(9)	284.483(8)	284.347(10)	284.124(11)	284.040(8)	284.045(9)	283.453(9)	283.250(8)	283.439(10)	283.127(8)	282.916(8)
R_{wp} / %	5.31	5	5.01	4.7	4.46	4.07	5.5	6.11	4.17	4.92	4.87	4.24	5.58	4.44	4.35
R_{exp} / %	20.1	20.39	20.3	20.13	19.77	14.37	14.4	14.5	14.65	14.66	14.73	14.7	14.51	14.68	14.79
χ	0.26	0.25	0.25	0.23	0.23	0.28	0.38	0.42	0.28	0.34	0.33	0.29	0.38	0.3	0.29

1400	1500	1600	1700	1800	1900	2000	2250	2500	2750	3000	3250	3500	3750	4000	1*
cubic	cubic	cubic	cubic	cubic	cubic	cubic	cubic	cubic	cubic	cubic	cubic	cubic	cubic	cubic	cubic
$Fm\bar{3}m$	$Fm\bar{3}m$	$Fm\bar{3}m$	$Fm\bar{3}m$	$Fm\bar{3}m$	$Fm\bar{3}m$	$Fm\bar{3}m$	$Fm\bar{3}m$	$Fm\bar{3}m$	$Fm\bar{3}m$	$Fm\bar{3}m$	$Fm\bar{3}m$	$Fm\bar{3}m$	$Fm\bar{3}m$	$Fm\bar{3}m$	$Fm\bar{3}m$
6.56423(8)	6.56266(7)	6.55830(7)	6.55864(9)	6.55790(7)	6.55605(8)	6.55461(8)	6.55223(7)	6.54846(6)	6.54424(6)	6.54172(8)	6.53814(7)	6.53651(7)	6.53177(7)	6.52923(8)	6.58352(7)
6.56423(8)	6.56266(7)	6.55830(7)	6.55864(9)	6.55790(7)	6.55605(8)	6.55461(8)	6.55223(7)	6.54846(6)	6.54424(6)	6.54172(8)	6.53814(7)	6.53651(7)	6.53177(7)	6.52923(8)	6.58352(7)
6.56423(8)	6.56266(7)	6.55830(7)	6.55864(9)	6.55790(7)	6.55605(8)	6.55461(8)	6.55223(7)	6.54846(6)	6.54424(6)	6.54172(8)	6.53814(7)	6.53651(7)	6.53177(7)	6.52923(8)	6.58352(7)
90	90	90	90	90	90	90	90	90	90	90	90	90	90	90	90
90	90	90	90	90	90	90	90	90	90	90	90	90	90	90	90
90	90	90	90	90	90	90	90	90	90	90	90	90	90	90	90
282.847(11)	282.644(9)	282.081(9)	282.125(11)	282.029(9)	281.790(10)	281.605(10)	281.299(9)	280.813(8)	280.270(8)	279.948(10)	279.487(9)	279.279(9)	278.671(9)	278.346(10)	285.348(9)
5.29	4.5	4.99	5.94	5.16	5.23	5.36	4.44	3.77	3.9	4.25	4.05	3.93	4.12	3.84	3.58
14.8	12.67	11.94	12.66	13.76	15.31	16.74	18.9	20.87	22.77	23.81	24.82	24.68	25.68	25.62	26.83
0.36	0.36	0.42	0.47	0.37	0.34	0.32	0.24	0.18	0.17	0.18	0.16	0.16	0.16	0.15	0.13

Table A3.5. Unit cell parameters and refinement quality indicators provided by sequential profile fits (Pawley method) performed on the HPPXRD patterns of MOF-74(Mg).

p / bar	50	100	200	300	400	500	600	700	800	900	1000	1100	1200	1300	1400
crystal system	trigonal	trigonal	trigonal	trigonal	trigonal	trigonal	trigonal	trigonal	trigonal	trigonal	trigonal	trigonal	trigonal	trigonal	trigonal
space group	$R\bar{3}$	$R\bar{3}$	$R\bar{3}$	$R\bar{3}$	$R\bar{3}$	$R\bar{3}$	$R\bar{3}$	$R\bar{3}$	$R\bar{3}$	$R\bar{3}$	$R\bar{3}$	$R\bar{3}$	$R\bar{3}$	$R\bar{3}$	$R\bar{3}$
a / Å	25.7776(5)	25.7803(4)	25.7777(4)	25.7784(4)	25.7672(4)	25.7673(3)	25.7647(3)	25.7650(3)	25.7614(3)	25.7684(2)	25.76598(20)	25.7524(3)	25.7555(4)	25.7455(5)	25.7542(4)
b / Å	25.7776(5)	25.7803(4)	25.7777(4)	25.7784(4)	25.7672(4)	25.7673(3)	25.7647(3)	25.7650(3)	25.7614(3)	25.7684(2)	25.76598(20)	25.7524(3)	25.7555(4)	25.7455(5)	25.7542(4)
c / Å	6.8351(18)	6.8323(15)	6.8311(14)	6.8296(14)	6.8289(14)	6.8285(12)	6.8261(11)	6.8235(11)	6.8220(9)	6.8182(8)	6.8166(8)	6.8177(0)	6.8165(12)	6.8160(17)	6.8132(13)
α / °	90	90	90	90	90	90	90	90	90	90	90	90	90	90	90
β / °	90	90	90	90	90	90	90	90	90	90	90	90	90	90	90
γ / °	120	120	120	120	120	120	120	120	120	120	120	120	120	120	120
V / Å^3	3933.4(10)	3932.5(9)	3931.0(8)	3930.4(8)	3926.6(8)	3926.4(7)	3924.2(7)	3922.8(6)	3920.8(6)	3920.8(4)	3919.2(5)	3915.6(6)	3915.9(7)	3912.6(1)	3913.6(7)
R_{wp} / %	2.55	2.2	1.96	2	1.95	1.7	1.61	1.59	1.32	1.08	1.08	1.35	1.83	2.59	1.92
R_{exp} / %	2.91	2.82	3.05	2.83	2.96	3.18	3.4	3.77	4.09	4.34	4.6	4.88	3.57	3.28	3.27
χ	0.88	0.78	0.64	0.71	0.66	0.53	0.47	0.42	0.32	0.25	0.23	0.28	0.51	0.79	0.59

1500	1600	1700	1800	1900	2000	2250	2500	2750	3000	3250	3500	3750	4000	1*
trigonal	trigonal	trigonal	trigonal	trigonal	trigonal	trigonal	trigonal	trigonal	trigonal	trigonal	trigonal	trigonal	trigonal	trigonal
$R\bar{3}$	$R\bar{3}$	$R\bar{3}$	$R\bar{3}$	$R\bar{3}$	$R\bar{3}$	$R\bar{3}$	$R\bar{3}$	$R\bar{3}$	$R\bar{3}$	$R\bar{3}$	$R\bar{3}$	$R\bar{3}$	$R\bar{3}$	$R\bar{3}$
25.7463(3)	25.7436(4)	25.7420(4)	25.7430(3)	25.7374(3)	25.7360(3)	25.7190(3)	25.7253(3)	25.7190(3)	25.7149(3)	25.7228(3)	25.7275(4)	25.7304(4)	25.7289(7)	25.8178(8)
25.7463(3)	25.7436(4)	25.7420(4)	25.7430(3)	25.7374(3)	25.7360(3)	25.7190(3)	25.7253(3)	25.7190(3)	25.7149(3)	25.7228(3)	25.7275(4)	25.7304(4)	25.7289(7)	25.8178(8)
6.8117(12)	6.8106(13)	6.8083(13)	6.8056(11)	6.8057(12)	6.8038(12)	6.8028(12)	6.7974(12)	6.7924(11)	6.7853(13)	6.7711(14)	6.7583(17)	6.742(2)	6.735(4)	6.783(3)
90	90	90	90	90	90	90	90	90	90	90	90	90	90	90
90	90	90	90	90	90	90	90	90	90	90	90	90	90	90
120	120	120	120	120	120	120	120	120	120	120	120	120	120	120
3910.4(7)	3908.9(8)	3907.1(8)	3905.8(6)	3904.2(7)	3902.7(7)	3897.0(7)	3895.7(7)	3891.0(6)	3885.7(7)	3880.0(8)	3874.0(10)	3865.3(13)	3860.9(20)	3915.3(20)
1.73	1.86	1.88	1.57	1.73	1.71	1.72	1.7	1.6	1.57	1.2	1.15	1.14	1.48	1.5
3.3	3.34	3.36	3.4	3.42	3.45	3.46	3.49	3.49	3.53	3.58	3.64	3.7	3.75	3.73
0.52	0.56	0.56	0.46	0.51	0.5	0.5	0.49	0.46	0.45	0.34	0.32	0.31	0.4	0.4

Table A3.6. Unit cell parameters and refinement quality indicators provided by sequential profile fits (Pawley method) performed on the HPPXRD patterns of MOF-74(Mn). Fitting results beyond a pressure of 1500 bar are not considered in the following data evaluation.

p / bar	1	50	100	200	300	400	500	600	700	800	900	1000	1100	1200	1300
crystal system	trigonal	trigonal	trigonal	trigonal	trigonal	trigonal	trigonal	trigonal	trigonal	trigonal	trigonal	trigonal	trigonal	trigonal	trigonal
space group	$R\bar{3}$	$R\bar{3}$	$R\bar{3}$	$R\bar{3}$	$R\bar{3}$	$R\bar{3}$	$R\bar{3}$	$R\bar{3}$	$R\bar{3}$	$R\bar{3}$	$R\bar{3}$	$R\bar{3}$	$R\bar{3}$	$R\bar{3}$	$R\bar{3}$
a / Å	26.2798(6)	26.2780(6)	26.2773(6)	26.2748(6)	26.2721(6)	26.2696(6)	26.2676(6)	26.2640(6)	26.2609(6)	26.2577(6)	26.2553(6)	26.2527(5)	26.2500(5)	26.2478(5)	26.2439(5)
b / Å	26.2798(6)	26.2780(6)	26.2773(6)	26.2748(6)	26.2721(6)	26.2696(6)	26.2676(6)	26.2640(6)	26.2609(6)	26.2577(6)	26.2553(6)	26.2527(5)	26.2500(5)	26.2478(5)	26.2439(5)
c / Å	7.0702(17)	7.0689(16)	7.0675(16)	7.0652(16)	7.0629(16)	7.0604(16)	7.0581(16)	7.0562(16)	7.0540(16)	7.0518(16)	7.0496(16)	7.0460(16)	7.0433(16)	7.0405(16)	7.0379(16)
α / °	90	90	90	90	90	90	90	90	90	90	90	90	90	90	90
β / °	90	90	90	90	90	90	90	90	90	90	90	90	90	90	90
γ / °	120	120	120	120	120	120	120	120	120	120	120	120	120	120	120
V / Å^3	4228.7(10)	4227.4(0)	4226.3(0)	4224.1(0)	4221.8(0)	4219.6(0)	4217.6(0)	4215.2(0)	4212.9(0)	4210.6(0)	4208.5(0)	4205.5(0)	4203.1(0)	4200.7(0)	4197.9(0)
R_{wp} / %	1.77	1.76	1.76	1.76	1.76	1.77	1.77	1.78	1.76	1.76	1.74	1.72	1.71	1.7	1.65
R_{exp} / %	0.54	0.53	0.54	0.54	0.54	0.54	0.54	0.54	0.54	0.54	0.54	0.54	0.54	0.54	0.54
χ	3.28	3.3	3.27	3.27	3.27	3.3	3.26	3.29	3.25	3.29	3.22	3.18	3.14	3.13	3.07

1400	1500	1600	1700	1800	1900	2000	2250	2500	2750	3000	3250	3500	3750	4000	1*
trigonal	trigonal	trigonal	trigonal	trigonal	trigonal	trigonal	trigonal	trigonal	trigonal	trigonal	trigonal	trigonal	trigonal	trigonal	trigonal
$R\bar{3}$	$R\bar{3}$	$R\bar{3}$	$R\bar{3}$	$R\bar{3}$	$R\bar{3}$	$R\bar{3}$	$R\bar{3}$	$R\bar{3}$	$R\bar{3}$	$R\bar{3}$	$R\bar{3}$	$R\bar{3}$	$R\bar{3}$	$R\bar{3}$	$R\bar{3}$
26.2401(5)	26.2359(5)	26.2304(5)	26.2254(5)	26.2205(7)	26.2155(10)	26.2143(14)	26.215(2)	26.224(2)	26.233(3)	26.246(3)	26.261(3)	26.278(3)	26.282(3)	26.293(4)	26.385(4)
26.2401(5)	26.2359(5)	26.2304(5)	26.2254(5)	26.2205(7)	26.2155(10)	26.2143(14)	26.215(2)	26.224(2)	26.233(3)	26.246(3)	26.261(3)	26.278(3)	26.282(3)	26.293(4)	26.385(4)
7.0349(15)	7.0308(16)	7.0257(16)	7.0198(18)	7.014(2)	7.007(4)	6.998(6)	6.966(0)	6.924(12)	6.911(12)	6.904(11)	6.900(10)	6.895(9)	6.894(9)	6.893(9)	6.902(9)
90	90	90	90	90	90	90	90	90	90	90	90	90	90	90	90
90	90	90	90	90	90	90	90	90	90	90	90	90	90	90	90
120	120	120	120	120	120	120	120	120	120	120	120	120	120	120	120
4194.9(9)	4191.1(0)	4186.3(0)	4181.2(11)	4176.3(14)	4171(2)	4165(4)	4146(6)	4124(7)	4118(7)	4118(7)	4121(6)	4124(6)	4124(6)	4127(6)	4161(6)
1.53	1.39	1.25	1.14	1.31	1.77	2.08	1.95	1.54	1.17	0.9	0.68	0.52	0.51	0.49	0.66
0.54	0.54	0.54	0.54	0.54	0.54	0.55	0.55	0.56	0.57	0.57	0.57	0.57	0.57	0.58	0.62
2.85	2.59	2.33	2.1	2.41	3.26	3.78	3.52	2.73	2.06	1.57	1.18	0.92	0.89	0.85	1.08

Table A3.7. Unit cell parameters and refinement quality indicators provided by sequential profile fits (Pawley method) performed on the HPPXRD patterns of MOF-74(Co). Fitting results beyond a pressure of 2500 bar are not considered in the following data evaluation.

p / bar	1	50	100	200	300	400	500	600	700	800	900	1000	1100	1200	1300
crystal system	trigonal	trigonal	trigonal	trigonal	trigonal	trigonal	trigonal	trigonal	trigonal	trigonal	trigonal	trigonal	trigonal	trigonal	trigonal
space group	$R\bar{3}$	$R\bar{3}$	$R\bar{3}$	$R\bar{3}$	$R\bar{3}$	$R\bar{3}$	$R\bar{3}$	$R\bar{3}$	$R\bar{3}$	$R\bar{3}$	$R\bar{3}$	$R\bar{3}$	$R\bar{3}$	$R\bar{3}$	$R\bar{3}$
a / Å	25.8844(5)	25.8813(7)	25.8800(6)	25.8789(6)	25.8776(6)	25.8704(7)	25.8718(7)	25.8703(7)	25.8668(7)	25.8592(7)	25.8599(7)	25.8540(6)	25.8478(7)	25.8446(6)	25.8435(7)
b / Å	25.8844(5)	25.8813(7)	25.8800(6)	25.8789(6)	25.8776(6)	25.8704(7)	25.8718(7)	25.8703(7)	25.8668(7)	25.8592(7)	25.8599(7)	25.8540(6)	25.8478(7)	25.8446(6)	25.8435(7)
c / Å	6.8545(12)	6.8546(16)	6.8538(15)	6.8511(14)	6.8488(15)	6.8481(16)	6.8457(17)	6.8442(16)	6.8427(17)	6.8422(17)	6.8394(18)	6.8381(16)	6.8370(17)	6.8350(15)	6.8326(17)
α / °	90	90	90	90	90	90	90	90	90	90	90	90	90	90	90
β / °	90	90	90	90	90	90	90	90	90	90	90	90	90	90	90
γ / °	120	120	120	120	120	120	120	120	120	120	120	120	120	120	120
V / Å^3	3977.2(7)	3976.3(0)	3975.5(9)	3973.6(8)	3971.9(9)	3969.3(0)	3968.3(10)	3966.9(0)	3965.0(10)	3962.4(0)	3961.0(10)	3958.4(9)	3955.9(0)	3953.8(9)	3952.0(0)
R_{wp} / %	2.73	3.2	2.86	2.69	2.96	3.17	3.31	3.18	3.31	3.25	3.39	3.06	3.19	2.94	3.2
R_{exp} / %	0.54	0.52	0.52	0.53	0.52	0.52	0.51	0.52	0.51	0.51	0.52	0.52	0.53	0.52	0.51
χ	5.03	6.2	5.48	5.1	5.69	6.1	6.43	6.13	6.45	6.32	6.57	5.94	6.06	5.63	6.21

p / bar	1400	1500	1600	1700	1800	1900	2000	2250	2500	2750	3000	3250	3500	3750	4000	1*
crystal system	trigonal	trigonal	trigonal	trigonal	trigonal	trigonal	trigonal	trigonal	trigonal	trigonal	trigonal	trigonal	trigonal	trigonal	trigonal	trigonal
space group	$R\bar{3}$	$R\bar{3}$	$R\bar{3}$	$R\bar{3}$	$R\bar{3}$	$R\bar{3}$	$R\bar{3}$	$R\bar{3}$	$R\bar{3}$	$R\bar{3}$	$R\bar{3}$	$R\bar{3}$	$R\bar{3}$	$R\bar{3}$	$R\bar{3}$	$R\bar{3}$
a / Å	25.8398(7)	25.8336(7)	25.8273(6)	25.8257(7)	25.8234(7)	25.8212(7)	25.8152(6)	25.8012(7)	25.8006(5)	25.8080(6)	25.8119(11)	25.817(2)	25.825(3)	25.836(4)	25.850(4)	25.974(4)
b / Å	25.8398(7)	25.8336(7)	25.8273(6)	25.8257(7)	25.8234(7)	25.8212(7)	25.8152(6)	25.8012(7)	25.8006(5)	25.8080(6)	25.8119(11)	25.817(2)	25.825(3)	25.836(4)	25.850(4)	25.974(4)
c / Å	6.8311(16)	6.8306(18)	6.8295(15)	6.8275(17)	6.8252(19)	6.8231(17)	6.8225(16)	6.8199(17)	6.8121(13)	6.8031(16)	6.795(4)	6.783(8)	6.771(10)	6.762(12)	6.755(13)	6.780(11)
α / °	90	90	90	90	90	90	90	90	90	90	90	90	90	90	90	90
β / °	90	90	90	90	90	90	90	90	90	90	90	90	90	90	90	90
γ / °	120	120	120	120	120	120	120	120	120	120	120	120	120	120	120	120
V / Å^3	3950.0(0)	3947.8(10)	3945.2(9)	3943.6(10)	3941.6(11)	3939.8(10)	3937.5(0)	3931.8(10)	3927.1(8)	3924.1(9)	3920(2)	3915(4)	3911(6)	3909(7)	3909(8)	3961(6)
R_{wp} / %	3.1	3.29	2.86	3.21	3.47	3.23	3.03	3.06	1.98	1.55	2.31	3.06	3.17	3.04	2.86	2.63
R_{exp} / %	0.52	0.52	0.52	0.52	0.52	0.51	0.51	0.52	0.52	0.53	0.54	0.55	0.56	0.56	0.57	0.6
χ	6.01	6.27	5.49	6.2	6.72	6.28	5.89	5.93	3.78	2.92	4.25	5.56	5.64	5.39	5.05	4.35

Table A3.8. Unit cell parameters and refinement quality indicators provided by sequential profile fits (Pawley method) performed on the HPPXRD patterns of MOF-74(Ni). Fitting results beyond a pressure of 3500 bar are not considered in the following data evaluation.

p / bar	1	50	100	200	300	400	500	600	700	800	900	1000	1100	1200	1300
crystal system	trigonal	trigonal	trigonal	trigonal	trigonal	trigonal	trigonal	trigonal	trigonal	trigonal	trigonal	trigonal	trigonal	trigonal	trigonal
space group	$R\bar{3}$	$R\bar{3}$	$R\bar{3}$	$R\bar{3}$	$R\bar{3}$	$R\bar{3}$	$R\bar{3}$	$R\bar{3}$	$R\bar{3}$	$R\bar{3}$	$R\bar{3}$	$R\bar{3}$	$R\bar{3}$	$R\bar{3}$	$R\bar{3}$
a / Å	25.7812(6)	25.7785(6)	25.7776(6)	25.7754(6)	25.7737(6)	25.7696(6)	25.7668(5)	25.7653(6)	25.7620(5)	25.7610(6)	25.7572(5)	25.7550(6)	25.7528(6)	25.7496(6)	25.7473(6)
b / Å	25.7812(6)	25.7785(6)	25.7776(6)	25.7754(6)	25.7737(6)	25.7696(6)	25.7668(5)	25.7653(6)	25.7620(5)	25.7610(6)	25.7572(5)	25.7550(6)	25.7528(6)	25.7496(6)	25.7473(6)
c / Å	6.7833(13)	6.7835(13)	6.7824(13)	6.7809(13)	6.7794(13)	6.7784(13)	6.7775(13)	6.7758(13)	6.7745(13)	6.7724(13)	6.7716(13)	6.7701(13)	6.7689(13)	6.7678(13)	6.7663(13)
α / °	90	90	90	90	90	90	90	90	90	90	90	90	90	90	90
β / °	90	90	90	90	90	90	90	90	90	90	90	90	90	90	90
γ / °	120	120	120	120	120	120	120	120	120	120	120	120	120	120	120
V / Å^3	3904.6(8)	3903.9(8)	3903.0(8)	3901.5(8)	3900.1(8)	3898.3(8)	3896.9(8)	3895.5(8)	3893.7(8)	3892.2(8)	3890.6(8)	3889.1(8)	3887.7(8)	3886.1(8)	3884.6(8)
R_{wp} / %	2.25	1.98	1.98	1.97	1.98	2.02	1.96	1.99	1.96	1.99	1.95	2.01	2.02	1.99	1.98
R_{exp} / %	0.58	0.56	0.55	0.55	0.55	0.56	0.56	0.56	0.56	0.55	0.56	0.56	0.56	0.57	0.56
χ	3.86	3.54	3.59	3.58	3.57	3.62	3.51	3.53	3.51	3.59	3.48	3.59	3.61	3.47	3.56

1400	1500	1600	1700	1800	1900	2000	2250	2500	2750	3000	3250	3500	3750	4000	1*
trigonal	trigonal	trigonal	trigonal	trigonal	trigonal	trigonal	trigonal	trigonal	trigonal	trigonal	trigonal	trigonal	trigonal	trigonal	trigonal
$R\bar{3}$	$R\bar{3}$	$R\bar{3}$	$R\bar{3}$	$R\bar{3}$	$R\bar{3}$	$R\bar{3}$	$R\bar{3}$	$R\bar{3}$	$R\bar{3}$	$R\bar{3}$	$R\bar{3}$	$R\bar{3}$	$R\bar{3}$	$R\bar{3}$	$R\bar{3}$
25.7448(6)	25.7416(6)	25.7395(5)	25.7351(6)	25.7330(6)	25.7296(6)	25.7281(6)	25.7212(6)	25.7151(6)	25.7079(6)	25.7000(6)	25.6940(6)	25.6898(6)	25.6970(9)	25.7067(14)	25.8105(11)
25.7448(6)	25.7416(6)	25.7395(5)	25.7351(6)	25.7330(6)	25.7296(6)	25.7281(6)	25.7212(6)	25.7151(6)	25.7079(6)	25.7000(6)	25.6940(6)	25.6898(6)	25.6970(9)	25.7067(14)	25.8105(11)
6.7645(13)	6.7635(14)	6.7621(13)	6.7613(14)	6.7600(14)	6.7588(13)	6.7571(13)	6.7542(14)	6.7508(14)	6.7478(13)	6.7438(14)	6.7403(14)	6.7353(15)	6.722(2)	6.707(5)	6.754(4)
90	90	90	90	90	90	90	90	90	90	90	90	90	90	90	90
90	90	90	90	90	90	90	90	90	90	90	90	90	90	90	90
120	120	120	120	120	120	120	120	120	120	120	120	120	120	120	120
3882.8(8)	3881.2(8)	3879.8(8)	3878.1(8)	3876.6(8)	3874.9(8)	3873.5(8)	3869.8(8)	3866.0(8)	3862.1(8)	3857.5(8)	3853.7(8)	3849.5(9)	3844.2(14)	3838(3)	3896(2)
2.02	2.07	1.97	2.08	2.04	2.01	2	2.05	2.08	2.04	2.05	2.03	2.09	2.48	2.98	2.31
0.56	0.55	0.56	0.56	0.55	0.56	0.56	0.56	0.56	0.56	0.56	0.56	0.57	0.57	0.58	0.6
3.64	3.75	3.56	3.74	3.69	3.57	3.57	3.63	3.71	3.65	3.67	3.62	3.69	4.34	5.12	3.83

Table A3.9. Unit cell parameters and refinement quality indicators provided by sequential profile fits (Pawley method) performed on the HPPXRD patterns of MOF-74(Cu).

p / bar	1	50	100	200	400	500	600	700	800	900	1000	1100	1200	1300	1400
crystal system	trigonal	trigonal	trigonal	trigonal	trigonal	trigonal	trigonal	trigonal	trigonal	trigonal	trigonal	trigonal	trigonal	trigonal	trigonal
space group	$R\bar{3}$	$R\bar{3}$	$R\bar{3}$	$R\bar{3}$	$R\bar{3}$	$R\bar{3}$	$R\bar{3}$	$R\bar{3}$	$R\bar{3}$	$R\bar{3}$	$R\bar{3}$	$R\bar{3}$	$R\bar{3}$	$R\bar{3}$	$R\bar{3}$
a / Å	25.8370(2)	25.8323(3)	25.8340(2)	25.8398(3)	25.8243(4)	25.8270(5)	25.8343(4)	25.8269(4)	25.8268(4)	25.8020(4)	25.8117(4)	25.7995(4)	25.7935(6)	25.8053(4)	25.7972(4)
b / Å	25.8370(2)	25.8323(3)	25.8340(2)	25.8398(3)	25.8243(4)	25.8270(5)	25.8343(4)	25.8269(4)	25.8268(4)	25.8020(4)	25.8117(4)	25.7995(4)	25.7935(6)	25.8053(4)	25.7972(4)
c / Å	6.2508(3)	6.2508(4)	6.2488(3)	6.2452(4)	6.2439(5)	6.2428(6)	6.2371(5)	6.2373(5)	6.2338(5)	6.2385(5)	6.2343(6)	6.2345(5)	6.2334(7)	6.2285(5)	6.2270(5)
α / °	90	90	90	90	90	90	90	90	90	90	90	90	90	90	90
β / °	90	90	90	90	90	90	90	90	90	90	90	90	90	90	90
γ / °	120	120	120	120	120	120	120	120	120	120	120	120	120	120	120
V / Å^3	3613.7(2)	3612.3(2)	3611.72(16)	3611.2(2)	3606.1(3)	3606.3(4)	3605.0(3)	3603.0(3)	3601.0(3)	3596.8(3)	3597.1(3)	3593.8(3)	3591.5(4)	3592.0(3)	3588.8(3)
R_{wp} / %	1.98	2.3	1.68	2.15	2.92	3.93	2.84	3.15	3.28	3.06	3.35	3.11	4.21	3.32	3.08
R_{exp} / %	3.48	4.09	4.44	4.16	3.74	3.7	3.54	3.58	3.59	3.65	3.65	3.71	3.71	3.71	3.8
χ	0.57	0.56	0.38	0.52	0.78	1.06	0.8	0.88	0.91	0.84	0.92	0.84	1.13	0.89	0.81

1500	1600	1700	1800	1900	2000	2250	2500	2750	3000	3250	3500	3750	4000	1*
trigonal	trigonal	trigonal	trigonal	trigonal	trigonal	trigonal	trigonal	trigonal	trigonal	trigonal	trigonal	trigonal	trigonal	trigonal
$R\bar{3}$	$R\bar{3}$	$R\bar{3}$	$R\bar{3}$	$R\bar{3}$	$R\bar{3}$	$R\bar{3}$	$R\bar{3}$	$R\bar{3}$	$R\bar{3}$	$R\bar{3}$	$R\bar{3}$	$R\bar{3}$	$R\bar{3}$	$R\bar{3}$
25.7922(4)	25.7937(4)	25.7912(4)	25.7844(3)	25.7780(3)	25.7746(3)	25.7518(6)	25.7531(3)	25.7470(3)	25.7362(4)	25.7267(5)	25.7119(4)	25.7043(6)	25.7008(8)	25.8529(10)
25.7922(4)	25.7937(4)	25.7912(4)	25.7844(3)	25.7780(3)	25.7746(3)	25.7518(6)	25.7531(3)	25.7470(3)	25.7362(4)	25.7267(5)	25.7119(4)	25.7043(6)	25.7008(8)	25.8529(10)
6.2250(4)	6.2220(5)	6.2213(4)	6.2207(4)	6.2194(4)	6.2166(4)	6.2163(7)	6.2089(4)	6.2027(4)	6.1985(5)	6.1956(6)	6.1926(7)	6.1887(9)	6.1835(15)	6.2448(18)
90	90	90	90	90	90	90	90	90	90	90	90	90	90	90
90	90	90	90	90	90	90	90	90	90	90	90	90	90	90
120	120	120	120	120	120	120	120	120	120	120	120	120	120	120
3586.3(3)	3585.0(3)	3583.9(3)	3581.7(2)	3579.1(2)	3576.6(2)	3570.1(4)	3566.2(2)	3561.0(2)	3555.5(3)	3551.3(4)	3545.4(4)	3541.1(6)	3537.2(9)	3614.7(11)
2.75	2.9	2.68	2.46	2.26	2.47	4.36	2.42	2.21	2.82	2.9	2.48	2.97	4.02	4.68
3.86	3.8	3.79	3.84	3.89	3.89	3.86	3.92	3.9	4.04	4.08	4	4.05	4.07	4.22
0.71	0.76	0.71	0.64	0.58	0.64	1.13	0.62	0.57	0.7	0.71	0.62	0.73	0.99	1.11

Table A3.10. Unit cell parameters and refinement quality indicators provided by sequential profile fits (Pawley method) performed on the HPPXRD patterns of MOF-74(Zn). Fitting results beyond a pressure of 2000 bar are not considered in the following data evaluation.

p / bar	1	200	400	600	800	1000	1200	1400	1600	1800	2000	2500	3000	3500	4000	1*
crystal system	trigonal	trigonal	trigonal	trigonal	trigonal	trigonal	trigonal	trigonal	trigonal	trigonal	trigonal	trigonal	trigonal	trigonal	trigonal	trigonal
space group	$R\bar{3}$	$R\bar{3}$	$R\bar{3}$	$R\bar{3}$	$R\bar{3}$	$R\bar{3}$	$R\bar{3}$	$R\bar{3}$	$R\bar{3}$	$R\bar{3}$	$R\bar{3}$	$R\bar{3}$	$R\bar{3}$	$R\bar{3}$	$R\bar{3}$	$R\bar{3}$
a / Å	25.7573(9)	25.7534(8)	25.7485(8)	25.7384(9)	25.7299(0)	25.7207(1)	25.7140(10)	25.7041(11)	25.7022(12)	25.6942(11)	25.6897(11)	25.6648(12)	25.5976(9)	25.610(3)	25.694(4)	25.956(3)
b / Å	25.7573(9)	25.7534(8)	25.7485(8)	25.7384(9)	25.7299(0)	25.7207(1)	25.7140(10)	25.7041(11)	25.7022(12)	25.6942(11)	25.6897(11)	25.6648(12)	25.5976(9)	25.610(3)	25.694(4)	25.956(3)
c / Å	6.801(2)	6.794(2)	6.788(2)	6.782(2)	6.775(3)	6.768(3)	6.760(3)	6.750(3)	6.738(3)	6.726(3)	6.711(3)	6.668(4)	6.602(4)	6.538(14)	6.51(2)	6.555(16)
α / °	90	90	90	90	90	90	90	90	90	90	90	90	90	90	90	90
β / °	90	90	90	90	90	90	90	90	90	90	90	90	90	90	90	90
γ / °	120	120	120	120	120	120	120	120	120	120	120	120	120	120	120	120
V / Å^3	3907.6(12)	3902.6(14)	3897.3(14)	3890.8(15)	3884.4(16)	3877.7(17)	3871.3(17)	3862.5(18)	3854.5(19)	3845.5(17)	3835.7(17)	3803.6(20)	3746(2)	3713(8)	3723(13)	3824(9)
R_{wp} / %	3.67	3.44	3.35	3.43	3.79	3.85	3.86	4.03	4.27	3.77	3.7	4.19	2.31	3.1	2.93	1.11
R_{exp} / %	3.51	3.45	3.45	3.46	3.41	3.4	3.34	3.26	3.19	3.16	3.15	3.16	3.27	3.51	3.61	3.38
χ	1.04	1	0.97	0.99	1.11	1.14	1.16	1.24	1.34	1.19	1.17	1.33	0.71	0.88	0.81	0.33

Table A3.11. Unit cell parameters and refinement quality indicators provided by sequential profile fits (Pawley method) performed on the HPPXRD patterns of Mg_2(dobpdc). Fitting results beyond a pressure of 1200 bar are not considered in the following data evaluation.

p / bar	1	200	400	600	800	1000	1200	1400	1600	1800	2000	3000	4000
crystal system	trigonal	trigonal	trigonal	trigonal	trigonal	trigonal	trigonal	trigonal	trigonal	trigonal	trigonal	trigonal	trigonal
space group	$P3_121$	$P3_121$	$P3_121$	$P3_121$	$P3_121$	$P3_121$	$P3_121$	$P3_121$	$P3_121$	$P3_121$	$P3_121$	$P3_121$	$P3_121$
a / Å	21.3779(4)	21.3218(4)	21.2664(4)	21.2053(4)	21.1458(4)	21.0835(7)	21.0301(12)	20.9676(19)	20.913(5)	20.886(13)	20.91(5)	20.86(15)	20.7(3)
b / Å	21.3779(4)	21.3218(4)	21.2664(4)	21.2053(4)	21.1458(4)	21.0835(7)	21.0301(12)	20.9676(19)	20.913(5)	20.886(13)	20.91(5)	20.86(15)	20.7(3)
c / Å	6.742(3)	6.732(3)	6.725(3)	6.723(3)	6.717(3)	6.719(5)	6.723(6)	6.820(7)	6.811(6)	6.808(9)	6.80(5)	6.77(20)	6.8(3)
α / °	90	90	90	90	90	90	90	90	90	90	90	90	90
β / °	90	90	90	90	90	90	90	90	90	90	90	90	90
γ / °	120	120	120	120	120	120	120	120	120	120	120	120	120
V / Å^3	2668.5(13)	2650.6(13)	2633.9(13)	2618.0(12)	2601.3(13)	2586.4(18)	2575(2)	2596(2)	2579(2)	2571(4)	2574(21)	2548(87)	2515(119)
R_{wp} / %	1.13	1.06	1.04	0.99	0.99	1.18	1.15	0.72	0.55	0.52	0.44	0.37	0.37
R_{exp} / %	2.76	2.67	2.67	2.68	2.69	2.77	2.84	2.90	2.94	2.98	3.02	3.08	3.14
χ	0.41	0.40	0.39	0.37	0.37	0.43	0.41	0.25	0.19	0.18	0.14	0.12	0.12

Table A3.12. Unit cell parameters and refinement quality indicators provided by sequential profile fits (Pawley method) performed on the HPPXRD patterns of mmen@Mg_2(dobpdc). Fitting results beyond a pressure of 1200 bar are not considered in the following data evaluation.

p / bar	1	200	400	600	800	1000	1200	1400	1600	1800	2000	2500	3000	3500	4000	1*
crystal system	trigonal	trigonal	trigonal	trigonal	trigonal	trigonal	trigonal	trigonal	trigonal	trigonal	trigonal	trigonal	trigonal	trigonal	trigonal	trigonal
space group	$P3_121$	$P3_121$	$P3_121$	$P3_121$	$P3_121$	$P3_121$	$P3_121$	$P3_121$	$P3_121$	$P3_121$	$P3_121$	$P3_121$	$P3_121$	$P3_121$	$P3_121$	$P3_121$
a / Å	21.5544(5)	21.5299(5)	21.4922(5)	21.4586(5)	21.4209(5)	21.3807(5)	21.3285(7)	21.2883(15)	21.253(3)	21.203(6)	21.158(9)	21.03(2)	22.21(2)	22.19(2)	22.145(17)	21.5048(6)
b / Å	21.5544(5)	21.5299(5)	21.4922(5)	21.4586(5)	21.4209(5)	21.3807(5)	21.3285(7)	21.2883(15)	21.253(3)	21.203(6)	21.158(9)	21.03(2)	22.21(2)	22.19(2)	22.145(17)	21.5048(6)
c / Å	6.926(3)	6.922(3)	6.913(3)	6.903(3)	6.897(3)	6.888(3)	6.879(4)	6.868(6)	6.860(8)	6.849(9)	6.838(9)	6.815(11)	6.97(11)	6.96(9)	6.95(8)	6.923(5)
α / °	90	90	90	90	90	90	90	90	90	90	90	90	90	90	90	90
β / °	90	90	90	90	90	90	90	90	90	90	90	90	90	90	90	90
γ / °	120	120	120	120	120	120	120	120	120	120	120	120	120	120	120	120
V / Å^3	2786.8(11)	2778.8(11)	2765.3(11)	2752.7(11)	2740.6(12)	2726.9(12)	2710.0(15)	2695(2)	2683(3)	2667(4)	2651(4)	2611(7)	2980(48)	2968(41)	2951(35)	2772.8(19)
R_{wp} / %	1.05	0.92	0.89	0.90	0.86	0.87	0.92	1.26	1.48	1.63	1.67	1.67	0.86	0.77	0.71	1.05
R_{exp} / %	3.03	2.98	3.01	3.03	3.04	3.07	3.09	3.16	3.22	3.24	3.26	3.32	3.34	3.38	3.38	3.16
χ	0.35	0.31	0.29	0.30	0.28	0.28	0.30	0.40	0.46	0.50	0.51	0.50	0.26	0.23	0.21	0.33

Table A3.13. Refined unit cell parameters and refinement quality indicators for the profile fits (Pawley method) performed on the HPPXRD patterns of MOF-74(Ni). The fits were performed with a constant z-value of -0.00085(10) (2Θ) with both crystal-size and macrostrain-broadening macros applied simultaneously. The pattern denoted with (*) refers to the pattern collected after pressure release. The trend observed for the microstrain ϵ_0 and domain size L_{Vol} is shown in Figure A3.34.

p / bar	1	500	1000	1500	2000	2500	3000	3500	4000	1*
Crystal system	trigonal	trigonal	trigonal	trigonal	trigonal	trigonal	trigonal	trigonal	trigonal	trigonal
Space group	$R\bar{3}$	$R\bar{3}$	$R\bar{3}$	$R\bar{3}$	$R\bar{3}$	$R\bar{3}$	$R\bar{3}$	$R\bar{3}$	$R\bar{3}$	$R\bar{3}$
a / Å	25.7788(6)	25.7644(6)	25.7526(6)	25.7391(6)	25.7257(6)	25.7126(6)	25.6975(6)	25.6872(6)	25.7023(13)	25.836(4)
b / Å	25.7788(6)	25.7644(6)	25.7526(6)	25.7391(6)	25.7257(6)	25.7126(6)	25.6975(6)	25.6872(6)	25.7023(13)	25.836(4)
c / Å	6.7836(12)	6.7777(13)	6.7701(14)	6.7636(14)	6.7571(13)	6.7510(14)	6.7442(14)	6.7356(15)	6.707(4)	6.750(3)
α / °	90	90	90	90	90	90	90	90	90	90
β / °	90	90	90	90	90	90	90	90	90	90
γ / °	120	120	120	120	120	120	120	120	120	120
V / Å^3	3904.1(7)	3896.3(8)	3888.4(8)	3880.6(8)	3872.8(8)	3865.4(8)	3856.9(8)	3848.9(9)	3837(2)	3902(2)
R_{wp} / %	2.24	1.97	2.02	2.08	2.01	2.09	2.02	2.07	2.59	1.75
R_{exp} / %	0.59	0.56	0.56	0.55	0.56	0.56	0.56	0.56	0.58	0.60
χ	3.82	3.54	3.62	3.78	3.59	3.74	3.64	3.67	4.50	2.94
ε_0 / %	0.08 ± 0.02	0.08 ± 0.02	0.09 ± 0.02	0.09 ± 0.02	0.10 ± 0.02	0.10 ± 0.02	0.10 ± 0.02	0.10 ± 0.02	0.18 ± 0.07	0.12 ± 0.07
L_{Vol} / nm	172 ± 24	190 ± 30	181 ± 28	155 ± 20	158 ± 20	147 ± 17	153 ± 19	129 ± 14	85 ± 20	169 ± 49

A3.8 Bulk Modulus and Linear Compressibility

To investigate the structural behavior of the MOFs upon pressure increase, the unit cell parameters obtained from sequential profile fitting were plotted against the applied hydrostatic pressure. For the individual unit cell parameters a, b and c (with $a = b$ in the trigonal crystal system), a linear compressibility α_L ($L = a$, b or c, and L_0 as the unit cell parameter at $p = 0$) was calculated via linear regression according to Equation A3.1.

$$\alpha_L = -\frac{1}{L_0}\frac{\mathrm{d}L}{\mathrm{d}p} \tag{A3.1}$$

The change of the unit cell volume V was quantified by performing a fit with the 2nd order Birch-Murnaghan equation of state (second-order BMEOS[282], Equation A3.2) providing the bulk modulus K_0 and the unit cell volume V_0 at $p = 0$.

$$p = -\frac{2}{3}K_0\left(\left(\frac{V}{V_0}\right)^{-\frac{7}{3}} - \left(\frac{V}{V_0}\right)^{-\frac{5}{3}}\right) \tag{A3.2}$$

To ensure the reliability of the structural analysis, data points exhibiting strong deviations from the expected pressure-dependent trend of the unit cell parameters were excluded from further evaluation. These excluded points, highlighted in pale colors in the corresponding plots, display unphysical behavior, for example an increase in unit cell volume with increasing hydrostatic pressure. Such anomalies are attributed to partial amorphization of the material at elevated pressures, which renders the refinement of lattice parameters unreliable in this regime. Consequently, only data collected below the onset of pressure-induced amorphization were considered for the determination of the linear compressibilities and for fitting the second-order BMEOS.

A3.8.1 Potassium bromide (KBr)

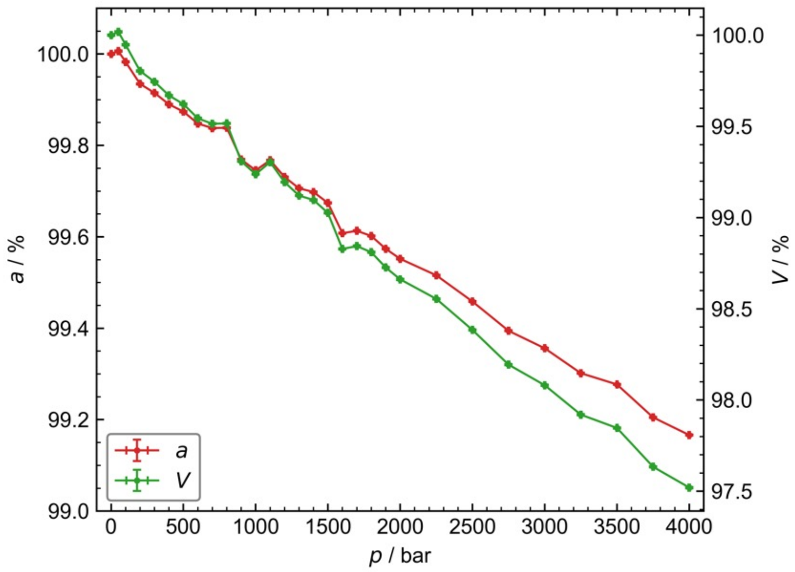

Figure A3.35. Relative progression of the unit cell parameter a and the unit cell volume V of KBr during pressure increase. The data were extracted via profile fits performed on the corresponding HPPXRD patterns (see Table A3.4). Lines are a guide to the eye.

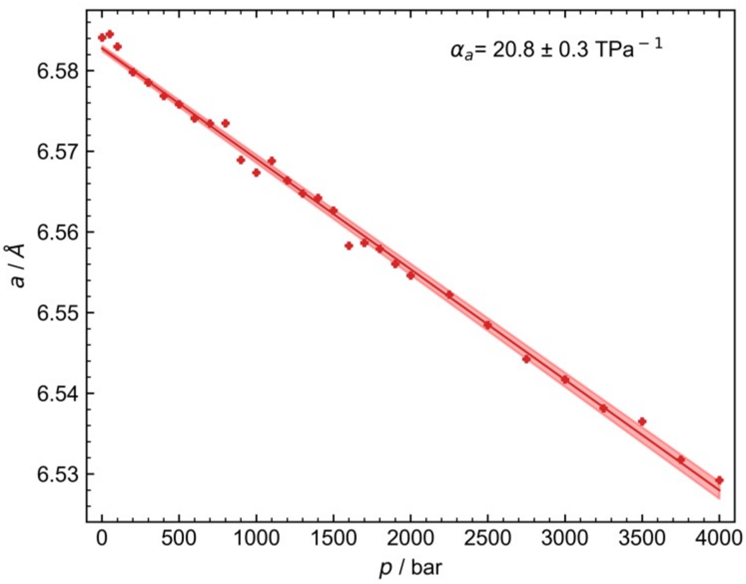

Figure A3.36. Linear fit on the progression of unit cell parameter a of KBr during pressure increase. The data were extracted via sequential profile fits performed on the corresponding HPPXRD patterns (see Table A3.4). The linear compressibility value α_a was calculated based on the linear fit. Filled areas indicate the confidence interval of one standard deviation. The obtained linear compressibility is in good agreement with a linear compressibility of 22.8 – 23.5 TPa^{-1} calculated based on the bulk modulus of 14.2−14.6 GPa for KBr reported in the literature.[233,234]

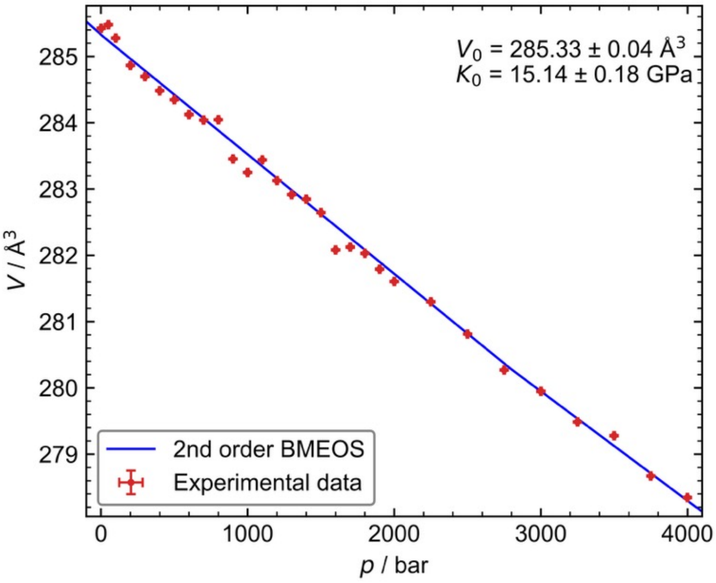

Figure A3.37. Fit of the 2nd order BMEOS on the progression of the unit cell volume V of KBr during pressure increase, providing the reference volume V_0 and the bulk modulus K_0. The data was extracted via profile fits performed on the corresponding HPPXRD pattern (see Table A3.4). The calculated bulk modulus is in good accordance with the literature value of 14.2−14.6 GPa.[233,234]

A3.8.2 MOF-74(Mg)

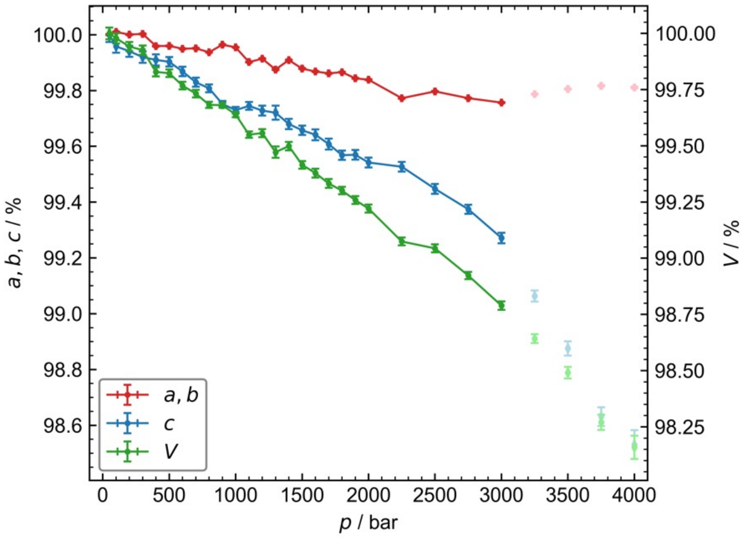

Figure A3.38. Relative progression of unit cell parameters a, b and c as well as the resulting unit cell volume V of MOF-74(Mg) during pressure increase. The data were extracted via profile fits performed on the HPPXRD patterns (see Table A3.5). Pale, non-interconnected points were removed from the evaluation due to limited reliability as a consequence of substantially reduced scattering intensity from the sample at high pressures. Lines are a guide to the eye.

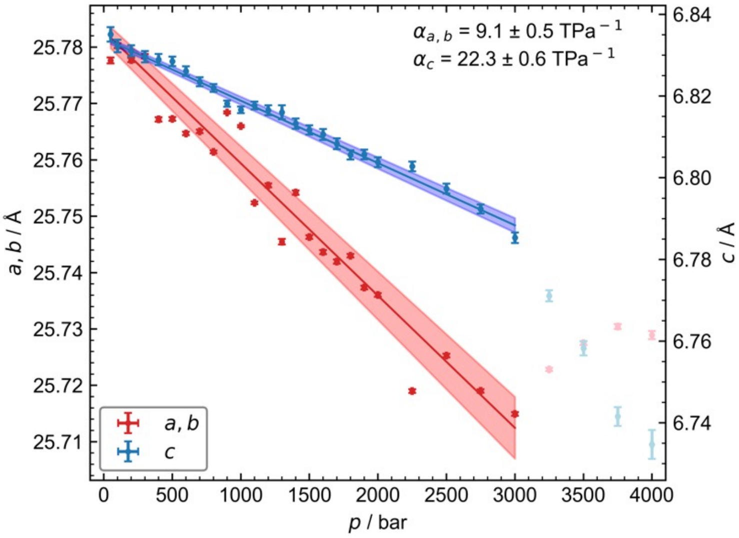

Figure A3.39. Linear fits on the progression of unit cell parameters of MOF-74(Mg) during pressure increase. The data were extracted via sequential profile fits performed on the HPPXRD patterns (see Table A3.5). The linear compressibility values α for the respective axes were calculated based on the linear fits. Pale points were removed from the evaluation due to limited reliability as a consequence of substantially reduced scattering intensity from the sample at high pressures. Pale colored areas indicate the confidence interval of one standard deviation.

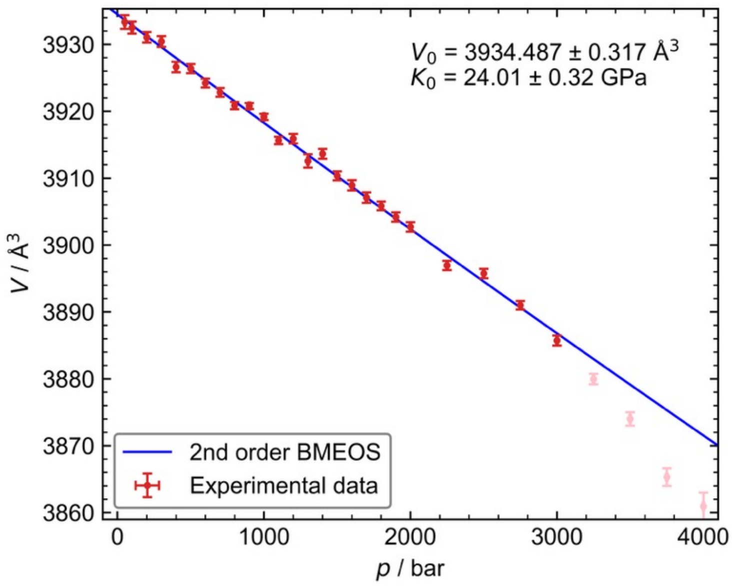

Figure A3.40. Fit of the second-order BMEOS on the progression of the unit cell volume V of MOF-74(Mg) during pressure increase, providing the reference volume V_0 and the bulk modulus K_0. The data were extracted via profile fits performed on the corresponding HPPXRD patterns (see Table A3.5). Pale points were removed from the evaluation due to limited reliability as a consequence of substantially reduced scattering intensity from the sample at high pressures.

A3.8.3 MOF-74(Mn)

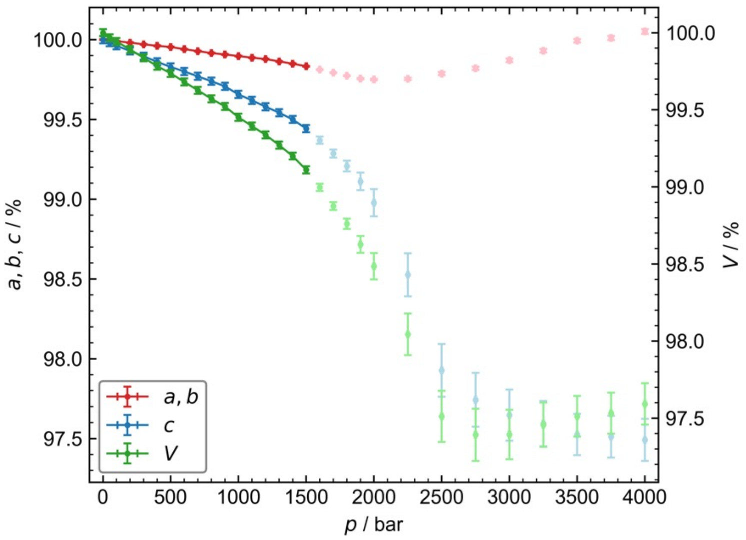

Figure A3.41. Relative progression of unit cell parameters a, b and c as well as the resulting unit cell volume V of MOF-74(Mn). The data were extracted via profile fits performed on the corresponding HPPXRD patterns (see Table A3.6). Pale, non-interconnected points were removed from the evaluation due to limited reliability as a consequence of substantially reduced scattering intensity from the sample at high pressures. Lines are a guide to the eye.

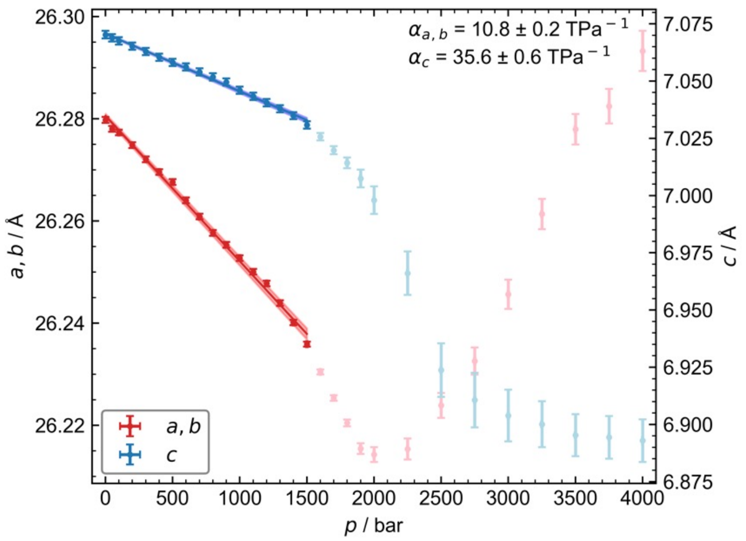

Figure A3.42. Linear fits on the progression of unit cell parameters of MOF-74(Mn) during pressure increase. The data were extracted via sequential profile fits performed on the HPPXRD patterns (see Table A3.6). The linear compressibility values α for the respective axes were calculated based on the linear fits. Pale points were removed from the evaluation due to limited reliability as a consequence of substantially reduced scattering intensity from the sample at high pressures. Pale colored areas indicate the confidence interval of one standard deviation.

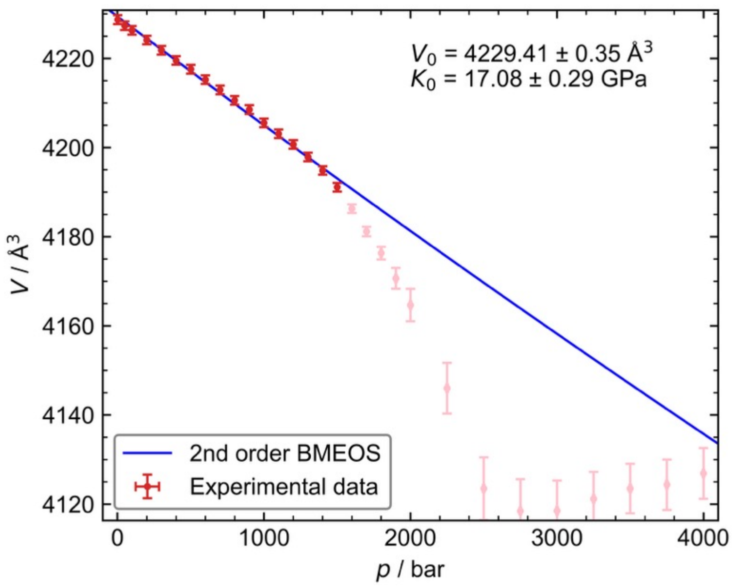

Figure A3.43. Fit of the second-order BMEOS on the progression of the unit cell volume V of MOF-74(Mn) during pressure increase, providing the reference volume V_0 and the bulk modulus K_0. The data were extracted via profile fits performed on the corresponding HPPXRD patterns (see Table A3.6). Pale points were removed from the evaluation due to limited reliability as a consequence of substantially reduced scattering intensity from the sample at high pressures.

A3.8.4 MOF-74(Co)

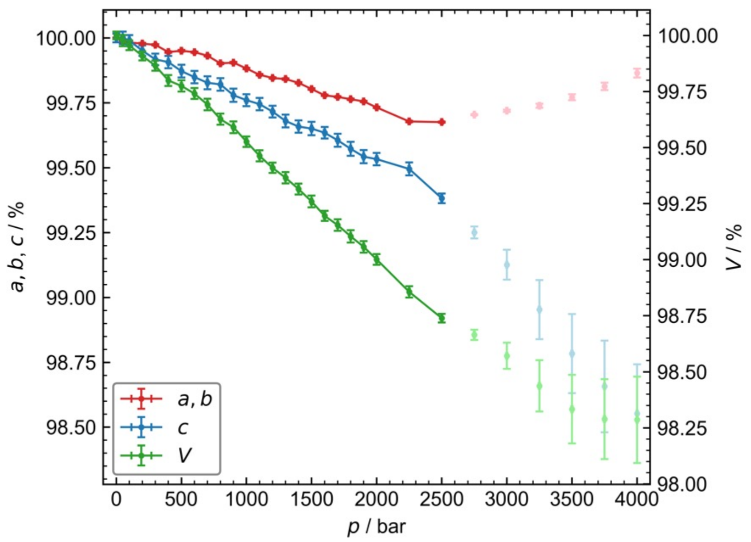

Figure A3.44. Relative progression of unit cell parameters a, b and c as well as the resulting unit cell volume V of MOF-74(Co) during pressure increase. The data were extracted via profile fits performed on the HPPXRD pattern (see Table A3.7). Pale, non-interconnected points were removed from the evaluation due to limited reliability as a consequence of substantially reduced scattering intensity from the sample at high pressures. Lines are a guide to the eye.

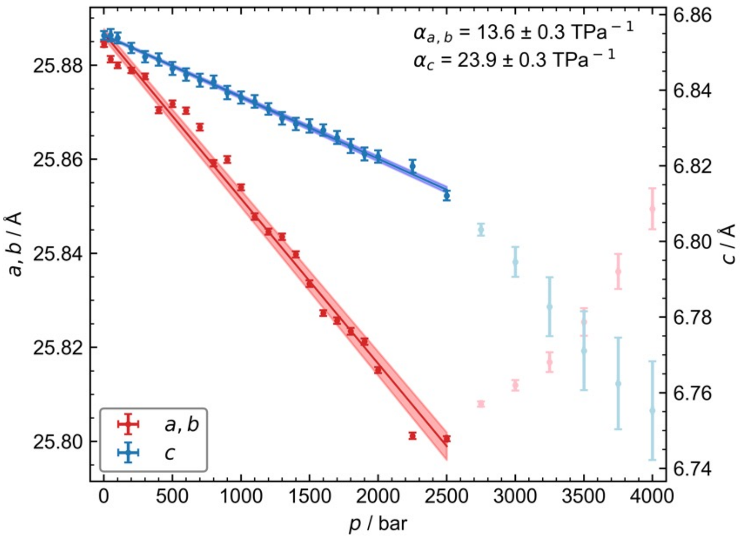

Figure A3.45. Linear fits on the progression of unit cell parameters of MOF-74(Co) during pressure increase. The data were extracted via sequential profile fits performed on the HPPXRD patterns (see Table A3.7). The linear compressibility values α for the respective axes were calculated based on the linear fits. Pale points were removed from the evaluation due to limited reliability as a consequence of substantially reduced scattering intensity from the sample at high pressures. Pale colored areas indicate the confidence interval of one standard deviation.

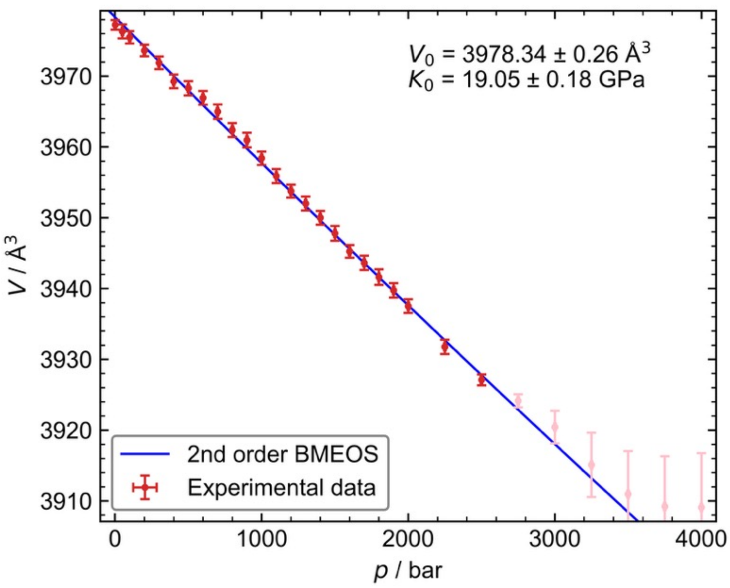

Figure A3.46. Fit of the second-order BMEOS on the progression of the unit cell volume V of MOF-74(Co) during pressure increase, providing the reference volume V_0 and the bulk modulus K_0. The data were extracted via profile fits performed on the corresponding HPPXRD patterns (see Table A3.7). Pale points were removed from the evaluation due to limited reliability as a consequence of substantially reduced scattering intensity from the sample at high pressures.

A3.8.5 MOF-74(Ni)

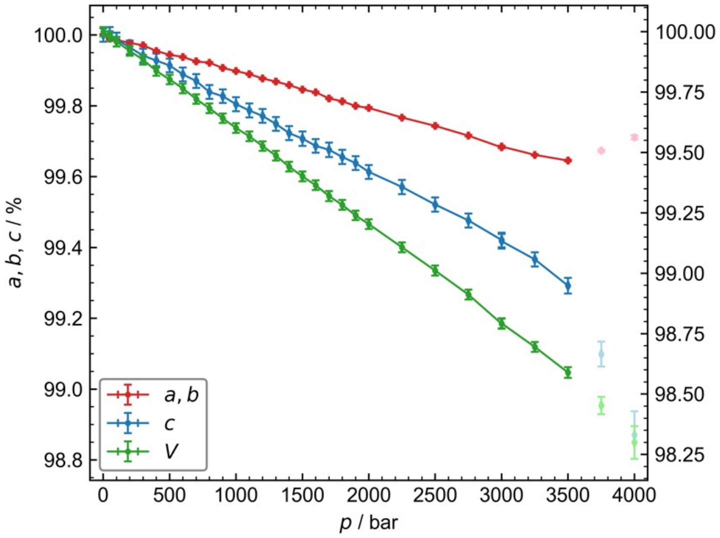

Figure A3.47. Relative progression of unit cell parameters a, b and c as well as the resulting unit cell volume V of MOF-74(Ni) during pressure increase. The data were extracted via profile fits performed on the HPPXRD patterns (see Table A3.8). Pale, non-interconnected points were removed from the evaluation due to limited reliability as a consequence of substantially reduced scattering intensity from the sample at high pressures. Lines are a guide to the eye.

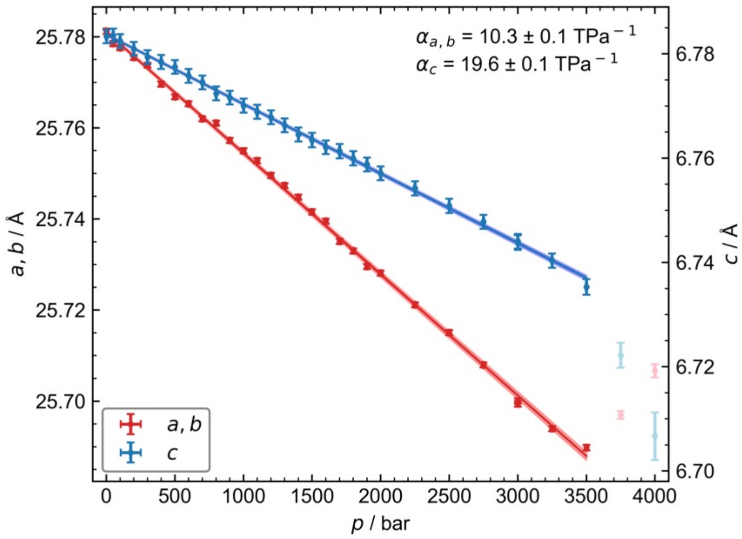

Figure A3.48. Linear fits on the progression of unit cell parameters of MOF-74(Ni) during pressure increase. The data were extracted via sequential profile fits performed on the HPPXRD patterns (see Table A3.8). The linear compressibility values α for the respective axes were calculated based on the linear fits. Pale points were removed from the evaluation due to limited reliability as a consequence of substantially reduced scattering intensity from the sample at high pressures. Pale colored areas indicate the confidence interval of one standard deviation.

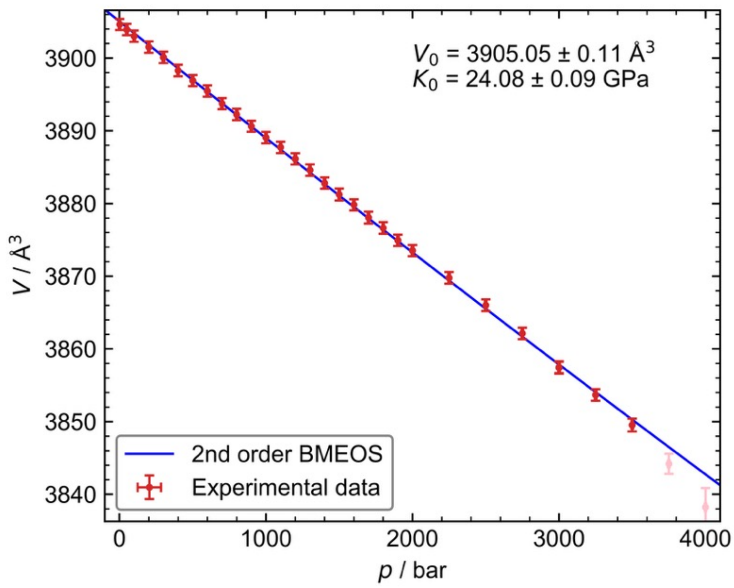

Figure A3.49. Fit of the second-order BMEOS on the progression of the unit cell volume V of MOF-74(Ni) during pressure increase, providing the reference volume V_0 and the bulk modulus K_0. The data were extracted via profile fits performed on the corresponding HPPXRD patterns (see Table A3.8). Pale points were removed from the evaluation due to limited reliability as a consequence of substantially reduced scattering intensity from the sample at high pressures.

A3.8.6 MOF-74(Cu)

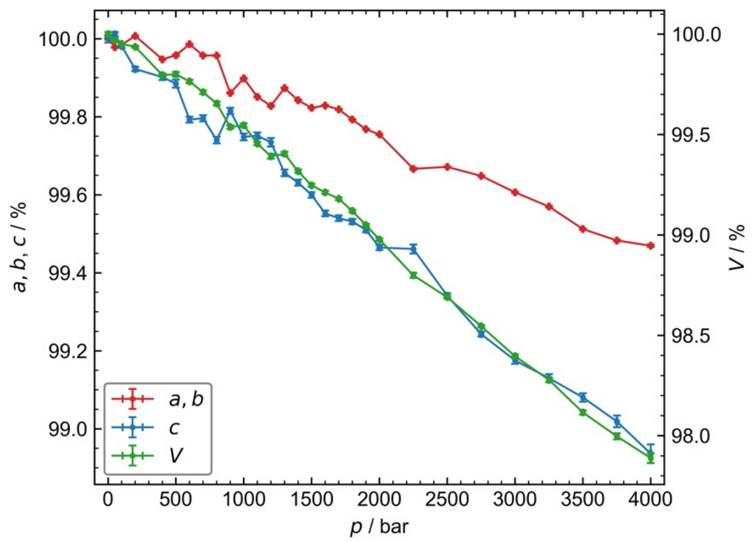

Figure A3.50. Relative progression of unit cell parameters a, b and c as well as the resulting unit cell volume V of MOF-74(Cu) during pressure increase. The data were extracted via profile fits performed on the HPPXRD patterns (see Table A3.9). Pale, non-interconnected points were removed from the evaluation due to limited reliability as a consequence of substantially reduced scattering intensity from the sample at high pressures. Lines are a guide to the eye.

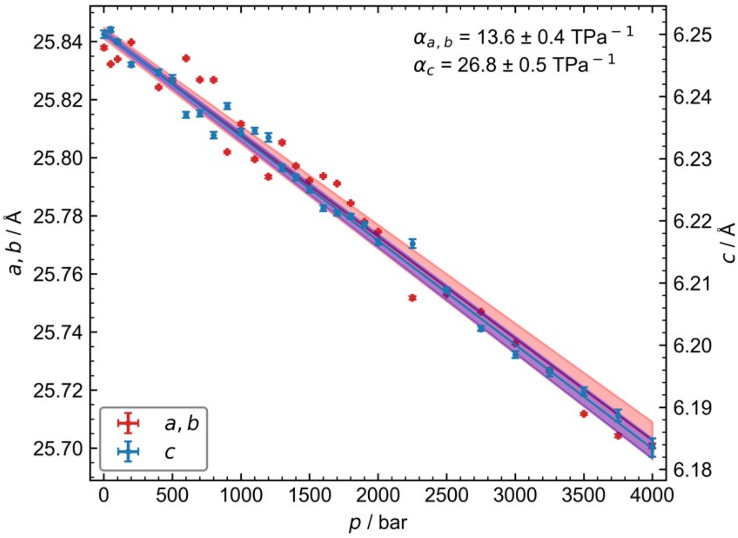

Figure A3.51. Linear fits on the progression of unit cell parameters of MOF-74(Cu) during pressure increase. The data were extracted via sequential profile fits performed on the HPPXRD patterns (see Table A3.9). The linear compressibility values α for the respective axes were calculated based on the linear fits. Pale points were removed from the evaluation due to limited reliability as a consequence of substantially reduced scattering intensity from the sample at high pressures. Pale colored areas indicate the confidence interval of one standard deviation.

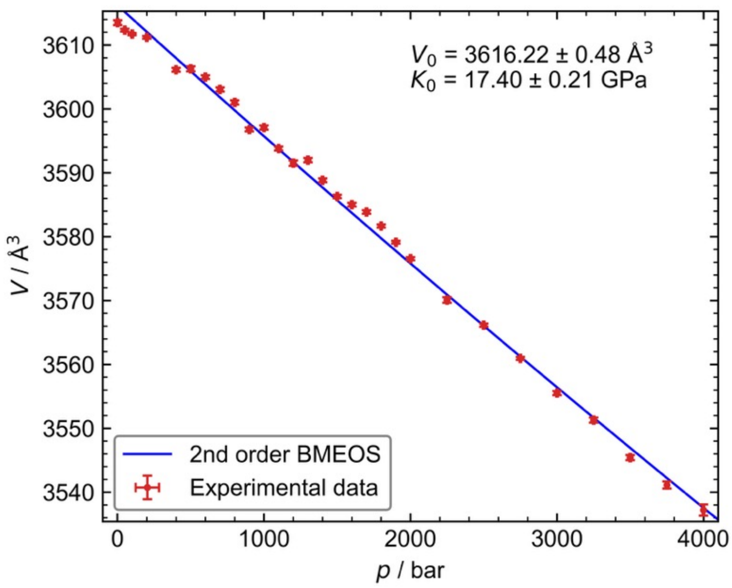

Figure A3.52. Fit of the second-order BMEOS on the progression of the unit cell volume V of MOF-74(Cu) during pressure increase, providing the reference volume V_0 and the bulk modulus K_0. The data were extracted via profile fits performed on the corresponding HPPXRD patterns (see Table A3.9). Pale points were removed from the evaluation due to limited reliability as a consequence of substantially reduced scattering intensity from the sample at high pressures.

A3.8.7 MOF-74(Zn)

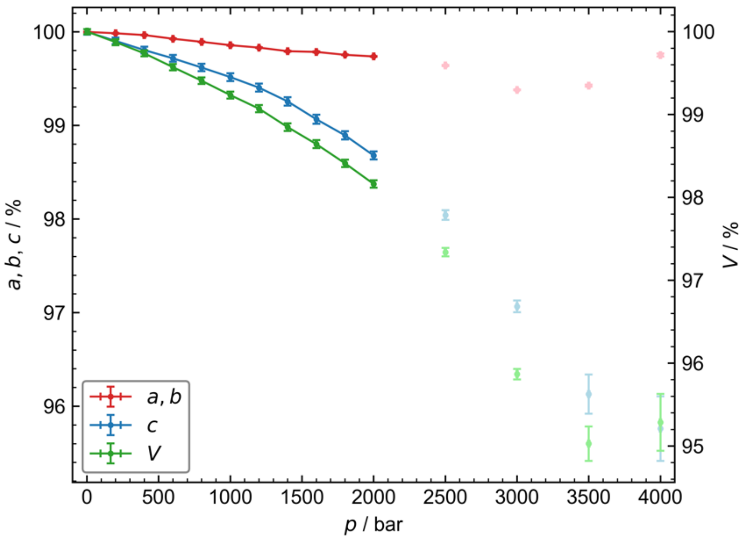

Figure A3.53. Relative progression of unit cell parameters a, b and c as well as the resulting unit cell volume V of MOF-74(Zn) during pressure increase. The data were extracted via profile fits performed on the HPPXRD patterns (see Table A3.10). Pale, non-interconnected points were removed from the evaluation due to limited reliability as a consequence of substantially reduced scattering intensity from the sample at high pressures. Lines are a guide to the eye.

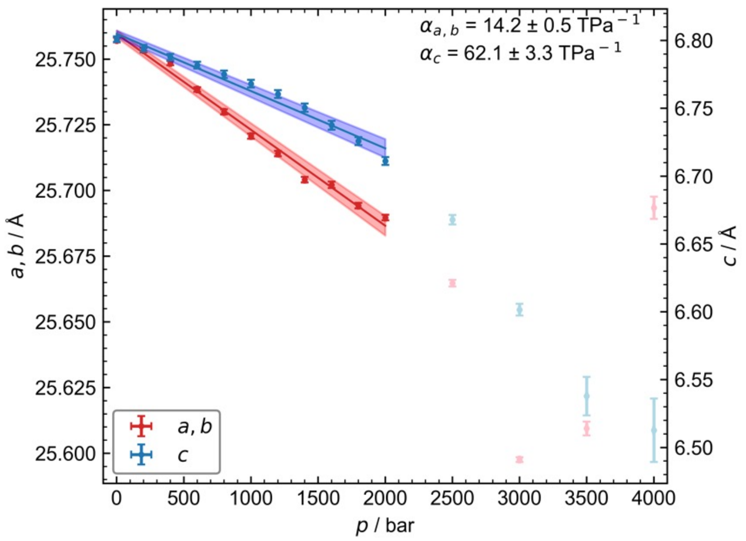

Figure A3.54. Linear fits on the progression of unit cell parameters of MOF-74(Zn) during pressure increase. The data were extracted via sequential profile fits performed on the HPPXRD patterns (see Table A3.10). The linear compressibility values α for the respective axes were calculated based on the linear fits. Pale points were removed from the evaluation due to limited reliability as a consequence of substantially reduced scattering intensity from the sample at high pressures. Pale colored areas indicate the confidence interval of one standard deviation.

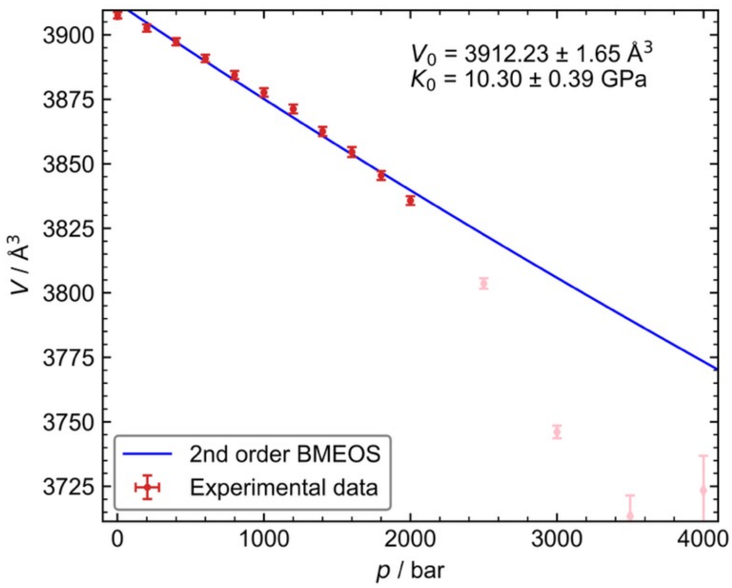

Figure A3.55. Fit of the second-order BMEOS on the progression of the unit cell volume V of MOF-74(Zn) during pressure increase, providing the reference volume V_0 and the bulk modulus K_0. The data were extracted via profile fits performed on the corresponding HPPXRD patterns (see Table A3.10). Pale points were removed from the evaluation due to limited reliability as a consequence of substantially reduced scattering intensity from the sample at high pressures.

A3.8.8 Mg_2(dobpdc)

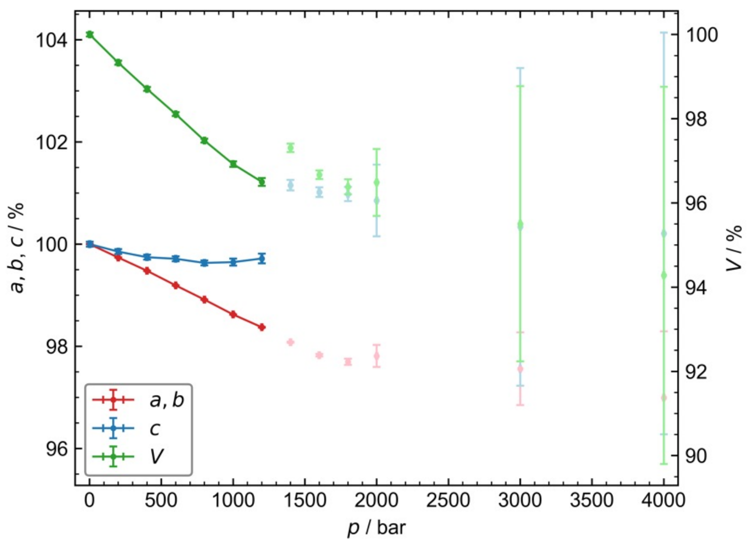

Figure A3.56. Relative progression of unit cell parameters a, b and c as well as the resulting unit cell volume V of Mg_2(dobpdc) during pressure increase. The data were extracted via profile fits performed on the HPPXRD patterns (see Table A3.11). Pale, non-interconnected points were removed from the evaluation due to limited reliability as a consequence of substantially reduced scattering intensity from the sample at high pressures. Lines are a guide to the eye.

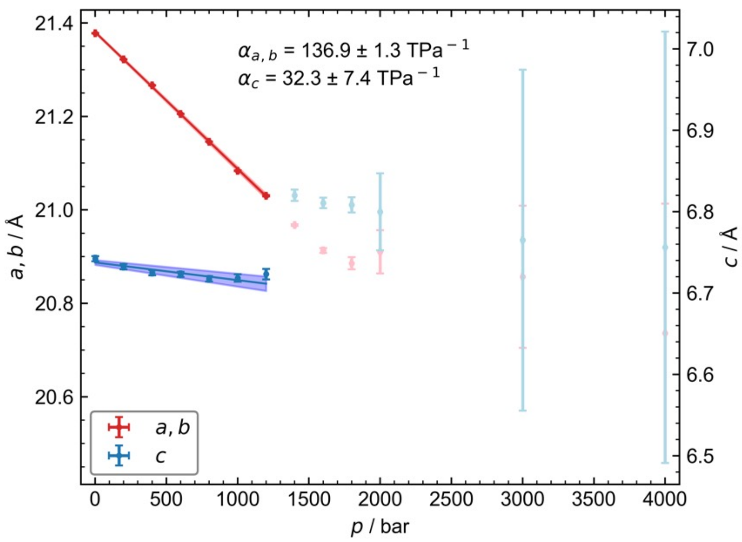

Figure A3.57. Linear fits on the progression of unit cell parameters of Mg_2(dobpdc) during pressure increase. The data were extracted via sequential profile fits performed on the HPPXRD patterns (see Table A3.11). The linear compressibility values α for the respective axes were calculated based on the linear fits. Pale points were removed from the evaluation due to limited reliability as a consequence of substantially reduced scattering intensity from the sample at high pressures. Pale colored areas indicate the confidence interval of one standard deviation.

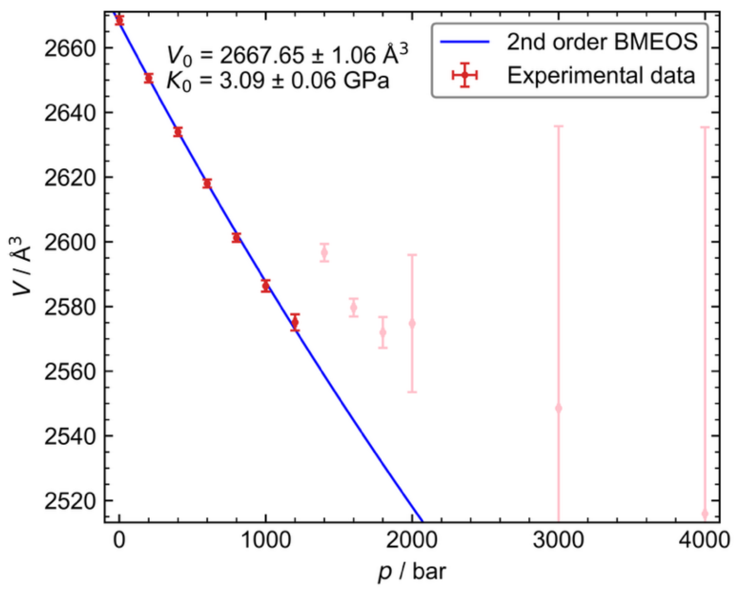

Figure A3.58. Fit of the second-order BMEOS on the progression of the unit cell volume V of Mg_2(dobpdc) during pressure increase, providing the reference volume V_0 and the bulk modulus K_0. The data were extracted via profile fits performed on the corresponding HPPXRD patterns (see Table A3.11). Pale points were removed from the evaluation due to limited reliability as a consequence of substantially reduced scattering intensity from the sample at high pressures.

A3.8.9 mmen@Mg_2(dobpdc)

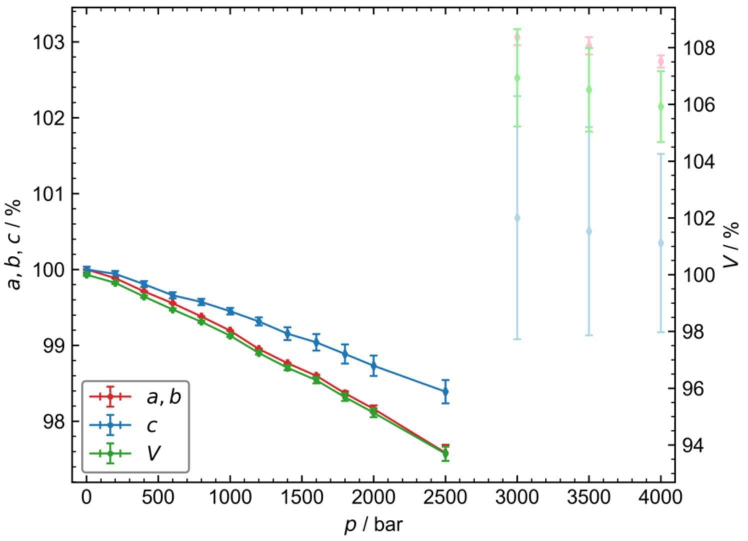

Figure A3.59. Relative progression of unit cell parameters a, b and c as well as the resulting unit cell volume V of mmen@Mg_2(dobpdc) during pressure increase. The data were extracted via profile fits performed on the HPPXRD patterns (see Table A3.12). Pale, non-interconnected points were removed from the evaluation due to limited reliability as a consequence of substantially reduced scattering intensity from the sample at high pressures. Lines are a guide to the eye.

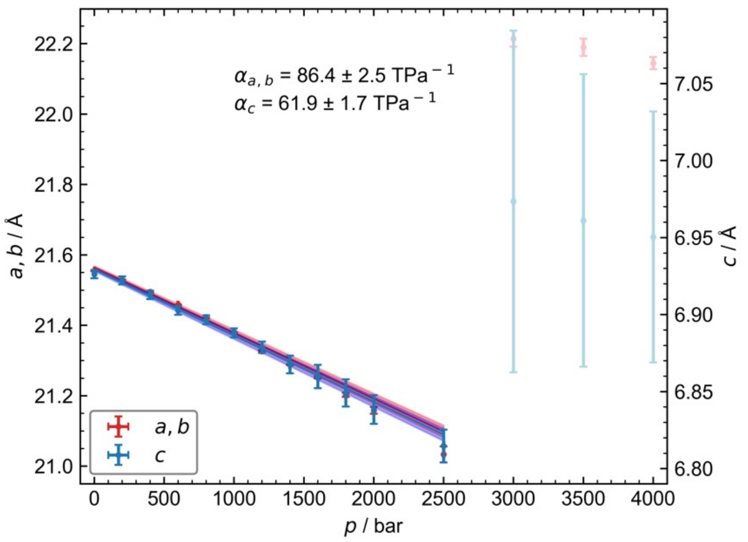

Figure A3.60. Linear fits on the progression of unit cell parameters of mmen@Mg_2(dobpdc) during pressure increase. The data were extracted via sequential profile fits performed on the HPPXRD patterns (see Table A3.12). The linear compressibility values α for the respective axes were calculated based on the linear fits. Pale points were removed from the evaluation due to limited reliability as a consequence of substantially reduced scattering intensity from the sample at high pressures. Pale colored areas indicate the confidence interval of one standard deviation.

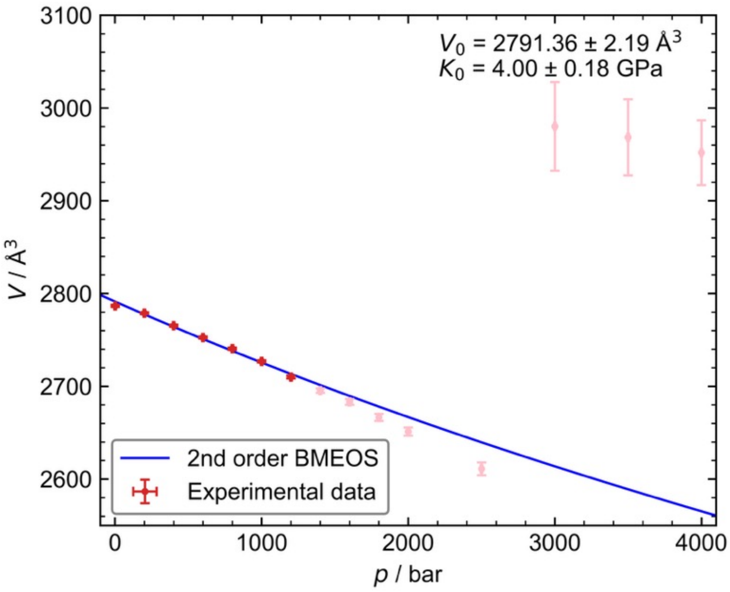

Figure A3.61. Fit of the second-order BMEOS on the progression of the unit cell volume V of mmen@Mg_2(dobpdc) during pressure increase, providing the reference volume V_0 and the bulk modulus K_0. The data were extracted via profile fits performed on the corresponding HPPXRD patterns (see Table A3.12). Pale points were removed from the evaluation due to limited reliability as a consequence of substantially reduced scattering intensity from the sample at high pressures.

A3.9 Linear Correlation Analysis

To explore potential correlations between the mechanical properties (specifically the bulk modulus) of the isoreticular MOF-74 derivatives and selected physical parameters of the corresponding metal ions or structural features of the ambient-pressure crystal structures reported in the literature, a linear correlation analysis was performed. Data of Cu_2(dobdc) were excluded from this analysis, as Cu_2(dobdc) exhibits a significantly smaller unit cell volume (8 – 14% lower) than the other M_2(dobdc) materials, a deviation attributed to the pronounced Jahn-Teller distortion of the Cu^{2+} coordination environment. Mg_2(dobdc) was further excluded as it is the only derivative incorporating a main group metal ion, resulting in substantially different bonding characteristics compared to the transition metal analogues.

A3.9.1 Metal Center Properties

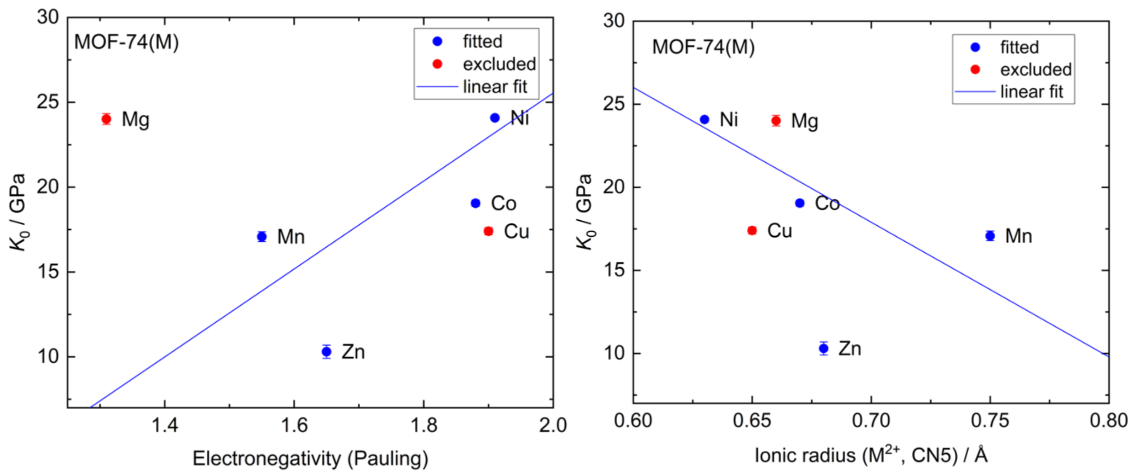

Figure A3.62. Linear correlation analysis for the correlation between the bulk modulus K_0 and the electronegativity of the incorporated metal ion M in the various MOF-74(M) materials (left) and the ionic radius of the metal ion (right). The electronegativity values correspond to the Pauling electronegativity scale.[283] The ionic radii correspond to the Shannon ion radii of divalent metal ions (M^{2+}) with a coordination number of five (CN5).[236] A clear correlation of the bulk moduli with the electronegativity of the metal and the ionic radius of the metal ion is not evident.

To evaluate possible correlations between the coordination geometry and coordination complex stability with the bulk modulus of the MOF-74(M) materials, the ligand field stabilization energy (LFSE) was estimated for an ideal square-pyramidal complex geometry (coordination number 5) with all metal ions in high-spin configurations as suggested by the literature.[238,239] The LFSE of the square-pyramidal environment can be estimated based on spectroscopically determined octahedral ligand field splitting Δ_O of corresponding hexa-aqua complexes $[M(H_2O)_6]^{2+}$ taken from the literature.[284]

In a square-pyramidal ligand field, the energy levels are arranged in the following order:[284] d_{xy}, d_{yz} (–4.57 Dq), d_{xy} (–0.86 Dq), d_{z2} (0.86 Dq), $d_{x2–y2}$ (9.14 Dq) and filled with maximum multiplicity (high-spin) according to the respective electron configuration in the metal ion (Table A3.14).[239] Based on the resulting occupation (number of electrons w, x, y, z) of the individual energy levels (–4.57 Dq, –0.86 Dq, 0.86 Dq, 9.14 Dq), the LFSE can be calculated according to Equation (A3.3) with 10 Dq corresponding to Δ_O.

$$\mathrm{LFSE} = (-4.75 \cdot w - 0.86 \cdot x + 0.86 \cdot y + 9.14 \cdot z)\,\mathrm{Dq} \tag{A3.3}$$

Table A3.14. Overview of the octahedral ligand field splitting of the corresponding hexa-aqua complexes $\Delta_O([\mathrm{M(H_2O)_6}]^{2+})$, the spin state of the metal ions in MOF-74(M) and the calculated LFSE in the square pyramidal coordination environment.

MOF-74(M)	d-electron config.	Δ_O / $\mathrm{cm^{-1}}$ [284][285]	Spin state[239]	LFSE / eV
Mg^{2+}	–	–	0	0
Mn^{2+}	$3d^5$	7774	5/2	0
Co^{2+}	$3d^7$	9200	3/2	-1.042
Ni^{2+}	$3d^8$	8500	1	-1.054
Cu^{2+}	$3d^9$	12000	1/2	-1.360
Zn^{2+}	$3d^{10}$	–	0	

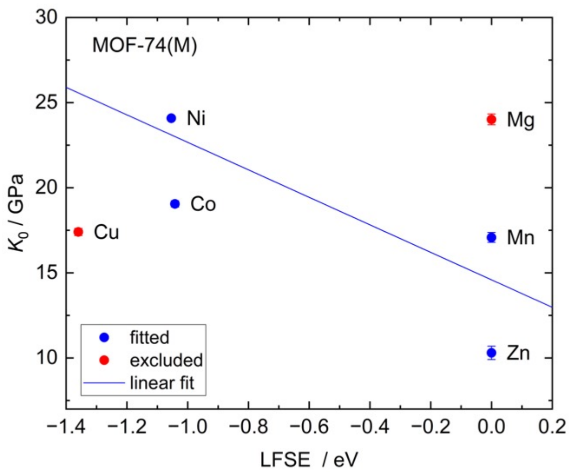

Figure A3.63. Linear correlation analysis for the correlation between the bulk modulus K_0 and the ligand field stabilization energy (LFSE) of the metal ion complexes in the various MOF-74(M) materials.

A3.10 Coordination Geometry and Distortion

However, the coordination environments of the metal ions in MOF-74(M) exhibit varying degrees of distortion, leading in some cases to substantial deviations from the ideal square-pyramidal [MO_5] coordination geometry. To quantify these distortions, a series of high-quality crystal structures reported in the literature, derived from high-resolution synchrotron PXRD data, we used as references for calculating of a set of geometric distortion parameters.[240]

Table A3.15. CCDC codes of the crystal structures of various MOF-74 derivatives derived from high-resolution synchrotron PXRD data[240] that were used for the geometric analysis performed herein.

Material	CCDC Code
Mg_2(dobdc)	1516645
Mn_2(dobdc)	1516646
Co_2(dobdc)	1516643
Ni_2(dobdc)	1516644
Cu_2(dobdc)	1516648
Zn_2(dobdc)	1516647

The bond valence sum SBV was calculated based on Equation A3.4 with the empirical parameter $B = 0.37\,\text{Å}$ describing the softness of the bonds,[286] r_i being the distances of all five M−O bond lengths in the coordination unit, and metal-ligand dependent r_0 values from the literature.[287]

$$S_{\mathrm{BV}} = \sum_i \exp\left(\frac{r_0 - r_i}{B}\right) \tag{A3.4}$$

A list of the valence bond parameters r_0 used in the calculation is given in Table A3.16.

Table A3.16. Overview over the bond valence parameter r_0 for the M−O bonds present in the coordination unit of MOF-74(M) materials.

M	r_0/Å
Mg	1.693(3)
Mn	1.790(3)
Co	1.692(5)
Ni	1.654(4)
Cu	1.679(2)
Zn	1.704(3)

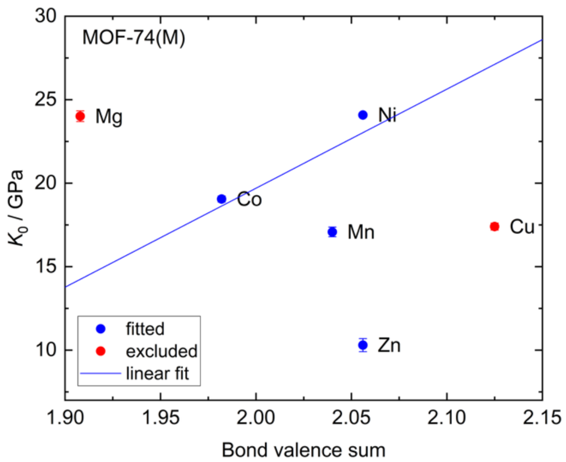

Figure A3.64. Linear correlation analysis for the correlation between the bulk modulus K_0 and the bond valence sum of the coordination complexes.

To investigate further structural correlations with the experimentally determined bulk moduli, two additional distortion indices were calculated.[288,289] The bond length distortion index quantifies the variation in M−O bond length within the $[MO_5]$ coordination unit and is defined as the root mean square deviation (RMSD) of the individual M−O distances (d_i) from the mean bond length ($\bar{d}$) over the five coordinating oxygen atoms ($N = 5$), as given in Equation A3.5:

$$\mathrm{RMSD}\,(\text{bond length}) = \sqrt{\frac{1}{N}\sum_{i=1}^{N}(d_i - \bar{d})^2} \tag{A3.5}$$

The angular distortion parameter serve as a measure of the deviation from ideal bond angles within the $[MO_5]$ coordination geometry. It is calculated as the RMSD of the four apex bond angles ($\Theta_{\text{ideal}} = 90°$), the four neighboring bond angles in the square base ($\Theta_{\text{ideal}} = 90°$), and the two diagonal bond angles in the square base ($\Theta_{\text{ideal}} = 180°$), covering a total number of 10 ($N = 10$) angles (see Equation A3.6).

$$\text{RMSD (bond angles)} = \sqrt{\frac{1}{N}\sum_{i=1}^{N}(\Theta_i - \Theta_{ideal})^2} \tag{A3.6}$$

The results of both distortion indices and their correlation with the bulk moduli are shown in Figure A3.65.

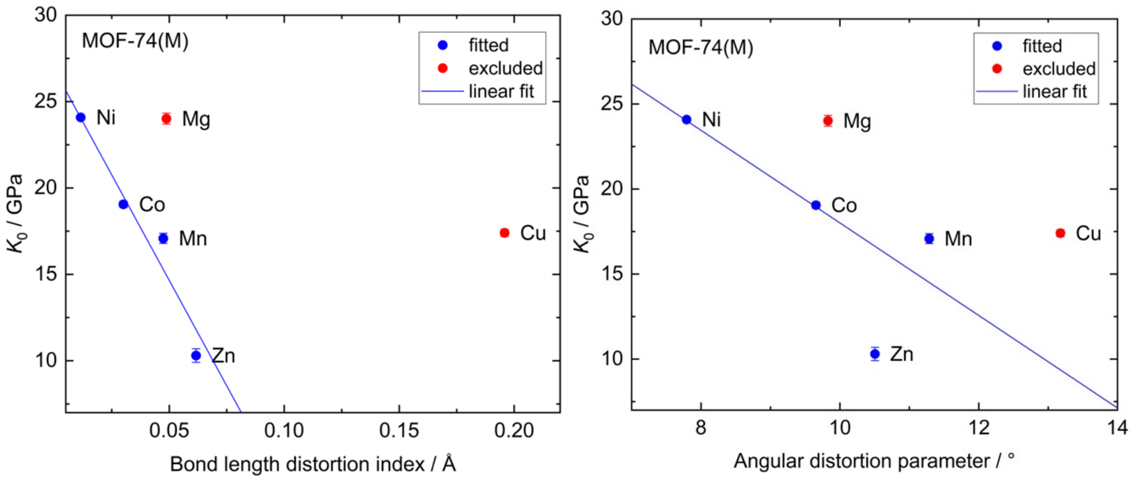

Figure A3.65. Linear correlation analysis for the correlation between the bulk modulus K_0 and the bond length distortion indices of the $[MO_5]$ coordination units in the various MOF-74(M) materials (left) as well as the angular distortion parameter of the same coordination units (right). The distortion indices were calculated according to Equation A3.5 and A3.6. Bond length and angle parameters were extracted for crystal structures summarized in Table A3.15.

Table A3.17. Results of the linear correlation analysis between the bulk modulus and various structural and inherent properties of the respective coordination unit of different MOF-74(M) materials. The corresponding fits with the slope m and intercept b are shown in Figure A3.62 – Figure A3.65. MOF-74(Mg) and Cu were excluded from the correlation analysis. Due to the small residual sample size of $n = 4$, only correlation coefficients with $|r| > 0.95$ are considered statistically significant at the 95% confidence level. Correlations with lower r are not considered statistically meaningful. Consequently, a statistically significant correlation is only evident for the bond length distribution of the coordination unit.

Correlation parameter	m	b/GPa	R^2	Pearson r
Electronegativity	26 ± 15 GPa	–26 ± 29	0.59	0.77
Ionic radius	–81 ± 46 GPa Å^{-1}	75 ± 30	0.61	–0.78
LFSE	–8 ± 5 GPa eV^{-1}	15 ± 5	0.60	–0.77
Bond valence sum	59 ± 74 GPa	–99 ± 151	0.24	0.49
Bond length dist.	–244 ± 31 GPa Å^{-1}	27 ± 1	0.97	–0.98
Angular dist.	-3 ± 1 GPa deg^{-1}	45 ± 8	0.83	–0.91

Bibliography

[1] T. M. McDonald, W. R. Lee, J. A. Mason, B. M. Wiers, C. S. Hong, J. R. Long, *J. Am. Chem. Soc.* **2012**, *134*, 7056–7065.

[2] R. W. Derlet, T. E. Albertson, *West. J. Med.* **1986**, *145*, 493–496.

[3] S. Sircar, T. C. Golden, *Sep. Sci. Technol.* **2000**, *35*, 667–687.

[4] Y. Li, J. Yu, *Nat. Rev. Mater.* **2021**, *6*, 1156–1174.

[5] C. Fruijtier-Pölloth, *Arch. Toxicol.* **2009**, *83*, 23–35.

[6] S. Karki, G. Hazarika, D. Yadav, P. G. Ingole, *Desalination* **2024**, *573*, 117200.

[7] O. M. Yaghi, H. Li, *J. Am. Chem. Soc.* **1995**, *117*, 10401–10402.

[8] O. M. Yaghi, G. Li, H. Li, *Nature* **1995**, *378*, 703–706.

[9] H. Furukawa, K. E. Cordova, M. O'Keeffe, O. M. Yaghi, *Science* **2013**, *341*, 974.

[10] S. R. Batten, N. R. Champness, X.-M. Chen, J. Garcia-Martinez, S. Kitagawa, L. Öhrström, M. O'Keeffe, M. P. Suh, J. Reedijk, *Pure Appl. Chem.* **2013**, *85*, 1715–1724.

[11] N. Stock, S. Biswas, *Chem. Rev.* **2012**, *112*, 933–969.

[12] A. D. Burrows, K. Cassar, R. M. W. Friend, M. F. Mahon, S. P. Rigby, J. E. Warren, *Cryst. Eng. Comm.* **2005**, *7*, 548–550.

[13] X. Zhang, Z. Chen, X. Liu, S. L. Hanna, X. Wang, R. Taheri-Ledari, A. Maleki, P. Li, O. K. Farha, *Chem. Soc. Rev.* **2020**, *49*, 7406–7427.

[14] Z. Chen, P. Li, R. Anderson, X. Wang, X. Zhang, L. Robison, L. R. Redfern, S. Moribe, T. Islamoglu, D. A. Gómez-Gualdrón, T. Yildirim, J. F. Stoddart, O. K. Farha, *Science* **2020**, *368*, 297–303.

[15] C. Healy, K. M. Patil, B. H. Wilson, L. Hermanspahn, N. C. Harvey-Reid, B. I. Howard, C. Kleinjan, J. Kolien, F. Payet, S. G. Telfer, P. E. Kruger, T. D. Bennett, *Coord. Chem. Rev.* **2020**, *419*, 213388.

[16] U. Mueller, M. Schubert, F. Teich, H. Puetter, K. Schierle-Arndt, J. Pastré, *J. Mater. Chem.* **2005**, *16*, 626–636.

[17] A. U. Czaja, N. Trukhan, U. Müller, *Chem. Soc. Rev.* **2009**, *38*, 1284–1293.

[18] framergy, Inc., www.framergy.com, Accessed: 2025/06/13.

[19] NUMAT Technologies, Inc. , www.numat.com, Accessed: 2025/06/13.

[20] novoMOF AG, www.novomof.com, Accessed: 2025/06/13.

[21] M. Eddaoudi, J. Kim, N. Rosi, D. Vodak, J. Wachter, M. O'Keeffe, O. M. Yaghi, *Science* **2002**, *295*, 469–472.

[22] O. M. Yaghi, M. O'Keeffe, N. W. Ockwig, H. K. Chae, M. Eddaoudi, J. Kim, *Nature* **2003**, *423*, 705–714.

[23] N. L. Rosi, J. Eckert, M. Eddaoudi, D. T. Vodak, J. Kim, M. O'Keeffe, O. M. Yaghi, *Science* **2003**, *300*, 1127–1129.

[24] Z. Chen, K. O. Kirlikovali, P. Li, O. K. Farha, *Acc. Chem. Res.* **2022**, *55*, 579–591.

[25] B. Tahmouresilerd, M. Moody, L. Agogo, A. F. Cozzolino, *Dalton Trans.* **2019**, *48*, 6445–6454.

[26] J. D. Humby, O. Benson, G. L. Smith, S. P. Argent, I. d. Silva, Y. Cheng, S. Rudić, P. Manuel, M. D. Frogley, G. Cinque, L. K. Saunders, I. J. Vitórica-Yrezábal, G. F. S. Whitehead, T. L. Easun, W. Lewis, A. J. Blake, A. J. Ramirez-Cuesta, S. Yang, M. Schröder, *Chem. Sci.* **2018**, *10*, 1098–1106.

[27] I. Senkovska, V. Bon, L. Abylgazina, M. Mendt, J. Berger, G. Kieslich, P. Petkov, J. L. Fiorio, J. Joswig, T. Heine, L. Schaper, C. Bachetzky, R. Schmid, R. A. Fischer, A. Pöppl, E. Brunner, S. Kaskel, *Angew. Chem. Int. Ed.* **2023**, *62*, e202218076.

[28] A. Schneemann, V. Bon, I. Schwedler, I. Senkovska, S. Kaskel, R. A. Fischer, *Chem. Soc. Rev.* **2014**, *43*, 6062–6096.

[29] N. Li, J. Pang, F. Lang, X.-H. Bu, *Acc. Chem. Res.* **2024**, *57*, 2279–2292.

[30] G. Scandura, S. Eid, A. A. Alnajjar, T. Paul, G. N. Karanikolos, D. Shetty, K. Omer, R. Alqerem, A. Juma, H. Wang, H. A. Arafat, L. F. Dumée, *Mater. Adv.* **2023**, *4*, 1258–1285.

[31] K. Yang, G. Zhou, Q. Xu, *RSC Adv.* **2016**, *6*, 37506–37514.

[32] Q. Li, K. Lin, Z. Liu, L. Hu, Y. Cao, J. Chen, X. Xing, *Chem. Rev.* **2022**, *122*, 8438–8486.

[33] S. C. McKellar, S. A. Moggach, *Acta Cryst. B* **2015**, *71*, 587–607.

[34] G. D. Gatta, Y. Lee, *Mineral. Mag.* **2014**, *78*, 267–291.

[35] R. N. Widmer, G. I. Lampronti, S. Chibani, C. W. Wilson, S. Anzellini, S. Farsang, A. K. Kleppe, N. P. Casati, S. G. Macleod, S. A. Redfern, F. X. Coudert, T. D. Bennett, *J. Am. Chem. Soc.* **2019**, *141*, 9330–9337.

[36] Y. H. Hu, L. Zhang, *Phys. Rev. B* **2010**, *81*, 174103.

[37] N. Ma, S. Horike, *Chem. Rev.* **2022**, *122*, 4163–4203.

[38] L. R. Redfern, O. K. Farha, *Chem. Sci.* **2019**, *10*, 10666–10679.

[39] Z. Wang, L. Liu, Z. Li, N. Goyal, T. Du, J. He, G. K. Li, *Energy Fuels* **2022**, *36*, 2927–2944.

[40] Y. Wang, H. Jin, Q. Ma, K. Mo, H. Mao, A. Feldhoff, X. Cao, Y. Li, F. Pan, Z. Jiang, *Angew. Chem. Int. Ed.* **2020**, *59*, 4365–4369.

[41] C. B. Carter, M. G. Norton, *Ceramic Materials, Science and Engineering*, Springer, New York, **2007**.

[42] K. T. Faber, F. Casadio, A. Masic, L. Robbiola, M. Walton, *Annu. Rev. Mater. Res.* **2021**, *51*, 460.

[43] A. J. Shortland, S. Kirk, K. Eremin, P. Degryse, M. Walton, *Archaeometry* **2017**, *60*, 764–783.

[44] J. W. Lankton, C. Pulak, B. Gratuze, *J. Archaeol. Sci.: Reports* **2022**, *42*, 103354.

[45] C. Jackson, P. Nicholson, *J. Archaeol. Sci.* **2010**, *37*, 295–301.

[46] *Springer Handbook of Glass*, 1st ed., (Eds.: L. Calvez, J. D. Musgraves, J. Hu), Springer, Cham, **2019**.

[47] Conradt, *Encyclopedia of Glass Science, Technology, History and Culture*, *Vol. 1*, (Eds.: P. Richet, R. Conradt, A. Takada, J. Dyon), John Wiley and Sons, Hoboken, New Jersey, **2021**.

[48] Q. Zheng, Y. Zhang, M. Montazerian, O. Gulbiten, J. C. Mauro, E. D. Zanotto, Y. Yue, *Chem. Rev.* **2019**, *119*, 7848–7939.

[49] P. G. Debenedetti, F. H. Stillinger, *Nature* **2001**, *410*, 259–267.

[50] J. W. Schmelzer, A. S. Abyzov, V. M. Fokin, C. Schick, E. D. Zanotto, *J. Non-Cryst. Solids* **2015**, *428*, 68–74.

[51] J. W. P. Schmelzer, V. M. Fokin, A. S. Abyzov, *Int. J. Appl. Glass Sci.* **2016**, *7*, 253–261.

[52] N. Karpukhina, R. G. Hill, R. V. Law, *Chem. Soc. Rev.* **2014**, *43*, 2174–2186.

[53] R. S. Welch, E. D. Zanotto, C. J. Wilkinson, D. R. Cassar, M. Montazerian, J. C. Mauro, *Acta Mater.* **2023**, *254*, 118994.

[54] J. Jiusti, E. D. Zanotto, S. A. Feller, H. J. Austin, H. M. Detar, I. Bishop, D. Manzani, Y. Nakatsuka, Y. Watanabe, H. Inoue, *J. Non-Cryst. Solids* **2020**, *550*, 120359.

[55] W. Kauzmann, *Chem. Rev.* **1948**, *43*, 219–256.

[56] S. Sakka, J. Mackenzie, *J. Non-Cryst. Solids* **1971**, *6*, 145–162.

[57] A. Qiao, T. D. Bennett, H. Tao, A. Krajnc, G. Mali, C. M. Doherty, A. W. Thornton, J. C. Mauro, G. N. Greaves, Y. Yue, *Sci. Adv.* **2018**, *4*, eaao6827.

[58] H. E. HAGY, H. N. RITLAND, *J. Am. Ceram. Soc.* **1957**, *40*, 436–442.

[59] E. D. Zanotto, J. C. Mauro, *J. Non-Cryst. Solids* **2017**, *471*, 490–495.

[60] G. Will, *Powder Diffr., The Rietveld Method and the Two Stage Method to Determine and Refine Crystal Structures from Powder Diffr. Data*, Springer, Berlin, Heidelberg, New York, **2006**.

[61] R. E. Dinnebier, A. Leineweber, J. S. O. Evans, *Rietveld Refinement*, De Gruyter, Berlin, Boston, **2019**.

[62] G. S. Pawley, *J. Appl. Cryst.* **1981**, *14*, 357–361.

[63] A. L. Bail, *Powder Diffr.* **2005**, *20*, 316–326.

[64] H. M. Rietveld, *J. Appl. Crystallogr.* **1969**, *2*, 65–71.

[65] E. Takeshi, S. J. Billinge, *Underneath the Bragg Peaks: Structural Analysis of Complex Materials*, *Vol. 7*, (Ed.: R. W. Cahn), Pergamon, Oxford, **2003**.

[66] L. C. Gallington, S. K. Wilke, S. Kohara, C. J. Benmore, *Quantum Beam Sci.* **2023**, *7*, 20.

[67] A. Singh, D. Dayton, D. M. Ladd, G. Reuveni, P. Paluch, L. Montagne, J. Mars, O. Yaffe, M. Toney, G. N. M. Reddy, D. B. Mitzi, *J. Am. Chem. Soc.* **2024**, *146*, 25656–25668.

[68] Y. Yang, H. Su, T. Wu, Y. Jiang, D. Liu, P. Yan, H. Tian, H. Yu, *Sci. Bull.* **2019**, *64*, 553–561.

[69] C. Angell, *J. Non-Cryst. Solids* **1991**, *131*, 13–31.

[70] C. A. Angell, *Science* **1995**, *267*, 1924–1935.

[71] Z. Chen, Z. Li, Y. Zhang, R. Liu, Y. Tian, L.-M. Wang, *Eur. Phys. J. E* **2014**, *37*, 52.

[72] C. Moynihan, S.-K. Lee, M. Tatsumisago, T. Minami, *Thermochim. Acta* **1996**, *280*, 153–162.

[73] D. L. Sidebottom, J. R. Changstrom, *Phys. Rev. B* **2008**, *77*, 020201.

[74] D. L. Sidebottom, *Front. Mater.* **2019**, *6*, 144.

[75] C. T. Moynihan, A. J. Easteal, M. A. D. Bolt, J. Tucker, *J. Am. Ceram. Soc.* **1976**, *59*, 12–16.

[76] G. W. H. Höhne, W. F. Hemminger, H.-J. Flammersheim, *Differential Scanning Calorimetry*, 2nd ed., Springer, Berlin, Heidelberg, **2003**.

[77] A. E. Slobozeanu, S. E. Bejan, I. A. Tudor, A.-M. Mocioiu, A. M. Motoc, M. D. Romero-Sanchez, M. Botan, C. G. Catalin, C. L. Madalina, R. R. Piticescu, C. Predescu, *Manuf. Rev.* **2021**, *8*, 1.

[78] C. T. Moynihan, A. J. Easteal, J. Wilder, J. Tucker, *J. Phys. Chem.* **1974**, *78*, 2673–2677.

[79] Q. Zheng, J. Zheng, M. Solvang, Y. Yue, J. C. Mauro, *J. Am. Ceram. Soc.* **2020**, *103*, 6070–6074.

[80] Q. Zheng, J. C. Mauro, Y. Yue, *J. Non-Cryst. Solids* **2017**, *456*, 95–100.

[81] H. Liu, M. M. Smedskjaer, H. Tao, L. R. Jensen, X. Zhao, Y. Yue, *Phys. Chem. Chem. Phys.* **2016**, *18*, 10887–10895.

[82] G. Ruocco, F. Sciortino, F. Zamponi, C. D. Michele, T. Scopigno, *J. Chem. Phys.* **2004**, *120*, 10666–10680.

[83] Y. Zhao, B. Shang, B. Zhang, X. Tong, H. Ke, H. Bai, W.-H. Wang, *Sci. Adv.* **2022**, *8*, eabn3623.

[84] T. D. Bennett, J. C. Tan, Y. Yue, E. Baxter, C. Ducati, N. J. Terrill, H. H. Yeung, Z. Zhou, W. Chen, S. Henke, A. K. Cheetham, G. N. Greaves, *Nat. Commun.* **2015**, *6*, 1–7.

[85] R. Banerjee, A. Phan, B. Wang, C. Knobler, H. Furukawa, M. O'Keeffe, O. M. Yaghi, *Science* **2008**, *319*, 939–943.

[86] E. Pérez-Botella, S. Valencia, F. Rey, *Chem. Rev.* **2022**, *122*, 17647–17695.

[87] K. S. Park, Z. Ni, A. P. Côté, J. Y. Choi, R. Huang, F. J. Uribe-Romo, H. K. Chae, M. O'Keeffe, O. M. Yaghi, *PNAS* **2006**, *103*, 10186–10191.

[88] J. López-Cabrelles, J. Romero, G. Abellán, M. Giménez-Marqués, M. Palomino, S. Valencia, F. Rey, G. M. Espallargas, *J. Am. Chem. Soc.* **2019**, *141*, 7173–7180.

[89] J. Sun, L. Semenchenko, W. T. Lim, M. F. B. Rivas, V. Varela-Guerrero, H. K. Jeong, *Microporous Mesoporous Mater.* **2018**, *264*, 35–42.

[90] Y. Q. Tian, S. Y. Yao, D. Gu, K. H. Cui, D. W. Guo, G. Zhang, Z. X. Chen, D. Y. Zhao, *Chem. Eur. J.* **2010**, *16*, 1137–1141.

[91] K. Kadota, E. Sivaniah, S. Bureekaew, S. Kitagawa, S. Horike, *Inorg. Chem.* **2017**, *56*, 8744–8747.

[92] S. Horike, K. Kadota, T. Itakura, M. Inukai, S. Kitagawa, *Dalton Trans.* **2015**, *44*, 15107–15110.

[93] D. Saliba, M. Ammar, M. Rammal, M. Al-Ghoul, M. Hmadeh, *J. Am. Chem. Soc.* **2018**, *140*, 1812–1823.

[94] Y. Q. Tian, Y. M. Zhao, Z. X. Chen, G. N. Zhang, L. H. Weng, D. Y. Zhao, *Chem. Eur. J.* **2007**, *13*, 4146–4154.

[95] Z. Zheng, Z. Rong, H. L. Nguyen, O. M. Yaghi, *Inorg. Chem.* **2023**, *62*, 20861–20873.

[96] L. Frentzel-Beyme, P. Kolodzeiski, J.-B. Weiß, A. Schneemann, S. Henke, *Nat. Commun.* **2022**, *13*, 7750.

[97] M. T. Wharmby, S. Henke, T. D. Bennett, S. R. Bajpe, I. Schwedler, S. P. Thompson, F. Gozzo, P. Simoncic, C. Mellot-Draznieks, H. Tao, Y. Yue, A. K. Cheetham, *Angew. Chem. Int. Ed.* **2015**, *54*, 6447–6451.

[98] T. D. Bennett, Y. Yue, P. Li, A. Qiao, H. Tao, N. G. Greaves, T. Richards, G. I. Lampronti, S. A. Redfern, F. Blanc, O. K. Farha, J. T. Hupp, A. K. Cheetham, D. A. Keen, *J. Am. Chem. Soc.* **2016**, *138*, 3484–3492.

[99] R. Gaillac, P. Pullumbi, K. A. Beyer, K. Chapman, D. A. Keen, T. D. Bennett, F. X. Coudert, *Nat. Mater.* **2017**, *16*, 1149–1155.

[100] R. S. K. Madsen, A. Qiao, J. Sen, I. Hung, K. Chen, Z. Gan, S. Sen, Y. Yue, *Science* **2020**, *367*, 1473–1476.

[101] Z. Yang, Y. Belmabkhout, L. N. McHugh, D. Ao, Y. Sun, S. Li, Z. Qiao, T. D. Bennett, M. D. Guiver, C. Zhong, *Nat. Mater.* **2023**, *22*, 888–894.

[102] G. Jiang, C. Qu, F. Xu, E. Zhang, Q. Lu, X. Cai, S. Hausdorf, H. Wang, S. Kaskel, *Adv. Funct. Mater.* **2021**, *31*, 2104300.

[103] L. Frentzel-Beyme, M. Kloß, P. Kolodzeiski, R. Pallach, S. Henke, *J. Am. Chem. Soc.* **2019**, *141*, 12362–12371.

[104] S. Li, R. Limbach, L. Longley, A. A. Shirzadi, J. C. Walmsley, D. N. Johnstone, P. A. Midgley, L. Wondraczek, T. D. Bennett, *J. Am. Chem. Soc.* **2019**, 1–13.

[105] J. Song, L. Frentzel-Beyme, R. Pallach, P. Kolodzeiski, A. Koutsianos, W.-L. Xue, R. Schmid, S. Henke, *J. Am. Chem. Soc.* **2023**, *145*, 9273–9284.

[106] O. Smirnova, S. Hwang, R. Sajzew, L. Ge, A. Reupert, V. Nozari, S. Savani, C. Chmelik, M. R. Reithofer, L. Wondraczek, J. Kärger, A. Knebel, *Nat. Mater.* **2024**, *23*, 262–270.

[107] Y. Zhang, Y. Wang, H. Xia, P. Gao, Y. Cao, H. Jin, Y. Li, *Chem. Commun.* **2022**, *58*, 9548–9551.

[108] I. Cornu, T. D. Bennett, C. Corcos, L. N. McHugh, P. Florian, *Small* **2023**, e2307034.

[109] W.-L. Xue, P. Kolodzeiski, H. Aucharova, S. Vasa, A. Koutsianos, R. Pallach, J. Song, L. Frentzel-Beyme, R. Linser, S. Henke, *Nat. Commun.* **2024**, *15*, 4420.

[110] C. Zhou, M. Stepniewska, J. M. Sørensen, L. Scarpa, G. Magnacca, V. Boffa, T. D. Bennett, Y. Yue, *Microporous Mesoporous Mater.* **2018**, *265*, 57–62.

[111] M. L. R. Gómez, G. I. Lampronti, Y. Yang, J. C. Mauro, T. D. Bennett, *Dalton Trans.* **2019**, *49*, 850–857.

[112] A. M. Bumstead, M. L. R. Gómez, M. F. Thorne, A. F. Sapnik, L. Longley, J. M. Tuffnell, D. S. Keeble, D. A. Keen, T. D. Bennett, *Cryst. Eng. Comm.* **2020**, *22*, 3627–3637.

[113] R. S. K. Madsen, S. Sarkar, B. B. Iversen, Y. Yue, *Chem. Commun.* **2021**, *58*, 823–826.

[114] J. Hou, M. L. R. Gómez, A. Krajnc, A. McCaul, S. Li, A. M. Bumstead, A. F. Sapnik, Z. Deng, R. Lin, P. A. Chater, D. S. Keeble, D. A. Keen, D. Appadoo, B. Chan, V. Chen, G. Mali, T. D. Bennett, *J. Am. Chem. Soc.* **2020**, *142*, 3880–3890.

[115] L. Frentzel-Beyme, M. Kloß, R. Pallach, S. Salamon, H. Moldenhauer, J. Landers, H. Wende, J. Debus, S. Henke, *J. Mater. Chem. A* **2018**, *7*, 985–990.

[116] L. León-Alcaide, R. S. Christensen, D. A. Keen, J. L. Jordá, I. Brotons-Alcázar, A. Forment-Aliaga, G. M. Espallargas, *J. Am. Chem. Soc.* **2023**, *145*, 11258–11264.

[117] W. Xue, C. Das, J. Weiß, S. Henke, *Angew. Chem. Int. Ed.* **2024**, *63*, e202405307.

[118] B. M. Goltsman, E. A. Yatsenko, *Open Ceram.* **2024**, *17*, 100540.

[119] L. Granados, R. Morena, N. Takamure, T. Suga, S. Huang, D. R. McKenzie, A. Ho-Baillie, *Mater. Today* **2021**, *47*, 131–155.

[120] M. Bengisu, *J. Mater. Sci.* **2016**, *51*, 2199–2242.

[121] U. Betke, P. V. D. Zander, M. Scheffler, *Adv. Eng. Mater.* **2024**, *26*, 2400521.

[122] J. O. Bockris, J. D. Mackenzie, J. A. Kitchener, *Trans. Faraday Soc.* **1955**, *51*, 1734–1748.

[123] P. Richet, M. Roskosz, J. Roux, *Chem. Geol.* **2006**, *225*, 388–401.

[124] G. S. Henderson, *The Can. Mineral.* **2005**, *43*, 1921–1958.

[125] G. Greaves, *J. Non-Cryst. Solids* **1985**, *71*, 203–217.

[126] B. Vessal, G. N. Greaves, P. T. Marten, A. V. Chadwick, R. Mole, S. Houde-Walter, *Nature* **1992**, *356*, 504–506.

[127] D. E. Clark, M. F. Dilmore, E. C. Ethridge, L. L. Hench, *J. Am. Ceram. Soc.* **1976**, *59*, 62–65.

[128] J. M. Tuffnell, C. W. Ashling, J. Hou, S. Li, L. Longley, M. L. R. Gómez, T. D. Bennett, *Chem. Commun.* **2019**, *55*, 8705–8715.

[129] V. Nozari, C. Calahoo, J. M. Tuffnell, D. A. Keen, T. D. Bennett, L. Wondraczek, *Nat. Commun.* **2021**, *12*, 5703.

[130] V. Nozari, O. Smirnova, J. M. Tuffnell, A. Knebel, T. D. Bennett, L. Wondraczek, *Adv. Mater. Technol.* **2022**, *7*, 2200343.

[131] S. S. Sørensen, A. K. R. Christensen, E. A. Bouros-Bandrabur, E. S. Andersen, H. F. Christiansen, S. Lang, F. Cao, M. F. U. Jalaludeen, J. F. S. Christensen, W. M. W. Winters, B. P. Andersen, A. B. Nielsen, N. C. Nielsen, D. B. Ravnsbæk, P. K. Kristensen, Y. Yue, M. M. Smedskjaer, *Chem. Mater.* **2024**, *36*, 2756–2766.

[132] S. Li, S. Yu, S. M. Collins, D. N. Johnstone, C. W. Ashling, A. F. Sapnik, P. A. Chater, D. S. Keeble, L. N. McHugh, P. A. Midgley, D. A. Keen, T. D. Bennett, *Chem. Sci.* **2020**, *11*, 9910–9918.

[133] C. W. Ashling, D. N. Johnstone, R. N. Widmer, J. Hou, S. M. Collins, A. F. Sapnik, A. M. Bumstead, P. A. Midgley, P. A. Chater, D. A. Keen, T. D. Bennett, *J. Am. Chem. Soc.* **2019**, *141*, 15641–15648.

[134] L. Longley, S. M. Collins, C. Zhou, G. J. Smales, S. E. Norman, N. J. Brownbill, C. W. Ashling, P. A. Chater, R. Tovey, C. B. Schönlieb, T. F. Headen, N. J. Terrill, Y. Yue, A. J. Smith, F. Blanc, D. A. Keen, P. A. Midgley, T. D. Bennett, *Nat. Commun.* **2018**, *9*, 1–10.

[135] L. Longley, S. M. Collins, S. Li, G. J. Smales, I. Erucar, A. Qiao, J. Hou, C. M. Doherty, A. W. Thornton, A. J. Hill, X. Yu, N. J. Terrill, A. J. Smith, S. M. Cohen, P. A. Midgley, D. A. Keen, S. G. Telfer, T. D. Bennett, *Chem. Sci.* **2019**, *10*, 3592–3601.

[136] F. Cao, S. S. Sørensen, A. K. R. Christensen, S. Mollick, X. Ge, D. Sun, A. B. Nielsen, N. C. Nielsen, N. Lock, R. Lu, R. Klemmt, P. K. Kristensen, L. R. Jensen, F. Dallari, J. Baglioni, G. Monaco, M. A. Karlsen, V. Baran, M. M. Smedskjaer, *Nat. Commun.* **2025**, *16*, 7001.

[137] P. Kolodzeiski, E. S. Grape, R. Pallach, L. Richter, A. K. Inge, S. Henke, *Cryst. Growth Des.* **2024**, *24*, 7278–7286.

[138] P. Kolodzeiski, E. S. Grape, R. Pallach, L. Richter, A. K. Inge, S. Henke, *ChemRxiv* **2024**, DOI 10.26434/chemrxiv-2024-j1mj2.

[139] B. Chen, Z. Yang, Y. Zhu, Y. Xia, *J. Mater. Chem. A.* **2014**, *2*, 16811–16831.

[140] H.-X. Zhang, C. Lu, J. Zhang, *Acc. Mater. Res.* **2023**, *4*, 995–1007.

[141] J. Zhang, T. Wu, C. Zhou, S. Chen, P. Feng, X. Bu, *Angew. Chem. Int. Ed.* **2009**, *48*, 2542–2545.

[142] D.-X. Zhang, H.-X. Zhang, T. Wen, D.-S. Li, J. Zhang, *Inorg. Chem. Frontiers* **2015**, *3*, 263–267.

[143] N. Ma, N. Horike, L. Lombardo, S. Kosasang, K. Kageyama, C. Thanaphatkosol, K. Kongpatpanich, K.-i. Otake, S. Horike, *J. Am. Chem. Soc.* **2022**, *144*, 18619–18628.

[144] J. Ding, T. Du, E. H. Thomsen, D. Andresen, M. R. Fischer, A. K. Møller, A. R. Petersen, A. K. Pedersen, L. R. Jensen, S. Wang, M. M. Smedskjaer, *Adv. Sci.* **2024**, *11*, 2306698.

[145] J. E. Bara, *Ind. Eng. Chem. Res.* **2011**, *50*, 13614–13619.

[146] Z. Z. Yang, L. N. He, Y. N. Zhao, B. Yu, *Environ. Sci. Technol.* **2013**, *47*, 1598–1605.

[147] H. Zhi, C. Lü, Q. Zhang, J. Luo, *Chem. Commun.* **2009**, 2878–2880.

[148] L. Niedzicki, M. Kasprzyk, K. Kuziak, G. Żukowska, M. Marcinek, W. Wieczorek, M. Armand, *J. Power Sources* **2011**, *196*, 1386–1391.

[149] M. Dranka, P. Jankowski, G. Z. Żukowska, *J. Phys. Chem. C* **2018**, *122*, 3201–3210.

[150] L. Niedzicki, G. Żukowska, M. Bukowska, P. Szczeciński, S. Grugeon, S. Laruelle, M. Armand, S. Panero, B. Scrosati, M. Marcinek, W. Wieczorek, *Electrochim. Acta* **2010**, *55*, 1450–1454.

[151] S. Burazer, F. Morelle, Y. Filinchuk, R. Černý, J. Popović, *Inorg. Chem.* **2019**, *58*, 6927–6933.

[152] F. Morelle, PhD thesis, Université Catholique de Louvain, **2017**.

[153] S. Burazer, K. Robeyns, L. Guénée, G. Mali, F. Morelle, V. Ban, T. Klaser, Y. Filinchuk, R. Černý, J. Popović, *Cryst. Growth Des.* **2021**, *21*, 770–778.

[154] L. Yang, D. R. Powell, R. P. Houser, *Dalton Trans.* **2007**, *0*, 955–964.

[155] P. Brázda, M. Klementová, Y. Krysiak, L. Palatinus, *IUCrJ* **2022**, *9*, 735–755.

[156] M. D. Radin, J. C. Thomas, A. V. d. Ven, *Phys. Rev. Mater.* **2020**, *4*, 043601.

[157] U. Müller, *Symmetry Relationships between Crystal Structures: Applications of Crystallographic Group Theory in Crystal Chemistry*, IUCr Texts on Crystallography, Oxford University Press, **2013**.

[158] I. E. Collings, M. G. Tucker, D. A. Keen, A. L. Goodwin, *Cryst. Eng. Comm.* **2014**, *16*, 3498–3506.

[159] W. Yao, X. Jiang, R. Huang, W. Li, C. Huang, Z. Lin, L. Li, C. Chen, *Chem. Commun.* **2014**, *50*, 13499–13501.

[160] S. M. Kronawitter, S. A. Hallweger, J. Meyer, C. Pedri, S. Burger, A. Alhadid, S. Henke, G. Kieslich, *APL Mater.* **2023**, *11*, 031119.

[161] P. Kolodzeiski, B. M. Gallant, L. Richter, M. A. T. Ongkiko, C. Franke, A. Kostka, W.-L. Xue, C. Das, J.-B. Weiß, E. Kolodzeiski, T. Kress, G. Kieslich, T. Li, A. J. Morris, D. Kubicki, S. Henke, *ChemRxiv* **2025**, DOI `10.26434/chemrxiv-2025-3m7vv`.

[162] D. Ramakanth, S. Singh, P. K. Maji, Y. S. Lee, K. K. Gaikwad, *Environ. Chem. Lett.* **2021**, *19*, 3597–3608.

[163] Y. Yang, H. Ren, T. Xie, H. Peng, S. Jiang, Y. Zhang, F. He, D. He, H. Lin, *J. Alloys Compd.* **2023**, *950*, 169892.

[164] Y. Wang, H. Jin, Q. Ma, K. Mo, H. Mao, A. Feldhoff, X. Cao, Y. Li, F. Pan, Z. Jiang, *Angew. Chem. Int. Ed.* **2020**, *59*, 4365–4369.

[165] M. Thorne, L. Rios, A. Bumstead, S. Li, T. Bennett, L. C. C. By-nc nd, C. Thorne, M. F. Thorne, M. Laura, R. Gómez, A. M. Bumstead, S. Li, D Thomas, *Green Chem.* **2020**, *22*, 2505–2512.

[166] M. E. Nordberg, H. P. Hood, *pat.*, US 2,106,744, **1934**.

[167] A. Inayat, B. Reinhardt, H. Uhlig, W.-D. Einicke, D. Enke, *Chem. Soc. Rev.* **2012**, *42*, 3753–3764.

[168] B. Gault, A. Chiaramonti, O. Cojocaru-Mirédin, P. Stender, R. Dubosq, C. Freysoldt, S. K. Makineni, T. Li, M. Moody, J. M. Cairney, *Nat. Rev. Methods Primers* **2021**, *1*, 51.

[169] T. Li, A. Devaraj, N. Kruse, *Cell Rep. Phys. Sci.* **2022**, *3*, 101188.

[170] P. Zhao, G. I. Lampronti, G. O. Lloyd, M. T. Wharmby, S. Facq, A. K. Cheetham, S. A. T. Redfern, *Chem. Mater.* **2014**, *26*, 1767–1769.

[171] Q. Zheng, J. Zheng, M. Solvang, Y. Yue, J. C. Mauro, *J. Am. Ceram. Soc.* **2020**, *103*, 6070–6074.

[172] Q. Zheng, J. C. Mauro, Y. Yue, *J. Non-Cryst. Solids* **2017**, *456*, 95–100.

[173] J. Jiusti, E. D. Zanotto, S. A. Feller, H. J. Austin, H. M. Detar, I. Bishop, D. Manzani, Y. Nakatsuka, Y. Watanabe, H. Inoue, *J. Non-Cryst. Solids* **2020**, *550*, 120359.

[174] K. I. Hadjiivanov, D. A. Panayotov, M. Y. Mihaylov, E. Z. Ivanova, K. K. Chakarova, S. M. Andonova, N. L. Drenchev, *Chem. Rev.* **2021**, *121*, 1286–1424.

[175] M. R. Ryder, B. Civalleri, T. Bennett, S. Henke, S. Rudić, G. Cinque, F. Fernandez-Alonso, J. C. Tan, *Phys. Rev. Lett.* **2014**, *113*, 215502.

[176] S. Elliott, *J. Non-Cryst. Solids* **1995**, *182*, 40–48.

[177] C. Crupi, G. Carini, G. Ruello, G. D'Angelo, *Philos. Mag.* **2016**, *96*, 788–799.

[178] K. W. Chapman, P. J. Chupas, *In-situ Characterization of Heterogeneous Catalysts, Chapter 5: Pair Distribution Function Analysis of High-energy X-ray Scattering Data*, 1st ed., (Eds.: J. A. Rodriguez, J. C. Hanson, P. J. Chupas), John Wiley & Sons, **2013**.

[179] C. Castillo-Blas, I. Romero-Muñiz, A. Mavrandonakis, L. Simonelli, A. E. Platero-Prats, *Chem. Commun.* **2020**, *56*, 15615–15618.

[180] S. Zhou, B. M. Gallant, J. Zhang, Y. Shi, J. Smith, J. N. Drysdale, P. Therdkatanyuphong, M. Taddei, D. P. McCarthy, S. Barlow, R. C. Kilbride, A. Dasgupta, A. R. Marshall, J. Wang, D. J. Kubicki, D. S. Ginger, S. R. Marder, H. J. Snaith, *J. Am. Chem. Soc.* **2024**, *146*, 27405–27416.

[181] C. J. Pickard, R. J. Needs, *J. Phys. Condens. Matter* **2011**, *23*, 053201.

[182] D. Enke, F. Janowski, W. Schwieger, *Microporous Mesoporous Mater.* **2003**, *60*, 19–30.

[183] D. W. Breck, *Zeolite Molecular Sieves - Structure, Chemistry, and Use*, John Wiley & Sons, New York, **1974**.

[184] S. Dantas, K. C. Struckhoff, M. Thommes, A. V. Neimark, *Langmuir* **2019**, *35*, 11291–11298.

[185] S. Samios, A. Stubos, G. Papadopoulos, N. Kanellopoulos, F. Rigas, *J. Colloid Interface Sci.* **2000**, *224*, 272–290.

[186] A. Vishnyakov, P. I. Ravikovitch, A. V. Neimark, *Langmuir* **1999**, *15*, 8736–8742.

[187] P. J. Branton, P. G. Hall, M. Treguer, K. S. W. Sing, *J. Chem. Soc. Faraday Trans.* **1995**, *91*, 2041–2043.

[188] P. Kolodzeiski, M. Strobl, L. Frentzel-Beyme, M. Paulus, C. Sternemann, C. Nelle, K. Terlinden, J. Song, S. Henke, *ChemRxiv* **2025**, DOI `10.26434/chemrxiv-2025-s9rsg`.

[189] T. Jia, Y. Gu, F. Li, *J. Environ. Chem. Eng.* **2022**, *10*, 108300.

[190] A. Bavykina, N. Kolobov, I. S. Khan, J. A. Bau, A. Ramirez, J. Gascon, *Chem. Rev.* **2020**, *120*, 8468–8535.

[191] Y. Shen, A. Tissot, C. Serre, *Chem. Sci.* **2022**, *13*, 13978–14007.

[192] S. Mahajan, M. Lahtinen, *J. Environ. Chem. Eng.* **2022**, *10*, 108930.

[193] M. P. Suh, H. J. Park, T. K. Prasad, D.-W. Lim, *Chem. Rev.* **2012**, *112*, 782–835.

[194] C. Jiang, X. Wang, Y. Ouyang, K. Lu, W. Jiang, H. Xu, X. Wei, Z. Wang, F. Dai, D. Sun, *Nanoscale Adv.* **2022**, *4*, 2077–2089.

[195] M. S. Alhumaimess, *J. Saudi Chem. Soc.* **2020**, *24*, 461–473.

[196] K. Hemmer, M. Cokoja, R. A. Fischer, *Chem. Cat. Chem.* **2021**, *13*, 1683–1691.

[197] Z. Zhang, Y. Zhao, Q. Gong, Z. Li, J. Li, *Chem. Commun.* **2012**, *49*, 653–661.

[198] M. Díaz-García, M. Sánchez-Sánchez, *Microporous Mesoporous Mater.* **2014**, *190*, 248–254.

[199] W. Zhou, H. Wu, T. Yildirim, *J. Am. Chem. Soc.* **2008**, *130*, 15268–15269.

[200] P. D. Dietzel, R. E. Johnsen, R. Blom, H. Fjellvåg, *Chem. Eur. J.* **2008**, *14*, 2389–2397.

[201] P. D. Dietzel, R. Blom, H. Fjellvåg, *Eur. J. Inorg. Chem.* **2008**, 3624–3632.

[202] R. Sanz, F. Martínez, G. Orcajo, L. Wojtas, D. Briones, *Dalton Trans.* **2013**, *42*, 2392–2398.

[203] S. Bhattacharjee, J. S. Choi, S. T. Yang, S. B. Choi, J. Kim, W. S. Ann, *J. Nanosci. Nanotechnol.* **2010**, *10*, 135–141.

[204] P. D. Dietzel, B. Panella, M. Hirscher, R. Blom, H. Fjellvåg, *Chem. Commun.* **2006**, *1*, 959–961.

[205] P. D. Dietzel, Y. Morita, R. Blom, H. Fjellvåg, *Angew. Chem. Int. Ed.* **2005**, *44*, 6354–6358.

[206] S. R. Caskey, A. G. Wong-Foy, A. J. Matzger, *J. Am. Chem. Soc.* **2008**, *130*, 10870–10871.

[207] Q. Zhang, B. Li, L. Chen, *Inorg. Chem.* **2013**, *52*, 9356–9362.

[208] J. Linke, T. Rohrbach, A. H. Clark, C. Borca, T. Huthwelker, F. L. Buchauer, M. R. Kraglund, C. Chatzichristodoulou, E. Meade, J. Guehl, M. Wojtas, M. Ranocchiari, T. J. Schmidt, E. Fabbri, *EES Catal.* **2025**, *3*, 505–514.

[209] G. Calleja, R. Sanz, G. Orcajo, D. Briones, P. Leo, F. Martínez, *Catal. Today* **2014**, *227*, 130–137.

[210] J. Shah, T. Wu, J. Lucero, M. A. Carreon, M. L. Carreon, *ACS Sustain. Chem. Eng.* **2019**, *7*, 377–383.

[211] M. J. Katz, A. J. Howarth, P. Z. Moghadam, J. B. DeCoste, R. Q. Snurr, J. T. Hupp, O. K. Farha, *Dalton Trans.* **2015**, *45*, 4150–4153.

[212] S. Zuluaga, E. M. A. Fuentes-Fernandez, K. Tan, F. Xu, J. Li, Y. J. Chabal, T. Thonhauser, *J. Mater. Chem. A* **2016**, *4*, 5176–5183.

[213] H. Jiang, Q. Wang, H. Wang, Y. Chen, M. Zhang, *ACS Appl. Mater. Interfaces* **2016**, *8*, 26817–26826.

[214] T. Zurrer, K. Wong, J. Horlyck, E. C. Lovell, J. Wright, N. M. Bedford, Z. Han, K. Liang, J. Scott, R. Amal, *Adv. Funct. Mater.* **2021**, *31*, 2007624.

[215] P. J. Milner, J. D. Martell, R. L. Siegelman, D. Gygi, S. C. Weston, J. R. Long, *Chem. Sci.* **2017**, *9*, 160–174.

[216] E. J. Kim, R. L. Siegelman, H. Z. H. Jiang, A. C. Forse, J.-H. Lee, J. D. Martell, P. J. Milner, J. M. Falkowski, J. B. Neaton, J. A. Reimer, S. C. Weston, J. R. Long, *Science* **2020**, *369*, 392–396.

[217] J. D. Martell, P. J. Milner, R. L. Siegelman, J. R. Long, *Chem. Sci.* **2020**, *11*, 6457–6471.

[218] Z. Zhu, H. Tsai, S. T. Parker, J.-H. Lee, Y. Yabuuchi, H. Z. H. Jiang, Y. Wang, S. Xiong, A. C. Forse, B. Dinakar, A. Huang, C. Dun, P. J. Milner, A. Smith, P. G. Martins, K. R. Meihaus, J. J. Urban, J. A. Reimer, J. B. Neaton, J. R. Long, *J. Am. Chem. Soc.* **2024**, *146*, 6072–6083.

[219] A. C. Forse, K. A. Colwell, M. I. Gonzalez, S. Benders, R. M. Torres-Gavosto, B. Blümich, J. A. Reimer, J. R. Long, *Chem. Mater.* **2020**, *32*, 3570–3576.

[220] T. Kamencek, E. Zojer, *The J. Phys. Chem. C* **2021**, *125*, 24728–24745.

[221] P. Canepa, K. Tan, Y. Du, H. Lu, Y. J. Chabal, T. Thonhauser, *J. Mater. Chem. A* **2014**, *3*, 986–995.

[222] M. Tagliabue, C. Rizzo, R. Millini, P. D. C. Dietzel, R. Blom, S. Zanardi, *J. Porous Mater.* **2011**, *18*, 289–296.

[223] P. Serra-Crespo, A. Dikhtiarenko, E. Stavitski, J. Juan-Alcañiz, F. Kapteijn, F.-X. Coudert, J. Gascon, *Cryst. Eng. Comm.* **2014**, *17*, 276–280.

[224] Y. Yan, A. E. O'Connor, G. Kanthasamy, G. Atkinson, D. R. Allan, A. J. Blake, M. Schröder, *J. Am. Chem. Soc.* **2018**, *140*, 3952–3958.

[225] P. Vervoorts, J. Stebani, A. S. J. Méndez, G. Kieslich, *ACS Mater. Lett.* **2021**, *3*, 1635–1651.

[226] K. W. Chapman, G. J. Halder, P. J. Chupas, *J. Am. Chem. Soc.* **2009**, *131*, 17546–17547.

[227] S. Dissegna, P. Vervoorts, C. L. Hobday, T. Düren, D. Daisenberger, A. J. Smith, R. A. Fischer, G. Kieslich, *J. Am. Chem. Soc.* **2018**, *140*, 11581–11584.

[228] P. G. Yot, Q. Ma, J. Haines, Q. Yang, A. Ghoufi, T. Devic, C. Serre, V. Dmitriev, G. Férey, C. Zhong, G. Maurin, *Chem. Sci.* **2011**, *3*, 1100–1104.

[229] T. M. McDonald, J. A. Mason, X. Kong, E. D. Bloch, D. Gygi, A. Dani, V. Crocellà, F. Giordanino, S. O. Odoh, W. S. Drisdell, B. Vlaisavljevich, A. L. Dzubak, R. Poloni, S. K. Schnell, N. Planas, K. Lee, T. Pascal, L. F. Wan, D. Prendergast, J. B. Neaton, B. Smit, J. B. Kortright, L. Gagliardi, S. Bordiga, J. A. Reimer, J. R. Long, *Nature* **2015**, *519*, 303–308.

[230] M. H. Rosnes, M. Opitz, M. Frontzek, W. Lohstroh, J. P. Embs, P. A. Georgiev, P. D. Dietzel, *J. Mater. Chem. A* **2015**, *3*, 4827–4839.

[231] L. Frentzel-Beyme, P. Kolodzeiski, K. Terlinden, S. Henke, *Adv. Funct. Mater.* **2023**, *33*, 2302033.

[232] C. Krywka, C. Sternemann, M. Paulus, M. Tolan, C. Royer, R. Winter, *Chem. Phys. Chem.* **2008**, *9*, 2809–2815.

[233] A. Dewaele, A. B. Belonoshko, G. Garbarino, F. Occelli, P. Bouvier, M. Hanfland, M. Mezouar, *Phys. Rev. B* **2012**, *85*, 1–7.

[234] C. S. Smith, L. Cain, *J. Phys. Chem. Solids* **1975**, *36*, 205–209.

[235] A. Coelho, *J. Appl. Crystallogr.* **2018**, *51*, 210–218.

[236] R. D. Shannon, *Acta Cryst. A* **1976**, *32*, 751–767.

[237] R. G. Parr, R. G. Pearson, *J. Am. Chem. Soc.* **1983**, *105*, 7512–7516.

[238] J. S. Griffith, L. E. Orgel, *Q. Rev. Chem. Soc.* **1957**, 381–393.

[239] D. Yu, A. O. Yazaydin, J. R. Lane, P. D. C. Dietzel, R. Q. Snurr, *Chem. Sci.* **2013**, *4*, 3544–3556.

[240] B. Pato-Doldán, M. H. Rosnes, P. D. C. Dietzel, *Chem. Sus. Chem.* **2017**, *10*, 1710–1719.

[241] R. L. Siegelman, T. M. McDonald, M. I. Gonzalez, J. D. Martell, P. J. Milner, J. A. Mason, A. H. Berger, A. S. Bhown, J. R. Long, *J. Am. Chem. Soc.* **2017**, *139*, 10526–10538.

[242] R. Pallach, J. Keupp, K. Terlinden, L. Frentzel-Beyme, M. Kloß, A. Machalica, J. Kotschy, S. K. Vasa, P. A. Chater, C. Sternemann, M. T. Wharmby, R. Linser, R. Schmid, S. Henke, *Nat. Commun.* **2021**, *12*, 4097.

[243] S. Jawahery, C. M. Simon, E. Braun, M. Witman, D. Tiana, B. Vlaisavljevich, B. Smit, *Nat. Commun.* **2017**, *8*, 13945.

[244] J. Deubener, R. Müller, H. Behrens, G. Heide, *J. Non-Cryst. Solids* **2003**, *330*, 268–273.

[245] M. Basham, J. Filik, M. T. Wharmby, P. C. Chang, B. E. Kassaby, M. Gerring, J. Aishima, K. Levik, B. C. Pulford, I. Sikharulidze, D. Sneddon, M. Webber, S. S. Dhesi, F. Maccherozzi, O. Svensson, S. Brockhauser, G. Náray, A. W. Ashton, *J. Synchrotron Rad.* **2015**, *22*, 853–858.

[246] J. Filik, A. W. Ashton, P. C. Chang, P. A. Chater, S. J. Day, M. Drakopoulos, M. W. Gerring, M. L. Hart, O. V. Magdysyuk, S. Michalik, A. Smith, C. C. Tang, N. J. Terrill, M. T. Wharmby, H. Wilhelm, *J. Appl. Cryst.* **2017**, *50*, 959–966.

[247] M. O. Cichocka, J. Ångström, B. Wang, X. Zou, S. Smeets, *J. Appl. Crystallogr.* **2018**, *51*, 1652–1661.

[248] W. Kabsch, *Acta Cryst. D* **2010**, *66*, 125–132.

[249] B. Wang, X. Zou, S. Smeets, *IUCrJ* **2019**, *6*, 854–867.

[250] G. M. Sheldrick, *Acta Cryst. A* **2015**, *71*, 3–8.

[251] G. Sheldrick, *Acta Cryst. A* **2008**, *64*, 112–122.

[252] L.-M. Peng, *Micron* **1999**, *30*, 625–648.

[253] J. A. M. Simões, M. M. d. Piedade, *Molecular Energetic: Condensed-Phase Thermochemical Techniques*, Oxford University Press, New York, **2008**.

[254] P. Juhás, T. Davis, C. L. Farrow, S. J. L. Billinge, *J. Appl. Crystallogr.* **2013**, *46*, 560–566.

[255] K. R. Thurber, R. Tycko, *J. Magn. Reson.* **2009**, *196*, 84–87.

[256] S. J. Clark, M. D. Segall, C. J. Pickard, P. J. Hasnip, M. I. J. Probert, K. Refson, M. C. Payne, *Z. Kristallogr. – Cryst. Mater.* **2005**, *220*, 567–570.

[257] C. Bonhomme, C. Gervais, F. Babonneau, C. Coelho, F. Pourpoint, T. Azaïs, S. E. Ashbrook, J. M. Griffin, J. R. Yates, F. Mauri, C. J. Pickard, *Chem. Rev.* **2012**, *112*, 5733–5779.

[258] J. R. Yates, C. J. Pickard, F. Mauri, *Phys. Rev. B* **2007**, *76*, 024401.

[259] M. Profeta, F. Mauri, C. J. Pickard, *J. Am. Chem. Soc.* **2003**, *125*, 541–548.

[260] C. J. Pickard, F. Mauri, *Phys. Rev. B* **2001**, *63*, 245101.

[261] J. P. Perdew, K. Burke, M. Ernzerhof, *Phys. Rev. Lett.* **1996**, *77*, 3865–3868.

[262] H. J. Monkhorst, J. D. Pack, *Phys. Rev. B* **1976**, *13*, 5188–5192.

[263] E. R. McNellis, J. Meyer, K. Reuter, *Phys. Rev. B* **2009**, *80*, 205414.

[264] S. Grimme, J. Antony, S. Ehrlich, H. Krieg, *J. Chem. Phys.* **2010**, *132*, 154104.

[265] D. J. Srivastava, M. Giammar, M. C. Venetos, L. McCarthy-Carney, P. J. Grandinetti, *J. Chem. Phys.* **2024**, *161*, 212501.

[266] J. L. Rowsell, O. M. Yaghi, *J. Am. Chem. Soc.* **2006**, *128*, 1304–1315.

[267] C. Krywka, M. Paulus, C. Sternemann, M. Volmer, A. Remhof, G. Nowak, A. Nefedov, B. Pöter, M. Spiegel, M. Tolan, *J. Synchrotron Radiat.* **2006**, *13*, 8–13.

[268] A.-C. Dippel, H.-P. Liermann, J. Delitz, P. Walter, H. Schulte-Schrepping, O. Seeck, H. Franz, *J. Synchrotron Radiat.* **2015**, *22*, 675–687.

[269] H. Marsmann, *29Si-NMR Spectroscopic Results. In: Oxygen-17 and Silicon-29. NMR Basic Principles and Progress*, *Vol. 17*, Springer, Berlin, Heidelberg, **1981**.

[270] P. Thompson, D. Cox, J. Hastings, *J. Appl. Crystallogr.* **1987**, *20*, 79–83.

[271] Y. Ye, R. A. Schwering, J. R. Smyth, *Am. Mineral.* **2009**, *94*, 899–904.

[272] G. Kresse, J. Furthmüller, *Comput. Mater. Sci* **1996**, *6*, 15–50.

[273] G Kresse, J Furthmüller, *Phys. Rev. B* **1996**, *54*, 11169–11186.

[274] S. Baroni, S. d. Gironcoli, A. D. Corso, P. Giannozzi, *Rev. Mod. Phys.* **2001**, *73*, 515–562.

[275] K. Esfarjani, Y. Hashi, J. Onoe, K. Takeuchi, Y. Kawazoe, *Phys. Rev. B* **1998**, *57*, 223–229.

[276] P. Giannozzi, S. Baroni, *J. Chem. Phys.* **1994**, *100*, 8537–8539.

[277] T. M. S. Moneeb, *New J. Glass Ceram.* **2016**, *06*, 37–46.

[278] M. Misawa, D. Price, K. Suzuki, *J. Non-Cryst. Solids* **1980**, *37*, 85–97.

[279] K. Chapman, S. Lapidus, P. Chupas, *J. Appl. Crystallogr.* **2015**, *48*, 1619–1626.

[280] B. Ravel, M. Newville, *J. Synchrotron Radiat.* **2005**, *12*, 537–541.

[281] M. Thommes, K. Kaneko, A. V. Neimark, J. P. Olivier, F. Rodriguez-Reinoso, J. Rouquerol, K. S. Sing, *Pure Appl. Chem.* **2015**, *87*, 1051–1069.

[282] T. Katsura, Y. Tange, *Minerals* **2019**, *9*, 745.

[283] L. Pauling, *J. Am. Chem. Soc.* **1932**, *54*, 3570–3582.

[284] A. F. Hollemann, E. Wiberg, N. Wiberg, *Lehrbuch der Anorganischen Chemie*, *Vol. 102*, Walter de Guyter, Berlin, **2007**.

[285] J. E. Huheey, E. A. Keiter, R. L. Keiter, *Inorg. Chem.: Principles of Structure and Reactivity*, 4th ed., Prentice Hall, New York, NY, **1993**.

[286] I. D. Brown, *Acta Cryst. B* **2006**, *62*, 692–694.

[287] I. D. Brown, D. Altermatt, *Acta Cryst. B* **1985**, *41*, 244–247.

[288] R. J. Deeth, A. Anastasi, C. Diedrich, K. Randell, *Coord. Chem. Rev.* **2009**, *253*, 795–816.

[289] K. Robinson, G. V. Gibbs, P. H. Ribbe, *Science* **1971**, *172*, 567–570.

List of Publications

1. P. Kolodzeiski, M. Strobl, L. Frentzel-Beyme, M. Paulus, C. Sternemann, C. Nelle, K. Terlinden, J. Song, S. Henke, Understanding the High-Pressure Behavior of MOF-74-Type Materials: The Influence of Metal Identity and Linker Extension, *ChemRxiv* **2025**, DOI:10.26434/chemrxiv-2025-s9rsg.

2. J.-B. Weiß, L. Fritsch, M. Tricarico, A. Schoch, S. Salamon, W.-L. Xue, C. Das, P. Kolodzeiski, H. Wende, J. C. Tan, M. Bauer, S. Henke, Organic flux-mediated ligand exchange enables coordination sphere engineering and topological reconstruction in metal-organic framework glasses, *ChemRxiv* **2025**, DOI:10.26434/chemrxiv-2025-2ss9r.

3. P. Kolodzeiski, B. M. Gallant, L. Richter, M. A. T. Ongkiko, C. Franke, A. Kostka, W.-L. Xue , C. Das, J.-B. Weiß, E. Kolodzeiski, T. Kress, G Kieslich, T. Li , A. J. Morris, D. Kubicki, S. Henke, Sodium-Ion-Modified Zeolitic Imidazolate Framework Glasses, *ChemRxiv* **2025**, DOI:10.26434/chemrxiv-2025-3m7vv.

4. C. Das, S. Salamon, J. Landers, J.-B. Weiß, W.-L. Xue, P. Kolodzeiski, R. Pallach, H. Wende, S. Henke, Emergent Spin-Glass Behavior in an Iron(II)-Based Metal–Organic Framework Glass, *Adv. Funct. Mater.* **2025**, e17854.

5. C. Yei, G. I. Lampronti, L. N. McHugh, C. Castillo-Blas, A. Kono, C. Chen, G. P. Robertson, L. A. V. Nagle-Cocco, W. Xu, S. D. Stranks, V. Martinez, I. Brekalo, B. Karadeniz, K. Užarević, W.-L. Xue, P. Kolodzeiski, C. Das, P. Chater, D. A. Keen, S. E. Dutton, T. D. Bennett, Mechanochemically-induced glass formation from two-dimensional hybrid organic–inorganic perovskites, *Chem. Sci.* **2024**, *15*, 7198-7205.

6. P. Kolodzeiski, E. S. Grape, R. Pallach, L. Richter, A. Ken Inge, S. Henke, Lithium and Sodium Benzimidazolate Coordination Networks: Syntheses, Structures, and Thermal Properties, *Cryst. Growth Des.* **2024**, *24* , 7278-7286.

7. W.-L. Xue, P. Kolodzeiski, H. Kavaleuskaya, S. Vasa, A. Koutsianos, R. Pallach, J. Song, L. Frentzel-Beyme, R. Linser, S. Henke, Highly porous metal-organic framework liquids and glasses via a solvent-assisted linker exchange strategy of ZIF-8, *Nat. Commun.* **2024**, *15*, 4420.

8. L. Frentzel-Beyme, P. Kolodzeiski, K. Terlinden, S. Henke, Microporous, Crystalline, and Water-Processable Framework Materials of Organic Amphiphile Salts, *Adv. Funct. Mater.* **2023**, 2302033.

9. J. Song, L. Frentzel-Beyme, R. Pallach, P. Kolodzeiski, A. Koutsianos, W.-L. Xue, R. Schmid, S. Henke, Modulating Liquid–Liquid Transitions and Glass Formation in Zeolitic Imidazolate Frameworks by Decoration with Electron-Withdrawing Cyano Groups, *J. Am. Chem. Soc.* **2023**, *145*, 9273–9284.

10. L. Frentzel-Beyme, P. Kolodzeiski, J.-B. Weiß, A. Schneemann, S. Henke, Quantification of gas-accessible microporosity in metal-organic framework glasses, *Nat. Commun.* **2022**, *13*, 7750.

11. J. Song, R. Pallach, L. Frentzel-Beyme, P. Kolodzeiski, G. Kieslich, P. Vervoorts, C. L. Hobday, S. Henke, Tuning the High-Pressure Phase Behaviour of Highly Compressible Zeolitic Imidazolate Frameworks: From Discontinuous to Continuous Pore Closure by Linker Substitution, *Angew. Chem. Int. Ed.* **2022**, *61*, e202117565.

12. L. Frentzel-Beyme, M. Kloß, P. Kolodzeiski, R. Pallach, S. Henke, Meltable Mixed-Linker Zeolitic Imidazolate Frameworks and Their Microporous Glasses: From Melting Point Engineering to Selective Hydrocarbon Sorption, *J. Am. Chem. Soc.* **2019**, *141*, 12362–12371.

Y con el cora lleno – On a wall in Granada

Eidesstattliche Versicherung (Affidavit)

Kolodzeiski, Pascal

Name, Vorname
(Surname, first name)

Matrikel-Nr.
(Enrolment number)

Belehrung:

Wer vorsätzlich gegen eine die Täuschung über Prüfungsleistungen betreffende Regelung einer Hochschulprüfungsordnung verstößt, handelt ordnungswidrig. Die Ordnungswidrigkeit kann mit einer Geldbuße von bis zu 50.000,00 € geahndet werden. Zuständige Verwaltungsbehörde für die Verfolgung und Ahndung von Ordnungswidrigkeiten ist der Kanzler/die Kanzlerin der Technischen Universität Dortmund. Im Falle eines mehrfachen oder sonstigen schwerwiegenden Täuschungsversuches kann der Prüfling zudem exmatrikuliert werden, § 63 Abs. 5 Hochschulgesetz NRW.

Die Abgabe einer falschen Versicherung an Eides statt ist strafbar.

Wer vorsätzlich eine falsche Versicherung an Eides statt abgibt, kann mit einer Freiheitsstrafe bis zu drei Jahren oder mit Geldstrafe bestraft werden, § 156 StGB. Die fahrlässige Abgabe einer falschen Versicherung an Eides statt kann mit einer Freiheitsstrafe bis zu einem Jahr oder Geldstrafe bestraft werden, § 161 StGB.

Die oben stehende Belehrung habe ich zur Kenntnis genommen:

Official notification:

Any person who intentionally breaches any regulation of university examination regulations relating to deception in examination performance is acting improperly. This offence can be punished with a fine of up to EUR 50,000.00. The competent administrative authority for the pursuit and prosecution of offences of this type is the chancellor of the TU Dortmund University. In the case of multiple or other serious attempts at deception, the candidate can also be unenrolled, Section 63, paragraph 5 of the Universities Act of North Rhine-Westphalia.

The submission of a false affidavit is punishable.

Any person who intentionally submits a false affidavit can be punished with a prison sentence of up to three years or a fine, Section 156 of the Criminal Code. The negligent submission of a false affidavit can be punished with a prison sentence of up to one year or a fine, Section 161 of the Criminal Code.

I have taken note of the above official notification.

Dortmund,

Ort, Datum
(Place, date)

Unterschrift
(Signature)

Titel der Dissertation:
(Title of the thesis):

Metal-Organic Frameworks: Concepts from Glass Science and High-Pressure Behavior

Ich versichere hiermit an Eides statt, dass ich die vorliegende Dissertation mit dem Titel selbstständig und ohne unzulässige fremde Hilfe angefertigt habe. Ich habe keine anderen als die angegebenen Quellen und Hilfsmittel benutzt sowie wörtliche und sinngemäße Zitate kenntlich gemacht.
Die Arbeit hat in gegenwärtiger oder in einer anderen Fassung weder der TU Dortmund noch einer anderen Hochschule im Zusammenhang mit einer staatlichen oder akademischen Prüfung vorgelegen.

I hereby swear that I have completed the present dissertation independently and without inadmissible external support. I have not used any sources or tools other than those indicated and have identified literal and analogous quotations.

The thesis in its current version or another version has not been presented to the TU Dortmund University or another university in connection with a state or academic examination.*

*Please be aware that solely the German version of the affidavit ("Eidesstattliche Versicherung") for the PhD thesis is the official and legally binding version.

Dortmund,

Ort, Datum
(Place, date)

Unterschrift
(Signature)